Factorisation: Applications in collider and flavour physics

DISSERTATION

zur Erlangung des Grades eines Doktors
der Naturwissenschaften

vorgelegt von
M.Sc. Marcel Wald

eingereicht bei der Naturwissenschaftlichen-Technischen Fakultät
der Universität Siegen

Siegen 2023

Betreuer und erster Gutachter
Prof. Dr. Guido Bell
Universität Siegen

Zweiter Gutachter
Prof. Dr. Alexander Khodjamirian
Universität Siegen

Tag der mündlichen Prüfung
08.11.2023

Promotionskommission: Prof. Dr. Guido Bell (Universität Siegen)
Prof. Dr. Markus Cristinziani (Universität Siegen)
Prof. Dr. Alexander Khodjamirian (Universität Siegen)
Priv.-Doz. Dr. Matthias Kleinmann (Universität Siegen)

Abstract

In many applications of particle physics, we encounter a variety of different energy scales, which tend to be widely separated in many cases. The concept of factorisation exploits this scale separation in order to simplify the intricate physics of scattering processes by disentangling the short-distance and long-distance effects. The theoretical description of these processes is usually provided by effective field theories (EFTs), which naturally implement factorisation for both collider and flavour physics applications. Asymptotic freedom allows to use techniques from perturbation theory to describe short-distance effects in typical problems of flavour physics, while additional methods like QCD sum rules or light-cone sum rules are necessary to parameterise long-distance effects. However, the physical situation is more complicated in the case of collider physics, since we additionally encounter a soft scale Λ_{soft}, which is still perturbatively treatable in the regime $\Lambda_{\text{soft}} \gg \Lambda_{\text{QCD}}$.
In the first project, we focus on Soft-Collinear Effective Theory (SCET). In this approach, a large hierachy of scales arises since the QCD radiation is restricted to the soft and collinear phase-space regions. While soft modes are characterised by small energies, collinear modes contain small virtualities with respect to the typical hard scales of the process. This defines a small power-counting parameter λ such that cross sections factorise in terms of hard, soft and collinear functions at every order in the power expansion. As long as the underlying scales are perturbative, these functions can be computed order-by-order for each observable. In order to streamline the calculation of the functions that arise at leading order in the power expansion, the computation of soft and final-state collinear (jet) functions has been automated in recent years for a general class of observables. The goal of this project consists in developing a similar automated setup for the computation of initial-state collinear (beam) functions to next-to-next-to-leading order (NNLO) in perturbation theory. In particular, our calculation provides the last missing ingredient to fully automate resummations at a modified next-to-next-to-leading logarithmic (NNLL$'$) accuracy using SCET.
In comparison to that, the second and third project deal with applications of factorisation in flavour physics. Specifically, we apply QCD sum rules in the second project and light-cone sum rules in the third project to parameterise non-perturbative effects. The second project aims to determine important parameters in the description of the B meson in the framework of Heavy-Quark Effective Theory (HQET), which are called $\lambda_{E,H}^2$. Contrary

to previous works, we make use of a diagonal correlation function containing two three-particle currents to resolve the discrepancies between two prior determinations. In our analysis, we include all contributions to leading order in the strong coupling constant α_s and all contributions up to vacuum condensates of mass dimension seven.
The third project ventures into the domain of new physics effects and investigates the two-particle decay $B \to p\Psi$ in the B-Mesogenesis model, where p denotes a proton, while Ψ corresponds to a new fermionic dark matter antibaryon, which interacts with the Standard Model via a colour-charged mediator boson Y. Light-cone sum rules are the appropriate framework to determine the relevant form factors up to twist six such that we can obtain an estimate for the branching fraction of this decay. Experimental facilities like Belle-II have recently started to look into decays of this particular model and our calculation is therefore particularly relevant for these studies.

Zusammenfassung

In vielen Anwendungen der modernen Teilchenphysik tauchen eine Vielzahl von Energieskalen auf, die in einigen Fällen weit voneinander getrennt liegen. Die Methode der Faktorisierung benutzt diese Skalentrennung zur Vereinfachung der zugrundeliegenden Physik von Streuprozessen, indem kurzreichweitige Effekte von langreichweitigen Effekten getrennt werden. Effektive Feldtheorien (EFTs) implementieren die Idee der Faktorisierung sowohl für Anwendungen in der Kolliderphysik als auch in der Flavourphysik. In typischen Problemen der Flavourphysik können wir Techniken aus der Störungstheorie, die auf asymptotischer Freiheit beruhen, verwenden, um kurzreichweitige Effekte zu beschreiben. Dahingegen benötigen wir zur Parameterisierung von langreichweitigen Effekten zusätzliche Methoden wie QCD-Summenregeln oder Lichtkegel-Summenregeln. Allerdings ist die physikalische Situation in der Kolliderphysik komplizierter, da wir zusätzlich auf eine softe Skala Λ_{soft} treffen, die jedoch immer noch in der Größenordnung $\Lambda_{\text{soft}} \gg \Lambda_{\text{QCD}}$ perturbativ behandelbar ist.
Im ersten Projekt konzentrieren wir uns auf die Soft-Collinear Effective Theory (SCET). In dieser Theorie beobachten wir eine große Hierarchie von Skalen, da die QCD-Strahlung auf die soften und kollinearen Phasenraumbereiche beschränkt ist. Während softe Moden durch kleine Energien charakterisiert werden, enthalten kollineare Moden kleine Virtualitäten im Vergleich zu den typischen harten Skalen des Prozesses. Darüber lässt sich ein kleiner Skalierungsfaktor λ definieren, sodass der Wirkungsquerschnitt durch harte, softe und kollineare Funktionen zu jeder Ordnung in der Entwicklung in λ ausgedrückt werden kann. Solange die zugrundeliegenden Skalen perturbativ sind, können diese Funktionen ordnungsgemäß für jede beobachtbare Größe berechnet werden. Um die Berechnung der Funktionen zu vereinfachen, die in führender Ordnung in der Störungsreihe auftreten, wurde die Berechnung von soften und kollinearen Funktionen für den Endzustand (Jetfunktionen) in den letzten Jahren für eine allgemeine Klasse von Observablen automatisiert. Das Ziel dieses Projekts besteht darin, einen ähnlichen automatisierten Ansatz für die Berechnung von kollinearen Funktionen für den Anfangszustand (Beamfunktionen) bis zur nächst-nächst führenden Ordnung (NNLO) in der Störungstheorie zu entwickeln. Insbesondere liefert unsere Berechnung die letzte fehlende Komponente, um Resummationen mit einer modifizierten nächst-nächst führenden logarithmischen (NNLL$'$) Genauigkeit unter Verwendung von SCET vollständig zu automatisieren.

Im Vergleich dazu beschäftigen sich das zweite und dritte Projekt mit Anwendungen der Faktorisierung in der Flavourphysik. Konkret verwenden wir im zweiten Projekt QCD-Summenregeln und im dritten Projekt Lichtkegel-Summenregeln, um nicht-perturbative Effekte zu parametrisieren. Das Ziel des zweiten Projekts besteht darin, wichtige Parameter in der Beschreibung des B Mesons im Rahmen der Heavy-Quark Effective Theory (HQET) zu bestimmen, die als $\lambda_{E,H}^2$ bezeichnet werden. Im Gegensatz zu früheren Arbeiten nutzen wir eine diagonale Korrelationsfunktion, die zwei Dreiteilchen-Ströme enthält, um die Diskrepanzen zwischen zwei früheren Bestimmungen aufzulösen. In unserer Analyse berücksichtigen wir alle Beiträge in führender Ordnung in der starken Kopplungskonstante α_s und alle Beiträge bis zu Vakuumkondensaten mit Massendimension sieben.
Im dritten Projekt untersuchen wir Effekte neuer Physik. Dabei analysieren wir den Zwei-Teilchen-Zerfall $B \to p\Psi$ im B-Mesogenesis-Modell, wobei p ein Proton und Ψ ein neues fermionisches wie auch antibaryonisches dunkle Materie Teilchen darstellt, das über ein farbgeladenes Vermittler-Boson Y mit dem Standardmodell wechselwirkt. Die geeignete Methode zur Untersuchung dieses Zerfalls sind Lichtkegel-Summenregeln, mittels derer die relevanten Formfaktoren bis zu Twist sechs bestimmt werden, um eine Abschätzung für die Zerfallsbreite dieses Zerfalls zu erhalten. Experimente wie Belle-II haben in letzter Zeit begonnen, sich mit Zerfällen dieses speziellen Modells zu beschäftigen, daher bieten unsere Berechnungen einen Anhaltspunkt für die theoretische Erwartung.

Contents

Chapter 1

Introduction

The physics of the universe involves a plethora of different energy scales ranging from cosmological scales like the Hubble length in the sub eV region to the Planck scale around 10^{18} GeV, where gravitational effects become dominant. Physicists dream to find a theory which incorporates all physical effects within this energy range. So far, all observed effects belong to four different classes mediated by four fundamental forces, which are electromagnetism, the weak nuclear force, the strong nuclear force and gravity. Other effects, which have not yet been tested by experiment, are assumed to interact via these fundamental forces with the known elementary particles such that they can be detected in principle.
Albeit the main purpose of the fundamental theory is to unify all forces, it is usually assumed to fulfil additional requirements. Besides basic principles like locality, which is closely related to causality, the theoretical description should be based on certain symmetries. Most important in this context is the concept of gauge invariance in order to quantise massless spin-1 particles. Second, renormalisability guarantees as another key element of the unified theory that quantum fluctuations yield well-defined results and that the theory is valid to arbitrary high energy scales.
The Standard Model (SM) of particle physics is the closest theory framework towards grand unification. It has been extensively studied experimentally and it has managed to withstand all precision tests so far. From the theoretical point of view, it combines the physics of strong interactions with the electroweak sector, which is yet another unification of physical effects induced by the weak nuclear force and electromagnetism. Thus, this theory treats three of the four fundamental forces on the same footing and it respects in addition important symmetries like gauge invariance, Lorentz invariance and renormalisability. However, gravity as the fourth fundamental force is not embedded in this framework. The current frontier to describe gravitational effects is set by General Relativity, which is a classical field theory solely describing long-distance interactions. A quantised version of it is currently unknown.
Precision tests in particle physics mostly rely on collisions of two particle beams at high energies, which produce a huge number of additional particles in the final state. Typical collider experiments, for instance the Large Hadron

Collider (LHC) at CERN, have perfomed tests of the theoretical framework to very high precision up to energies of several TeV. But despite recent experimental discoveries like the Higgs boson at the ATLAS [1] and CMS [2] experiment at CERN, there still exist several open questions that cannot be explained within the SM. Examples for these new physics effects are dark matter, dark energy, the matter-antimatter asymmetry of the universe or neutrino masses. In this context, the experimental proof of neutrino oscillations, which are only observable for non-zero neutrino masses, constitutes a prominent example for the direct measurement of new physics effects which are not captured by the SM [3–5]. This is why experimental searches, especially in the current Run-3 of the LHC [6], or at the dedicated flavour experiments like Belle-II [7] perform increasingly precise measurements to look for deviations between theoretical predictions and experimental measurements or to search directly for new non-SM particles. These measurements are supposed to shed light on the many possible theoretical explanations for new physics effects and provide the path for future theoretical investigations.
From a theoretical point of view, the SM is a local, relativistic and renormalisable theory based on gauge invariance under the $SU(3)_c \times SU(2)_L \times U(1)_Y$ group. Each gauge group implements different physical effects associated with the fundamental forces. For instance, quantum electrodynamics (QED), the quantised version of electromagnetism, arises from invariance under the group $U(1)_{\mathrm{EM}}$ after spontaneous symmetry breaking [8] of the gauge group $SU(2)_L \times U(1)_Y$.
The fundamental building blocks of matter in the SM are quarks and leptons, which are grouped into multiplets of the various gauge groups. In general, there exist three categories (families) with the same gauge couplings, but organised according to their charges and masses. Bosons, which are particles whose spin only takes integer values, are responsible for the interaction between matter. As an example, gluons are the interaction particles of the strong interaction, while photons mediate electromagnetic interactions. Notice that the Higgs particle is of particular importance in the group of SM bosons. It can be interpreted as fluctuations of the Higgs field which generates the mass for all massive particles in the SM via the Higgs mechanism [9, 10], including quarks, leptons and gauge bosons. However, it does not explain the observed neutrino masses, since the SM assumes massless neutrinos.
The electroweak sector is particularly suited for precision tests of SM parameters. Especially the field of flavour physics is adequate for accurate measurements as it allows for the study of transitions between different types (flavours) of quarks and leptons. Typical parameters in these transitions are the components of the quark-mixing matrix due to Cabibbo, Kobayashi and Maskawa (CKM) [11, 12] or directly the masses of the gauge bosons M_W, M_Z. Due to the large number of possible transitions, the electroweak sector exhibits a rich phenomenology, in particular for B-meson decays. The investigation of central properties of the B mesons, i.e. quark-antiquark bound states that involve a bottom quark (and additional virtual particles), as well as channels hinting towards new physics effects in form of dark matter

are among the central elements of this work.
Contrary to that, the physical nature of the strong interaction is completely different compared to the electroweak interaction. In this case, the gauge group is the $SU(3)_c$ and quarks as well as antiquarks are grouped according to their colour charge in triplets, while gluons form an octet since they belong to the adjoint representation of the $SU(3)_c$. A direct comparison of the behaviour of the coupling constant α_s in quantum chromodynamics (QCD) and α_{EM} for electromagnetic interactions provides hints for the different theoretical foundations. The β-function is particularly suited to illustrate this behaviour

$$\beta(\alpha(\mu)) \equiv \frac{\mathrm{d}\alpha(\mu)}{\mathrm{d}\log\mu} = -2\beta_0\frac{\alpha(\mu)^2}{4\pi} + \mathcal{O}(\alpha^3) \tag{1.1}$$

with $\beta_0 = \frac{11}{3}C_A - \frac{2}{3}n_f > 0$ in QCD and $\beta_0 < 0$ in QED. Notice that Eq. (1.1) corresponds to a renormalisation group equation (RGE), which describes the running of the coupling in the $\overline{MS}$ scheme. This running indicates that physical parameters are scale-dependent in renormalisable theories and they change their value depending on the probed energy. In general, we are able to derive such RGEs for any parameter and coupling of the SM. They can subsequently be used to switch between different scales.
Generally, the running of the QCD coupling constant $\alpha_s(\mu)$ helps to understand the fundamental theoretical properties of the strong interaction. At large energies, i.e. short distances, the coupling tends to zero, underlining the fact that constituents inside bound states in QCD, namely quarks and gluons, are quasi-free particles and perturbative methods are applicable. This fundamental characteristic is called asymptotic freedom [13–15]. But on the other end of the energy scale at low energies, the coupling becomes stronger. We refer to this effect as confinement. Quarks and gluons are not separately visible, since only bound states are observed in nature. The formation of bound states takes place at characteristic scales around $\Lambda_{\mathrm{QCD}} \sim$ 200 - 300 MeV.
Many physical observables are furthermore sensitive to widely separated scales such that a power expansion in the small scale ratio may be performed. This expansion naturally leads to the factorisation of short-distance and long-distance effects in form of an operator product expansion, where short-distance contributions can be computed with perturbation theory due to asymptotic freedom, while long-distance contributions are usually parameterised with methods like QCD sum rules, light-cone sum rules or extracted from lattice QCD. Factorisation is the key concept in the construction of effective field theories. Prominent examples like Soft-Collinear Effective Theory (SCET) [16–19] or Heavy-Quark Effective Theory (HQET) [20–23] exploit this fundamental property and allow, as effective theories of QCD, for a simplified description of the low-energy physics based on factorised expressions at different scales.
For QED however, the β-function has an opposite sign, which induces the opposite physical picture compared to QCD. In particular, the gauge group is now the $U(1)_{\mathrm{EM}}$, which has a simpler algebraic structure. This is represented

by the behaviour of the electromagnetic coupling constant as the coupling becomes weaker with larger distances and stronger as the particle approaches an electromagnetic source. Note that this is also reflected in particle interactions: The gauge bosons of QCD, the gluons, are self-interacting particles, while photons, the mediators of electromagnetic interactions in QED, do not interact with each other. Furthermore, the self-interaction of gluons is responsible for the formation of bound states on long-distance scales.
Asymptotic freedom is crucial for the theoretical description of QCD. Perturbation theory is an effective and systematic tool to compute scattering processes of SM particles at large energies $\mu \gg \Lambda_{\mathrm{QCD}}$. Physical observables are expressed in terms of an asymptotic expansion of the small coupling constant α_s such that corrections become smaller at higher orders in perturbation theory. These corrections in fact often turn out to be divergent due to quantum fluctuations with arbitrarily large ($k^\mu \to \infty$) or small ($k^\mu \to 0$) momenta. At this point, the renormalisability of the theory becomes important, because this ingredient ensures that divergences from large loop momenta can be absorbed into the parameters of the theory. Singularities due to small momenta of the interacting particles in virtual and real corrections cancel because of the Kinoshita-Lee-Nauenberg (KLN) theorem [24, 25].
There exist many tools in the literature that automate the calculation of next-to-leading order (NLO) corrections in QCD. Prominent examples are MadGraph [26–28], HELAC-NLO [29] or WHIZARD [30, 31] among many others. In the past decades, several approaches for the automated computation of NNLO corrections emerged, which are mostly based on global or local substraction schemes at NLO [29, 32–37] that have been subsequently extended to NNLO. Frameworks like ANTENNA-substraction [38], q_T-slicing [39], STRIPPER [40, 41] or Nested soft-collinear substraction [42, 43] are typical examples for setups to automatically evaluate NNLO corrections on the basis of the previously mentioned substraction techniques.
However, the perturbative predictions may be spoilt by large logarithmic corrections for observables that are not fully inclusive. In particular, Sudakov double logarithms arise whenever the QCD radiation is constrained to be low-energetic (soft) or aligned (collinear) to some external hard partons. As an example, the transverse-momentum spectrum of the Higgs boson suffers from large corrections of the order of $\alpha_s^n \ln^{2n}(p_T/m_H)$, which become large and spoil the convergence of the perturbative series for $p_T \ll m_H$. As the transverse momentum of the Higgs boson must be balanced by the QCD radiation, this implies that the QCD radiation is either soft or collinear to the beam directions in this case. The particular method to sum these corrections of order $\alpha_s^n \ln^{2n}(p_T/m_H)$ to all orders in perturbation theory is called resummation.
Effective field theories (EFTs) provide a natural framework to resum large logarithms based on the factorisation of different modes characterised by widely separated scales. High-energy modes are usually integrated out in these type of theories such that only low-energetic degrees of freedoms are left and the infrared (IR) physics of the full theory is correctly reproduced. An example for an EFT is again Soft-Collinear Effective Theory, which relies

on the factorisation of collinear and soft modes to describe complicated collider processes in terms of simple building blocks accounting for soft, collinear and the hard QCD radiation. Large logarithms are systematically resummed, thus very precise results for many different collider observables can be obtained.
In the literature, there exist automated setups for the resummation of Sudakov corrections to next-to-leading logarithmic (NLL) [44] or next-to-next-to-leading logarithmic (NNLL) [45] accuracy, which are based on the direct QCD framework [46] and make it obsolete to perform resummation case-by-case for each observable. But automated frameworks for resummation beyond this order do not exist, since crucial ingredients for the description of the initial-state radiation at NNLO are still unknown for many observables. The first part of this thesis is devoted to the construction of an automated approach that captures collinear initial-state radiation at hadron colliders to NNLO in QCD. These effects are encoded in so-called beam functions and they have been computed for many observables to high accuracy either analytically or semi-numerically, but there does not exist a consistent setup which automatises these calculations for arbitrary observables. For soft and jet functions, similar approaches have been developed recently [47–50]. With the development of such an automated framework for beam functions, we provide the last ingredient for automated high precision resummations to NNLL$'$ in SCET.
In order to discuss our implementation coherently, we introduce general concepts of SCET in section 2.1 with a focus on a particular reference observable for which we choose transverse-momentum (p_T-) resummation. Chapter 3 is devoted to the discussion of the basics of the approach, in particular the definition as well as general properties of quark and gluon beam functions in section 3.1 and which type of observables are suitable for our automated evaluation in section 3.2. After this, we turn to the general determination of the matrix elements at NLO in chapter 4 and at NNLO in chapter 5. Moreover, we discuss the renormalisation of the beam functions in chapter 6 both in momentum and Mellin space for SCET-I and SCET-II observables. After discussing the numerical implementation in chapter 7, we present various results in chapter 8. The conclusion in chapter 9 closes the first project.
Furthermore, a second example for an effective field theory is Heavy-Quark Effective Theory (HQET), which is suited for the study of B-meson properties. Depending on the structure of these decays, it is possible to extract parameters of the SM like the CKM matrix elements. HQET is suited for the treatment of perturbative contributions, but the parameterisation of non-perturbative effects is difficult due to hadronisation. Nevertheless, techniques like QCD sum rules [51–53] or light-cone sum rules [54, 55] are well established methods allowing for the extraction of particle properties in the non-perturbative domain. These methods make it possible to determine the decay constants or form factors of processes under consideration. The second project is centered around the determination of fundamental parameters of the B-meson distribution amplitude using QCD sum rules. For this, we provide a basic introduction to HQET in section 2.2, where we also present

the fundamental parameters $\lambda_{E,H}^2$, which we intend to extract with QCD sum rules. Therefore, chapter 10 provides the basics of this method. Subsequently, we derive the corresponding QCD sum rules in chapter 11 to leading order in α_s and include vacuum condensates up to mass dimension seven. We first review the current status of the determination of these parameters and go through the various steps from the sum rule approach to the application of the quark-hadron duality and finally to the discussion of the QCD vacuum condensates as well as the perturbative contributions. A numerical analysis in chapter 12 yields estimates for the desired parameters and we summarise the work in chapter 13.
The third project enters the domain of new physics effects. We determine the branching fraction of the exclusive $B \to p\Psi$ decay in the B-Mesogenesis model with light-cone sum rules. For this, we include all contributions up to twist six into our analysis. Starting with a general overview on LCSRs in section 14.1, we discuss the main idea of the underlying B-Mesogenesis model in section 14.2. We establish the form factor decomposition in section 14.3 and we derive the sum rules in chapter 15 as well as evaluate the OPE in section 15.1 in the following. In order to extrapolate the form factors into the physical domain, we need to perform an additional transformation, which is done in section 15.2. In the end, we perform a numerical analysis in chapter 16 and obtain the branching fractions with respect to the mass m_Ψ of the new dark matter particle Ψ. Notice that the appendix provides supplementary details on the discussions. We refer to this part throughout this thesis at appropriate places.

Chapter 2

Factorisation

Factorisation is one of the most important concepts in modern applications of particle physics. These applications are characterised by largely separated scales, which are usually given by the kinematics of the underlying process. As an example, we typically observe that the masses of particles or the energy of colliding particles are large compared to low-energy scales like the hadronisation scale $\Lambda_{\text{QCD}} \sim 200 - 300$ MeV. Many modern experiments at the Large Hadron Collider (LHC) or experiments like Belle-II exploit fundamental properties like asymptotic freedom to probe processes which show widely separated energy scales.
Effective field theories are perfectly suited to provide the theoretical description of this physical situation, because factorisation is naturally implemented into these frameworks. They usually introduce a small parameter λ, defined as the small ratio of scales occurring in the problem at hand. A systematic power expansion in the parameter λ allows to describe the factorisation of short- and long-distance effects in form of an operator product expansion (OPE). This expansion disentangles the physics at large and small energies and therefore simplifies the theoretical description of the underlying process. We can make use of important properties of QCD like asymptotic freedom to investigate the short-distance physics, while we need to rely on other methods like QCD sum rules, light-cone sum rules or lattice QCD to parameterise the long-distance effects. Another possibility to characterise the low-energy physics is to extract the necessary information from experimental data.
Throughout the calculation of short-distance effects, we usually encounter complicated Feynman integrals, which are in general hard to evaluate. In order to simplify the computations, it is possible to exploit factorisation and perform an asymptotic expansion of these integrals with respect to the power counting parameter λ. This asymptotic expansion is incorporated in the method of regions, which has first been presented in [56]. In this approach, we directly use the hierarchy of different scales appearing in the underlying problem to simplify the occurring Feynman integrals. The power counting parameter λ is used to split the full integration domain of a multi-loop integral into various subregions [57, 58]. Subsequently, the integrand in each region is expanded in the parameter λ up to the desired order. Furthermore, the integrals in each region are evaluated individually, keeping in mind that

scaleless integrals vanish in dimensional regularisation. Notice that a complete mathematical proof of this method is missing so far, albeit the approach has been partially formalised in [57].
The method of regions is a key concept used to identify the relevant degrees of freedom in an effective field theory. Its application is universal, hence it also plays an important role in Soft-Collinear Effective Theory (SCET) [16–19] or Heavy-Quark Effective Theory (HQET) [20–23], which are the central frameworks in project I and II of this thesis. We begin our discussion with a short and general introduction to SCET, followed by an introduction to HQET. After that, we merge both effective field theories into the concept of QCD factorisation.

2.1 Soft-Collinear Effective Theory

Soft-Collinear Effective Theory (SCET) is a prominent example for an effective field theory of QCD. This theory has been established in the fundamental works [16–19]. In the spirit of an effective field theory, it captures the low-energy physics of QCD and separates physics at different scales by introducing different modes based on their momentum scaling. For the characterisation of the momentum modes, it is convenient to use the previously defined expansion parameter λ which is helpful in the kinematical description of factorisation in this effective theory. Furthermore, we introduce light-cone coordinates, which are defined in terms of two light-like four-vectors n^μ and $\bar{n}^\mu$ satisfying $n^2 = \bar{n}^2 = 0$ as well as $n \cdot \bar{n} = 2$. From a kinematical point of view, we see that the two incoming particles are aligned along these two light-cone vectors and we can further state them explicitly in the lab frame

$$n^\mu = (1, 0, 0, 1)^T , \qquad \bar{n}^\mu = (1, 0, 0, -1)^T . \tag{2.1}$$

The general idea is that we can express any four-vector p^μ in terms of these light-cone components

$$p^\mu = p_- \frac{n^\mu}{2} + p_+ \frac{\bar{n}^\mu}{2} + p_\perp^\mu \tag{2.2}$$

with $\bar{n} \cdot p = p_-$ and $n \cdot p = p_+$. For later convenience, it is useful to introduce the Euclidean form of the vector $p_\perp$, which satisfies the relation $p_\perp^2 = -p_T^2$. With these light-cone coordinates, we can define the virtuality of a particle as its invariant mass and use it to characterise different modes. Typical modes and their scaling together with their virtuality are shown in the table below:

Modes	Momentum scaling	Virtuality
collinear	$p \sim (\lambda^2, 1, \lambda)Q$	$\lambda^2 Q^2$
anti-collinear	$p \sim (1, \lambda^2, \lambda)Q$	$\lambda^2 Q^2$
ultrasoft	$p \sim (\lambda^2, \lambda^2, \lambda^2)Q$	$\lambda^4 Q^2$
soft	$p \sim (\lambda, \lambda, \lambda)Q$	$\lambda^2 Q^2$
hard	$p \sim (1, 1, 1)Q$	Q^2

For collider processes, we observe that typical modes are collinear modes accounting for particles that are emitted along a jet (or beam) direction and a soft mode describing isotropic low-energetic radiation. In the table above, p denotes the momentum of the particle under investigation, while Q represents the relevant hard scale of the process. The notation stems from the idea that we decompose the momentum p into light-cone coordinates with three different components $(p_+, p_-, p_\perp)$. Its virtuality is then given by $p^2 = p_+ p_- + p_\perp^2$.
In general, we observe that computations in the SCET framework follow a certain pattern, at least if we focus on leading power effects. This typical procedure can be summarised as follows:

1. Momentum modes:

   The method of regions helps us to identify the class of the observable under investigation. This classification is connected to the virtuality of the various regions. The figures below illustrate the virtualities of the different modes in SCET-I and -II for a general scaling parameter λ and allow for a direct comparison of these two classes.

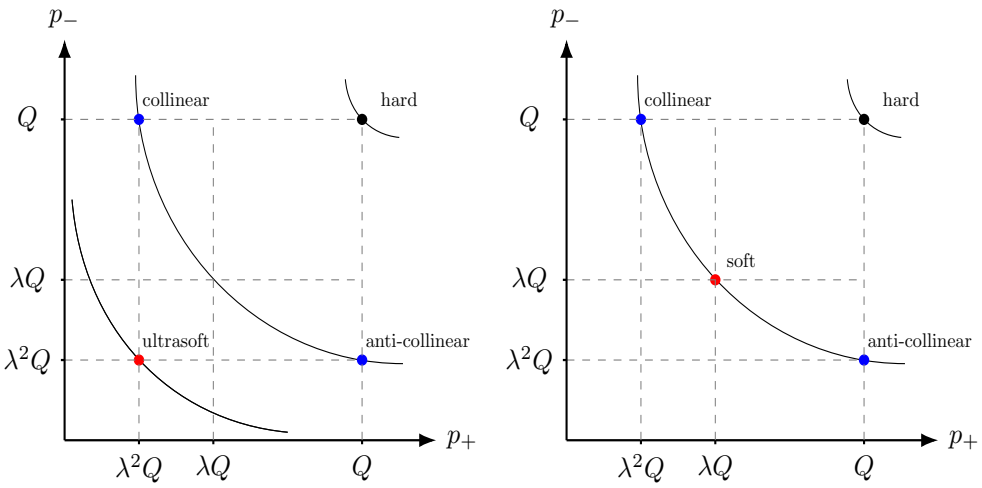

   In the left panel, we see that the collinear and anti-collinear mode share the same virtuality $\lambda^2 Q^2$ and lie on the same hyperbola in the $p_+ - p_-$ plane. But the soft mode, which has now the virtuality of an ultrasoft

mode according to the table above, is located on another hyperbola. Observables which show these characteristic modes and scaling belong to the class of SCET-I observables. Soft modes with a virtuality of $\lambda^2 Q^2$ do not contribute in this case.
Contrary, we observe in the right panel for SCET-II observables that the collinear, anti-collinear and soft region share the same virtuality $\lambda^2 Q^2$ and therefore lie on the same hyperbola in the $p_+ - p_-$-plane. The only distinct region with a different virtuality is the hard region. This situation is typical for SCET-II problems: In many cases, the ultrasoft region leads to scaleless integrals in dimensional regularisation if we only consider leading power contributions in λ, while the soft region becomes non-trivial. This causes additional complications for SCET-II, since we observe an overlap between the soft and collinear or anti-collinear region in certain kinematical configurations, which generates new type of divergences called rapidity divergences. The naming of this new type of divergences is intuitive. Generally, the rapidity is defined in terms of the ratio $y_p = \frac{1}{2} \ln \left(\frac{p_+}{p_-} \right)$. For large p_+, the soft rapidity ends up in the vicinity of the anti-collinear region, while for large p_- it enters the opposite collinear region and induces divergences. We are going to discuss in detail how to tackle these divergences in chapter 6.

2. Factorisation:

   After identifying the relevant degrees of freedom, we decompose the field operators in the QCD Lagrangian density into various sectors in line with the introduction of different modes based on the scaling with respect to the parameter λ from before. However, it is possible to show that these modes completely decouple at leading power in λ for both SCET-I and SCET-II observables after expanding the Lagrangian in λ. In the SCET-I case, one performs a field redefinition in order to decouple all sectors, while soft and collinear modes do not interact in the SCET-II case from the beginning due to the power scaling of the different modes. On top of that, we need to analyse the observable in the power expansion to derive a factorisation theorem of the underlying process. In this work, we focus on observables that are free of complications like endpoint divergences [59–66] or Glauber gluons [67–72]. The general form of a factorisation theorem at leading power is given by

$$\mathrm{d}\sigma = H \cdot B \otimes \bar{B} \otimes S \otimes \Pi_i J_i \,. \tag{2.3}$$

   The factorisation theorem in Eq. (2.3) consists of an observable independent hard function H, which encodes the physics at the hard scale Q, collinear beam and jet functions and soft functions. These functions are defined in terms of the different fields which were introduced in accordance with the different momentum regions obtained from the method of regions. Through the decoupling transformation, we can decompose the full state into collinear, anti-collinear and soft states, which yields operator expressions for the functions in Eq. (2.3) that

will be specified below.
The beam functions account for collinear initial-state radiation, while the soft function describes the soft partons in the scattering process. Note that the functions in gray in Eq. (2.3) represent jet functions, which encode the physics of collinear final-state radiation. However, they are not relevant for this work here, since we focus on processes which only contain initial-state radiation. Nevertheless, isotropic soft radiation naturally occurs for these specific processes, since they are relevant for both initial-state and final-state radiation. An automated framework to compute these functions has been proposed in [48, 49].

3. Renormalisation:

Once we have derived a factorisation theorem and established the operator definition of the relevant quantities, we can in principle go ahead and compute them with known perturbative techniques as long as the collinear and soft scale are larger compared to Λ_{QCD}. In perturbative calculations, one encounters UV and IR divergences that are usually regularised in dimensional regularisation with the dimension $d = 4-2\epsilon$. These divergences become visible in form of poles in the dimensional regulator ϵ, but they are unphysical and need to be removed with proper procedures. For SCET-I observables, this is in general straightforward, since only poles in ϵ occur. Soft functions can be immediately computed with perturbative methods and subsequently regularised as well as renormalised. However, this does not apply for beam functions, since they are non-perturbative objects due to their operator definition. For these functions, we need to disentangle short- and long-distance physics via an operator product expansion (OPE) such that so called matching kernels describe the short-distance contributions. Those are again treated with perturbation theory and, at least for SCET-I observables, renormalised in the usual way. But for SCET-II problems, additional rapidity divergences generate complications, because dimensional regularisation is not sufficient to regularise these type of singularities.
There exist many different ways to regularise rapidity divergences in SCET. One possibility consists of implementing an analytic regulator on the level of the phase-space measure [73], which we use in this work, another possibility which is commonly applied is to use an exponential regulator [74].
With this regularisation of the rapidity divergences, which is for instance done with a regulator α in the case of an analytic regulator, techniques like the collinear anomaly approach [75] or the rapidity renormalisation group equations [76, 77] can be used to perform the renormalisation for these type of problems. We make use of the collinear anomaly approach throughout this work, which refactorises the beam functions and resums the rapidity divergences in the same step. After renormalisation, we are left with finite expressions which we can use

to perform predictions in phenomenological analyses and to extract information on the underlying physics.

4. Resummation:

   Following the renormalisation procedure, we need to choose a renormalisation scheme. Common schemes are the on-shell scheme or the $\overline{MS}$-scheme. In the latter case, like in any mass-independent renormalisation scheme, the renormalised parameters depend on the renormalisation scheme μ and this scale dependence is controlled by a renormalisation group equation (RGE). However, the renormalisation procedure introduces logarithms of this scale μ and the different scales of the process, which can in general become large and spoil the asymptotic behaviour of the perturbative expansion. Therefore, they need to be resummed, i.e. we use renormalisation group equations to run the renormalisation scale μ to a common matching scale $\mu_{\text{res.}}$. In this step, we observe another advantage of SCET: the EFT approach allows for a straightforward resummation of large logarithms via RGEs.

These four steps usually appear during the investigation of a SCET problem. In the following sections, we are going to discuss the details of these basic steps by considering a benchmark observable for which we choose the production of a Drell-Yan pair at hadron colliders at small transverse momentum (p_T). This process was investigated with SCET methods in the literature to great extent. Results to the desired NNLO order are known analytically [58, 78, 79] and we follow closely the discussion from [58]. The current state-of-the-art precision for this observable was elaborated in [80, 81].

Kinematics and momentum modes for p_T-resummation

In general, experiments at hadron colliders like the LHC study the interaction of two colliding hadron beams. Since we work in the domain of high energies, we can use asymptotic freedom for the theoretical description of the underlying short-distance physics and therefore assume that two partons within the proton, in particular quarks or gluons, scatter among each other. The final state consists of a high-energetic Drell-Yan pair. We denote the large virtuality of the photon by Q^2 and its transverse momentum with respect to the colliding beam by p_T.
In the domain of small transverse momenta $\Lambda^2_{\text{QCD}} \ll p_T^2 \ll Q^2$, it is convenient to define the small parameter

$$\lambda = \frac{p_T}{Q}\,, \tag{2.4}$$

which we will use to identify the different momentum modes. It is the small expansion parameter of the theory and therefore suitable to illustrate factorisation for the problem at hand.
With the help of the method of regions, we know which regions contribute to our analysis. We observe that, besides the collinear, anti-collinear and

hard mode, the soft mode becomes relevant here, since it shares the same counting for the transverse components as the collinear modes. This leads to the same virtuality of soft and collinear modes, rendering this observable to be of SCET-II type. According to the discussion in [75], other modes do not contribute at leading power in the expansion parameter λ, are kinematically not possible or lead to scaleless integrals in dimensional regularisation.
Transverse momentum resummation belongs to the class of SCET-II observables, therefore we encounter additional rapidity divergences. We implement a symmetric analytic regulator on the phase space level in order to account for these divergences in all SCET-II applications. For this particular regulator choice, the collinear and anti-collinear beam function are related by a $n-\bar{n}$-symmetry. With the help of the collinear anomaly approach, we resum the rapidity divergences and perform the renormalisation subsequently.

Factorisation theorem for p_T-resummation

Once we have identified the relevant momentum modes, we can derive the factorisation theorem for the Drell-Yan cross section at small transverse momenta p_T. For simplicity, we focus here on the correction from the virtual photon exchange. Generally, the steps to derive the factorisation theorem have been performed many times and to a great extend in the literature [58, 78], thus we follow this discussion closely.
Starting point is the cross section, which includes the correlation function describing the underlying process and a momentum integration over the external momentum q of the photon

$$\mathrm{d}\sigma = \frac{4\pi\alpha_{EM}^2}{3q^2 s}\frac{\mathrm{d}^4 q}{(2\pi)^4}\int \mathrm{d}^4 x_\perp e^{-iqx}(-g_{\mu\nu})\,\langle h_1(p)h_2(\bar{p})|\,(j^\mu)^\dagger(x)j^\nu(0)\,|h_1(p)h_2(\bar{p})\rangle\,. \tag{2.5}$$

The current $j^\mu = \sum_q e_q \bar{q}\gamma^\mu q$ is the electromagnetic current for the light quarks q with charges $|e_q| = \frac{1}{3}, \frac{2}{3}$ and $\alpha_{EM} = \frac{e^2}{4\pi}$ is the electromagnetic coupling constant. Moreover, the two initial-state hadrons h_1 and h_2 have momenta p and $\bar{p}$, respectively. Additionally, we work in Feynman gauge, which yields the tensor $-g_{\mu\nu}$ from the sum over the photon polarizations.
In order to treat this production process in SCET, we need to perform a matching from the full QCD expression for the current j^μ onto SCET operators. Thus, the current operator j^μ becomes [58]

$$j^\mu(x) = \int \mathrm{d}s \int \mathrm{d}t_\perp\, C_V(s,t)\,\bar{\chi}_c(x+s\bar{n})\gamma_\perp^\mu S_n^\dagger(x) S_{\bar{n}}(x)\chi_{\bar{c}}(x+tn)\,. \tag{2.6}$$

Along this matching procedure, the high-energy physics component is encoded in the Wilson coefficient $C_V(s,t)$. In the SCET language, we rewrite expressions in the QCD Lagrangian in terms of hard, collinear, anti-collinear and soft fields with the momentum scaling from the table above. Thereafter, modes with high virtuality are integrated out. This leads to the introduction of collinear and anti-collinear quark fields in (2.6), which we further

decompose into

$$q_{c,\bar{c}}(x) = \xi_{c,\bar{c}}(x) + \eta_{c,\bar{c}}(x)\,. \tag{2.7}$$

The Dirac spinors $q_{c,\bar{c}}$ are therefore reduced to two two-component Weyl spinors obeying the relations $\not{n}\xi_c(x) = 0$ as well as $\not{\bar{n}}\xi_{\bar{c}}(x) = 0$ for the ξ-fields and similar relations for the η-fields after replacing $\xi \to \eta$ combined with $\not{n} \leftrightarrow \not{\bar{n}}$. With proper projection operators, they can be related to the spinor $q_{c,\bar{c}}$

$$\xi_c(x) = \frac{\not{n}\not{\bar{n}}}{4} q_c(x)\,, \tag{2.8}$$

$$\xi_{\bar{c}}(x) = \frac{\not{\bar{n}}\not{n}}{4} q_{\bar{c}}(x) \tag{2.9}$$

and similarly for the η-fields with the same replacements from before.
Furthermore, we can derive the scaling of the subfields $\xi_{c,\bar{c}}(x), \eta_{c,\bar{c}}(x)$ from the scaling of the fields $q_{c,\bar{c}}(x)$. We obtain that the field $\xi_{c,\bar{c}}(x)$ scales with λ, while $\eta_{c,\bar{c}}(x)$ scales with λ^2 [58] and we identify the η-fields as subleading due to their scaling. For this reason, they do not appear in Eq. (2.6). Rather, we express the collinear quark fields in Eq. (2.7) in terms of gauge-invariant building blocks

$$\chi_{c,\bar{c}}(x) = W^\dagger_{c,\bar{c}}(x)\xi_{c,\bar{c}}(x)\,, \tag{2.10}$$

$$\mathcal{A}^\mu_{c,\bar{c}}(x) = W^\dagger_{c,\bar{c}}(x)\left[iD^\mu_{c,\bar{c}} W_{c,\bar{c}}(x)\right], \tag{2.11}$$

where $D^\mu_{c,\bar{c}} = \partial_\mu - ig_s A^\mu_{c,\bar{c}}$ corresponds to the covariant derivative containing the collinear gluon field. $W_{c,\bar{c}}$ are collinear and anti-collinear Wilson lines including collinear and anti-collinear gluon fields in order to guarantee gauge invariance of the expression in Eq. (2.6)

$$W_c(x) = P\exp\left[ig_s\int_{-\infty}^{0} \mathrm{d}s\; \bar{n}\cdot A_c(x+s\bar{n})\right], \tag{2.12}$$

$$W_{\bar{c}}(x) = P\exp\left[ig_s\int_{-\infty}^{0} \mathrm{d}t\; n\cdot A_{\bar{c}}(x+tn)\right]. \tag{2.13}$$

After introducing the basic notation, we can now focus on the derivation of the factorisation theorem. First, we consider the combination of two vector currents

$$j^{\dagger,\mu}(x)j^\nu(0) \to \int \mathrm{d}s \int \mathrm{d}t \int \mathrm{d}s' \int \mathrm{d}t'\, C_V(s,t)C_V^*(s',t') \left[S_n^\dagger(x)S_{\bar{n}}(x)\right]^{ad}$$
$$\times\, \bar{\chi}^a_c(x+t'\bar{n})\gamma^\mu_\perp \chi^d_{\bar{c}}(x+s'n)\; \bar{\chi}^b_{\bar{c}}(sn)\gamma^\nu_\perp \chi^c_c(t\bar{n})\left[S^\dagger_{\bar{n}}(0)S_n(0)\right]^{bc}. \tag{2.14}$$

In this context, we remind ourselves that

$$\gamma^\mu = \gamma^\mu_\perp + \not{n}\frac{\bar{n}^\mu}{2} + \not{\bar{n}}\frac{n^\mu}{2}\,. \tag{2.15}$$

Due to the relations $\bar{\not{n}}\chi_{\bar{c}} = 0$ and $\not{n}\chi_c = 0$, we can effectively replace $\gamma_\perp^\mu$ by γ^μ in Eq. (2.14). This will become useful in the following step, where we apply Fierz transformations [82] on the expression in the second line of Eq. (2.14), after contracting it with the metric tensor $-g_{\mu\nu}$:

$$\begin{aligned}\bar{\chi}_c^a(x+t'\bar{n})\gamma_\perp^\mu\chi_{\bar{c}}^d(x+s'n)\;&\bar{\chi}_{\bar{c}}^b(sn)\gamma_\perp^\nu\chi_c^c(t\bar{n})\\ &= \bar{\chi}_c^a(x+t'\bar{n})\frac{\bar{\not{n}}}{2}\chi_c^c(t\bar{n})\;\bar{\chi}_{\bar{c}}^b(sn)\frac{\not{n}}{2}\chi_{\bar{c}}^d(x+s'n)\\ &\quad+\bar{\chi}_c^a(x+t'\bar{n})\frac{\bar{\not{n}}}{2}\gamma_5\chi_c^c(t\bar{n})\;\bar{\chi}_{\bar{c}}^b(sn)\frac{\not{n}}{2}\gamma_5\chi_{\bar{c}}^d(x+s'n)\end{aligned} \tag{2.16}$$

In the relation above, we exploited that $\bar{\chi}_c\gamma^\mu\chi_c = n^\mu\bar{\chi}_c\frac{\bar{\not{n}}}{2}\chi_c$ and $\bar{\chi}_c\chi_c = 0$. We express the currents in terms of the gauge invariant building blocks from Eq. (2.11) and a, b, c, d are colour indices in the fundamental representation of $SU(N_c)$. However, the second term in Eq. (2.16) vanishes due to parity invariance of the strong interaction such that we are only left with the first line.

In SCET-II, collinear, anti-collinear and soft modes do not interact with each other to leading power in the expansion parameter λ. Hence, we can decompose the initial state according to $|h_1(p)h_2(\bar{p})\rangle = |h_1(p)\rangle_c \otimes |h_2(\bar{p})\rangle_{\bar{c}} \otimes |0\rangle_S$ such that the full matrix element factorises into individual pieces. We can furthermore average over colour indices. Finally, we obtain

$$\begin{aligned}&\langle h_1(p)|\,\bar{\chi}_c^a(x+t'\bar{n})\gamma_\perp^\mu\chi_c^c(t\bar{n})\,|h_1(p)\rangle\\ &\qquad= \frac{1}{N_c}\delta^{ac}\,\langle h_1(p)|\bar{\chi}_c^e(x+t'\bar{n})\gamma_\perp^\mu\chi_c^e(t\bar{n})\,|h_1(p)\rangle\\ &\langle h_2(\bar{p})|\,\bar{\chi}_{\bar{c}}^b(sn)\gamma_\perp^\nu\chi_{\bar{c}}^d(x+s'n)\,|h_2(\bar{p})\rangle\\ &\qquad= \frac{1}{N_c}\delta^{bd}\,\langle h_2(\bar{p})|\bar{\chi}_{\bar{c}}^f(sn)\gamma_\perp^\nu\chi_{\bar{c}}^f(x+s'n)\,|h_2(\bar{p})\rangle\,.\end{aligned} \tag{2.17}$$

Ultimately, we arrive at the matrix element

$$\begin{aligned}&\langle h_1(p)h_2(\bar{p})|-j^{\dagger,\mu}(x)j_\mu(0)\,|h_1(p)h_2(\bar{p})\rangle\\ &\qquad\to\frac{|C_V(-q^2,\mu)|^2}{N_c^2}\,\langle h_1(p)|\,\bar{\chi}_c(x_+ + x_\perp)\frac{\bar{\not{n}}}{2}\chi_c(0)\,|h_1(p)\rangle\\ &\qquad\quad\times\langle h_2(\bar{p})|\,\bar{\chi}_{\bar{c}}(0)\frac{\not{n}}{2}\chi_{\bar{c}}(x_- + x_\perp)\,|h_2(\bar{p})\rangle\\ &\qquad\quad\times\langle 0|\,\mathrm{Tr}\Big[\bar{T}\big[S_n^\dagger(x_\perp)S_{\bar{n}}(x_\perp)\big]T\big[S_{\bar{n}}^\dagger(0)S_n(0)\big]\Big]\,|0\rangle\;.\end{aligned} \tag{2.18}$$

In the last equation, we perform several steps at once. First, we need to do an additional multipole expansion, hence we drop all subleading components in the power expansion parameter λ. The scaling of the momentum q of the photon turns out to be $(1, 1, \lambda^{-1})Q$, thus we need to drop x_- for the collinear field, while we neglect x_+ for the anti-collinear field. In the case of the soft field, both the x_- and x_+ components are subleading. T and $\bar{T}$ denote the

time-ordered and anti-time-ordered product respectively. Moreover, we use translation invariance to shift the arguments of the collinear fields χ and perform the substitutions $x_+ \to x_+ + t'\bar{n} - t\bar{n}$ as well as $x_- \to x_- + s'n - sn$. This helps us to simplify the Wilson coefficients after performing a Fourier transformation such that we obtain the factor in Eq. (2.21). For more details on the explicit calculation, we refer to [58, 78].
After decomposing the integral

$$\int \mathrm{d}^4x e^{-iqx} = \frac{1}{2}\int \mathrm{d}^2x_\perp e^{-iq_\perp\cdot x_\perp}\int \mathrm{d}t_1 e^{-it_1\bar{n}\cdot q}\int \mathrm{d}t_2 e^{-it_2 n\cdot q}\,, \tag{2.19}$$

we can identify the collinear, anti-collinear and soft function

$$\begin{aligned}
\mathcal{B}_{q/h_1}(x_1, x_T^2, \mu) &= \frac{1}{2\pi}\int_{-\infty}^{\infty}\mathrm{d}t_1 e^{-ix_1 t_1\bar{n}\cdot p}\,\langle h_1(p)|\,\bar{\chi}_c(x_+ + x_\perp)\frac{\bar{n}\!\!\!/}{2}\chi_c(0)\,|h_1(p)\rangle\ ,\\
\bar{\mathcal{B}}_{\bar{q}/h_2}(x_2, x_T^2, \mu) &= \frac{1}{2\pi}\int_{-\infty}^{\infty}\mathrm{d}t_2 e^{-ix_2 t_2 n\cdot p}\,\langle h_2(\bar{p})|\,\bar{\chi}_{\bar{c}}(0)\frac{n\!\!\!/}{2}\chi_{\bar{c}}(x_- + x_\perp)\,|h_2(\bar{p})\rangle\ ,\\
\mathcal{S}(x_T^2, \mu) &= \frac{1}{N_c}\,\langle 0|\,\mathrm{Tr}\Big[\bar{T}\big[S_n^\dagger(x_\perp)S_{\bar{n}}(x_\perp)\big]T\big[S_{\bar{n}}^\dagger(0)S_n(0)\big]\Big]\,|0\rangle\ .
\end{aligned} \tag{2.20}$$

Here, we have introduced the transverse component $x_T^2 = -x_\perp^2$. From a physical point of view, the quantity $\mathcal{B}_{q/h_1}$ represents the transverse parton distribution function, which illustrates the distribution of collinear quarks and longitudinal momentum fraction x_1 inside the hadron h_1. With the definitions from Eq. (2.20), the expressions in Eq. (2.5) becomes

$$\begin{aligned}
\mathrm{d}\sigma = \frac{4\pi\alpha_{EM}^2}{3N_c q^2 s}|C_V(-q^2,\mu)|^2\frac{\mathrm{d}^4q}{2(2\pi)^2}\int \mathrm{d}^2x_\perp e^{-iq_\perp\cdot x_\perp}\mathcal{S}(x_T^2,\mu)\\
\times\sum_q e_q^2\Big[\mathcal{B}_{q/h_1}(x_1,x_T^2,\mu)\bar{\mathcal{B}}_{\bar{q}/h_2}(x_2,x_T^2,\mu) + (q\leftrightarrow\bar{q})\Big]\,.
\end{aligned} \tag{2.21}$$

This is a typical form of a factorisation theorem in SCET to leading power in λ. Hard, soft, collinear and anti-collinear contributions to the cross section are factorised and can be computed independently. Factorisation theorems for other observables share a similar structure, albeit the specific form of factors like $e^{-iq_\perp\cdot x_\perp}$ depend on the measurement function which incorporates the full characteristics of the observable. Although we demand several requirements for this function, the ansatz is still general enough to allow for a large class of observables. In the following chapter, we discuss in more detail the definition of the beam and the measurement function.
Since p_T-resummation is a SCET-II observable, we encounter rapidity divergences which need a special treatment as discussed before. Regularising these singularities with a symmetric analytic regulator and applying the collinear anomaly approach subsequently resums those divergences and refactorises the beam function expressions. We discuss these issues in chapter 6 in more detail. Once we obtain renormalised expressions, we finally reach our goal to provide the finite renormalised NNLO beam function expressions which are missing to push the automation of resummation to NNLL$'$ accuracy. This is

related to the last step in our general introduction from before. Albeit renormalised expressions are finite and have no poles in the dimensional regulator ϵ or in the rapidity regulator α, the renormalisation procedure introduces logarithms of the renormalisation scale μ and the different scales of the underlying process. These logarithms might become large, depending on the choice of μ, and might spoil the perturbative series. Resummation techniques account for this issue and run the scale μ via the RGEs to a common scale, where the logarithms are small, such that the perturbative series retains its predictive power. Therefore, resummation is crucial for phenomenological analyses. However, this is beyond the scope of this work, since we aim to provide NNLO predictions for the beam functions, which can be used in phenomenological studies. For a detailed discussion on resummation of transverse-momentum resummation, we refer to [58, 78].

2.2 Heavy-Quark Effective Theory

Heavy-Quark Effective Theory (HQET) [20–23] is another well-established example for an effective field theory. One of its main advantages is to enable the study of heavy quarks, such as charm and bottom quarks, in a more simplified framework compared to the full Standard Model. Within this approach, one exploits that the mass of a heavy quark is much larger than the typical energy scale of strong interactions Λ_{QCD}. Therefore, the heavy quark can be treated as nearly static embedded in a cloud of lighter degrees of freedom such as gluons or light quarks. In this physical picture, the heavy meson state H is decomposed into valence and non-valence contributions

$$|H\rangle = |Q\bar{q}\rangle \oplus |Q\bar{q}g\rangle \oplus \sum_{q'=u,d,s} |Q\bar{q}q'\bar{q}'\rangle \oplus \dots , \tag{2.22}$$

where Q denotes the heavy quark like the b- or c-quark and q the corresponding light u, d, s-quark. The masses of the light quarks are negligible compared to the hard scale of typical processes such that we restrict our discussion to a B- or D-meson. Through this effective framework, we have direct access to SM parameters like the weak mixing angle θ_W, the Cabbibo-Kobayashi-Maskawa (CKM) matrix elements and their unitarity relation or CP-violating effects in a model-independent way. Theoretical predictions are then compared to experimental data from dedicated flavour physics experiments like BaBar or Belle-II. Besides that, it is even possible to determine decay constants from leptonic decays or form factors of heavy hadrons from semileptonic decays if we combine the HQET formalism with methods like QCD sum rules [51–53], light-cone sum rules [54, 55] or lattice QCD.
Since heavy mesons involve two widely separated energy scales $m_Q \gg \Lambda_{\text{QCD}}$, we can again exploit factorisation techniques to separate short-distance and long-distance physics with an operator product expansion (OPE). Short-distance effects can be studied within perturbation theory, while long-distance effects like hadronisation need different methods for an appropriate treatment. The aforementioned QCD sum rule and the light-cone sum rule (LCSR) approach are used in an attempt to parameterise these low-energy physical effects. Throughout this work, we employ the QCD sum rule method to determine two essential HQET parameters called $\lambda^2_{E,H}$, while we consider light-cone sum rules to investigate a B-meson decay into a new dark matter particle which extends the Standard Model.
In general, the theoretical description of this framework is based on the observation that the large mass of the heavy meson H allows us to introduce its velocity via the relation

$$v^\mu = \frac{p_H^\mu}{m_H} \tag{2.23}$$

with $v^2 = 1$ such that we can even identify $v = (1, \vec{0})^T$ in the rest frame of the heavy meson.
Since the heavy quark Q is nearly at rest, it is useful to define

$$p_Q^\mu = m_Q v^\mu + k^\mu , \tag{2.24}$$

where $k^\mu \sim \Lambda_{\rm QCD}$ describes the fluctuations around its mass shell. Because it is of the order of $\Lambda_{\rm QCD}$, its effects are usually negligible in the expansion around the heavy quark mass m_Q.
Following the usual spirit of effective field theories, we aim to construct a theory which captures the low-energy physics of the full theory (QCD) by integrating out the small components of the heavy quark field. But contrary to the usual effective field theory approaches, we only remove the small components in the heavy-quark momentum decomposition such that we can treat the effective heavy quark as a degree of freedom of the theory. But since we modify the high-energy physics by integrating out parts of the heavy-quark components, we can not capture the full UV physics of QCD. For this, we need to adjust the scale of the Wilson coefficients of the effective operators in a matching calculation. The OPE appears in this framework when we rewrite the effective theory, which is at first non-local, into an infinite series of local terms which are systematically expanded in inverse powers of m_Q.
At this point, it is convenient to split the heavy-quark field into large and small components

$$h_v(x) = e^{im_Q v\cdot x} P_+ Q(x)\,, \qquad H_v(x) = e^{im_Q v\cdot x} P_- Q(x) \tag{2.25}$$

with the projection operator $P_\pm = \frac{1\pm\not{v}}{2}$. The projection operators guarantee that the relations $\not{v} h_v = h_v$ and $\not{v} H_v = -H_v$ hold for the large and small components of the heavy-quark field respectively.
We are able to rewrite the Lagrangian density for the heavy quark field in terms of the large and small components h_v and H_v

$$\begin{aligned}\mathcal{L}_Q = \bar{Q}(i\not{D} - m_Q)Q = {}& \bar{h}_v iv\cdot D h_v - \overline{H}_v(iv\cdot D + 2m_Q)H_v + \bar{h}_v i\not{D}_\perp H_v \\ & + \overline{H}_v i\not{D}_\perp h_v\end{aligned} \tag{2.26}$$

with $D^\mu_\perp = D^\mu - v^\mu v\cdot D$, which satisfies $v\cdot D_\perp = 0$. Additionally, we use equations of motion to express the field H_v by h_v

$$H_v = \frac{1}{2m_Q + iv\cdot D} i\not{D}_\perp h_v\,. \tag{2.27}$$

Indeed, we observe in this relation that the small components H_v scale as $1/m_Q$. However, we can insert Eq. (2.27) into Eq. (2.26) to obtain an effective non-local Lagrangian

$$\mathcal{L}_{\rm eff} = \bar{h}_v iv\cdot D h_v + \bar{h}_v i\not{D}_\perp \frac{1}{2m_Q + iv\cdot D} i\not{D}_\perp h_v\,. \tag{2.28}$$

Formally, we can manipulate at this stage the generating functional for the QCD Greens′ functions containing heavy-quark fields in order to get rid of the non-local effects [23, 83]. This effectively means that we expand the Lagrangian in terms of the small residual momentum k^μ, which is much smaller than m_Q. Therefore, we obtain the following effective Lagrangian

$$\mathcal{L}_{\rm eff} = \bar{h}_v iv\cdot D h_v + \sum_{n=0}^{\infty} \frac{1}{2m_Q} \bar{h}_v i\not{D}_\perp \left(-\frac{iv\cdot D}{2m_Q}\right)^n i\not{D}_\perp h_v\,. \tag{2.29}$$

This step naturally introduces a tower of local terms in form of an OPE as we argued before. By exploiting the relation

$$P_+ i\not{D}_\perp i\not{D}_\perp P_+ = P_+ \left[(iD_\perp)^2 + \frac{g_s}{2}\sigma_{\mu\nu}G^{\mu\nu} \right] P_+ \tag{2.30}$$

with $G^{\mu\nu} = \frac{i}{g_s}[D^\mu, D^\nu]$, we arrive at the following form of the Lagrangian

$$\mathcal{L}_{\text{eff}} = \bar{h}_v iv\cdot D h_v + \frac{1}{2m_Q}\bar{h}_v (iD_\perp)^2 h_v + \frac{g_s}{4m_Q}\bar{h}_v \sigma_{\mu\nu}G^{\mu\nu}h_v + \mathcal{O}\left(\frac{1}{m_Q^2}\right). \tag{2.31}$$

Notice that in the limit $m_Q \to \infty$ only the first term survives, which describes the kinetic term of the large component of the heavy quark field in form of a linear propagator and its interaction with soft gluons. The large component field h_v becomes important in the determination of the HQET parameters $\lambda^2_{E,H}$. However, we can prove that the interaction terms do not contribute in our considerations and only the propagator becomes important, since we work only to leading power in the heavy quark expansion.
Moreover, the factorisation in HQET leads in this particular limit to another advantage in the description of long-distance effects. It is possible to identify approximate symmetries in some kinematical regimes, which simplify the underlying problem and allow for statements beyond perturbation theory at energy scales $\mu \sim \Lambda_{\text{QCD}}$. The HQET framework allows to identify two important symmetries, which become exact for $m_Q \to \infty$, namely the heavy-quark flavour and spin symmetries.
The heavy-quark flavour symmetry becomes apparent if we consider the binding energy $\bar{\Lambda} = m_H - m_Q + \mathcal{O}\left(\frac{1}{m_Q}\right)$. Comparing the values for $\bar{\Lambda}$ for B- and D-mesons, we see that they are nearly identical. This particular feature is called the flavour symmetry in HQET. The spin symmetry becomes obvious by studying the difference between the masses of vector and pseudoscalar heavy mesons. They just differ by the spin orientation of the heavy quark Q inside the heavy meson H and are also nearly identical.
Besides, it is also possible to understand these two symmetries in a more direct physical picture [83]. For this, we assign the heavy meson system H a characteristic size R_H. The heavy quark is embedded in a cluster of light partons like quarks, antiquarks and gluons around the energy scale Λ_{QCD} . Since the heavy quarks constitutes the large scale in this problem, its wavelength is of the order of $\lambda_Q \ll R_H$. Soft gluons, which live at the characteristic scale $\Lambda_{\text{QCD}} \sim R_H$, can not resolve the quantum numbers of the heavy quark, in particular its spin and flavour. The light degrees of freedom view the heavy quark as a colour charge source confined inside the hadron. Relativistic effects like colour magnetism allow the soft gluons to distinguish different heavy quarks. But since these relativistic effects vanish in the heavy quark limit $m_Q \to \infty$, heavy mesonic states containing $b-$ or c-quarks become indistinguishable. Interestingly, the nature of this symmetry is quite different to approximate symmetries of QCD like the chiral symmetry, because it is

not a symmetry of the full theory in a certain parametrical limit, but rather an approximate symmetry of an effective theory. Especially the fact that the symmetry holds only in the limit $m_Q \to \infty$ illustrates the difference to ordinary symmetries in QCD.
After establishing the fundamental framework in HQET, we are in principle able to investigate many properties of the Standard Model, as we described before. But apart from the determination of SM parameters, it is also possible to investigate parameters and quantities directly defined in the HQET framework. For instance, they are used to describe the properties of the B-meson by studying matrix elements of operators of the form

$$\mathcal{O}(z) = \bar{q}(0)W(0,z)\Gamma h_v(z)\,. \tag{2.32}$$

In this context, q denotes the light quark field, h_v represents the heavy quark field in HQET and $W(0,z)$ is the Wilson line rendering the expression in Eq. (2.32) gauge invariant. It is defined in a similar manner to Eq. (2.12) with z denoting a light-like vector on the light-cone, i.e. $z^2 = 0$.
One of the most important parameters in HQET is the HQET decay constant defined in terms of the relation

$$\langle 0|\,\bar{q}(0)\gamma_\mu\gamma_5 h_v(0)\,|\bar{B}(v)\rangle = iF(\mu)v_\mu\,. \tag{2.33}$$

It is related to the physical QCD decay constant f_B via the expression

$$f_B\sqrt{m_B} = F(\mu)\left[1 + \frac{C_F\alpha_s}{4\pi}\left(3\cdot\ln\Big(\frac{m_b}{\mu}\Big) - 2\right) + ...\right] + \mathcal{O}\Big(\frac{1}{m_b}\Big) \tag{2.34}$$

up to corrections of $\frac{1}{m_b}$. Notice that in this relation up to order α_s, we expect that the explicit scale dependence of the decay constant cancels on the right side such that the physical decay constant f_B is scale independent. Another interesting parameter, which we have already discussed before, is the binding energy $\bar{\Lambda}$ introduced through the matrix element

$$\langle 0|\,\bar{q}\Gamma iD^\mu h_\nu\,|\bar{B}\rangle = \frac{-i}{6}\,\bar{\Lambda}\,F(\mu)\,\mathrm{Tr}\Big[\Gamma P_+\gamma_5(4v^\mu - \gamma^\mu)\Big]\,. \tag{2.35}$$

Its definition is given by $\bar{\Lambda} = m_B - m_b + \mathcal{O}\Big(\frac{1}{m_b}\Big)$ and it is relevant for the first moments of the leading and subleading twist amplitude, which we discuss in the following section.
In addition to that, there are other interesting parameters called λ_H^2 and λ_E^2, which contribute to the second moments of the B-meson DAs. Originally, they have been defined as [84]

$$\langle 0|\,g_s\bar{q}\,\vec{\alpha}\cdot\vec{E}\,\gamma_5 h_v\,|\bar{B}(v)\rangle = F(\mu)\,\lambda_E^2\,, \tag{2.36}$$

$$\langle 0|\,g_s\bar{q}\,\vec{\sigma}\cdot\vec{H}\,\gamma_5 h_v\,|\bar{B}(v)\rangle = iF(\mu)\,\lambda_H^2. \tag{2.37}$$

and can be physically interpreted as chromoelectric and chromomagnetic moments. This fact becomes apparent if we consider the definition of the quantities in Eqs. (2.36), (2.37). Both $\vec{E}$ and $\vec{H}$ are related to the field

strength tensor $G_{\mu\nu} = G^a_{\mu\nu} T^a$ via $E^i = G^{0i}$ and $H^i = -\frac{1}{2}\epsilon^{ijk} G^{jk}$, which is similar to the definition of the electric and magnetic fields in QED. This field strength tensor is defined as $G_{\mu\nu} = \frac{i}{g_s}[D_\mu, D_\nu]$ with g_s denoting the strong coupling constant, which is related to α_s by

$$\alpha_s = \frac{g_s^2}{4\pi} \,. \tag{2.38}$$

$\vec{\alpha}$ and $\vec{\sigma}$ are combinations of Dirac γ-matrices in order to project out the parameters $\lambda^2_{E,H}$

$$\alpha^i = \gamma^0 \gamma^i \gamma_5 \,, \qquad \sigma^i = \gamma^i \,. \tag{2.39}$$

The explicit choice of these projections in Eq. (2.39) guarantees that the expressions are invariant under parity transformations.
In the second project of this thesis, we plan to determine these parameters with QCD sum rules within HQET. Instead of analysing a correlation function of one two-particle and one three-particle current, which has been studied in the previous works [84, 85], we propose an alternative diagonal sum rule based on a correlation function containing two three-particle currents. One of the advantages of this particular correlation function is its positive definiteness, which allows for a more reliable application of the quark-hadron duality. The tension between the two determinations from [84] and [85], where the central values differ by a factor of three, makes it interesting to investigate these parameters in an independent approach. These parameters become relevant in the modelling of the shape of the B-meson in the subleading power expansion. Due to the large discrepancy between the two extractions, many authors express their relations through the ratio $\mathcal{R} = \lambda_E^2/\lambda_H^2$, which is approximately equal, and work with this quantity instead of choosing an explicit parameter set.
In our determination, we work to leading order in α_s and include local vacuum condensates up to mass dimension seven into our analysis, therefore we neglect α_s and $1/m_b$-corrections in Eq. (2.34) and the definition of $\bar{\Lambda}$. However, it is convenient for our analysis to rewrite the definitions in Eq. (2.36) and (2.37) into a covariant form

$$\begin{aligned}\langle 0|\, \bar{q}(0) \Gamma_1^{\mu\nu} g_s G_{\mu\nu}(0) h_v(0)\, |\bar{B}\rangle = \frac{-i}{6} F(\mu) \{ &\lambda_H^2(\mu)\ \mathrm{Tr}[\Gamma_1^{\mu\nu} P_+ \gamma_5 \sigma_{\mu\nu}] \\ &+ [\lambda_H^2(\mu) - \lambda_E^2(\mu)]\ \mathrm{Tr}[\Gamma_1^{\mu\nu} P_+ \gamma_5 v_{\mu\nu}]\}. \end{aligned} \tag{2.40}$$

In Eq. (2.40), we make use of the covariant trace formalism [84]. We define $\sigma_{\mu\nu} = \frac{i}{2}[\gamma_\mu, \gamma_\nu]$, while $v_{\mu\nu}$ is given by $i(v_\mu \gamma_\nu - v_\nu \gamma_\mu)$. Although $\Gamma_1^{\mu\nu}$ represents in general an arbitrary combination of Dirac γ-matrices, it is possible to go back to the original definitions in Eq. (2.36) and (2.37) by choosing Eq. (2.39) for Γ_1.

2.3 QCD Factorisation

Another important milestone in the description of exclusive hadronic two-body decays of B-mesons has been the introduction of the QCD factorisation approach [86–88]. It is based on the heavy-quark expansion (HQE) within HQET from section 2.2 combined with collinear factorisation, which describes the factorisation of hard-exclusive processes. HQE exploits that the mass of the heavy quark Q inside the mesonic state H is much larger than the typical hadronic scale Λ_{QCD}, while collinear factorisation operates at energies where the final-state particles of the exclusive processes, which are supposed to be on the light-cone, are much larger than the hadronic scales. Therefore, HQE is applicable in the description of the B-meson in the expansion $\Lambda_{\text{QCD}} \ll m_b$, whereas collinear factorisation uses the energy $E \sim \mathcal{O}(m_b)$ of the light final-state particle in the B-meson rest frame and works in the limit $\Lambda_{\text{QCD}} \ll E$. The modern formulation of QCD factorisation therefore uses methods from both SCET and HQET [89–95].
This framework is perfectly suited for the investigation of heavy B-meson decays into light (charmless) energetic mesons. As we deal with widely separated scales, the corresponding decay amplitudes can again be factorised in the HQE. For this specific case, it takes for a generic operator $\mathcal{O}_i$ of the weak effective Hamiltonian the following form [87]

$$\begin{aligned}\langle M_1 M_2|\,\mathcal{O}_i\,|\bar{B}\rangle = \sum_j F_j^{B\to M_1}(m_2^2)\int_0^1 \mathrm{d}u\, T_{ij}^I(u)\Phi_{M_2}(u) + (M_1 \leftrightarrow M_2) \\ + \int_0^1 \mathrm{d}\xi \int_0^1 \mathrm{d}u \int_0^1 \mathrm{d}v\, T_i^{II}(\xi,u,v)\Phi_B(\xi)\Phi_{M_1}(v)\Phi_{M_2}(u) \qquad (2.41)\end{aligned}$$

for M_1 and M_2 being both light. In Eq. (2.41), we have introduced the form factors $F_j^{B\to M_{1,2}}(m_{2,1}^2)$ for $B \to M_{1,2}$ decays, which can be determined with methods like light-cone sum rules or lattice QCD. Correspondingly, $m_{1,2}$ are the masses of the light mesons $M_{1,2}$. $\Phi_X(u)$ with $X \in \{M_1, M_2, B\}$ represent the leading twist light-cone distribution amplitudes of the meson X. These light-cone distribution amplitudes are non-perturbative objects and do not depend on the process under investigation. In addition to that the quantities $T_{ij}^I(u)$ and $T_i^{II}(\xi,u,v)$ correspond to the hard-scattering functions, which are, contrary to the distribution amplitudes, process dependent. Moreover, perturbation theory can be applied to determine those functions.
Typical applications of the QCD factorisation approach are for instance the radiative leptonic $B \to \gamma l\nu$ decays or the hadronic $B \to \pi\pi$ decays. These examples are perfectly suited to determine the properties of the B-meson distribution amplitude like the first inverse moment λ_B^{-1} of the LCDA [96–103]. In this work, we are interested in the extraction of the parameters $\lambda_{E,H}^2$, which are used to model the shape of the B-meson DA [84, 104–107]. The properties of the B-meson DAs are less known, albeit they are subject of many studies recently. However, there occur many problems in their description, especially if we include subleading power corrections [108–113].

In order to characterise distribution amplitudes, the quantity twist is defined as

$$t = d - s\,, \tag{2.42}$$

where d denotes the mass dimension of the operator, while s describes its canonical spin. Its determination for arbitrary local operators is not always immediately clear, since it requires to expand quark and gluon fields in terms of longitudinal and transverse projections to the light-cone direction [114]. For light-meson distribution amplitudes like the pion DAs or for nucleon distribution amplitudes, which we encounter in the third project of this thesis, the quantity twist is well defined. Matrix elements can be parameterised based on symmetries like Lorentz covariance, spin and parity invariance and can be subsequently related to distribution amplitudes. However, there is no proper definition for twist in the case of B-meson distribution amplitudes, albeit it is for convenience artificially introduced in many cases [110]. This parameter becomes important in the application of light-cone sum rules, where twist corresponds to the mass dimension of local operators in the QCD sum rule approach.
We are now able to state the definition of the leading- and subleading-twist two-particle B-meson distribution amplitudes, which are defined by the operator in Eq. (2.32) [84]

$$\langle 0|\,\mathcal{O}(z)\,|\bar{B}(v)\rangle = -\frac{i}{2}F(\mu)\,\mathrm{Tr}\Big[\gamma_5\Gamma\frac{1+\not{v}}{2}\Big\{\tilde{\phi}_+(u) - \frac{\not{z}}{2u}[\tilde{\phi}_+(u) - \tilde{\phi}_-(u)]\Big\}\Big] \tag{2.43}$$

for a pseudoscalar initial-state B-meson. $\tilde{\phi}_+$ and $\tilde{\phi}_-$ denote the leading- and subleading quark-antiquark distribution amplitudes in position space, respectively. Furthermore, z^μ describes a light-like four vector satisfying $z^2 = 0$ and v^μ represents the B-meson velocity in HQET with $v^2 = 1$. The quantity u is defined as $u = v \cdot z$. Notice that we are able to reproduce Eq. (2.33) by choosing $z = 0$ and $\Gamma = \gamma_\mu\gamma_5$ in Eq. (2.43).
Analogously, it is also possible to introduce three-particle distribution amplitudes [110, 115]

$$\begin{aligned}\langle 0|\,\bar{q}(z)g_sG_{\mu\nu}(wz)\Gamma h_v(0)\,|\bar{B}(v)\rangle = \frac{1}{2}F(\mu)\,\mathrm{Tr}\Big\{&\gamma_5\Gamma P_+\Big[-iv_{\mu\nu}\Big[\widetilde{\Psi}_A - \widetilde{\Psi}_V\Big]\\ &- i\sigma_{\mu\nu}\widetilde{\Psi}_V - (z_\mu v_\nu - z_\nu v_\mu)\widetilde{X}_A + (z_\mu\gamma_\nu - z_\nu\gamma_\mu)\Big[\widetilde{W} + \widetilde{Y}_A\Big]\\ &- i\epsilon_{\mu\nu\alpha\beta}z^\alpha v^\beta\gamma_5\widetilde{\widetilde{X}}_A + i\epsilon_{\mu\nu\alpha\beta}z^\alpha\gamma^\beta\gamma_5\widetilde{\widetilde{Y}}_A - (z_\mu v_\nu - z_\nu v_\mu)\not{z}\widetilde{W}\\ &+ (z_\mu\gamma_\nu - z_\nu\gamma_\mu)\not{z}\widetilde{\widetilde{Z}}\Big]\Big\}(u,w,\mu)\,,\end{aligned} \tag{2.44}$$

which contain in total eight different distribution amplitudes. In particular, we observe that in the limit $z \to 0$, i.e. when we go over to a local matrix element, we reduce Eq. (2.44) to a similar form as in Eq. (2.40). In this

context, the role of the HQET parameters $\lambda^2_{E,H}$ becomes obvious. They serve as hadronic parameters to describe the shape of the higher twist B-meson distribution amplitudes of non-local matrix elements including three-particle operators. Moreover, they are used as normalisation of the three-particle DAs $\tilde{\Psi}_{V,A}$.
Furthermore, these distribution amplitudes are often also considered in momentum space, where one defines Mellin moments of these amplitudes. While the first Mellin moment only depends on the HQET parameter $\bar{\Lambda}$, the second moments also depend on a combination of $\bar{\Lambda}$ and $\lambda^2_{E,H}$ [84, 115].
In the third part of this thesis, we compute the branching fraction of the new physics decay $B \to p\Psi$. For this, we evaluate the form factors for the $p \to B$ transition, which involve proton distribution amplitudes in the light-cone expansion. These amplitudes have been studied to great extent in the literature [116–119] and they are defined via the matrix element

$$\langle 0| T\{u(x)u(0)d(0)\} |p\rangle \ . \tag{2.45}$$

Therefore, they only involve light constituents and a decomposition based on Lorentz invariance, spin and parity makes it possible to relate this matrix element to definite twist amplitudes. We provide these details in appendix E. Currently, they are known to leading order in α_s up to twist six, which corresponds to the precision of our computation in project three.

Project I:

An automated framework to calculate beam functions to next-to-next-to leading order

Partial results of this project led to the publications [120–122].

Chapter 3

Theoretical framework

3.1 Beam functions

Beam functions are important objects which enter factorisation theorems in EFTs like SCET, since they describe the initial-state radiation at hadron colliders. In Eq. (2.3), we have encountered a typical example for a factorisation theorem including beam functions which account for collinear initial-state radiation. Moreover, we have examined a specific example in section 2.1, namely transverse-momentum resummation in Drell-Yan production, but here we aim to start from a more general definition that is valid for arbitrary observables. This is in the spirit of this work to construct an automated setup to compute beam functions to NNLO accuracy.
The definition of the quark beam function for a general observable take the form [123]

$$\frac{1}{2}\left[\frac{\bar{n}\!\!\!/}{2}\right]_{\beta\alpha}\mathcal{B}_{q/h}(x,\tau,\mu)=\sum_X \delta\Big((1-x)P_- - \sum_i k_{i,-}\Big)\,\mathcal{M}(\tau;\{k_i\}) \\ \times \langle h(P)|\,\bar{\chi}_\alpha\,|X\rangle\,\langle X|\,\chi_\beta\,|h(P)\rangle\ . \tag{3.1}$$

The δ-distribution in Eq. (3.1) accounts for the energy conservation in the collinear region. In this context, the quantity x denotes the energy fraction of the quark q going into the hard interaction. Furthermore, the phase space integral over the emitted partons X with momenta $\{k_i\}$ is implicit here. The last two important quantities are the matrix element and the measurement function $\mathcal{M}(\tau;\{k_i\})$. First of all, the measurement function $\mathcal{M}(\tau;\{k_i\})$ incorporates the full observable dependence and will be further discussed in the following section. It depends on both the momenta $\{k_i\}$ as well as the variable τ, which is the Laplace variable defining the particular measurement. Besides, the matrix element contains the SCET collinear quark field $\chi = W_c^\dagger \frac{\bar{n}\!\!\!/ n\!\!\!/}{4} q$, where W_c represents the collinear Wilson line from Eq. (2.12) pointing in the $\bar{n}$-direction, while q corresponds to the usual QCD quark field. The external state $|h(P)\rangle$ refers to a hadronic state of momentum $P^\mu = P_- \frac{n^\mu}{2}$, which renders the beam function a non-perturbative object. Nevertheless, it is a physical object encoding physical information since it

enters the factorisation theorems in SCET, although applying methods from perturbation theory for their determination is not possible at first sight. Before we show how to extract the perturbatively calculable information from Eq. (3.1), we introduce the corresponding definition of the gluon beam function [123]

$$\begin{aligned}\mathcal{B}_{g/h}(x,\tau,\mu) = &- xP_- \sum_X \delta\Big((1-x)P_- - k_{i,-}\Big)\,\mathcal{M}(\tau;\{k_i\}) \\ &\times \langle h(P)|\,\mathcal{A}^{\mu,A}_{c,\perp}\,|X\rangle\,\langle X|\,\mathcal{A}^{A}_{c,\perp,\mu}\,|h(P)\rangle\ . \end{aligned} \tag{3.2}$$

Due to the external hadronic state $|h(P)\rangle$, the gluon beam function is also genuinely a non-perturbative object. The other quantities in Eq. (3.2) are defined similarly to Eq. (3.1) and $\mathcal{A}^{\mu}_{c,\perp}$ is the gauge-invariant building block from Eq. (2.11).
In order to tackle the non-perturbative nature of Eqs. (3.1) and (3.2), we perform an operator product expansion in the regime $1/\tau \gg \Lambda_{\rm QCD}$. This requires the assumption that we predominantly work in the small τ region. The OPE introduces a perturbatively calculable matching kernel $\mathcal{I}_{i\leftarrow j}(x,\tau,\mu)$, which captures the short-distance physics at the scale $1/\tau$, whereas the long-distance non-perturbative effects are encoded in the well-known parton distribution functions (PDFs) $f_{i/h}(x,\mu)$ via

$$\mathcal{B}_{i/h}(x,\tau,\mu) = \sum_{j\in\{q,g,\bar{q}\}} \int_x^1 \frac{\mathrm{d}z}{z}\,\mathcal{I}_{i\leftarrow j}\left(\frac{x}{z},\tau,\mu\right) f_{j/h}(z,\mu) + \mathcal{O}(\tau\Lambda_{\rm QCD}),\ \ i\in\{q,g\}\ . \tag{3.3}$$

Notice that Eq. (3.3) is valid for both the quark and gluon beam function. However, the case $i=\bar{q}$ does not need to be considered separately, because it is related to the other channels via charge-conjugation invariance.
The matching kernels $\mathcal{I}_{i\leftarrow j}(x,\tau,\mu)$ are independent of the IR physics and they can therefore be obtained from partonic rather than hadronic beam functions. Due to the OPE in Eq. (3.3), they only account for the perturbative physics such that asymptotic freedom allows us to work with partons instead of complicated bound states like hadrons during the computation. As the matching kernels are defined in terms of a operator matrix element in the factorisation theorem, they do not depend on the representation of the external states [124, 125]. In this context, the partonic beam functions $\mathcal{B}_{i\leftarrow j}(x,\tau,\mu)$ are defined in analogy to Eqs. (3.1) and (3.2) except that the hadronic states are interpreted now as partonic states. If the matching is performed on-shell in dimensional regularisation, the partonic PDFs evaluate to $f_{i\leftarrow j}(x,\mu) = \delta_{ij}\delta(1-x)$ to all orders in perturbation theory and the extraction of the matching kernels reduces to the calculation of the bare partonic beam functions.
The above definitions of beam functions are valid for both SCET-I and SCET-II observables. From the technical point of view, the main difference between these two classes of observables consists in the fact that the latter are subject to rapidity divergences that are not regularised in dimensional regularisation.

$k_- \gg k_+$	$k_+ \gg k_-$	$k_+ \sim k_-$
$\left(\frac{\nu}{k_-}\right)^\alpha$	$\left(\frac{\nu}{k_+}\right)^\alpha$	$\left(\frac{\nu}{k_+ + k_-}\right)^\alpha$

Table 3.1: Implementation of symmetric analytic regulator in the collinear, anti-collinear and soft region. For each final state emission, a regulator needs to be introduced to account for rapidity divergences in the SCET-II case. For the collinear and anti-collinear region, we exploit the momentum scaling of these modes, while there is no ordering in the soft function case.

Therefore, it becomes necessary to introduce a second regulator α, which we introduce on the level of the phase-space measure [73]

$$\int \mathrm{d}^d k_i \left(\frac{\nu}{k_{i,+} + k_{i,-}}\right)^\alpha \delta(k_i^2)\Theta(k_i^0)\,. \tag{3.4}$$

Thus, we make use of a symmetric regulator in this work, which has the advantage that collinear and anti-collinear beam functions are directly related by replacing $n \leftrightarrow \bar{n}$. Table 3.1 shows the specific form of this regulator in the different phase-space regions. In the collinear and anti-collinear region, we can simplify the regulator by exploiting the different scaling of the light-cone components.
Up to NNLO, the pertubative expansion of the bare matching kernels then takes the form

$$\begin{aligned}\mathcal{I}^0_{i\leftarrow j}(x,\tau) = \delta_{ij}\,\delta(1-x) + \left(\frac{\alpha_s}{4\pi}\right)\left(\frac{\nu}{q_-}\right)^\alpha \mathcal{I}^{0,(1)}_{i\leftarrow j}(x,\tau) + \left(\frac{\alpha_s}{4\pi}\right)^2\left(\frac{\nu}{q_-}\right)^\alpha \\ \times\, \mathcal{I}^{0,(2,\mathrm{RV})}_{i\leftarrow j}(x,\tau) + \left(\frac{\alpha_s}{4\pi}\right)^2\left(\frac{\nu}{q_-}\right)^{2\alpha} \mathcal{I}^{0,(2,\mathrm{RR})}_{i\leftarrow j}(x) + \mathcal{O}\big(\alpha_s^3\big)\,.\end{aligned} \tag{3.5}$$

Note that the real-virtual (RV) and double real (RR) corrections at NNLO have different exponents in Eq. (3.5). NLO and RV contributions contain only one-particle final states, while RR contributions consist of a two-particle final state. This is why we observe the factor ν/q_- twice in Eq. (3.5). q represents the momentum going into the hard interaction and we identify $q_- = xP_-$.
Generally, the matching kernels are distribution valued, as anticipated in Eq. (3.5). In the explicit calculation, the distributions arise from terms like

$$\begin{aligned}&\text{SCET-I}: \mathcal{I}^0_{i\leftarrow j}(x,\tau) \sim (1-x)^{-1-m\epsilon}\,,\\ &\text{SCET-II}: \mathcal{I}^0_{i\leftarrow j}(x,\tau) \sim (1-x)^{-1-m\alpha}\,.\end{aligned} \tag{3.6}$$

We have developed two independent frameworks to work with these distributions: In the first approach (x-space), we expand the x-dependence in terms

of distributions

$$(1-x)^{-1-m\epsilon} = -\frac{1}{m\epsilon}\,\delta(1-x) + \left[\frac{1}{1-x}\right]_+ - m\epsilon\left[\frac{\log(1-x)}{1-x}\right]_+ + \dots\,, \tag{3.7}$$

where the plus-distribution acting on a test function $f(x)$ is defined as

$$\int_0^1 \mathrm{d}x\, f(x)\left[\frac{g(x)}{1-x}\right]_+ = \int_0^1 \mathrm{d}x\, \frac{f(x)-f(1)}{1-x}\cdot g(x)\,. \tag{3.8}$$

We will later rewrite Eq. (3.6) into a more convenient form for numerical evaluations, which has the advantage that the coefficients in front of the distributions are x-independent and the remaining (grid) contribution is finite in the limit $x \to 1$. In order to deal with the SCET-II case, we just need to replace $\epsilon \to \alpha$.
However, we will resolve the distributions via

$$\widehat{\mathcal{I}}^0_{i\leftarrow j}(N,\tau) = \int_0^1 \mathrm{d}x\; x^{N-1}\,\mathcal{I}^0_{i\leftarrow j}(x,\tau) \tag{3.9}$$

in the second approach (N-space). The transformed matching kernels are thus regular functions of the Mellin variable N, although this comes with the disadvantage of one additional integration affecting the numerical accuracy.

3.2 Measurement function

According to the definitions in Eqs. (3.1) and (3.2), the beam functions consist schematically of three parts, namely the collinear matrix element, the measurement function and an integration over the phase space of the emitted particles. Moreover, the bare beam functions are subject to divergences in the dimensional regulator ϵ and possibly in the rapidity regulator α. These divergences only depend on the underlying matrix element and are observable independent. Hence, the dependence on the observable is solely encoded in the measurement function $\mathcal{M}(\tau;\{k_i\})$, which acts like a weight function in the phase space enhancing and suppressing certain contributions depending on the observable. This observation is the key ingredient of our approach. Our goal consists of isolating the divergences into monomial form first and then performing the remaining phase-space integrations numerically. To this end, we have to find a suitable parameterisation of the measurement function. Specifically, we assume that the measurement function can be written as

$$\mathcal{M}(\tau;\{k_i\}) = \exp[-\tau\omega(\{k_i\})]\,, \tag{3.10}$$

which typically arises as the result of a Laplace transformation and τ is the corresponding Laplace variable. The generic form of the function $\omega(\{k_i\})$ is constrained by a few assumptions that are similar to the requirements postulated for soft functions in the `SoftSERVE` framework [48, 49]:

(i) **Measurement function:** Our framework requires the measurement function to be strictly positive $\mathrm{Re}(\omega(\{k_i\})) > 0$ such that the convergence of the phase space integrals is guaranteed. We only allow for a vanishing measurement in configurations with zero weight in the phase space.

(ii) **Mass dimension**: The Laplace variable τ is supposed to have mass dimension 1/mass, therefore the measurement $\omega(\{k_i\})$ possesses mass dimension 1.

(iii) **Azimuthal dependence:** We restrict the function $\omega(\{k_i\})$ to only depend on one angle Θ_i per emitted particle in the $(d-2)$-dimensional transverse plane. Therefore, the emissions are measured with respect to a reference vector v^μ. But the function $\omega(\{k_i\})$ is in addition allowed to contain relative angles Θ_{ij} in the transverse plane between two emissions with transverse momenta $k_\perp^i$ and $k_\perp^j$.

Generally, assumption (ii) could be relaxed in the future. Although we did not encounter any observable in the beam function case so far which possesses a mass dimension different from one, there are examples like jet rates in the jet function case, which violate this assumption. The generalisation to an arbitrary mass dimension is, however, rather straight-forward in our approach. In contrast to that we identify requirements (i) and (iii) as crucial to our framework. According to requirement (i), the measurement $\omega(\{k_i\})$ should be strictly positive to ensure convergence of the numerical integrations. Though, we also face observables like transverse-momentum resummation, which seem to violate this condition at first sight. Due to an additional Fourier transformation, the measurement becomes imaginary. In chapter 8, we show explicitly how we can rewrite the measurement function such that it becomes positive and vanishes only for phase-space points with zero weight. Whereas the original measurement is formulated as a δ-function for most observables, which transforms into the form in Eq. (3.10) after a Laplace transformation, there are some observables like jet-veto resummation which are expressed in terms of a Θ-function. We will explain later in chapter 8 that these type of measurements can also be brought into the form of Eq. (3.10) via a Laplace transformation and that they can also be handled by our approach [49]. The azimuthal dependence required in assumption (iii) becomes important in the parameterisation of the angular integrations, which we discuss in section 5.2.2.

3.3 Accuracy of the framework and connection to phenomenology

After discussing the general form of the beam function and the constraints on the allowed measurements, we focus now on the phenomenological accuracy and how the new results of this work influence the current state-of-the-art precision in the literature. In order to accomplish that, we need to introduce a counting scheme for the logarithmic accuracy as well as the ingredients that are needed to realise this accuracy. In SCET, logarithms are resummed by solving the corresponding RGEs. For instance, a typical RGE is of the form

$$\frac{\mathrm{d}H(Q,\mu)}{\mathrm{d}\ln\mu} = \left[-2C_F\Gamma^i_{\mathrm{cusp}}(\alpha_s)\ln\left(\frac{\mu^2}{Q^2}\right) + \gamma_H(\alpha_s)\right] H(Q,\mu)\,, \tag{3.11}$$

where

$$\Gamma^i_{\mathrm{cusp}}(\alpha_s) = \sum_{m=0}^{\infty}\left(\frac{\alpha_s}{4\pi}\right)^{m+1}\Gamma^i_m \tag{3.12}$$

is the cusp anomalous dimension and

$$\gamma^{i,H}(\alpha_s) = \sum_{m=0}^{\infty}\left(\frac{\alpha_s}{4\pi}\right)^{m+1}\gamma^{i,H}_m \tag{3.13}$$

denotes the non-cusp anomalous dimension of the hard function $H(Q,\mu)$. The solution of the RGE requires a boundary term, which we call c_H. Similar relations hold for the beam and soft functions and for the former we denote the corresponding boundary terms by $\mathcal{I}^{(m)}_{i\leftarrow j}(x)$ as they are boundary terms of the matching kernels from Eq. (3.5). We will also see later that the relevant anomalous dimension for SCET-II observables are the anomaly coefficients d_m. Finally, we need as an input for the renormalisation of the strong coupling constant α_s the QCD β-function.
With these general ingredients for renormalisation and resummation, we can now define a proper counting for the logarithmic accuracy in table 3.2 and state individually to which order in α_s we need each quantity. In order to achieve resummation up to NNLL′ accuracy, we need the observable independent cusp anomalous dimension Γ^i_{cusp} to $\mathcal{O}(\alpha_s^3)$, which is currently known up to four loop order [126–128]. Furthermore, we require the QCD β-function to order $\mathcal{O}(\alpha_s^3)$, which is currently known up to $\mathcal{O}(\alpha_s^5)$ [129, 130]. Its expansion in α_s is given by

$$\beta(\alpha_s) = \sum_{m=0}^{\infty}\left(\frac{\alpha_s}{4\pi}\right)^{m+1}\beta_m\,. \tag{3.14}$$

In addition to that we need the hard non-cusp anomalous dimension $\gamma^{i,H}$ and c_H to NNLO. These quantities are related to the underlying hard scattering process and encode the UV physics according to the factorisation theorem

	LL	NLL	NNLL	NNLL′	N^{3}LL
Γ^i_{cusp}	Γ^i_0	Γ^i_1	Γ^i_2	Γ^i_2	Γ^i_3
β	β_0	β_1	β_2	β_2	β_3
$\gamma^{i,H}$	-	$\gamma^{i,H}_0$	$\gamma^{i,H}_1$	$\gamma^{i,H}_1$	$\gamma^{i,H}_2$
$c_{H,S}$	$c^{(0)}_{H,S}$	$c^{(0)}_{H,S}$	$c^{(1)}_{H,S}$	$c^{(2)}_{H,S}$	$c^{(2)}_{H,S}$
$F_{i\bar{i}}$	-	d^i_1	d^i_2	d^i_2	d^i_3
$\gamma^{i,\{B,S\}}$	-	$\gamma^{i,\{B,S\}}_0$	$\gamma^{i,\{B,S\}}_1$	$\gamma^{i,\{B,S\}}_1$	$\gamma^{i,\{B,S\}}_2$
$\mathcal{I}_{i\leftarrow j}(x)$	$\mathcal{I}^{(0)}_{i\leftarrow j}(x)$	$\mathcal{I}^{(0)}_{i\leftarrow j}(x)$	$\mathcal{I}^{(1)}_{i\leftarrow j}(x)$	$\mathcal{I}^{(2)}_{i\leftarrow j}(x)$	$\mathcal{I}^{(2)}_{i\leftarrow j}(x)$

Table 3.2: Inputs for the anomalous dimensions and matching corrections in order to obtain the desired logarithmic accuracy. Notice that the expressions in blue correspond to the input to the NNLL′ accuracy which are either provided by this work or the `SoftSERVE` framework. The index i indicates the parton going into the hard interaction and defines the channel. Depending on the channel, we can identify by this index whether the cusp and non-cusp anomalous dimensions are taken in fundamental or adjoint representation.

in Eq. (2.3). Specifically, for colour-singlet processes like Drell-Yan or Higgs production, quark and gluon form factors [131, 132] provide values for the non-cusp anomalous dimension $\gamma^{i,H}$ as well as the matching correction c_H. Generally, these quantities are observable independent, but the soft function and the collinear anomaly exponent in the SCET-II case depend on the observable. For most observables in this work, the non-cusp anomalous dimension is known to $\mathcal{O}(\alpha_s^2)$ [78, 79, 124, 125]. But for generic observables, it becomes necessary to use `SoftSERVE` which provides $\gamma^{i,S}$, c_S and $d^i_{1,2}$ numerically. Especially in the SCET-II case, the soft function depends on the regulator choice for the rapidity divergences and hence some analytical results from the literature might not be applicable for specific problems. In general, the `SoftSERVE` framework allows for both the rapidity renomalisation group approach as well as the collinear anomaly approach to resum rapidity divergences such that the user has more freedom here.
Finally, at least for processes with only initial-state radiation which we consider here, we need the non-cusp anomalous dimension $\gamma^{i,B}$ and matching correction for the beam function for resummation. In principle, it is possible to extract the quantity $\gamma^{i,B}$ from our computation, however we use the soft non-cusp anomalous dimension via the consistency relation

$$\gamma^{i,H} + \gamma^{i,S} + \underbrace{\gamma^{i,B} + \gamma^{i,\bar{B}}}_{=2\gamma^{i,B}} = 0 \tag{3.15}$$

for the factorisation theorem in Eq. (2.3) in order to check our renormalisation procedure. In the case of final-state radiation described by jet functions,

we would need to add the jet non-cusp anomalous dimension as well. The advantage in using the soft anomalous dimension lies in the better numerical accuracy, since the expressions in the soft function calculation, i.e. the matrix element and the phase space are considerably simpler compared to the beam function computation. Therefore, we make use of the input from the soft function as a check of our calculation.
By providing the NNLO boundary term for the matching kernels $\mathcal{I}_{i\leftarrow j}(x)$, automated setups for resummation can be pushed to NNLL$'$ accuracy, which is beyond reach for many observables so far. The blue quantities in table 3.2 illustrate the expressions which we are able to provide within our automated framework. As we have discussed above, the NNLO non-cusp anomalous dimensions $\gamma_1^{i,\{B,S\}}$ or the NNLO anomaly coefficients d_2^i are known to this order for both quark and gluon channels, hence they are a useful check for our setup. For SCET-II observables, renormalisation is more involved due to the rapidity divergences, but the counting in table 3.2 is still valid if the SCET-I matching kernels $\mathcal{I}_{i\leftarrow j}(x)$ get replaced by the so-called refactorised matching kernels $I_{i\leftarrow j}(x)$. Moreover, this scheme works similarly for N-space expressions, the expressions in x-space just need to be Mellin transformed with Eq. (3.9).

Chapter 4

NLO beam functions

This chapter is devoted to the careful analysis of beam function expressions up to next-to leading order (NLO) accuracy in the strong coupling constant α_s. They are related to the matching kernels via Eq. (3.3). In order to evaluate the matching kernels to NLO, we derive a master formula which has a closed analytical form and with which we are capable of calculating these terms to NLO accuracy for a general class of observables. We treat quark and gluon channels separately, although the computational steps are closely related to each other. The considerations in this chapter are based on bare quantities denoted by the index "0", we translate all these quantities to renormalised objects in chapter 6.

4.1 The quark beam function at NLO

As argued in section 3.1, the matching kernels can be determined from partonic instead of hadronic beam functions. We thus start from the relation

$$\frac{1}{2}\left[\frac{\not{n}}{2}\right]_{\beta\alpha}\mathcal{I}^0_{q\leftarrow j}(x,\tau) = \sum_X \delta\Big((1-x)P_- - \sum_i k_{i,-}\Big)\,\mathcal{M}(\tau;\{k_i\}) \times \langle j(P)|\,\bar{\chi}_\alpha\,|X\rangle\,\langle X|\,\chi_\beta\,|j(P)\rangle\ . \tag{4.1}$$

Since we only work to NLO accuracy for now, the final state $|X\rangle$ consists of a gluon or antiquark with momentum k. Furthermore, the pure virtual corrections at NLO lead to scaleless integrals in dimensional regularisation and therefore vanish. As a consequence, the sum over X will be replaced by the phase-space integral over k.
We now start to calculate the matrix element in Eq. (4.1), which is shown in form of a Feynman diagram in figure 4.1.

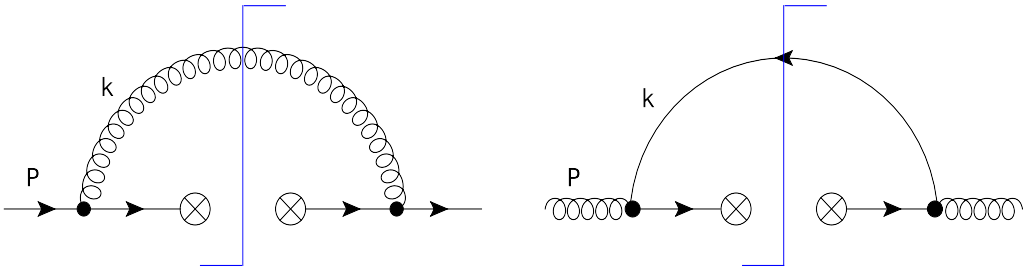

Figure 4.1: NLO Feynman diagram for the diagonal $q \to q$ and off-diagonal $g \to q$ matching kernels. These diagrams are the only contributions in light-cone gauge.

Since we work in light-cone gauge, we only need to evaluate the diagrams in figure 4.1 for the two quark channels, while the diagrams in figure 4.2 vanish for this particular gauge. Moreover, it is convenient for the calculation to project out the spinor structure by multiplying the expression in Eq. (4.1) with $\left[\frac{\bar{n}\!\!\!/}{2}\right]_{\alpha\beta}$. The matrix element can then be computed with QCD Feynman rules. As an example, we evaluate the matrix element for the $q \to q$ matching kernel

$$\begin{aligned}
\mathcal{M}^{(1)}_{q\leftarrow q} &:= \langle q(P)|\,\bar{\chi}_\alpha\,|k\rangle\,\frac{\bar{n}\!\!\!/_{\alpha\beta}}{2}\,\langle k|\,\chi_\beta\,|q(P)\rangle \\
&= \frac{i(g_s^0)^2}{2}\frac{1}{N_c}\Big(-g_{\mu\nu}+\frac{\bar{n}_\mu k_\nu+\bar{n}_\nu k_\mu}{\bar{n}\cdot k}\Big)\frac{1}{k^2+i0^+}\mathrm{tr}\Big[T^A T^B\delta^{AB}\Big] \\
&\quad\times \mathrm{Tr}\Big[P\!\!\!/\gamma^\nu\frac{(P\!\!\!/-k\!\!\!/)}{(P-k)^2+i0^+}\frac{\bar{n}\!\!\!/ n\!\!\!/}{4}\frac{\bar{n}\!\!\!/}{2}\frac{n\!\!\!/\bar{n}\!\!\!/}{4}\frac{(P\!\!\!/-k\!\!\!/)}{(P-k)^2+i0^+}\gamma^\mu\Big] \\
&\equiv \frac{\alpha_s^0}{4\pi}\,\overline{\mathcal{M}}^{(1)}_{q\leftarrow q}\cdot\frac{i}{k^2+i0^+}\,.
\end{aligned} \tag{4.2}$$

Although we work in the framework of SCET, it is possible to use ordinary QCD Feynman rules for the computation [58]. We observe that the SCET Lagrangian for the collinear and anti-collinear fields are form-invariant with respect to the Lagrangian density in QCD for both the SCET-I and -II case after the corresponding transformations. A Lorentz boost, which leaves the Dirac bilinears inside the Lagrangian density invariant, transforms the collinear and anti-collinear fields back to the ordinary QCD fields [1].

[1] This statement only holds to leading power in λ as the decoupling transformation factorises each region only at this order.

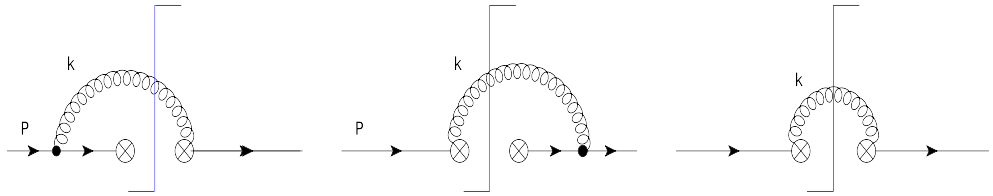

Figure 4.2: NLO Feynman diagrams, which additionally to figure 4.1 contribute in Feynman gauge for the $q \to q$ matching kernel at NLO. In light-cone gauge, we can prove that these diagrams vanish. Similar diagrams exist for the other channels and vanish due to the same reason.

In Eq. (4.2), we have already included the spin averaging factor $\frac{1}{2}$ from the incoming quark as well as the colour averaging factor $\frac{1}{N_c}$. The next step is to evaluate the traces and express the scalar products in light-cone coordinates

$$\overline{\mathcal{M}}^{(1)}_{q\leftarrow q} = 32\pi^2\, C_F\, \frac{(1-\epsilon)k_-^2 + 2P_-^2 - 2k_-P_-}{(2k\cdot P)k_-}\,. \tag{4.3}$$

We assume that the incoming quark is aligned along the n-axis, hence $P^\mu = P_-\frac{n^\mu}{2}$. For the off-diagonal quark channel, i.e. the $g \to q$ channel, we can proceed similarly to Eq. (4.2) and obtain for the matrix element

$$\overline{\mathcal{M}}^{(1)}_{q\leftarrow g} = 32\pi^2\, T_F \left[\frac{1}{k_+} + \frac{2}{1-\epsilon}\Big(\frac{k_-^2}{k_+P_-^2} - \frac{k_-}{k_+P_-}\Big)\right]. \tag{4.4}$$

Until now, we have treated the Feynman diagram in figure 4.1 as an ordinary loop integral. But since there is a cut through the gluon line in these diagrams, which is indicated by the introduction of a full set of states in Eq. (4.1), we need to apply Cutkosky rules [133]. They can be summarised as follows [2]:

- Cut through a Feynman diagram in all possible ways. In physical terms, this corresponds to putting cut particles on-shell.
- Replace every propagator with a cut by

$$\frac{1}{k^2 - m^2 + i0^+} = -2\pi i\delta(k^2 - m^2)\Theta(k^0)\,. \tag{4.5}$$

- Sum over all possible cuts to obtain the complete contribution.

Therefore, we need to replace the gluon propagator $\frac{1}{k^2+i0^+}$ in Eq. (4.2) by $-2\pi i\delta(k^2)\Theta(k^0)$. The quark matching kernels become

$$\begin{aligned}\mathcal{I}^0_{q\leftarrow j}(x,\tau) = \delta_{qj}\,\delta(1-x) + \left(\frac{\alpha_s^0}{4\pi}\right)\cdot\frac{1}{2}\int\frac{\mathrm{d}k_+}{(2\pi)}\int\frac{\mathrm{d}k_-}{(2\pi)}\int\frac{\mathrm{d}^{d-2}k_\perp}{(2\pi)^{d-2}}\left(\frac{\nu}{k_-}\right)^\alpha \\ \times\,\delta\Big((1-x)P_- - k_-\Big)\cdot i\,\overline{\mathcal{M}}^{(1)}_{q\leftarrow j}\,(-2\pi i)\delta(k^2)\Theta(k^0)\,\mathcal{M}(\tau;k) \\ + \mathcal{O}\Big(\big(\alpha_s^0\big)^2\Big)\,,\end{aligned} \tag{4.6}$$

[2] These rules are strictly speaking only applicable in the physical timelike region. We refer to [134] for a generalisation to other regions.

where we have expressed the phase-space integral in terms of light-cone coordinates.
We can make use of the two δ-distributions to remove the integration over k_+ and k_-, since $k^2 = k_+k_- - k_T^2$. In this context, we remind ourselves that $\vec{k}_\perp^2 = -\vec{k}_T^2 \equiv k_T^2$. Furthermore, the $(d-2)$-dimensional integral over the transverse components can be rewritten by using spherical coordinates

$$\begin{aligned}\int \mathrm{d}^{d-2}k_\perp &= \int \mathrm{d}\Omega_{d-3} \int_0^\infty \mathrm{d}k_T\, k_T^{d-3} \\ &= \frac{2\pi^{1-\epsilon}}{\sqrt{\pi}\,\Gamma\left(\frac{1}{2}-\epsilon\right)} \int_{-1}^{1} \mathrm{d}\cos\Theta_k \sin^{-1-2\epsilon}(\Theta_k) \int_0^\infty \mathrm{d}k_T\, k_T^{d-3}\,. \end{aligned} \tag{4.7}$$

In the last line, we have parameterised the angular integration by an angle Θ_k, which describes the angle between a reference vector $v_\perp^\mu$ that is imposed by the observable and the emitted gluon in the transverse plane. Since we work in the $(d-2)$-dimensional plane, one angle is sufficient to specify the kinematic structure of this process.
Similar to the work on soft and jet functions, we can state a general ansatz for the measurement function obeying all conditions from section 3.2. For this, we parameterise the phase-space integrals in the form

$$k_- = (1-x)P_-\,, \qquad\qquad k_+ = \frac{k_T^2}{(1-x)P_-} \tag{4.8}$$

with the momentum fraction $x \in [0,1]$. As we can deduce from Eq. (4.6), the large k_- - component in the collinear region is parameterised by $(1-x)P_-$ and hence the fraction xP_- goes into the hard interaction. The advantage of this parameterisation is that we can write the divergences of the expressions in Eq. (4.6) explicitly in terms of monomials, which is easier for the investigation later. Moreover, the integration domain is restricted between $[0,1]$, which is convenient for numerical Monte-Carlo integrations, albeit numerical integrations are not necessary at the NLO level. Since we only encounter a one-particle phase space generated by the emitted gluon with momentum k, we can state the beam function expressions completely analytically, at least for the examples presented in this work.
Using the parameterisation in Eq. (4.8), we propose the following general ansatz for the measurement function:

$$\mathcal{M}_1(\tau;k) = \exp\left[-\tau k_T \left(\frac{k_T}{(1-x)P_-}\right)^n f(\Theta_k)\right]. \tag{4.9}$$

It has precisely the form as we indicate in Eq. (3.10), thus we identify the measurement $\omega(\{k_i\})$ to be

$$\omega(k) = k_T \left(\frac{k_T}{(1-x)P_-}\right)^n f(\Theta_k)\,. \tag{4.10}$$

Since we work in Laplace space according to the discussion in section 3.2, the variable τ represents again the Laplace variable with mass dimension

$[\tau] = -1$ in this context. Therefore, we include an additional factor k_T in Eq. (4.9) to render the argument of the exponential function dimensionless. The last factor is inspired by the definition of the NLO measurement function for the soft function [48, 49] and jet function [50]. In fact, we can derive the exact form of these factors by exploiting that the collinear limit of the NLO soft function and the soft limit of Eq. (4.9) commute [50]. Generally, there is also a possible angular dependence hidden inside the measurement function $\mathcal{M}(\tau; k)$ in Eq. (4.6), thus we need to investigate the form of this expression in more detail. As long as the observable belongs to the class of observables that are allowed in our framework, see section 3.2 for more details, it is possible to characterise this observable solely by a function f and a number n at this order in α_s. The angular dependence is then captured by the function f, while n corresponds to the same number which has been introduced in the case of soft functions [48, 49] as well as jet functions [50]. It is related to the power counting of the momentum modes. In particular the value $n = 0$ defines observables which belong to the class of SCET-II, values $n \neq 0$ define SCET-I observables [48] [3]. Furthermore, the function $f(\Theta_k)$ might depend on the variable x, but so far we did not see any observable with an explicit x-dependence at NLO.
Applying the parameterisation from Eq. (4.8) and the ansatz for the measurement function (4.9), we finally derive the master formula to compute the $q \to q$ and $g \to q$ matching kernels to $\mathcal{O}(\alpha_s)$

$$\begin{aligned}\mathcal{I}^0_{q\leftarrow q}(x,\tau) = \; & \delta(1-x) + \frac{4}{\sqrt{\pi}(n+1)}\frac{\alpha_s C_F}{4\pi}\left(\frac{\mu^2\bar{\tau}^{\frac{2}{n+1}}}{q_-^{\frac{2n}{n+1}}}\right)^{\epsilon}\left(\frac{\nu}{q_-}\right)^{\alpha}\frac{\Gamma\left(\frac{-2\epsilon}{n+1}\right)}{\Gamma\left(\frac{1}{2}-\epsilon\right)} \\ & \times x^{\frac{2n\epsilon}{n+1}+\alpha}\exp\left(\gamma_E\epsilon\left(\frac{-2}{n+1}+1\right)\right)\Big(1-x\Big)^{-1-\frac{2n\epsilon}{n+1}-\alpha}\left[(1-\epsilon)(1-x)^2+2x\right] \\ & \times \int_{-1}^{1}\mathrm{d}\cos(\Theta_k)\;\sin^{-1-2\epsilon}(\Theta_k) f^{\frac{2\epsilon}{n+1}}(\Theta_k) + \mathcal{O}\Big(\alpha_s^2\Big)\,, \end{aligned} \tag{4.11}$$

$$\begin{aligned}\mathcal{I}^0_{q\leftarrow g}(x,\tau) = & \frac{4}{\sqrt{\pi}(n+1)}\frac{\alpha_s T_F}{4\pi}\left(\frac{\mu^2\bar{\tau}^{\frac{2}{n+1}}}{q_-^{\frac{2n}{n+1}}}\right)^{\epsilon}\left(\frac{\nu}{q_-}\right)^{\alpha}\frac{\Gamma\left(\frac{-2\epsilon}{n+1}\right)}{\Gamma\left(\frac{1}{2}-\epsilon\right)}\Big(1-x\Big)^{-\frac{2n\epsilon}{n+1}-\alpha} \\ & \times x^{\frac{2n\epsilon}{n+1}+\alpha}\exp\left(\gamma_E\epsilon\left(\frac{-2}{n+1}+1\right)\right)\left[1-\frac{2x(1-x)}{1-\epsilon}\right] \\ & \times \int_{-1}^{1}\mathrm{d}\cos(\Theta_k)\;\sin^{-1-2\epsilon}(\Theta_k) f^{\frac{2\epsilon}{n+1}}(\Theta_k) + \mathcal{O}\Big(\alpha_s^2\Big). \end{aligned} \tag{4.12}$$

Here, q_- corresponds to the momentum going into the hard interaction and is defined via $q_- = xP_-$. Moreover, we have already replaced the bare coupling

[3] In Ref. [50], it is explicitly shown that it is necessary to use the same parameter n for soft and jet functions in order for the soft limit of the jet function measurement and for the collinear limit of the soft function measurement to coincide. This argumentation applies similarly to the beam function case.

α_s^0 by its renormalised counterpart, which is given by

$$\alpha_s^0 = Z_{\alpha_s}\mu^{2\epsilon}\alpha_s e^{\gamma_E\epsilon}(4\pi)^{-\epsilon} \qquad \text{and} \qquad Z_{\alpha_s} = 1 - \frac{\alpha_s}{4\pi}\frac{\beta_0}{\epsilon} + \mathcal{O}\Big(\alpha_s^2\Big)\,. \quad (4.13)$$

We will elaborate in chapter 6 more on these relations.
In Eqs. (4.11) and (4.12), we perform the k_T-integration analytically, but leave the angular integration open due to the observable-dependent function $f(\Theta_k)$. On top of that we implement the notation $\bar{\tau} = \tau e^{\gamma_E}$. By fixing the number n as well as the measurement function $f(\Theta_k)$, we specify an observable completely. Moreover, we notice that the matrix element expressions from Eqs. (4.3) and (4.4) are already embedded into the master formulae after applying the NLO parametrisation in Eq. (4.8).
There is a direct relation between the timelike splitting functions, which also show up in the master formulae for the jet function [50] and the expressions in (4.11) and (4.12) via crossing symmetry [135]:

Jet function		Beam function
• $q^* \to q$: $k_- = z\,Q_-$ $Q_- = P_- + k_-$	$\xrightarrow{Q_-\to -Q_-;\;\; P_-\to -P_-}$	• $q \to q^*$: $k_- = (1-x)\,P_-$ $Q_- = P_- - k_- \equiv q_-$
• $q^* \to g$: $k_- = (1-z)\,Q_-$ $Q_- = P_- + k_-$	$\xrightarrow{P_-\to -P_-}$	• $g \to q^*$: $k_- = (1-x)\,Q_-$ $Q_- = -P_- + k_-$

Figure 4.3 illustrates the assignments of the energy fractions in the jet function and beam function case. For the jet function, the quantity z corresponds to the energy fraction of the gluon in the diagonal channel, which we denote by $(1-x)$ in the beam function case.

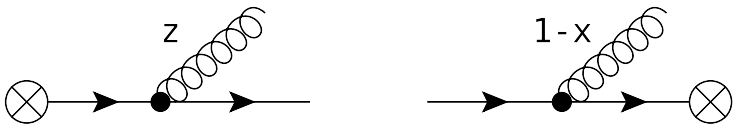

Figure 4.3: Momentum fraction assignment for the jet function and beam function on the left and right respectively. The momenta P and k are assigned according to figure 4.1.

In order to obtain the expressions for the beam function, crossing requires to flip the incoming quark from the hard interaction in the jet function case

to the final state, while the final state quark q is moved to the initial state. This corresponds to the momentum change $Q_- \to -Q_-$ and $P_- \to -P_-$. Additionally, we can immediately relate the different energy fractions with each other

$$\frac{k_-}{Q_-} = z \to -\frac{k_-}{Q_-} = \frac{1-x}{x} \tag{4.14}$$

and therefore

$$z \to -\frac{1-x}{x}\,. \tag{4.15}$$

Eq. (4.15) allows us in principle to take the jet function expression, for instance provided in [50], and extract the beam function expression. The matrix elements are directly related to each other via the crossing relation, while we need to adjust the phase-space factors. Furthermore, the colour factor does not change for this particular channel since we interchange two quarks between initial and final state. However, the situation changes once we consider the off-diagonal $g \to q$ channel. The relations are now slightly modified compared to the diagonal case, since we first interchange the final-state quark and gluon in the timelike domain, before we perform the crossing. Hence, we only need to flip the momentum $P_- \to -P_-$ of the initial-state quark to the final-state quark now. Thus, the crossing relation for the energy fractions changes slightly

$$\frac{k_-}{Q_-} = 1 - z \to -\frac{1-x}{x} \quad \Leftrightarrow \quad z \to \frac{1}{x}\,. \tag{4.16}$$

In addition to that the colour factors of the contributions change according to

$$C_F = \frac{(N_c^2-1)}{N_c}\,T_F \to \frac{-2N_c}{(d-2)(N_c^2-1)}\,\frac{(N_c^2-1)}{N_c}\,T_F = \frac{-T_F}{1-\epsilon}\,. \tag{4.17}$$

The factor $2N_c$ in the numerator in Eq. (4.17) corrects for the spin average factor $1/2$ and for the colour average factor $1/N_c$, which occur in the case of an initial-state quark. Since we interchange the final-state gluon with the initial-state quark during the crossing procedure in the off-diagonal channel, the corresponding averaging factors are now $1/(d-2)$ for the polarisation of a gluon in dimensional regularisation and N_c^2-1 for the colour average. Notice that the additional minus appears because we only flip one quark instead of two in the diagonal case.
With Eqs. (4.15) and (4.16), we can relate the timelike splitting functions from e.g. [136] to our expressions in Eq. (4.11) and (4.12). For this, it is convenient to write the splitting functions in terms of an expansion in α_s, similar as for the different quantities in section 3.3

$$\mathbb{P}_{q\to gq^*}(x) = \sum_{k=0}^{\infty} \left(\frac{\alpha_s}{4\pi}\right)^{k+1} \mathbb{P}^{(k)}_{q\to gq^*}(x) \tag{4.18}$$

and analogously for splitting functions with different particle content. The leading order quark splitting functions, transform under Eqs. (4.15) and (4.16) in the following way

$$\begin{aligned}\mathbb{P}^{(0)}_{q^*\to gq}(z) &= \frac{C_F}{z}((1-\epsilon)z^2+2(1-z)) \\ &\xrightarrow{(4.15)} \frac{-C_F}{(1-x)x}\left[(1-\epsilon)(1-x)^2+2x\right] \equiv -\frac{1}{x}\,\mathbb{P}^{(0)}_{q\to gq^*}(x) \quad (4.19)\\ \mathbb{P}^{(0)}_{q^*\to gq}(z) &= \frac{C_F}{z}((1-\epsilon)z^2+2(1-z)) \\ &\xrightarrow{(4.16)} -\frac{1}{x}\,T_F\left[1-\frac{2x(1-x)}{1-\epsilon}\right] \equiv -\frac{1}{x}\,\mathbb{P}^{(0)}_{g\to\bar{q}q^*}(x)\,. \quad (4.20)\end{aligned}$$

We encounter an additional factor $-\frac{1}{x}$, which will be cancelled by a factor $Q_- \to -q_- = -xP_-$ from the phase space. The relation in Eq. (4.20) is an example for a off-diagonal channel, where we first need to interchange the final-state quark and gluon in the jet function expression and subsequently perform the crossing. This is reflected by the crossing in Eq. (4.16), but also in the change of the colour factors. In the following discussion, in particular in the investigation of the real-virtual (RV) and real-real (RR) contributions which are part of the $\mathcal{I}^{(2)}_{i\leftarrow j}$ matching kernels, we will heavily exploit this symmetry.

From Eqs. (4.11) and (4.12), we can read off the divergence structure of the matching kernels. In addition to the singularity expressed in terms of the Γ-function $\Gamma\big(\frac{-2\epsilon}{n+1}\big)$, which originates from the quark becoming collinear to the gluon, there is another singularity located at $x\to 1$ for the diagonal matching kernel. Here, this singularity accounts for the emitted gluon becoming soft. In the following, we resolve this kind of singularities in terms of distributions

$$(1-x)^{-1-\frac{2n\epsilon}{n+1}} = -\frac{n+1}{2n\epsilon}\delta(1-x)+\left[\frac{1}{1-x}\right]_+ - \frac{2n\epsilon}{n+1}\left[\frac{\log(1-x)}{1-x}\right]_+ + \dots\,, \quad (4.21)$$

which has the advantage that the poles become explicit now.

The special case $n=0$ requires further investigation as it characterises SCET-II observables. According to the discussion below Eq. (3.5), we introduce analytic regulators for each final-state emission to regularise rapidity divergences. We can also explicitly observe the regularisation problem in Eq. (4.11). If we set $n=0$, the divergence in $x\to 1$ would not be properly regularised. We will encounter several SCET-II observables in chapter 8, where poles in the rapidity variable α will occur.

4.2 The gluon beam function at NLO

Similarly to the previous section, we can investigate the gluon beam function at NLO in more detail. For this, we start from

$$\begin{aligned}\mathcal{I}^0_{g\leftarrow j}(x,\tau) =& -xP_- \sum_X \delta\Big((1-x)P_- - \sum_i k_{i,-}\Big)\,\mathcal{M}(\tau;\{k_i\}) \\ &\times \langle j(P)|\,\mathcal{A}^{\mu,A}_{c,\perp}\,|X\rangle\,\langle X|\,\mathcal{A}^{A}_{c,\perp,\mu}\,|j(P)\rangle\ . \end{aligned} \tag{4.22}$$

Since we also work to $\mathcal{O}(\alpha_s)$ for the gluon beam function, we encounter again a one-particle final state consisting of an emitted quark or gluon with momentum k. For the measurement function $\mathcal{M}(\tau;\{k_i\})$, we still use the general ansatz provided in Eq. (4.9) as well as the parameterisation (4.8) due to the similar kinematical situation.

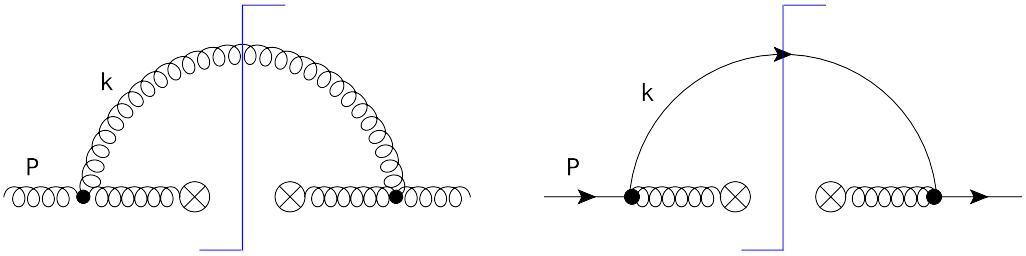

Figure 4.4: NLO Feynman diagram for the diagonal $g \to g$ and off-diagonal $q \to g$ matching kernels, which give the only contributions in light-cone gauge.

Applying QCD Feynman rules for the diagrams depicted in figure 4.4, we obtain the matrix elements in light-cone coordinates

$$\overline{\mathcal{M}}^{(1)}_{g\leftarrow g} = -\,64\pi^2 C_A \frac{(k_-^2 + P_-^2 - k_- P_-)^2}{(2k\cdot P)k_- P_-(k_- - P_-)^2} \tag{4.23}$$

$$\overline{\mathcal{M}}^{(1)}_{g\leftarrow q} = -\,\frac{16\pi^2 C_F}{2k\cdot P}\left[2(1-\epsilon) + \frac{4k_- P_-}{(k_- - P_-)^2}\right] \tag{4.24}$$

Proceeding similarly to section 4.1, we finally end up with the following master formulae for the two channels:

$$\begin{aligned}\mathcal{I}^0_{g\leftarrow g}(\tau,x) =& \,\delta(1-x) + \frac{4}{\sqrt{\pi}(n+1)}\frac{\alpha_s C_A}{4\pi}\left(\frac{\mu^2\bar{\tau}^{\frac{2}{n+1}}}{q_-^{\frac{2n}{n+1}}}\right)^{\epsilon}\left(\frac{\nu}{q_-}\right)^{\alpha} x^{\frac{2n\epsilon}{n+1}+\alpha}\frac{\Gamma\left(\frac{-2\epsilon}{n+1}\right)}{\Gamma\left(\frac{1}{2}-\epsilon\right)} \\ &\times \exp\left(\gamma_E\epsilon\left(\frac{-2}{n+1}+1\right)\right)\Big(1-x\Big)^{-1-\frac{2n\epsilon}{n+1}-\alpha}\left[\frac{2(1-(1-x)x)^2}{x}\right] \\ &\times \int_{-1}^{1} \mathrm{d}\cos(\theta)\ \sin^{-1-2\epsilon}(\theta) f^{\frac{2\epsilon}{n+1}}(\theta) + \mathcal{O}\Big(\alpha_s^2\Big)\,, \end{aligned} \tag{4.25}$$

$$\mathcal{I}^0_{g\leftarrow q}(\tau,x) = \frac{4}{\sqrt{\pi}(n+1)}\frac{\alpha_s C_F}{4\pi}\left(\frac{\mu^2\bar{\tau}^{\frac{2}{n+1}}}{q_-^{\frac{2n}{n+1}}}\right)^{\epsilon}\left(\frac{\nu}{q_-}\right)^{\alpha}\frac{\Gamma\left(\frac{-2\epsilon}{n+1}\right)}{\Gamma\left(\frac{1}{2}-\epsilon\right)}\Big(1-x\Big)^{-\frac{2n\epsilon}{n+1}-\alpha}$$
$$\times\exp\left(\gamma_E\epsilon\left(\frac{-2}{n+1}+1\right)\right)\left[(1-\epsilon)x+\frac{2(1-x)}{x}\right]x^{\frac{2n\epsilon}{n+1}+\alpha}$$
$$\times\int_{-1}^{1}\mathrm{d}\cos(\theta)\ \sin^{-1-2\epsilon}(\theta)f^{\frac{2\epsilon}{n+1}}(\theta)+\mathcal{O}\Big(\alpha_s^2\Big)\,. \tag{4.26}$$

The divergences are again factorised in terms of monomials and possible rapidity divergences for $n=0$ are again regularised by the analytic regulator α. Moreover, the matrix element can be related to the timelike splitting functions [136] via the same crossing relation as in Eq. (4.15)

$$\mathbb{P}^{(0)}_{g^*\to gg}(z) = 2C_A\left[\frac{z}{1-z}+\frac{1-z}{z}+z(1-z)\right]$$
$$\xrightarrow{(4.15)} -\frac{C_A}{(1-x)x^2}\left[2\Big(1-(1-x)x\Big)^2\right]\equiv -\frac{1}{x}\,\mathbb{P}^{(0)}_{g\to gg^*}(x) \tag{4.27}$$

$$\frac{1}{1-\epsilon}\,\mathbb{P}^{(0)}_{g^*\to q\bar{q}}(z) = \frac{T_F}{1-\epsilon}\left[z^2+(1-z)^2-\epsilon\right]$$
$$\xrightarrow{(4.15)} -\frac{1}{x}\,C_F\left[(1-\epsilon)x+\frac{2(1-x)}{x}\right]\equiv -\frac{1}{x}\,\mathbb{P}^{(0)}_{q\to qg^*}(z)\,. \tag{4.28}$$

As for the quark beam function, the factor $-\frac{1}{x}$ gets cancelled by $Q_-\to -q_- = -xP_-$. The crossing works analogously to the quark case.

Chapter 5

NNLO beam functions

In this chapter, we extend our automated framework for the computation of the beam function matching kernels to $\mathcal{O}(\alpha_s^2)$. At this order, there are up to two emitted particles in the final state, which leads to various contributions with different colour structures. Specifically, the real-virtual (RV) contributions involve a one-loop correction to the matrix elements that we have considered in the previous chapter and they can be computed with similar techniques. In contrast to this, the real-real (RR) contributions are the most challenging part of the evaluation as they require a novel parameterisation of the measurement function and the two-particle phase space. Virtual-virtual (VV) corrections, which correspond to two-loop corrections to the matrix elements from chapter 4, lead to scaleless integrals in dimensional regularisation. We will now address each of these contributions in turn.

5.1 Real-virtual contributions

The RV contributions contain a one-particle cut and therefore require a one-loop integration over the second emitted (virtual) particle according to the Cutkosky rules from chapter 4. Following sections 4.1 and 4.2, we assign the momentum k to the real emitted particle, while the virtual particle has momentum l. In total, there are again four different channels which we need to consider if we do not count the hermitian conjugate Feynman diagrams separately. A full list of all contributions can be found for instance in [124, 125]. As an example to show the basic steps for the evaluation of these contributions, we apply the usual Feynman rules for the diagram in figure 5.1 such that they can be transferred to the other diagrams.

$$\begin{aligned}\mathcal{M}_{q\leftarrow q}^{\mathrm{RV},1} = \frac{\left(g_s^0\right)^4}{2N_c}\int\frac{\mathrm{d}^d l}{(2\pi)^d}\,\mathrm{Tr}\Bigg[\not{P}\gamma^\mu\frac{(\not{P}-\not{k})}{(P-k)^2+i0^+}\frac{\bar{\not{n}}\not{n}}{4}\frac{\bar{\not{n}}}{2}\frac{\not{n}\bar{\not{n}}}{4}\frac{(\not{P}-\not{k})}{(P-k)^2+i0^+}\\ \times\gamma^\rho\frac{(\not{P}-\not{k}-\not{l})}{(P-k-l)^2+i0^+}\gamma^\nu\frac{(\not{P}-\not{l})}{(P-l)^2+i0^+}\gamma^\sigma\Bigg]\frac{i}{l^2+i0^+}\frac{i}{k^2+i0^+}\\ \times\Big(-g_{\mu\nu}+\frac{k_\mu\bar{n}_\nu+k_\nu\bar{n}_\mu}{k\cdot\bar{n}}\Big)\Big(-g_{\rho\sigma}+\frac{l_\rho\bar{n}_\sigma+l_\sigma\bar{n}_\rho}{l\cdot\bar{n}}\Big)\end{aligned}$$

$$\times \operatorname{tr}\Big[T^A\, T^C\, T^B\, T^D\, \delta^{AB}\delta^{CD}\Big]\,. \tag{5.1}$$

As in the NLO case, we leave the indices of the generators implicit, since they give rise to non-trivial colour structures. The capital Latin letters $A, B, ...$ indicate indices from the adjoint representation, which allow for values in the range 1 to $N_c^2 - 1 = 8$. Thus, we can conclude from the matrix element in Eq. (5.1) that the colour structure here is $C_F^2 - \frac{C_F C_A}{2}$.
Performing the spin sum over the Dirac spinors $u(P)\bar{u}(P)$, we obtain a trace over the Dirac γ-matrices, which we can evaluate with the usual trace technology [133]. The trace expression contains a sum of many different scalar products in the momenta P, k, l that we can use to simplify the denominator structure of the loop integral

$$\begin{aligned}\mathcal{M}_{q\leftarrow q}^{\mathrm{RV},1} &= \frac{i\big(g_s^0\big)^4}{128 s^2}\Big(C_F^2 - \frac{C_F C_A}{2}\Big)\int \frac{\mathrm{d}^d l}{(2\pi)^d}\frac{N(P\cdot k, P\cdot l, n\cdot l, l\cdot\bar{n}, ...)}{A(P;k,l)} \\ &\quad\times \frac{i}{k^2 + i0^+} \\ &= \left(\frac{\alpha_s^0}{4\pi}\right)^2 \overline{\mathcal{M}}_{q\leftarrow q}^{\mathrm{RV},1}\frac{i}{k^2+i0^+}\end{aligned} \tag{5.2}$$

with

$$A(P;k,l) := \big((P-k-l)^2 + i0^+\big)\big((P-l)^2 + i0^+\big)\big(l^2 + i0^+\big)\big(-\bar{n}\cdot l + i0^+\big) \tag{5.3}$$

and the invariant mass $s = 2\,k\cdot P$. Of particular importance is the linear propagator originating from the polarisation sum of the gluon propagator in light-cone gauge. For this propagator, it may not be immediately obvious which $i0^+$-prescription needs to be chosen, but since it is crucial in the application of the Feynman parameterisation in the following steps, it has to be reconstructed carefully from the QCD diagrams [1].

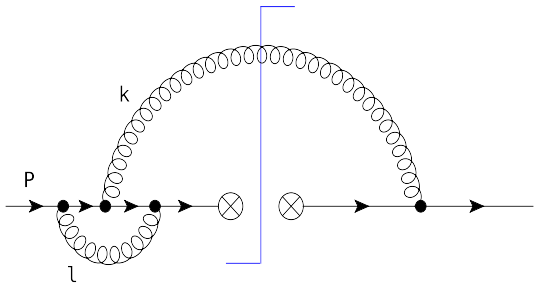

Figure 5.1: RV Feynman diagram, which contributes to the $q \to q$ channel. The h.c. diagrams are obtained by mirroring these diagrams along the cut.

In order to evaluate the loop integral in Eq. (5.2), it is useful to simplify the integrand as much as possible. This is accomplished by rewriting the scalar

[1] This has for instance been done explicitly in [50] for the jet function case. The beam function case works similarly.

products inside $N(P\cdot k, P\cdot l, n\cdot l, l\cdot\bar{n}, ...)$ in terms of the expressions in the denominator as

$$\begin{aligned} P\cdot l &= -\frac{1}{2}\Big[(P-l)^2 - l^2\Big] \\ k\cdot l &= \frac{1}{2}\Big[(P-k-l)^2 - (P-l)^2 + 2k\cdot P\Big]\,. \end{aligned} \tag{5.4}$$

With these replacements, we can separate the integral over the momentum l into 8 different contributions:

$$\begin{aligned} I_1 &= \int \frac{\mathrm{d}^d l}{(2\pi)^d} \frac{N_1(\bar{n}\cdot k, k\cdot P, \bar{n}\cdot P, l\cdot P, k\cdot l, l^2)}{\big((P-l)^2+i0^+\big)\big(l^2+i0^+\big)\big(-\bar{n}\cdot l+i0^+\big)} \\ I_2 &= \int \frac{\mathrm{d}^d l}{(2\pi)^d} \frac{N_2(\bar{n}\cdot k, k\cdot P, \bar{n}\cdot P, l\cdot P, l^2)}{\big((P-k-l)^2+i0^+\big)\big(l^2+i0^+\big)\big(-\bar{n}\cdot l+i0^+\big)} \\ I_3 &= \int \frac{\mathrm{d}^d l}{(2\pi)^d} \frac{N_3(\bar{n}\cdot k, k\cdot P, \bar{n}\cdot P, l\cdot P, k\cdot l, l^2)}{\big((P-k-l)^2+i0^+\big)\big((P-l)^2+i0^+\big)\big(-\bar{n}\cdot l+i0^+\big)} \\ I_4 &= \int \frac{\mathrm{d}^d l}{(2\pi)^d} \frac{N_4(\bar{n}\cdot k, k\cdot P, \bar{n}\cdot P, \bar{n}\cdot l)}{\big((P-k-l)^2+i0^+\big)\big((P-l)^2+i0^+\big)\big(l^2+i0^+\big)} \\ I_5 &= \int \frac{\mathrm{d}^d l}{(2\pi)^d} \frac{N_5(\bar{n}\cdot k, k\cdot P, \bar{n}\cdot P)}{\big((P-k-l)^2+i0^+\big)\big((P-l)^2+i0^+\big)\big(l^2+i0^+\big)\big(-\bar{n}\cdot l+i0^+\big)} \\ I_6 &= \int \frac{\mathrm{d}^d l}{(2\pi)^d} \frac{N_6(\bar{n}\cdot k, k\cdot P, \bar{n}\cdot P, l\cdot P, l^2)}{\big((P-k-l)^2+i0^+\big)\big(l^2+i0^+\big)} \\ I_7 &= \int \frac{\mathrm{d}^d l}{(2\pi)^d} \frac{N_7(\bar{n}\cdot k, k\cdot P, \bar{n}\cdot P, l\cdot P, l^2)}{\big((P-k-l)^2+i0^+\big)\big(-\bar{n}\cdot l+i0^+\big)} \\ I_8 &= \int \frac{\mathrm{d}^d l}{(2\pi)^d} \frac{N_8(\bar{n}\cdot k, k\cdot P, \bar{n}\cdot P, l\cdot P, l^2)}{\big((P-l)^2+i0^+\big)\big(-\bar{n}\cdot l+i0^+\big)}\,, \end{aligned} \tag{5.5}$$

which are then part of the matrix element

$$\overline{\mathcal{M}}^{\mathrm{RV},1}_{q\leftarrow q} = \frac{i}{8s^2}\left(C_F^2 - \frac{C_F C_A}{2}\right)\sum_{k=1}^{8} I_k\,. \tag{5.6}$$

In order to compute these eight contributions, we first use the formulae in appendix A to introduce the Feynman parameterisation and rescale the loop momentum l such that we obtain the form in Eq. (A.4). For integrals containing the linear propagator $(-\bar{n}\cdot l + i0^+)$, we use the slightly modified Feynman parameterisation in Eq. (A.2). Tensor integrals with an even power of the loop momentum l in the numerator are symmetrised according to Eq. (A.5), while contributions with an odd number vanish due to the antisymmetry of the numerator under the change $l \to -l$. It turns out that the integrals I_1, I_3, I_7, I_8 vanish, since they lead to scaleless integrals in

dimensional regularisation. Combining all integrals, we obtain

$$\begin{aligned}\overline{\mathcal{M}}_{q\leftarrow q}^{\mathrm{RV},1} = &\frac{2^{4\epsilon}\pi^{\frac{3}{2}+\epsilon}\csc(\pi\epsilon)P_-}{(1-x)\epsilon\Gamma\left(\frac{3}{2}-\epsilon\right)s^{1+\epsilon}}\left(C_F^2-\frac{C_FC_A}{2}\right)\Bigg[-2(2\epsilon-1)\Big(x^2(\epsilon-1)\\ &-2x\epsilon+\epsilon-1\Big)\,{}_2F_1(1,-\epsilon;1-\epsilon;1-x)+x^2\left(2\epsilon^3-3\epsilon^2+3\epsilon-2\right)\\ &+x\left(-4\epsilon^2+3\epsilon-4\right)\epsilon+2\epsilon^3-2\epsilon^2+3\epsilon-2\Bigg]. \end{aligned} \tag{5.7}$$

In Eq. (5.7), we have implemented the NLO parameterisation from Eq. (4.8) since we still encounter a one-particle phase space. This matrix element for the diagram in figure 5.1 is directly related to the corresponding jet function diagram via the crossing

$$z \to -\frac{1-x}{x}\,, \tag{5.8}$$

which corresponds exactly to the NLO crossing relation in Eq. (4.15). Notice that the prefactors do not match immediately, because the replacement in Eq. (5.8) introduces the variable change $s \to -s$ leading to an additional imaginary part. After adding the hermitian conjugate diagram, this results in a factor of $2\cos(\pi\epsilon)$ instead of the factor 2.
The other two diagrams for the $q \to q$ channel can be evaluated similarly to the discussion above [2]. However, the diagram involving the non-Abelian three-gluon vertex requires an additional transformation. The computation leads to the hypergeometric function

$${}_2F_1\left(1,-\epsilon;1-\epsilon;\frac{1}{1-x}\right), \tag{5.9}$$

where the last argument is a priori troublesome. The radius of convergence for this hypergeometric function is supposed to be 1 in order to observe absolute convergence, however we identify in Eq. (5.9) that $\frac{1}{1-x} \geq 1$ for $x \in [0,1]$. This requires an additional remapping of this hypergeometric function for the case that $|\arg(-z)| < \pi$ such that the argument is again in the region of convergence:

$$\begin{aligned}{}_2F_1(a,b;c;z) = &\frac{\Gamma(c)\Gamma(b-a)}{\Gamma(b)\Gamma(c-a)}(-z)^{-a}\,{}_2F_1(a,1+a-c;1+a-b;1/z)\\ &+\frac{\Gamma(c)\Gamma(a-b)}{\Gamma(a)\Gamma(c-b)}(-z)^{-b}\,{}_2F_1(b,1+b-c;1+b-a;1/z)\,. \end{aligned} \tag{5.10}$$

By setting $z := 1/(1-x)$, we trade one hypergeometric function for two of these functions, which are now in the allowed region of convergence. Moreover, this remapping in Eq. (5.10) introduces a small imaginary part, which

[2] One of those has been evaluated for the jet function case in [50]. Applying the crossing from Eq. (5.8) and correcting for the prefactor provides the expression for the beam function case.

becomes explicit now and is of importance if we add the hermitian conjugate diagram in order to obtain the full RV contribution. Convergence at the point $x = 0$ is guaranteed for the function in Eq. (5.9), because the sum of all arguments is greater than 0.
Finally, we are able to calculate the full matrix element in the RV case for the $q \to q$ channel:

$$\overline{\mathcal{M}}^{\mathrm{RV}}_{q\leftarrow q} = \sum_{i=1}^{3} \overline{\mathcal{M}}^{\mathrm{RV},i}_{q\leftarrow q} + \mathrm{h.c.} = \frac{2^{5+2\epsilon}\pi^{3+\epsilon}}{s^{1+\epsilon}} \frac{\Gamma(1-\epsilon)\csc(\pi\epsilon)}{\epsilon\,\Gamma(2-2\epsilon)} \widetilde{\mathcal{M}}^{\mathrm{RV}}_{q\leftarrow q} \tag{5.11}$$

In this result, we first perform the remapping in Eq. (5.10) and add up all contributions as well as their hermitian conjugates. For convenience, we have defined the pure matrix element without any prefactors:

$$\begin{aligned}
\widetilde{\mathcal{M}}^{\mathrm{RV}}_{q\leftarrow q} = \; & -2(x+1)\epsilon^2(C_F C_A - C_F^2) + 2\left(x^2 + (x-1)^2(-\epsilon) + 1\right)\Bigg((1-2\epsilon) \\
& \times (C_F C_A - 2C_F^2)\,{}_2F_1(1,-\epsilon,1-\epsilon;1-x) + (\epsilon(\epsilon+2)-1)(C_F C_A - C_F^2) \\
& + C_F C_A \epsilon(2\epsilon-1)\Big((x-1)\Gamma(1+\epsilon)\,{}_2F_1(1,1+\epsilon,2+\epsilon;1-x) \\
& + \pi\,(1-x)^{-\epsilon}\cot(\pi\epsilon)\Big) - 2C_F^2\epsilon + C_F^2\Bigg).
\end{aligned} \tag{5.12}$$

Excluding prefactors in Eq. (5.12) is useful when we state the final form of the master formula. For the diagonal channels, in particular also for the $g \to g$ channel, we also pull out an additional factor $(1-x)^{-1}$, which results in a singularity at $x \to 1$.
As we have seen in the previous chapter, the collinear matrix elements are related to the well-known splitting functions. In the RV case, this corresponds to the one-loop splitting functions [135, 137] after performing the crossing in Eq. (5.8) and the mapping (5.10). The same observation also applies to the other channels. In general, it is possible to either calculate the matrix elements directly using the techniques from above or to extract them from the splitting functions in the timelike region using appropriate crossing relations.
For the off-diagonal $g \to q$ channel, the crossing works analogously to the crossing for the off-diagonal quark channel in the NLO case and we can therefore apply Eq. (4.16). Consequently, the colour structure needs to be modified accordingly. These modifications ensure that we obtain the correct colour structures $C_F T_F$ and $C_A T_F$ in the $g \to q$ channel. Ultimately, we end up with the following matrix element

$$\begin{aligned}
\widetilde{\mathcal{M}}^{\mathrm{RV}}_{q\leftarrow g} = \frac{-2\,T_F\,(1-x)}{1-\epsilon}\Bigg(& (2\epsilon-1)\left(2x^2-2x-\epsilon+1\right)(C_A - 2C_F)\Bigg((1-x)^{-\epsilon} \\
& \times \cos(\pi\epsilon)\Gamma(1-\epsilon)\Gamma(\epsilon+1) + \frac{(x-1)\epsilon\,{}_2F_1(1,\epsilon+1;\epsilon+2;1-x)}{\epsilon+1}\Bigg) \\
& - (2\epsilon-1)C_A\left(2x^2-2x-\epsilon+1\right)\,{}_2F_1(1,-\epsilon;1-\epsilon;1-x) \\
& + C_A\left(x^2(2-4\epsilon) - x((\epsilon-4)\epsilon+2) + (\epsilon-1)\epsilon(\epsilon+3)+1\right)
\end{aligned}$$

$$+ C_F \left(x^2(8\epsilon-4) + x((\epsilon-8)\epsilon+4) - \epsilon(\epsilon(\epsilon+4)-6) - 2\right)\Bigg), \tag{5.13}$$

where we still remove the prefactors for further simplifications in the master formula.
The two remaining gluon channels follow the same strategy. In the off-diagonal $q \to g$ channel, we take the timelike splitting function from [137] and perform the crossing from Eq. (5.8) [3].

$$\begin{aligned}\widetilde{\mathcal{M}}^{\mathrm{RV}}_{g\leftarrow q} = \frac{2\left(x^2(\epsilon-1)+2x-2\right)C_F}{x\left(3-2\epsilon\right)}\Bigg(& C_A\left(4\epsilon^2-8\epsilon+3\right){}_2F_1(1,-\epsilon;1-\epsilon;1-x)\\ &+ C_A\left(4\epsilon^2-8\epsilon+3\right)\Bigg(\frac{(x-1)\epsilon\,{}_2F_1(1,\epsilon+1;\epsilon+2;1-x)}{\epsilon+1} + (1-x)^{-\epsilon}\\ &\times\cos(\pi\epsilon)\,\Gamma(1-\epsilon)\,\Gamma(\epsilon+1)\Bigg) + 2C_A\epsilon^3 - 8C_A\epsilon^2 + 13C_A\epsilon - 9C_A\\ &- 4C_F\epsilon^3 + 8C_F\epsilon^2 - 7C_F\epsilon + 6C_F - 2n_f\epsilon^2 + 2n_f\epsilon\Bigg)\cdot(1-x)\end{aligned} \tag{5.14}$$

Finally, the missing matrix element belongs to the $g \to g$ channel. After performing the crossing on the splitting function from Ref. [137], we get

$$\begin{aligned}\widetilde{\mathcal{M}}^{\mathrm{RV}}_{g\leftarrow g} = \frac{2C_A}{x(\epsilon-1)^2\left(3-2\epsilon\right)}\Bigg(&\left(-2C_A\left(x^2-x+1\right)^2(\epsilon-1)^2\left(4\epsilon^2-8\epsilon+3\right)\right.\\ &\times {}_2F_1(1,-\epsilon;1-\epsilon;1-x) - 2C_A\left(x^2-x+1\right)^2(\epsilon-1)^2\left(4\epsilon^2-8\epsilon+3\right)\\ &\times\Big(\frac{(x-1)\epsilon\,{}_2F_1(1,\epsilon+1;\epsilon+2;1-x)}{\epsilon+1} + (1-x)^{-\epsilon}\cos(\pi\epsilon)\Gamma(1-\epsilon)\\ &\times\Gamma(\epsilon+1)\Big) + C_A(\epsilon-1)\Big(2(x(x(4(x-2)x+13)-10)+5)\epsilon^3\\ &+(-(x-1)x(x(24x-23)+48)-24)\epsilon^2 + 22((x-1)x+1)^2\epsilon\\ &\left.-6((x-1)x+1)^2\Big) - 2\,T_F n_f\,(x-1)\epsilon^2\left(x^2-2x\epsilon+2\epsilon\right)\right).\end{aligned} \tag{5.15}$$

With these matrix elements, we can state the master formulae for all four channels. From a computational point of view, we follow the same steps as in chapter 4. We still start with the expressions in Eq. (4.6), perform the k_T-integration analytically according to Eq. (4.7) and use the ansatz (4.9) for the measurement function. Thus, we obtain for the bare RV matching

[3] Ref. [137] works in the convention $T_F = \frac{1}{2}$, therefore we need to correct these results accordingly.

kernel for all channels

$$\begin{aligned}\mathcal{I}_{i\leftarrow j}^{0,(2,\mathrm{RV})} = &\frac{4\sqrt{\pi}}{\Gamma\Big(\frac{1}{2}-\epsilon\Big)} C_F \frac{\Gamma(1-\epsilon)\csc(\pi\epsilon)}{\Gamma(2-2\epsilon)\epsilon} \left(\frac{\mu\bar{\tau}^{\frac{1}{n+1}}}{q_-^{\frac{n}{n+1}}}\right)^{4\epsilon} \frac{\Gamma\Big(-\frac{4\epsilon}{n+1}\Big)}{n+1}\, x^{\frac{4n\epsilon}{n+1}+\alpha} \\ &\times \exp\left(\epsilon\gamma_E\Big(-\frac{4}{n+1}+2\Big)\right)(1-x)^{-1+\epsilon-\frac{4n\epsilon}{n+1}-\alpha}\widetilde{\mathcal{M}}_{i\leftarrow j}^{\mathrm{RV}} \\ &\times \int_{-1}^{1} \mathrm{d}\cos(\Theta_k)\, \sin^{-1-2\epsilon}(\Theta_k) f^{\frac{4\epsilon}{n+1}}(\Theta_k) \end{aligned} \tag{5.16}$$

with $i \in \{q, g\}$. The case $i = \bar{q}$ coincides with the $i = q$ case due to the charge-conjugation invariance of the collinear splitting functions. In Eq. (5.13) and (5.14), we include an additional factor $(1-x)$ to compensate for the divergent factor $(1-x)^{-1+\epsilon-\frac{4n\epsilon}{n+1}}$, which does not lead to an explicit divergence in the off-diagonal channels. Moreover, the matrix elements $\widetilde{\mathcal{M}}_{i\leftarrow i}^{\mathrm{RV}}$ correspond to the two-loop splitting functions as discussed above. Since the RV contributions contain by construction one particle in the final state, we only need to include one analytic regulator into the phase space measure, which we pull out in Eq. (3.5). However, this factor is crucial in the derivation of the master formulae, as we have shown in the NLO case, and has to be included following table 3.1.

Furthermore, we still need to work with the NLO measurement function $f(\Theta_k)$, albeit with a different exponent now. Similar to the NLO case in sections 4.1 and 4.2, the singularities are again completely factorised. While the Γ-function $\Gamma\big(-\frac{4\epsilon}{n+1}\big)$ accounts for the collinear divergence, the factor $(1-x)^{-1+\epsilon-\frac{4n\epsilon}{n+1}-\alpha}$ denotes the soft divergence. In addition to that there occur two more ϵ-poles from the $\csc(\pi\epsilon)$- and the $1/\epsilon$-factor such that the highest divergence is of the order $1/\epsilon^4$ in the SCET-I case and $1/(\alpha\epsilon^3)$ in the SCET-II case.

The overall factor $(1-x)^{-1+\epsilon-\frac{4n\epsilon}{n+1}-\alpha}$ requires further investigation. As we previously mentioned, the SCET-II case corresponds to the parameter choice $n = 0$. Hence, one would naively assume that the factor $(1-x)^{-1+\epsilon-\alpha}$ is regularised due to the ϵ-term in the exponent and thus the α-regulator is not needed at all. But it turns out that there occur additional terms of the form $(1-x)^{-\epsilon}$ in Eq. (5.12) and (5.15) after the remapping in Eq. (5.10). This cancellation of the ϵ-term leads to the necessity to introduce the α-regulator.

To summarise, we have stated the master formulae for the RV contributions for all four matching kernels in Eq. (5.16) in the SCET-I and SCET-II case. Since we encounter a one-particle phase space here, we can present the master formulae completely analytically and work with the NLO measurement function $f(\Theta_k)$. They can be used to extract the RV contributions to the complete NNLO matching kernels according to Eq. (3.5).

5.2 Real-real contributions

In this section, we focus on the most complicated NNLO structures, namely the real emission process of two massless partons. For the first time in this work, we encounter a two-particle final state. The necessary methods and techniques, as well as numerical aspects related to their application, are discussed in the following. Before we study each contribution in detail, we start by deriving the respective master formula.
Our starting point are again the partonic beam function definitions (4.1) and (4.22), which we now expand to order α_s^2. In particular, we now obtain a contribution with two emitted particles with momenta k and l. For the quark channels, we get

$$\begin{aligned}\mathcal{I}^0_{q\leftarrow j}(x,\tau) = \delta_{qj}\,\delta(1-x) + \left(\frac{\alpha_s}{4\pi}\right)\left(\frac{\nu}{q_-}\right)^\alpha \left[\mathcal{I}^{0,(1)}_{q\leftarrow j}(x,\tau) + \left(\frac{\alpha_s}{4\pi}\right)\mathcal{I}^{0,(2,\mathrm{RV})}_{q\leftarrow j}(x,\tau)\right] \\ + \int \frac{\mathrm{d}^d k}{(2\pi)^d}\left(\frac{\nu}{k_-}\right)^\alpha \int \frac{\mathrm{d}^d l}{(2\pi)^d}\left(\frac{\nu}{l_-}\right)^\alpha \delta\Big((1-x)P_- - k_- - l_-\Big) \\ \times \langle j(P)|\,\bar\chi\,|k,l\rangle\,\frac{\bar{\not n}}{2}\,\langle k,l|\,\chi\,|j(P)\rangle\;(-2\pi i)\delta(k^2)\Theta(k^0)\,(-2\pi i)\delta(l^2) \\ \times \Theta(l^0)\mathcal{M}_2(\tau;k,l) + \mathcal{O}\Big(\alpha_s^3\Big)\,, \qquad (5.17)\end{aligned}$$

where we wrote the RR contribution from Eq. (3.5) explicitly.
If we generalise the NLO discussion from chapter 4, we see that we now need to integrate over two emitted particles with momenta k and l instead of a single emission. From the definition of the RR contributions, we know that these two particles are on-shell, which is indicated by the on-shell conditions in the last two lines of Eq. (5.17). They get introduced into this expression after applying the Cutkosky rules due to the cuts on the two emitted final state particles. Additionally, we have included the analytic regulators in order to account for SCET-II observables. Energy conservation is guaranteed by the δ-distribution restricting the large components in the collinear sector. The momentum fraction x denotes the energy fraction of the parton going into the hard interaction, see figure 4.3. Moreover, $\mathcal{M}_2(\tau;k,l)$ denotes the two-emission measurement function in Eq. (5.17), which again completely determines the observable under investigation.
Similarly, we can also state the starting point for the gluon channels

$$\begin{aligned}\mathcal{I}^0_{g\leftarrow j}(x,\tau) = \;\delta_{gj}\,\delta(1-x) + \left(\frac{\alpha_s}{4\pi}\right)\left(\frac{\nu}{q_-}\right)^\alpha \left[\mathcal{I}^{0,(1)}_{g\leftarrow j}(x,\tau) + \left(\frac{\alpha_s}{4\pi}\right)\right. \\ \left.\times\,\mathcal{I}^{0,(2,\mathrm{RV})}_{g\leftarrow j}(x,\tau)\right] - xP_-\int \frac{\mathrm{d}^d k}{(2\pi)^d}\left(\frac{\nu}{k_-}\right)^\alpha \int \frac{\mathrm{d}^d l}{(2\pi)^d}\left(\frac{\nu}{l_-}\right)^\alpha (-2\pi i)\delta(k^2) \\ \times \langle j(P)|\,\mathcal{A}^{\mu,A}_{c,\perp}\,|k,l\rangle\,\langle k,l|\,\mathcal{A}^{A}_{c,\perp,\mu}\,|j(P)\rangle\;\delta\Big((1-x)P_- - k_- - l_-\Big) \\ \times (-2\pi i)\delta(l^2)\Theta(k^0)\Theta(l^0)\mathcal{M}_2(\tau;k,l) + \mathcal{O}\big(\alpha_s^3\big)\,. \qquad (5.18)\end{aligned}$$

Since the computational steps are the same as for the quark beam function, we continue our explanations with the quark channels.

The first step is to introduce light-cone coordinates

$$\int \frac{\mathrm{d}^d k}{(2\pi)^d} \to \frac{1}{2}\int \frac{\mathrm{d}k_+}{2\pi}\int \frac{\mathrm{d}k_-}{2\pi}\int \frac{\mathrm{d}^{d-2}k_\perp}{(2\pi)^{d-2}}$$
$$\int \frac{\mathrm{d}^d l}{(2\pi)^d} \to \frac{1}{2}\int \frac{\mathrm{d}l_+}{2\pi}\int \frac{\mathrm{d}l_-}{2\pi}\int \frac{\mathrm{d}^{d-2}l_\perp}{(2\pi)^{d-2}} \tag{5.19}$$

and to use the δ-distributions to perform some integrations

$$k_+ \to \frac{k_T^2}{k_-}, \qquad l_+ \to \frac{l_T^2}{l_-}, \qquad l_- \to (1-x)P_- - k_- \,. \tag{5.20}$$

This leaves us with an integration over $k_-, k_\perp$ and $l_\perp$. For both integrations over $k_\perp$ and $l_\perp$, we go over to spherical coordinates. Ultimately, we end up with

$$\begin{aligned}\mathcal{I}^0_{q\leftarrow j}(x,\tau) = \delta_{qj}\,\delta(1-x) + \left(\frac{\alpha_s}{4\pi}\right)\left(\frac{\nu}{q_-}\right)^\alpha \left[\mathcal{I}^{0,(1)}_{q\leftarrow j}(x,\tau) + \left(\frac{\alpha_s}{4\pi}\right)\mathcal{I}^{0,(2,\mathrm{RV})}_{q\leftarrow j}(x,\tau)\right] \\ + \frac{1}{4}\int_0^\infty \frac{\mathrm{d}k_-}{(2\pi)^2}\int \mathrm{d}\Omega^{(k)}_{d-2}\int \mathrm{d}\Omega^{(l)}_{d-2}\frac{(-i)^2}{(2\pi)^{2d-4}}\int_0^\infty \mathrm{d}k_T\, k_T^{d-3} \\ \times \int_0^\infty \mathrm{d}l_T\, l_T^{d-3}\frac{\nu^{2\alpha}}{k_-^{1+\alpha}((1-x)P_- - k_-)^{1+\alpha}}\,\langle j(P)|\,\bar\chi\,|k,l\rangle\,\frac{\not{\bar n}}{2} \\ \times \langle k,l|\,\chi\,|j(P)\rangle\,\mathcal{M}_2(\tau;k,l) + \mathcal{O}\Big((\alpha_s)^3\Big)\end{aligned} \tag{5.21}$$

for the matching kernels of the quark channels and we obtain similarly for the gluon channels

$$\begin{aligned}\mathcal{I}^0_{g\leftarrow j}(x,\tau) = \;\delta_{gj}\,\delta(1-x) + \left(\frac{\alpha_s}{4\pi}\right)\left(\frac{\nu}{q_-}\right)^\alpha \left[\mathcal{I}^{0,(1)}_{g\leftarrow j}(x,\tau) + \left(\frac{\alpha_s}{4\pi}\right)\right. \\ \left.\times\,\mathcal{I}^{0,(2,\mathrm{RV})}_{g\leftarrow j}(x,\tau)\right] - xP_-\,\frac{1}{4}\int_0^\infty \frac{\mathrm{d}k_-}{(2\pi)^2}\int \mathrm{d}\Omega^{(k)}_{d-2}\int \mathrm{d}\Omega^{(l)}_{d-2}\frac{(-i)^2}{(2\pi)^{2d-4}} \\ \times \int_0^\infty \mathrm{d}k_T\, k_T^{d-3}\int_0^\infty \mathrm{d}l_T\, l_T^{d-3}\frac{\nu^{2\alpha}}{k_-^{1+\alpha}((1-x)P_- - k_-)^{1+\alpha}} \\ \times \langle j(P)|\,\mathcal{A}^{\mu,A}_{c,\perp}\,|k,l\rangle\,\langle k,l|\,\mathcal{A}^A_{c,\perp,\mu}\,|j(P)\rangle\,\mathcal{M}_2(\tau;k,l) + \mathcal{O}\big(\alpha_s^3\big)\,.\end{aligned} \tag{5.22}$$

In the following, we introduce a suitable parameterisation of the phase-space integrals, investigate the angular integrations in the transverse space, propose a specific form of the two-emission measurement function $\mathcal{M}_2(\tau;k,l)$ and evaluate the corresponding matrix elements, before we derive a suitable master formula for the computation of the RR contributions.

5.2.1 Phase-space parameterisation

In order to parameterise the two-particle phase space, we use the variables

$$a = \frac{k_- l_T}{l_- k_T}\,, \quad x_{12} = \frac{k_- + l_-}{P_-}\,, \quad b = \frac{k_T}{l_T}\,, \quad q_T = \sqrt{(k_+ + l_+)(k_- + l_-)} \tag{5.23}$$

with the inverse transformation

$$k_- = \frac{abx_{12}P_-}{1+ab}\,, \quad k_+ = \frac{q_T^2 b}{(a+b)x_{12}P_-}\,, \quad l_- = \frac{x_{12}P_-}{1+ab}\,, \quad l_+ = \frac{q_T^2 a}{x_{12}P_-(a+b)}\,. \tag{5.24}$$

We call this parameterisation the physical parameterisation, since there is a direct physical meaning attached to it. The variable a is a measure of the rapidity difference between the two rapidities $y_k = \frac{1}{2}\ln\left(\frac{k_+}{k_-}\right)$ and $y_l = \frac{1}{2}\ln\left(\frac{l_+}{l_-}\right)$ of the two emissions, while x_{12} describes the energy fraction of the two emissions. Based on momentum conservation, we identify $x_{12} = 1-x$. b accounts for the single soft limit in this particular parameterisation.
We remark that this parameterisation is particularly useful since the divergence in x_{12} will be factorised in all cases. This is essential in our x-space approach, where the matching kernels are distribution valued in $(1-x)$.
However, it may be convenient to use different parameterisations for some contributions, which have the advantage that the singularities are immediately factorised. For instance, the parameterisation

$$x_1 = \frac{k_-}{P_-}\,, \qquad x_2 = \frac{l_-}{P_-}\,, \qquad b = \frac{k_T}{l_T}\,, \qquad q_T = k_T + l_T \tag{5.25}$$

and its inverse transformation

$$k_- = x_1 P_-\,, \qquad k_+ = \frac{q_T^2 b^2}{(1+b)^2 x_1 P_-}\,, \quad l_- = x_2 P_-\,, \quad l_+ = \frac{q_T^2}{(1+b)^2 x_2 P_-} \tag{5.26}$$

are helpful for some contributions to the $q \to q$ channel, since the divergences factorise directly in this case. This parameterisation is inspired by the uncorrelated emission contributions to soft functions [49] [4]. Nevertheless, we point out that this parameterisation is only useful for our N-space approach where we integrate over x_{12}, whereas it becomes difficult to extract the distributions in the x-space framework. Another slightly modified parameterisation is given by

$$\tilde{a} = \frac{l_- k_T}{k_- l_T}\,, \quad x_{12} = \frac{k_- + l_-}{P_-}\,, \quad r = \frac{k_-}{l_-}\,, \quad q_T = \sqrt{(k_+ + l_+)(k_- + l_-)} \tag{5.27}$$

and the inverse transformation

$$k_- = \frac{r x_{12} P_-}{1+r}\,, \quad k_+ = \frac{q_T^2 r \tilde{a}^2}{(1+r\tilde{a}^2)x_{12}P_-}\,, \quad l_- = \frac{x_{12}P_-}{1+r}\,, \quad l_+ = \frac{q_T^2(1+r)}{x_{12}P_-\tilde{a}^2 r^2}\,. \tag{5.28}$$

[4] So far, we investigated this parameterisation only for SCET-II observables. Therefore, we can set $n = 0$ in [49] and expand the remaining terms according to the momentum scaling in the collinear region. For our x-space approach, we rather stick to the parameterisation in Eq. (5.23) for both SCET-I and SCET-II observables.

This parameterisation simplifies the calculation of the $C_F T_F$ colour structure of the $q \to q$ channel. Generally, it remaps the divergence for $a \to \infty$ to $\tilde{a} \to 0$, because of $\tilde{a} \to \frac{1}{a}$ and disentangles overlapping divergences by using the new variable r.
When using the parameterisation from Eq. (5.23), the integration domain is restricted to

$$a, b, q_T \in [0, \infty) \qquad\qquad x_{12} \in [0, 1]\,. \tag{5.29}$$

As we will see, we integrate out the dimensionful variable q_T analytically, and we find it convenient to map the integration domain of the variables (a, b) to the interval $[0, 1]$, since we intend to perform numerical Monte Carlo integrations due to the complicated phase-space structure. This can be done by splitting the integrations

$$\int_0^\infty \mathrm{d}a \int_0^\infty \mathrm{d}b\, I(a, b, ...) = \left[\int_0^1 \mathrm{d}a + \int_1^\infty \mathrm{d}a\right]\left[\int_0^1 \mathrm{d}b + \int_1^\infty \mathrm{d}b\right] I(a, b, ...) \tag{5.30}$$

and substituting $a \to \frac{1}{a}$ or $b \to \frac{1}{b}$ in the integrals with integration range $[1, \infty)$. Here, the integrand $I(a, b, ...)$ is an abbreviation for all components present in Eqs. (5.21) and (5.22). Thus, the integration splits into four regions:

Region	Abbreviation	Substitution	Integrand
Region A	R_A	-	$I(a, b, ...)$
Region B	R_B	$a \to 1/a$	$a^{-2}\, I\left(\frac{1}{a}, b, ...\right)$
Region C	R_C	$b \to 1/b$	$b^{-2}\, I\left(a, \frac{1}{b}, ...\right)$
Region D	R_D	$a \to 1/a$, $b \to 1/b$	$a^{-2}b^{-2}\, I\left(\frac{1}{a}, \frac{1}{b}, ...\right)$

Table 5.1: List of the various substitutions in order to define the specific regions. We perform the remapping such that we only work on the unit hypercube when we perform numerical integrations.

However, we observe in many cases that the functions in the integrand $I(a, b, ...)$ like the matrix element, the measurement function and the Jacobian are invariant under some of the substitutions listed in table 5.1. As a consequence, the number of regions and the necessary numerical integrations are reduced significantly.
Generally, the discussion from above also holds for the parameterisations in Eqs. (5.25) and (5.27). In the second case, the variables $\tilde{a}$ and r need to be remapped onto the unit hypercube, while the first case only requires the remapping of $b \to \frac{1}{b}$ and therefore it only introduces two subregions.

5.2.2 Angular integrations

After parameterising the phase-space integrations in terms of the variables in Eq. (5.23), we turn towards the investigation of the angular variables. They stem from the integrals over the transverse coordinates $k_\perp$ and $l_\perp$, therefore it is natural that they should encode the relative position of these vectors.

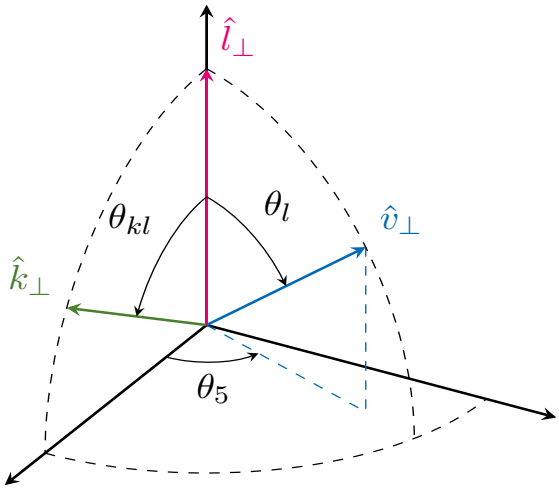

Figure 5.2: Angular parameterisation in the transverse plane. We parameterise the angular integration by introducing two angles Θ_l and Θ_5 with respect to a reference vector $\vec{v}_\perp$. $\hat{v}_\perp, \hat{k}_\perp$ and $\hat{l}_\perp$ denote in this context unit vectors pointing into the $\vec{v}_\perp, \vec{k}_\perp$ as well as $\vec{l}_\perp$ direction, respectively. For the third angle, it is convenient to choose the angle Θ_{kl} between the k and l emission in the transverse plane. We can reduce this to the NLO case by choosing the reference vector to be the $\bar{n}$-axis. The picture is taken from [48].

Following our general assumptions in section 3.2, we only allow for one angle per particle which is measured with respect to a reference vector $\vec{v}_\perp$ that is imposed by the observable. We can then apply the same angular parameterisations as in the `SoftSERVE` approach [48, 49]. The transverse plane is $(d-2)$-dimensional, therefore we define the transverse components of the two emissions as depicted in figure 5.2 with

$$\begin{aligned}
\vec{l}_\perp &= |\vec{l}_\perp|(1,0,...,0)^T\,, \\
\vec{k}_\perp &= |\vec{k}_\perp|(\cos\Theta_{kl}, \sin\Theta_{kl}, 0, ..., 0)^T\,, \\
\vec{v}_\perp &= |\vec{v}_\perp|(\cos\Theta_l, \sin\Theta_l\cos\Theta_5, \sin\Theta_l\sin\Theta_5, 0, ..., 0)^T\,.
\end{aligned} \tag{5.31}$$

The choice for the angles in Eq. (5.31) is useful for our applications, since the invariant mass $s_{12} = (k+l)^2$ depends only on the angle Θ_{kl}, i.e. the angle between the two transverse vectors $\vec{k}_\perp$ and $\vec{l}_\perp$, $\Theta_{kl} = \angle(\vec{k}_\perp, \vec{l}_\perp)$. Contrary, the other two angles are defined with respect to some reference vector $\vec{v}_\perp$

$$\Theta_k = \angle(\vec{k}_\perp, \vec{v}_\perp)\,, \tag{5.32}$$

$$\Theta_l = \angle(\vec{l}_\perp, \vec{v}_\perp)\,, \tag{5.33}$$

where

$$\cos\Theta_k = \cos\Theta_{kl}\cos\Theta_l + \sin\Theta_{kl}\sin\Theta_l\cos\Theta_5\,. \tag{5.34}$$

If we parametrise now the angular integrations in Eqs. (5.21) and (5.22) by these variables, we obtain

$$\begin{aligned}\int \mathrm{d}\Omega^{(k)}_{d-2}\,\mathrm{d}\Omega^{(l)}_{d-2} =& \frac{4\pi^{\frac{1}{2}-2\epsilon}}{\Gamma(1/2-\epsilon)\Gamma(-\epsilon)}\int_0^\pi \mathrm{d}\Theta_{kl}\mathrm{d}\Theta_l\mathrm{d}\Theta_5\sin^{d-4}(\Theta_{kl})\sin^{d-4}(\Theta_l)\cdot\\ &\times\sin^{d-5}(\Theta_5)\\ =& \frac{32\pi^{\frac{1}{2}-2\epsilon}}{\Gamma(1/2-\epsilon)\Gamma(-\epsilon)}\int_0^1 \mathrm{d}t_{kl}\mathrm{d}t_l\mathrm{d}t_5(4t_{kl}\bar{t}_{kl})^{-\frac{1}{2}-\epsilon}(4t_l\bar{t}_l)^{-\frac{1}{2}-\epsilon}\cdot\\ &\times(4t_5\bar{t}_5)^{-1-\epsilon}\end{aligned} \tag{5.35}$$

In the last line, we have substituted

$$\cos(\Theta_y) = 1-2t_y \quad \text{with} \quad y\in\{kl,l,5\} \tag{5.36}$$

such that the integration boundary lies on the unit hypercube and we define $\bar{t}_x = 1-t_x$ with $x\in\{kl,l,5\}$.
We observe that the t_5-integration becomes divergent at the integration endpoints $t_5\to\{0,1\}$. These singularities are spurious and unphysical. They stem from the fact that we have parameterised the transverse plane with more angles than there exist in four space-time dimensions, but their unphysical nature guarantees that this singularity cancels against the prefactor $\frac{1}{\Gamma(-\epsilon)} = \mathcal{O}(\epsilon)$.
In our framework, we aim to factorise all singularities in monomial form such that an expansion in ϵ is possible. However, the spurious divergence does not allow for a simple ϵ expansion since there are divergences at both endpoints. Hence, we deal with this issue by splitting the integration range at $t_5 = 1/2$ and performing the substitutions

$$\begin{aligned}&\mathrm{I}_1 : t_5 \to t_5'/2\\ &\mathrm{I}_2 : t_5 \to 1-t_5'/2\end{aligned} \tag{5.37}$$

with $t_5'\in[0,1]$ to end up with unit integration boundaries suitable for numerical integrations.
As can be seen from above, the angle Θ_5 enters our calculation only via relation (5.34), which turns to

$$t_k^{\pm} = t_l + t_{kl} - 2t_lt_{kl} \pm 2\sqrt{t_l\bar{t}_lt_{kl}\bar{t}_{kl}}(1-t_5')\,. \tag{5.38}$$

according to Eqs. (5.36) and (5.37) for the regions I_1 and I_2 respectively. We are going to discuss the implications of this relation in the next section, when we focus on the measurement function. After substituting Eq. (5.37), the final form of the angular parameterisation reads

$$\begin{aligned}\int \mathrm{d}\Omega^{(k)}_{d-2}\,\mathrm{d}\Omega^{(l)}_{d-2} =& \frac{16\pi^{\frac{1}{2}-2\epsilon}}{\Gamma(1/2-\epsilon)\Gamma(-\epsilon)}\int_0^1 \mathrm{d}t_{kl}\mathrm{d}t_l\mathrm{d}t_5(4t_{kl}\bar{t}_{kl})^{-\frac{1}{2}-\epsilon}(4t_l\bar{t}_l)^{-\frac{1}{2}-\epsilon}\\ &\times\left(t_5'(2-t_5')\right)^{-1-\epsilon}.\end{aligned} \tag{5.39}$$

At this point, it is important to keep in mind that we integrate over two copies of the integrand in Eq. (5.39), one with the substitution I_1 from Eq. (5.38), the other with the substitution I_2.

5.2.3 Measurement function

Since we encounter now two emissions with momenta k and l in the final state, the measurement function requires some modification. For the purpose of a coherent discussion, we state our ansatz for the NLO measurement function from Eq. (4.9) after making use of Eq. (5.36)

$$\mathcal{M}_1(\tau;k) = \exp\left[-\tau k_T \left(\frac{k_T}{(1-x)P_-}\right)^n f(t_k)\right]. \tag{5.40}$$

The NLO argumentation applies similarly to the NNLO case. We can propose the following ansatz

$$\mathcal{M}_2(\tau;k,l) = \exp\left[-\tau q_T \left(\frac{q_T}{(1-x)P_-}\right)^n \rho\, F(a,b,x_{12},t_k,t_l,t_{kl})\right]. \tag{5.41}$$

We are working in Laplace space, so τ is the corresponding Laplace variable with mass dimension $[\tau] = -1$. This is the reason for the exponential form of the measurement function. In order to guarantee that the argument of the exponential function is then dimensionless, we need to introduce an additional factor of q_T, which is the only dimensionful variable in our parameterisation. The n-dependent factor is chosen according to the NLO case, since the underlying physics for the NLO and NNLO case are the same: the dimensionful variable is now q_T and the energy fraction going into the hard interaction is $x = 1 - x_{12}$.
Moreover, we have introduced an additional factor ρ which accounts for the issue that we need to pull out factors from the function $F(a,b,x_{12},t_k,t_l,t_{kl})$ in order to render this function finite and non-zero in all singular limits of the matrix elements. While this factor is necessary for both SCET-I and SCET-II observables, it is particularly important in the SCET-II case. The reason is that these additional factors produce $1/\alpha^2$ poles in some contributions, as we will see below.
Besides this factor ρ, the function $F(a,b,x_{12},t_k,t_l,t_{kl})$ possesses other interesting properties. This function is in general a complicated object, which depends on the parameterisation, as well as on the angles in the transverse plane $\Theta_k, \Theta_l, \Theta_{kl}$ that were defined in section 5.2.2. Note that the dependence on x_{12} is an observable-dependent and parameterisation-dependent statement. However, for the physical (a,b)-parameterisation, which we use for both our x-space and N-space formalism, we can safely drop the x_{12}-dependence in the argument of the function $F(a,b,x_{12},\Theta_k,\Theta_l,\Theta_{kl})$ for all observables under investigation. An explicit x_{12} would cause in principle no additional problems in our setup, but it leads to simplifications if the measurement does not depend on this variable as well.

Furthermore, this function has certain limits which are protected by infrared-collinear (IRC) safety. First of all, the limit $a \to 1$ and $\Theta_{kl} \to 0$ corresponds to the case in which the two emitted particles become collinear to each other. This limit occurs for instance in the $C_F T_F n_f$ colour structure of the $q \to q$ channel, where we observe a quark-antiquark bubble. In this limit, the NNLO measurement function $\mathcal{M}_2(\tau; k, l)$ reduces to the NLO measurement function $\mathcal{M}_1(\tau; k)$ in certain physical limits

$$k^\mu \,||\, l^\mu : F(1, b, x_{12}, t_k, t_k, 0) \to f(t_k) \tag{5.42}$$

and therefore

$$\mathcal{M}_2(\tau; k, l) \to \mathcal{M}_1(\tau; k)\,. \tag{5.43}$$

Furthermore, the limit $b \to 0$ represents the limit of particle k becoming soft. This can be seen from the inverse transformation in Eq. (5.24), since the components k_+, k_- tend in the same scaling to zero for $b \to 0$. However, the limit $b \to \infty$ represents the opposite limit with particle l becoming soft.

$$b \to 0 : F(a, 0, x_{12}, t_k, t_l, t_{kl}) \to f(t_l) \tag{5.44}$$

$$b \to \infty : F(a, \infty, x_{12}, t_k, t_l, t_{kl}) \to f(t_k) \tag{5.45}$$

Notice that the measurement function has an explicit dependence on the angle Θ_k. According to Eq. (5.38), we see that the complete expression of the measurement function $F(a, b, x_{12}, t_k, t_l, t_{kl})$ consists of two different components, in which we consider in the first part the measurement $F(a, b, ...)$ and replace in the second part $t_k^+ \to t_k^-$. There are observables with an explicit dependence on this angle like transverse-momentum resummation in which the colour-singlet particle singles out a specific direction in the transverse plane, while there are others that do not. In the latter case, the two contributions then simply give a factor of two.
From the discussion of the parameterisations in section 5.2.1, one might assume that it is necessary to use different measurement functions for different regions in the phase space defined in table 5.1. As it turns out, we can exploit symmetry arguments between different regions. One symmetry uses the fact that the measurement function can not distinguish between the two emissions and it is therefore symmetric under the substitution $a \to 1/a$ and $b \to 1/b$. Therefore, the measurement function coincides in regions A and D as well as in regions B and C.

5.2.4 Crossing symmetry

As we have already pointed out in sections 4.1, 4.2 and 5.1, the collinear matrix elements correspond to the spacelike splitting functions [135]. This connection has been extensively used in the jet function computation at NNLO [50] for timelike splitting functions and it can also be extended to the beam function case to NNLO accuracy. Since we now consider two-particle emissions, the relevant splitting functions are now the triple-collinear

splitting functions [135, 136, 138] and require a more complicated crossing than in the NLO or RV case. The relevant crossing relations are

$$z_1 \to -\frac{x_1}{x}\,, \qquad z_2 \to -\frac{x_2}{x}\,, \qquad z_3 \to \frac{1}{x}\,, \tag{5.46}$$

$$s_{12} \to s_{12}\,, \qquad s_{13} \to -s_{13}\,, \qquad s_{23} \to -s_{23}\,, \qquad s_{123} \to s^B_{123}\,, \tag{5.47}$$

where we define the invariant masses $s^B_{123} = s_{12} - s_{13} - s_{23}$, $s_{12} = (k+l)^2$, $s_{13} = (k+P)^2$ and $s_{23} = (l+P)^2$. $x_{1,2}$ and x indicate the momentum fractions of the constituents inside the beam function with $x = 1 - x_1 - x_2$ due to momentum conservation. Depending on the matching kernel under consideration, it might be necessary to interchange some particles in the timelike splitting functions first, before the crossing is applied.
The derivation of these crossing relations follows closely the discussion from chapter 4. For the jet functions, we identify the relations

$$\begin{aligned} k_- &= z_1\, Q_- \\ l_- &= z_2\, Q_- \\ P_- &= z_3\, Q_- \\ Q_- &= k_- + l_- + P_-\,. \end{aligned}$$

In the diagonal quark channel, we need to perform the interchanges $Q \to -Q$ and $P \to -P$. With this, we obtain the relations:

$$\begin{aligned} k_- &= x_1\, Q_- \\ l_- &= x_2\, Q_- \\ P_- &= x\, Q_- \\ Q_- &= P_- - k_- - l_-\,. \end{aligned}$$

In order to obtain the crossing in Eq. (5.46), we consider similarly to chapter 4 the ratio between the different components k_-/Q_-, l_-/Q_-, P_-/Q_- and perform the interchanges from above. Following the argumentation from chapter 4, we arrive at Eq. (5.46). Furthermore, the invariant masses change due to the interchange $P_- \to -P_-$. For instance, $s_{13} = (k+P)^2 = 2k\cdot P \to -2k\cdot P = -s_{13}$ and analogous considerations apply for the other invariant masses. In general, the crossing works similarly for the other channels as well.
Moreover, we observe a plethora of different colour structures for the various matching kernels, which do not arise in timelike splitting functions. This is related to the interchanges between a quark and gluon in the initial and final state. However, this works exactly as in the NLO case, therefore we refer to chapter 4 for details.

5.2.5 Master formula

After studying each part of Eqs. (5.21) and (5.22) individually, we now combine all ingredients and state the master formulae for the RR contributions

in the physical parameterisation in Eq. (5.23). First, we notice that the integration over the only dimensionful variable q_T can always be performed analytically,

$$\int_0^\infty \mathrm{d}q_T\, q_T^{2d-9}\mathcal{M}_2(\tau;k,l) = \tau^{\frac{4\epsilon}{n+1}}\,(1-x)^{-\frac{4n\epsilon}{n+1}}\,P_-^{-\frac{4n\epsilon}{n+1}}\,\frac{\Gamma\big(-\frac{4\epsilon}{n+1}\big)}{n+1} \times \rho^{\frac{4\epsilon}{n+1}}F^{\frac{4\epsilon}{n+1}}(a,b,x_{12},t_k,t_l,t_{kl})\,. \tag{5.48}$$

The factor q_T^{2d-9} arises on dimensional grounds from the Jacobian of the variable transformation and the matrix element.
Finally, we conclude our general considerations by showing the master formula for the RR NNLO matching kernels in the physical parameterisation

$$\begin{aligned}\mathcal{I}_{i\leftarrow j}^{0,(2,\mathrm{RR})}(x,\tau) = {}& \frac{16\pi^{-3/2}}{\Gamma(-\epsilon)\Gamma(1/2-\epsilon)}\exp\left(\left(-\frac{4\epsilon}{n+1}+2\epsilon\right)\gamma_E\right)\frac{\Gamma\big(-\frac{4\epsilon}{n+1}\big)}{n+1}\\ &\times(1-x)^{-1-\frac{4n\epsilon}{n+1}-2\alpha}\int_0^1\mathrm{d}t_{kl}\int_0^1\mathrm{d}t_l\int_0^1\mathrm{d}t_5'\int_0^\infty\mathrm{d}a\int_0^\infty\mathrm{d}b\,(4t_l\bar{t}_l)^{-\frac{1}{2}-\epsilon}\\ &\times(4t_{kl}\bar{t}_{kl})^{-\frac{1}{2}-\epsilon}\big(t_5'(2-t_5')\big)^{-1-\epsilon}\frac{(ab)^{1-2\epsilon-\alpha}}{(a+b)^{2-2\epsilon}(1+ab)^{2-2\epsilon-2\alpha}}\,|M_{i\leftarrow j}^{(2)}|^2\\ &\times x^{\frac{4n\epsilon}{n+1}+2\alpha}\left[\rho^{\frac{4\epsilon}{n+1}}F^{\frac{4\epsilon}{n+1}}(a,b,x_{12},t_k^+,t_l,t_{kl})+(t_k^+\to t_k^-)\right]\end{aligned} \tag{5.49}$$

In Eq. (5.49), we consider the complete RR master formula without the remapping onto the unit integration range. Since the integration domain of the variables a and b spans from 0 to ∞, we need to perform the substitutions in table 5.1 to end up with integrations over the unit hypercube. As we have already mentioned, further simplifications are possible due to symmetries of the matrix element, the Jacobian and the measurement function. Notice also that the term $|M_{i\leftarrow j}^{(2)}|^2$ corresponds to the squared matrix element without the q_T-factors and the factor $\left(\frac{\alpha_s}{4\pi}\right)^2$.
Furthermore, we see that we have two isolated singularities in Eq. (5.49), the first one is given by the Γ-function $\Gamma\big(-\frac{4\epsilon}{n+1}\big)$, while we also observe a singularity in $x_{12}=1-x$, which is one of the reasons of choosing the parameterisation in Eq. (5.23). This divergence is characteristic for the diagonal channels in the quark and gluon case. In the x-space formalism, we translate this factor into distributions according to

$$\begin{aligned}(1-x)^{-1-\frac{4n\epsilon}{n+1}} = {}& -\frac{n+1}{4n\epsilon}\,\delta(1-x)+\left[\frac{1}{1-x}\right]_+-\left(\frac{4n\epsilon}{n+1}\right)\left[\frac{\ln[1-x]}{1-x}\right]_+\\ &+\frac{1}{2}\left(\frac{4n\epsilon}{n+1}\right)^2\left[\frac{\ln[1-x]^2}{1-x}\right]_+-\frac{1}{6}\left(\frac{4n\epsilon}{n+1}\right)^3\left[\frac{\ln[1-x]^3}{1-x}\right]_++\dots\,,\end{aligned} \tag{5.50}$$

for SCET-I observables, while in the SCET-II case we only need an expansion to $\mathcal{O}(\alpha)$

$$(1-x)^{-1-2\alpha} = -\frac{1}{2\alpha}\,\delta(1-x) + \left[\frac{1}{1-x}\right]_+ - 2\alpha\left[\frac{\ln[1-x]}{1-x}\right]_+ + \dots\,, \quad (5.51)$$

since $n=0$ here. In the N-space approach, the distributions get removed by an additional Mellin transformation on top of the Laplace transformation, i.e. we evaluate the integrals of the form

$$\int_0^1 \mathrm{d}x\, x^{N-1+\frac{4n\epsilon}{n+1}+2\alpha}\,(1-x)^{-1-\frac{4n\epsilon}{n+1}-2\alpha}\,I(a,b,x,\dots)\,, \quad (5.52)$$

where the expression $I(a,b,x,\dots)$ is similarly to section 5.2.1 an abbreviation for all contributions in Eq. (5.49) apart from the explicit factors in x and $(1-x)$. Due to the integration over x, the matching kernels become regular functions of the Mellin parameter N and they are not distribution valued anymore. Nevertheless, this does not apply in x-space. In this case, it is more convenient to rewrite the distributions such that we obtain x-independent coefficients in front of the distributions and finite grid contributions

$$\begin{aligned}
(1-x)^{-1-\frac{4n\epsilon}{n+1}} I(a,b,x,\dots) = \Bigg\{ & -\frac{n+1}{4n\epsilon}\,\delta(1-x) + \left[\frac{1}{1-x}\right]_+ \\
& - \left(\frac{4n\epsilon}{n+1}\right)\left[\frac{\ln[1-x]}{1-x}\right]_+ + \frac{1}{2}\left(\frac{4n\epsilon}{n+1}\right)^2\left[\frac{\ln[1-x]^2}{1-x}\right]_+ \\
& - \frac{1}{6}\left(\frac{4n\epsilon}{n+1}\right)^3\left[\frac{\ln[1-x]^3}{1-x}\right]_+ \Bigg\} I(a,b,1,\dots) \\
& + \frac{\mathrm{I}(a,b,x,\dots) - \mathrm{I}(a,b,1,\dots)}{1-x}\left(1 - \frac{4n\epsilon}{n+1}\ln[1-x]\right. \\
& \left. + \frac{1}{2}\left(\frac{4n\epsilon}{n+1}\right)^2\ln[1-x]^2 - \frac{1}{6}\left(\frac{4n\epsilon}{n+1}\right)^3\ln[1-x]^3\right), \quad (5.53)
\end{aligned}$$

which applies similarly for the SCET-II case by replacing $\frac{4n\epsilon}{n+1} \to 2\alpha$. As we anticipated in the beginning, we now have x-independent coefficients in front of the distributions. The grid contributions in the last two lines then consist of the original x-dependent integrand $I(a,b,x,\dots)$, which is now substracted by the same function $I(a,b,1,\dots)$ that appears in front of the distributions. This renders these contributions finite in the limit $x \to 1$, therefore the distributions become ordinary functions. However, this substraction is in general numerically difficult, especially in the limit $x \to 1$, and requires a careful treatment in order to keep the uncertainties in a reasonable range. Another advantage of the ordering in Eq. (5.53) is that we only need to compute the coefficients $I(a,b,1,\dots)$ once. This will be further investigated in chapter 7, where we describe the numerical implementation of our framework.

To summarise, we observe two factorised divergences in Eq. (5.49) yielding $1/\epsilon^2$ - poles (or $\frac{1}{\alpha\epsilon}$ - poles in the SCET-II case). However, the highest possible poles at $\mathcal{O}(\alpha_s^2)$ are $1/\epsilon^4$-poles for SCET-I observables and $1/(\alpha^2\epsilon^2), 1/(\alpha\epsilon^3)$-poles for SCET-II observables. The remaining singularities arise from the phase-space integration in Eq. (5.49). In particular, they tend to be entangled in form of overlapping divergences in the denominators of the matrix element. We solve this issues with the help of sector decomposition [139–141] and selector functions [142]. Besides, the measurement function is designed to be finite and non-zero in all singular limits if we pull out factors ρ appropriately.
With all these considerations in mind, we are now able to turn to individual contributions and discuss the additional steps which are needed to obtain factorised singularities in monomial form from Eq. (5.49).

Matching kernel $\mathcal{I}_{q\leftarrow q}$: $C_F T_F n_f$ - contribution

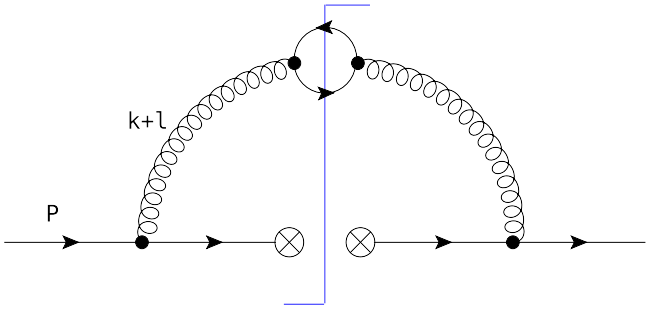

Figure 5.3: Feynman diagram for the $C_F T_F n_f$ colour structure.

One of the easiest structures in the calculation of all matching kernels is the $C_F T_F n_f$ colour structure in the $q \to q$ channel. This contribution occurs when a gluon is emitted from the incoming quark line and subsequently decaying into a quark-antiquark pair. Due to the quark bubble, the flavour of the quark-antiquark pair is unknown, hence we sum over all n_f quark flavours. We depict the corresponding diagram in figure 5.3.
In order to compute this structure, we start with Eq. (5.49). The following steps, which are necessary to obtain completely factorised singularities in terms of monomials, depend on the matrix element and partly also on the measurement function under consideration. In principle, the measurement might contain entangled singularities in form of overlapping zeroes, which need to be treated properly in our approach.
As we already pointed out in section 5.2.4, the matrix elements are related to the triple-collinear splitting functions [135]. In particular, the $C_F T_F n_f$ matrix element is related to the $\mathbb{P}_{q^*\to\bar{q}qq}$ splitting function from [136] after performing the crossing from Eqs. (4.15) and (4.16). We can decompose the complete $C_F T_F n_f$ colour structure according to

$$\mathbb{P}^{C_F T_F n_f}_{q\to\bar{q}qq^*} = \mathbb{P}^{(I_1)}_{C_F T_F n_f} + \mathbb{P}^{(I_2)}_{C_F T_F n_f} + \mathbb{P}^{(I_3)}_{C_F T_F n_f} \,. \tag{5.54}$$

$$\mathbb{P}^{(I_1)}_{C_F T_F n_f} = \frac{\left((s_{12}-2s_{23})x_1-(s_{12}-2s_{13})x_2\right)^2}{(s^B_{123})^2 s_{12}^2(1-x)^2}\left[-\frac{4xP_-}{2}\right],$$
$$\mathbb{P}^{(I_2)}_{C_F T_F n_f} = \frac{-4P_-}{s^B_{123}s_{12}(1-x)}\left[\bar{x}_1^2+\bar{x}_2^2-\epsilon\,(1-x)^2\right],$$
$$\mathbb{P}^{(I_3)}_{C_F T_F n_f} = \frac{4xP_-}{(s^B_{123})^2}\left[-\frac{1-2\epsilon}{2}\right]. \tag{5.55}$$

For later considerations, it is useful to split these contributions into three independent pieces, although we will immediately compute the sum in the numerical implementation. The next steps are to replace the invariant masses by scalar products, rewrite them in terms of light-cone coordinates and use the parameterisation from Eq. (5.23). In addition to that we need to drop the q_T-dependence, since they have been accounted for in Eq. (5.48). Afterwards, the matrix element is in such a form that it can be implemented into the master formula in Eq. (5.49).
Further investigation of the matrix element leads to the conclusion that the singularities are yet not completely factorised. The reason is that we observe an overlapping singularity in the denominator

$$s_{12} = (k+l)^2 \sim ((1-a)^2+4at_{kl}) \tag{5.56}$$

in the combined limit $a \to 1$ and $t_{kl} \to 0$, which needs to be resolved. At this point, we introduce an additional non-linear transformation, which separates the singularity [48]

$$a \to 1-u(1-v), \qquad t_{kl} \to \frac{u^2 v}{1-u(1-v)}, \qquad \{u,v\} \in [0,1]\,. \tag{5.57}$$

After performing this additional transformation, we end up with divergences in monomial form. We can state the modified version of Eq. (5.49)

$$\begin{aligned}
\mathcal{I}^{0,(2,\mathrm{RR},n_f)}_{q\leftarrow q}(x,\tau) = {}& \frac{16\pi^{-3/2}}{\Gamma(-\epsilon)\Gamma(1/2-\epsilon)}\exp\left(\left(-\frac{4\epsilon}{n+1}+2\epsilon\right)\gamma_E\right)\frac{\Gamma\left(-\frac{4\epsilon}{n+1}\right)}{n+1}\\
&\times x^{\frac{4n\epsilon}{n+1}+2\alpha}(1-x)^{-1-\frac{4n\epsilon}{n+1}-2\alpha}\int_0^1\mathrm{d}u\int_0^1\mathrm{d}t_l\int_0^1\mathrm{d}t_5'\int_0^1\mathrm{d}v\int_0^1\mathrm{d}b\,(4t_l\bar{t}_l)^{-\frac{1}{2}-\epsilon}\\
&\times (4v\bar{u}(1+uv))^{-\frac{1}{2}-\epsilon}\left(t_5'(2-t_5')\right)^{-1-\epsilon}\frac{(1-u\bar{v})^{1-\alpha}b^{-2\epsilon-\alpha}u^{-1-2\epsilon}}{(1-u\bar{v}+b)^{-2\epsilon}(1+(1-u\bar{v})b)^{2-2\epsilon-2\alpha}}\\
&\times \frac{4P_-}{(1+v)^3\left(-bu^2(1+v)^2x_{12}+b(1-u\bar{v})(1+b-u\bar{v})+b-u\bar{v}+1\right)^2}\\
&\times\Bigg(-(1+v)^2(1+b-bu\bar{v})\Big(b^2(1-u\bar{v})^3\left(x_{12}^2(1+\epsilon)-2\right)+b(1-u\bar{v})^2\\
&\times\left(b^2(x_{12}(x_{12}(\epsilon-1)+2)-2)+2x_{12}(x_{12}(\epsilon-1)+3)-4\right)+(1-u\bar{v})\\
&\times\left(2b^2(x_{12}(x_{12}(\epsilon-1)+3)-2)+x_{12}(x_{12}(\epsilon-1)+2)-2\right)+b\left(x_{12}^2(\epsilon+1)-2\right)\Big)\\
&+bu^2(v+1)^4x_{12}\Big(x_{12}\epsilon(1+b-bu\bar{v})^2+b(1-u\bar{v})(b(x_{12}-2)(1-u\bar{v})\\
&+4(x_{12}-1))+x_{12}-2\Big)+2b(1-v)^2(x_{12}-1)(2-u\bar{v})^2(bu(v-1)+b+1)^2\Bigg)
\end{aligned}$$

$$\times \left[\rho^{\frac{4\epsilon}{n+1}} F^{\frac{4\epsilon}{n+1}}(a,b,x_{12},t_k^+,t_l,t_{kl}) + (t_k^+ \to t_k^-)\right] + (b \to 1/b) \tag{5.58}$$

Here, we use the notation from Eq. (3.5) and compute the $C_F T_F n_f$ colour structure of the $q \to q$ channel. We obtain Eq. (5.58) by taking our master formula from Eq. (5.49) and insert Eq. (5.54) after removing the q_T-factor in the denominator. All singularities appear in monomial form, as we have originally desired. Notice that the derivation of the master formula for the remaining contributions works similarly. All individual sectors are listed in appendix C. Each sector needs to be implemented into Eq. (5.49) after removing the q_T-dependence in the corresponding splitting function contributions $\mathbb{P}$ and needs to be subsequently combined according to the decompositions in appendix C to yield the complete colour structures.
The $C_F T_F n_f$ colour structure is a prominent example in which the measurement function and matrix element obey symmetries, which can be exploited to reduce the number of integrations. Both the matrix element and measurement function coincide in regions A and D as well as B and C, which are obtained according to the substitutions in table 5.1.

Matching kernel $\mathcal{I}_{q\leftarrow q}$: C_F^2 - contribution

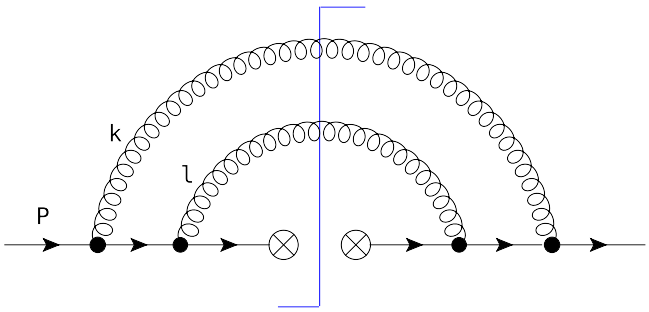

Figure 5.4: Sample Feynman diagram for the C_F^2 colour structure. The full list of diagrams which is necessary to determine this structure is provided in [124, 125].

The colour structure C_F^2 of the $q \to q$ channel requires more advanced techniques in order to disentangle all singularities. As the Feynman diagram in figure 5.4 already suggests, there are many symmetries hidden in the matrix element, which we will exploit extensively. In general, the complete contribution to this colour structure is given by

$$\mathbb{P}_{C_F^2} = \mathbb{P}^{C_F^2}_{q\to ggq^*} + \mathbb{P}^{id}_{q\to \bar{q}qq^*} \tag{5.59}$$

with

$$\begin{aligned}\mathbb{P}^{C_F^2}_{q\to ggq^*} &= \frac{1}{2}\left[\mathbb{P}^{(I_1)}_{C_F^2} + \mathbb{P}^{(I_{23})}_{C_F^2} + 2\cdot\mathbb{P}^{(I_{4A})}_{C_F^2}\right] \\ \mathbb{P}^{id}_{\bar{q}qq^*} &= \mathbb{P}^{(I_1)}_{id} + \mathbb{P}^{(I_2)}_{id} + \mathbb{P}^{(I_{3A})}_{id} + \mathbb{P}^{(I_{3B})}_{id} + \mathbb{P}^{(I_4)}_{id}\,.\end{aligned} \tag{5.60}$$

In Eq. (5.59), we have included the symmetry factor $\frac{1}{2}$, which becomes necessary because we encounter two identical particles in the final state. But in contrast to the corresponding timelike splitting function, we do not need to include this symmetry factor in front of the identical splitting function here. While we encounter two identical final state quarks in the jet function case [50], we obtain in the beam function case a quark and an antiquark due to the crossing procedure, which are now distinguishable.
We list the various contributions similarly to the $C_F T_F n_f$ case:

$$\begin{aligned}
\mathbb{P}^{(I_1)}_{C_F^2} &= \frac{4P_-}{s_{13}s_{23}x_1x_2}\left[\left\{1+x^2-\epsilon(x_1^2+x_1x_2+x_2^2)-\epsilon^2x_1x_2\right\}\right],\\
\mathbb{P}^{(I_2)}_{C_F^2} &= \frac{4xP_-}{(s^B_{123})^2}\left[2\epsilon(1-\epsilon)\right],\\
\mathbb{P}^{(I_3)}_{C_F^2} &= 4xP_-\frac{s_{13}^2+s_{23}^2}{(s^B_{123})^2 s_{13}s_{23}}\left[-(1-\epsilon)^2\right],\\
\mathbb{P}^{(I_{4A})}_{C_F^2} &= \frac{-4P_-}{s^B_{123}s_{13}x_1x_2}\left[\bar{x}_1^3+x\bar{x}_2-\epsilon(x_1^2+x_1x_2+x_2^2)\bar{x}_1+\epsilon^2x_1x_2(1+x)\right]\\
\mathbb{P}^{(I_{4B})}_{C_F^2} &= \frac{-4P_-}{s^B_{123}s_{23}x_1x_2}\left[\bar{x}_2^3+x\bar{x}_1-\epsilon(x_1^2+x_1x_2+x_2^2)\bar{x}_2+\epsilon^2x_1x_2(1+x)\right].
\end{aligned} \tag{5.61}$$

Each piece is obtained in the same way as for the $C_F T_F n_f$ structure: First, we take the $\mathbb{P}_{q\to ggq^*}$ timelike splitting functions from [135, 136], apply the crossing relations from section 5.2.4 including the transformation of the colour structures and split the contributions into the parts I_1 to I_4. For the numerical integrations, we group the contributions depending on the power of the invariant mass s^B_{123} in the denominator. Therefore, we calculate $\mathbb{P}^{(I_1)}_{C_F^2}$ separately and combine $\mathbb{P}^{(I_2)}_{C_F^2}$ and $\mathbb{P}^{(I_3)}_{C_F^2}$. For the piece $\mathbb{P}^{(I_4)}_{C_F^2} = \mathbb{P}^{(I_{4A})}_{C_F^2} + \mathbb{P}^{(I_{4B})}_{C_F^2}$, we make use of the fact that the components $\mathbb{P}^{(I_{4A})}_{C_F^2}$ and $\mathbb{P}^{(I_{4B})}_{C_F^2}$ are related by a $1 \leftrightarrow 2$, i.e. $k \leftrightarrow l$, symmetry. Hence, we only compute the contribution $\mathbb{P}^{(I_{4A})}_{C_F^2}$ and account for the second contribution by a factor of two.
There appears an additional contribution, which is induced by the so-called identical splitting function piece $\mathbb{P}_{id}$:

$$\begin{aligned}
\mathbb{P}^{(I_1)}_{id} &= 4xP_-\frac{s_{23}(s_{12}-s_{13})}{(s^B_{123})^2 s_{12}s_{13}}\left[2(1-\epsilon)\right] + (2\leftrightarrow 3),\\
\mathbb{P}^{(I_2)}_{id} &= \frac{4xP_-}{(s^B_{123})^2}\left[-2\epsilon(1-\epsilon)\right] + (2\leftrightarrow 3),\\
\mathbb{P}^{(I_{3A})}_{id} &= \frac{4P_-}{s^B_{123}s_{12}\bar{x}_1\bar{x}}\Big[(x_1^2+x^2)\bar{x}-2x_2x\bar{x}_1+\epsilon\Big\{-\bar{x}^3-(x-x_1)\bar{x}_1\bar{x}\\
&\quad +2x_2x\bar{x}_1\Big\}+\epsilon^2\bar{x}_1\bar{x}^2\Big] + (2\leftrightarrow 3),\\
\mathbb{P}^{(I_{3B})}_{id} &= \frac{4P_-}{s^B_{123}s_{13}\bar{x}_1\bar{x}}\Big[(x_1^2+x^2)\bar{x}_1+2x\bar{x}-\epsilon\Big\{\bar{x}_1^3-(x-x_1)\bar{x}_1\bar{x}+2x\bar{x}\Big\}\\
&\quad +\epsilon^2\bar{x}_1^2\bar{x}\Big] + (2\leftrightarrow 3),
\end{aligned}$$

$$\mathbb{P}_{id}^{(I_4)} = \frac{4x_1 P_-}{s_{12}s_{13}\bar{x}_1\bar{x}}\left[\left\{(x_1^2+x^2)-\epsilon\left(\bar{x}_1^2-\bar{x}_1\bar{x}+\bar{x}^2\right)+\epsilon^2\bar{x}_1\bar{x}\right\}\right] + (2\leftrightarrow 3)\,. \tag{5.62}$$

The interchange $(2 \leftrightarrow 3)$ indicates that we have to add the term in front after interchanging the indices 2 and 3.
Similar to Eq. (5.61), we group these contributions according to their powers in the invariant mass s_{123}^B. From a computational point of view, it is appropriate to combine these structures, because this leads to numerically stable and reliable results. If we consider all components together, we observe that numerical integrations become time consuming and unstable.
When we now try to implement these contributions, we encounter problems in form of overlapping divergences in the denominators of various terms. Another source of these overlapping singularities are terms in the Jacobian or the measurement function, which generate logarithmic divergences after expansion in ϵ. For example, the component $\mathbb{P}_{C_F^2}^{(I_1)}$ shares this issue. If we express the contribution in terms of light-cone coordinates and subsequently introduce the parameterisation from Eq. (5.23), the situation becomes apparent. Symbolically, we get

$$a^{1-2\epsilon}b^{1-2\epsilon}(a+b)^{2\epsilon-2}\,\mathbb{P}_{C_F^2}^{(I_1)} \sim a^{-1-2\epsilon}b^{-1-2\epsilon}(a+b)^{2\epsilon}\mathcal{N}\,. \tag{5.63}$$

The term $\mathcal{N}$ represents the remaining factors including phase-space factors, the Jacobian, the matrix element with the troublesome denominators and the measurement function. For this particular part of the C_F^2-contribution, we also observe overlapping divergences in the denominator of the matrix element, which we do not show explicitly here.
The factors $1/a^2$ and $1/b^2$ from $\mathbb{P}_{C_F^2}^{(I_1)}$ introduce a singularity in a and b, as illustrated above. We can visualise the problem in the following way: According to Eq. (5.63), we rewrite the singularities $a^{-1-2\epsilon}$ and $b^{-1-2\epsilon}$ to leading order as $\frac{-1}{2\epsilon}\delta(a)$ or $\frac{-1}{2\epsilon}\delta(b)$ and expand the second term $(a+b)^{2\epsilon}$ in ϵ such that we obtain

$$\frac{\mathcal{N}}{2\epsilon}\delta(a)\delta(b)\ln(a+b)+\mathcal{O}(\epsilon)\,, \tag{5.64}$$

which is an ill-defined expression upon integration over a and b.

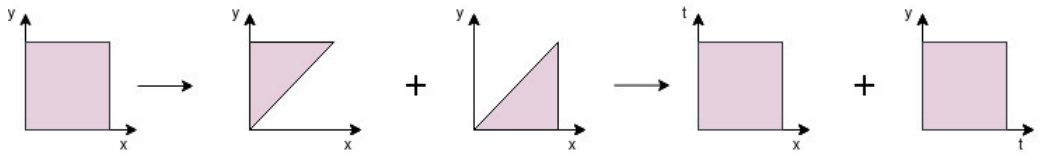

Figure 5.5: Sector decomposition in a schematic form taken from [50]. In our discussion, x corresponds to a, while y is b.

The problem is clearly related to the structure $(a+b)^{2\epsilon}$, which is an example of an overlapping zero that needs to be disentangled properly. To do so, we make

use of sector decomposition [139–141]. The idea of this approach is simple. Singularities in integrals with overlapping divergences are disentangled by splitting the integrals according to figure 5.5 first and by remapping them in the next step to the unit integration domain. Let us demonstrate the basic steps of this method for the integral above in a slightly simplified form

$$\widetilde{I} = \int_0^1 \mathrm{d}a \int_0^1 \mathrm{d}b\, a^{-1-2\epsilon} b^{-1-2\epsilon} (a+b)^{2\epsilon}\,. \tag{5.65}$$

First, we insert unity in terms of a sum of two Θ-functions

$$\widetilde{I} = \int_0^1 \mathrm{d}a \int_0^1 \mathrm{d}b\, a^{-1-2\epsilon} b^{-1-2\epsilon} (a+b)^{2\epsilon} \Big[\Theta(a-b) + \Theta(b-a)\Big] \tag{5.66}$$

which induces an ordering in the integrations over a and b. In each part of the sum, we perform a substitution which remaps the integration domain to the unit interval. First, we substitute $b \to t \cdot a$ in the domain $a > b$

$$\begin{aligned}\int_0^1 \mathrm{d}a \int_0^1 \mathrm{d}b\, a^{-1-2\epsilon} b^{-1-2\epsilon} (a+b)^{2\epsilon}\, \Theta(a-b) \\ = \int_0^1 \mathrm{d}a \int_0^1 \mathrm{d}b\, a^{-1-2\epsilon} t^{-1-2\epsilon} (1+t)^{2\epsilon}\end{aligned} \tag{5.67}$$

and similarly for $b > a$ in the second integral with $a \to t \cdot b$

$$\begin{aligned}\int_0^1 \mathrm{d}a \int_0^1 \mathrm{d}b\, a^{-1-2\epsilon} b^{-1-2\epsilon} (a+b)^{2\epsilon}\, \Theta(b-a) \\ = \int_0^1 \mathrm{d}t \int_0^1 \mathrm{d}b\, b^{-1-2\epsilon} t^{-1-2\epsilon} (1+t)^{2\epsilon}\,.\end{aligned} \tag{5.68}$$

The full result in Eq. (5.65) consists now of the sum of Eqs. (5.67) and (5.68). However, the advantage is that we have factorised all singularities in form of monomials and no overlapping zero in the factor $(1+t)^{2\epsilon}$ is present anymore. This method is sufficient to disentangle all overlapping divergences in our approach. In particular, it is enough to perform one sector decomposition step in each part of the matrix element in order to disentangle all singularities.

Moreover, we note that the parameterisation in Eq. (5.23) is particularly useful in the x-space framework since we obtain the singularity in x immediately in factorised form. Although this parameterisation also works in the N-space approach, we can use the parameterisation from Eq. (5.25) in this case. The advantage of the latter is that we do not need to perform the additional sector decomposition step.

Albeit this sector becomes particularly simple, we see that the structure $\mathbb{P}_{C_F^2}^{(I_{4A})}$ becomes more involved due to overlapping divergences. Even more problematic is the fact that this parameterisation is the first case where we explicitly observe a $x_{1,2}$-dependence in the measurement function for the observable p_T-veto, which requires additional sector decomposition steps. This complication is for example absent in the (a,b)-parameterisation. In our

N-space formalism, we use both parameterisations and see that the results agree. From the numerical side, we do not encounter major differences in terms of precision and runtime.

Matching kernel $\mathcal{I}_{q\leftarrow q}$: $C_F C_A$ - contribution

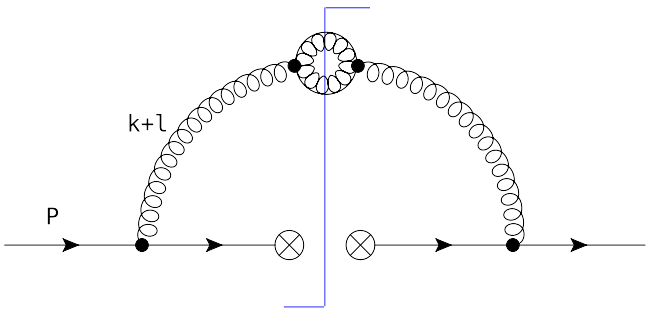

Figure 5.6: An example for a Feynman diagram for the $C_F C_A$ colour structure. The full list of diagrams, which is necessary to determine this structure is provided in [124, 125].

We next investigate the $C_F C_A$ colour structure of the $q \to q$ channel, where we will find the last complication in the computation of the RR contributions. The complete expression is

$$\mathbb{P}_{C_F C_A} = \mathbb{P}^{C_F C_A}_{q\to ggq^*} - \frac{1}{2}\left\{\mathbb{P}_{id} + \mathbb{P}^{(I_1)}_{C_F^2} + 2\cdot\mathbb{P}^{(I_{4A})}_{C_F^2}\right\} - \frac{1-\epsilon}{2}\left\{\mathbb{P}^{(I_{13})}_{C_F T_F n_f}\right\} \tag{5.69}$$

with

$$\mathbb{P}^{C_F C_A}_{q\to ggq^*} = \mathbb{P}^{(I_3)}_{C_F C_A} + \mathbb{P}^{(I_5)}_{C_F C_A} + \mathbb{P}^{(I_6)}_{C_F C_A}\,. \tag{5.70}$$

In order to obtain the contribution $\mathbb{P}^{(I_{13})}_{C_F T_F n_f}$, we combine $\mathbb{P}^{(I_1)}_{C_F T_F n_f}$ and $\mathbb{P}^{(I_3)}_{C_F T_F n_f}$ from Eq. (5.55).
Besides the expressions from the C_F^2 colour structure and parts of the $C_F T_F n_f$ colour structure discussed above, which also occur in the complete $C_F C_A$ structure, we encounter pure $C_F C_A$ contributions of the form

$$\begin{aligned}
\mathbb{P}^{(I_3)}_{C_F C_A} =& \frac{4P_-}{s_{12}s_{13}s_{23}x_1x_2\bar{x}}\left[x_1 s_{23}\left\{\bar{x}_1x_2x + x\bar{x} + \frac{\bar{\epsilon}}{2}(x_2^3+\bar{x}^3)\right\}\right.\\
&\left. + x_2 s_{13}\left\{x_1\bar{x}_2x + x\bar{x} + \frac{\bar{\epsilon}}{2}(x_1^3+\bar{x}^3)\right\}\right]\\
\mathbb{P}^{(I_5)}_{C_F C_A} =& \frac{-4P_-}{s_{12}s^B_{123}x_1x_2\bar{x}}\left[\frac{1}{2}\left\{\bar{x}_1^4+\bar{x}_2^4-2x^4-x_1x_2(x_1^2+x_2^2+12x^2)\right.\right.\\
&\left.\left. - 4(x_1\bar{x}_2+\bar{x}_1x_2)x^2 - 2x_3\bar{x}^3 - \epsilon(x_1-x_2)^2(x_1^2+x_1x_2+x_2^2)\right\}\right]\\
\mathbb{P}^{(I_6)}_{C_F C_A} =& \frac{-4P_-}{s_{13}s_{23}s^B_{123}x_1x_2\bar{x}}\left[x_1 s_{23}\left\{\frac{\bar{\epsilon}}{2}\left(\bar{x}_1^3 + x(1+x_2x)\right) + \epsilon\bar{x}_1x(1+x_2)\right.\right.
\end{aligned}$$

$$- \frac{\epsilon\bar{\epsilon}}{2} x_2 \bar{x}_2 \bar{x} \Bigg\} + x_2 s_{13} \Bigg\{ \frac{\bar{\epsilon}}{2} \left(\bar{x}_2^3 + x(1 + x_1 x) \right) + \epsilon \bar{x}_2 x (1 + x_1) - \frac{\epsilon\bar{\epsilon}}{2} x_1 \bar{x}_1 \bar{x} \Bigg\} \Bigg] \tag{5.71}$$

The pure $C_F C_A$ structure with the individual parts I_3, I_5, I_6 are of particular interest since they contain a different kind of singularity structure, which we did not observe so far. For instance, if we parameterise the I_5 term in Eq. (5.71) in terms of the physical parameterisation from Eq. (5.23), we symbolically get

$$a^{1-2\epsilon} \, \mathbb{P}^{(I_5)}_{C_F C_A} = a^{-1-2\epsilon} \frac{\mathcal{N}_2}{(1-a)^2 + 4 a t_{kl}} \, . \tag{5.72}$$

Here, we included the factor $a^{1-2\epsilon}$ from the Jacobian and isolate from Eq. (5.71) only the troublesome term in the denominator. Therefore, we see that there occur divergences for the variable a at both endpoints, i.e. for $a \to 0$ and additionally the overlapping singularity for $a \to 1$ and $t_{kl} \to 0$. These singularities at both endpoints need to be disentangled in order to obtain completely factorised divergences. One possibility would be to split the phase space integration at $a = 1/2$, similar to the discussion in section (5.2.2), where we split the t_5-integration as well at $t_5 = \frac{1}{2}$ to deal with singularities at $t_5 = 0$ and $t_5 = 1$. But in this case, we have decided to follow a different approach by introducing selector functions [142]. We multiply each contribution with a singularity structure of the type (5.72) a function of the form

$$1 = \frac{\mathcal{S}_1 + \mathcal{S}_2}{\mathcal{S}} = \frac{\mathcal{S}_1 + \mathcal{S}_2}{a + (1-a)^2 + 4 a t_{kl}} \tag{5.73}$$

and identify

$$\mathcal{S}_1 = a, \qquad \mathcal{S}_2 = (1-a)^2 + 4 a t_{kl} \quad \text{and} \quad \mathcal{S} = \mathcal{S}_1 + \mathcal{S}_2 \, . \tag{5.74}$$

In this way, we split the integration such that in one case $\mathcal{S}_1$ cancels the divergence at $a = 0$, while in the other case $\mathcal{S}_2$ removes the overlapping singularity at $a \to 1$ and $t_{kl} \to 0$. In the first part containing the selector function $\mathcal{S}_1$, we deal with the overlapping divergence by using once more the non-linear transformation from Eq. (5.57). Contrary to that, we can just continue to work in the physical parameterisation in the expression including the second selector function $\mathcal{S}_2$, since the singularity in $a \to 0$ is immediately factorised. Notice that we also encounter, similar to the previous C_F^2 contribution, overlapping divergences, where sector decomposition is necessary to factorise all singularities. In some cases, it is even necessary to split the divergences at both endpoints for the variable a with Eq. (5.74) first and subsequently apply a sector decomposition step to obtain fully factorised results.
In appendix C, we show all steps explicitly in order to obtain fully factorised singularities. Furthermore, we also highlight that it becomes necessary in some cases to pull out certain factors in the measurement to guarantee that the measurement function stays finite and non-zero. This complication will be the topic of the next paragraph.

Additional treatment of the measurement function

The methods developed so far were focussed around the manipulation of the matrix element in order to disentangle singularities therein and obtain them in monomial form. In this section, we intend to ensure that the measurement function is finite and non-zero. Albeit the singularities are in monomial form, there occur several cases in which the measurement becomes zero or even diverges in the singular limits. So far we have not encountered these cases in the physical parameterisation from Eq. (5.23) for the observables that we mainly focus on here, namely transverse-momentum resummation, jet-veto resummation and beam thrust, although this is an observable-dependent and phase-space parameterisation dependent statement. But for angularities in deep-inelastic scattering (DIS) as a class of observables, we leave the value of n, which is a parameter defining the measurement, open. More specifically, we require $n \in (0, \infty)$ based on infrared-collinear safety. These type of measurements introduce additional complications for which we have included the factor ρ in Eq. (5.41). One sector decomposition step is in general not enough to account for this issue, because the variables inside the measurement function do not scale homogeneously. In order to reduce the total number of sectors, we perform a rescaling in the variables first before we apply sector decomposition. Generally, we encounter two different types of this problem

$$\begin{aligned} \text{Type-I}: F(t, b, x_{12}, t_k, t_l, t_{kl}) &= F_I(t, b, x_{12}, t_k, t_l, t_{kl}) \cdot t^{\frac{n-1}{2}} \cdot \left[t^n + b^{1-n}\right] \\ \text{Type-II}: F(t, a, x_{12}, t_k, t_l, t_{kl}) &= F_{II}(t, a, x_{12}, t_k, t_l, t_{kl}) \cdot \left[1 + t \cdot a^{1-n}\right]. \end{aligned} \tag{5.75}$$

For Type-I, we observe that for $n > 1$ we do not encounter any difficulties. It is possible to pull out the factor $\rho^{n>1} = b^{1-n}$ such that the overlap is resolved. However for $0 < n < 1$, we still see overlapping divergences in the limit $\{b, t\} \to 0$. At this point, the idea is to rescale the variables t, b such that they scale homogeneously and subsequently perform a sector decomposition step to factorise the singularities. Hence, the following substitutions are necessary to obtain all singularities in monomial form

$$t \to s^{1-n};\ b \to g^n;\ s \to g\tilde{s};\ g \to s\tilde{s}\,. \tag{5.76}$$

These singularities lead to the factor $\rho^{n<1} = g^{\frac{1-n^2}{2}} \tilde{s}^{\frac{(1-n)^2}{2}}$, which we ultimately pull out of the measurement function.
For the second type in Eq. (5.75), we observe the opposite behaviour. In the case that $0 < n < 1$, we encounter no additional problems. But for $n > 1$, a factor a^{1-n} has to be pulled out of the measurement function, which introduces an overlapping divergence between the variables a and t for $\{a, t\} \to 0$ with an inhomogeneous scaling. We resolve this problem in a similar manner

$$t \to s^{n-1};\ a \to gs;\ s \to ga\,. \tag{5.77}$$

The factor ρ now takes the form $\rho^{n<1} = s^{\frac{1-n^2}{2}}$.
These steps are in general sufficient to disentangle all singularities that we

encounter in the measurement function on top of those in the matrix element. Notice that we have already discussed the special case $n = 0$ previously. Here, the expressions in Eq. (5.75) do not require any additional steps and we identify for the Type-I scenario that $\rho^{n=0} = t^{2\epsilon}$. This is in accordance with our previous findings and provides the explanation for the occurence of $1/\alpha^2$-poles. The factor $t^{2\epsilon}$ cancels the ϵ-dependence in the singularity $t^{-1-2\epsilon-\alpha}$, which leads to the second α-pole besides the explicit divergence in x_{12}.
In appendix C, we explicitly state in which sector we need to introduce the additional rescaling and sector decomposition.

Remaining contributions

In the previous sections, we have discussed all techniques which are necessary to obtain fully factorised singularities in the $C_F T_F n_f$, C_F^2 and $C_F C_A$ colour structure of the $q \to q$ channel. However, these methods have to be applied similarly for the other channels to end up with factorised divergences. We summarise the necessary steps in appendix C. Moreover, we have shown a few diagrams illustrating typical contributions which we need to evaluate. The full list of diagrams is given in [124, 125].
This completes our discussion on the contributions which enter at NNLO level. Since these expressions still contain poles in the dimensional regulator ϵ and in the case of SCET-II also in the rapidity regulator α, we turn our attention to the renormalisation in the next chapter.

Chapter 6

Renormalisation

In this chapter, we turn our attention to the renormalisation of the bare matching kernels $\mathcal{I}^0_{i\leftarrow j}$, which we construct from the computations in chapters 4 and 5 by using the corresponding master formulae for the NLO, RV and RR contributions. As we will see in this chapter, the renormalisation procedure works differently for SCET-I and SCET-II observables. While the bare results in the SCET-I case contain only poles in the dimensional regulator ϵ, one encounters additional rapidity divergences in the SCET-II case. This new type of singularities requires a different method to remove all divergences and to obtain a finite result which is free of rapidity and ϵ divergences. The renormalisation of the beam function matching kernels then proceeds similarly to the renormalisation of soft [48, 49] and jet [50] functions, except that the renormalisation group equations include an additional term associated with the scale dependence of the PDFs in the matching relation in Eq. (3.3). We will now first investigate the renormalisation in the SCET-I framework and then generalise this framework to the SCET-II case.

6.1 SCET-I observables

6.1.1 Renormalisation in x-space

So far, we have considered bare quantities throughout this work, i.e. Laurent expansions with poles in the dimensional regulator ϵ in the SCET-I case. We distinguished bare from renormalised quantities by a different superscript "0" for bare quantities, while renormalised quantities have no superscript.
Based on our explicit computations above, we are able to state the most general ansatz for the bare matching kernels

$$\begin{aligned}\mathcal{I}^0_{i\leftarrow j}(x,\tau) = \;& \delta_{ij}\,\delta(1-x) \\ & + \left(\frac{Z_{\alpha_s}\alpha_s}{4\pi}\right)\left(\frac{\mu\bar{\tau}^{\frac{1}{n+1}}}{q_-^{\frac{n}{n+1}}}\right)^{2\epsilon}\left\{\frac{h_2}{\epsilon^2}+\frac{h_1}{\epsilon}+h_0+h_{-1}\,\epsilon+h_{-2}\,\epsilon^2+\mathcal{O}(\epsilon^3)\right\} \\ & + \left(\frac{Z_{\alpha_s}\alpha_s}{4\pi}\right)^2\left(\frac{\mu\bar{\tau}^{\frac{1}{n+1}}}{q_-^{\frac{n}{n+1}}}\right)^{4\epsilon}\left\{\frac{y_4}{\epsilon^4}+\frac{y_3}{\epsilon^3}+\frac{y_2}{\epsilon^2}+\frac{y_1}{\epsilon}+y_0+\mathcal{O}(\epsilon)\right\}\end{aligned}$$

$$+ \mathcal{O}(\alpha_s^3)\,. \tag{6.1}$$

The second line in Eq. (6.1) can be obtained from the NLO master formulae in Eqs. (4.11), (4.12), (4.26) and (4.25). Notice that the NLO coefficients h_i are functions of x and in some cases distribution valued. This depends on the observable under investigation.
In the third line, we can identify the NNLO contributions. We combine the RV and RR contributions from sections 5.1 and 5.2 into the NNLO coefficients y_i, which again depend in general on x. All previous considerations have intended to construct an automated framework which provides these coefficients for a general class of observables within the constraints from section 3.2.
The connection between bare and renormalised quantities is provided by two renormalisation factors. In x-space, this relation is given by a convolution, which simplifies to a simple product after performing a Mellin transformation as we will see below

$$\begin{aligned}\mathcal{I}_{i\leftarrow j}(x,\tau) &= \sum_{k\in\{q,g,\bar{q}\}} Z_i^B \int_x^1 \frac{\mathrm{d}z}{z}\, \mathcal{I}^0_{i\leftarrow k}\Big(\frac{x}{z},\tau\Big) Z^f_{k\leftarrow j}(z) \\ &\equiv \sum_{k\in\{q,g,\bar{q}\}} \int_x^1 \frac{\mathrm{d}z}{z}\, \mathcal{I}^0_{i\leftarrow k}\Big(\frac{x}{z},\tau\Big) \tilde{Z}^f_{i;k\leftarrow j}(z)\,, \qquad i,j\in\{q,g,\bar{q}\}\,.\end{aligned} \tag{6.2}$$

In general, it is possible to combine the two terms Z_i^B and $Z_{k\leftarrow j}$, but a separation of those terms is more convenient in order to avoid confusions regarding the representation of the cusp and non-cusp anomalous dimensions inside Z_i^B. Here, Z_i^B substracts the UV divergences, while $Z^f_{k\leftarrow j}$ incorporates the IR divergences that match the UV divergences of the PDF.
Starting from the fact that bare quantities do not possess any μ-dependence, one can derive renormalisation group equations (RGEs) for the counterterms Z_i^B as well as $Z^f_{k\leftarrow j}$ and the renormalised matching kernels $\mathcal{I}_{i\leftarrow j}(x)$. The corresponding RGEs for the renormalisation factors are

$$\frac{d}{d\ln\mu}\, Z_i^B(\tau,\mu) = \left[4f(n)\Gamma^i_{\mathrm{cusp}}(\alpha_s)\, L - g(n)\gamma^{i,B}(\alpha_s)\right] Z_i^B(\tau,\mu)\,, \tag{6.3}$$

and

$$\frac{d}{d\ln\mu}\, Z^f_{k\leftarrow j}(x,\tau,\mu) = -\,2\sum_{l\in\{q,g,\bar{q}\}} \int_x^1 \frac{\mathrm{d}z}{z}\, Z^f_{k\leftarrow l}\Big(\frac{x}{z},\tau,\mu\Big)\, P_{l\leftarrow j}(z,\alpha_s)\,, \tag{6.4}$$

where we leave the expressions $f(n) := \frac{n+1}{2n}$ and $g(n)$ general, since they are determined by the observable. The remaining quantities in Eq. (6.3) are the cusp anomalous dimensions $\Gamma^i_{\mathrm{cusp}}(\alpha_s)$ and the non-cusp anomalous dimension $\gamma^{i,B}(\alpha_s)$. Their expansion in α_s is given in section 3.3. Generally, the cusp anomalous dimension is an observable-independent quantity and it is known at the considered two-loop order. In contrast to that the non-cusp anomalous dimension is observable dependent. One way to determine this quantity

is to compute it directly with our framework, another way makes use of consistency relations between the hard and soft anomalous dimensions, see for example Eq. (3.15). But even if the non-cusp anomalies can be determined in this way, a direct calculation provides a useful check of our calculation. As mentioned before, the index i indicates the representation of the anomalous dimensions, which ultimately depends on the channel under investigation. For the quark channel, we need to use the fundamental representation, while the gluon channels live in the adjoint representation.
The differential equations in Eqs. (6.3) and (6.4) can be used to extract general expressions for the renormalisation factors. For the UV part, we get

$$\begin{aligned} Z_i^B(\tau,\mu) &= 1 + \left(\frac{\alpha_s}{4\pi}\right)\left\{-\frac{f(n)\Gamma_0^i}{\epsilon^2} - \frac{2f(n)\Gamma_0^i L - g(n)\frac{\gamma_0^{i,B}}{2}}{\epsilon}\right\} \\ &+ \left(\frac{\alpha_s}{4\pi}\right)^2\left\{\frac{f(n)^2(\Gamma_0^i)^2}{2\epsilon^4} + \left(2f(n)^2\Gamma_0^i L - f(n)g(n)\frac{\gamma_0^{i,B}}{2} + f(n)\frac{3\beta_0}{4}\right)\frac{\Gamma_0^i}{\epsilon^3}\right. \\ &+ \left(2f(n)^2(\Gamma_0^i)^2L^2 - \Gamma_0^i\Big(f(n)g(n)\gamma_0^{i,B} - f(n)\beta_0\Big)L - f(n)\frac{\Gamma_1^i}{4} + \frac{g(n)^2(\gamma_0^{i,B})^2}{8}\right. \\ &\left.\left. - \frac{g(n)\beta_0\gamma_0^{i,B}}{4}\right)\frac{1}{\epsilon^2} - \frac{4f(n)\Gamma_1^i L - g(n)\gamma_1^{i,B}}{4\epsilon}\right\}. \end{aligned} \tag{6.5}$$

In this expression, the factors $L = \ln\Big(\mu\bar{\tau}^{\frac{1}{n+1}}/q_-^{\frac{n}{n+1}}\Big)$ stems from the prefactors in Eq. (6.1) after expansion in ϵ. Furthermore, $\beta_0 = \frac{11}{3}C_A - \frac{4}{3}T_F n_f$ represents the lowest coefficient in the expansion of the QCD β-function. Note that the origin of these terms lies in the renormalisation of the QCD coupling α_s. The relation between the bare and renormalised coupling is given by

$$\alpha_s^0 = Z_{\alpha_s}\mu^{2\epsilon}\alpha_s e^{\gamma_E\epsilon}(4\pi)^{-\epsilon} \qquad \text{and} \qquad Z_{\alpha_s} = 1 - \frac{\alpha_s}{4\pi}\frac{\beta_0}{\epsilon} + \mathcal{O}\Big(\alpha_s^2\Big)\,. \tag{6.6}$$

The second renormalisation factor has the solution

$$\begin{aligned} Z^f_{k\leftarrow j}(x,\tau,\mu) &= \delta_{kj}\delta(1-x) + \left(\frac{\alpha_s}{4\pi}\right)\left\{P^{(0)}_{k\leftarrow j}(x)\,\frac{1}{\epsilon}\right\} + \left(\frac{\alpha_s}{4\pi}\right)^2\left\{-P^{(0)}_{k\leftarrow j}(x)\,\frac{\beta_0}{2\epsilon^2}\right. \\ &\left. + \frac{1}{2\epsilon^2}\sum_l\int_x^1\frac{\mathrm{d}z}{z}P^{(0)}_{k\leftarrow l}\Big(\frac{x}{z}\Big)\;P^{(0)}_{l\leftarrow j}(z) + P^{(1)}_{k\leftarrow j}(x)\,\frac{1}{2\epsilon}\right\}. \end{aligned} \tag{6.7}$$

Here, the main quantities are the one- and two-loop splitting functions $P^{(0)}_{k\leftarrow j}(x)$ and $P^{(1)}_{k\leftarrow j}(x)$ respectively, which we take from [135, 136].
For the renormalised matching kernels, we can state a RGE as well

$$\begin{aligned} \frac{d}{d\ln\mu}\,\mathcal{I}_{i\leftarrow j}(x,\tau,\mu) &= \big[4f(n)\Gamma^i_{\text{cusp}}(\alpha_s)\,L - g(n)\gamma^{i,B}(\alpha_s)\big]\,\mathcal{I}_{i\leftarrow j}(x,\tau,\mu) \\ &\quad - 2\sum_k\int_x^1\frac{\mathrm{d}z}{z}\,\mathcal{I}_{i\leftarrow k}\Big(\frac{x}{z},\tau,\mu\Big)\,P_{k\leftarrow j}(z,\alpha_s)\,. \end{aligned} \tag{6.8}$$

Its solution is given by

$$\begin{aligned}
&\mathcal{I}_{i\leftarrow j}(x,\tau,\mu) = \delta_{ij}\cdot\delta(1-x)\\
&+\left(\frac{\alpha_s}{4\pi}\right)\left\{\Big(2f(n)\Gamma_0^i\,L^2 - g(n)\gamma_0^{i,B}\,L\Big)\delta_{ij}\delta(1-x) - 2L\,P^{(0)}_{i\leftarrow j}(x) + \mathcal{I}^{(1)}_{i\leftarrow j}(x)\right\}\\
&+\left(\frac{\alpha_s}{4\pi}\right)^2\left\{\left(2f(n)^2(\Gamma_0^i)^2L^4 - 4f(n)\Gamma_0^i\Big(g(n)\frac{\gamma_0^{i,B}}{2} - \frac{\beta_0}{3}\Big)L^3 + \Big(2f(n)\Gamma_1^i\right.\right.\\
&\left.+\,g(n)^2\frac{(\gamma_0^{i,B})^2}{2} - g(n)\beta_0\gamma_0^{i,B}\Big)L^2 - g(n)\gamma_1^{i,B}L\Big)\delta_{ij}\delta(1-x) - 2\Big(2f(n)\Gamma_0^iL^3\\
&\times\delta(1-x) + \big(\beta_0 - g(n)\gamma_0^{i,B}\big)L^2\Big)P^{(0)}_{i\leftarrow j}(x) + \left(2f(n)\Gamma_0^iL^2 - 2L\Big(g(n)\frac{\gamma_0^{i,B}}{2}\right.\\
&\left.-\,\beta_0\Big)\right)\times\mathcal{I}^{(1)}_{i\leftarrow j}(x) + 2\sum_k\int_x^1\frac{\mathrm{d}z}{z}\left(L^2\,P^{(0)}_{i\leftarrow k}\Big(\frac{x}{z}\Big) - L\,\mathcal{I}^{(1)}_{i\leftarrow k}\Big(\frac{x}{z}\Big)\right)P^{(0)}_{k\leftarrow j}(z)\\
&\left.-\,2L\,P^{(1)}_{i\leftarrow j}(x) + \mathcal{I}^{(2)}_{i\leftarrow j}(x)\right\}. \qquad (6.9)
\end{aligned}$$

As the various anomalous dimensions and splitting functions are known, the non-logarithmic terms $\mathcal{I}^{(1)}_{i\leftarrow j}(x)$ and $\mathcal{I}^{(2)}_{i\leftarrow j}(x)$ are of particular interest for us. For many observables, this provides a new input for phenomenological analyses and pushes the frontier to NNLL′ accuracy, as we discussed in section 3.3.

The next step is to derive explicit expressions for the NLO and NNLO renormalised matching kernel as well as consistency relations between the general coefficients of the bare matching kernels in Eq. (6.1) and the renormalised quantities. For the $\mathcal{O}(\alpha_s)$ contribution, we obtain

$$\begin{aligned}
\mathcal{I}^{(1)}_{i\leftarrow j}(x,\tau,\mu) &= \int_x^1\frac{\mathrm{d}z}{z}\left[\mathcal{I}^{0,(1)}_{i\leftarrow k}\Big(\frac{x}{z},\tau\Big)\delta_{kj}\delta(1-z) \;+\; \delta_{ik}\delta\Big(1-\frac{x}{z}\Big)\tilde{Z}^{(1)}_{i;k\leftarrow j}(z)\right]\\
&= \mathcal{I}^{0,(1)}_{i\leftarrow j}(x,\tau) \;+\; \tilde{Z}^{(1)}_{i;i\leftarrow j}(x)\,. \qquad (6.10)
\end{aligned}$$

Thus, we can extract consistency relations between cusp and non-cusp anomalous dimensions and bare coefficients

$$\begin{aligned}
h_2(x) &= f(n)\;\Gamma_0^i\;\delta(1-x)\,,\\
h_1(x) &= g(n)\frac{\gamma_0^{i,B}}{2}\;\delta(1-x) - P^{(0)}_{i\leftarrow j}(x)\,,\\
h_0(x) &= \mathcal{I}^{(1)}_{i\leftarrow j}(x)\,. \qquad (6.11)
\end{aligned}$$

Furthermore, the expression for the NNLO renormalised matching kernel is

$$\mathcal{I}^{(2)}_{i\leftarrow j}(x) = \mathcal{I}^{0,(2)}_{i\leftarrow j}(x,\mu) + \tilde{Z}^{(2)}_{i;i\leftarrow j}(x) + \sum_{k=q,g,\bar{q}}\int_x^1\frac{\mathrm{d}z}{z}\,\mathcal{I}^{0,(1)}_{i\leftarrow k}\Big(\frac{x}{z},\bar{\tau}\Big)\tilde{Z}^{(1)}_{i;k\leftarrow j}(z)\,. \qquad (6.12)$$

Notice that the matching kernel $\mathcal{I}^{(1)}_{q\leftarrow\bar{q}} = 0$, since the leading contribution of this kernel is $\mathcal{O}(\alpha_s^2)$. Moreover, we observe that $\mathcal{I}^{(1)}_{g\leftarrow\bar{q}} = \mathcal{I}^{(1)}_{g\leftarrow q}$ and $\tilde{Z}^{(1)}_{\bar{q}\leftarrow g} = \tilde{Z}^{(1)}_{q\leftarrow g}$ due to invariance under the discrete charge-conjugation symmetry. We are again able to connect the anomalous dimensions to the bare coefficients via

$$\begin{aligned}\Gamma_1^i\,\delta(1-x) = \frac{4}{f(n)}\Bigg(& y_2(x) - \beta_0 h_1(x) - \Gamma_0^i f(n) h_0(x) - \frac{g(n)}{2}\gamma_0^{i,B} h_1(x) \\ &+ \int_x^1 \frac{\mathrm{d}z}{z} P^{(0)}_{i\leftarrow i}\Big(\frac{x}{z}\Big) h_1(z) + \Big(\beta_0 g(n)\frac{\gamma_0^{i,B}}{4} + g(n)^2\frac{(\gamma_0^{i,B})^2}{8}\Big)\delta(1-x) \\ &- \Big(\frac{\beta_0}{2} + g(n)\frac{\gamma_0^{i,B}}{2}\Big) P^{(0)}_{i\leftarrow i}(x) + \frac{1}{2}\sum_k \int_x^1 \frac{\mathrm{d}z}{z} P^{(0)}_{i\leftarrow k}\Big(\frac{x}{z}\Big) P^{(0)}_{k\leftarrow i}(z)\Bigg), \quad (6.13)\end{aligned}$$

$$\begin{aligned}\gamma_1^{i,B}\,\delta(1-x) = \frac{4}{g(n)}\Bigg(& y_1(x) - \beta_0 h_0(x) - \Gamma_0^i f(n) h_{-1}(x) - \frac{g(n)}{2}\gamma_0^{i,B} h_0(x) \\ &+ \int_x^1 \frac{\mathrm{d}z}{z} P^{(0)}_{i\leftarrow i}\Big(\frac{x}{z}\Big) h_0(z) + \frac{1}{2} P^{(1)}_{i\leftarrow i}(x)\Bigg). \quad (6.14)\end{aligned}$$

Furthermore, one can make use of Eq. (6.12) to extract the expression $\mathcal{I}^{(2)}_{i\leftarrow j}(x)$, which represents a new prediction for some observables. Observables, for which this term is known, provide a useful check of our approach. In the SCET-I case, we exploit that the results for beam thrust [124, 125] are known analytically and choose this observable to test our framework.

6.1.2 Renormalisation in N-space

In addition to the x-space framework, we also implement our approach in Mellin (N)-space. This includes an additional integration over the variable x, which leads to simplifications in the renormalisation procedure. As we pointed out before, this is one of the main motivations to work in N-space. But since factorisation theorems require in general the beam functions in x-space, it would be necessary to transform the matching kernels back by using an inverse Mellin transformation. The contour integrals introduce numerical uncertainties which have a major impact on the accuracy of our results. But in general, the N-space results provide a useful check. Besides, there are also some observables for which the factorisation theorems are naturally stated in Mellin space. Hence, our N-space framework would be perfectly suited to study such observables.

In the following, we separate x-space expressions from N-space quantities by putting an additional hat symbol for expressions in Mellin space, similar to Eq. (3.9).

Generally, the renormalisation procedure works as in x-space except that the convolutions in the variable x become products of regular functions in the Mellin variable N due to the Mellin transformation in Eq. (3.9). For

instance, we observe for two test functions $f(x)$ and $g(x)$

$$\int_0^1 \mathrm{d}x\, x^{N-1} f \otimes_x g \equiv \int_0^1 \mathrm{d}x\, x^{N-1} \int_x^1 \frac{\mathrm{d}z}{z}\, f\Big(\frac{x}{z}\Big) \cdot g(z) = \widehat{f}(N) \cdot \widehat{g}(N)\,. \tag{6.15}$$

In order to obtain all expressions and relations from the previous section in Mellin space, we only need to perform the Mellin transformation in (3.9) on each relation and apply Eq. (6.15).

6.2 SCET-II observables

Contrary to the SCET-I case, we observe additional rapidity divergences for SCET-II observables due to the overlap of the soft with the collinear and anti-collinear regions. The reason for this issue is that the soft modes have the same virtuality as the collinear ones in SCET-II. This new type of divergences requires a modification of the renormalisation procedure. We split the following discussion for different channels in both the x-space and N-space formalisms. The diagonal channels need a slightly different approach compared to the off-diagonal channels, since the leading contributions to the off-diagonal channels start one order higher in the expansion in α_s.

6.2.1 Renormalisation in x-space

In order to account for the additional rapidity divergences in the SCET-II case, the collinear anomaly approach has been introduced in the literature [75, 143]. The idea is that in the combination of collinear, anti-collinear and soft regions the rapidity divergences have to cancel and as a result the associated rapidity logarithms will be resummed in terms of an anomaly coefficient $F^0_{i\bar{i}}(\tau)$

$$\big[\mathcal{I}^0_{i\leftarrow j}(x_1,\tau,\nu)\, \mathcal{I}^0_{\bar{i}\leftarrow k}(x_2,\tau,\nu)\, \mathcal{S}^0_{i\bar{i}}(\tau,\nu)\big]_Q = (Q\bar{\tau})^{-2F^0_{i\bar{i}}(\tau)}\; I^0_{i\leftarrow j}(x_1,\tau)\, I^0_{\bar{i}\leftarrow k}(x_2,\tau)\,. \tag{6.16}$$

At this point, we consider the collinear anomaly approach in the most general form. The index i belongs to $i \in \{q, g\}$ and therefore determines whether we work with quark or gluon kernels. In comparison to that the indices $j, k \in \{q, g\}$ are not fixed here and it is possible to choose them such that we either investigate diagonal or off-diagonal channels. Notice that Eq. (6.16) is directly stated on the level of the matching kernels rather than the (non-perturbative) beam functions. Generally, there exists the freedom to work with bare or renormalised quantities in the renormalisation procedure, thus we decide to use the bare version in our approach. As we have previously mentioned, we obtain the bare matching kernel $\mathcal{I}^0_{i\leftarrow j}(x_1,\tau,\nu)$ from the master formulae in chapters 4 and 5. Moreover, using the $n-\bar{n}$-symmetry provides an expression for the anti-collinear matching kernel $\mathcal{I}^0_{\bar{i}\leftarrow k}(x_2,\tau,\nu)$. The last ingredient is the soft function, which we obtain from the fully automated

framework `SoftSERVE` [48, 49]. This setup computes soft functions for a general class of observables to NNLO accuracy based on similar considerations as in section 3.2.

On the right-hand side of Eq. (6.16), we observe that the rapidity logarithms are resummed into the anomaly coefficient $F^0_{i\bar{i}}(\tau)$ and only the hard scale $Q^2 = q_+ q_-$ appears. Since the collinear anomaly approach operates at the scale Q, we can now understand why we have introduced the momentum q_- in the general ansatz in Eq. (6.1).

In Eq. (6.16), the Laplace variable τ encodes the observable dependence. However, the most interesting objects are the refactorised matching kernels $I^0_{i\leftarrow j}(x_1, \tau)$. Their bare version contains only poles in the dimensional regulator ϵ and their renormalisation works similarly to the SCET-I case. Additionally, the renormalised matching kernels are interesting for phenomenological studies and they are for most observables unknown at NNLO.

Both the renormalised anomaly coefficient $F_{i\bar{i}}(\tau, \mu)$ and the refactorised matching kernels $I_{i\leftarrow j}$ satisfy well-defined RGEs in the $\overline{\text{MS}}$ scheme. Before we investigate these further, it is convenient to factor out the terms related to the anomaly coefficient $F^0_{i\bar{i}}(\tau)$ in the bare matching kernels on the left-hand side of Eq. (6.16). For this, we introduce the remainder functions $W^0_{i\leftarrow j}(x, \tau)$ which contain only poles in ϵ

$$\begin{aligned}
\mathcal{I}^0_{i\leftarrow j}(x_1, \tau, \nu) &= \left(\frac{\nu}{q_-}\right)^{F^0_{i\bar{i}}(\tau)} W^0_{i\leftarrow j}(x_1, \tau)\,, \\
\mathcal{I}^0_{\bar{i}\leftarrow k}(x_2, \tau, \nu) &= \left(\frac{\nu}{q_+}\right)^{F^0_{i\bar{i}}(\bar{\tau})} W^0_{\bar{i}\leftarrow k}(x_2, \tau)\,, \\
\mathcal{S}_{i\bar{i}}(\tau, \nu) &= \left(\nu^2 \bar{\tau}^2\right)^{-F^0_{i\bar{i}}(\tau)} W^{S,0}_i(\tau)\,.
\end{aligned} \tag{6.17}$$

At this stage it becomes obvious why we need to perform the transformation from the momentum P_- to q_-. The rapidity logarithms transform with $q_- = xP_-$ according to

$$\left(\frac{\nu}{P_-}\right)^{m\cdot\alpha} \to \left(\frac{\nu}{q_-}\right)^{m\cdot\alpha} x^{m\cdot\alpha} \qquad \text{with}\, m \in \{1, 2\}\,. \tag{6.18}$$

If we now multiply the relations in Eq. (6.17), we notice that the coefficients in front of the remainder functions combine to

$$\left(\frac{\nu}{q_-}\right)^{F_{i\bar{i}}(\bar{\tau})} \left(\frac{\nu}{q_+}\right)^{F_{i\bar{i}}(\bar{\tau})} \left(\nu^2 \bar{\tau}^2\right)^{-F_{i\bar{i}}(\bar{\tau})} = \left(Q^2 \bar{\tau}^2\right)^{-F_{i\bar{i}}(\bar{\tau})} \tag{6.19}$$

such that we reproduce the resummed anomaly coefficient from Eq. (6.16) and the dependence on the scale ν drops out. Hence, the introduction of the remainder functions in Eq. (6.17) provides a possibility to connect these functions directly to the refactorised matching kernels in Eq. (6.16)

$$W^0_{i\leftarrow j}(x_1, \tau)\, W^0_{\bar{i}\leftarrow k}(x_2, \tau)\, W^{S,0}_i(\tau) = I^0_{i\leftarrow j}(x_1, \tau)\, I^0_{\bar{i}\leftarrow k}(x_2, \tau)\,. \tag{6.20}$$

Due to the $n-\bar{n}$ symmetry, it is sufficient to compute the kernels $I^0_{i\leftarrow j}(x_1,\tau)$ in order to extract the final renormalised refactorised matching kernels. But for now, we discuss the renormalisation of the anomaly coefficients and the extraction of the relevant finite piece.
Based on the collinear anomaly approach, we know that the anomaly exponent for the beam and soft function are the same. Therefore, we can use the same ansatz as analysed in [48]

$$\begin{aligned} F^0_{i\bar{i}}(x,\tau) = &-\frac{1}{2}\left(\frac{Z_{\alpha_s}\alpha_s}{4\pi}\right)(\mu^2\bar{\tau}^2)^\epsilon\left\{\frac{h^1_1}{\epsilon}+h^1_0+h^1_{-1}\,\epsilon+h^1_{-2}\,\epsilon^2+\mathcal{O}(\epsilon^3)\right\} \\ &-\left(\frac{Z_{\alpha_s}\alpha_s}{4\pi}\right)^2(\mu^2\bar{\tau}^2)^{2\epsilon}\Bigg\{\left(y^1_3+\frac{z^1_3}{2}-h^0_2\otimes_x h^1_1\right)\frac{1}{\epsilon^3}+\left(y^1_2+\frac{z^1_2}{2}-h^0_2\otimes_x h^1_0\right. \\ &\left.-h^0_1\otimes_x h^1_1\right)\frac{1}{\epsilon^2}+\left(y^1_1+\frac{z^1_1}{2}-h^0_2\otimes_x h^1_{-1}-h^0_1\otimes_x h^1_0-h^0_0\otimes_x h^1_1\right)\frac{1}{\epsilon}+y^1_0 \\ &+\frac{z^1_0}{2}-h^0_2\otimes_x h^1_{-2}-h^0_1\otimes_x h^1_{-1}-h^0_0\otimes_x h^1_0-h^0_{-1}\otimes_x h^1_1+\mathcal{O}(\epsilon)\Bigg\}. \end{aligned} \tag{6.21}$$

Similar to Eq. (6.1), the coefficients h^j_i denote the NLO coefficients, however we introduce the superscript j in order to account for the additional poles in the regulator α in the SCET-II case. The lower index i still describes the order of the ϵ-poles. The same notation applies to the NNLO coefficients. In contrast to the SCET-I case, we need to split the RV contributions, illustrated by the coefficients z^j_i, from the RR contributions with the coefficients y^j_i due to the decomposition in Eq. (3.5). There, we implement the analytic regulator on the level of the phase space measure for each final state emission in order to account for the rapidity divergences. Since the RR contribution consists of two final-state emissions, while the RV contribution has only one parton in the final state, we observe different prefactors $\left(\frac{\nu}{q_-}\right)^{2\alpha}$ and $\left(\frac{\nu}{q_-}\right)^{\alpha}$, respectively.
All coefficients in Eq. (6.21) are functions of the variable x and for convenience we have introduced the abbreviation from Eq. (6.15).
The anomaly coefficient renormalises additively via the relation

$$F^0_{i\bar{i}}(\tau) = F_{i\bar{i}}(\tau,\mu) + Z_F(\mu)\,. \tag{6.22}$$

and obeys the RGE

$$\frac{d}{d\ln\mu}\,F_{i\bar{i}}(\tau,\mu) = 2\,\Gamma^i_{\text{cusp}}(\alpha_s) \qquad i\in\{q,g\}\,. \tag{6.23}$$

For the quark channel, Γ^q_{cusp} belongs to the fundamental representation, while the gluon channel lives in the adjoint representation. After solving the RGE in Eq. (6.23), we get the solution

$$\begin{aligned} F_{i\bar{i}}(\tau,\mu) = &\left(\frac{\alpha_s}{4\pi}\right)\left\{2\Gamma^i_0\,L+d_1\right\}+\left(\frac{\alpha_s}{4\pi}\right)^2\left\{2\beta_0\Gamma^i_0\,L^2+2\left(\Gamma^i_1+\beta_0 d^i_1\right)L\right. \\ &\left.+d^i_2\right\}+\mathcal{O}\Big(\alpha_s^3\Big) \end{aligned} \tag{6.24}$$

for the anomaly coefficient and for the counterterm, which satisfies a similar RGE, we obtain

$$Z_F^i(\tau,\mu) = \left(\frac{\alpha_s}{4\pi}\right)\left\{\frac{\Gamma_0^i}{\epsilon}\right\} + \left(\frac{\alpha_s}{4\pi}\right)^2\left\{-\frac{\beta_0\Gamma_0^i}{2\epsilon^2} + \frac{\Gamma_1^i}{2\epsilon}\right\} + \mathcal{O}\left(\alpha_s^3\right). \tag{6.25}$$

The interesting quantities are the $d_{1,2}^i$ coefficients, which are observable dependent and provide a useful check of our approach, because they are known in most of the cases. Furthermore, they can be expressed in terms of the bare coefficients from Eq. (6.21) as

$$\begin{aligned} d_1^i\,\delta(1-x) &= h_0^1\,,\\ \frac{-d_2^i}{2}\,\delta(1-x) &= -y_0^1 - \frac{z_0^1}{2} + h_{-1}^0 \otimes_x h_1^1 + h_0^0 \otimes_x h_0^1 + h_1^0 \otimes_x h_{-1}^1 + h_2^0 \otimes_x h_{-2}^1 \\ &\quad + \frac{\beta_0 h_{-1}^1}{2}\,. \end{aligned} \tag{6.26}$$

In addition to that we can state consistency relations for the α - poles,

$$-y_3^1 - \frac{z_3^1}{2} = 0\,, \tag{6.27}$$

$$-y_2^1 - \frac{z_2^1}{2} + h_1^1 \otimes_z h_1^0 + \beta_0\frac{h_1^1}{2} - \Gamma_0^i\frac{\beta_0}{4}\delta(1-x) = 0\,, \tag{6.28}$$

$$-y_1^1 - \frac{z_1^1}{2} + h_1^1 \otimes_z h_0^0 + \frac{\Gamma_1^i}{4}\delta(1-x) = 0\,. \tag{6.29}$$

Next, we turn to the refactorised matching kernels $I^0_{i\leftarrow j}(x,\tau)$. As we have mentioned before, these quantities renormalise similarly to the SCET-I case, since the relation between the bare and renormalised kernels is similar to Eq. (6.2)

$$\begin{aligned} I_{i\leftarrow j}(x,\tau) &= \sum_{k\in\{q,g,\bar{q}\}} Z_i^B \int_x^1 \frac{\mathrm{d}z}{z}\, I^0_{i\leftarrow k}\Big(\frac{x}{z},\tau\Big) Z^f_{k\leftarrow j}(z) \\ &\equiv \sum_{k\in\{q,g,\bar{q}\}} \int_x^1 \frac{\mathrm{d}z}{z}\, I^0_{i\leftarrow k}\Big(\frac{x}{z},\tau\Big) \tilde{Z}^f_{i;k\leftarrow j}(z)\,, \qquad i\in\{q,g,\bar{q}\}\,. \end{aligned} \tag{6.30}$$

Hence, the kernels satisfy a similar RGE compared to Eq. (6.8). It is possible to reconstruct the RGE for the refactorised matching kernels from this equation by choosing $f(n) = \frac{1}{2}$ and $g(n) = 2$ such that

$$\begin{aligned} \frac{d}{d\ln\mu}\, I_{i\leftarrow j}(x,\tau,\mu) &= 2\left[\Gamma^i_{\mathrm{cusp}}(\alpha_s)\, L - \gamma^{i,B}(\alpha_s)\right] I_{i\leftarrow j}(x,\tau,\mu) \\ &\quad - 2\sum_k \int_x^1 \frac{\mathrm{d}z}{z}\, I_{i\leftarrow k}\Big(\frac{x}{z},\tau,\mu\Big)\, P_{k\leftarrow j}(z,\alpha_s)\,. \end{aligned} \tag{6.31}$$

The solution to this RGE is then determined by Eq. (6.9) for the same choice of $f(n)$ and $g(n)$. The interesting term is the expression $I^{(2)}_{i\leftarrow j}(x)$, which is

for many observables a new prediction. It depends on the energy fraction x and is usually stated in terms of the coefficients of the distributions and a grid for $x \in [0,1]$. Similar to the SCET-I case, the determination of this expression for various observables is one of the main tasks in this thesis and is discussed in the following chapters.
Similarly, the RGEs for the two renormalisation factors Z_i^B and $Z_{k\leftarrow j}^f$ take the form in Eqs. (6.3) and (6.4) with $f(n) = 1/2$ as well as $g(n) = 2$ with their solution given in Eqs. (6.5) and (6.7). The last step is to relate the bare refactorised matching kernels to the renormalised ones and to state explicit expressions for the anomalous dimensions and the finite refactorised matching kernels $I_{i\leftarrow j}^{(1)}(x)$ and $I_{i\leftarrow j}^{(2)}(x)$. For this discussion, it is convenient to consider diagonal and off-diagonal channels separately, since they start at different orders in the perturbative expansion in α_s.

Diagonal channels

The starting point for this discussion is Eq. (6.20), which connects the bare remainder functions that only contain poles in ϵ, to the bare refactorised matching kernels $I_{i\leftarrow j}^0(x,\tau)$. However, we need to choose the indices j,k in Eq. (6.16) explicitly to make any further statements. With the choice $j = i$ and $k = \bar{i}$, we consider diagonal matching kernels with

$$\left[\mathcal{I}_{i\leftarrow i}^0(x_1,\tau,\nu)\,\mathcal{I}_{\bar{i}\leftarrow\bar{i}}^0(x_2,\tau,\nu)\,\mathcal{S}_{i\bar{i}}^0(\tau,\nu)\right]_Q = (Q\bar{\tau})^{-2F_{i\bar{i}}^0(\tau)}\; I_{i\leftarrow i}^0(x_1,\tau)\; I_{\bar{i}\leftarrow\bar{i}}^0(x_2,\tau) \tag{6.32}$$

such that the relation for the remainder functions in Eq. (6.20) becomes

$$W_{i\leftarrow i}^0(x_1,\tau)\,W_{\bar{i}\leftarrow\bar{i}}^0(x_2,\tau)\,W_i^{S,0}(\tau) = I_{i\leftarrow i}^0(x_1,\tau)\,I_{\bar{i}\leftarrow\bar{i}}^0(x_2,\tau)\,. \tag{6.33}$$

Based on the decompositions in Eq. (6.17), we are able to propose a general ansatz for the remainder functions with $i \in \{q,g\}$

$$\begin{aligned} W_{i\leftarrow i}^0(x,\tau) = {}& \delta(1-x) + \left(\frac{Z_{\alpha_s}\alpha_s}{4\pi}\right)(\mu\bar{\tau})^{2\epsilon} W_{i\leftarrow i}^{(1)}(x) + \left(\frac{Z_{\alpha_s}\alpha_s}{4\pi}\right)^2 (\mu\bar{\tau})^{4\epsilon} W_{i\leftarrow i}^{(2)}(x) \\ & + \mathcal{O}(\alpha_s^3) \end{aligned} \tag{6.34}$$

with the NLO

$$W_{i\leftarrow i}^{0,(1)}(x) = \frac{h_2^0}{\epsilon^2} + \frac{h_1^0}{\epsilon} + h_0^0 + h_{-1}^0\epsilon + h_{-2}^0\epsilon^2 + h_2^{-1}\frac{\alpha}{\epsilon^2} + h_1^{-1}\frac{\alpha}{\epsilon} + h_0^{-1}\alpha + h_{-1}^{-1}\alpha\epsilon\,, \tag{6.35}$$

and NNLO remainder function:

$$\begin{aligned} W_{i\leftarrow i}^{0,(2)}(x) = {}& \frac{y_4^0}{\epsilon^4} + \frac{y_3^0}{\epsilon^3} + \frac{y_2^0}{\epsilon^2} + \frac{y_1^0}{\epsilon} + y_0^0 + \frac{z_4^0}{\epsilon^4} + \frac{z_3^0}{\epsilon^3} + \frac{z_2^0}{\epsilon^2} + \frac{z_1^0}{\epsilon} + z_0^0 - \frac{h_3^{-1}\otimes_x h_1^1}{\epsilon^4} \\ & - \frac{h_2^{-1}\otimes_x h_1^1}{\epsilon^3} - \frac{h_1^{-1}\otimes_x h_1^1}{\epsilon^2} - \frac{h_2^{-1}\otimes_x h_0^1}{\epsilon^2} - \frac{h_3^{-1}\otimes_x h_{-1}^1}{\epsilon^2} - \frac{h_0^{-1}\otimes_x h_1^1}{\epsilon} \\ & - \frac{h_1^{-1}\otimes_x h_0^1}{\epsilon} - \frac{h_2^{-1}\otimes_x h_{-1}^1}{\epsilon} - \frac{h_3^{-1}\otimes_x h_{-2}^1}{\epsilon}\,. \end{aligned} \tag{6.36}$$

Notice that the mixing terms appear here in order to account for the mixing of the $1/\alpha$-poles from the NLO anomaly coefficient $F^0_{i\bar{i}}$ and the $\mathcal{O}(\alpha)$ contributions from the NLO remainder function $W^0_{i\leftarrow i}(x)$. In the SCET-I case, these mixing terms would not occur and since there is no distinction between RV and RR contributions necessary, we would obtain the ansatz from Eq. (6.1). The same ansatz holds for the anti-collinear beam function and the soft function, albeit the coefficients for the collinear and anti-collinear beam function coincide due to the $n - \bar{n}$ symmetry.
Furthermore, we can express the refactorised matching kernels in terms of the collinear remainder function and the soft function from our calculations. For this, we take Eq. (6.33) and expand both sides in α_s. After exploiting the $n - \bar{n}$ symmetry between the collinear and anti-collinear expressions, we get at NLO

$$I^{0,(1)}_{i\leftarrow i}(x) = W^{0,(1)}_{i\leftarrow i}(x) + \frac{1}{2} W^{S,0,(1)}_i \tag{6.37}$$

with $i \in \{q, g\}$, while the corresponding NNLO expression involves more mixing terms

$$I^{0,(2)}_{i\leftarrow i}(x) = W^{(2)}_{i\leftarrow i}(x) + \frac{1}{2} W^{S,0,(2)}_i + \frac{1}{2} W^{0,(1)}_{i\leftarrow i}(x) W^{S,0,(1)}_i - \frac{1}{8} \left[W^{S,0,(1)}_i\right]^2 . \tag{6.38}$$

Note that the case $i = \bar{q}$ is related to $i = q$ by charge-conjugation invariance. The remaining step is to relate the bare refactorised matching kernel to the renormalised refactorised matching kernel via Eq. (6.30). At NLO, we obtain

$$I^{(1)}_{i\leftarrow i}(x, \mu) = I^{0,(1)}_{i\leftarrow i}(x, \bar{\tau}) \; + \; \tilde{Z}^{(1)}_{i;i\leftarrow i}(x) \, , \tag{6.39}$$

while the corresponding NNLO expression reads

$$I^{(2)}_{i\leftarrow i}(x, \tau, \mu) = I^{0,(2)}_{i\leftarrow i}(x, \mu) + \tilde{Z}^{(2)}_{i\leftarrow i}(x) + \sum_{k=q,g,\bar{q}} \int_x^1 \frac{\mathrm{d}z}{z} \, I^{0,(1)}_{i\leftarrow k}\Big(\frac{x}{z}, \bar{\tau}, \mu\Big) \tilde{Z}^{(1)}_{i;k\leftarrow i}(z) \, . \tag{6.40}$$

After inserting all insights, the extraction of the renormalised refactorised matching kernels becomes apparent. For the diagonal channels, we can express the cusp and non-cusp anomalous dimensions in terms of the NLO as well as NNLO coefficients in the bare remainder functions. Similar to the RGE solution in Eq. (6.9), we can go back to Eqs. (6.11) as well as (6.14) and set $f(n) = \frac{1}{2}$ and $g(n) = 2$. In the following chapters, we extract these quantities for several observables to prove that we can indeed reproduce the literature values. But as we have stressed several times before, this provides rather a check of our framework than a new prediction.

Off-diagonal channels

We can proceed similarly to extract the refactorised matching kernels for the off-diagonal channels. For these channels, we start from Eq. (6.16) with one

diagonal and off-diagonal channel

$$\begin{aligned}\left[\mathcal{I}^0_{i\leftarrow j}(x_1,\tau,\nu)\,\mathcal{I}^0_{\bar{i}\leftarrow\bar{i}}(x_2,\tau,\nu)\,\mathcal{S}^0_{i\bar{i}}(\tau,\nu)\right]_Q \\ = (Q\bar{\tau})^{-2F^0_{i\bar{i}}(\tau,\mu)}\; I^0_{i\leftarrow j}(x_1,\tau)\,I^0_{\bar{i}\leftarrow\bar{i}}(x_2,\tau)\,. \end{aligned} \tag{6.41}$$

From Eq. (6.41), we can read off that we leave the index $j \neq i$ open and set $k = \bar{i}$. The reason for this modification lies in the expansion of the off-diagonal matching kernel in α_s. While the leading contribution to the diagonal matching kernels and the soft function is of $\mathcal{O}(1)$, the contribution to the off-diagonal matching kernels with $j \neq i$ reads

$$\mathcal{I}^0_{i\leftarrow j}(x_1,\tau,\nu) = \frac{\alpha_s}{4\pi}\,\mathcal{I}^{0,(1)}_{i\leftarrow j}(x_1,\tau,\nu) + \left(\frac{\alpha_s}{4\pi}\right)^2 \mathcal{I}^{0,(2)}_{i\leftarrow j}(x_1,\tau,\nu) + \mathcal{O}\Big(\alpha_s^3\Big)\,. \tag{6.42}$$

In order to extract the refactorised matching kernel $I^0_{i\leftarrow j}(x)$ to $\mathcal{O}(\alpha_s^2)$, we have to combine the off-diagonal matching kernel $\mathcal{I}^0_{i\leftarrow j}(x_1)$ with the diagonal kernel $\mathcal{I}^0_{\bar{i}\leftarrow\bar{i}}(x_2)$. Combining two off-diagonal matching kernels would only allow for the extraction of the NLO contribution at $\mathcal{O}(\alpha_s^2)$.
The ansatz for this remainder function is slightly different from Eq. (6.36)

$$W^{0,(1)}_{i\leftarrow j}(x) = \frac{h^0_2}{\epsilon^2} + \frac{h^0_1}{\epsilon} + h^0_0 + h^0_{-1}\epsilon + h^0_{-2}\epsilon^2\,,$$

$$\begin{aligned} W^{0,(2)}_{i\leftarrow j}(x) = {} & \frac{y^0_4}{\epsilon^4} + \frac{y^0_3}{\epsilon^3} + \frac{y^0_2}{\epsilon^2} + \frac{y^0_1}{\epsilon} + y^0_0 + \frac{z^0_4}{\epsilon^4} + \frac{z^0_3}{\epsilon^3} + \frac{z^0_2}{\epsilon^2} + \frac{z^0_1}{\epsilon} + z^0_0 - \frac{h_3^{-1}\otimes_x \bar{h}^1_1}{\epsilon^4} \\ & - \frac{h_2^{-1}\otimes_x \bar{h}^1_1}{\epsilon^3} - \frac{h_1^{-1}\otimes_x \bar{h}^1_1}{\epsilon^2} - \frac{h_2^{-1}\otimes_x \bar{h}^1_0}{\epsilon^2} - \frac{h_3^{-1}\otimes_x \bar{h}^1_{-1}}{\epsilon^2} \\ & - \frac{h_0^{-1}\otimes_x \bar{h}^1_1}{\epsilon} - \frac{h_1^{-1}\otimes_x \bar{h}^1_0}{\epsilon} - \frac{h_2^{-1}\otimes_x \bar{h}^1_{-1}}{\epsilon} - \frac{h_3^{-1}\otimes_x \bar{h}^1_{-2}}{\epsilon}\,. \end{aligned} \tag{6.43}$$

In this particular case, the mixing terms connect coefficients from the collinear and anti-collinear beam function, which coincide in our approach due to the $n-\bar{n}$-symmetry. The coefficients of the anti-collinear beam function are denoted by the bar symbol.
In the off-diagonal case, the construction of the NNLO remainder function is not as simple as in Eq. (6.17) for the diagonal function, where we can derive the expression for the remainder function for each sector individually. The reason lies in the fact that the leading order in the off-diagonal case is $\mathcal{O}(\alpha_s)$. It becomes necessary at this point to consider the complete product in Eq. (6.41) for the derivation of Eq. (6.43). Then, we see that the counterterms in Eq. (6.43) in form of a product of NLO collinear and anti-collinear beam function coefficients need to be naturally inserted to account for the combination of $1/\alpha$-poles from the anomaly exponent, which occur in the decomposition of $\mathcal{I}^0_{\bar{i}\leftarrow\bar{i}}$, with $\mathcal{O}(\alpha_s)$ terms from the remainder function of the anti-collinear beam function.

Similar to Eq. (6.20), it is possible to relate the refactorised matching kernels to the remainder function at NLO and NNLO

$$\begin{aligned} I^{0,(1)}_{i\leftarrow j}(x,\tau) &= W^{0,(1)}_{i\leftarrow j}(x,\tau) \\ I^{0,(2)}_{i\leftarrow j}(x,\tau) &= W^{0,(2)}_{i\leftarrow j}(x,\tau) + \frac{1}{2}\, W^{0,(1)}_{i\leftarrow j}(x,\tau) W^{S,0,(1)}_{i}(\tau)\,. \end{aligned} \tag{6.44}$$

Notice that we can not make use of the off-diagonal channels to extract the NNLO anomaly coefficient to $\mathcal{O}(\alpha_s^2)$, since the leading order of this coefficient is α_s here. Renormalisation for the off-diagonal channels works according to Eq. (6.30) such that we obtain the relations

$$I^{(1)}_{i\leftarrow j}(x,\tau,\mu) = I^{0,(1)}_{i\leftarrow j}(x,\tau) \;+\; \tilde{Z}^{(1)}_{i;i\leftarrow j}(x)\,, \tag{6.45}$$

$$I^{(2)}_{i\leftarrow j}(x) = I^{0,(2)}_{i\leftarrow j}(x,\mu) + \tilde{Z}^{(2)}_{i\leftarrow j}(x) + \sum_{k=q,g,\bar{q}} \int_x^1 \frac{\mathrm{d}z}{z}\, I^{0,(1)}_{i\leftarrow k}\Big(\frac{x}{z},\tau,\mu\Big) \tilde{Z}^{(1)}_{i;k\leftarrow j}(z)\,. \tag{6.46}$$

for $i \neq j$.
Notice that the matching kernel $I_{q\leftarrow\bar{q}}(x)$ starts to contribute at order $\mathcal{O}(\alpha_s^2)$ and therefore $I^{(1)}_{q\leftarrow\bar{q}}(x) = 0$. As a consequence, the third term in Eq. (6.46) vanishes. Additionally, the NLO kernels $I^{(1)}_{g\leftarrow q}(x)$ and $I^{(1)}_{g\leftarrow\bar{q}}(x)$ are equal due to the C-invariance of QCD.

6.2.2 Renormalisation in N-space

For completeness, we also show the relevant relations for renormalisation in N-space. The collinear anomaly relation from Eq. (6.16) gets slightly modified

$$\begin{aligned} \Big[\widehat{\mathcal{I}}^0_{i\leftarrow j}(N_1,\tau,\nu)\, \widehat{\mathcal{I}}^0_{\bar{i}\leftarrow k}(N_2,\tau,\nu)\, \mathcal{S}^0_{i\bar{i}}(\bar{\tau},\nu)\Big]_Q \\ = (Q\bar{\tau})^{-2F^0_{i\bar{i}}(\tau)}\; \widehat{I}^0_{i\leftarrow j}(N_1,\tau)\, \widehat{I}^0_{\bar{i}\leftarrow k}(N_2,\tau)\,. \end{aligned} \tag{6.47}$$

Instead of the convolution variables $x_{1,2}$, the matching kernels depend now on the Mellin parameters $N_{1,2}$, which we have introduced via the Mellin transformation in Eq. (3.9). Moreover, we also see, as we intuitively expect, that the collinear and anti-collinear matching kernels are still related by the $n-\bar{n}$-symmetry, thus the additional Mellin transformation does not affect this symmetry. Quantities with a hat denote again that they belong to N-space.
Similar to the SCET-I case, we can extract all expressions and relations for the SCET-II renormalisation from our discussion in x-space after performing a Mellin transformation. According to Eq. (6.15), convolutions in x between two terms turn into a product in Mellin space.

Chapter 7

Numerical implementation

This chapter is devoted to the numerical implementation of our novel automated framework for the calculation of beam function matching kernels. It relies on numerical Monte Carlo integrations, which we perform with the publicly available library `Cuba` [144–146]. More specifically, we have implemented the master formulae from chapters 4 and 5 into the public code `pySecDec` [147–149], which performs the expansions in the various regulators and provides an interface to the `Cuba` library. In order to improve the numerical convergence and to obtain reliable uncertainty estimates, we have added a few further refinements that will be described in this chapter. But before we come to this part, we give a short introduction to the program `pySecDec`.

7.1 `pySecDec`

`pySecDec` is the newer version of the original program `SecDec` [141, 150, 151]. `SecDec` was originally designed for the factorisation and evaluation of parameter and multi-loop integrals based on sector decomposition of the integrands. In general, the workflow is implemented in a hybrid format between `python` and `C++`. The starting point of our implementation consists in providing the master formulae for each sector in `python`[1]. This input is then further processed with `FORM` [152–154] to produce optimised `C++` functions, which can subsequently be integrated with the numerical integrator `Cuba`. Within the `Cuba` library, we can choose between several integration methods. The most prominent ones are the `Vegas`, as well as the `Divonne`, routine, which mainly differ in their strategy to perform variance reduction. In figure 7.1, we visualise the workflow of `pySecDec`. General inputs into `pySecDec` are either loop integrals or parameter integrals. The next step in the `pySecDec` framework is connected to the parameterisation of loop inte-

[1]Notice that there is a caveat in this implementation, which we solve later in section 7.2.3. It is connected to the physical parameterisation from Eq. (5.23) in our master formulae.

grals, which is not necessary in our case since we only consider parameter integrals. After that, `pySecDec` takes the input from parameter integrals or the parameterised loop integrals to perform sector decomposition in order to disentangle overlapping singularities and to obtain completely factorised singularities. This step also becomes obsolete in our approach, since we have already obtained fully factorised divergences in each sector by using the methods described in chapter 5 in `Mathematica`. Therefore, the expressions we implement in the SCET-I case are schematically of the form

$$I(\{x_i\}) = \Pi_i \, x_i^{-1+a_i\epsilon} R(\{x_i\}) \tag{7.1}$$

with integration on a multi-dimensional unit hypercube in the variables $\{x_i\}$. In the SCET-II case, we have

$$I(\{x_i\}) = \Pi_i \, x_i^{-1+a_i\epsilon+b_i\alpha} R(\{x_i\}) \,, \tag{7.2}$$

where some of the variables a_i may be zero, which requires the rapidity regulator α to make the integral well-defined. In the above expression, we have in fact assumed that all divergences arise in the limit $x_i \to 0$, while the function $R(\{x_i\})$ is finite and non-zero in this limit. The next step in the workflow, namely the contour deformation, is not relevant, because we only evaluate parameter integrals and we can immediately proceed to step 5, which corresponds to the substraction of the poles. It aims to isolate poles in the regulators ϵ or α with the help of integration by parts. In the general case

$$I(\{x_i\}) = \Pi_i \, x_i^{a+a_i\epsilon} R(\{x_i\}) \tag{7.3}$$

or

$$I(\{x_i\}) = \Pi_i \, x_i^{a+a_i\epsilon+b_i\alpha} R(\{x_i\}) \,, \tag{7.4}$$

partial integrations need to be employed for $|a| > 1$. However, we only encounter the case $a = -1$ in our setup, therefore we can also skip this step. Besides, we already implement the singularities in monomial form into `pySecDec`, an internal isolation inside the `pySecDec` framework is therefore not necessary.
Factorising the singularities explicitly has the advantage that we can expand the integrand in terms of distributions and perform a Laurent expansion in the regulators ϵ and α. The order of expansion is relevant in the SCET-II case, the α expansion needs to be performed first.

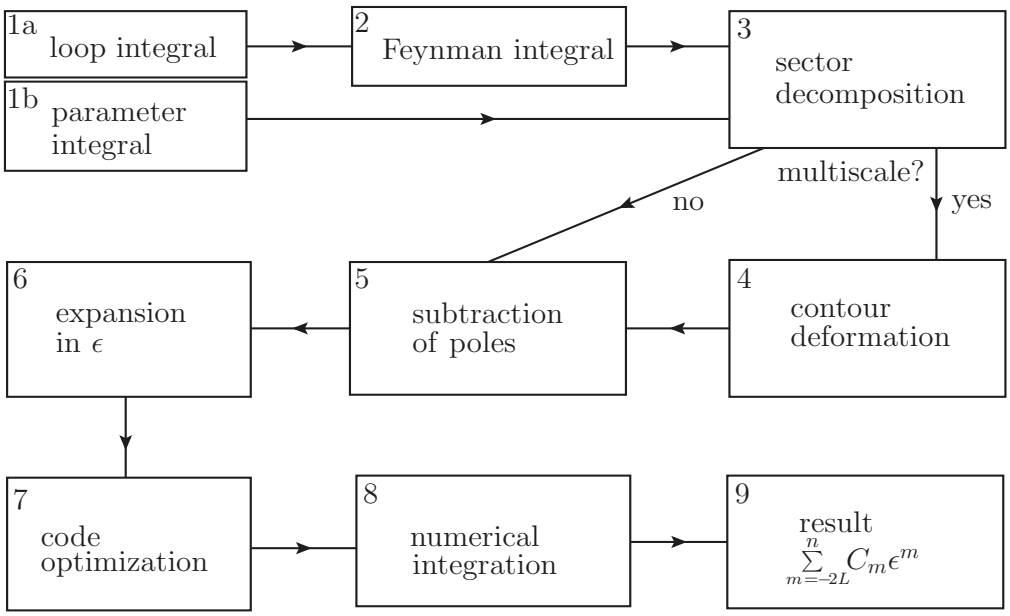

Figure 7.1: Workflow for the code `pySecDec` taken from [147].

Furthermore, `pySecDec` optimises the code for a more efficient numerical integration in the following step. In older versions, like the 1.4.4 version which we make use of in our implementation, `pySecDec` relies on the `Cuba` library to integrate these optimised expressions numerically with Monte Carlo techniques. Here, the user has the freedom to choose between different integrators, although we stick to the integrator `Vegas`. In the last step, `pySecDec` provides the result of the numerical integration in form of a Laurent expansion in the regulators ϵ and α. We take these bare results and perform the renormalisation subsequently based on our discussion in chapter 6.

7.2 Error estimation

In this section, we discuss methods to quantify the uncertainties of our numerical implementation. This topic is of importance in order to obtain reliable and well-defined results and it provides information regarding the feasibility as well as competitiveness compared to direct analytical or semi-numerical calculations. For this, we investigate the basics of Monte Carlo integrations first and study the uncertainty estimates based on optimisation techniques like importance sampling.

7.2.1 Monte Carlo integration

Monte Carlo (MC) integration is a powerful technique to evaluate integrals numerically by treating the integrals as discrete sums over a large number of sampling points. While there exist many different MC algorithms, they all share the same characteristics [155]:

- The integrand does not need to be smooth or even continuous. In particular, step functions or other irregular functional dependencies do not pose any problems.
- The convergence rate of the integrals does not depend on their dimension per integration, but solely on the sampling points.

In order for this characteristics to hold and in order to obtain a reasonable estimate, the number of sampling points should be at least around 10^6. Although MC techniques are usually applied for the evaluation of multidimensional integrals, it is sufficient at this stage to work for simplicity with one-dimensional integrals. Consider for example the integral of the form

$$I[f] = \int_G \mathrm{d}x\, f(x)\,. \tag{7.5}$$

The true value of $I[f]$ can be estimated by the relation

$$\langle I^N[f]\rangle_p = \frac{1}{N}\sum_{k=1}^{N}\frac{f(x_k)}{p(x_k)}\,, \tag{7.6}$$

where x_k are uniform random points. In Eq. (7.6), we discretise the original integral for $I[f]$ by using N random points inside the domain G with normalised probability density $p(x)$ to scan the behaviour of the test function $f(x)$. For a proper estimate, N should be sufficiently large. The strong law of large numbers guarantees that in the limit $N \to \infty$ we observe

$$\lim_{N\to\infty}\langle I^N[f]\rangle_p = I[f]\,. \tag{7.7}$$

However, in most cases we do not know the value for $I[f]$ and hence its variance is also unknown. To obtain an estimate for the uncertainty on the Monte Carlo integration, it is possible to make use of the empirical variance

$$\sigma_N^2[f] = \frac{1}{N(N-1)}\left(\sum_{k=1}^{N}\left(\frac{f(x_k)}{p(x_k)}\right)^2 - \frac{1}{N}\left(\sum_{k=1}^{N}\frac{f(x_k)}{p(x_k)}\right)^2\right)^2\,. \tag{7.8}$$

If we now increase the number of sampling points N, the variance σ_N^2 reduces at the cost of an increasing runtime of the integration. This naive error estimate can be further optimised with certain sampling methods. A prominent example is used in the `Vegas` algorithm called importance sampling. We use this routine for our numerical integrations.

7.2.2 `Vegas`

The `Vegas` method is based on calculating the estimate in Eq. (7.6) for the integral $I[f]$ M times [155]. In each evaluation, we get an error estimate $\sigma_{N,i}^2[f]$ according to Eq. (7.8). The idea is now to vary the probability function $p(x)$ such that the uncertainties $\sigma_{N,i}^2[f]$ get reduced step by step

until they are minimised. From a theoretical point of view, the explicit choice

$$p(x) = \frac{|f(x)|}{\int_G \mathrm{d}x |f(x)|} \tag{7.9}$$

minimises the error $\sigma_N^2[f]$, meaning that the sampling points are concentrated in the region where the magnitude is the largest. `Vegas` evaluates now M estimates to approximate the integral $I[f]$ in the best way. In this method, the integral $I[f]$ is not just given approximately by Eq. (7.6), but rather by the cumulative estimate

$$I[f] \approx \bar{\sigma}^2 \sum_{i=1}^{M} \frac{\langle I^N[f] \rangle_{p,i}}{\sigma_{N,i}^2} \tag{7.10}$$

with

$$\bar{\sigma}^2 = \left[\sum_{i=1}^{M} \frac{1}{\sigma_{N,i}^2} \right]^{-1} . \tag{7.11}$$

In the first step, the algorithm starts with uniformly distributed random variables and obtains an approximate estimate $\langle I^N[f] \rangle_{p,1}$. The integration domain is divided into a large number of hypercubes such that the average number of points per cube is nearly constant. After this first iteration step, the density $p(x)$ gets modified such that $\sigma_{N,2}^2 < \sigma_{N,1}^2$ in the next iteration. We proceed M times with the aim that $\sigma_{N,M}^2 \leq \sigma_{N,M-1}^2 < ... < \sigma_{N,1}^2$. The number of evaluations N during one iteration step remains constant. This implies that, due to the change of the probability density, the grid of hypercubes is narrow in regions with large $|f(x)|$ and therefore samples these regions in more detail, while other regions get suppressed. In this way, `Vegas` tries to find the optimal grid to reduce the variance. This method is called importance sampling, i.e. depending on the magnitude of the test function $f(x)$, the algorithm samples these regions with more points. This step is iterated a fixed number of times, until the parameter χ^2 per degree of freedom

$$\chi^2/\mathrm{dof} = \frac{1}{M-1} \sum_{i=1}^{M} \frac{\left(\langle I^N[f] \rangle_{p,i} - \langle I^N[f] \rangle \right)^2}{\sigma_{N,i}^2} \tag{7.12}$$

tends to approximately one. Thus, the estimate $\langle I^N[f] \rangle_p$ becomes reasonably close to the original expression $I[f]$.

7.2.3 Computational parameterisation

The previous discussion on the basics of MC integration and importance sampling methods is helpful to understand why the phase-space parameterisations that we have introduced in chapters 4 and 5 are not yet suited for

numerical evaluations. In particular, problems arise for the angular integrations over the variables t_l, t_{kl}, which are of the form

$$\Big(4x(1-x)\Big)^{-\frac{1}{2}-\epsilon} \qquad \text{with} \quad x \in \{t_l, t_{kl}\}\,, \tag{7.13}$$

and from other terms like $y^{-2\epsilon}$. Especially the first type of divergences leads to problems at the both endpoints if we expand the expression in ϵ

$$\Big(4x(1-x)\Big)^{-\frac{1}{2}-\epsilon} = \frac{1}{\sqrt{4x(1-x)}} \sum_{n=0}^{\infty} \frac{(-\epsilon)^n}{n!} \ln^n\Big[4x(1-x)\Big] \tag{7.14}$$

and induces square root singularities at $x = \{0, 1\}$.
Contrary to that, logarithmic divergences result from the phase-space measure and become singular in the limit $y \to 0$

$$y^{-2\epsilon} = 1 - 2\epsilon \ln(y) + \mathcal{O}(\epsilon^2)\,. \tag{7.15}$$

Both square-root and logarithmic singularities are integrable divergences, however they potentially cause problems during numerical evaluations. In regions near singularities, it becomes difficult to sample the integrand which has an unbounded peak in this area. In particular, square-root divergences cause a major problem for Monte Carlo integrations based on variance reduction techniques. This is the case for both the `Vegas` and `Divonne` routines, although `Vegas` is less affected by this issue. The reason for the stability of the `Vegas` algorithm lies in the fact that this routine suppresses phase space points at endpoints. Only for high precision runs with a large number of sampling points, the algorithm starts to probe the regions near the endpoints and breaks down due to square-root and logarithmic singularities.
Moreover, variance reduction techniques use the empirical variance to compute an error estimate for the numerical evaluation, which depends on the underlying probabilistic function $p(x)$ to sample the points and on the number of evaluation points N. Therefore, the sample variance is always finite, but the variance of the integral itself is unbounded due to the integrable singularities. Adaptive integration techniques are based on the assumption that the variance of the integrand is finite and subsequently use the empirical variance to reduce the error estimate. Thus, the error estimates are in general unreliable, since the basic requirement for adaptive integration techniques is not fulfilled.
We intend to use the `Vegas` routine for our numerical evaluations, so we need to find a way to avoid these type of singularities. In principle, we are able to resolve this issue by appropriate substitutions. For logarithmic singularities, it is sufficient to perform the following substitution

$$\begin{aligned}\int_0^1 \mathrm{d}y\, y^{-2\epsilon} f(y) &= \int_0^1 \mathrm{d}y^2\, y^{-4\epsilon} f(y^2) = 2\int_0^1 \mathrm{d}y\, y^{1-4\epsilon} f(y^2) \\ &= 2\int_0^1 \mathrm{d}y\, f(y^2)\Big(y - 4\epsilon y \ln(y) + \mathcal{O}(\epsilon^2)\Big)\,,\end{aligned} \tag{7.16}$$

where the function $f(y)$ is a finite test function. We observe that this substitution leads to a suppression of the form $y\ln(y)$. In our specific case, we use this transformation for the t_5'-integration and thus replace $t_5' \to s_5^2$.
Square-root divergences in the variable u, which appears after making use of the non-linear transformation in Eq. (5.57), can also be removed by the substitution

$$\begin{aligned}\int_0^1 \mathrm{d}u\, u^{-1-2\epsilon}\,(1-u)^{-\frac{1}{2}-\epsilon} f(u)&\\ &= 2\int_0^1 \mathrm{d}u_t\,(1-u_t)\left[1-(1-u_t)^2\right]^{-1-2\epsilon}(1-u_t)^{-1-2\epsilon} f\Big(1-(1-u_t)^2\Big)\\ &= 2\int_0^1 \mathrm{d}u_t\,(1-u_t)^{-2\epsilon}u_t^{-1-2\epsilon}(2-u_t)^{-1-2\epsilon} f\Big(1-(1-u_t)^2\Big)\,. \qquad (7.17)\end{aligned}$$

Rather than substituting a squared variable, we apply $u \to 1-(1-u_t)^2$ here. We trade the square root divergence at $u=1$ for a logarithmic divergence in $u_t = 1$, which is less problematic for numerical integrations in `Vegas`. Besides, in most regions we get additional terms of the form $(1-u_t)^m$ with $m > 1$ from the Jacobian and matrix element such that the logarithmic singularity is ultimately removed. In the case where numerical integrations are not stable in one sector, we observe that the transformation $u \to 1-(1-u_t^2)^4$ removes the logarithmic divergence completely.
Finally, we turn our attention to the most prominent square root divergence given in Eq. (7.13). For this type of divergence, we use

$$t_x \to 1-(1-s_x^4)^4 \qquad\qquad x \in \{l, kl\} \qquad (7.18)$$

in order to remove singularities at 0 and 1 for the angular integrations. Notice that we also perform this substitution for the angular variable v which enters due to the non-linear transformation in Eq. (5.57).
With this set of substitutions, we get rid of all problematic square root divergences. We call this parameterisation in the end the computational parameterisation as it has no direct physical meaning like the physical parameterisations in Eqs. (5.23), (5.25) or (5.27) and as it is only included to account for numerical issues during Monte Carlo integrations. Our `pySecDec` input in the `python` files is expressed in terms of this parameterisation instead of the physical parameterisation.

7.2.4 Error propagation

In this section, we explain how we obtain the final uncertainties of the renormalised matching kernels in the SCET-I and -II case. Prior to the discussion on the numerical implementation, we have discussed the various contributions, which enter the final result. Besides the NLO and the RV contributions in chapters 4 and section 5.1 respectively, there are the more complicated RR contributions, which are characterised by a two-particle final state. This makes it necessary to perform numerical Monte Carlo integrations to evaluate the phase-space integrals. We parameterise the phase space with the

physical parameterisation from section 5.2.1, which has the advantage that the singularities in the variable x are immediately factorised. Our N-space formalism performs an additional Mellin transformation (3.9), which removes the distributions in x according to Eqs. (5.50) as well as (5.51). However, we notice that the physical parameterisation suffers from square-root divergences originating from the angular integrations and logarithmic singularities, which we need to remove in order to apply MC techniques based on variance reduction like importance sampling in the `Vegas` routine. The computational parametrisation achieves precisely this goal such that we can obtain numerically reliable error estimates from `Cuba`. Chapter 8 states all channels and independent matching kernels which we need to evaluate. We observe three quark channels, which lead to seven independent kernels which we define according to their colour structure, and analogously two gluon channels with five independent kernels. Each kernel has various sectors, which we need to combine following the decompositions in chapter 5 for the quark channels or the decompositions in appendix C for the remaining contributions. Thus, each of these sectors is independently implemented in our `pySecDec` framework and provides bare numbers from the numerical integrations, which we need to combine according to the decompositions. We add the uncertainties from each sector quadratically in `Mathematica`, since we assume that the error estimates are uncorrelated and have a Gaussian nature. At this point it becomes obvious why we aim to have completely factorised singularities in each sector, which we achieve with the methods described in chapter 5. Although `pySecDec` would be in principle able to compute integrals with overlapping singularities as well, we see now the advantage of the divergences in monomial form. Compared to a direct input into `pySecDec` without any disentanglement, we observe that it is numerically more stable to remove overlapping divergences by hand. On top of that, we obtain better error estimates, while we also reduce the runtime significantly at the cost that we need to implement more sectors. Nevertheless, runtime reduction and better numerics support our framework.

This procedure yields the uncertainties on the level of the bare matching kernels in (6.1) and (6.36). But the final expression for the matching kernels consists of NLO and RV contributions as well. In our framework for both x- and N-space, we calculate those terms fully analytically for the observables under investigation. Therefore, these coefficients do not represent a new source of uncertainties. However we notice that, especially for the N-space formalism, we can evaluate these contributions also numerically, which provides a useful check of the analytic computation. But if we consider these coefficients from the numerical evaluations, we see that they increase the errors up to 50% due to the large uncertainties stemming from the RV contributions. Using the analytic results instead of the numerical estimates is thus desirable.

In order to obtain the renormalised matching kernels, we need to combine these various contributions during the renormalisation procedure. For instance, the error propagation for the anomaly coefficient d_2^i in Eq. (6.26)

works in the following way

$$\sigma_{d_2^i} = 2 \cdot \Bigg[\sigma^2_{y_0^1} + \frac{1}{4}\sigma^2_{z_0^1} + \sigma^2_{h^0_{-1}} \left(h_1^1\right)^2 + \left(h_{-1}^0\right)^2 \sigma^2_{h_1^1} + \sigma^2_{h_0^0} \left(h_0^1\right)^2 + \left(h_0^0\right)^2 \sigma^2_{h_0^1} + \sigma^2_{h_1^0} \left(h_{-1}^1\right)^2 + \left(h_1^0\right)^2 \sigma^2_{h^1_{-1}} + \sigma^2_{h_2^0} \left(h_{-2}^1\right)^2 + \left(h_2^0\right)^2 \sigma^2_{h^1_{-2}} + \frac{\beta_0^2}{4} \sigma^2_{h^1_{-1}} \Bigg]^{\frac{1}{2}}. \tag{7.19}$$

In our discussion, we are able to extract the NLO and RV coefficients completely analytically, hence they do not contribute. As a consequence, the error on the RR coefficients y directly propagates to the anomaly coefficient d_2^i. This observation holds for all expressions in the off-diagonal channels. But we see that the diagonal channels contain another source of uncertainties due to the contributions from the soft functions in Eqs. (6.16) and (6.47). These coefficients are provided by `SoftSERVE` and introduce uncertainties, in particular for the finite matching kernels. The errors on the NLO and RV coefficients are in general negligible, while the errors on the RR contribution become sizeable.

Notice that the level of precision in the individual sectors lies around 0.1% to 0.2% for our high precision setup, but during the combination of all sectors the total uncertainty tends to become as large as 1%. But we also observe for many observables large cancellations of RR and RV contributions such that these combined errors become sizeable and exceed the sub per mille level, although we manage to maintain this level of precision in each sector of the RR contributions individually. This is one disadvantage of introducing many sectors. Uncertainties seem to be overestimated since the central values from our computation tend to be in very good agreement with the results from the literature.

Furthermore, we notice that in our N-space approach the additional integration over x increases the runtime of the numerical evaluations and provides worse central values with larger uncertainties compared to the results in x-space. Factorisation theorems for most observables are stated in x-space, hence a calculation in N-space is not necessary. In particular, the inverse transformation from Mellin space to x-space is additionally non-trivial and introduces unknown systematic errors. Nevertheless as we have mentioned before, there exist some observables in the literature which are defined in Mellin space and where our setup is useful.

But the x-space approach comes with its own complications, especially the grid contribution. This contribution is problematic, as it can be seen from Eq. (5.53). We substract from the complicated function $I(a, b, x, ...)$ the function at $x = 1$ rendering this difference finite in the limit $x \to 1$. We implement this exactly in our framework in order to guarantee that large contributions cancel internally. This works from the numerical perspective quite well. However, we encounter a different critical behaviour at the endpoint $x \to 0$. Here, there occur logarithmic divergences in x in every colour structure, which result from the factor $x^{\frac{4n\epsilon}{n+1}+2\alpha}$. A similar behaviour is also possible for the limit $x \to 1$, which is induced by the NLO splitting functions during renormalisation. In order to capture the correct behaviour at these

points, a larger number of sampling points is required. Numerical integrations in the direct vicinity of $x = 0$ become unreliable and need a careful study. This aspect will be more important when it comes to the implementation of this approach into a novel standalone `C++` code, which is beyond the scope of this work.

Chapter 8

Results

In this chapter, we collect all results obtained with the outlined automated framework to compute beam function matching kernels both in momentum and Mellin space. Specifically, we consider transverse-momentum (p_T) resummation, jet-veto resummation, the hadron collider event shape beam thrust and angularities in deep inelastic scattering. p_T-resummation and beam thrust play a special role in this context, because analytic results are known in this case and hence they provide a useful test of the SCET-II and SCET-I setup, respectively. In contrast to that our results for jet-veto resummation and DIS angularities are new [122].
For the characterisation of the different renormalised matching kernels, we follow the notation from chapter 6. At NLO, we encounter four different channels, which we denote by $\mathcal{I}^{(1)}_{i\leftarrow j}(x)$. In the NNLO case, there are many different channels containing different colour structures. We separate the quark matching kernels based on the various colour structures and follow for this the notation from [122]:

$$\begin{aligned}
\mathcal{I}^{(2)}_{q\leftarrow q}(x) &= C_F^2\,\mathcal{I}^{(2,C_F)}_{q\leftarrow q}(x) + C_F C_A\,\mathcal{I}^{(2,C_A)}_{q\leftarrow q}(x) + C_F T_F n_f\,\mathcal{I}^{(2,n_f)}_{q\leftarrow q}(x) \\
&\quad + C_F T_F\,\mathcal{I}^{(2,T_F)}_{q\leftarrow q}(x)\,, \\
\mathcal{I}^{(2)}_{q\leftarrow g}(x) &= C_F T_F\,\mathcal{I}^{(2,C_F)}_{q\leftarrow g}(x) + C_A T_F\,\mathcal{I}^{(2,C_A)}_{q\leftarrow g}(x)\,, \\
\mathcal{I}^{(2)}_{q\leftarrow \bar{q}}(x) &= C_F(C_A - 2C_F)\,\mathcal{I}^{(2,C_{AF})}_{q\leftarrow \bar{q}}(x) + C_F T_F\,\mathcal{I}^{(2,T_F)}_{q\leftarrow q}(x)\,, \\
\mathcal{I}^{(2)}_{q\leftarrow q'}(x) &= \mathcal{I}^{(2)}_{q\leftarrow \bar{q}'}(x) = C_F T_F\,\mathcal{I}^{(2,T_F)}_{q\leftarrow q}(x)\,.
\end{aligned} \tag{8.1}$$

The notation q' denotes a quark with different flavour than the quark q. Charge-conjugation invariance reduces the number of independent matching kernels as well. We also observe that some matching kernels can be expressed in terms of contributions, which we already computed for another kernel, leaving us with seven independent contributions that we need to calculate.
For the gluon channels at NNLO, we can state a similar decomposition according to different colour structures:

$$\begin{aligned}
\mathcal{I}^{(2)}_{g\leftarrow q}(x) &= C_F^2\,\mathcal{I}^{(2,C_F)}_{g\leftarrow q}(x) + C_F C_A\,\mathcal{I}^{(2,C_A)}_{g\leftarrow q}(x) + C_F T_F n_f\,\mathcal{I}^{(2,n_f)}_{g\leftarrow q}(x) \\
\mathcal{I}^{(2)}_{g\leftarrow g}(x) &= C_A^2\,\mathcal{I}^{(2,C_A)}_{g\leftarrow g}(x) + C_A T_F n_f\,\mathcal{I}^{(2,C_A n_f)}_{g\leftarrow g}(x) + C_F T_F n_f\,\mathcal{I}^{(2,C_F n_f)}_{g\leftarrow g}(x)\,.
\end{aligned} \tag{8.2}$$

This decomposition also holds for the refactorised renormalised matching kernels $I^{(2)}_{i\leftarrow j}(x)$ in the SCET-II case. For our Mellin space framework, we replace each expression in Eqs. (8.1) and (8.2) by the corresponding Mellin transformed N-dependent functions. Before we study the individual observables, it is convenient to introduce the decomposition into distributions and the remainder, which we call grid, in our x-space approach. For the diagonal $q \to q$ channel, we perform the decomposition

$$\begin{aligned}\mathcal{I}^{(2,y)}_{q\leftarrow q}(x) = \; & c^q_{-1}\,\delta(1-x) + c^q_0 \left[\frac{1}{1-x}\right]_+ + c^q_1 \left[\frac{\ln(1-x)}{1-x}\right]_+ \\ & + c^q_2 \left[\frac{\ln^2(1-x)}{1-x}\right]_+ + c^q_3 \left[\frac{\ln^3(1-x)}{1-x}\right]_+ + \mathcal{I}^{(2,y),\text{Grid}}_{q\leftarrow q}(x)\end{aligned} \tag{8.3}$$

with $y \in \{n_f, T_F, C_F, C_A\}$ and for the diagonal gluon channel, we decompose similarly

$$\begin{aligned}\mathcal{I}^{(2,y)}_{g\leftarrow g}(x) = \; & c^g_{-1}\,\delta(1-x) + c^g_0 \left[\frac{1}{1-x}\right]_+ + c^g_1 \left[\frac{\ln(1-x)}{1-x}\right]_+ \\ & + c^g_2 \left[\frac{\ln^2(1-x)}{1-x}\right]_+ + c^g_3 \left[\frac{\ln^3(1-x)}{1-x}\right]_+ + \mathcal{I}^{(2,y),\text{Grid}}_{g\leftarrow g}(x)\end{aligned} \tag{8.4}$$

where now $y \in \{C_F n_f, C_A n_f, C_A\}$. The off-diagonal channels do not contain a singularity in $(1-x)$ such that we only obtain a grid contribution in this case. Therefore, we can identify

$$\mathcal{I}^{(2,y)}_{q\leftarrow g}(x) = \mathcal{I}^{(2,y),\text{Grid}}_{q\leftarrow g}(x)\,, \qquad y \in \{C_F, C_A\} \tag{8.5}$$

$$\mathcal{I}^{(2,y)}_{g\leftarrow q}(x) = \mathcal{I}^{(2,y),\text{Grid}}_{g\leftarrow q}(x)\,, \qquad y \in \{n_f, C_F, C_A\}\,, \tag{8.6}$$

$$\mathcal{I}^{(2,C_{AF})}_{q\leftarrow \bar{q}}(x) = \mathcal{I}^{(2,C_{AF}),\text{Grid}}_{q\leftarrow \bar{q}}(x)\,. \tag{8.7}$$

In order to obtain the corresponding SCET-II relations, we need to replace the matching kernels in Eqs. (8.1) to (8.7) by the refactorised matching kernels from chapter 6.

As we have discussed earlier in section 3.1, the coefficients in front of the distributions are numbers and thus independent of x, while the whole x-dependence is contained in the grid contribution. For our N-space setup, it is not necessary to perform such a decomposition since we integrate over the singularity in x and transform all distributions into regular functions in the Mellin parameter N.

To conclude our general considerations here, we state the decompositions for the anomaly coefficients d^i_2 into different colour structures here. For the NNLO anomaly coefficient, we perform the decomposition

$$\begin{aligned} d^q_2 &= d^{n_f}_2\, C_F T_F n_f + d^{C_F}_2\, C^2_F + d^{C_A}_2\, C_F C_A\,, \\ d^g_2 &= d^{n_f}_2\, C_A T_F n_f + d^{C_A}_2\, C^2_A\,, \end{aligned} \tag{8.8}$$

for the quark and gluon channel, respectively. At this point, we notice that these expressions are related via Casimir scaling. Casimir scaling is a property which originates from the similar structure of quark and gluon soft functions and allows to extract the gluon soft function from the quark soft function by replacing $C_F \to C_A$. Therefore, the quark channel colour factors C_F^2 and $C_F C_A$ are combined to yield C_A^2, while the $C_F T_F n_f$ structure in the quark channel becomes $C_A T_F n_f$ for the gluon channel.
Casimir scaling is only applicable for soft function matrix elements, which are in general expressed in terms of Wilson lines. There, it becomes immediately obvious that replacing a quark Wilson line by a gluon Wilson line only amounts for the change of the Casimir operator. In the beam function case, we can exploit this scaling relation whenever we work in the threshold limit $x \to 1$, which describes the physical situation that the complete energy goes into the hard interaction and the radiation becomes soft. Hence, the matrix elements simplify to the soft matrix elements for each colour structure, for which we know the replacement is valid. Due to the decompositions from Eqs. (8.3) and (8.4), we see that the coefficients $c^{q,g}_{-1,0,1,2,3}$ are defined in the limit $x \to 1$ and therefore related via Casimir scaling. The same is also true for the anomaly coefficients d_2^i for SCET-II observables. In addition to that we also use Casimir scaling for the soft function in the collinear anomaly approach. The quark soft function is provided by `SoftSERVE`, while we obtain the gluon soft function via Casimir scaling. An example where Casimir scaling is not applicable are the quark and gluon anomalous dimensions $\gamma_1^{\{q,g\},B}$, since this quantity requires the full collinear matrix element for its determination.

8.1 Transverse-momentum resummation

The first observable we are going to present is p_T-resummation, which has been extensively studied in section 2.1. For this observable, the measurement function is given by:

$$\omega_{p_T}(\{k_i\}) = -2i \sum_i k_{i,T} \cos(\Theta_i)\,. \tag{8.9}$$

We observe an explicit dependence on the angle Θ_i in the transverse plane, since the QCD radiation has to balance the transverse momentum of the colour-singlet particle, which thus singles out a specific direction in the transverse plane. On top of this, we note that the measurement function is purely imaginary in this case, which is in conflict with the assumptions specified in section 3.2. In order to solve this problem, we follow a procedure that was introduced for the calculation of the Fourier-space soft functions in [48, 49]. To this end, one considers the auxiliary measurement function

$$\omega^{\text{aux}}_{p_T}(\{k_i\}) = 2 \left| \sum_i k_{i,T} \cos(\Theta_i) \right|$$

for which the requirement $\omega \geq 0$ is now satisfied. We follow the argumentation in [48], where the treatment of Fourier-space soft functions is described

in detail. The same argumentation also holds in the beam function case. Ultimately, it is possible to compute the measurement from Eq. (8.9) by taking the absolute value of Eq. (8.9) and multiply it by an additional factor. According to [48], this factor is $\cos(\pi\epsilon)$ in the NLO case and $\cos(2\pi\epsilon)$ for both the RV and RR case.
At NLO, the auxiliary function, which we use from now on to compute p_T-resummation, takes the form

$$f_{p_T}^{\text{aux}} = 2|1 - 2t_k|\,, \tag{8.10}$$

whereas it is given at NNLO in terms of the variables in Eq. (5.23) by

$$F_{p_T}^{\text{aux}} = 2\sqrt{\frac{a}{(a+b)(1+ab)}} \cdot \left|1 - 2t_l + b \cdot \left(1 - 2t_k^{\pm}\right)\right|. \tag{8.11}$$

Notice that the auxiliary observable vanishes for special configurations with

$$\Theta_i = \frac{\pi}{2}\,, \tag{8.12}$$

which corresponds to

$$t_l = t_k^{\pm} = \frac{1}{2} \tag{8.13}$$

in Eq. (8.11). As the measurement function contributes in form of logarithms after expanding in the regulators, this leads to an integrable divergence, which is complicated to treat numerically since it leads to a logarithmic divergence similar to the one we have encountered in chapter 7. In principle, it is possible to split the phase space such that the integrable divergences lie at the endpoints rather than inside the integration region, but this approach would be observable dependent and not within the idea of our approach.
From the numerical perspective, we make use of the fact that contributions with $F_{p_T}^{\text{aux}} = 0$ have zero weight in the phase space. Hence, we can set $F_{p_T}^{\text{aux}} = 1$ for these specific points without changing the result.
p_T-resummation is an example for a SCET-II observable, therefore we use the collinear anomaly framework discussed in chapter 6 in order to arrive at renormalised results. During renormalisation, we can extract the observable-dependent constants d_1^i and d_2^i entering the anomaly coefficient $F_{i\bar{i}}$, but also the non-cusp anomalous dimensions $\gamma_0^{i,B}$, $\gamma_1^{i,B}$ as well as the refactorised matching coefficients from chapter 6. For most observables that we encounter, the non-cusp anomalous dimensions as well as the anomaly coefficients are known at NNLO and provide a useful check for our computation. For p_T-resummation, the renormalised matching kernels are also known analytically from [78, 79], as we will see in the following.

x-space

We start by stating the results in x-space. At NLO, we can compare the non-cusp anomalous dimension $\gamma_0^{i,B}$ and the anomaly coefficient d_1^i to the results

d_2^q	analytic	this work
$C_F T_F n_f$	-8.2963	$-8.2956(50)$
C_F^2	0	0.0009(468)
$C_F C_A$	-3.7317	$-3.6882(526)$

d_2^g	analytic	this work
$C_F T_F n_f$	0	0
$C_A T_F n_f$	-8.2963	$-8.2970(54)$
C_A^2	-3.7317	$-3.7325(450)$

Table 8.1: NNLO anomaly coefficients for the quark and gluon channels. We take the analytic results from [78, 79]. Notice that we can obtain the gluon anomaly coefficient from the quark anomaly coefficient via Casimir scaling.

$\gamma_1^{q,B}$	analytic	this work
$C_F T_F n_f$	11.3946	11.3948(3)
C_F^2	-10.6102	$-10.6102(432)$
$C_F C_A$	-4.6371	$-4.6471(419)$

$\gamma_1^{g,B}$	analytic	this work
$C_F T_F n_f$	4	4
$C_A T_F n_f$	7.2882	7.2884(29)
C_A^2	-17.1941	$-17.1951(15)$

Table 8.2: Non-cusp anomalous dimension $\gamma_1^{i,B}$ for the quark and gluon channel. The analytic results are known from [78, 79].

in the literature, as well as the finite refactorised renormalised matching kernel for the four different channels. We can extract the NLO quantities analytically, since they only contain a one-particle final state as discussed in chapter 4. We find that $\gamma_0^{q,B} = -3C_F$ and $\gamma_0^{g,B} = -\beta_0$ for the $q \to q$ and $g \to g$ channel, respectively, as well as $d_1^q = d_1^g = 0$. For the refactorised matching kernels defined in Eq. (6.45), we obtain

$$I_{q\leftarrow q}^{(1)}(x) = 2C_F\,(1-x) - \frac{\pi^2}{6} C_F\,\delta(1-x)\,, \tag{8.14}$$

$$I_{q\leftarrow g}^{(1)}(x) = 4T_F\,x(1-x), \tag{8.15}$$

$$I_{g\leftarrow q}^{(1)}(x) = 2C_F\,x, \tag{8.16}$$

$$I_{g\leftarrow g}^{(1)}(x) = -\frac{\pi^2}{6} C_A\,\delta(1-x)\,. \tag{8.17}$$

These results are in agreement with the literature [78, 79].
We proceed to the comparison of the NNLO results. Our results for the NNLO anomaly coefficient d_2^i are collected in table 8.1, which are in agreement with the analytic results for both the quark as well as the gluon channel. Even the uncertainties on the most complicated colour structure, the $C_F C_A$-structure in the diagonal quark channel, are under good control and the central value is in good agreement with the expected value. The quark and gluon coefficients are related to each other through Casimir scaling, as we have discussed in the beginning of this chapter.

c_{-1}^q	analytic	this work
$C_F T_F n_f$	5.1735	5.1740(28)
C_F^2	1.3529	1.3463(749)
$C_F C_A$	−8.2534	−8.1352(1385)

c_{-1}^g	analytic	this work
$C_F T_F n_f$	0	0
$C_A T_F n_f$	5.1735	5.1928(64)
C_A^2	−6.9005	−6.9551(761)

Table 8.3: Coefficients c_{-1}^i in front of the δ-distribution in Eqs. (8.3) and (8.4). These coefficients are again related by Casimir scaling.

c_0^q	analytic	this work
$C_F T_F n_f$	8.2963	8.2956(50)
C_F^2	0	$7 \cdot 10^{-6}$
$C_F C_A$	3.7317	3.6883(526)

c_0^g	analytic	this work
$C_F T_F n_f$	0	0
$C_A T_F n_f$	8.2963	8.2970(54)
C_A^2	3.7317	3.7325(450)

Table 8.4: Coefficients c_0^i in front of the plus distribution in Eqs. (8.3) and (8.4). These coefficients are again related by Casimir scaling.

Next, we turn to the NNLO non-cusp anomalous dimension $\gamma_1^{i,B}$, which is also analytically known [78, 79] and for completeness given in appendix A. Our numbers are shown in table 8.2 and we observe perfect agreement within the uncertainties. Moreover, we extract the x-independent coefficients in front of the distributions in x in Eqs. (8.3) and (8.4). As the distributions only occur in the case of explicit divergences in x, they arise only for the diagonal quark and gluon channels. We show the results for the $q \to q$ channel and the $g \to g$ channel in tables 8.3 and 8.4.
It turns out that the coefficients $c_1^{q,g}, c_2^{q,g}, c_3^{q,g}$ vanish, which is a common feature of every SCET-II observable. The reason is that we only need to expand the SCET-II case in Eq. (3.6) up to $\mathcal{O}(\alpha)$ since the highest possible pole in the regulator α is $1/\alpha^2$. Furthermore, the deviations of the central values show the same pattern as for the anomaly coefficients and the non-cusp anomalous dimensions and therefore agree with the analytic results within one standard deviation. But besides the $C_F C_A$ structure, other colour structures show larger uncertainties as well since we expand the integrand to higher orders in the regulator. Note also that we are again able to relate both channels via Casimir scaling, i.e. it is sufficient to compute the quark channel to this order and extract the values for the gluon channels by replacing $C_F \to C_A$ in the quark channel results. In addition to that we observe a direct relation between the anomaly coefficient d_2^i and the coefficient in front of the plus distribution c_0^i. These two coefficients only differ by a global minus sign. This is related to the construction of these contributions. For both the d_2^i and c_0^i coefficients, the same $\mathcal{O}(\alpha^0)$-terms multiply the singularity $(1-x)^{-1-2\alpha}$, which provides after an expansion in α the d_2^i coefficient from the first term and the c_i^0 coefficient from the second term in the expression. This relations also hold for the other observables which we consider in

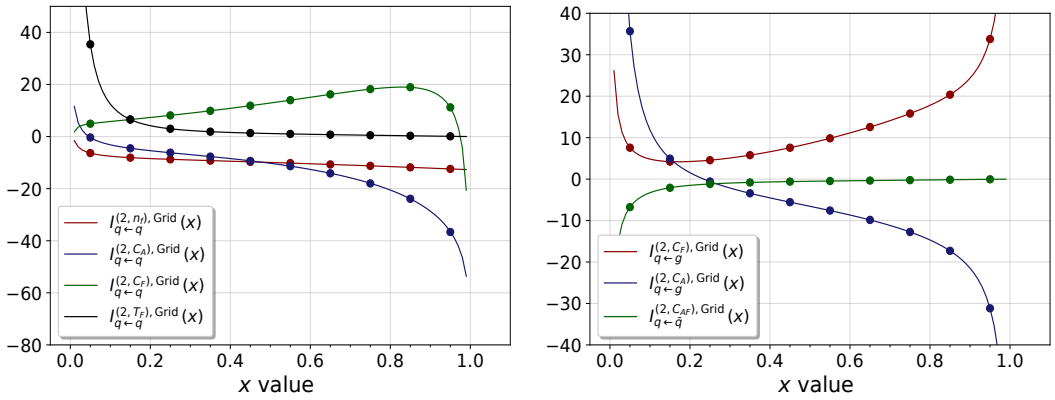

Figure 8.1: Grid contribution to the refactorised matching kernels for all quark channels for the observable transverse-momentum resummation in x-space. The dots indicate numbers from our numerical approach, the solid lines the analytical expressions taken from [78, 79]. Uncertainties on our computation are included, but not visible.

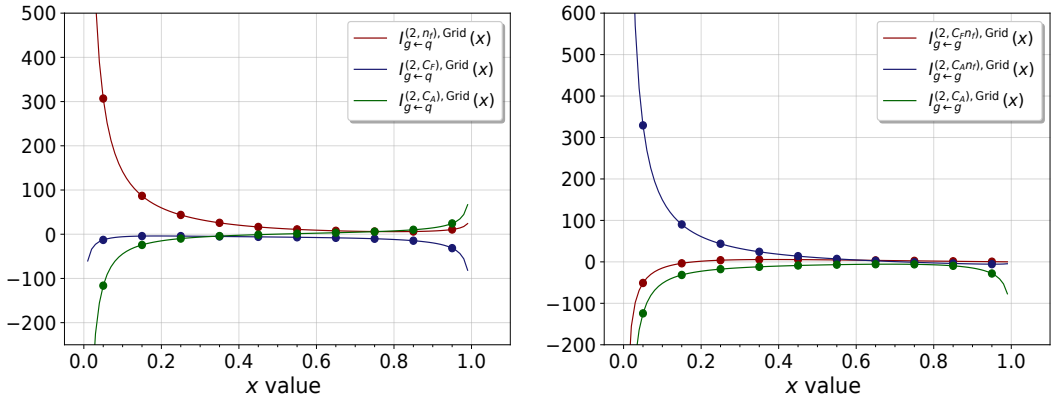

Figure 8.2: This plot shows the same as in figure 8.1 for the gluon channels.

this work. Notice that the values in $\gamma_1^{i,B}$ are not related via Casimir scaling, because we need the full collinear matrix element in this case.
Finally, we plot the grid contribution of the NNLO refactorised matching kernels in the conventions of Eqs. (8.3) and (8.4). The results are also analytically known in this case [78, 79]. Therefore, this observable constitutes a useful check of our approach. The dots indicate the prediction obtained with our framework, which lie perfectly on the solid lines provided by the analytic expressions from [78, 79]. We include the uncertainties in the plots, albeit they are not visible.
This observable proves that our approach is able to reproduce the known results for p_T-resummation. Notice that the low and high x values provide critical limits, which need to be tested in general more carefully with a finer grid. This is left for a more dedicated study of specific observables in the future; the goal at this stage is to prove the applicability of our setup. Figures 8.1 and 8.2 reproduce this behaviour, since the analytic predictions illustrated by the solid lines diverge for each colour structure in the limit $x \to 0$

and also for some structures for $x \to 1$. As we have already pointed out, this is related to logarithms in the variable x occurring in the expressions of the master formula in Eq. (5.49) after expansion in α and ϵ and to diverging factors in the limit $x \to 1$ originating from prefactors inside the splitting function.
From the numerical perspective, this observable is the most expensive observable that we consider in this work because of the angular dependence which allows for zeroes inside the integration domain. However, the very good agreement with the analytic results underlines the precision and applicability of our approach.

N-space

The observable p_T-resummation provides also an immediate check for our N-space formalism. Similar to the x-space results at NLO, we can extract the non-cusp anomalous dimension $\gamma_0^{i,B}$ and anomaly coefficient d_1^i together with the finite refactorised matching kernels at NLO. While the former can again be obtained analytically, the refactorised matching kernels are now functions of the Mellin value N introduced during the Mellin transformation from Eq. (3.9). We find

$$\widehat{I}^{(1)}_{q\leftarrow q}(N) = \frac{2C_F}{N(1+N)} - \frac{\pi^2}{6}C_F, \tag{8.18}$$

$$\widehat{I}^{(1)}_{q\leftarrow g}(N) = \frac{4T_F}{(N+1)(N+2)}, \tag{8.19}$$

$$\widehat{I}^{(1)}_{g\leftarrow q}(N) = \frac{2C_F}{N+1}, \tag{8.20}$$

$$\widehat{I}^{(1)}_{g\leftarrow g}(N) = -\frac{\pi^2}{6}C_A\,. \tag{8.21}$$

In principle, the two-loop anomaly coefficient d_2^i and non-cusp anomalous dimension γ_1^B can be extracted for different Mellin values N. Since we evaluate the beam function for ten different Mellin values, we obtain ten different estimates for these quantities. We decide to choose the Mellin value $N = 12$, because it lies in the middle of our Mellin parameter range and represents the central values as well as the corresponding uncertainties well. Our results are shown in tables 8.5 and 8.6. These results agree with the results from the literature and they are comparable to the numbers we found in the x-space approach in tables 8.1 and 8.2. We can move on and consider again the refactorised matching kernels for all partonic channels. As we have already seen at NLO, they depend now on the Mellin parameter N. Besides that, the integration over x removes all distributions and a decomposition according to Eqs. (8.3) and (8.4) is not needed in this case. Our results are displayed in figure 8.3, where we see that the our computation, illustrated in form of the dots with uncertainties, agrees again with the analytic results represented by the solid lines.

d_2^q	analytic	this work
$C_F T_F n_f$	-8.2963	$-8.2932(41)$
C_F^2	0	0.0155(389)
$C_F C_A$	-3.7317	$-3.7236(191)$

d_2^g	analytic	this work
$C_F T_F n_f$	0	0
$C_A T_F n_f$	-8.2963	$-8.2969(68)$
C_A^2	-3.7317	$-3.7287(558)$

Table 8.5: NNLO quark and gluon anomaly coefficient d_2^i. The analytic results are given in [78, 79].

$\gamma_1^{q,B}$	analytic	this work
$C_F T_F n_f$	11.3946	11.3915(89)
C_F^2	-10.6102	$-10.5959(420)$
$C_F C_A$	-4.6371	$-4.6520(528)$

$\gamma_1^{g,B}$	analytic	this work
$C_F T_F n_f$	4	4
$C_A T_F n_f$	7.2882	7.2884(73)
C_A^2	-17.1941	$-17.1951(579)$

Table 8.6: Non-cusp anomalous dimensions $\gamma_1^{i,B}$ for the quark and gluon channels. Analytic results are extracted from [78, 79].

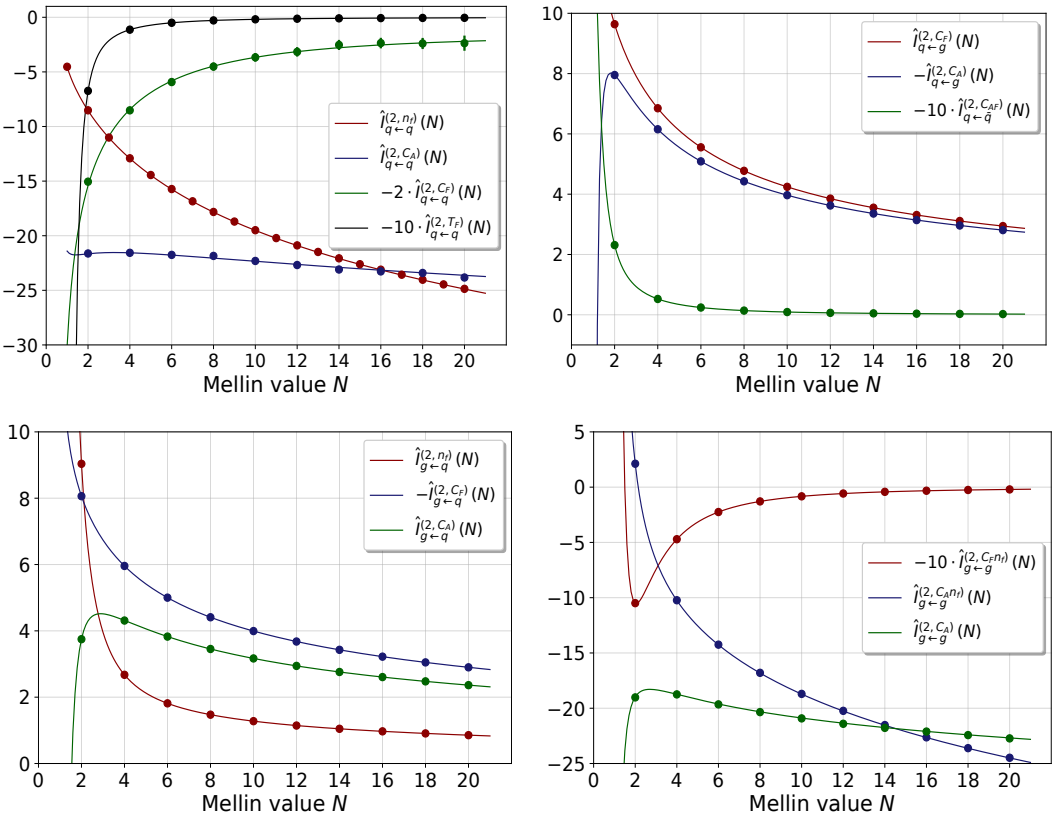

Figure 8.3: Refactorised matching kernel for all quark channels (upper row) and gluon channels (lower row) for the observable transverse-momentum resummation in Mellin space. The dots indicate numbers from our numerical approach, the solid line the analytical expression taken from [78, 79]. Uncertainties on our computation are included, but not visible.

Furthermore, we find that the critical behaviour for $x \to 0$ in x-space is mapped onto the small N-range due to the Mellin transformation in Eq. (3.9). We expect in this limit logarithmic divergences or explicit divergences of the form $\frac{1}{x}$, which transform under a Mellin transformation like

$$\int_0^1 \mathrm{d}x \, \frac{\ln^b(x)}{x^a} x^{N-1} = \frac{(-1)^b b!}{(N-a)^{1+b}} \,. \tag{8.22}$$

For $N \to 1$, the analytic predictions start to diverge if there appears a factor of $\frac{1}{x}$ in x-space, but the large N limit seems to be under good control, at least for the parameter range investigated in this work.
However, we notice another interesting fact regarding the numerics. The integration over x has a direct impact on the numerical accuracy of our approach. This is already visible in the values for d_2^i and $\gamma_1^{i,B}$, especially for the NNLO non-cusp quark anomalous dimension. While the central values in x-space, in particular for the C_F^2 colour structure, are particularly close to the analytic result, there is a slight deviation in N-space, which is still well within the uncertainties. The same observation applies for the refactorised matching kernels. This is remarkable, especially in the context that the number of evaluations we used in our Mellin space approach is $2.5 \cdot 10^8$ points instead of the 10^8 points in momentum space. But performing more precise numerical integrations in order to achieve the same level of agreement as for the x-space results might lead to a breakdown of the integration with the `Vegas` routine, as has been discussed in chapter 7. In this case, it might become necessary to use another numerical integrator like `Divonne`, which is also implemented in `SoftSERVE` [48, 49].

8.2 Jet-veto resummation

The next observable we consider is jet-veto resummation. Jet vetoes are often applied in LHC analyses to suppress backgrounds. In order to extract for instance the $H \to W^+W^-$ signal, one imposes a veto on additional jets to suppress the background from $t\bar{t}$-production that also end up in a W^+W^- pair and two additional b-jets.
Due to its phenomenological importance, this jet-veto resummation has been studied in many physical applications, ranging from Drell-Yan and Higgs production to the resummation of arbitrary electroweak final states in [156–161], specific analyses of associated Higgs production [162, 163], gauge boson pair production [164–166] to beyond-standard-model computations [167–170]. With the methods developed in this work, it is possible to extend the resummation to NNLL$'$ accuracy. In fact, our calculation in [122] has provided the NNLO refactorised matching kernels for the quark channels in Mellin space for the first time, while they were published in momentum space for all channels in [171]. The current state-of-the-art for the prediction of the jet-vetoed Higgs boson includes a resummation of logarithms up to NNLL matched onto N^{3}LO fixed order computations [172].
The general form of the measurement function is complicated as it depends

on the details of the jet algorithm, which clusters the particles according to a pair-wise recombination scheme. For one emission, the veto is directly imposed on this emission and one has

$$\mathcal{M}_1(\tau;k) = \Theta(p_T^{\text{veto}} - k_T)\,. \tag{8.23}$$

By taking a Laplace transform with respect to the variable p_T^{veto}, we can bring this measurement function into the form in Eq. (4.9) with $n = 0$, $f(\Theta_k) = 1$ and an additional factor $1/\tau$. The method for inverting the Laplace transform before renormalisation was described in [49] and it amounts to multiplying the NLO computation by a factor $\frac{e^{2\epsilon\gamma_E}}{\Gamma(1-2\epsilon)}$ and the NNLO contribution by $\frac{e^{4\epsilon\gamma_E}}{\Gamma(1-4\epsilon)}$. These factors are, in fact, slightly different compared to the ones in [49], because the analytic regulator does not include any τ-dependence in the beam function case. Therefore, we can take the factors from [49] and set $\alpha = 0$ in order to obtain our correction factors. By including these factors, we are able to use our approach without any further restrictions.
At NNLO, the jet algorithm distinguishes between regions in which the two emissions are clustered together and those where they are treated separately. The distinction depends on the distance measure

$$\Delta^2 = \frac{1}{4}\ln^2\left(\frac{l_+k_-}{l_-k_+}\right) + \Theta_{lk}^2 \tag{8.24}$$

in terms of which the measurement becomes

$$\mathcal{M}_2(\tau;k,l) = \Theta(p_T^{\text{veto}} - \omega_{\text{veto}}(k,l)) \tag{8.25}$$

with

$$\omega_{\text{veto}}(k,l) = \Theta(\Delta - R)\max\Big(k_T, l_T\Big) + \Theta(R-\Delta)\Big|\vec{k}_T + \vec{l}_T\Big|, \quad .$$

Depending on the size of the distance measure, the algorithm identifies the particle with the largest transverse momentum as an independent jet if $\Delta > R$ or groups them together into a single jet if the measure is less than the jet radius R. In terms of the parameterisation from Eq. (5.23), the measurement function then becomes

$$\begin{aligned} F_{\text{veto}}(a,b,x_{12},t_k^{\pm},t_l,t_{kl}) = \sqrt{\frac{a}{(a+b)(1+ab)}}\Bigg[\sqrt{(1+b)^2-4bt_{kl}} \\ \times\,\Theta\Big(R-\Delta(a,t_{kl})\Big) + \Theta\Big(\Delta(a,t_{kl})-R\Big)\Bigg]\,, \end{aligned} \tag{8.26}$$

where $\Delta(a,t_{kl}) = \sqrt{\ln^2(a) + \arccos^2(1-2t_{kl})}$, which we obtain from Eq. (8.24) after inserting the physical parameterisation from Eq. (5.23). We can now go on and extract the same quantities as for the observable p_T-resummation.

x-space

We start our discussion again with the NLO non-cusp anomalous dimension $\gamma_0^{i,B}$ and the NLO anomaly coefficient d_1^i, which we can extract analytically. In particular, we find $\gamma_0^{q,B} = -3C_F, \gamma_0^{g,B} = -\beta_0$ and $d_1^i = 0$ as before for the quark (gluon) channel. For the refactorised matching kernels at NLO, we get

$$I_{q\leftarrow q}^{(1)}(x) = 2C_F\,(1-x) - \frac{\pi^2}{6} C_F\;\delta(1-x)\,, \tag{8.27}$$

$$I_{q\leftarrow g}^{(1)}(x) = 4T_F\,x(1-x), \tag{8.28}$$

$$I_{g\leftarrow q}^{(1)}(x) = 2C_F\,x, \tag{8.29}$$

$$I_{g\leftarrow g}^{(1)}(x) = -\frac{\pi^2}{6} C_A\;\delta(1-x)\,, \tag{8.30}$$

which is in agreement with [160] and the same result that we found for p_T-resummation. Due to the fact that the jet algorithm needs at least two particles to work, the NLO results do not depend on the jet radius R. This dependence enters at NNLO. The anomaly coefficient d_2^i at NNLO is a function of this radius R and we can compare our computation to the semi-analytic results from [160] for the three values of the jet radius $R = \{0.2, 0.5, 0.8\}$. We perform this analysis in more detail for the N-space results and explicitly show that our computation for different jet radii R captures the behaviour of the semi-analytic results correctly. The same observation holds for the NNLO non-cusp anomalous dimension $\gamma_1^{i,B}$, which is R-independent. We state its value later in our N-space analysis.
Furthermore, we can investigate the x-independent coefficients in front of the distributions defined in Eqs. (8.3) and (8.4). As for p_T-resummation, the coefficients $c_1^{q,g}, c_2^{q,g}, c_3^{q,g}$ vanish. Our result for the remaining coefficients are shown in tables 8.7 to 8.10 for the different values of the jet radius. Again, we observe that these coefficients for the diagonal quark and gluon channels are related to each other by Casimir scaling.

c_{-1}^q	$R = 0.2$		$R = 0.5$		$R = 0.8$	
	[171, 173]	this work	[171, 173]	this work	[171, 173]	this work
$C_F T_F n_f$	0.3161	0.3112(140)	1.3849	1.3807(135)	1.9419	1.9386(132)
C_F^2	1.5462	1.5463(425)	2.5921	2.5932(425)	4.6614	4.6617(427)
$C_F C_A$	−24.8692	−24.8629(1093)	−19.5692	−19.5651(1110)	−16.9469	−16.9474(1106)

Table 8.7: Coefficients of the δ-distribution for the three different colour structures of the diagonal quark channel. We extract these coefficients for three different values of the jet radius $R = \{0.2, 0.5, 0.8\}$.

c_{-1}^g	$R = 0.2$		$R = 0.5$		$R = 0.8$	
	[171, 173]	this work	[171, 173]	this work	[171, 173]	this work
$C_F T_F n_f$	0	0	0	0	0	0
$C_A T_F n_f$	0.3161	0.3100(123)	1.3849	1.3817(59)	1.9419	1.9387(122)
C_A^2	−23.3230	−23.3174(910)	−16.9771	−16.9812(914)	−12.2855	−12.2876(915)

Table 8.8: We show the same as in table 8.7 for the three colour structures of the diagonal gluon channel.

c_0^q	$R = 0.2$		$R = 0.5$		$R = 0.8$	
	[171, 173]	this work	[171, 173]	this work	[171, 173]	this work
$C_F T_F n_f$	16.4363	16.4362(130)	11.4000	11.4013(121)	9.0121	9.0118(114)
C_F^2	−1.0496	−1.0496(211)	−6.4547	−6.4546(212)	−16.0249	−16.0254(212)
$C_F C_A$	80.0687	80.0692(780)	49.6549	49.6546(780)	36.2145	36.2156(773)

Table 8.9: Coefficients in front of the plus distribution for the three different colour structures of the diagonal quark channel. We extract these coefficients for three different values of the jet radius $R = \{0.2, 0.5, 0.8\}$.

c_0^g	$R = 0.2$		$R = 0.5$		$R = 0.8$	
	[171, 173]	this work	[171, 173]	this work	[171, 173]	this work
$C_F T_F n_f$	0	0	0	0	0	0
$C_A T_F n_f$	16.4363	16.4376(105)	11.4000	11.4001(56)	9.0121	9.0124(99)
C_A^2	79.0192	79.0202(596)	43.2002	43.2014(594)	20.1896	20.1909(597)

Table 8.10: The same as in table 8.9 for the three colour structures of the diagonal gluon channel.

Finally, we can show the contributions to the grid for the refactorised matching kernels and compare it to the results in [171, 173]. In these works, the authors have followed a different approach since they have computed the difference between the p_T-veto observable and a reference observable that can be obtained from the transverse-momentum resummation results in the previous section. Moreover, the authors of [171, 173] used a different rapidity regulator and it is therefore interesting to validate these results which appeared only recently.
Similarly to the previous discussion, we observe again the critical behaviour at the endpoints, in particular for the limit $x \to 0$. Nevertheless, the results from both works agree very well, since the central values coincide within the uncertainties of our computation, which are not visible on the scale of the

plot. We show the plots for the remaining channels in appendix B.1.

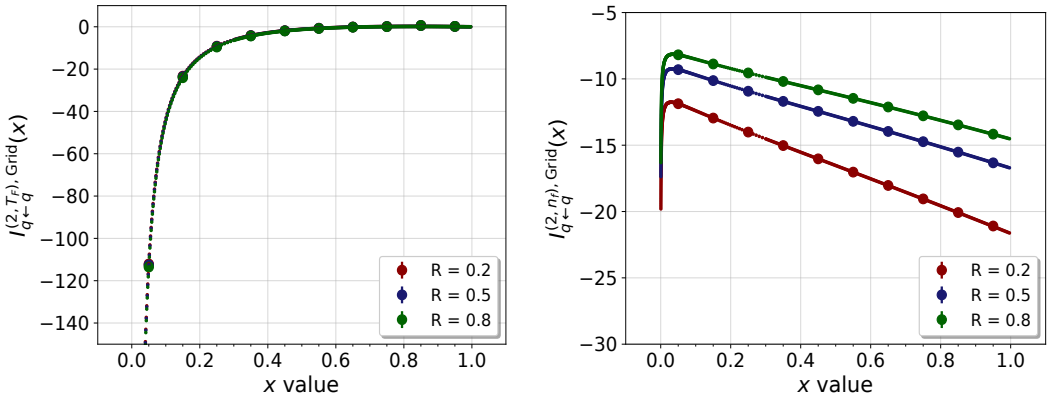

Figure 8.4: Grid for the refactorised renormalised matching kernel for the colour structures $C_F T_F$ and $C_F T_F n_f$ for the observable p_T-veto in x-space. The large dots indicate numbers from our numerical approach, the small dots the semi-analytical expressions extracted from [171, 173]. Uncertainties on our computation are included, but not visible. However, there are no errors for a direct comparison stated in [171, 173].

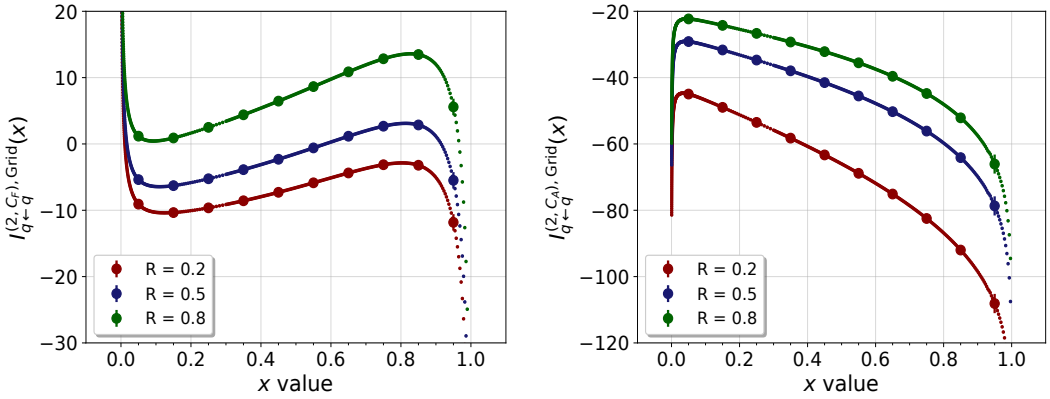

Figure 8.5: We show the same as in figure 8.4 for the colour structures C_F^2 and $C_F C_A$ of the diagonal quark channel.

N-space

We also consider the jet-veto resummation in our N-space formalism. The results for the quark channels were in fact published by us in [122] before [171] appeared. In the following, we present additional values for the jet radius $R = \{0.4, 1.0\}$, which are also commonly used in the literature. First, we extract the non-cusp anomalous dimension $\gamma_0^{i,B}$ and anomaly coefficient d_1^i together with the refactorised matching kernels at NLO. While we again find $\gamma_0^{q,B} = -3C_F$, $\gamma_0^{g,B} = -\beta_0$ and $d_1^i = 0$, the refactorised matching kernels

are now functions of the Mellin value N. Specifically, we find

$$\widehat{I}^{(1)}_{q\leftarrow q}(N) = \frac{2C_F}{N(1+N)} - \frac{\pi^2}{6}C_F\,, \tag{8.31}$$

$$\widehat{I}^{(1)}_{q\leftarrow g}(N) = \frac{4T_F}{(N+1)(N+2)}, \tag{8.32}$$

$$\widehat{I}^{(1)}_{g\leftarrow q}(N) = \frac{2C_F}{N+1}, \tag{8.33}$$

$$\widehat{I}^{(1)}_{g\leftarrow g}(N) = -\frac{\pi^2}{6}C_A\,. \tag{8.34}$$

As we have mentioned in the discussion of our x-space results, we investigate the anomaly coefficient d_2^i and $\gamma_1^{i,B}$ in more detail here. In particular, the anomaly coefficient d_2^i is now R-dependent, therefore we analyse its behaviour for ten different values of R in figure 8.6. We decompose the quark anomaly coefficient d_2^q and the gluon anomaly coefficient d_2^g according to Eq. (8.8).

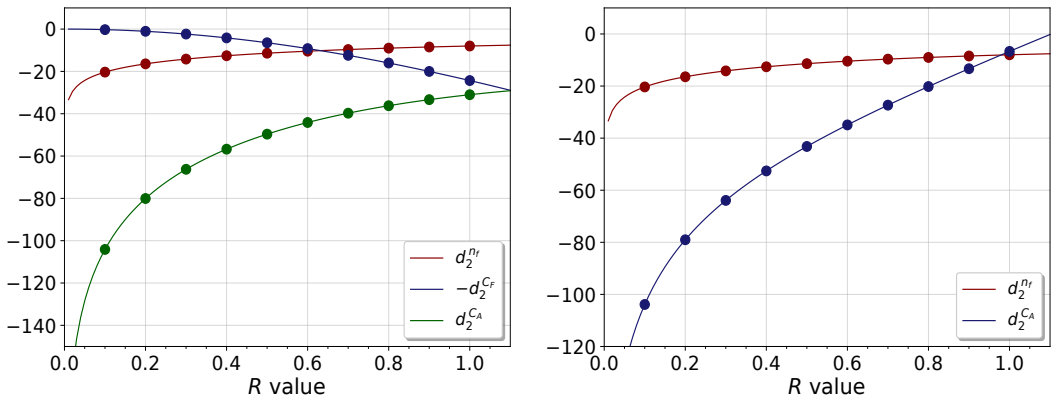

Figure 8.6: NNLO anomaly coefficient d_2^i for the quark (left) and gluon (right) channel as a function of the jet radius R. The dots indicate our computation and the solid lines illustrate the semi-analytic results from [160]. Uncertainties on our calculations are included, but not visible. The anomaly coefficients are again related to each other via Casimir scaling.

We observe very good agreement for all colour structures. Next, we extract the NNLO non-cusp anomalous dimension $\gamma_1^{i,B}$. We expect its value to be the same as for p_T-resummation due to the similar renormalisation procedure. In accordance with our analysis in 8.1, we choose $N = 12$ for our extraction and $R = 0.5$, although a specification of R is not necessary since the $\gamma_1^{i,B}$ are independent of the value R.

$\gamma_1^{q,B}$	analytic	this work
$C_F T_F n_f$	11.3946	11.3948(22)
C_F^2	−10.6102	−10.6105(185)
$C_F C_A$	−4.6371	−4.64397(168)

$\gamma_1^{g,B}$	analytic	this work
$C_F T_F n_f$	4	4
$C_A T_F n_f$	7.2882	7.2879(51)
C_A^2	−17.1941	−17.1932(322)

Table 8.11: Non-cusp anomalous dimension $\gamma_1^{i,B}$ for the quark and gluon channel. We compare the results in our work to the analytic results from [78, 79].

These quantities agree both very well with the analytic results and values we found for p_T-resummation in table 8.6. Finally, we turn our attention to the refactorised matching kernels in Mellin space. We show these expressions for five different values of R for the diagonal quark channel, other channels are stated in appendix B.2.

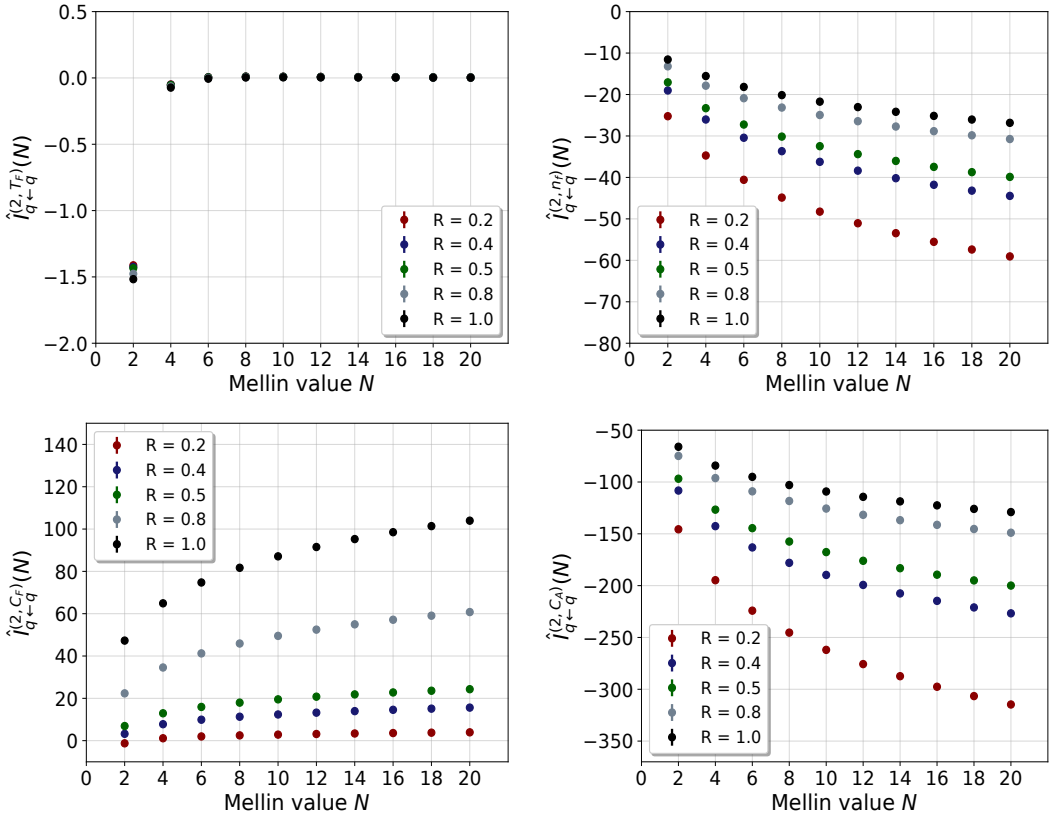

Figure 8.7: Refactorised matching kernels for the four colour structures of the diagonal quark channel for the observable jet-veto resummation in Mellin space. The dots indicate numbers from our numerical approach. Uncertainties on our computation are included, but not visible.

Notice that the uncertainties are included in the plots, however they are not visible here. By verifying that our momentum-space numbers agree with the numbers from [171, 173], we directly confirm our N-space calculation as well,

since they only include an additional integration. We have also confirmed that our numbers for the x- and N-space formalism agree by performing this additional integration explicitly.

8.3 Beam thrust

As a first SCET-I observable, we are going to analyse the hadronic event-shape variable beam thrust. The measurement function consists in this case of the sum of the small light-cone components of the emissions. At NLO, we identify that $n = 1$ and the measurement function $f(t_k) = 1$ becomes trivial. The same observation holds at NNLO as well, i.e. we find that $n = 1$ and $F(a, b, x_{12}, t_k^{\pm}, t_l, t_{kl}) = 1$. From a physical point of view, beam thrust quantifies how the emitted partons are grouped around the beam axis. The limit $\omega_{BT} \ll 1$ corresponds to the kinematical configuration where the emitted particles are aligned along the beam axis, while $\omega_{BT} \sim 1$ illustrates hard radiation with the order of the hard scale Q emitted perpendicularly to the beam axis.
Beam thrust is a SCET-I observable and its renormalisation has been discussed in chapter 6. Due to the particularly simple measurement function, we are able to extract the NLO matching kernels and the RV contribution analytically as well.
The expressions for the NLO and NNLO non-cusp anomalous dimensions as well as the NLO and NNLO refactorised matching kernels are known analytically [124, 125]. However, we need to perform an additional Laplace transformation of these results in order to transform the measurement into the desired exponential form in Eq. (3.10). We explicitly show the impact of the Laplace transformation in appendix A.4.

x-space

In analogy to the analysis of the two previous SCET-II observables, we start by considering the NLO contributions to beam thrust. In our framework, we are able to extract all relevant quantities at this order analytically. The diagonal quark and gluon channels allow us to extract the NLO quark and gluon non-cusp anomalous dimension with $\gamma_0^{q,B} = -3C_F$ and $\gamma_0^{g,B} = -\beta_0$, respectively. For the refactorised matching kernels, we obtain at NLO

$$\mathcal{I}_{q\leftarrow q}^{(1)}(x) = 2\,C_F\left(1 - x - \frac{1+x^2}{1-x}\ln(x) + (1+x^2)\left[\frac{\ln(1-x)}{1-x}\right]_+\right), \tag{8.35}$$

$$\mathcal{I}_{q\leftarrow g}^{(1)}(x) = 2\,T_F\left(2x(1-x) + \Big((1-x)^2 + x^2\Big)\ln\left(\frac{1-x}{x}\right)\right), \tag{8.36}$$

$$\mathcal{I}_{g\leftarrow q}^{(1)}(x) = 2\,C_F\left(x + \frac{1}{x}\cdot\Big(2 - (2-x)x\Big)\ln\left(\frac{1-x}{x}\right)\right), \tag{8.37}$$

$$\mathcal{I}^{(1)}_{g\leftarrow g}(x) = -4\,C_A\,\frac{\Big(1-(1-x)x\Big)^2}{x}\left(\frac{\ln(x)}{1-x} - \left[\frac{\ln(1-x)}{1-x}\right]_+\right), \tag{8.38}$$

which are in agreement with the results from the literature [124, 125, 174]. At NNLO, the non-cusp anomalous dimension is also known at this order and our results are summarised in table 8.12.

$\gamma_1^{q,B}$	analytic	this work
$C_F T_F n_f$	13.3495	13.3494(117)
C_F^2	−10.6102	−10.6102(114)
$C_F C_A$	3.2601	3.2599(171)

$\gamma_1^{g,B}$	analytic	this work
$C_F T_F n_f$	4	4
$C_A T_F n_f$	9.2431	9.2432(33)
C_A^2	−9.2968	−9.2970(167)

Table 8.12: NNLO non-cusp anomalous dimension $\gamma_1^{i,B}$. We compare our results to the analytic results provided in [124, 125].

We observe excellent agreement between the results from the literature [124, 125] and our computation also for SCET-I observables. Finally, we can compare the refactorised matching kernels at NNLO.

c_{-1}^q	analytic	this work
$C_F T_F n_f$	−1.238	−1.2380(220)
C_F^2	−2.165	−2.1647(153)
$C_F C_A$	−12.732	−12.7313(294)

c_{-1}^g	analytic	this work
$C_F T_F n_f$	0	0
$C_A T_F n_f$	−1.2379	−1.2379(53)
C_A^2	−14.8965	−14.8962(294)

Table 8.13: Coefficients of the δ-distribution for the diagonal quark and gluon matching kernels in Eqs. (8.3) and (8.4). We compare our computation to the analytic results from [124, 125]. Additionally, we observe Casimir scaling between both coefficients.

c_0^q	analytic	this work
$C_F T_F n_f$	3.9098	3.9098(117)
C_F^2	19.2329	19.2329(114)
$C_F C_A$	15.7945	15.7943(172)

c_0^g	analytic	this work
$C_F T_F n_f$	0	0
$C_A T_F n_f$	3.9098	3.9098(33)
C_A^2	35.0274	35.0273(167)

Table 8.14: We show the same as in table 8.13, but for the distribution $\left[\frac{1}{1-x}\right]_+$.

c_1^q	analytic	this work
$C_F T_F n_f$	-8.8889	$-8.8889(33)$
C_F^2	-26.3189	$-26.3189(81)$
$C_F C_A$	16.6183	16.6186(89)

c_1^g	analytic	this work
$C_F T_F n_f$	0	0
$C_A T_F n_f$	-8.8889	$-8.8889(12)$
C_A^2	-9.7006	$-9.7005(87)$

Table 8.15: We show the same as in table 8.14, but for the distribution $\left[\frac{\ln(1-x)}{1-x}\right]_+$.

c_2^q	analytic	this work
$C_F T_F n_f$	2.6667	2.6667(5)
C_F^2	0	0
$C_F C_A$	-7.3333	$-7.3333(15)$

c_2^g	analytic	this work
$C_F T_F n_f$	0	0
$C_A T_F n_f$	2.6667	2.6667(1)
C_A^2	-7.3333	$-7.3333(15)$

Table 8.16: We show the same as in table 8.14, but for the distribution $\left[\frac{\ln^2(1-x)}{1-x}\right]_+$.

c_3^q	analytic	this work
$C_F T_F n_f$	0	0
C_F^2	8	8 ± 10^{-4}
$C_F C_A$	0	0

c_3^g	analytic	this work
$C_F T_F n_f$	0	0
$C_A T_F n_f$	0	0
C_A^2	8	8 ± 10^{-4}

Table 8.17: We show the same as in table 8.14, but for the distribution $\left[\frac{\ln^3(1-x)}{1-x}\right]_+$.

Here, we perform the same decomposition as in Eqs. (8.3) and (8.4) for the diagonal quark and gluon channels, albeit the coefficients $c_1^{q,g}, c_2^{q,g}, c_3^{q,g}$ do not vanish for SCET-I observables, because we observe poles up to ϵ^{-4}. Our results are given in tables 8.13 to 8.17. We see again, similarly to the SCET-II case, that the coefficients between the diagonal quark and gluon channel are related to each other via Casimir scaling. The reason is the same as before: the limit $x \to 1$ corresponds to the threshold limit in which the matrix elements satisfy Casimir scaling. Additionally, we see perfect agreement between the known analytic results and our calculation, which is related to the fact that the measurement function is particularly simple in this case. This is also reflected in the grid contributions to the refactorised matching kernels shown in figures 8.8 and 8.9. Again, our results, indicated by the points, are in perfect agreement with the analytical computation illustrated by the solid lines [124, 125]. Notice that the errors on our evaluation are not visible on these scales. This proves that our setup is also applicable for SCET-I observables, albeit we have chosen a particular value for the parameter n.

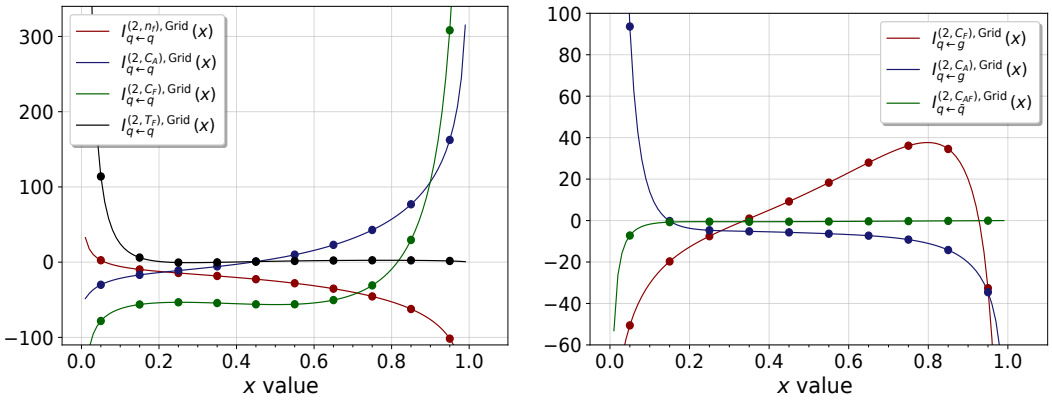

Figure 8.8: Grid contribution to the refactorised matching kernels for all quark channels for the observable beam thrust. The dots indicate numbers from our numerical approach, the solid lines the analytical expression taken from [124, 125]. Uncertainties on our computation are included, but not visible.

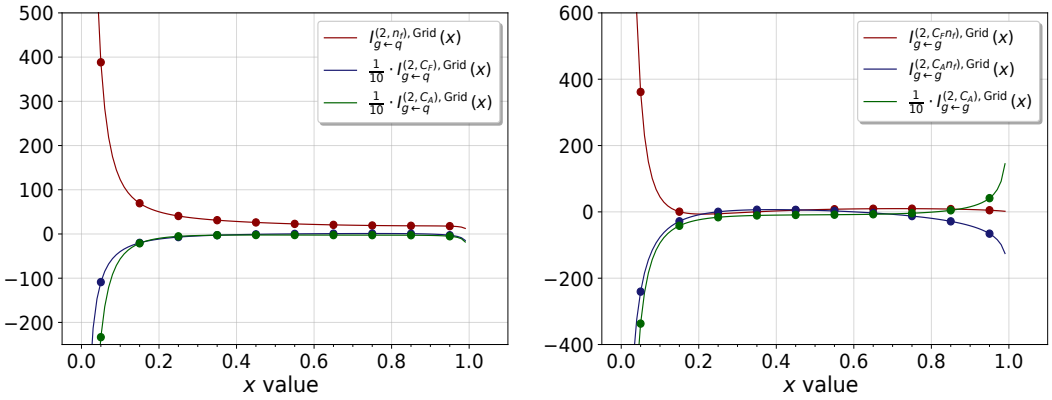

Figure 8.9: We show the same as in figure 8.8 for the grid contribution of the gluon channels.

Next, we perform a similar analysis in N-space in order to test this framework for SCET-I observables as well.

N-space

In Mellin space, the NLO refactorised matching kernels read

$$\begin{aligned}\widehat{\mathcal{I}}^{(1)}_{q\leftarrow q}(N) = \frac{C_F}{3N^2(N+1)}\Bigg(&\pi^2(N+1)N^2 + 6\Big(\gamma_E N(\gamma_E N+\gamma_E+2)+\gamma_E \\ &+3\Big)N + 6N\Big(N(N+1)\psi(N)^2 + \big(2N(\gamma_E N+\gamma_E+1)+1\big) \\ &\times\psi(N) + N(N+1)\psi'(N+1)\Big)+6\Bigg),\end{aligned} \tag{8.39}$$

$$\widehat{\mathcal{I}}^{(1)}_{q\leftarrow g}(N) = T_F\,\frac{4-2\left(N^2+N+2\right)\left(\psi(N)+\gamma_E\right)}{N(N+1)(N+2)}, \tag{8.40}$$

$$\widehat{\mathcal{I}}^{(1)}_{g\leftarrow q}(N) = C_F \frac{-2\left(N^2+N+2\right)H_{N-2}+2(N-1)N+6}{N\left(N^2-1\right)}, \tag{8.41}$$

$$\begin{aligned}\widehat{\mathcal{I}}^{(1)}_{g\leftarrow g}(N) = \frac{1}{3}C_A\Bigg(&\frac{12\left(N\left(N^2+\gamma_E(N-1)(N+1)(N+2)-3\right)-4\right)\psi(N)}{(N-1)N(N+1)(N+2)}\\ &+6\left(\frac{4\gamma_E-1}{N}+\frac{4-2\gamma_E}{N+1}+\frac{2\gamma_E-3}{N+2}-\frac{2\gamma_E}{N-1}+\frac{2}{(N-1)^2}+\gamma_E^2\right)\\ &+6\psi(N)^2+6\psi'(N)+\pi^2\Bigg),\end{aligned} \tag{8.42}$$

where $\psi'(N)$ denotes the first derivative of the digamma function $\psi(N)$. Moreover, H_N corresponds to the harmonic number $H_N = \sum_{k=1}^{N} 1/k$.
In addition to that we can also determine the NNLO non-cusp anomalous dimension $\gamma_1^{i,B}$, which is shown in table 8.18.

$\gamma_1^{q,B}$	analytic	this work
$C_F T_F n_f$	13.3495	13.3494(76)
C_F^2	−10.6102	−10.6106(528)
$C_F C_A$	3.2602	3.2564(503)

$\gamma_1^{g,B}$	analytic	this work
$C_F T_F n_f$	4	4
$C_A T_F n_f$	9.2431	9.2432(71)
C_A^2	−9.2968	−9.2976(604)

Table 8.18: NNLO non-cusp anomalous dimension $\gamma_1^{i,B}$ for the quark and gluon channel extracted from our Mellin-space setup. We compare our results to [124, 125].

We observe once more good agreement within the uncertainties, albeit the central values are slightly worse compared to the x-space extraction. This can be traced back to the additional x-integration, as we discussed before.

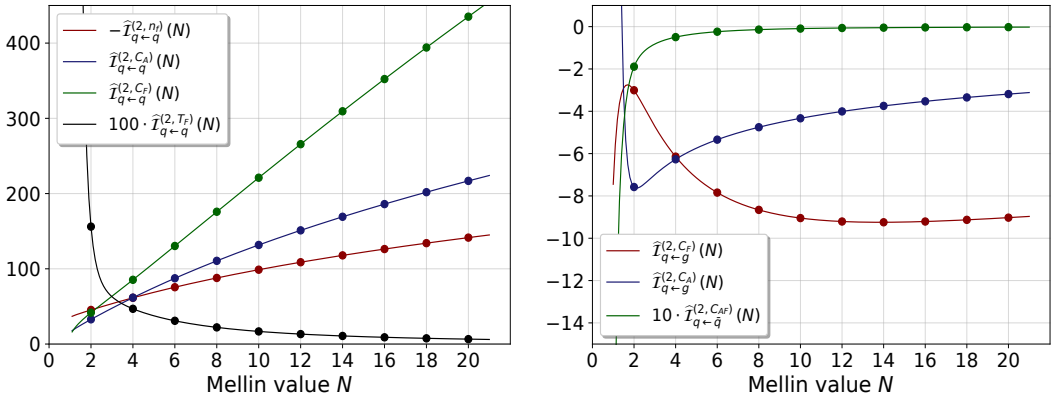

Figure 8.10: Refactorised matching kernels for all quark channels for the observable beam thrust. The dots indicate numbers from our numerical approach, the solid line the analytical expression extracted from [124]. Uncertainties on our computation are included, but not visible.

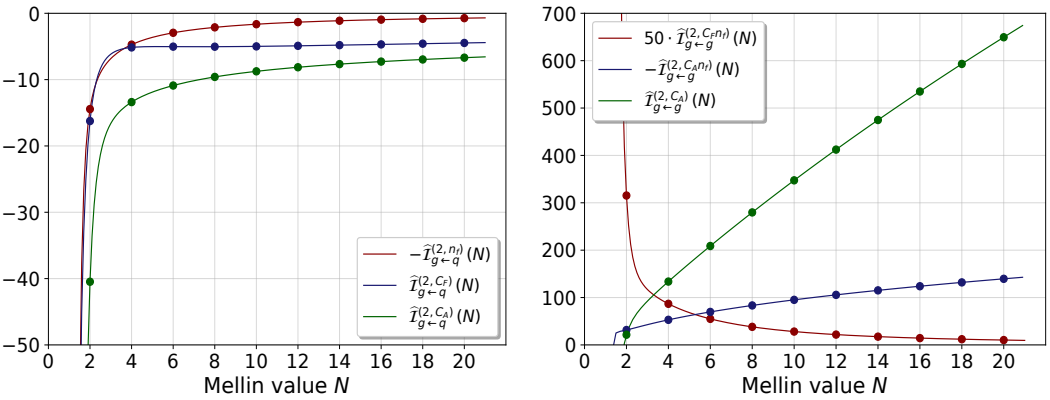

Figure 8.11: We show the same as in figure 8.10 for the gluon channels.

Finally, we compare the refactorised matching kernels against the Mellin and Laplace transformed results of [124, 125]. The dots correspond to our calculation, while the solid lines are the analytic results, which we extract from [124, 125]. Furthermore, the uncertainties on the computed values are not visible on the scales shown here. This proves that our N-space formalism can also deal with SCET-I observables.

8.4 DIS-angularities

Contrary to the discussion of the other observables, DIS-angularities correspond to a class of observables since we leave the parameter n open and allow it to be in the range $n \in (0, \infty)$. Therefore, this whole class of observables belongs to SCET-I. Note that this parameter range also includes beam thrust, namely if we set $n = 1$.
This class of observables is special in the sense that it introduces a mixing of small and large light-cone components for the first time. At NLO, we see that the measurement function is trivial as in the beam thrust case, i.e. $f(t_k) = 1$, while the measurement function takes a more complicated form at NNLO in the physical parameterisation from Eq. (5.23)

$$F_{\text{DIS}}(a, b, x_{12}, t_k^{\pm}, t_l, t_{kl}) = (a+b)^{\frac{A}{2}-1}(1+ab)^{-\frac{A}{2}} \cdot \left[b \cdot a^{\frac{A}{2}} + a^{1-\frac{A}{2}} \right], \quad (8.43)$$

where we introduce the angularity parameter $A \equiv 1 - n$.
As we have discussed in chapter 5, this class of observables leads to additional complications in our analysis since the measurement function might become infinite or zero. This requires additional treatment in form of a rescaling and more sector decomposition steps to disentangle all divergences.
In the following, we consider in total three different values of the angularity parameter $A \in \{-1, 0, 0.5\}$, which translates into different n-values $n \in \{0.5, 1, 2\}$. We consider this particular choice, because it is used on the one hand for instance in [175], on the other hand we treat both cases $n > 1$ and $n < 1$, which require different computational steps according to chapter 5. The case $n = 1$ is a check since we expect to recover beam thrust.

The NLO quark and gluon non-cusp anomalous dimension as well as the quark NLO matching kernels are known analytically [175]. Furthermore, we can use the NNLO non-cusp anomalous dimension $\gamma_1^{\{q,g\},B}$ from the analysis of event-shape angularities [176] via a similar consistency relation as in Eq. (3.15) as a check of our renormalisation procedure. In [50], a similar analysis has been performed in the jet function case and since the jet and beam function factorisation theorems for event-shape and hadronic angularities are similar, the same relation between the different non-cusp anomalous dimensions holds. Thus, we take the expected value for the non-cusp anomalous dimensions from [50], which are extracted from [176].

x-space

Similar to the previous observables, we begin our discussion by considering the NLO contributions to DIS-angularities. Thus, we can extract the NLO non-cusp anomalous dimensions analytically in our framework and obtain $\gamma_0^{q,B} = -3C_F$ and $\gamma_0^{g,B} = -\beta_0$ for the quark and gluon case, respectively. Furthermore, we compute the NLO matching kernels:

$$\begin{aligned}\mathcal{I}^{(1)}_{q\leftarrow q}(x) = &-\frac{C_F}{6n(n+1)}\Bigg[\pi^2(n-1)(n+3)\delta(1-x)+12n\Bigg(\Bigg(2n\,\frac{1+x^2}{1-x}\\ &\times\ln(x)-(1+n)(1-x)\Bigg)-2n\left(1+x^2\right)\left[\frac{\ln(1-x)}{1-x}\right]_+\Bigg)\Bigg],\end{aligned} \tag{8.44}$$

$$\mathcal{I}^{(1)}_{q\leftarrow g}(x) = T_F\left[\frac{4n}{n+1}\left(2x^2-2x+1\right)\ln\left(\frac{1-x}{x}\right)+4(1-x)x\right], \tag{8.45}$$

$$\mathcal{I}^{(1)}_{g\leftarrow q}(x) = C_F\left[\frac{4n}{n+1}\left(x-2+\frac{2}{x}\right)\ln\left(\frac{1-x}{x}\right)+2x\right], \tag{8.46}$$

$$\begin{aligned}\mathcal{I}^{(1)}_{g\leftarrow g}(x) = &-\frac{C_A}{6n(n+1)}\,\frac{\Big(1-(1-x)x\Big)^2}{x}\Bigg[(n-1)(n+3)\pi^2\delta(1-x)+48n^2\\ &\times\left(\frac{\ln(x)}{1-x}-\left[\frac{\ln(1-x)}{1-x}\right]_+\right)\Bigg].\end{aligned} \tag{8.47}$$

We notice that we are able to reproduce beam thrust if we choose $n = 1$. Moreover, we can compare Eqs. (8.44) and (8.45) with [175] and see that both results agree.

Next, we turn our analysis to the NNLO contributions. For convenience, we only focus on the $q \to q$ channel here, the other results are provided in appendix B.3. The first relevant check which we employ is the comparison of the quark non-cusp anomalous dimension $\gamma_1^{q,B}$ to the results in [176]. As we have already pointed out, the factorisation theorems for event-shape angularities relevant for the jet function case and hadronic angularities in the beam function case share the same structure, thus we can derive an analogous consistency relation for the non-cusp anomalous dimensions as in the jet function case. The input for the soft and hard function are the same

in both cases, hence we expect both the jet and beam non-cusp anomalous dimension to coincide.

$\gamma_1^{q,B}$	$A=-1$		$A=0$		$A=0.5$	
	[176]	this work	[176]	this work	[176]	this work
$C_F T_F n_f$	11.16	11.1553(29)	13.35	13.3495(37)	16.56	16.5558(186)
C_F^2	−10.61	−10.6100(235)	−10.61	−10.6102(114)	−10.61	−10.6111(1916)
$C_F C_A$	−4.38	−4.3762(485)	3.26	3.2595(509)	14.49	14.4939(2740)

Table 8.19: NNLO quark non-cusp anomalous dimensions for the three different angularity values $A = \{-1, 0, 0.5\}$. We compare the results obtained here to [176].

Table 8.19 shows the comparison of the non-cusp anomalous dimension values computed in this work to the results from [176]. In general a comparison to the jet function case [50] would be possible as well, however we expect better numerics from the soft function extraction. We observe very good agreement between both results for all three angularity values.
In the next step, we extract the x-independent coefficients c_{-1}^q to c_3^q in Eq. (8.3). We only focus on the diagonal quark channel here, as we show the rest of the results in appendix B.3:

c_{-1}^q	$A=-1$	$A=0$	$A=0.5$
$C_F T_F n_f$	6.3202(53)	−1.2379(70)	−17.4888(606)
C_F^2	−2.9089(440)	−2.1647(153)	6.4092(4087)
$C_F C_A$	−4.0903(1196)	−12.7298(892)	−2.6909(6790)

Table 8.20: x-independent coefficients in front of the δ-distribution for the colour structures of the diagonal quark channel. We extract these coefficients for three different angularity values $A = \{-1, 0, 0.5\}$.

c_0^q	$A=-1$	$A=0$	$A=0.5$
$C_F T_F n_f$	−0.1494(38)	3.9098(37)	8.1559(37)
C_F^2	34.1920(313)	19.2329(114)	8.5473(1277)
$C_F C_A$	17.5791(647)	15.7938(509)	8.6366(1826)

Table 8.21: We show the same as in table 8.20, but for the $\left[\frac{1}{1-x}\right]_+$-distribution.

c_1^q	$A=-1$	$A=0$	$A=0.5$
$C_F T_F n_f$	$-11.8519(14)$	$-8.8889(10)$	$-5.9260(16)$
C_F^2	$-54.0999(261)$	$-26.3189(81)$	$-1.4623(308)$
$C_F C_A$	22.1584(324)	16.6189(252)	11.0796(398)

Table 8.22: We show the same as in table 8.20, but for the $\left[\frac{\ln(1-x)}{1-x}\right]_+$-distribution.

c_2^q	$A=-1$	$A=0$	$A=0.5$
$C_F T_F n_f$	4.7407(3)	2.6667(3)	1.1852(1)
C_F^2	$-0.0001(23)$	0	0
$C_F C_A$	$-13.0371(49)$	$-7.3333(42)$	$-3.2592(28)$

Table 8.23: We show the same as in table 8.20, but for the $\left[\frac{\ln^2(1-x)}{1-x}\right]_+$-distribution.

c_3^q	$A=-1$	$A=0$	$A=0.5$
$C_F T_F n_f$	0	0	0
C_F^2	14.2222(4)	8 ± 10^{-4}	3.5556(1)
$C_F C_A$	0	0	0

Table 8.24: We show the same as in table 8.20, but for the $\left[\frac{\ln^3(1-x)}{1-x}\right]_+$-distribution.

These numbers constitute a new prediction. The same is true for the various grid contributions, which we show for the four different colour structures in the quark channel in figure 8.12. Here, the dots indicate the new predictions, which are currently unknown for the angularity values $A = \{0, 5, 2\}$ but necessary to push the resummation of this observable to NNLL$'$ accuracy. Furthermore, we include the uncertainties of our computation, albeit they are not visible at the scales shown here. However, we need to make a final remark regarding the accuracy of our approach: As it is to be seen from the measurement function in Eq. (8.43), the expression becomes complicated since the variables occur with fractional numbers in their exponents. If we encounter regions where we observe explicit divergences in $\{a, b\}$ in our physical parameterisation from Eq. (5.23), the implementation of the computational parameterisation becomes necessary to account for logarithmic

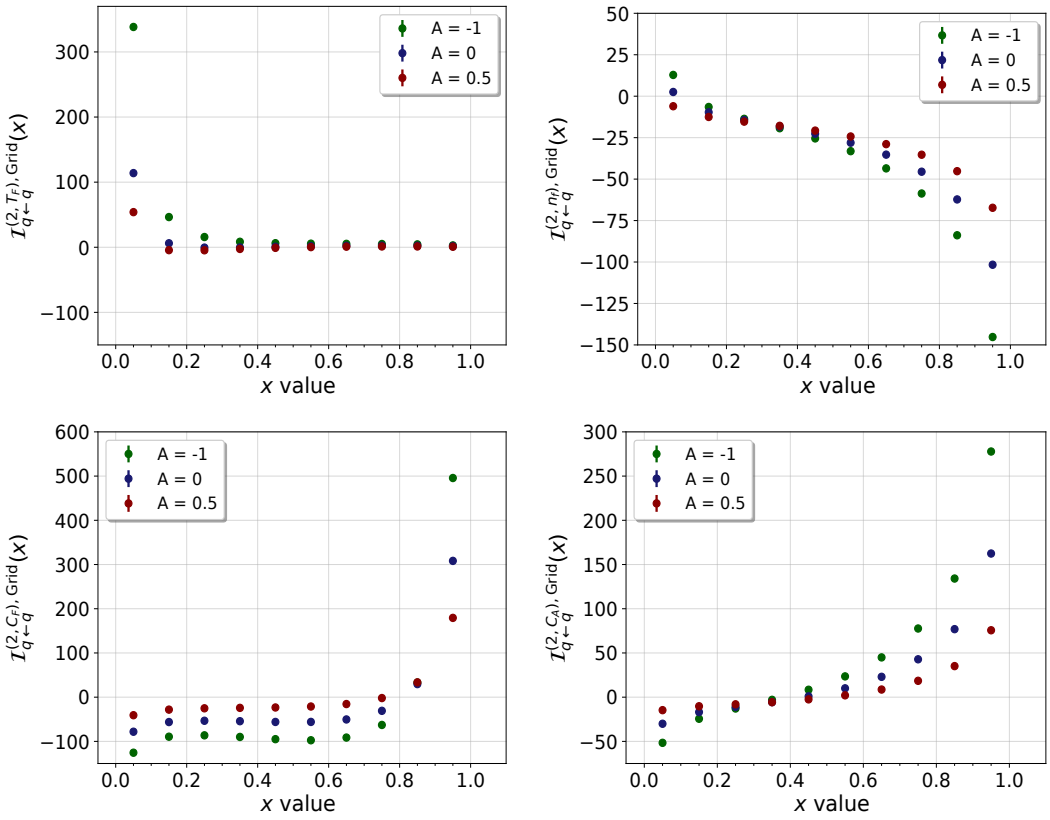

Figure 8.12: Refactorised matching kernels for the four colour structures of the diagonal quark channel for the observable DIS-angularities for angularity values $A = \{-1, 0, 0.5\}$. The dots indicate numbers from our numerical approach. Uncertainties on our computation are included, but not visible.

and sqaure-root divergences, especially in regions where additional rescaling and sector decomposition steps are necessary. Since we do not include this additional modification on the physical parameterisation, this has a sizeable effect on our central values. While the angularity value $A = 0.5$ is particularly sensitive to this feature, the impact on the other two angularity values is less prominent. But we also see this feature for $n = 1$, i.e. $A = 0$, i.e. beam thrust. If we compare the results in this section to the explicit beam thrust results from the section before, we conclude that the central values of both calculations are in very good agreement, but the uncertainties are larger for the DIS-angularities case. Notice that we observe similar issues for the remaining contributions shown in appendix B.3.

Chapter 9

Conclusions and Outlook

In the era of high-precision physics, collider experiments like the LHC search for deviations from the Standard Model (SM) predictions. These deviations would provide a window to new-physics effects, which are not incorporated in the SM and therefore require new developments in the field of theoretical particle physics. The new run at the LHC will provide data with unprecedented precision, which requires the theoretical predictions to become more and more precise. Fixed-order computations in the SM are to a large extent automated to NLO and NNLO in perturbation theory, however they suffer from large logarithmic corrections in some regions of the phase space. These logarithms spoil the convergence of the perturbative series and therefore need to be resummed to all orders. Effective field theories (EFTs) provide a systematic framework to resum these logarithms.
Soft-Collinear Effective Theory (SCET) is the EFT applied throughout this project. Different momentum modes are factorised according to their scaling with respect to a power counting parameter λ in the SCET framework. Typical modes are energetic modes of the invariant mass (collinear) and low-energetic isotropic (soft) radiation. The soft region is described by the soft function in the factorisation theorem, while final-state collinear radiation is captured by jet functions. For these functions, there already exist automated frameworks for their computation to NNLO accuracy for a general class of observables. But the automated calculation of initial-state collinear radiation, which is described by beam functions, for a general class of observables to NNLO was up to now missing. In particular, this is the only missing ingredient to automate resummations at NNLL$'$ accuracy.
Until now, beam functions have rather been computed case-by-case for specific observables, which led to many results in the literature at NNLO. In particular, we could use the available results for beam thrust, which is a SCET-I observable, and transverse-momentum (p_T) resummation, which is a SCET-II observable, to test our novel setup.
Our framework is based on general, observable-independent master formulae, which incorporate completely disentangled phase-space divergences in monomial form and which we have implemented in the publicly accessible code `pySecDec`. In general, we have achieved this specific form of the master formulae using methods like sector decomposition, selector functions and

non-linear transformations. We have further used `pySecDec` as an interface to the `Cuba Vegas` library, which evaluates the phase-space integrals numerically and provides bare results for the beam function matching kernels. After renormalisation, we have obtained finite results useful for phenomenological applications.
Besides the test observables p_T-resummation and beam thrust, we have also determined the matching kernels for jet-veto resummation and angularities in deep-inelastic scattering. The results for the former were unknown for a long time and they were first determined by us in Mellin space for the quark channels [122] and subsequently in momentum space for all channels by another group [171].
In the current work, we have computed the remaining channels for jet-veto resummation and DIS angularities directly in x-space, which is an important extension compared to our previous work [122]. We use our independent N-space setup to compute the observable p_T-veto independently and also show the gluon channels which were not discussed in [122].
In general, there are some aspects that one might consider to further improve the setup in the future. We list the most important ideas below:

- First of all, one should implement the master formulae from this work in a standalone `C++` code in the spirit of `SoftSERVE` [48, 49]. This has the advantage that several optimisations can be implemented that are not possible with a multi-purpose program like `pySecDec`. For instance, the integrands could be further simplified and processed more efficiently by the numerical integrator. Moreover, this would allow one to be independent of future `pySecDec` updates and the code could be made public in this specific form.

- Connected to the last point is an optimised computational parameterisation, which helps to suppress logarithmic and in particular square-root divergences. So far we treat the square-root divergences from the angular integrations and critical logarithmic singularities induced by the matrix element and the Jacobian, however there exists another source for square-root divergences, which is in particular problematic for DIS-angularities. These additional singularities are related to the measurement function itself and they could be treated by introducing an additional parameter as it was also done in `SoftSERVE`. This would further improve the numerics for observables like DIS angularities.

- It would also be interesting to better understand the behaviour of the matching kernels at the endpoints $x \to 0$ and $x \to 1$. Once the divergent behaviour has been properly isolated, this would allow us to use an optimised grid and thus to significantly reduce the runtime of our code.

- Finally, for some observables like transverse-momentum resummation, one may also consider polarised beam functions. So far, we have worked with unpolarised beam functions, where we perform spin averages and where the matrix elements are connected to the unpolarised timelike

splitting functions via crossing. Polarised beam functions generalise this setup, because one splits matrix elements according to different spin structures. Nevertheless, the methods derived in this project should be powerful enough to tackle these kind of beam functions as well.

Project II:

QCD sum rules for parameters of the B - meson distribution amplitudes

This project led to the publication [177].

Chapter 10

QCD sum rules: Overview

In the following, we are going to discuss the framework of QCD sum rules (QCD SRs), which has been first proposed in [51, 52] for light mesons (ρ, K^*, ϕ) and charmonium resonances. Generally, this method can be used to determine properties of hadrons like hadron masses, decay constants, form factors or characteristic parameters for the modelling of distribution amplitudes (DAs). The goal in this work is to apply the QCD SR method to extract two characteristic parameters, $\lambda^2_{E,H}$, of the B-meson DA, as we will elaborate later.
Starting point of the QCD SR framework is the correlation function (for the relevant cases here we are focussing on two-point sum rules) of the form

$$\Pi_{KL}(q) = i \int \mathrm{d}^d x \, e^{iqx} \, \langle 0 | \, T\{ j_K(x), j_L(0) \} \, | 0 \rangle \equiv T_{KL} \Pi(q^2) \,, \tag{10.1}$$

which will be expressed as a dispersion relation containing a ground state resonance as well as excited and multihadron continuum states located above a threshold s^{th}.

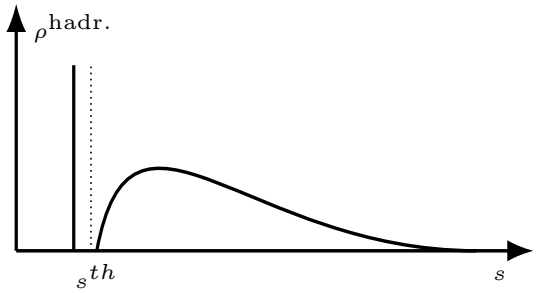

Figure 10.1: Schematic representation of the hadronic spectral density $\rho^{\mathrm{hadr.}}$. The peak denotes the ground state contribution, which gets separated from the continuum contribution and higher excited states starting at a threshold s^{th} illustrated by the dashed line. However, there are also cases where a separation with a proper choice of s^{th} is not immediately obvious, for instance if there is an overlap between the ground state and the lowest continuum contributions.

The general structure of the currents in Eq. (10.1) is $j_K(x) = \bar{q}(x) \Gamma_K q'(x)$

and $j_L(0) = \bar{q}'(0)\Gamma_L q(0)$, where q and q' allow for all quarks apart from the top quark and $\Gamma_{K,L}$ are combinations of Dirac γ-matrices which determine the spin and parity of the currents. The sum over the colour indices is implied such that the currents are in total colour-neutral. Section 11.2 provides more details on the correlation function in Eq. (10.1) and specifies the exact form of the currents $j_K(x)$ as well as $j_L(0)$. Furthermore, the concept of quark-hadron duality is used in order to relate the hadronic spectral density to the operator product expansion (OPE) density [178], see section 11.3. In general, the OPE employed in the QCD SR approach has the form [1]

$$j_K(x)j_L(0) = \sum_i C_i(x)O_i(0) \tag{10.2}$$

in the limit $x \to 0$. The OPE in Eq. (10.2) allows to separate the currents in the correlation function (10.1) into short-distance contributions represented by perturbatively calculable Wilson coefficients $C_i(x)$ and into a long-distance part denoted by vacuum matrix elements of the operators $O_i(0)$. Here, the important property is the locality of these operators, which leads to local vacuum condensates of increasing mass dimension in the QCD SR approach. The values of these condensates can be derived from lattice QCD or from comparisons of sum rules with experiments and are input parameters. Their properties and parameterisation are further investigated in section 11.4. The explicit computation of the Wilson coefficients is performed in section 11.5. Notice that based on dimensional analysis, the Wilson coefficient of the unit operator with mass dimension $d = 0$ is singular at $x^2 \to 0$, which emphasises that at large q^2, i.e. small distances, this contribution becomes dominant. Finally, the numerical analysis to extract the parameters $\lambda^2_{E,H}$ is done in chapter 12 and the problems and solutions regarding the SRs in section 11.5 are discussed there.

[1] This separation of scales holds strictly speaking only in the spacelike region with $-q^2 \gg \Lambda^2_{\rm QCD}$. Analytic continuation links Eq. (10.2) to timelike physical momentum regions [133].

Chapter 11

Derivation of QCD sum rules in HQET

11.1 Grozin-Neubert approach

Before we start to discuss the derivation of the sum rules for the problem at hand, it is convenient to explore the previous works which have already determined the parameters $\lambda_{E,H}^2$. As mentioned before, these parameters have been introduced by Grozin and Neubert [84] and a first value has been determined by considering an off-diagonal correlation function between a two-particle quark-antiquark current and a three-particle current

$$\Pi_{\mathrm{GN}}(\omega) = i \int \mathrm{d}^d x e^{-i\omega v\cdot x} \left\langle 0\right| T\{\bar{q}(0)\Gamma_1^{\mu\nu} g_s G_{\mu\nu}(0) h_v(0) \bar{h}_v(x)\gamma_5 q(x)\} \left|0\right\rangle \ . \tag{11.1}$$

Since the underlying framework to treat B-mesons is HQET, the field $h_v(x)$ denotes the effective heavy-quark field from section 2.2. The parameter ω corresponds to the energy of the B-meson. For correlation functions in QCD, we generally encounter the factor e^{-iqx}, where q denotes the external momentum. Since we work in the B-meson rest frame, we set $q = \omega v$ and exploit that in HQET the usual choice for the velocity is $v = (1, \vec{0})^T$. Thus, the energy of the B-meson q^0 is given by ω. With this special choice of the reference system, we obtain the factor $e^{-i\omega vx}$ in Eq. (11.1).
Furthermore, $\Gamma_1^{\mu\nu}$ has to be chosen accordingly to project out λ_H^2 and λ_E^2. In order to extract these parameters from the correlation function in Eq. (11.1), they apply the QCD SR framework and include all leading contributions to the operator-product expansion (OPE) up to vacuum condensates of mass dimension five. While the leading contribution to the condensates up to mass dimension four start at $\mathcal{O}(\alpha_s)$, the leading order contribution to the mass dimension five condensate already contributes at $\mathcal{O}(\alpha_s^0)$.
But as it turns out, this extraction is connected to large uncertainties due to the unstable behaviour of the sum rules with respect to the Borel parameter M. This instability increases the difficulty to assign a proper Borel window for the numerical analysis. Notice that this dependence on the Borel parameter is expected since condensates with higher mass dimension tend to give

larger contributions to correlation functions of higher dimensional operators. The extracted parameters are [84]

$$\begin{aligned} \lambda_H^2(1\text{ GeV}) &= (0.18 \pm 0.07)\text{ GeV}^2 \\ \lambda_E^2(1\text{ GeV}) &= (0.11 \pm 0.06)\text{ GeV}^2\,. \end{aligned} \tag{11.2}$$

In order to tackle this uncertainty evoked by the instability of the sum rules, Nishikawa and Tanaka [85] include $\mathcal{O}(\alpha_s)$ corrections to the quark-gluon condensate, which is of mass dimension five. Moreover, they also add contributions originating from condensates of mass dimension six starting at $\mathcal{O}(\alpha_s)$ to show that the sum rules start to converge. Besides that the HQET decay constant $F(\mu)$ is also incorporated up to $\mathcal{O}(\alpha_s)$ accuracy. Although these additional contributions lead to a good convergence of the sum rule for the decay constant $F(\mu)$, these higher order corrections turn our to be around 50% [179, 180]. Finally, the large logarithmic contributions occuring in this computation are resummed, which leads to more stable sum rules with respect to the Borel parameter and to a more convergent OPE compared to [84]. The final values are stated to be [85]:

$$\begin{aligned} \lambda_H^2(1\text{ GeV}) &= (0.06 \pm 0.03)\text{ GeV}^2 \\ \lambda_E^2(1\text{ GeV}) &= (0.03 \pm 0.02)\text{ GeV}^2 \end{aligned} \tag{11.3}$$

Comparing Eq. (11.2) to (11.3), we see that the values from the two extractions differ by a factor of three, albeit the ratio $\mathcal{R} = \lambda_E^2/\lambda_H^2$ is similar. This is why many studies rely on the ratio $\mathcal{R}$ rather than the separate parameters in order to eliminate the choice dependence between these two results.
In the following sections, we analyse an alternative sum rule to predict the parameters $\lambda_{E,H}^2$. Rather than investigating a correlation of the form in Eq. (11.1), we focus on a diagonal correlation function between two quark-antiquark-gluon three-particle currents

$$\Pi_{\text{diag}}(\omega) = i \int \mathrm{d}^d x\; e^{-i\omega v\cdot x}\, \langle 0|\, T\{\bar{q}(0)\Gamma_1^{\mu\nu} g_s G_{\mu\nu}(0) h_v(0) \bar{h}_v(x) \Gamma_2^{\rho\sigma} g_s G_{\rho\sigma}(x) q(x)\}\, |0\rangle\,. \tag{11.4}$$

This diagonal sum rule is positive definite and therefore the quark-hadron duality, which is a central assumption in the QCD SR framework, is more accurate compared to the off-diagonal case in [84, 85]. But since two three-particle currents lead to operators with even higher mass dimension as in the off-diagonal case, the OPE does not show better convergence, although we include all contributions up to condensates of mass dimension seven. In addition to that we observe that the continuum and higher excited states dominate the sum rules for the parameters $\lambda_{E,H}^2$, so we resolve this issue by investigating combinations of these parameters which suppress these dominating effects. In this context, we use the ratio $\mathcal{R}$ as one combination to suppress continuum contributions.

11.2 Diagonal QCD sum rule approach

Generally, both correlation functions in Eqs. (11.1) and (11.4) describe physical effects in two different energy regimes. For large spacelike momenta $-q^2 \equiv Q^2 \gg \Lambda^2_{\rm QCD}$, we observe quasi-free particles instead of colour-neutral bound states due to asymptotic freedom. Therefore, we can apply perturbative methods in this region and describe the underlying physics in terms of quarks and gluons, which propagate and interact with each other. Contrary, we deal with physical bound states of quarks in form of hadrons in the timelike region $q^2 > m_b^2$ such that perturbation theory is not adequate to explain the underlying physical phenomena. Beyond a certain branch point, which is given by the lowest possible hadron generated by the currents inside the correlation function at $q^2 = m_h^2$, we observe a plethora of excited higher resonances, multihadron states and continuum contributions. They all lie on the positive real axis, where $\mathrm{Re}(q^2) > m_h^2$ and are encoded into the spectral density $\rho^{\rm hadr.}$. Since this spectral density is in general a complicated and unknown function, it is desirable to work out a method which can tackle the physics of both regions and which naturally links them in the theoretical description.

In the framework of QCD sum rules, the OPE disentangles these short-distance perturbative effects in the spacelike region from the long-distance low-energy physics. These short-distance contributions are encoded in perturbatively calculable Wilson coefficients, while the non-perturbative effects in the long-distance regime are parameterised in terms of a series of local vacuum matrix elements of increasing mass dimension due to the non-trivial QCD vacuum structure. These vacuum averaged matrix elements are called condensates, which are in addition to that scalar and colour-neutral quantities.

$$\begin{aligned}\Pi_{\rm X}^{\rm OPE}(\omega) = {} & C_{\rm X}^{\rm pert}(\omega) + C_{\rm X}^{\bar{q}q}(\omega)\,\langle 0|\,\bar{q}q\,|0\rangle + C_{\rm X}^{G^2}(\omega)\,\langle 0|\,\frac{\alpha_s}{\pi}G^a_{\mu\nu}G^{a,\mu\nu}\,|0\rangle \\ & + C_{\rm X}^{\bar{q}Gq}(\omega)\,\langle 0|\,\bar{q}g_s G^{\mu\nu}\sigma_{\mu\nu}q\,|0\rangle + C_{\rm X}^{G^3}(\omega)\,\langle 0|\,g_s^3 f^{abc}G^a_{\mu\nu}G^{b,\nu\rho}G^{c,\mu}_{\rho}\,|0\rangle \\ & + C_{\rm X}^{\bar{q}qG^2}(\omega)\,\langle 0|\,\bar{q}q\,|0\rangle\,\langle 0|\,\frac{\alpha_s}{\pi}G^a_{\mu\nu}G^{a,\mu\nu}\,|0\rangle + \ldots \end{aligned} \tag{11.5}$$

The quantities C_X^i denote the Wilson coefficients, whose determination is covered in detail in section 11.5, while the condensates are ordered by their mass dimension and carry the quantum numbers of the QCD vacuum. We are going to comment in more detail on the structure of Eq. (11.5) and the parameterisation of the different condensates in section 11.4. In particular, we will also discuss the factorisation of the mass dimension seven condensate in the last line of Eq. (11.5).

It is important to stress that Eq. (11.5) only holds in the deep spacelike region since non-perturbative effects become dominant in the low-energy domain $-|\omega| \sim \Lambda_{QCD}$ and violate the separation between the different distance scales in the OPE. On the other end of the energy scale at $\omega \ll 0$, we can use the methods known from perturbation theory to compute the Wilson coefficients and the non-perturbative effects are power suppressed. Thus, it is necessary to work in the transition region, where the condensates give sizeable, but still

small enough contributions such that we can treat them as local and retail only a few condensates with low mass dimension.
The quark-hadron duality, which is further investigated in the next section, makes it possible to connect the physics of spacelike and timelike regions. But first, we need to find an appropriate representation of the correlation function which is valid for any point in the complex plane, in particular in the deep-spacelike and timelike domain. For this, we make use of the fact that the correlation function is an analytic function in the complex variable q^2 except on the positive real axis above the threshold $q^2 \geq m_h^2$, where singularities and branch cuts in form of particle poles and multihadron states occur. Therefore, the threshold parameters s_0 and s_1, which are used to parameterise the singularities and branch cut on the positive real axis, need to be chosen based on the situation at hand. In our case, we intend to investigate the properties of the B-meson and thus work in HQET, which introduces the scale ω instead of q^2. As a consequence, we choose $s_0 > 0$ and determine s_1 in the following. However to stay as general as possible in the following discussion, we leave s_0 and s_1 unspecified.
Based on the structure of the correlation function in the spacelike region $\mathrm{Re}[q^2] < 0$, we can conclude that the correlation function has no imaginary part in this region, i.e. $\mathrm{Im}\Big[\Pi(q^2)\Big] = 0$. But as we have pointed out above, we expect that $\Pi(q^2)$ acquires an imaginary part beyond the threshold s_0 due to singularities in form of isolated poles at particle masses of higher resonances and due to continuum contributions. We prove this statement with the Schwartz reflection principle [181]. It states that if an analytic function is real-valued on some part of the real axis, then the function is equal to its complex conjugate reflected along this real axis. This is true in our case, since $\Pi(q^2)$ is real-valued below s_0. Hence, we know that $\Pi(q^2 - i\epsilon) = \Pi^*(q^2 + i\epsilon)$ for $q^2 < s_0$ and we get for $q^2 \geq s_0$

$$\begin{aligned}\Delta\Pi(q^2) &\equiv \lim_{\epsilon\to 0}\Big(\Pi(q^2+i\epsilon) - \Pi(q^2-i\epsilon)\Big)\\ &= \lim_{\epsilon\to 0}\Big(\Pi(q^2+i\epsilon) - \Pi^*(q^2+i\epsilon)\Big)\\ &= 2i\,\mathrm{Im}\Big[\Pi(q^2)\Big]\,. \end{aligned} \tag{11.6}$$

Therefore, Eq. (11.6) indicates that there is a branch cut starting at the branch point $q^2 \geq s_0$. The next step is to employ the Cauchy integration formula, since $\Pi(q^2)$ is an analytic function except on the branch cut on the positive real axis

$$\Pi(q^2) = \frac{1}{2\pi i}\oint_C \mathrm{d}s\,\frac{\Pi(s)}{s-q^2}\,. \tag{11.7}$$

We choose the contour C according to figure 11.1, which we parameterise in the following way:

1. we start with the upper line C_1 parallel to the real axis shifted by an infinitesimal distance ϵ:

$$q^2 = s + i\epsilon \qquad \text{with} \quad s_0 \leq s \leq R$$

2. large circle C_2 with radius R: $q^2 = Re^{i\varphi}\,, \quad \epsilon/R < \varphi < 2\pi - \epsilon/R$

3. small half circle C_3 with radius ϵ: $q^2 = s_0 + \epsilon e^{i\varphi}\,, \quad -\pi/2 \leq \varphi \leq \pi/2$

4. lower line C_4 parallel to real axis shifted by ϵ:

$$q^2 = s - i\epsilon \qquad \text{with} \quad R \leq s \leq s_0$$

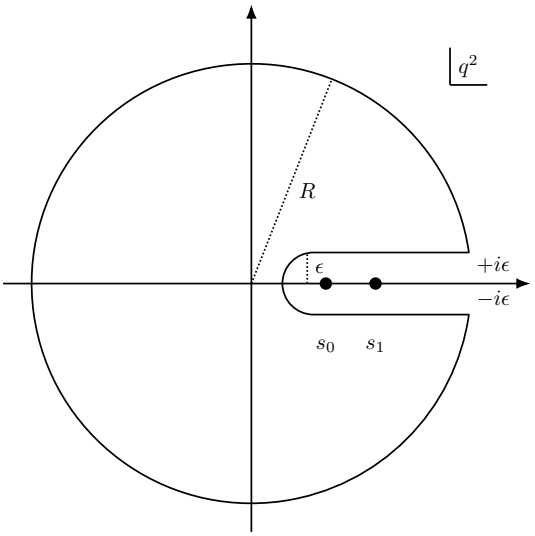

Figure 11.1: Contour $C = C_1 + C_2 + C_3 + C_4$ for the integral in Eq. (11.7). The small half-circle with radius ϵ vanishes for $\epsilon \to 0$, the bigger circle with radius R vanishes for $R \to \infty$ if the correlation function $\Pi(q^2)$ converges for $|q^2| \to \infty$. Otherwise, substraction terms are needed to remove the singularities.

Decomposing Eq. (11.7) into the different parts, we get

$$\Pi(q^2) = \frac{1}{2\pi i}\int_{s_0}^{R} \mathrm{d}s\, \frac{\Pi(s+i\epsilon) - \Pi(s-i\epsilon)}{s - q^2} + \frac{1}{2\pi i}\oint_{C_2} \mathrm{d}p^2\, \frac{\Pi(p^2)}{p^2 - q^2} + \frac{1}{2\pi i}\oint_{C_3} \mathrm{d}p^2\, \frac{\Pi(p^2)}{p^2 - q^2}\,. \tag{11.8}$$

We can argue that the small half-circle C_3 vanishes if we introduce spherical coordinates and take the limit $\epsilon \to 0$. The integral over the large circle C_2 requires further investigation, since the function $\Pi(q^2)$ might diverge in the limit $|q^2| \to \infty$ for $R \to \infty$. This depends on the currents in the correlation function. In this case, it is necessary to introduce an additional substraction term at a specific point q_0^2 and perform the analysis with this substraction. But in the end these substraction terms are not of importance, because we perform a Borel transformation on the sum rule expressions in order to suppress continuum contributions and higher resonances in the hadronic spectral density. This transformation removes all substraction terms and improves in

the same step the convergence of the OPE.
Hence, the contour integrals C_2 and C_3 in Eq. (11.8) vanish. Inserting Eq. (11.6) and taking the limit $R \to \infty$, we finally obtain

$$\Pi(q^2) = \frac{1}{\pi} \int_{s_0}^{\infty} \mathrm{d}s \, \frac{\mathrm{Im}\Pi(s)}{s - q^2} \,. \tag{11.9}$$

This is the desired form of the correlation function, which we use in the following discussion. In the next section, we connect the spacelike region with the timelike region in order to derive sum rule expressions for the parameters $\lambda^2_{E,H}$.

11.3 Application of the quark-hadron duality

In this section, we investigate the correlation function stated in Eq. (11.4) in two different regimes. In particular, the deep-spacelike region $-q^2 \equiv Q^2 \gg \Lambda^2_{\mathrm{QCD}}$ can be tackled with perturbative methods, while the timelike region is given by the hadronic spectrum. Since this correlation function is embedded into a dispersion relation in the sum rule approach, we need to consider the imaginary part of Eq. (11.4) and use the unitary condition

$$\begin{aligned}
\frac{1}{\pi}\mathrm{Im}\Pi_{\mathrm{diag}}(\omega) = & \sum_n (2\pi)^3 \delta(\omega - p_n) \, \langle 0| \, \bar{q}(0) \Gamma_1^{\mu\nu} g_s G_{\mu\nu}(0) h_v(0) \, |n\rangle \\
& \times \langle n| \, \bar{h}_v(x) \Gamma_2^{\rho\sigma} g_s G_{\rho\sigma}(x) q(x) \, |0\rangle \, \mathrm{d}\Phi_n \\
= & \, \delta(\omega - \bar{\Lambda}) \, \langle 0| \, \bar{q}(0) \Gamma_1^{\mu\nu} g_s G_{\mu\nu}(0) h_v(0) \, |\bar{B}\rangle \\
& \langle \bar{B}| \, \bar{h}_v(0) \Gamma_2^{\rho\sigma} g_s G_{\rho\sigma}(0) q(0) \, |0\rangle + \rho^{\mathrm{hadr.}}(\omega) \Theta(\omega - \omega^{th})
\end{aligned} \tag{11.10}$$

including a full set of intermediate states in Eq. (11.10). In this case, the ground state corresponds to the B-meson and we set an appropriate threshold ω^{th} such that higher excited states like the radially excited B-meson or the continuum contributions are collected in the hadronic spectral density $\rho^{\mathrm{hadr.}}(\omega)$. This procedure is symbolically shown in figure 10.1. In general, the choice of ω^{th} depends on the problem at hand. Moreover, there also might occur problems where the ground state can not be separated from the hadronic spectrum by a good choice of the threshold, for instance if the ground state contribution is broad. But for B-mesons, this procedure is well established since the ground is isolated. The parameter $\bar{\Lambda} = m_B - m_b$ is the binding energy, which has already been introduced in section 2.2.
After applying the unitary condition, we make use of the residue theorem and the Schwartz reflection principle in order to rewrite the correlation function in Eq. (11.4) into a standard dispersion integral. The details of this procedure are discussed in section 11.2.

$$\begin{aligned}
\Pi_{\mathrm{diag}}(\omega) = & \frac{1}{\pi} \int_0^{\infty} \mathrm{d}s \frac{\mathrm{Im}\Pi_{\mathrm{diag}}(s)}{s - \omega - i0^+} \\
= & \frac{1}{\bar{\Lambda} - \omega - i0^+} \, \langle 0| \, \bar{q}(0) \Gamma_1^{\mu\nu} g_s G_{\mu\nu}(0) h_v(0) \, |\bar{B}\rangle \\
& \times \langle \bar{B}| \, \bar{h}_v(0) \Gamma_2^{\rho\sigma} g_s G_{\rho\sigma}(0) q(0) \, |0\rangle + \int_{s^{th}}^{\infty} \mathrm{d}s \frac{\rho^{\mathrm{hadr.}}(s)}{s - \omega - i0^+} \,.
\end{aligned} \tag{11.11}$$

The threshold parameter ω^{th} transforms into s^{th} once the hadronic contribution is expressed in terms of a dispersion integral. With the help of Eq. (2.40), the ground state contribution can be simplified

$$\begin{aligned}
&\langle 0|\,\bar{q}(0)\Gamma_1^{\mu\nu} g_s G_{\mu\nu}(0) h_v(0)\,|\bar{B}\rangle\,\langle \bar{B}|\,\bar{h}_v(0)\Gamma_2^{\rho\sigma} g_s G_{\rho\sigma}(0) q(0)\,|0\rangle \\
&= \frac{-i}{6}F(\mu)\Big[\lambda_H^2(\mu)\mathrm{Tr}[\Gamma_1 P_+\gamma_5\sigma_{\mu\nu}] + [\lambda_H^2(\mu)-\lambda_E^2(\mu)]\mathrm{Tr}[\Gamma_1 P_+\gamma_5 v_{\mu\nu}]\Big] \\
&\times \frac{-i}{6}F^\dagger(\mu)\Big[\lambda_H^2(\mu)\mathrm{Tr}[\gamma_5 P_+\Gamma_2\sigma_{\rho\sigma}] - [\lambda_H^2(\mu)-\lambda_E^2(\mu)]\mathrm{Tr}[\gamma_5 P_+\Gamma_2 v_{\rho\sigma}]\Big]\,.
\end{aligned} \tag{11.12}$$

For convenience, we suppress the Lorentz indices at $\Gamma_{1,2}^{\mu\nu}$.
To derive the sum rules for combinations of the parameters $\lambda_{E,H}^2$, we choose appropriate expressions for Γ_1 and Γ_2. To this end, we consider

$$\Gamma_1 = \frac{i}{2}\sigma_{\mu\nu}\gamma_5\,, \tag{11.13}$$

and get the sum rule for $(\lambda_H^2+\lambda_E^2)^2$. The sum rule for λ_H^4 can be derived by requiring that

$$\Gamma_1 = i\left(\frac{1}{2}\delta_\alpha^{\ \nu} - v_\nu v^\alpha\right)\sigma_{\mu\alpha}\gamma_5\,, \tag{11.14}$$

while we designate Γ_1 to be

$$\Gamma_1 = i v_\nu v^\alpha \sigma_{\mu\alpha}\gamma_5 \tag{11.15}$$

to obtain λ_E^4. Contrary to Eqs. (2.36) and (2.37), these choices are Lorentz covariant. Since we consider diagonal sum rules, Γ_2 is related to Γ_1 through the change of indices $\mu\to\rho, \nu\to\sigma$.
Using the projections in Eqs. (11.13) to (11.15), it is possible to derive the expressions for $\Pi_{\mathrm{diag}}(\omega)$ in (11.11) depending on the projection

$$\Pi_{E,H}(\omega) = F(\mu)^2\cdot\lambda_{E,H}^4\cdot\frac{1}{\bar{\Lambda}-\omega-i0^+} + \int_{s^{th}}^\infty \mathrm{d}s\frac{\rho_{E,H}^{\mathrm{hadr.}}(s)}{s-\omega-i0^+}\,, \tag{11.16}$$

$$\Pi_{HE}(\omega) = F(\mu)^2\cdot(\lambda_H^2+\lambda_E^2)^2\cdot\frac{1}{\bar{\Lambda}-\omega-i0^+} + \int_{s^{th}}^\infty \mathrm{d}s\frac{\rho_{HE}^{\mathrm{hadr.}}(s)}{s-\omega-i0^+}\,. \tag{11.17}$$

It is important to keep in mind that the threshold parameter s^{th} differs for the sum rules in Eqs. (11.16) and (11.17), since the hadronic spectral densities $\rho_{E,H,HE}^{\mathrm{hadr.}}$ are in principle different. Now we also see that we choose $s_1 = s_{E,H,HE}^{th}$ in section 11.2.
In order to parameterise the hadronic spectral density, we use the global and semi-local quark-hadron duality (QHD) [182, 183]. The essential idea of this approximation is to connect the physical hadronic spectral density to the spectral density from the OPE [53, 178, 184, 185]. However, we consider the OPE in the deep-spacelike region with $\omega \ll 0$, where we observe quasi-free particles in form of quarks and gluons due to asymptotic freedom, while

the hadronic spectral density is defined for $\omega \in \Re$. As mentioned before, the hadronic spectral density incorporates observable bound states of quarks and gluons due to confinement, therefore we work in the timelike region with $\omega > 0$. Nevertheless, in the region $\omega \ll 0$, we can use that the hadronic and OPE spectral density functions agree at the global level

$$\Pi_X^{\text{hadr.}} = \Pi_X^{\text{OPE}} \quad \text{for } X \in \{H, E, HE\}. \tag{11.18}$$

This equality holds since the components of the bound states like mesons and baryons, i.e. the quarks and gluons, obey asymptotic freedom and appear as quasi-free particles in the process. Additionally, we need to apply the semi-local quark-hadron duality, which connects the spectral integrals over the two densities

$$\int_{s_X^{th}}^{\infty} \mathrm{d}s \frac{\rho_X^{\text{hadr.}}(s)}{s - \omega - i0^+} = \int_{s_X^{th}}^{\infty} \mathrm{d}s \frac{\rho_X^{\text{OPE}}(s)}{s - \omega - i0^+} \,. \tag{11.19}$$

The quantity X is to be chosen according to Eq. (11.18). Moreover, the threshold parameter s^{th} might differ between the left and right side of Eq. (11.19).
Here, the next step is to apply the QHD (11.18) and (11.19) and to obtain the following expression for the sum rules:

$$\begin{aligned} F(\mu)^2 \cdot \lambda_{E,H}^4 \cdot \frac{1}{\bar{\Lambda} - \omega - i0^+} &= \int_0^{s_{E,H}^{th}} \mathrm{d}s \, \frac{\rho_{E,H}^{\text{OPE}}(s)}{s - \omega - i0^+} \\ &= \int_0^{s_{E,H}^{th}} \mathrm{d}s \, \frac{\frac{1}{\pi}\text{Im}\Pi_{E,H}^{\text{OPE}}(s)}{s - \omega - i0^+} \,, \end{aligned} \tag{11.20}$$

$$\begin{aligned} F(\mu)^2 \cdot (\lambda_H^2 + \lambda_E^2)^2 \cdot \frac{1}{\bar{\Lambda} - \omega - i0^+} &= \int_0^{s_{HE}^{th}} \mathrm{d}s \, \frac{\rho_{HE}^{\text{OPE}}(s)}{s - \omega - i0^+} \\ &= \int_0^{s_{HE}^{th}} \mathrm{d}s \, \frac{\frac{1}{\pi}\text{Im}\Pi_{HE}^{\text{OPE}}(s)}{s - \omega - i0^+} \,. \end{aligned} \tag{11.21}$$

The last step to derive the final expressions for the sum rules is to perform an additional Borel transformation on Eqs. (11.20) and (11.21). Since this transformation is also relevant in the light-cone sum rule approach, we state the details in appendix A.5. Furthermore, the advantage of this step lies in the fact that higher resonances and the continuum are exponentially suppressed and possible substraction terms in the dispersion integral are removed. Besides, the convergence of the sum rule is improved. After applying this additional transformation, the final sum rule expressions are

$$\begin{aligned} F(\mu)^2 \cdot \lambda_{E,H}^4 \cdot e^{-\bar{\Lambda}/M} &= \int_0^{\omega_{E,H}^{th}} \mathrm{d}\omega \, \rho_{E,H}^{\text{OPE}}(\omega) \, e^{-\omega/M} \\ &= \int_0^{\omega_{E,H}^{th}} \mathrm{d}\omega \, \frac{1}{\pi}\text{Im}\Pi_{E,H}^{\text{OPE}}(\omega) \, e^{-\omega/M} \,, \end{aligned} \tag{11.22}$$

$$F(\mu)^2 \cdot (\lambda_H^2 + \lambda_E^2)^2 \cdot e^{-\bar{\Lambda}/M} = \int_0^{\omega_{HE}^{th}} \mathrm{d}\omega\ \rho_{HE}^{\mathrm{OPE}}(\omega)\ e^{-\omega/M} = \int_0^{\omega_{HE}^{th}} \mathrm{d}\omega\ \frac{1}{\pi}\mathrm{Im}\Pi_{HE}^{\mathrm{OPE}}(\omega)\ e^{-\omega/M}\,. \tag{11.23}$$

These sum rules (11.22) and (11.23) are one of the main results in this project. By choosing the Borel parameter M and the threshold parameter ω^{th} accordingly, we can extract values for the parameters $\lambda_{E,H}^2$. Details for the determination of the Borel window and the threshold are provided in chapter 12, where we discuss the numerics and point out several strategies to pin down the parameters. Additionally, we also notice that the Borel transformation is not sufficient to suppress continuum contributions and excited states. This observation tends to be the case for correlation functions of currents with large mass dimension, similar to the function in Eq. (11.4). We cover this issue in the numerical analysis as well. The next subsections are devoted to the detailed discussion of the components of Eq. (11.5).

11.4 QCD vacuum condensates and parameterisation in the OPE

The OPE is the central element of the QCD sum rule framework, since it allows for the factorisation of perturbative and non-perturbative contributions. As discussed before, the non-perturbative effects are parameterised by vacuum condensates of increasing mass dimension. We state the OPE from Eq. (11.5) introducing a more compact notation

$$\begin{aligned}&\langle\bar{q}q\rangle := \langle 0|\,\bar{q}q\,|0\rangle\,, \langle G^2\rangle := \langle 0|\,G^a_{\mu\nu}G^{a,\mu\nu}\,|0\rangle\,, \langle\bar{q}g_s\sigma\cdot Gq\rangle := \langle 0|\,\bar{q}g_sG^{\mu\nu}\sigma_{\mu\nu}q\,|0\rangle\,,\\ &\langle g_s^3 f^{abc}G^aG^bG^c\rangle := \langle 0|\,g_s^3 f^{abc}G^a_{\mu\nu}G^{b,\nu\rho}G^{c,\mu}_{\rho}\,|0\rangle\,.\end{aligned} \tag{11.24}$$

such that the OPE becomes

$$\begin{aligned}\Pi_{\mathrm{X}}^{\mathrm{OPE}}(\omega) = C_{\mathrm{X}}^{\mathrm{pert}}(\omega) + C_{\mathrm{X}}^{\bar{q}q}\,\langle\bar{q}q\rangle + C_{\mathrm{X}}^{G^2}\,\langle\frac{\alpha_s}{\pi}G^2\rangle + C_{\mathrm{X}}^{\bar{q}Gq}\,\langle\bar{q}g_s\sigma\cdot Gq\rangle\\ + C_{\mathrm{X}}^{G^3}\,\langle g_s^3 f^{abc}G^aG^bG^c\rangle + C_{\mathrm{X}}^{\bar{q}qG^2}\,\langle\bar{q}q\rangle\,\langle\frac{\alpha_s}{\pi}G^2\rangle + ...\end{aligned} \tag{11.25}$$

In order to derive the vacuum condensates contributions from the correlation function given in Eq. (11.24), we need to average over the Lorentz, Dirac and colour indices. For this, we closely follow the discussion in [186]. Starting point is the matrix element $\langle 0|\,\bar{q}(0)\Gamma_1 P_+\Gamma_2\,q(x)\,|0\rangle$, which we Taylor expand near $x = 0$:

$$\begin{aligned}\langle 0|\,\bar{q}(0)\Gamma_1 P_+\Gamma_2\,q(x)\,|0\rangle = \langle 0|\,\bar{q}(0)\Gamma_1 P_+\Gamma_2 q(0)\,|0\rangle + x^\mu\,\langle 0|\,\bar{q}(0)\Gamma_1 P_+\Gamma_2 D_\mu q(0)\,|0\rangle\\ + \frac{x^\mu x^\nu}{2}\,\langle 0|\,\bar{q}(0)\Gamma_1 P_+\Gamma_2 D_\mu D_\nu q(0)\,|0\rangle + \cdots\end{aligned} \tag{11.26}$$

Notice that we drop for simplicity all indices in the beginning. The first term in Eq.(11.26) yields the quark condensate

$$\langle 0|\,\bar{q}^i_\alpha(0)\Gamma_{1,\alpha\beta}P_{+,\beta\gamma}\Gamma_{2,\gamma\delta}\,q^j_\delta(0)\,|0\rangle = \frac{1}{4N_c}\cdot\mathrm{Tr}[\Gamma_1 P_+\Gamma_2]\cdot\langle\bar{q}q\rangle\,\delta^{ij}, \tag{11.27}$$

where (i, j) are colour indices and $(\alpha, \beta, \gamma, \delta)$ are spinor indices. The factor N_c represents the number of colour degrees of freedom. Taking the Dirac equation into consideration, we see that the second term in Eq. (11.26) vanishes, because we consider light quarks with $m_q = 0$.

$$\not{D} q = -i m_q q \,. \tag{11.28}$$

The third term is directly related to the dimension five matrix element, which is parameterised as the quark-gluon condensate

$$\langle 0| \, \bar{q}^i_\alpha(0) g_s G_{\mu\nu}(0) q^j_\delta(0) \, |0\rangle = \langle 0| \, \bar{q} g_s \sigma \cdot G q \, |0\rangle \cdot \frac{1}{4 N_c d(d-1)} \cdot \delta^{ij} \cdot (\sigma_{\mu\nu})_{\delta\alpha} \,. \tag{11.29}$$

Thus, for the third term in Eq. (11.26) we obtain

$$\frac{x^\mu x^\nu}{2} \langle 0| \, \bar{q}^i_\alpha(0) D_\mu D_\nu q^j_\delta(0) \, |0\rangle = \frac{x^2}{16 N_c d} \, \delta^{ij} \delta_{\alpha\delta} \langle 0| \, \bar{q} g_s \sigma \cdot G q \, |0\rangle \,. \tag{11.30}$$

Next, the gluon condensate can be parametrised as

$$\langle 0| \, G^a_{\mu\nu} G^b_{\rho\sigma} \, |0\rangle = \frac{\delta^{ab}}{d(d-1)(N_c^2 - 1)} \langle G^2 \rangle \left(g_{\mu\rho} g_{\nu\sigma} - g_{\mu\sigma} g_{\nu\rho} \right) , \tag{11.31}$$

where $d = 4 - 2\epsilon$ and a, b are colour indices in the adjoint representation. Finally, we are left with the triple-gluon condensate. According to [187], the triple-gluon condensate is given by

$$\begin{aligned} \langle g_s^3 f^{abc} G^a_{\mu\nu} G^b_{\rho\sigma} G^c_{\alpha\lambda} \rangle = \frac{\langle g_s^3 f^{abc} G^a G^b G^c \rangle}{d(d-1)(d-2)} \cdot \Big(& g_{\mu\lambda} g_{\rho\nu} g_{\sigma\alpha} + g_{\mu\sigma} g_{\rho\alpha} g_{\lambda\nu} + g_{\rho\lambda} g_{\mu\alpha} g_{\nu\sigma} \\ & + g_{\alpha\nu} g_{\mu\rho} g_{\sigma\lambda} - \; g_{\mu\sigma} g_{\rho\lambda} g_{\alpha\nu} - g_{\mu\lambda} g_{\rho\alpha} g_{\nu\sigma} - g_{\rho\nu} g_{\mu\alpha} g_{\sigma\lambda} \\ & - g_{\sigma\alpha} g_{\mu\rho} g_{\nu\lambda} \Big) \\ \equiv \frac{\langle g_s^3 f^{abc} G^a G^b G^c \rangle}{d(d-1)(d-2)} \cdot & B_{\mu\lambda\rho\nu\sigma\alpha} \,. \end{aligned} \tag{11.32}$$

The last condensate encountered in Eq. (11.25) is the condensate of mass dimension seven, where we apply an additional simplification. While there exist many estimates for the values of the lower dimensional condensates in the literature from lattice QCD or sum rule computations (see chapter 12 for more details), contributions arising with higher mass dimension are hard to tackle due to mixing with lower dimensional terms. This lack of values requires to make use of the vacuum saturation approximation [51], where a full set of intermediate states is inserted into the condensate expression. After assuming that only the ground state, i.e. the vacuum, leads a sizeable effect, these higher dimensional condensates are effectively reduced to a product of condensates with lower mass dimension. In our case in Eq. (11.25), the dimension seven condensate is rewritten into a product of a quark condensate and a gluon condensate.

After discussing the averaging and parameterisation of the vacuum condensates in the OPE (11.5) and (11.25), one might wonder whether the condensates are parameterised uniquely by the terms stated above. In general, this is indeed the case for condensates up to mass dimension five. Beyond this dimension, there arise many different combinations which are in some cases related by QCD equations of motions or Fierz identities [188]. We only consider condensates of mass dimension six and seven in the OPE in Eq. (11.25), which give a leading power contribution to the parameters $\lambda_{E,H}^2$. This is consistent with our general setup, since we plan the extraction of these parameters to leading order in α_s. Note that the general counting is not related to the parameter α_s which is not matching between different condensates. The prefactors in the gluon, quark-gluon and triple-gluon condensate are purely chosen according to the convention in [185].

11.5 Perturbative contributions in the OPE

As we have discussed before, we can identify the perturbative part of the OPE in Eq. (11.25) as the Wilson coefficients C_X^i. They encode the short-distance effects, which can be determined by perturbative methods. We are working to leading order in α_s throughout this project, which turns out to be $\mathcal{O}(\alpha_s)$ for a diagonal correlation function (11.4) of two three-particle currents. This leads to the observation that the computation of $C_X^{\text{pert.}}$ is related to a two-loop integral, while the other Wilson coefficients up to mass dimension seven require either the calculation of one-loop integrals or tree level diagrams. Since there is only one scale involved in this evaluation, we can perform a direct computation of these integrals on completely analytical basis. Nevertheless, we also use LiteRED [189] to reduce the two-loop integral via IBP-reduction [190] in order to check the analytic computation. During the analytic computation it is useful to work in Feynman gauge.
In the QCD SR method, the long-distance effects are parameterised in terms of local vacuum matrix elements of increasing mass dimension (11.25). Locality in these matrix elements require that the fields inside the vacuum condensates are expanded in the spacetime coordinate x. Moreover, the gluon fields do not interact with the HQET heavy quark field $h_v(x)$ as we have proven in appendix D. In total, there are three subdiagrams, which lead to vanishing contributions and which we show in figure 11.2

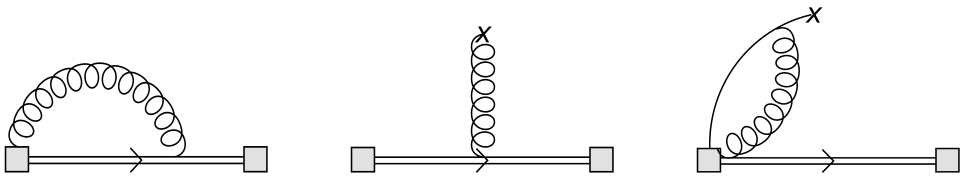

Figure 11.2: Vanishing subdiagrams during the computation. The double line denotes the heavy quark field, while the curly lines denote the gluon field.

Since we perform the computations in momentum space, we also use the heavy-quark propagator in this space

$$\langle 0|\, T\{h_v^i(0)\bar{h}_v^j(x)\}\,|0\rangle = \int \frac{\mathrm{d}^d k}{(2\pi)^d}\, e^{ikx} \frac{i}{v\cdot k + i0^+} P_+ \delta^{ji} \tag{11.33}$$

for the vanishing diagrams in figure 11.2 as well as the contributions in the following discussion. Additionally, i, j denote the colour indices of the heavy quark fields and $P_+ = (1+\not{v})/2$ corresponds to the projection operator in HQET. In general, linear propagators like the above one often appear in effective field theories and are for instance also a fundamental part of SCET. We regularise the divergences appearing in the computation of the Wilson coefficients C_X^i with dimensional regularisation [191], i.e. we work in $d = 4-2\epsilon$ dimensions. As it is known for a long time, this specific regularisation is useful since it preserves symmetries like gauge invariance or Lorentz invariance. For the calculation, we follow two different roads. On the one hand, we perform each integral completely analytically in momentum space by applying the Feynman parameterisation and solving the occurring integrals. Due to the linear propagator which appears in the evaluation, it is necessary to use a slightly modified Feynman parameterisation stated in appendix A.1. Furthermore, we encounter tensor integrals in the loop momenta, which we rewrite into scalar integrals by projecting the tensor structures in the loop momenta onto invariant Lorentz structures according to appendix A.1. On the other hand, we use FeynCalc [192] to decompose the tensor integrals in the evaluation to scalar integrals. These scalar integrals are additionally reduced to master integrals by integration-by-parts (IBP) identities [190] with the `Mathematica` package LiteRed [189]. For both the perturbative contribution as well as for the Wilson coefficients related to vacuum condensates, this ultimately boils down to a master integral of the form [193]

$$\int \frac{\mathrm{d}^d k_1}{i\pi^{d/2}} \frac{1}{(-k_1^2)^{a_1}[-2(k_1+k_2)\cdot v + 1]^{a_2}} = (-2k_2\cdot v + 1)^{d-2a_1-a_2}\, I(a_1, a_2) \tag{11.34}$$

with

$$I(a_1, a_2) = \frac{\Gamma(2a_1 + a_2 - d)\,\Gamma(d/2 - a_1)}{\Gamma(a_1)\Gamma(a_2)}\,. \tag{11.35}$$

By applying the machinery from above, we can solve the two-loop integral for the determination of $C_X^{\text{pert.}}$ iteratively and obtain the following expression:

$$\begin{aligned} C_{\mathrm{X}}^{\mathrm{pert}}(\omega) = {} & \frac{2\alpha_s}{\pi^3}\cdot C_F N_c \cdot \mathrm{Tr}[\Gamma_1 P_+ \Gamma_2 \not{v}]\cdot \bar{\mu}^{4\epsilon}\Gamma(-6+4\epsilon)\cdot\Gamma(2-\epsilon)\cdot\omega^{6-4\epsilon} e^{4i\pi\epsilon} \\ & \times \left[\Gamma(2-\epsilon)\cdot T_1^{\mu\rho\nu\sigma} + \Gamma(3-\epsilon)\cdot T_2^{\mu\rho\nu\sigma}\right], \end{aligned} \tag{11.36}$$

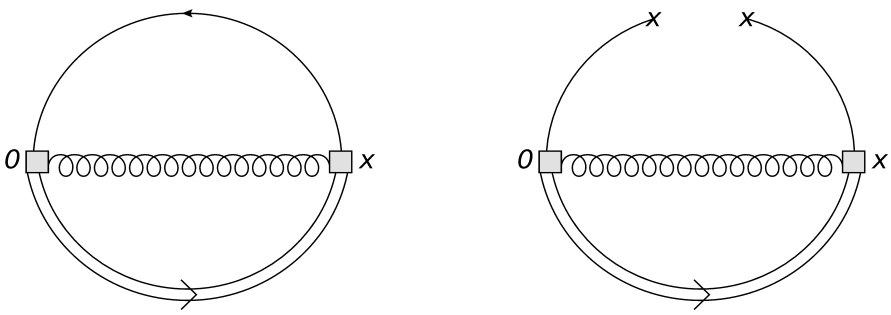

Figure 11.3: Diagrams for the perturbative and condensate of mass dimension three Wilson coefficients $C_{\mathrm{X}}^{\mathrm{pert.}}$ and $C_{\mathrm{X}}^{\bar{q}q}$. The double line indicates the heavy quark field h_v in HQET, while the single line corresponds to the light antiquark $\bar{q}$. Furthermore, the curvy line denotes the gluon field.

We introduce several abbreviations, which are also relevant for the other contributions. Notice that we depict the diagram corresponding to this Wilson coefficient on the left in figure 11.3

$$\begin{aligned}
\bar{\mu}^2 &:= \frac{\mu^2 e^{\gamma_E}}{4}\,, \\
T_1^{\mu\rho\nu\sigma} &:= g_{\mu\rho}g_{\nu\sigma} - g_{\mu\sigma}g_{\nu\rho}\,, \\
T_2^{\mu\rho\nu\sigma} &:= -g_{\nu\sigma}v_\mu v_\rho + g_{\mu\sigma}v_\nu v_\rho + g_{\nu\rho}v_\mu v_\sigma - g_{\mu\rho}v_\nu v_\sigma\,.
\end{aligned} \tag{11.37}$$

The above definitions in Eq. (11.37) are chosen such that they satisfy all symmetries imposed by the field strength tensors $G_{\mu\nu}$ and $G_{\rho\sigma}$. Notably, they are anti-symmetric under the exchange $\{\mu \leftrightarrow \nu\}, \{\rho \leftrightarrow \sigma\}$ and symmetric under the simultaneous exchange $\{\mu \leftrightarrow \nu, \rho \leftrightarrow \sigma\}$.
The remaining one-loop integrals for the other Wilson coefficients are of simpler nature and an analytic computation can be performed easily. Thus, we obtain for the factor $C_X^{\bar{q}q}$ in front of the quark condensate

$$\begin{aligned}
C_{\mathrm{X}}^{\bar{q}q}(\omega) = &-\frac{\alpha_s}{\pi}\cdot C_F \cdot \mathrm{Tr}[\Gamma_1 P_+ \Gamma_2]\cdot \bar{\mu}^{2\epsilon}\cdot\Gamma(-3+2\epsilon)\cdot\omega^{3-2\epsilon}e^{2i\pi\epsilon} \\
&\times\left[\Gamma(2-\epsilon)\cdot T_1^{\mu\rho\nu\sigma} + \Gamma(3-\epsilon)\cdot T_2^{\mu\rho\nu\sigma}\right].
\end{aligned} \tag{11.38}$$

Both coefficients are stated in a completely general form for all sum rules in Eqs. (11.22) and (11.23) since they are expressed in terms of $\Gamma_{1,2}$. Choosing these matrices accordingly leads to the contributions to the individual sum rules, thus we follow this notation for the rest of the coefficients. For the gluon condensate diagrams, which is shown in figure 11.4, we can proceed similarly and obtain

$$\begin{aligned}
C_{\mathrm{X}}^{G^2}(\omega) = &\,\mathrm{Tr}[\Gamma_1 P_+ \Gamma_2 \not{v}]\cdot\frac{\bar{\mu}^{2\epsilon}}{(4-2\epsilon)(3-2\epsilon)}\Gamma(-2+2\epsilon)\cdot\Gamma(2-\epsilon)\cdot\omega^{2-2\epsilon}e^{2i\pi\epsilon} \\
&\times T_1^{\mu\rho\nu\sigma}\,.
\end{aligned} \tag{11.39}$$

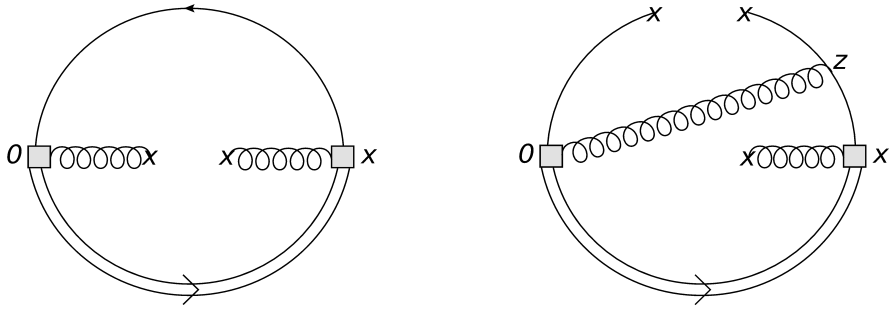

Figure 11.4: Diagrams for the gluon condensate and condensate of mass dimension five Wilson coefficients $C_{\mathrm{X}}^{G^2}$ and $C_{\mathrm{X}}^{\bar{q}Gq,1}$. The double line indicates the heavy quark field h_v in HQET, while the single line corresponds to the light antiquark $\bar{q}$. Furthermore, the curvy line denotes the gluon field.

The quark-gluon condensate of mass dimension five receives several contributions depending on the location of the gluon line. Moreover, there is an additional correction term originating from the higher order expansion in x in the expression for the quark condensate (11.30). We show the corresponding Feynman diagrams in figures 11.4 and 11.5.

$$C_{\mathrm{X}}^{\bar{q}Gq,1}(\omega) = -\frac{\alpha_s}{\pi}\cdot C_F\cdot \mathrm{Tr}[\Gamma_1 P_+ \Gamma_2]\cdot \frac{\bar{\mu}^{2\epsilon}}{(4-2\epsilon)}\Gamma(-3+2\epsilon)\cdot\Gamma(3-\epsilon)\cdot\omega^{1-2\epsilon} \times e^{2i\pi\epsilon} T_1^{\mu\rho\nu\sigma}\,, \tag{11.40}$$

$$C_{\mathrm{X}}^{\bar{q}Gq,2}(\omega) = \frac{\alpha_s}{4\pi}\cdot\frac{C_F\cdot\bar{\mu}^{2\epsilon}}{(4-2\epsilon)(3-2\epsilon)}\cdot\Gamma(-1+2\epsilon)\cdot\Gamma(1-\epsilon)\cdot\omega^{1-2\epsilon}e^{2i\pi\epsilon} \times\Big[\mathrm{Tr}[\Gamma_1 P_+\Gamma_2\sigma_{\mu\nu}\sigma_{\rho\sigma}] - (1-\epsilon)\cdot\mathrm{Tr}[\Gamma_1 P_+\Gamma_2 \not{v}\sigma_{\mu\nu}\sigma_{\rho\sigma}]\Big]\,, \tag{11.41}$$

$$C_{\mathrm{X}}^{\bar{q}Gq,3}(\omega) = \frac{\alpha_s}{4\pi}\cdot\frac{C_F\cdot\bar{\mu}^{2\epsilon}}{(4-2\epsilon)(3-2\epsilon)}\Gamma(-1+2\epsilon)\cdot\Gamma(1-\epsilon)\cdot\omega^{1-2\epsilon}e^{2i\pi\epsilon} \times\Big[\mathrm{Tr}[\Gamma_1 P_+\Gamma_2\sigma_{\mu\nu}\sigma_{\rho\sigma}] + (1-\epsilon)\cdot\mathrm{Tr}[\Gamma_1 P_+\Gamma_2\sigma_{\mu\nu}\not{v}\sigma_{\rho\sigma}]\Big]\,, \tag{11.42}$$

$$\begin{aligned} C_{\mathrm{X}}^{\bar{q}Gq,4}(\omega) = {}& \frac{i\alpha_s}{32\pi}\cdot\frac{C_A C_F\cdot\bar{\mu}^{2\epsilon}}{(2-\epsilon)(3-2\epsilon)}\cdot\mathrm{Tr}[\Gamma_1 P_+\Gamma_2\sigma^{\chi\beta}]\cdot\Gamma(-1+2\epsilon)\cdot\Gamma(1-\epsilon) \\ &\times\omega^{1-2\epsilon}e^{2i\pi\epsilon}\Big[\{g_{\mu\chi}T_1^{\nu\rho\beta\sigma} - (\beta\leftrightarrow\chi)\} + (1-\epsilon) \\ &\times\big(\{v_\beta g_{\mu\rho}(v_\sigma g_{\nu\chi} - v_\nu g_{\sigma\chi}) - (\rho\leftrightarrow\sigma)\} + \\ &\{v_\nu g_{\mu\chi}(v_\sigma g_{\beta\rho} - v_\rho g_{\beta\sigma}) - (\beta\leftrightarrow\chi)\}\big)\Big] - (\mu\leftrightarrow\nu)\,, \end{aligned} \tag{11.43}$$

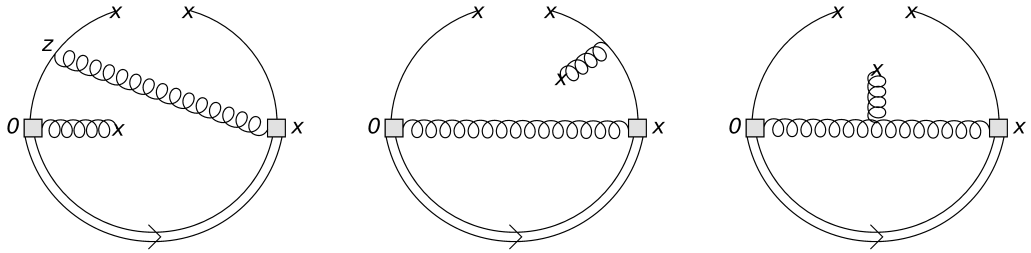

Figure 11.5: Diagrams for the remaining mass dimension five vacuum condensates. The double line indicates the heavy quark field h_v in HQET, while the single line corresponds to the light antiquark $\bar{q}$. Furthermore, the curvy line denotes the gluon field.

Apart from the definitions in Eq. (11.37) which appear in Eqs. (11.40) to (11.43), we encounter additional complicated tensor structures as well. Nevertheless, all symmetries based on the properties of the field strength tensor are still satisfied. In order to obtain the complete Wilson coefficient for the mass dimension five condensate, we need to add up the contributions in Eqs. (11.40) to (11.43)

$$C_{\mathrm{X}}^{\bar{q}Gq} = \sum_{k=1}^{4} C_X^{\bar{q}Gq,k} \,. \tag{11.44}$$

Finally, the two remaining diagrams are shown in figure 11.6. The corresponding condensates are of mass dimension six and seven. Since the OPE is supposed to converge in the sense that condensates of higher mass dimension tend to give smaller contributions to the sum rules, we expect these terms to be small in comparison to the other expressions. But as we will discuss in detail in the numerical analysis, the condensate contributions are in general larger compared to the perturbative contribution. This behaviour spoils the converge of the OPE at first sight, albeit it is not unusual for the types of correlation functions (11.4) that we encounter.
Notice that in general the triple-gluon condensate and the condensate of mass dimension seven have more than one contribution to the OPE in Eq. (11.25). Due to our leading order analysis, which is $\mathcal{O}(\alpha_s)$ in this case, we end up with one contribution for each condensate, which are depicted in figure 11.6. We can state those to be

$$\begin{aligned} C_{\mathrm{X}}^{G^3}(\omega) = \frac{\bar{\mu}^{2\epsilon}}{64\pi^2} \cdot B_{\mu\lambda\rho\nu\sigma\alpha} \cdot \Gamma(2\epsilon) \cdot \Gamma(1-\epsilon) \cdot \omega^{-2\epsilon} e^{2i\pi\epsilon} \cdot (-i) \\ \times \Big[\mathrm{Tr}[\Gamma_1 P_+ \Gamma_2 \not{v} \sigma^{\lambda\alpha}] + \mathrm{Tr}[\Gamma_1 P_+ \Gamma_2 v^{\alpha\lambda}]] \Big] \,, \end{aligned} \tag{11.45}$$

$$C_{\mathrm{X}}^{\bar{q}qG^2}(\omega) = -\mathrm{Tr}[\Gamma_1 P_+ \Gamma_2] \cdot \frac{T_1^{\mu\rho\nu\sigma}}{\omega + i0^+} \cdot \frac{\pi^2}{2N_c(4-2\epsilon)(3-2\epsilon)} \,. \tag{11.46}$$

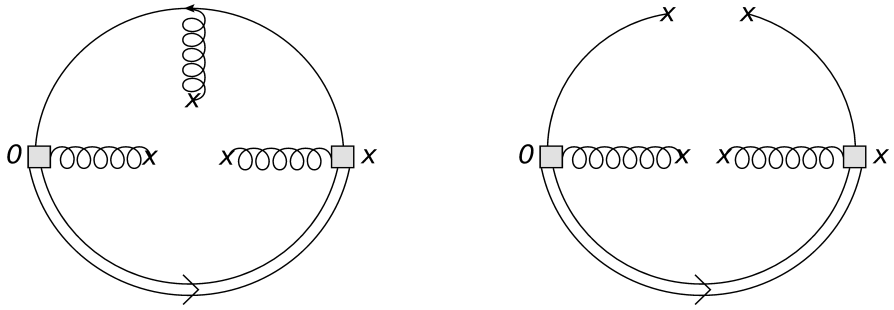

Figure 11.6: Diagrams for the condensates of mass dimension six and seven Wilson coefficients $C_{\mathrm{X}}^{G^3}$ and $C_{\mathrm{X}}^{\bar{q}qG^2}$. The double line indicates the heavy quark field h_v in HQET, while the single line corresponds to the light anti-quark $\bar{q}$. Furthermore, the curvy line denotes the gluon field.

The expression $B_{\mu\lambda\rho\nu\sigma\alpha}$ in Eq. (11.45) is defined in Eq. (11.32). Note that the computation of the triple-gluon condensate involves a subtlety, in particular the final expression needs to be symmetrised in order to preserve all symmetries with respect to the Lorentz indices μ, ν, ρ, σ. This is related to an additional factor of x in the integration over the exponential functions such that we can not immediately identify this integral as the momentum conserving δ-distribution.
According to Eq. (11.22) or Eq. (11.23), the dispersion integral states that we need to include the imaginary part of our results into these sum rules. In Eqs. (11.36) to (11.45), we see factors of $e^{i\pi n\epsilon}$ yielding the imaginary part after expansion in ϵ. These factors originate from terms of the form $(-1+i0^+)^\epsilon$ in the computation. The last contribution in Eq. (11.46) constitutes a factor of $\frac{1}{\omega+i0^+}$, which we relate to the corresponding imaginary part via

$$\frac{1}{\omega \pm i0^+} = \mathrm{PV}\left[\frac{1}{\omega}\right] \mp i\pi\delta(\omega)\,, \tag{11.47}$$

where PV indicates the principal value.
After the extraction of the imaginary part, we can now derive the sum rules in their complete form. In order to obtain the final expression for the sum rules in Eqs. (11.22) and (11.23), we integrate ω up to ω^{th} and state the result in terms of the function

$$G_n(x) := 1 - \sum_{k=0}^{n} \frac{x^k}{k!} e^{-x} \tag{11.48}$$

in a completely analytical form. With the abbreviation in Eq. (11.48), we can state the final result for the sum rules for the parameters $\lambda_{E,H}^4$ and the combination $(\lambda_E^2 + \lambda_H^2)^2$:

$$\begin{aligned} F(\mu)^2 \cdot (\lambda_H^2 + \lambda_E^2)^2\, e^{-\bar{\Lambda}/M} = {} & \frac{\alpha_s C_A C_F}{\pi^3} \cdot 24M^7 \cdot G_6\Big(\frac{\omega^{th}}{M}\Big) \\ & - \frac{\alpha_s C_F C_A}{4\pi} \cdot \langle \bar{q} g_s \sigma \cdot G q \rangle \cdot M^2 \cdot G_1\Big(\frac{\omega^{th}}{M}\Big) - \frac{3\alpha_s C_F}{2\pi} \cdot \langle \bar{q} g_s \sigma \cdot G q \rangle \cdot M^2 \end{aligned}$$

$$\times G_1\Big(\frac{\omega^{th}}{M}\Big) - \frac{\pi^2}{2N_c}\,\langle\bar{q}q\rangle\,\langle\frac{\alpha_s}{\pi}G^2\rangle\;, \tag{11.49}$$

$$\begin{aligned} F(\mu)^2\cdot\lambda_H^4\,e^{-\bar{\Lambda}/M} \;&=\; \frac{\alpha_s C_A C_F}{\pi^3}\cdot 12M^7\cdot G_6\Big(\frac{\omega^{th}}{M}\Big) - \frac{\alpha_s C_F}{\pi}\,\langle\bar{q}q\rangle\cdot 6M^4 \\ &\times G_3\Big(\frac{\omega^{th}}{M}\Big) + \frac{1}{2}\,\langle\frac{\alpha_s}{\pi}G^2\rangle\cdot M^3\cdot G_2\Big(\frac{\omega^{th}}{M}\Big) - \frac{\alpha_s C_F C_A}{8\pi}\cdot\langle\bar{q}g_s\sigma\cdot Gq\rangle\cdot M^2 \\ &\times G_1\Big(\frac{\omega^{th}}{M}\Big) - \frac{3\alpha_s C_F}{4\pi}\cdot\langle\bar{q}g_s\sigma\cdot Gq\rangle\cdot M^2\cdot G_1\Big(\frac{\omega^{th}}{M}\Big) + \frac{\langle g_s^3 f^{abc}G^aG^bG^c\rangle}{64\pi^2} \\ &\times M\cdot G_0\Big(\frac{\omega^{th}}{M}\Big) - \frac{\pi^2}{4N_c}\,\langle\bar{q}q\rangle\,\langle\frac{\alpha_s}{\pi}G^2\rangle\;, \end{aligned} \tag{11.50}$$

$$\begin{aligned} F(\mu)^2\cdot\lambda_E^4\,e^{-\bar{\Lambda}/M} \;&=\; \frac{\alpha_s C_A C_F}{\pi^3}\cdot 12M^7\cdot G_6\Big(\frac{\omega^{th}}{M}\Big) + \frac{\alpha_s C_F}{\pi}\,\langle\bar{q}q\rangle\cdot 6\cdot M^4 \\ &\times G_3\Big(\frac{\omega^{th}}{M}\Big) - \frac{1}{2}\,\langle\frac{\alpha_s}{\pi}G^2\rangle\cdot M^3\cdot G_2\Big(\frac{\omega^{th}}{M}\Big) - \frac{\alpha_s C_F}{2\pi}\cdot\langle\bar{q}g_s\sigma\cdot Gq\rangle\cdot M^2 \\ &\times G_1\Big(\frac{\omega^{th}}{M}\Big) - \frac{\langle g_s^3 f^{abc}G^aG^bG^c\rangle}{64\pi^2}\cdot M\cdot G_0\Big(\frac{\omega^{th}}{M}\Big) - \frac{\pi^2}{4N_c}\,\langle\bar{q}q\rangle\,\langle\frac{\alpha_s}{\pi}G^2\rangle\;. \end{aligned} \tag{11.51}$$

Notice that the perturbative contribution for the sum rules in $\lambda_{E,H}^4$ in Eqs. (11.50), (11.51) are identical, in particular they share the same sign. This positive sign is expected since we investigate a positive definite correlation function in Eq. (11.4). In addition to that the condensate with mass dimension seven agrees in these sum rules as well. But we also recognise that the quark, gluon and triple-gluon condensate in Eqs. (11.50) and (11.51) have different signs. Furthermore, the Wilson coefficients in Eqs. (11.41), (11.42), (11.43) do not contribute to the sum rule for λ_E^4. This turns out to be crucial for the stability of this sum rule, since the mass dimension five condensate gives rise to the largest contribution. The consequences of this behaviour are studied in chapter 12 in more detail. Finally, we note that in Eq. (11.49) the quark, the gluon and the triple-gluon condensate do not appear, because they enter the sum with opposite signs.
Besides, all sum rules involve the HQET decay constant $F(\mu)$, which was defined in Eq. (2.33). We only include leading order contributions in the sum rule expression in order to be consistent in our sum rule analysis. The sum rule can be found in e.g. [85]

$$F^2(\mu)\cdot e^{-\bar{\Lambda}/M} = \frac{2N_c M^3}{\pi^2}\cdot G_2\Big(\frac{\omega_{th}}{M}\Big) \;-\langle\bar{q}q\rangle + \frac{1}{16M^2}\,\langle\bar{q}g_s G\cdot\sigma q\rangle\,. \tag{11.52}$$

By inserting the sum rule for the decay constant $F(\mu)$ into Eqs. (11.49) to (11.51), it is possible to extract the parameters $\lambda_{E,H}^2$. Besides, the dependence on the low-energy parameter $\bar{\Lambda}$ drops out due to the insertion above. In the next section, we perform the numerical analysis and study the behaviour of the sum rules in more detail.

Chapter 12

Numerical analysis

In this section, we compute the parameters $\lambda_{E,H}^2$ by employing the sum rules stated in Eqs. (11.49) to (11.51). As mentioned before, we make use of the sum rule in Eq. (11.52) in order to eliminate the dependence on the decay constant $F(\mu)$ and on the HQET parameter $\bar{\Lambda}$. The numerical inputs for the condensates and other parameters are collected in table 12.1.

Parameters	Value	Ref.
$\alpha_s(1\text{ GeV})$	0.471	[194, 195]
$\langle\bar{q}q\rangle$	$(-0.242 \pm 0.015)^3$ GeV^3	[196]
$\langle\frac{\alpha_s}{\pi}G^2\rangle$	(0.012 ± 0.004) GeV^4	[51, 197]
$\langle\bar{q}gG\cdot\sigma q\rangle$ / $\langle\bar{q}q\rangle$	(0.8 ± 0.2) GeV^2	[198]
$\langle g_s^3 f^{abc} G^a G^b G^c\rangle$	(0.045 ± 0.045) GeV^6	[51]
$\bar{\Lambda}$	(0.55 ± 0.06) GeV	[199]

Table 12.1: List of the numerical inputs, which we use in our analysis. The renormalisation scale is chosen to be $\mu = 1$ GeV. For the strong coupling constant we use the two-loop expression with $\Lambda_{\text{QCD}}^{(4)} = 0.31$ GeV taken from [194, 195].

During the determination of the optimal window for the Borel parameter M for the sum rules in Eqs. (11.49) to (11.51), we find that these sum rules are dominated by contributions from excited states and the continuum. Thus, the estimation for the parameters $\lambda_{E,H}^2(1\text{ GeV})$ and their ratio

$$\mathcal{R}(\mu) = \frac{\lambda_E^2(\mu)}{\lambda_H^2(\mu)} \tag{12.1}$$

at $\mu = 1$ GeV is unreliable since we are not able to separate out the ground states in the dispersion integrals in Eqs. (11.20), (11.21) by a proper choice of ω^{th}. This is a crucial step in the sum rule analysis. In order to avoid this issue, we consider different combinations of Eqs. (11.49) to (11.52) such

that the separation of the ground state is possible and continuum and higher excited states are suppressed.

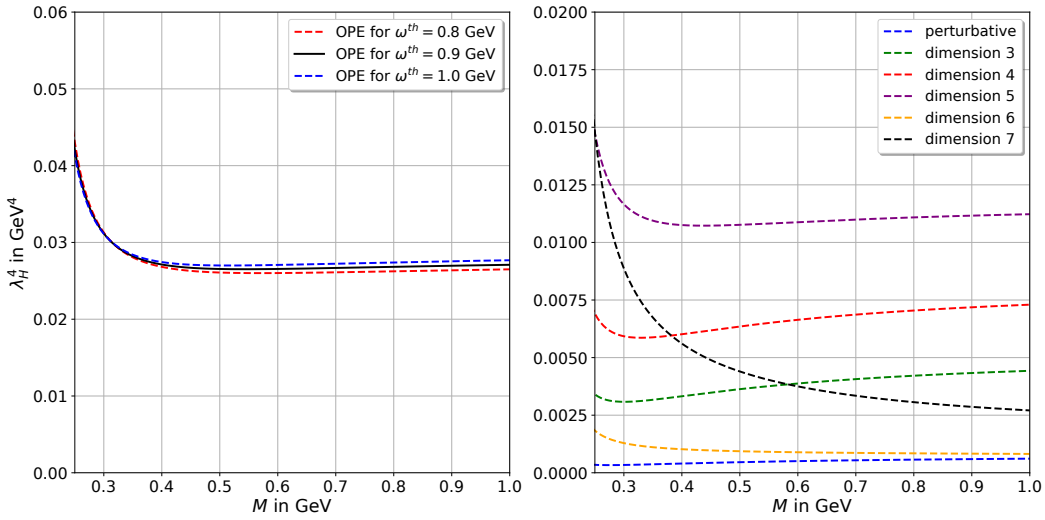

Figure 12.1: Analysis for the continuum dominated sum rule (11.50). The left plot shows the complete sum rule for different choices of ω^{th} with respect to the Borel parameter M. Contrary, the right plot illustrates each contribution individually up to the vacuum condensate of mass dimension seven and hence indicates the relative sizes of each contribution.

Before we study these combinations in more detail, we investigate the original sum rules in Eqs. (11.49) to (11.51) first to determine whether the continuum dominance in these sum rules have a great effect on the parameter extraction. In figure 12.1, we plot the contributions for λ_H^4 from each vacuum condensate and we notice that each correction enhances the total value of this parameter. Interestingly, the quark-gluon condensate contributes the most to the sum rule. Usually, we expect that the size of the contributions are ordered in the sense that the Wilson coefficient for the perturbative contribution is the largest among the Wilson coefficients in the power expansion and condensates contribute less with increasing mass dimension. Therefore, the OPE shows good convergence and the extracted quantities are reliable within this framework. In our case, we observe a different behaviour due to the large Wilson coefficient in front of the quark-gluon condensate. Nevertheless, we see that beyond this condensate, the contributions become increasingly smaller indicating that the OPE starts to converge. This particular behaviour is a well-known fact if correlation functions of currents with a large mass dimension are considered, because local condensates with a large mass dimension dominate for small values of the Borel parameter M. The left plot in figure 12.1 illustrates the sum of all contributions up to the condensate with mass dimension seven for different choices of the threshold parameter ω^{th}. We conclude that the value of the sum rule with fixed threshold parameter ω^{th} is stable under the variation of the Borel parameter M. Additionally, this is also emphasised by the small error bands due to the variation of ω^{th} within

its uncertainties. This observation turns out to be crucial in the study of the correlation of ω^{th} and M. In general, the determination of ω^{th} depends on the Borel parameter M, while the determination of the Borel window requires a particular choice for the threshold parameter ω^{th}. In order to obtain the optimal values for both the threshold parameter and the Borel window, it is possible to scan each value independently until the conditions for the determination of those parameters are satisfied. However, due to the small variation of ω^{th} with respect to the Borel parameter M, it is sufficient to choose one point in the parameter space spanned by ω^{th} and M such that the conditions are met. We account for the correlation by varying both ω^{th} and M within their uncertainties and take the maximal deviation as an estimate for the error induced by the Borel parameter M.
We continue to determine the optimal window for the threshold ω^{th} in two different ways, in the end it turns out that both results coincide. In the first method, we make use of the HQET decay constant $F(\mu)$ and vary this function in figure 12.2 for different values of ω^{th}. The decay constant yields reliable estimates for the particular choice 0.8 GeV $\leq \omega^{th} \leq$ 1.0 GeV due to its stable behaviour. Nevertheless, we need to prove that this window provides reasonable results. For this check, we extract the physical decay constant f_B from $F(\mu)$ within the range 0.8 GeV $\leq \omega^{th} \leq$ 1.0 GeV via relation (2.34) and provide the comparison in figure 12.3.

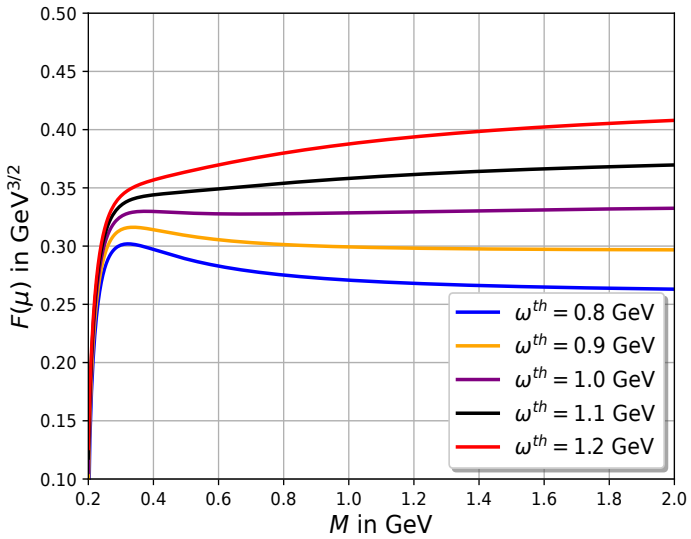

Figure 12.2: Analysis for the sum rule (11.52) for the HQET decay constant. We plot the constant for different choices for ω^{th} in order to investigate the stability of $F(\mu)$ with respect to the Borel parameter M.

According to figure 12.2, the dependence on the threshold parameter ω^{th} in the desired range is minimised if $M \geq 0.8$ GeV is chosen, since the sum rules become stable and reliable beyond this boundary. We need to keep in mind that we neglect higher order corrections in α_s to the decay constant $F(\mu)$, which are known to be large [179], especially the $\mathcal{O}(\alpha_s)$ corrections.

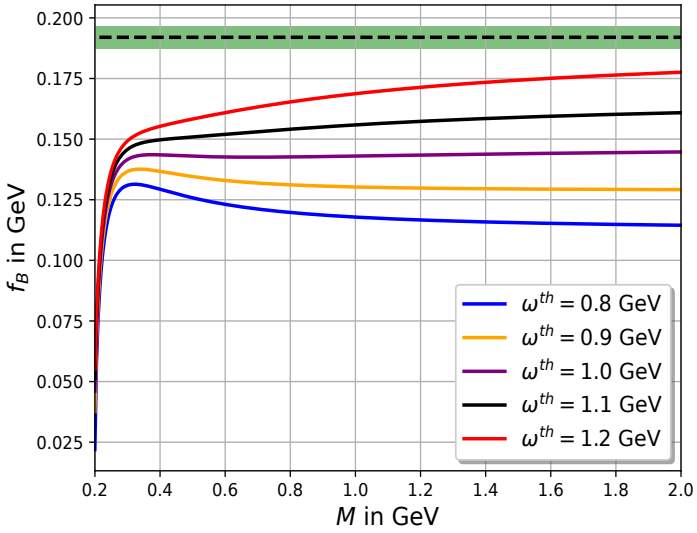

Figure 12.3: Translation of the HQET decay constant $F(\mu)$ to the physical decay constant f_B for various threshold parameters ω^{th} via Eq. (2.34). The dashed black line denotes the value for f_B from lattice QCD [200], while the green band indicates the corresponding error.

Additionally, we cut off the OPE expansion in vacuum condensates at mass dimension seven and neglect all the contributions beyond this dimension. Hence, it is appropriate to assume a conservative uncertainty of 50%. The authors in [85] discuss the impact of these corrections and conclude that the overall uncertainty on $F(\mu)$ gets reduced to $15\% - 20\%$.
The second method is more established in the literature and relies on direct manipulation of the sum rules. Here, the idea is to take the derivative of the sum rule under investigation with respect to the inverse Borel parameter $\partial/\partial(-1/M)$ and divide this new expression by the original sum rule. This provides a direct method to determine an estimate for the parameter $\bar{\Lambda}$, which can be adjusted by choosing a range for ω^{th} such that $\bar{\Lambda}$ coincides with values from the literature, i.e. the value stated in table 12.1. In the end, both methods provide the same interval 0.8 GeV $\leq \omega^{th} \leq$ 1.0 GeV.
The analysis of the sum rule in Eq. (11.49) proceeds similarly. In figure 12.4, we plot again the contribution from each vacuum condensate individually. For this particular case, the contributions from the quark, gluon and triple-gluon condensate get cancelled in the sum rule for the combination $(\lambda_H^2 + \lambda_E^2)^2$. Moreover, the quark-gluon condensate with mass dimension five gives rise to the largest contribution again. Beyond this order the size of the contributions decreases indicating the convergence of the OPE. The second plot illustrates the complete sum rule for this combination as a function of the Borel parameter M for different choices of ω^{th}. We fix this parameter by applying both methods from above and obtain again the range 0.8 GeV $\leq \omega^{th} \leq$ 1.0 GeV.

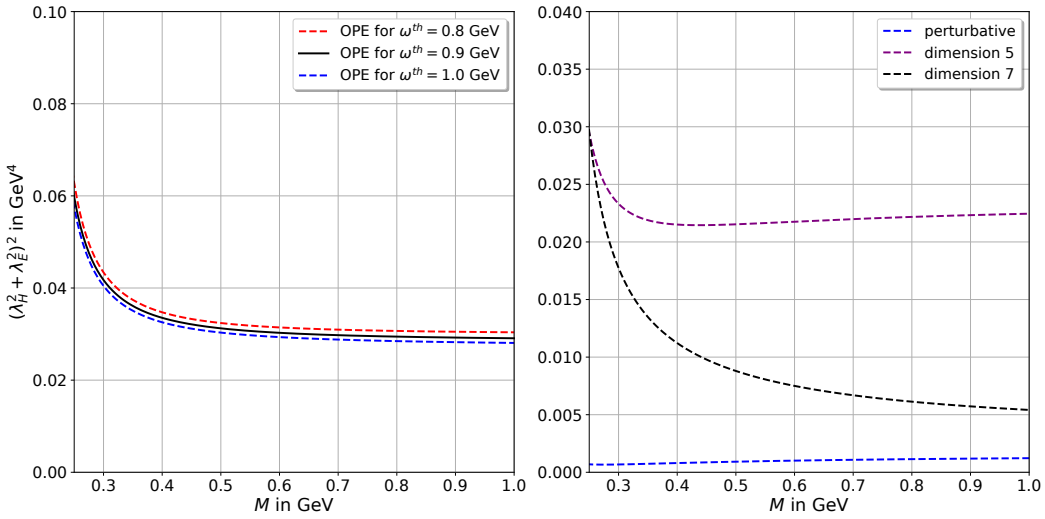

Figure 12.4: Analysis for the continuum dominated sum rule (11.49). The left plot shows the complete sum rule for different choices of ω^{th} with respect to the Borel parameter M. Contrary, the right plot illustrates each contribution individually up to the vacuum condensate of mass dimension seven and hence indicates the relative sizes of each contribution.

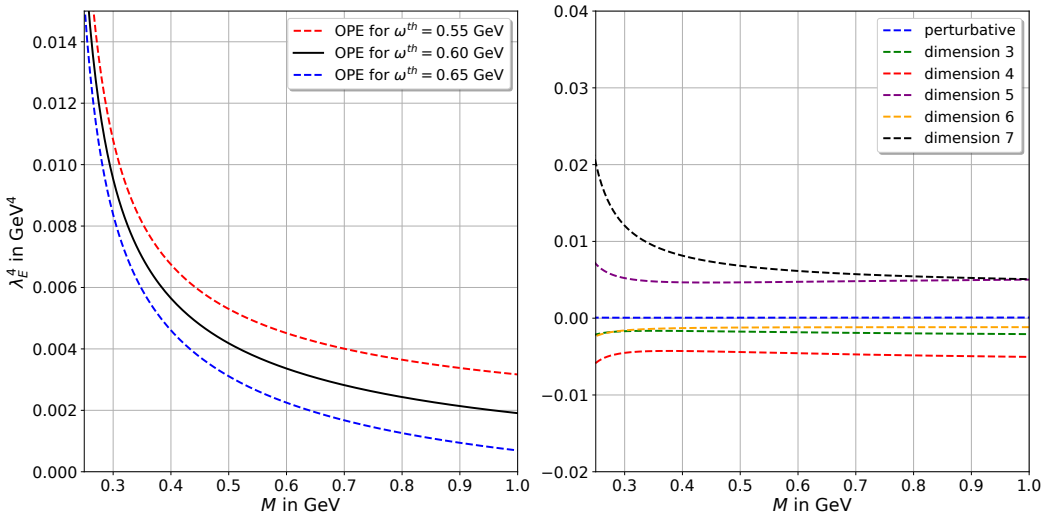

Figure 12.5: Analysis for the continuum dominated sum rule (11.51). The left plot shows the complete sum rule for different choices of ω^{th} with respect to the Borel parameter M. Due to larger deviations from the central values, this sum rule seems less stable compared to Eqs. (11.49), (11.50). The right plot illustrates each contribution individually up to the vacuum condensate of mass dimension seven and provides an explanation for the lack of convergence.

While the extraction of the threshold for the parameters λ_H^4 and $(\lambda_H^2 + \lambda_E^2)^2$ is straightforward due to the convergence of the OPE and the stability of the sum rule, we encounter several problems in the analysis of the sum rule for the parameter λ_E^4. Figure 12.5 is structured similarly to the plots for the

previous sum rules. The left panel shows the combination of all contributions up to condensates of mass dimension seven, the right panel presents each contribution individually. We notice for this particular sum rule that the quark and the gluon condensate enter with opposite signs in Eq. (11.51) compared to Eqs. (11.49) and (11.50). This leads to an unreliable and therefore unstable sum rule. Furthermore, the dominant condensate with mass dimension five is significantly reduced in comparison to the sum rules in Eqs. (11.49), (11.50) since the Wilson coefficients in Eqs. (11.41), (11.42), (11.43) vanish in this case. In addition to that the vacuum condensate with mass dimension seven seems to be another sizeable correction, hence the convergence of the OPE itself is not guaranteed. In order to ensure the convergence of the OPE, it would be necessary to include condensates of even higher mass dimension and higher order corrections in α_s to the computation of the Wilson coefficients C_X^i. Adding condensates of higher mass dimension to the OPE generates additional problems, because their values are not numerically known from lattice QCD or sum rule analyses. A possibility here is to use the vacuum saturation approximation, although the applicability and accuracy is unknown. Higher order corrections in α_s require a detailed loop integral computation similar to the evaluation in [85] for a correlation function containing a two-particle and a three particle current. Albeit this calculation requires some effort, it is nevertheless feasible.

These issues have a direct impact on the determination of the threshold interval ω^{th}. It follows that the determination via the derivative method fails and we are only left to use the decay constant $F(\mu)$ and its relation to the physical constant f_B to obtain the threshold range. Additionally, the deviation from the central values by varying the threshold ω^{th} is also enhanced compared to the sum rules in Eqs. (11.49), (11.50). This fact points towards less stable sum rules with larger uncertainties. Ultimately, we end up with a parameter range of $0.55\ \text{GeV} \leq \omega^{th} \leq 0.65\ \text{GeV}$.

Next, we investigate the determination of the optimal Borel window by using figures 12.1 to 12.5. Notice that we show all sum rules for the Borel parameter range between 0.2 and 1 GeV. The optimal window is ideally chosen in the mid-range such that the condensate contributions are not too dominant for small values of M as well as the perturbative contribution for large values of M. As it can be seen from Eqs. (11.49) to (11.51), the Borel parameter occurs with the highest power in the perturbative contribution and the condensate with mass dimension seven has no M dependence at all. This explains the behaviour which is relevant for the choice of the Borel window: For small M, the condensates tend to contribute the most, especially the condensate with mass dimension seven, while for larger M the perturbative part dominates. Hence, we fix the lower bound of the Borel window by requiring that the contribution of the condensate with the highest mass dimension, i.e. with mass dimension seven, does not exceed 40% of the total OPE. As a result, the lower bound for the sum rules (11.49) and (11.50) is set to be at $0.5\ \text{GeV} \geq M$. If we compare this choice with figures 12.1 and 12.4, we note that at this bound the sum rule becomes stable and thus reliable. But for the parameter λ_E^4 in Eq. (11.51), the sum rule is unstable and the above method

does not apply. Nevertheless, we still choose the lower bound to be at 0.5 GeV by investigating the behaviour of the sum rule depicted in figure 12.5 and reading off the bound from this plot based on its stability. We account for this rough estimation of the lower bound in the error analysis.
In order to determine the upper bound, we define a new quantity

$$R_{\text{cont.}} = 1 - \frac{\int_0^{\omega^{th}} \mathrm{d}\omega \frac{1}{\pi} \mathrm{Im}\Pi_X^{\mathrm{OPE}}(\omega) e^{-\omega/M}}{\int_0^{\infty} \mathrm{d}\omega \frac{1}{\pi} \mathrm{Im}\Pi_X^{\mathrm{OPE}}(\omega) e^{-\omega/M}} \qquad X \in \{H, E, HE\} \; . \tag{12.2}$$

The idea is that the integral in the numerator in the above Eq. (12.2) captures the duality interval of the ground state, which is an isolated pole if we choose the threshold ω^{th} properly. The integral in the denominator describes the contribution from the entire hadronic spectrum including the ground state, as well as the continuum and excited states. Thus, Eq. (12.2) measures the role of the continuum and higher resonances in the sum rules. For a reliable extraction of the parameters $\lambda_{E,H}^2$, we expect the upper bound to be $R_{cont.} \leq 50\%$ for $M \leq M_{max}$. But when we apply this criterion for the sum rules in Eqs. (11.49) to (11.51), we notice that the continuum and excited states dominate the sum rule such that $R_{cont.} \sim 96\%$. This is an expected feature for a correlation function with currents of large mass dimension, thus this method to determine the upper bound for M is not applicable.
In order to nevertheless establish the upper boundary of the Borel window, we consider combinations of $\lambda_{E,H}^2$ together with the HQET decay constant $F(\mu)$. These combinations should be chosen such that the continuum and excited states are suppressed. One possible choice for these combinations is the following:

$$\begin{aligned} \frac{(\lambda_H^2 + \lambda_E^2)^2}{\lambda_H^4} &= (1 + \mathcal{R})^2 \\ \frac{F(\mu)^2 M^4 e^{-\bar{\Lambda}/M} + \frac{1}{\pi} F(\mu)^2 \lambda_H^4 e^{-\bar{\Lambda}/M}}{F(\mu)^2 M^4 e^{-\bar{\Lambda}/M} - \frac{1}{\pi} F(\mu)^2 \lambda_E^4 e^{-\bar{\Lambda}/M}} &, \end{aligned} \tag{12.3}$$

where the quantity $\mathcal{R}$ is defined according to Eq. (12.1). We choose the first combination, because the quark-gluon condensate contribution in the sum rule for λ_H^4 (11.49) reduces the value of $R_{cont.}$ as this combination is the dominant part in the sum rule expression. The second combination is useful since it is dominated by large $\mathcal{O}(\alpha_s^0)$ contributions from $F(\mu)$ such that $\lambda_{E,H}^4$ become numerically small. This ordering gets spoiled if we introduce an additional factor of M^4 into the sum rule for $F(\mu)$ which is necessary on dimensional grounds. But we are able to restore the desired ordering by adding a suppression factor $\frac{1}{\pi}$ in front of $\lambda_{E,H}^2$. In the end, both combinations yield a continuum suppression of less than 50% ($R_{cont.} \leq 50\%$) for $M_{max} = 0.8$ GeV. The lower bound can be determined from the arguments given above and is around $M_{min} = 0.5$ GeV. Before we derive the parameters $\lambda_{E,H}^2$ from the combinations in Eq. (12.3), we present the finally adopted Borel window and the threshold range and finally plot the combinations in figure 12.6 with respect to the Borel parameter M for different thresholds ω^{th}. Here, the green shaded area denotes the Borel window and we observe that within

Sum rule	Borel window	threshold interval
Eq. (12.3)	$0.5\ \text{GeV} \leq M \leq 0.8\ \text{GeV}$	$0.8\ \text{GeV} \leq \omega^{th} \leq 1.0\ \text{GeV}$

Table 12.2: Summary of the threshold and Borel window for the combination in Eq. (12.3).

this specific window the sum rules are stable and therefore suitable for an extraction of the distribution amplitude parameters.

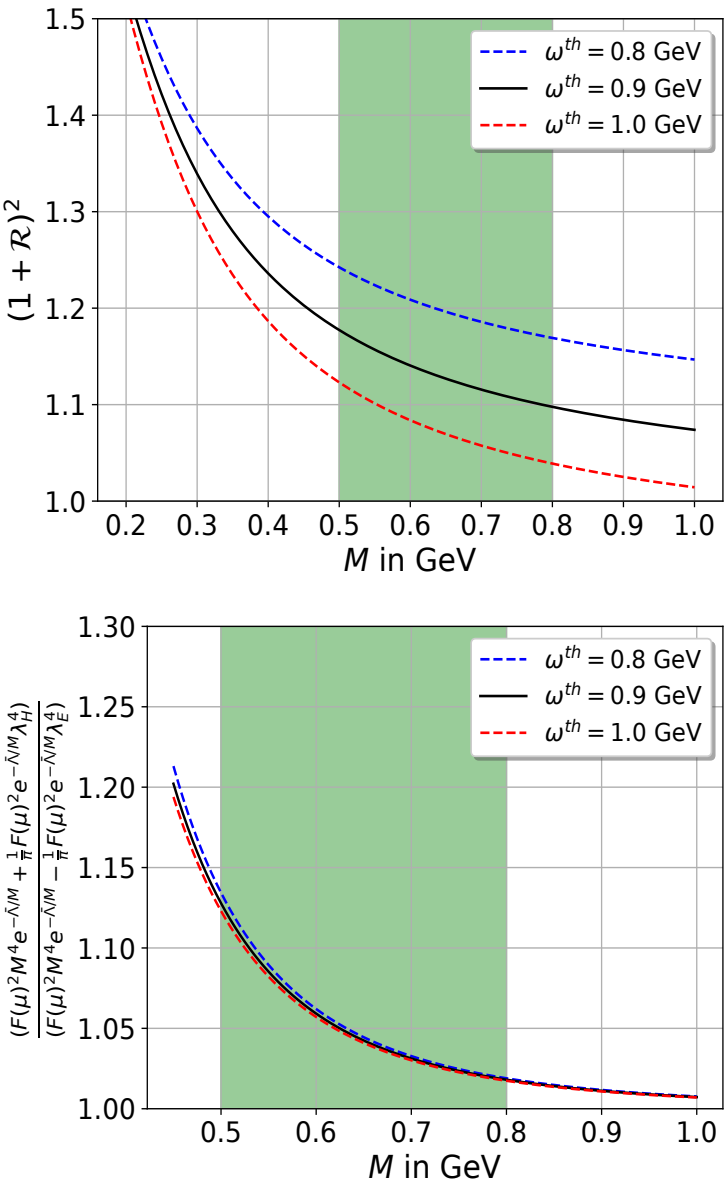

Figure 12.6: Combinations of the sum rules in Eqs. (11.49) to (11.51) chosen to suppress the continuum contributions and the excited states for different threshold parameters ω^{th}.

We are now set to determine the parameters $\lambda^2_{E,H}$ from the combinations

shown in Eq. (12.3). Notice that there are several sources for total uncertainty in the final ranges of the parameters. Apart from the intrinsic error of the OPE expansion related to the truncation of vacuum condensates beyond mass dimension seven and to the neglect of higher order terms in α_s in the Wilson coefficients in Eq. (11.25), there occur uncertainties generated by the input parameters. We account for them by varying each input parameter individually within their uncertainty and add them in the end in quadrature. Besides, there is also an error induced by the sum rule approach itself which is connected to the application of the quark-hadron duality. These intrinsic errors are in general hard to estimate, thus we assume a conservative error of $30\% - 50\%$.
In order to derive the value of the strong coupling constant $\alpha_s(1\text{ GeV}) = 0.471$ in table 12.1, we make use of the QCD scale $\Lambda^{(4)}_{QCD} = 0.31$ GeV up to two-loop order. The uncertainty is determined by varying the scale $\Lambda^{(4)}_{QCD}$ in the range $0.29\,\text{GeV} \leq \Lambda^{(4)}_{QCD} \leq 0.33\,\text{GeV}$, which results into a parameter range for α_s of $0.44 \leq \alpha_s \leq 0.50$. For the $\mathcal{R}$-ratio, we get the following estimate

$$\begin{aligned}\mathcal{R}(1\,\text{GeV}) = 0.1 &+ \begin{pmatrix} +0.03 \\ -0.03 \end{pmatrix}_{\omega_{th}} + \begin{pmatrix} +0.01 \\ -0.02 \end{pmatrix}_{M} \\ &+ \begin{pmatrix} +0.01 \\ -0.01 \end{pmatrix}_{\alpha_s} + \begin{pmatrix} +0.01 \\ -0.01 \end{pmatrix}_{\langle\bar{q}q\rangle} + \begin{pmatrix} +0.02 \\ -0.03 \end{pmatrix}_{\langle\frac{\alpha_s}{\pi}G^2\rangle} \\ &+ \begin{pmatrix} +0.05 \\ -0.04 \end{pmatrix}_{\langle\bar{q}gG\cdot\sigma q\rangle} + \begin{pmatrix} +0.02 \\ -0.02 \end{pmatrix}_{\langle g_s^3 f^{abc} G^a G^b G^c\rangle} \\ &= 0.1 \pm 0.07 \end{aligned} \tag{12.4}$$

while for λ_H^2 we obtain

$$\begin{aligned}\lambda_H^2(1\,\text{GeV}) = \Big[0.154 &+ \begin{pmatrix} +0.002 \\ -0.003 \end{pmatrix}_{\omega_{th}} + \begin{pmatrix} +0.002 \\ -0.004 \end{pmatrix}_{M} \\ &+ \begin{pmatrix} +0.001 \\ -0.001 \end{pmatrix}_{\langle\frac{\alpha_s}{\pi}G^2\rangle} + \begin{pmatrix} +0.001 \\ -0.001 \end{pmatrix}_{\langle\bar{q}gG\cdot\sigma q\rangle} \\ &+ \begin{pmatrix} +0.001 \\ -0.001 \end{pmatrix}_{\langle g_s^3 f^{abc} G^a G^b G^c\rangle} \Big]\,\text{GeV}^2 \\ &= (0.154 \pm 0.006)\,\text{GeV}^2\,. \end{aligned} \tag{12.5}$$

We do not include the uncertainties caused by α_s and the vacuum condensates of mass dimension three as well as six since they do not change the central value significantly. However, they are inserted into the final result for λ_E^2 due to their sizeable effect.

$$\begin{aligned}\lambda_E^2(1\,\text{GeV}) = \Big[0.009 &+ \begin{pmatrix} +0.004 \\ -0.005 \end{pmatrix}_{\omega_{th}} + \begin{pmatrix} +0.002 \\ -0.003 \end{pmatrix}_{M} \\ &+ \begin{pmatrix} +0.001 \\ -0.001 \end{pmatrix}_{\alpha_s} + \begin{pmatrix} +0.003 \\ -0.003 \end{pmatrix}_{\langle\bar{q}q\rangle} \\ &+ \begin{pmatrix} +0.003 \\ -0.004 \end{pmatrix}_{\langle\frac{\alpha_s}{\pi}G^2\rangle} + \begin{pmatrix} +0.007 \\ -0.006 \end{pmatrix}_{\langle\bar{q}gG\cdot\sigma q\rangle} \end{aligned}$$

$$+ \left(\begin{array}{c} +0.002 \\ -0.002 \end{array} \right)_{\langle g_s^3 f^{abc} G^a G^b G^c \rangle} \Big] \, \mathrm{GeV}^2$$
$$= (0.009 \pm 0.009) \, \mathrm{GeV}^2 \, . \tag{12.6}$$

There are several comments on the error analysis in Eqs. (12.4), (12.5) and (12.6) in order. First, there generally exists a correlation between the threshold parameter ω^{th} and the Borel parameter M, especially in the uncertainty estimation. As have previously discussed, we follow two different paths for the determination of the threshold, i.e. the derivative method and the method via the HQET decay constant. In the derivative method, we obtain the low-energy parameter $\bar{\Lambda}$ as a function of ω^{th} and fix the threshold parameter such that we are able to reproduce the value of $\bar{\Lambda}$ from table 12.1. This value naturally introduces an error which we use to determine the error on ω^{th}. Hence, this method provides a more rigorous uncertainty estimate than the method via the HQET decay constant, where the errors are introduced by estimating the effects of higher order corrections in α_s to $F(\mu)$ in order to compare this constant to the value of the physical decay constant f_B known from lattice QCD [200]. At this point, it is already necessary to choose the Borel parameter M to fix ω^{th}. But since the variation of ω^{th} with respect to M is negligible, we can argue that it is sufficient to choose one point in the parameter space of both parameters, i.e. set M to a value which is supposed to be in the mid range such that neither the condensate contributions for small M or the continuum and excited states for large M dominate. The variation of ω^{th} with respect to M usually provides a guidance for the first choice of M based on the stability of the sum rule. After fixing ω^{th}, we can determine the Borel window by the arguments from above. If the benchmark value for M to set ω^{th} lies within this window, this choice is justified a posteriori. In order to consider the uncertainties of these parameters, we vary the parameters within their errors and choose the maximal possible deviation from the sum rule from the central values. Thus, we account for the correlation between these parameters, as we described above in more detail.

Notice that the diagonal structure of the correlation function allows us to state an upper bound for $\lambda^2_{E,H}$ due to the positive definiteness of the spectral density. The idea is to perform the limit $\omega^{th} \to \infty$ in Eqs. (11.49) to (11.51) and consequently include all contributions, in particular the continuum and higher excited states. This leads to an upper bound on these parameters similarly to the f_D and f_{D_s} decay constants [201]. The uncertainties on these bounds are determined by varying the input parameters within their range in table 12.1 and add them in quadrature. Note that the intrinsic error due to the QHD approximation in the sum rule approach does not appear in this case.

$$\lambda^2_H < 0.48^{+0.17}_{-0.24} \ \mathrm{GeV}^2 \, , \tag{12.7}$$
$$\lambda^2_E < 0.41^{+0.19}_{-0.24} \ \mathrm{GeV}^2 \, . \tag{12.8}$$

When we now finally extract $\lambda^2_{E,H}$ at $\mu = 1$ GeV, these estimates are expected to lie below the bounds stated in Eqs. (12.7), (12.8). We add the uncertain-

ties from neglecting higher order corrections as well as from the sum rule approach itself to the uncertainties originating from the input parameters in Eqs. (12.4), (12.5) and (12.6) in order to obtain the final numbers with a conservative error estimate.

$$\lambda_E^2(1\text{ GeV}) = (0.01 \pm 0.01)\text{ GeV}^2\,, \tag{12.9}$$
$$\lambda_H^2(1\text{ GeV}) = (0.15 \pm 0.05)\text{ GeV}^2\,, \tag{12.10}$$
$$\mathcal{R} = 0.1 \pm 0.1\,. \tag{12.11}$$

Interestingly, we note that if we directly consider Eqs. (11.49), (11.50) and take the Borel window and the threshold parameter ω^{th} as shown in table 12.2, we obtain the values:

$$\lambda_E^2(1\text{ GeV}) = (0.05 \pm 0.03)\text{ GeV}^2\,, \tag{12.12}$$
$$\lambda_H^2(1\text{ GeV}) = (0.16 \pm 0.05)\text{ GeV}^2\,, \tag{12.13}$$
$$\mathcal{R} = 0.3 \pm 0.2\,. \tag{12.14}$$

An extraction for λ_E^2 is in general possible if we make use of (11.51) with the threshold window $0.55\text{ GeV} \leq \omega^{th} \leq 0.65\text{ GeV}$ depicted in figure 12.5, although we expect this value to be not reliable due to the stability issues in this sum rule. Thus, we observe that the values in Eqs. (12.12) to (12.14), which are dominated by the continuum contributions and excited states in our chosen Borel window from table 12.2, agree with the parameters in Eqs. (12.9) to (12.11) within their uncertainties. In particular the parameter λ_H^2 matches nearly perfectly, which indicates the stability and reliability of the sum rule, even in the presence of dominating effects from the continuum. However, the value for λ_E^2 changes significantly, which is expected since the convergence of the OPE is not guaranteed and the sum rule in Eq. (11.51) is rather unstable with respect to the variation of the Borel parameter and threshold parameter ω^{th}. This is in general reflected in the determination of ω^{th}, where we observe that the methods are not immediately applicable as for the other sum rules. Nevertheless, all estimates stated above lie below the upper bounds in Eqs. (12.7), (12.8).
In table 12.3, we compare our results with all currently known values.

Parameters	[84]	[85]	this work ([177])
$\mathcal{R}(1\text{ GeV})$	(0.6 ± 0.4)	(0.5 ± 0.4)	(0.1 ± 0.1)
$\lambda_H^2(1\text{ GeV})$	$(0.18 \pm 0.07)\text{ GeV}^2$	$(0.06 \pm 0.03)\text{ GeV}^2$	$(0.15 \pm 0.05)\text{ GeV}^2$
$\lambda_E^2(1\text{ GeV})$	$(0.11 \pm 0.06)\text{ GeV}^2$	$(0.03 \pm 0.02)\text{ GeV}^2$	$(0.01 \pm 0.01)\text{ GeV}^2$

Table 12.3: Comparison of our results for the parameters $\lambda_{E,H}^2$ and $\mathcal{R}$ at $\mu = 1\text{ GeV}$.

We are now able to explain the deviation between the works [84] and [85]. One reason surely lies in the sum rule for the HQET decay constant $F(\mu)$ in Eq. (11.52). While [84] includes only $\mathcal{O}(\alpha_s)$ contributions, which is indeed

justified since the OPE itself shows good convergence, [85] also add $\mathcal{O}(\alpha_s)$ corrections to obtain a consistent $\mathcal{O}(\alpha_s)$ extraction of the parameters $\lambda^2_{E,H}$. But these additional $\mathcal{O}(\alpha_s)$ contributions turn out to be large, especially for the perturbative Wilson coefficient [179]. This fact already explains a factor of two deviation between the two analyses. Furthermore, the authors of [85] add $\mathcal{O}(\alpha_s)$ corrections to the quark-gluon condensate, add the corresponding triple-gluon condensate with $\mathcal{O}(\alpha_s)$ accuracy to prove the convergence of the OPE and resum their result in the end. These steps finally lead to the deviation which we observe.

Turning to our results, we first note that the central value for λ^2_H is in the ballpark of [84], but does not agree with [85] within the errors. Due to the fact that the continuum dominated result in Eq. (12.13) agrees with the modified value (12.10) and due to the convergence of the OPE, we conclude that this value is an reliable estimate. Based on these observations, we do not expect that the inclusion of $\mathcal{O}(\alpha_s)$ corrections to the Wilson coefficients or the inclusion of vacuum condensates with higher mass dimension change the final value significantly.

This observation certainly does not apply to the parameter λ^2_E. The values from the continuum dominated sum rule in Eq. (12.12) and the modified sum rules in Eq. (12.9) differ significantly, which follows from the instability of the sum rule and the lack of convergence of the OPE, see figure 12.5. Our extracted estimate largely deviates from previous extractions and has a large uncertainty. It is clear that further studies of this parameter using a correlation function with two three-particle currents is necessary in order to check the convergence of the OPE in general, but also to remove the large uncertainty. Here, we expect that the value starts to approach the values in [84] and [85]. This will also alter the value of $\mathcal{R}$-ratio towards the other values stated in table 12.3.

Chapter 13

Conclusion

The decay of B mesons into light mesons can be described within the QCD factorisation approach. This factorisation introduces B-meson distribution amplitudes as well as distribution amplitudes for the two light mesons, which capture the long-distance effects of the underlying process. While the properties of light meson distribution amplitudes are in general quite well known, the properties for B-meson distribution amplitudes are less well known, especially beyond leading power in the $1/m_b$-expansion. The HQET parameters $\lambda^2_{E,H}$ are important quantities in the description of the B-meson distribution amplitude since they are for instance used in the normalisation of B-meson three-particle distribution amplitude. These parameters have been studied in previous works [84, 85]. Albeit they both use the same off-diagonal correlation function, which consists of one three-particle and one two-particle current, their final results differ by roughly a factor of three, although the ratio $\mathcal{R} = \lambda^2_E/\lambda^2_H$ is nearly equal. The work [84] performs a leading order analysis in α_s up to vacuum condensates of mass dimension five, while the discussion in [85] includes condensates up to mass dimension six and a rigorous treatment of all $\mathcal{O}(\alpha_s)$ contributions. In particular, this includes loop corrections for the quark-gluon condensate as well as the $\mathcal{O}(\alpha_s)$ corrections for the HQET decay constant $F(\mu)$.
In order to resolve this tension, we have investigated alternative QCD sum rules, which are based on a diagonal correlation function including two three-particle currents. The advantage of this approach is that the sum rules are positive definite, thus we expect that the quark-hadron duality holds much better than for an off-diagonal correlation function. In our evaluation, we have considered all vacuum condensates up to mass dimension seven to leading order in α_s. For consistency, we have also worked with the leading order expression for the HQET decay constant $F(\mu)$. However, we have noticed that the sum rules are dominated by continuum contributions and excited states, hence we have constructed combinations of our sum rules to guarantee that the ground state becomes the dominant contribution in the Borel parameter range which we apply for our analysis.
We have observed that the two sum rules in Eqs. (11.49) and (11.50) show good convergence, since the contributions beyond the vacuum condensate of mass dimension five become smaller indicating the convergence of the OPE.

But this is not the case for the sum rule in Eq. (11.51), because the contributions from the quark-gluon condensate and condensate of mass dimension seven are still sizeable. The combination of sum rules in Eq. (12.3) shows good convergence and allows for the extraction of the parameters $\lambda^2_{E,H}$, which are more reliable due to the suppression of the continuum and excited state contributions.

Our final results are listed in table 12.3. The parameter λ^2_H is in good agreement with the original work [84], but the parameter λ^2_E differs from the previous analysis, which illustrates that the sum rules are not reliable due to the lack of convergence of the OPE. Interestingly, we found that the original sum rules from Eqs. (11.49) to (11.51), which are still dominated by contributions from the hadronic spectrum, yield a similar value for $\lambda^2_{E,H}$.

As future improvements, one might include $\mathcal{O}(\alpha_s^2)$-contributions into the analysis to obtain even more accurate results. Moreover, the inclusion of vacuum condensates of even higher mass dimension into the OPE is also desirable, especially for the sum rules for λ^2_E, where the convergence of the OPE is not clear and therefore the result not fully reliable. However, one encounters different problems at this point, for instance the values of the vacuum condensates with high mass dimension are not known. Usually, one applies the vacuum saturation approximation at this stage and relates these condensates to a product of lower dimensional condensates for which the values are known. But there exists no reliable estimate regarding the applicability of the vacuum saturation approximation. Although the computation becomes more accurate by including $\mathcal{O}(\alpha_s^2)$ corrections, we are not able to reduce the intrinsic uncertainties of the sum rule approach itself. Nevertheless, we expect that these corrections will improve the convergence of the OPE for the parameter λ^2_E such that the extracted value will move towards the values from [84, 85]. A similar effect on the $\mathcal{R}$-ratio is also expected.

Project III:

B-meson decay into a proton and dark antibaryon from QCD light-cone sum rules

This project led to the publications [202, 203].

Chapter 14

Introductory Remarks

14.1 Light-cone sum rules: Overview

In the QCD sum rule approach described in section 11.2, the OPE is used to treat a correlation function with two local operators at different points in position space in the limit $x \to 0$. Within this framework, short- and long-distance physics are disentangled such that high-energy effects are then encoded in perturbatively calculable Wilson coefficients and non-perturbative effects are parameterised by local vacuum matrix elements of increasing mass dimension.
Light-cone sum rules (LCSRs) [54, 55] can be viewed as an extension of the QCD SR approach in a sense that the QCD SR method is merged with the physics of hard-exclusive processes. Instead of considering correlation functions with vacuum initial and final states, we now examine transitions between a hadronic initial state to the vacuum final state. Thus, the correlation functions are now typically of the form

$$\Pi_{KL}(q^2) = i \int \mathrm{d}^d x \, e^{iqx} \, \langle 0| \, T\{j_K(x) j_L(0)\} \, |M\rangle \ . \tag{14.1}$$

In this context, the initial state $|M\rangle$ might stand for a light meson like pions, a heavy meson like the B-meson or even a baryon like a proton or neutron. In our case, we are particularly interested in a proton as the initial state. To explain the light-cone dominance, we contract for simplicity the open indices K, L in the correlation function by multiplying the metric tensor g^{KL}. But this depends on the particular choice of the Lorentz structure of the currents in the correlation function. Moreover, we assume only light quark content inside the currents $j_{K,L}$ in order to drop dependencies on the quark masses [204]. From Eq. (14.1), we can identify the correlation function as a purely x-dependent piece

$$\Pi(x^2) \equiv i \, \langle 0| \, T\{j_K(x) j^K(0)\} \, |M\rangle \ . \tag{14.2}$$

In general, the exponential factor e^{iqx} in Eq. (14.1) acts as a cutoff due to its oscillating behaviour and thus determines essentially the size of the dominating contribution inside $\Pi(x^2)$ to good approximation as a function

of q^2. After Fourier transforming $\Pi(x^2)$

$$\Pi(x^2) = \int \mathrm{d}\omega \; e^{i\omega x^2} \Pi(\omega) \tag{14.3}$$

we can rewrite Eq. (14.1)

$$\Pi(q^2) = \int \mathrm{d}^d x \, e^{iqx} \int \mathrm{d}\omega \, e^{i\omega x^2} \, \Pi(\omega) = \int \mathrm{d}\omega \, \Pi(\omega) \int \mathrm{d}^d x \, e^{i(qx+\omega x^2)} \,. \tag{14.4}$$

Completing the square and redefining $y := x + q/(2\omega)$, we end up with

$$\Pi(q^2) = \int \mathrm{d}^d x \int \mathrm{d}\omega e^{i\omega x^2} e^{iQ^2/(4\omega)} \Pi(\omega) \tag{14.5}$$

with $Q^2 \equiv -q^2$. Since the measure in Eq. (14.5) is invariant under constant shifts, we can immediately switch back from y to x in the integration measure. We observe for large ω that at least one of the integrands $|\omega x^2|$ or $|Q^2/(4\omega)|$ strongly oscillates and hence suppresses the contribution to the integral. Therefore, we obtain only sizeable contributions to Eq. (14.1) if two conditions are satisfied simultaneously:

$$|\omega x^2| \leq 1 \,, \qquad\qquad \frac{Q^2}{4|\omega|} \leq 1 \,. \tag{14.6}$$

This leads to the final constraint

$$|x^2| \leq \frac{4}{Q^2} \,. \tag{14.7}$$

For large $Q^2 \to \infty$, we work in the domain of small $|x^2| \to 0$, i.e. near the light-cone. Moreover, in the limit $x^2 \to 0$, or more general in the region of small x^2, it is possible to rewrite the time-ordered product of Eq. (14.1) in terms of an expansion in bilocal operators

$$T\{j_K(x) j_L(0)\} = \sum_t C_t(x^2) \mathcal{O}_t(x, 0) \,. \tag{14.8}$$

This is exactly in the spirit of the OPE expression which we have encountered during the discussion of QCD SRs in section 11.2. Notice that in the discussion in section 11.2 the argumentation from above is also possible, in particular the region near the light-cone $x^2 \sim 0$ is also dominating in this method. The difference lies in the correlation function under consideration as well as in the general structure of the OPE. While the QCD SR approach uses vacuum matrix elements and the OPE encodes the long-distance effects in terms of local composite operators, which are then parameterised in form of vacuum condensates of increasing mass dimension, the LCSR approach makes use of more complicated transitions between a hadronic initial state and the vacuum. In addition to that the low-energy physics is described by matrix elements of bilocal operators $\mathcal{O}_t(x, 0)$, as follows from substituting Eq. (14.8) into (14.2). Furthermore, the ordering parameter is now twist

instead of the mass dimension of the operators.
In general, the expansion in Eq. (14.8) works since the short-distance physics is encoded in the Wilson coefficients $C_t(x^2)$ for large Q^2 and asymptotic freedom guarantees that perturbation theory can be applied for the determination of those coefficients. Additionally, it is possible to truncate Eq. (14.8) in the limit $x^2 \to 0$ at sufficiently large twists to obtain a reasonable accuracy, similar to the OPE in the QCD sum rule approach. But as it has been seen for instance in the determination of the parameter λ_E^2 in chapter 12, this might become tricky since the convergence of the OPE is not obvious at first sight. This makes it necessary to include higher twist contributions into the analysis in order to extract reasonable and reliable results.
The direct physical connection of twist to a conformal partial wave expansion makes it apparent to parameterise the matrix elements of bilocal operators $\mathcal{O}_t(x, 0)$ in terms of distribution amplitudes of increasing twist. As it has been stressed before, this is one of the major differences between the light-cone sum rule approach and the QCD sum rule approach. In section 2.3, we have already introduced the B-meson distribution amplitudes, which describe the transition between an initial B-meson to a vacuum state. For the following discussion, which belongs to the domain of new physics scenarios, we encounter three particle distribution amplitudes with a proton in the initial state. Details on the parameterisation of these objects and their connection to the definite twist amplitudes are provided in appendix E. Before we elaborate more on computational steps, we first introduce the main aspects of the underlying model and emphasise the particular importance of the channel $B \to p +$ missing energy in a very brief manner.

14.2 B-Mesogenesis model

In the following sections, we investigate two different versions of the B-Mesogenesis model. This model has been proposed in [205–207] and provides, besides the explanation of the relic dark matter abundance in the universe, the explanation for observed matter-antimatter asymmetry in the universe

$$Y_B \equiv (n_{\mathcal{B}} - n_{\bar{\mathcal{B}}})/s = (8.718 \pm 0.004) \cdot 10^{-11} \,, \tag{14.9}$$

which can be deduced from measurement of the Cosmic Microwave Background (CMB) [208, 209] and Big Bang Nucleosynthesis (BBN) [210, 211]. But in order to guarantee the existence of this asymmetry in Eq. (14.9), the three Sakharov conditions [212] have to be satisfied:

- Processes that violate baryon number symmetry appear in the universe;
- C and CP - violation appear in the universe;
- universe is in departure from thermal equilibrium.

In other words, one consequence of the departure from thermal equilibrium is the violation of the discrete time reversal symmetry (T-symmetry) such that the combined discrete symmetry CPT is conserved, as it is supposed to

be for every Poincare invariant theory. In this model, the main mechanism relies on these three conditions. First, we start with a heavy scalar particle Φ with a mass $M_\Phi > 11$ GeV which decays at a temperature of $T_R \sim 15$ MeV, at which the universe is in a non-equilibrium state, into $b\bar{b}$-pairs. Due to the low temperature involved in this mechanism, we observe to a large amount the hadronisation of these quasi-free particles to bound states in form of mesons and anti-mesons, in particular to bound states like the $B^{\pm}$-, $B^0_{d,s}$- and $\bar{B}^0_{d,s}$-mesons. From the SM we know that there occur oscillations in the neutral $B^0_{d,s} - \bar{B}^0_{d,s}$-systems as typical examples for CP-violating effects [211], which are known to be sizeable for B-meson systems. These observations can be parameterised in terms of the observable A^q_{SL} [206]

$$A^q_{\mathrm{SL}} = \frac{\Gamma(\bar{B}^0_q \to B^0_q \to f) - \Gamma(B^0_q \to \bar{B}^0_q \to \bar{f})}{\Gamma(\bar{B}^0_q \to B^0_q \to f) + \Gamma(B^0_q \to \bar{B}^0_q \to \bar{f})}\,, \tag{14.10}$$

which can also be expressed in terms of the physical mass and width differences $\Delta M^q = 2|M^q_{12}|$ as well as $\Delta\Gamma^q = 2|\Gamma^q_{12}|\cos\phi^q_{12}$

$$A^q_{\mathrm{SL}} = -\left|\frac{\Gamma^q_{12}}{M^q_{12}}\right| \sin(\phi^q_{12})\,. \tag{14.11}$$

Here, ϕ^q_{12} denotes the relative phase between M^q_{12} and Γ^q_{12}. Such CP-violating effects trigger various decays with a mixing between the dark sector and the SM sector [205–207]. Of particular interest in the following work is the decay of a B-meson into a SM baryon $\mathcal{B}$ and a dark matter particle Ψ, $B \to \mathcal{B}\Psi$, but decays into additional mesons in the final states are also possible. The introduction of the dark matter particle Ψ has an impact on the baryon number conservation. By considering each sector individually, we observe baryon number violation, which yields the matter-antimatter asymmetry, but in combination with the dark sector, which interacts only via gravity or via a heavy scalar mediator boson Y with the SM, we see that the total baryon number of the universe is conserved if we assign the particle Ψ a baryon number of -1. Notice that it is crucial for this model that we work at low reheating temperature $T_R = 15$ MeV such that it is possible to obtain distinctive experimental signatures in experiments like Belle-II [205, 206].
In the minimal version of this model, it is necessary to introduce two additional particles, a SM singlet scalar anti-baryon ϕ and a SM singlet Majorana fermion ξ. The dark matter particle Ψ has a mass of the order of a few GeV and decays into these additional particles $\Psi \to \phi\,\xi$. Without this restriction, the particle Ψ would just decay into light anti-baryons such that the conserved baryon number symmetry would be violated again. Furthermore, we assume the existence of a Z_2-symmetry which stabilises the ϕ and ξ particles such that further decays via proton or electron exchange are not allowed and forbidden by kinematics. The corresponding interaction is then given by a renormalisable Yukawa type interaction, i.e.

$$\mathcal{L} \in -y_d \bar{\Psi}\phi\xi + \mathrm{h.c.}\,. \tag{14.12}$$

Besides these particles, we need to claim the existence of another boson, namely a colour-triplet scalar particle Y serving as the mediator for the interaction with the dark sector. Since the mediator boson is supposed to interact

with SM quarks, we require it to be a colour triplet. Furthermore, this boson is a singlet under the weak isospin symmetry $SU(2)_L$, thus it does not distinguish between left- and right-handed particles. But for the hypercharge, we see that the model allows for two possibilities, i.e. $Q_Y = \{-1/3, 2/3\}$. We focus in the following on the model with $Q_Y = -1/3$ and refer to [205–207] for more details on the other version of this model. Nevertheless, the general approach and the computational methods elaborated in this thesis can be also applied to the second model after a few modifications. With this particle content, we have built the minimal realisation of the B-Mesogenesis model. In table 14.1, we summarise all additional particles together with their quantum numbers:

Field	Spin	Q_{EM}	B	colour	Z_2	mass
Φ	0	0	0	3	+1	$11 - 100$ GeV
Y	0	$-\frac{1}{3}$	$-\frac{2}{3}$	3	+1	$\mathcal{O}$(TeV)
Ψ	$\frac{1}{2}$	0	-1	1	+1	$\mathcal{O}$(GeV)
ξ	$\frac{1}{2}$	0	0	1	-1	$\mathcal{O}$(GeV)
ϕ	0	0	-1	1	-1	$\mathcal{O}$(GeV)

Table 14.1: Quantum numbers of minimal realisation of the B-Mesogenesis model with hypercharge $Q_Y = -1/3$. In general, the model also allows for the hypercharge $Q_Y = 2/3$, which we disregard in this work.

Although this model exhibits a rich phenomenology, we restrict ourselves in this work to the decay mode $B \to p\Psi$, because the application of the LCSR approach is straightforward and comparable to previous works for $\Lambda_b \to p$ form factors [213]. Moreover, the nucleon DAs have been studied in a detailed fashion [116–118, 214] and the parameters in the conformal expansion are known from QCD sum rule [116, 117], from model consideration [214], from light-cone sum rules [116, 215] or lattice calculations [119]. The overall goal is to provide the fundamental framework to treat two-particle decays like $B \to p\Psi$ such that this framework can be extended in a similar manner to the other phenomenological interesting cases, which has been done in Ref. [216] to leading twist approximation. The Lagrangian in our specific case takes the form

$$\begin{aligned}\mathcal{L}_{(Q_Y=-1/3)} = &- y_{ud}\epsilon_{ijk}Y^{*i}\bar{u}_R^j d_R^{ck} - y_{ub}\epsilon_{ijk}Y^{*i}\bar{u}_R^j b_R^{ck} - y_{\Psi d}Y_i\bar{\Psi}d_R^{ci} - y_{\Psi b}Y_i\bar{\Psi}b_R^{ci} \\ &+ \text{h.c.}\,,\end{aligned} \tag{14.13}$$

where the $y_{ud}, y_{\Psi d}$ and $y_{ub}, y_{\Psi b}$ are the (antisymmetric) Yukawa couplings between the dark sector and the SM sector. The c-notation denotes charge-conjugated fields such that fields q^c ($\bar{q}^c$) have the quantum numbers of an (anti)particle. Furthermore, the index R represents right-handed $SU(2)_L$-singlet Weyl fields, which can be obtained from ordinary Dirac fields with

the projection operator $P_R = \frac{1+\gamma_5}{2}$. Since the scalar field Y is a singlet under the $SU(2)_L$ symmetry, it only couples to right-handed SM particles. The Latin indices i, j, k correspond to colour indices running between one to three, so we can additionally check that the Lagrangian in Eq. (14.13) is indeed gauge-invariant under the $SU(3)_c$ transformation. In the first two terms, all fields belong to the anti-fundamental representation $\bar{\mathbf{3}}$ of the colour $SU(3)$, thus we observe an antisymmetric combination of three $\bar{\mathbf{3}}$-fields which is gauge invariant. The last two terms are gauge singlet under $SU(3)_c$, because we combine a charge-conjugated quark field in the $\bar{\mathbf{3}}$-representation with a Y-boson which is a $\mathbf{3}$-field [205].
During our calculation, we will perform an additional simplification by exploiting that the mass of the Y-boson is of the order of a few TeV (see table 14.1).

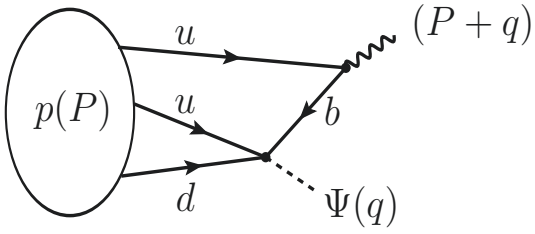

Figure 14.1: Diagram for the $p \to B$ transition, which differs from the $B \to p$ transition relevant for the $B \to p\Psi$ decay by an unobservable global phase. The mediator particle Y has been integrated out such that we obtain an effective four-fermion interaction.

Hence, we can integrate out the mediator Y and obtain an effective interaction. The spin-0 propagator is expanded for large masses M_Y similar to Fermi's theory

$$\frac{i}{k^2 - M_Y^2} = -\frac{i}{M_Y^2} \cdot \left(1 + \frac{k^2}{M_Y^2} + ...\right) \approx -\frac{i}{M_Y^2} \tag{14.14}$$

and we get as a result a four-fermion interaction between the SM quarks and the fermionic dark anti-baryon Ψ depicted in figure 14.1. We can derive the corresponding effective Lagrangian

$$\begin{aligned}\mathcal{L}_{(Q_Y=-1/3)} =& \frac{y_{ub} y_{\Psi d}}{M_Y^2} i\epsilon_{ijk} \left(\bar{\Psi} d_R^{ci}\right) \left(\bar{u}_R^j b_R^{ck}\right) + \frac{y_{ub}^* y_{\Psi d}^*}{M_Y^2} i\epsilon_{ijk} \left(\bar{b}_R^{ci} u_R^j\right) \left(\bar{d}_R^{ck} \Psi\right) \\ &+ \{d \leftrightarrow b\}\end{aligned} \tag{14.15}$$

and therefore the effective Hamiltonian is given by

$$\begin{aligned}\mathcal{H}_{(Q_Y=-1/3)} =& -\frac{y_{ub} y_{\Psi d}}{M_Y^2} i\epsilon_{ijk} \left(\bar{\Psi} d_R^{ci}\right) \left(\bar{u}_R^j b_R^{ck}\right) - \frac{y_{ub}^* y_{\Psi d}^*}{M_Y^2} i\epsilon_{ijk} \left(\bar{b}_R^{ci} u_R^j\right) \left(\bar{d}_R^{ck} \Psi\right) \\ &+ \{d \leftrightarrow b\}\,.\end{aligned} \tag{14.16}$$

Note that it is in principle possible to consider more complicated Dirac structures in (14.15), but after performing Fierz transformations [82], they can be

reduced to the bilinear form above [206].
In order to derive the expressions for the effective operators of the underlying four-fermion interaction, we attach the charge conjugation matrix to the field Ψ by performing an additional Fierz transformation [82]. For this transformation, we use

$$\bar{\Psi} d_R^c = \bar{d}_R \Psi^c, \quad \bar{d}_R^c \Psi = \bar{\Psi}^c d_R \,, \tag{14.17}$$

and factorise the field Ψ from the effective Hamiltonian:

$$\mathcal{H}_{(Q_Y=-1/3)} = - G_{(d)} \bar{\mathcal{O}}_{(d)} \Psi^c - G^*_{(d)} \bar{\Psi}^c \mathcal{O}_{(d)} + \{d \leftrightarrow b\} \,. \tag{14.18}$$

For brevity, we introduce the effective four-fermion coupling $G_{(d)} = \frac{y_{ub} y_{\Psi d}}{M_Y^2}$, which consists of the antisymmetric Yukawa-type couplings y_{ub} and $y_{\Psi d}$ from Eq. (14.13), and define in Eq. (14.18) the following local three-quark operator and its conjugate

$$\bar{\mathcal{O}}_{(d)} = i\epsilon_{ijk} \left(\bar{u}_R^i b_R^{c\,j}\right) \bar{d}_R^k, \quad \mathcal{O}_{(d)} = i\epsilon_{ijk} d_R^i \left(\bar{b}_R^{c\,j} u_R^k\right) \tag{14.19}$$

The coupling $G_{(d)}$ is one of the input parameters which need to be determined from experiment and its choice is discussed in chapter 16. The index (d) in the relations in Eqs. (14.18) and (14.19) denotes that we consider the coupling of the d-quark to ΨY. Another possibility in this context is the coupling of the b-quark to ΨY, which we indicate with the index (b). Notice that it is possible to obtain the equations for the (b)-type version by replacing in above equations $(d) \leftrightarrow (b)$. This introduces the effective coupling $G_{(b)} = (y_{ud} y_{\Psi b})/M_Y^2$ and the three-quark operators

$$\bar{\mathcal{O}}_{(b)} = i\epsilon_{ijk} \left(\bar{u}_R^i d_R^{c\,j}\right) \bar{b}_R^k, \quad \mathcal{O}_{(b)} = i\epsilon_{ijk} b_R^i \left(\bar{d}_R^{c\,j} u_R^k\right) \,. \tag{14.20}$$

These operators (14.19), (14.20) play a crucial role in our framework, since they enter the correlation function for the determination of the $B \to p\Psi$ decay. As for the QCD SR approach, the correlation function is the fundamental object for the LCSR method as well. In the following, we treat the operators in Eqs. (14.19) and (14.20) as two different versions of the B-Mesogenesis model, indicated by the indices (d) and (b) respectively. In comparison to [206], they correspond to the "type 2" and "type 1" operators introduced therein.

14.3 Form factor decomposition

The central element in our analysis is the following correlation function

$$\Pi^{(d)}(P,q) = i \int \mathrm{d}^4x \; e^{i(P+q)\cdot x} \, \langle 0| \, T\left\{ j_B(x), \mathcal{O}_{(d)}(0) \right\} |p(P)\rangle \tag{14.21}$$

with $j_B(x)$ denoting the B-meson current $j_B(x) = i m_b \bar{b}(x) \gamma_5 u(x)$ and with $\mathcal{O}_{(d)}$ corresponding to the three-quark operator in Eq. (14.19), which enters the four-fermion interaction in (14.16) including the new hypothetical

fermionic dark matter particle Ψ. In the second version of the B-Mesogenesis model, the operator $\mathcal{O}_{(d)}$ needs to be replaced by $\mathcal{O}_{(b)}$ from Eq. (14.20).
This correlation function (14.21) can be decomposed into different kinematical structures according to all possible Lorentz-invariant amplitudes $\Pi_{R,L}, \widetilde{\Pi}_{R,L}$:

$$\begin{aligned}\Pi^{(d)}(P,q) = \Pi_R^{(d)}((P+q)^2,q^2)u_{p,R}(P) + \Pi_L^{(d)}((P+q)^2,q^2)u_{p,L}(P) \\ +\widetilde{\Pi}_R^{(d)}((P+q)^2,q^2)\not{q}u_{p,R}(P) + \widetilde{\Pi}_L^{(d)}((P+q)^2,q^2)\not{q}u_{p,L}(P)\,. \quad (14.22)\end{aligned}$$

The Dirac spinors $u_{p,\{R,L\}}(P)$ are the right-handed and left-handed components of the Dirac spinor $u_p(P)$, i.e. $u_{p,\{R,L\}}(P) = P_{\{R,L\}}u_p(P) = \frac{1}{2}(1 \pm \gamma_5)u_p(P)$. Notice that there is another Lorentz structure of the form $\not{P}u_{p,R/L}$, which can be reduced to the decomposition in the first line of Eq. (14.22) by using the Dirac equation.
We are interested in the decay $B \to p\Psi$, for which we can state the corresponding decay amplitude:

$$\begin{aligned}\mathcal{A}_{(d)}(B^+ \to p\Psi) &= G_{(d)}\,\langle p(P)\Psi^c|\,\bar{\mathcal{O}}_{(d)}\,|B^+(P+q)\rangle \\ &= G_{(d)}\,\langle p(P)|\,\bar{\mathcal{O}}_{(d)}\,|B^+(P+q)\rangle\,u^c_\Psi(q) \quad (14.23)\end{aligned}$$

with the effective operator $\bar{\mathcal{O}}_{(d)}$ from Eq. (14.19). Following the derivation of section 14.2, we start with interaction vertices including Standard Model quarks and a heavy scalar complex field Y which provides the link between the SM and dark matter sector. During the computation of the Hamiltonian, we exploit that the mass M_Y of the Y-boson is much larger than the momentum transfer. Hence, we can integrate out the heavy particle and obtain an effective Fermi-type 4-fermion coupling, which couples the SM quarks to the dark matter particle Ψ.
The momentum assignment can be read off Eq. (14.23): the B meson has the momentum $P+q$ satisfying the on-shell condition $(P+q)^2 = m_B^2$, the proton the momentum P with the on-shell condition $P^2 = m_p^2$ and the Dirac fermion Ψ the momentum q with $q^2 = m_\Psi^2$. Since the mass m_Ψ of the fermion is unknown, we keep it as a free parameter in our analysis. The hadronic matrix element in Eq. (14.23) can be parameterised in terms of four independent $B \to p$ form factors:

$$\begin{aligned}\langle p(P)|\bar{\mathcal{O}}_{(d)}|B^+(P+q)\rangle = F^{(d)}_{B\to p_R}(q^2)\bar{u}_{p,R}(P) + F^{(d)}_{B\to p_L}(q^2)\bar{u}_{p,L}(P) \\ +\widetilde{F}^{(d)}_{B\to p_R}(q^2)\bar{u}_{p,R}(P)\frac{\not{q}}{m_p} + \widetilde{F}^{(d)}_{B\to p_L}(q^2)\bar{u}_{p,L}(P)\frac{\not{q}}{m_p}\,. \quad (14.24)\end{aligned}$$

Notice that we introduce the factor $1/m_p$ in the second line of Eq. (14.24) in order to guarantee that the form factors are dimensionless. This set of form factors will be determined in the following using the light-cone sum rule approach.

Chapter 15

Derivation of the LCSRs

Starting point of the derivation of the sum rules is the correlation function in Eq. (14.21)

$$\Pi^{(d)}(P,q) = i \int \mathrm{d}^4x \; e^{i(P+q)\cdot x} \, \langle 0| \, T \left\{ j_B(x), \mathcal{O}_{(d)}(0) \right\} |p(P)\rangle \; .$$

According to this correlation function, we investigate the $p \to B$ rather than the $B \to p$ form factors, where the latter accounts for the physically relevant $B^+ \to p\Psi$ decay. This is possible since these form factors only differ by a global phase, which is irrelevant for physical observables like decay widths. Long-distance contributions are parameterised by proton distribution amplitudes of increasing twist, which have been extensively studied in [116–118, 214] and are summarised in appendix E. Advanced lattice QCD calculations and sum rule analyses have determined the input parameters in the conformal expansion to good accuracy [116, 117, 119, 214, 215]. Alternatively, it would be necessary to investigate B-meson distribution amplitudes. On the one hand, the B meson needs to be studied in the framework of HQET, which adds not completely understood $1/m_b$ corrections to the correlation functions, on the other hand the key parameter of these DAs is the inverse moment λ_B [97–103], which suffers from a rather large uncertainty of around 30%. In addition to that the nucleon interpolating current would cause additional problems in this approach. First, the current is not unique and the sum rule results are therefore choice dependent [213]. Furthermore, we would need to consider an additional pole besides the proton in the dispersion relation ansatz due to the negative parity baryon with proton valence quark content [213]. Finally, the advantage of the $p \to B$ transition is that similar computations have been performed in LCSRs for $\Lambda_b \to p$ form factors [213], so we can guide our calculation along this work. For these particular reasons, it is therefore easier to work with the nucleon DAs instead of the B-meson DAs.

The light-cone sum rule approach works in the region where the external momenta $P+q$ and q are far off-shell, thus we work in the regions $(P+q)^2 \ll m_b^2$ and $q^2 \ll m_b^2$. As shown in section 14.1, the x-integration region shrinks to a domain near the light-cone $x^2 \approx 0$ and in this kinematical region we achieve the separation of short- and long-distance physics in form of an operator

product expansion. Here, short-distance effects are encoded in perturbatively calculable matching coefficients, while long-distance contributions are parameterised in terms of the nucleon distribution amplitudes of increasing twist.
In order to obtain an expression for the different form factors from Eq. (14.21), we use our considerations from section 11.2 to express the correlation function in terms of a dispersion integral. These steps are similar to the QCD sum rules derivation, since the major difference between these two methods lies in the paramerisation of the non-perturbative effects. After we have obtained a dispersion integral, we use the unitarity condition and write down a hadronic dispersion relation in the variable $(P+q)^2$

$$\Pi^{(d)}(P,q) = \frac{\langle 0|j_B|B^+(P+q)\rangle\langle B^+(P+q)|\mathcal{O}_{(d)}|p(P)\rangle}{m_B^2-(P+q)^2} + \int\limits_{s_h}^{\infty} ds \frac{\rho^{h(d)}(s,P,q)}{s-(P+q)^2}\,. \tag{15.1}$$

Here, we isolate the ground state contribution in form of a B^+-meson and introduce a cutoff $s_h = (m_B+2m_\pi)^2$ in the integral over the hadronic density $\rho^{h(d)}$ accounting for excited resonances like the B^*- or ρ-mesons and continuum contributions. The threshold s_h is chosen based on the lowest possible mass of the combination of mesons conserving the quantum numbers of the initial B meson. Possible substractions in Eq. (15.1) are neglected, because they vanish after performing the Borel transformation in the next steps. The hadronic dispersion relation in Eq. (15.1) incorporates all dispersion relations for the different invariant amplitudes in Eq. (14.22) for the (d)-model. By inserting the decomposition for the hermitian conjugate matrix element in Eq. (14.22) into Eq. (15.1) and by ordering the contributions according to different Dirac structures, we can for instance write down the hadronic dispersion relation for the form factor $F^{(d)}_{B\to p_R}$:

$$\Pi^{(d)}_R((P+q)^2,q^2) = \frac{m_B^2 f_B\, F^{(d)}_{B\to p_R}(q^2)}{m_B^2-(P+q)^2} + \int\limits_{s_h}^{\infty} ds \frac{\rho^{h(d)}_R(s,q^2)}{s-(P+q)^2}\,. \tag{15.2}$$

Notice that we use that $\langle 0|j_B|B^+\rangle = m_B^2 f_B$ and that we separate the hadronic spectral density $\rho^{h(d)}$ according to the different Dirac structures as well. Moreover, we also replace the original form factor for $p\to B$ transition by the $B\to p$ form factor and neglect the additional global phase. The other three form factors can be obtained by the following replacements:

$$\begin{aligned} &\Pi^{(d)}_R \to \Pi^{(d)}_L,\ \widetilde{\Pi}^{(d)}_R,\ \widetilde{\Pi}^{(d)}_L, \quad F^{(d)}_{B\to p_R} \to F^{(d)}_{B\to p_L},\ m_p^{-1}\widetilde{F}^{(d)}_{B\to p_R},\ m_p^{-1}\widetilde{F}^{(d)}_{B\to p_L}\,, \\ &\rho^{h(d)}_R \to \rho^{h(d)}_L,\ \widetilde{\rho}^{h(d)}_R,\ \widetilde{\rho}^{h(d)}_L\,. \end{aligned} \tag{15.3}$$

In the next section, we are going to calculate the correlation function in Eq. (14.21) employing an OPE. The various contributions can be transformed

into the dispersive integral form, e.g. for the amplitude $\Pi_R^{(d)}$

$$\Pi_R^{(d),\mathrm{OPE}}((P+q)^2,q^2) = \frac{1}{\pi}\int\limits_{m_b^2}^{\infty} ds \frac{\mathrm{Im}\Pi_R^{(d),\mathrm{OPE}}(s,q^2)}{s-(P+q)^2}\,, \tag{15.4}$$

where we rewrite $\rho_R^{(d),\mathrm{OPE}} = \frac{1}{\pi}\mathrm{Im}\Pi_R^{(d),\mathrm{OPE}}$. With the help of the (semi-local) quark-hadron duality, we can replace the integral over the hadronic spectral density $\rho^{h(d)}$ by the integral over the spectral density obtained from the OPE $\mathrm{Im}\Pi^{(d),\mathrm{OPE}}$

$$\int\limits_{s_h}^{\infty} ds \frac{\rho_R^{h(d)}(s,q^2)}{s-(P+q)^2} = \frac{1}{\pi}\int\limits_{s_0^B}^{\infty} ds \frac{\mathrm{Im}\Pi_R^{(d),\mathrm{OPE}}(s,q^2)}{s-(P+q)^2}\,. \tag{15.5}$$

As we have previously mentioned, this step is useful in order to get rid of the hadronic spectral density, which is in general hard to estimate and in many cases unknown. However, this introduces the effective threshold s_0^B, which needs to be determined in the numerical analysis and constitutes an additional uncertainty.
With all these steps at hand, we can now substitute Eq. (15.4) into Eq. (15.2) and perform simplifications on the integration region after applying Eq. (15.5). Finally, we perform a Borel transformation, see appendix A.5, in the variable $(P+q)^2$ to arrive at the desired form of the sum rules:

$$m_B^2 f_B\, F_{B\to p_R}^{(d)}(q^2) e^{-m_B^2/M^2} = \frac{1}{\pi}\int\limits_{m_b^2}^{s_0^B} ds\, e^{-s/M^2}\mathrm{Im}\Pi_R^{(d),\mathrm{OPE}}(s,q^2)\,. \tag{15.6}$$

As we will see in the next section, the OPE contributions $\mathrm{Im}\Pi_R^{(d),\mathrm{OPE}}(s,q^2)$ also depend for the higher twist contributions on inverse powers of the Borel parameter M^2. This indicates that higher twist contributions tend to be suppressed. The sum rules for the other form factors are obtained in a similar way by using the replacements in Eq. (15.3).
If we now turn to the second model under consideration in this work, the (b)-model, we can start again in Eq. (14.21) and replace the operator $\mathcal{O}_{(d)}$ by $\mathcal{O}_{(b)}$. Besides this replacement, the derivations follow the same steps as presented above.

15.1 Evaluating the OPE

The explicit calculation follows the usual steps for evaluating correlation functions: First, we use Wicks theorem to contract the b-quarks. Since we recognise that there is a transposed b-quark field in the operator $\mathcal{O}_(d)$ in Eq. (14.19) instead of an ordinary b-quark field, we perform an additional Fierz transformation:

$$\bar{u}_R b_R^c = \bar{b}_R u_R^c, \quad \bar{b}_R^c u_R = \bar{u}_R^c b_R\,. \tag{15.7}$$

After that the trace over the Dirac indices of the spinor fields can be evaluated using the well-known trace technologies from the literature. However, there remain uncontracted quark fields between a vacuum and a proton state of the form:

$$\langle 0|\, T\{u(x)u(0)d(0)\}\, |p\rangle \tag{15.8}$$

These terms are related to the nucleon DAs via the relations Eqs. (E.1) and (E.6) in appendix E in the light-cone limit $x^2 \to 0$. Moreover, they are sorted according to increasing twist and become increasingly more complicated in terms of computation. The leading-twist contributions have been worked out in [202, 216] for both operators. They read:

$$\Pi^{(d)}(P,q) = \left[-\frac{m_b}{2} \int_0^1 \mathrm{d}\alpha \frac{\big((1-\alpha)m_p^2 + P\cdot q\big)(V_1+A_1)(\alpha)}{((1-\alpha)P+q)^2 - m_b^2} \right] u_{p,R}(P) \tag{15.9}$$

$$\begin{aligned}\Pi^{(b)}(P,q) = &\left[-\frac{m_b m_p}{4} \int_0^1 \mathrm{d}\alpha \frac{(1-\alpha)m_p(V_1+A_1)(\alpha) - 3m_b T_1(\alpha)}{((1-\alpha)P+q)^2 - m_b^2} \right] u_{p,R}(P) \\ &- \left[\frac{m_b m_p}{4} \int_0^1 \mathrm{d}\alpha \frac{(V_1+A_1)(\alpha)}{((1-\alpha)P+q)^2 - m_b^2} \right] \not{q}\, u_{p,L}(P)\,. \end{aligned} \tag{15.10}$$

We see that at leading twist only one form factor enters for the operator $\mathcal{O}_{(d)}$, while for the operator $\mathcal{O}_{(b)}$ also the contribution from the Lorentz structure $\not{q}u_{p,L}(P)$ appears. The integration variable α denotes the energy fraction of the u-quark inside the proton bound state, while we have already integrated the other two components α_2 and α_3. The leading-twist amplitudes V_1, A_1, T_1 are stated in appendix E together with the other distribution amplitudes up to twist six. Furthermore, there occurs a scalar product $P\cdot q$ in Eq. (15.9), which needs to be replaced by

$$2P\cdot q = (P+q)^2 - m_p^2 - q^2\,, \tag{15.11}$$

allowing for the cancellation of the $(P+q)^2$-dependence in the denominator in Eq. (15.9). This introduces constant terms which vanish when we perform the Borel transformation. We replace this scalar product similarly in the other contributions as well.
When we now start to include higher twist corrections, explicit x-dependencies appear for the first time in Eqs. (14.21) and (E.1). These dependencies prevent us from immediately rewriting the exponential functions into the momentum conserving δ-distributions, see table 15.1.

twist 3	$\int \mathrm{d}^d x\; e^{ikx} e^{i(P+q)x} e^{-iP\alpha x} = (2\pi)^d \delta^{(d)}(k+q+P\bar{\alpha})$
twist 4, 5, 6	$\int \mathrm{d}^d x\; e^{ikx} e^{i(P+q)x} e^{-iP\alpha x} x_\nu = -i(2\pi)^d \frac{\partial}{\partial k^\nu} \delta^{(d)}(k+q+P\bar{\alpha})$
	$\int \mathrm{d}^d x\; e^{ikx} e^{i(P+q)x} e^{-iP\alpha x} x_\mu x_\nu = (-i)^2 (2\pi)^d \frac{\partial}{\partial k^\mu} \frac{\partial}{\partial k^\nu} \delta^{(d)}(k+q+P\bar{\alpha})$
	$\int \mathrm{d}^d x\; e^{ikx} e^{i(P+q)x} e^{-iP\alpha x} x_\mu x^\mu = (-i)^2 (2\pi)^d \frac{\partial}{\partial k^\mu} \frac{\partial}{\partial k_\mu} \delta^{(d)}(k+q+P\bar{\alpha})$

Table 15.1: Integration over the position variable x in order to obtain the momentum conserving δ-distributions. For brevity, we introduce the notation $\bar{\alpha} = 1 - \alpha$.

Second, we encounter scalar products $P \cdot x$ from the light-cone expansion in Eq. (E.1), which prevent us to use the relations in table 15.1. At this point we need to perform an additional partial integration with respect to α. It turns out that the surface terms vanish during this partial integration, even in the case where we need to perform partial integration steps twice. The complete higher twist contributions for both models up to twist six are provided in appendix F.1. We also include the $\mathcal{O}(x^2)$ contributions to the twist-three contributions, while we neglect the $\mathcal{O}(x^2)$ corrections to twist four, since they are numerically small and correspond to a power-suppressed contribution [117]. In general, the computations for the operator $\mathcal{O}_{(b)}$ are of similar complexity, albeit the various $\mathcal{T}$-structures in the proton matrix element decomposition in Eq. (E.1) contribute for this operator. In addition to that we notice that the form factor $\widetilde{F}_{B\to p_L}$ originating from the Dirac structure $\not{q} u_{p,L}(P)$ also starts to contribute beyond twist three for the $\mathcal{O}_{(d)}$ operator. Hence, our numerical discussion will include four kinematically independent form factors for both models instead of three in previous works [202, 216].
In order to obtain similar relations as in Eqs. (15.9) and (15.10) including all corrections up to twist six, we need to take all contributions listed in appendix F.1 and add them up based on the different spinor structures. We continue the discussion with the complete contributions by modifying the denominator such that we obtain the usual form of a dispersion relation. Therefore, we rewrite the expression $((1-\alpha)P+q)^2$

$$((1-\alpha)P+q)^2 = (1-\alpha)(P+q)^2 + \alpha q^2 - \alpha(1-\alpha)m_p^2 \tag{15.12}$$

and perform the following substitution

$$s := \frac{m_b^2 - \alpha q^2 + \alpha(1-\alpha)m_p^2}{1-\alpha}\,. \tag{15.13}$$

The integral $\int_0^1 \mathrm{d}\alpha$ in the leading-twist contributions in Eqs. (15.9) and (15.10), as well as the contributions in appendix F.1, are replaced by $\int_{m_b^2}^\infty \mathrm{d}s$ due to the substitution in Eq. (15.13) and we obtain the desired dispersion integral relation.
Now we can use Eq. (A.32) to execute the Borel transformation of the contributions such that we can insert our result into Eq. (15.6). Subsequently,

it is useful to replace the variable s in the dispersion relation by α.
After performing the Borel transformation, we derive the LCSR for the form factor $F^{(d)}_{B\to p_R}(q^2)$ and for the remaining form factors by using the replacements in Eq. (15.3) and $(d) \leftrightarrow (b)$ in Eq. (15.6) after inserting our complete contributions up to twist six from appendix E. For completeness, we state the $F^{(d)}_{B\to p_R}(q^2)$ form factor in Eq. (15.14), while the three remaining form factors are shown in appendix in Eqs. (F.41) to (F.43).

$$\begin{aligned}
F^{(d)}_{B\to p_R}(q^2) = \frac{1}{m_B^2 f_B}\int_0^{\alpha_0^B} \mathrm{d}\alpha\, e^{\frac{m_B^2 - s(\alpha)}{M^2}} \Bigg\{ & \frac{m_b^3}{4}\left(1+\frac{\bar\alpha^2 m_p^2 - q^2}{m_b^2}\right)\frac{(V_1+A_1)(\alpha)}{\bar\alpha^2} \\
& - \frac{m_b^2 m_p}{2}\frac{P_1(\alpha)+S_1(\alpha)}{\bar\alpha} + \frac{m_b m_p^2}{4}\Big(V_3(\alpha)-A_3(\alpha)\Big) + \frac{m_b^3 m_p^2}{4M^2} \\
& \times \frac{\widetilde{V}_{123}(\alpha)-\widetilde{A}_{123}(\alpha)}{\bar\alpha^2}\left(1+\frac{m_p^2\bar\alpha^2-q^2}{m_b^2}\right) + \frac{m_b^2 m_p^3}{2}\frac{\widetilde{S}_{12}(\alpha)-\widetilde{P}_{21}(\alpha)}{\bar\alpha M^2} \\
& - \frac{m_b m_p^2}{4}\frac{\widetilde{V}_{1345}(\alpha)+\widetilde{A}_{1345}(\alpha)}{\bar\alpha}\left(1+\frac{m_b^2}{\bar\alpha M^2}\right) + \frac{m_b m_p^2}{4\bar\alpha^2}\Big(\widetilde{A}_1^M - \widetilde{V}_1^M\Big) \\
& \times \left(1+\frac{q^2-m_p^2\bar\alpha^2+m_b^2}{\bar\alpha M^2} + \frac{m_b^2}{\bar\alpha^2 M^4}\Big(q^2-m_p^2\bar\alpha^2-m_b^2\Big)\right) \\
& + \frac{m_b m_p^4}{2}\frac{\widetilde{\widetilde{V}}_{123456}(\alpha)-\widetilde{\widetilde{A}}_{123456}(\alpha)}{\bar\alpha M^2}\left(1+\frac{m_b^2}{\bar\alpha M^2}\right)\Bigg\}. \qquad (15.14)
\end{aligned}$$

Besides the notation $\bar\alpha = 1-\alpha$, we introduce the abbreviation

$$\widetilde{V}(\alpha) = \int_0^\alpha \mathrm{d}\alpha'\, V(\alpha') \qquad (15.15)$$

$$\widetilde{\widetilde{V}}(\alpha) = \int_0^\alpha \mathrm{d}\alpha' \int_0^{\alpha'} \mathrm{d}\alpha''\, V(\alpha''), \qquad (15.16)$$

where we have already integrated over the momentum fractions α_2 as well as α_3 and where we have performed additional integrations in $\alpha_1 = \alpha$ due to the partial integrations. We exploit this notation to a great extent in the form factors in Eqs. (15.14) and (F.41) to (F.43). Moreover, we introduce the various distribution amplitudes in Eq. (15.14) in appendix E.
However, these form factors are strictly speaking only valid in the region $q^2 \ll m_b^2$, while we intend to extract predictions in the physical timelike region with $q^2 = m_\Psi^2$. Since the mass of the particle Ψ might be in the region $m_\Psi \sim m_b$, we need to extrapolate the form factors to these q^2 values. The next section is devoted to this issue.

15.2 Transition to large m_Ψ-region

In the last section, we have discussed the derivation of the form factors and stated the results in appendix F.2 for the (d)- and (b)-model, which are an essential part of the decay width for the process $B \to p\Psi$. However, the derivation within the LCSR approach requires that we work in the limit

$q^2 \ll m_b^2$ in order to use the light-cone OPE. In the physical region, we can identify that $q^2 = m_\Psi^2$ and see that the form factors need to be modified such that reliable results can be obtained in the region $m_\Psi \sim m_b$. Although it is in general possible to extract the form factors in the lower part of the interval $m_p \leq m_\Psi \leq (m_B - m_p) \approx 4.34\,\text{GeV}$, an extrapolation to the upper region of the interval is necessary to obtain a reliable prediction, also for large masses m_Ψ. While the lower bound of this interval is set by the requirement that the model prevents proton decays, the upper bound is given by the kinematics of a two-body decay of the B meson in the specific decay channel $B \to p\Psi$. The corresponding extrapolation which we adopt here is the BCL version [217] of the z-expansion [218], which has the advantage that it is a model-independent parameterisation of the form factors. Thus, the idea is to perform a conformal mapping of the variable q^2 onto the complex variable z which lives on a unit circle in the complex plane:

$$z(q^2) = (\sqrt{t_+ - q^2} - \sqrt{t_+ - t_0})/(\sqrt{t_+ - q^2} + \sqrt{t_+ - t_0})\,. \tag{15.17}$$

This reparameterisation is based on the assumption that the form factors in (15.14) and (F.41) to (F.43) are free from singularities in the complex q^2 plane apart from the positive real axis. Notice that this physical picture is reflected in the choice of the parameters $t_\pm$ and t_0 in Eq. (15.17). A common choice for the default parameter t_0 is given by $(m_B + m_p) \cdot (\sqrt{m_B} - \sqrt{m_p})^2$, while the variables $t_\pm$ are determined by $(m_B \pm m_p)^2$. With this default parameter choice, the maximum truncation error gets minimised. The bound $t_- = m_B - m_p$ constitutes the upper bound of the kinematics of the decay $B \to p\Psi$, the bound $t_+ = m_B + m_p$ represents the threshold where the timelike form factors develop an imaginary part due to intermediate states and higher resonances. Therefore, the variable z becomes imaginary in the region $q^2 > t_+$. However, there is one subthreshold pole below t_+, namely the Λ_b-baryon, which takes the form of an isolated pole at $q^2 = m_{\Lambda_b}^2$. By isolating the singularity, we can define a function

$$f(z) = (1 - q^2/m_{\Lambda_b}^2)F(q^2)\,, \qquad F(q^2) \in \{F_{B\to p_R}^{(d),(b)}, \widetilde{F}_{B\to p_L}^{(d),(b)}\} \tag{15.18}$$

which is an analytic function in q^2 apart from the cut on the positive real axis with $q^2 \geq t_+$ and finite for $q^2 \to \infty$. Since the physical region of the dark baryon mass m_Ψ for the particular mapping in Eq. (15.17) is expressed in terms of small z values between $0.077 > z > -0.083$, a Taylor expansion of the function $f(z)$ can be performed such that we end up with a parameterisation of the form [217]

$$F(q^2) = \frac{1}{1 - q^2/m_{\Lambda_b}^2} \sum_{n=0}^{N} \bar{b}_n z(q^2, t_0)^n \tag{15.19}$$

From restrictions imposed by the threshold t_+ onto the variable z [217], it is possible to derive an additional constraint on the expansion coefficients

$$\bar{b}_N = -\frac{(-1)^N}{N} \sum_{n=0}^{N-1} (-1)^n n \bar{b}_n\,. \tag{15.20}$$

For our purposes, it is convenient to rewrite the expansion coefficients as $\bar{b}_n = F(0)b_n$, where $F(0)$ is the form factor evaluated at $q^2 = 0$. Thus, we can express the lowest coefficient b_0 by

$$b_0 = 1 - \sum_{n=1}^{N-1} b_n \Big[z(0,t_0)^n - (-1)^{n-N} \frac{n}{N} z(0,t_0)^N \Big] \tag{15.21}$$

and therefore end up with the final form of the form factors in the z-expansion

$$F(q^2) = \frac{F(0)}{1 - q^2/m_{\Lambda_b}^2} \Bigg[1 + \sum_{n=1}^{N-1} b_n \Bigg(z(q^2,t_0)^n - z(0,t_0)^n - (-1)^{n-N} \frac{n}{N} \cdot \Big[z(q^2,t_0)^N - z(0,t_0)^N \Big] \Bigg) \Bigg] . \tag{15.22}$$

The form factors $F(q^2)$ are chosen according to Eq. (15.18). It is sufficient to truncate the expansion at $\mathcal{O}(z^2)$ such that we have two free parameters.

$$F_{B\to p_R}^{(d)}(q^2) = \frac{F_{B\to p_R}^{(d)}(0)}{1 - q^2/m_{\Lambda_b}^2} \Bigg[1 + b_{B\to p_R}^{(d)} \Bigg(z(q^2) - z(0) + \frac{1}{2} \Big[z(q^2)^2 - z(0)^2 \Big] \Bigg) \Bigg] \tag{15.23}$$

First, we have the form factors evaluated at $q^2 = 0$, which corresponds to the normalisation of this form factor, and the slope parameter $b_{B\to p_R}^{(d)}$. This slope parameter is determined by a fit for each of the form factors individually. The other form factor expressions are obtained from the replacement rule in Eq. (15.3) and from the replacement $(d) \leftrightarrow (b)$.
The form factors in Eq. (15.23) are the final expressions which will be used in the following analysis to determine the decay width and subsequently the branching fraction.

Chapter 16

Numerical analysis

This chapter is devoted to the numerical evaluation of the sum rules in Eq. (15.6) and the determination of the decay width and branching fractions of the decay $B \to p\Psi$.

Parameter	interval	Ref.
b-quark $\overline{MS}$ mass	$\overline{m}_b(3\text{ GeV}) = 4.47^{+0.04}_{-0.03}$ GeV	[219]
Renormalization scale	$\mu = 3.0^{+1.5}_{-0.5}$ GeV	[220, 221]
Borel parameter squared	$M^2 = 16.0 \pm 4.0$ GeV^2	
Duality threshold	$s_0^B = 39.0^{-1.0}_{+1.5}$ GeV^2	
B-meson decay constant	$f_B = 190.0 \pm 1.3$ MeV	[200]
Nucleon decay constant	$f_N(\mu = 2\text{ GeV}) = \left(3.54^{+0.06}_{-0.04}\right) \times 10^{-3}$ GeV^2	[119]
Parameters of nucleon DAs	$\varphi_{10}(\mu = 2\text{ GeV}) = 0.182^{+0.021}_{-0.015}$	[119]
	$\varphi_{11}(\mu = 2\text{ GeV}) = 0.118^{+0.024}_{-0.023}$	
	$\lambda_1(\mu = 2\text{ GeV}) = \left(-44.9^{+4.2}_{-4.1}\right) \times 10^{-3}$ GeV^2	
	$\lambda_2(\mu = 2\text{ GeV}) = \left(93.4^{+4.8}_{-4.8}\right) \times 10^{-3}$ GeV^2	
	$\eta_{10}(\mu = \sqrt{2}\text{ GeV}) = -0.039^{+0.005}_{-0.005}$	[215]
	$\eta_{11}(\mu = \sqrt{2}\text{ GeV}) = 0.14^{+0.016}_{-0.016}$	
	$\xi_{10}(\mu = 2\text{ GeV}) = -0.042^{+0.313}_{-0.312}$	[214]

Table 16.1: Input parameters for the LCSRs.

The various input parameters for the LCSRs are given in table 16.1. We work at a renormalisation scale of $\mu = 3$ GeV, because recent studies of LCSRs for $B \to \pi$ or $B^*B\pi$ strong couplings [220, 221] indicate that this choice with the corresponding uncertainties is optimal for B-meson interpolating currents. Furthermore, we take the b-quark mass in the $\overline{MS}$-scheme and use the same value for the B-meson decay constant f_B as in the determination of the parameters $\lambda^2_{E,H}$ in Project II, which has been obtained from lattice QCD computations with $n_f = 2 + 1 + 1$ [200].
The input parameters of the nucleon DAs require a more detailed investigation. We take some of these parameters at a scale $\mu_0 = 2$ GeV from a recent

lattice determination [119], while others from a LCSR computation [215] at a scale $\mu_0 = \sqrt{2}$ GeV. Since we perform our analysis at the scale $\mu = 3$ GeV, we need to run these parameters to this scale by using their RGE [215]

$$\frac{\mathrm{d}}{\mathrm{d}\ln\mu}\,\varphi(\mu) = -\gamma_\varphi\,\varphi(\mu)\,. \tag{16.1}$$

γ_φ denotes the anomalous dimension for the parameter φ. Its solution to NLO order is given by

$$\varphi(\mu) = \varphi(\mu_0)\left(\frac{\alpha_s(\mu)}{\alpha_s(\mu_0)}\right)^{\frac{\gamma_\varphi^0}{2\beta_0}}\,. \tag{16.2}$$

Here, γ_φ^0 indicates the one-loop anomalous dimension according to the expansion in Eq. (3.13). We are able to simplify Eq. (16.2) if we include the one-loop RGE solution for α_s

$$\alpha_s(\mu^2) \approx \left(\beta_0 \ln\left(\frac{\mu^2}{\Lambda^2_{\mathrm{QCD}}}\right)\right)^{-1} \tag{16.3}$$

such that we obtain

$$\varphi(\mu) = \varphi(\mu_0)\left(\frac{\ln(\mu_0/\Lambda_{\mathrm{QCD}})}{\ln(\mu/\Lambda_{\mathrm{QCD}})}\right)^{\frac{\gamma_\varphi^0}{2\beta_0}}\,. \tag{16.4}$$

We take the value for $\Lambda_{\mathrm{QCD}} = 0.288$ GeV from [194] for $n_f = 4$. Notice that Eq. (16.4) can be used for all parameters of the nucleon DA. The non-cusp anomalous dimension γ^0 is given for instance in [215] for various parameters. We collect them for completeness in table 16.2. The advantage of using

Parameter φ	f_N	φ_{10}	φ_{11}	η_{10}	η_{11}	λ_1	λ_2	ξ_{10}
γ_φ^0	$\frac{4}{3}$	$\frac{40}{9}$	$\frac{16}{3}$	$\frac{40}{9}$	8	4	4	$\frac{20}{3}$

Table 16.2: Non-cusp anomalous dimensions for different parameters of the nucleon DA.

these parameters instead of the parameters in the conformal expansion in appendix E is that they satisfy a well-defined RGE. They can be related to the parameters of the conformal expansion via [215]

$$\begin{aligned}
A_1^u &= \varphi_{10} + \varphi_{11}\\
V_1^d &= \frac{1}{3} - \varphi_{10} + \frac{1}{3}\varphi_{11}\\
f_1^d &= \frac{3}{10} - \frac{1}{6}\frac{f_N}{\lambda_1} + \frac{1}{5}\eta_{10} - \frac{1}{3}\eta_{11}\\
f_1^u &= \frac{1}{10} - \frac{1}{6}\frac{f_N}{\lambda_1} - \frac{3}{5}\eta_{10} - \frac{1}{3}\eta_{11}\\
f_2^d &= \frac{4}{15} + \frac{2}{5}\xi_{10}\,.
\end{aligned} \tag{16.5}$$

16.1 Numerical analysis: Form factors

After performing the running of the nucleon DA parameters to the desired scale $\mu = 3$ GeV, we can estimate the uncertainties on the form factors as they are the relevant input parameters. For this, we consider these form factors before the z-expansion and vary each input parameter individually within the given uncertainty range. For each variation of one parameter, we perform a z-expansion and obtain two additional slope parameters representing the upper and lower bound on central value of the slope parameter b. After performing these steps for each input parameter, we determine the upper uncertainty $\Delta^{\uparrow}$ on the central value b by considering the difference of b with each upper slope parameter, obtained by inserting the upper limit of each input parameter into the different form factor expressions individually, and adding all the differences in quadrature. The same steps apply for the lower uncertainty $\Delta^{\downarrow}$ on the parameter b by inserting the lower uncertainties on each input parameter into the form factors. We show these steps for the slope parameter of the form factor $F^{(d)}_{B\to p_R}$ in Eq. (16.6)

$$\begin{aligned}\Delta^{\uparrow}_{b^{(d)}_{B\to p_R}} &= \left[\sum_k (b^{(d)}_{B\to p_R} - b^{(d),\uparrow}_{B\to p_R;k})^2\right]^{\frac{1}{2}} \\ \Delta^{\downarrow}_{b^{(d)}_{B\to p_R}} &= \left[\sum_k (b^{(d)}_{B\to p_R} - b^{(d),\downarrow}_{B\to p_R;k})^2\right]^{\frac{1}{2}}\end{aligned} \tag{16.6}$$

with $k \in \{M^2, \mu, \varphi_{10}, \varphi_{11}, f_B, f_N, m_b, \eta_{10}, \eta_{11}, \lambda_1, \lambda_2, \xi_{10}\}$. In this context, the parameter $b^{(d),\uparrow}_{B\to p_R;\phi_{10}}$ illustrates for instance the slope parameter from the z-expansion if we insert the upper bound on the parameter ϕ_{10} into the form factor $F^{(d)}_{B\to p_R}$. We keep correlations between different parameters in mind, for example the Borel parameter M^2 and the threshold parameter s_0^B are correlated, hence upper and lower limits need to be inserted into the form factor before z-expansion simultaneously. Furthermore, the variation of the scale μ leads to different values of the b-quark mass as well, since this mass has an explicit scale dependence. In the end, we notice that the parameters $\Delta^{\uparrow,\downarrow}_{b^{(d)}_{B\to p_R}}$ in Eq. (16.6) are precisely the deviations which we show in table 16.3 as uncertainties on the slope parameters.

Moreover, the second input parameter in the z-expansion is the form factors at $q^2 = 0$. We determine its uncertainties as in Eq. (16.6). In order to obtain the error estimates on the other three form factors, we need to perform a similar analysis for the three remaining form factors.

We provide the several slope parameters and the form factor at $q^2 = 0$ within their uncertainties in table 16.3 for the (d)-model and in table 16.4 for the (b)-model:

$F^{(d)}_{B\to p_R}(0)$	$b^{(d)}_{B\to p_R}$	$\widetilde{F}^{(d)}_{B\to p_L}(0)$	$b^{(d)}_{B\to p_L}$
$0.022^{+0.013}_{-0.013}$	$4.46^{+0.97}_{-1.72}$	$0.005^{+0.002}_{-0.001}$	$-2.27^{+0.10}_{-0.08}$

Table 16.3: Parameters of the z-expansion for the (d)-model form factors including all contributions up to twist six. Notice that the parameters $F^{(d)}_{B\to p_R}(0)$ and $\widetilde{F}^{(d)}_{B\to p_L}(0)$ have the dimension GeV^2, while the slope parameters $b^{(d)}_{B\to p_R}$,$b^{(d)}_{B\to p_L}$ are dimensionless.

$F^{(b)}_{B\to p_R}(0)$	$b^{(b)}_{B\to p_R}$	$\widetilde{F}^{(b)}_{B\to p_L}(0)$	$b^{(b)}_{B\to p_L}$
$-0.041^{+0.019}_{-0.018}$	$-2.00^{+1.58}_{-3.62}$	$-0.007^{+0.003}_{-0.002}$	$-2.85^{+0.17}_{-0.15}$

Table 16.4: We show the same as in table 16.3, but for the parameters of the (b)-model.

With these input parameters, we are able to perform the z-expansion and investigate the four different form factors for the two models individually.

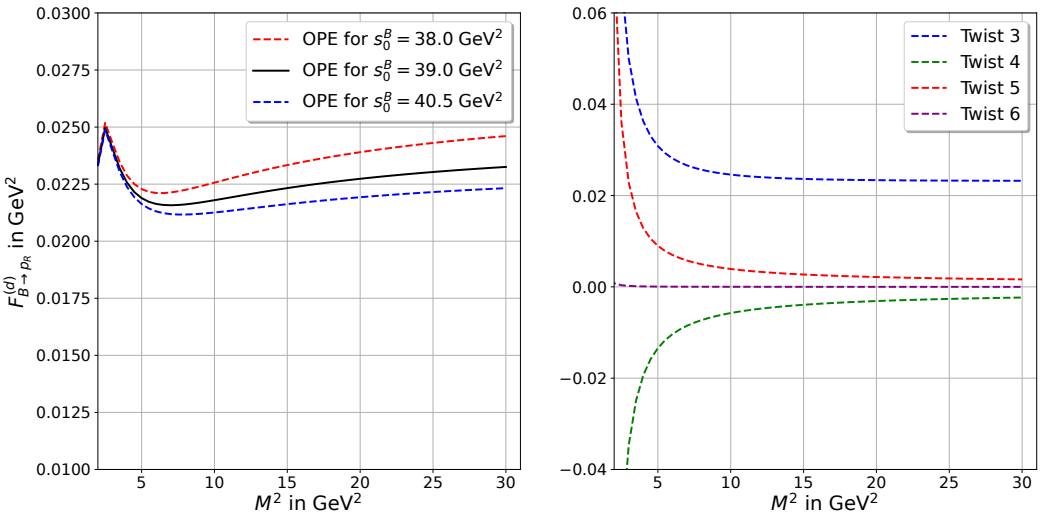

Figure 16.1: Analysis for the form factor $F^{(d)}_{B\to p_R}(q^2)$ in the (d)-model for different Borel parameter M^2. The right plot shows each higher twist correction individually, while the left plot illustrates all contributions combined up to twist six for various choices of the threshold parameter s_0^B. We choose for the mass of the dark matter particle m_Ψ the benchmark value $m_\Psi = 2$ GeV [206].

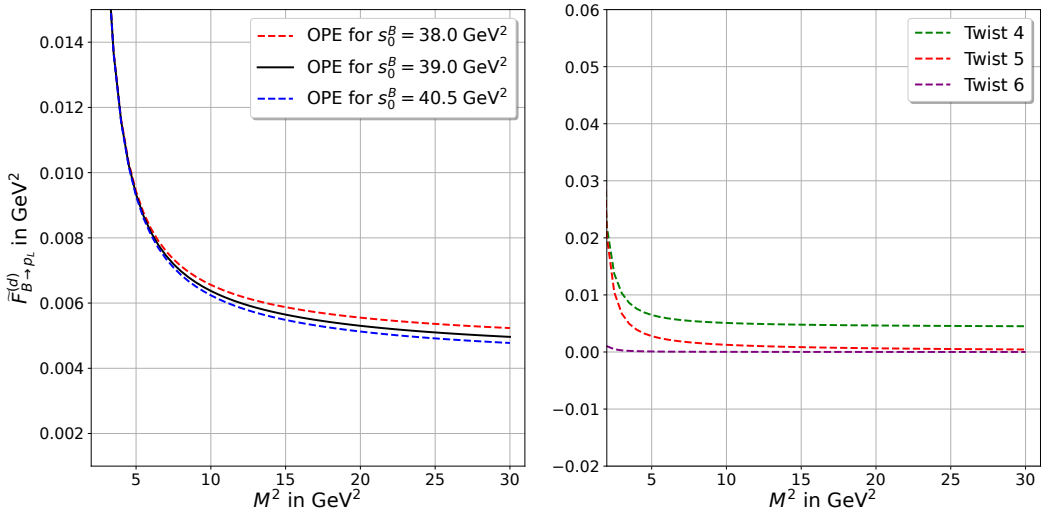

Figure 16.2: Similar analysis as in figure 16.1 for the form factor $\widetilde{F}^{(d)}_{B\to p_L}(q^2)$.

We plot in figures 16.1 to 16.4 the four different form factors with respect to the Borel parameter M^2. The plot on the right side illustrates each twist correction individually and provides a relative estimate of the magnitude of the different corrections to the leading twist three contribution. The leading contributions have been investigated in [202], see also [216].

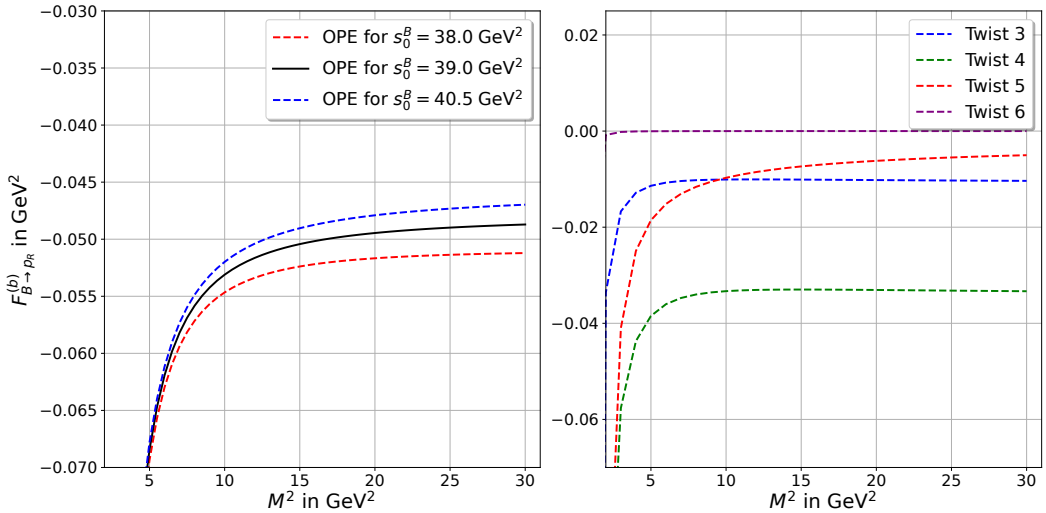

Figure 16.3: Analysis for the form factor $F^{(b)}_{B\to p_R}(q^2)$ in the (b)-model for different Borel parameter M^2. The right plot shows each higher twist correction individually, while the left plot illustrates all contributions combined up to twist six for various choices of the threshold parameter s_0^B. We choose for the mass of the dark matter particle m_Ψ the benchmark value $m_\Psi = 2$ GeV [206].

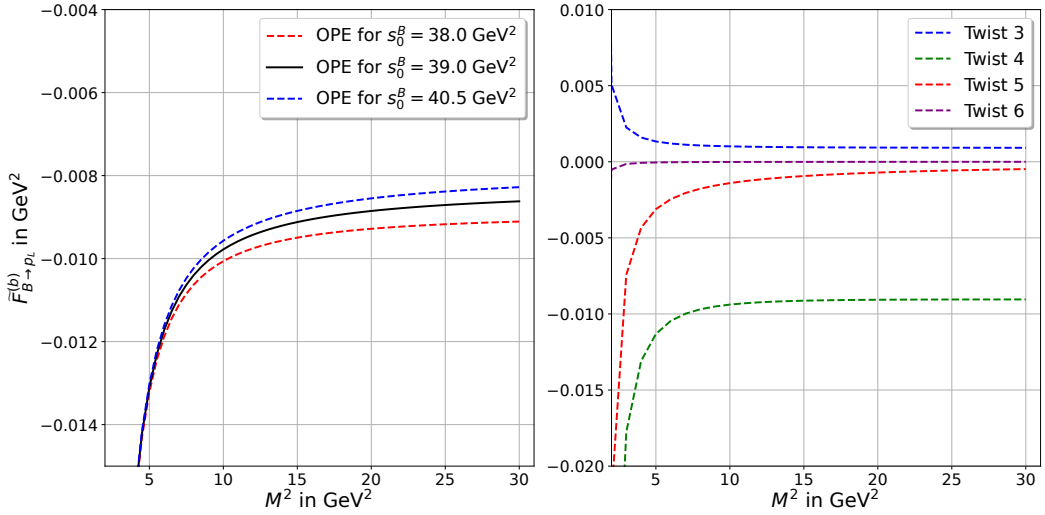

Figure 16.4: Similar analysis as in figure 16.1 for the form factor $\widetilde{F}^{(b)}_{B\to p_L}(q^2)$.

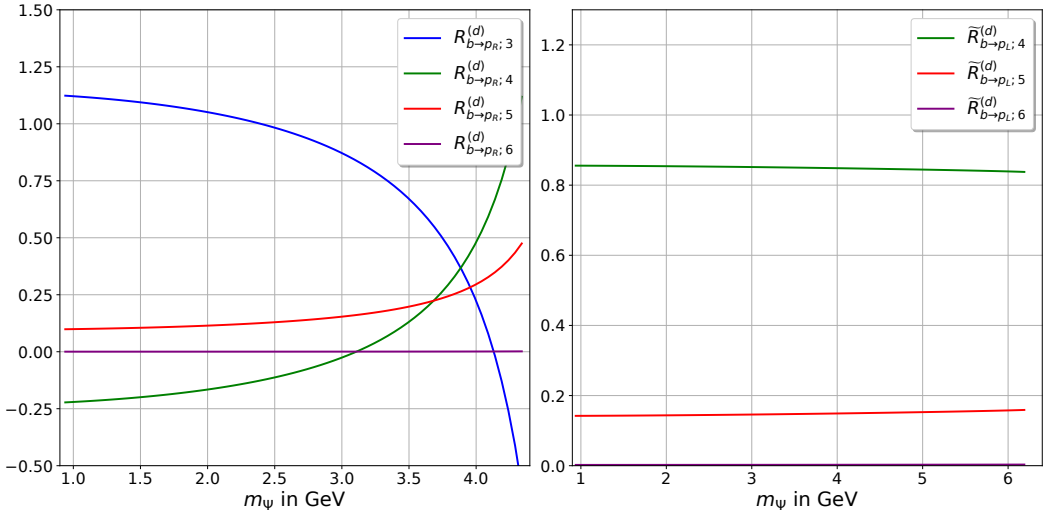

Figure 16.5: Plot for the ratios $R^{(d)}_{B\to p_R;i}$ and $\widetilde{R}^{(d)}_{B\to p_L;i}$ defined in Eqs. (16.7) and (16.8) with respect to the dark fermion mass m_Ψ. The left panel contains the contributions from the form factor $F^{(d)}_{B\to p_R}$, while the right panel shows the ratios for the form factor $\widetilde{F}^{(d)}_{B\to p_L}$.

Notice that the form factor $\widetilde{F}^{(d)}_{B\to p_L}(q^2)$ starts to contribute at twist four accuracy, while the other three form factors already give rise to contributions at twist three. As it is expected from various different sum rules analyses including B-meson interpolating currents, the OPE shows good convergence. While the form factors in the (d)-model show the typical hierarchy of twist contributions at the benchmark value $m_\Psi = 2$ GeV, we observe that the twist four correction is large for the (b)-model, in particular for the form factor $F^{(b)}_{B\to p_R}(q^2)$, where the twist four contribution is larger than the leading-twist contribution. This can be traced back to the large $\mathcal{T}_{2,4}$-contributions in Eq.

(E.1), which enhance the twist four correction in the (b)-model, but vanish for the (d)-model in the computation of the correlation function. These contributions introduce for the first time the sizeable and not very precisely known parameter ξ_{10} via Eq. (16.5). Beyond twist four, we also observe in the (b)-model convergence of the OPE indicated by the fact that higher twist corrections tend to become smaller.
The left panel shows the complete form factor after including all higher twist corrections for different choices of the threshold parameter s_0^B within the bounds stated in table 16.1. Due to the small variation of the form factors for different thresholds with respect to different Borel parameter, we again conclude that the sum rules for the four form factors are stable at the benchmark value $m_\Psi = 2$ GeV and hence reliable.
The range for the Borel parameter M^2 is chosen in accordance to table 16.1 and in agreement with the work in [202], although we include higher twist corrections up to twist six here. Besides that, it is also possible to verify this Borel window by investigating the behaviour of the form factors over a wider range of the Borel parameter and by choosing this window based on the stability of the sum rule. As shown in figures 16.1 to 16.4, we see that the sum rules are stable for the specific Borel window provided in table 16.1, thus this parameter range seems to be adequate. Furthermore, it turns out that for this particular choice of the Borel parameter the contributions of the excited and continuum states are reasonably suppressed due to the Borel transformation from Eq. (A.32) and lie around $20 - 30\%$. Therefore, our result does not depend sensitively on the QHD approximation.
In addition to that the threshold parameter s_0^B is determined by taking the derivative of the sum rules in Eq. (15.6) with respect to $-1/M^2$ and by combining the result such that we obtain an estimate for the B-meson mass m_B, which we fit to the literature [211]. The stability of the sum rules in figures 16.1 to 16.4 underline that this choice is appropriate in order to obtain reliable estimates.
The argumentation on the stability of the sum rule is based around the parameter choice $m_\Psi = 2$ GeV. We know that the LCSR approach works for $q^2 = m_\Psi^2 \ll m_b^2$, therefore we expect that the OPE shows good convergence as well for values m_Ψ below 2 GeV. However, we can now take the analysis one step further and investigate whether the OPE is still applicable for larger values of m_Ψ, in particular at which point the expansion starts to break down. We perform this analysis for the (d)-model in figure 16.5 for the form factor $F^{(d)}_{B\to p_R}(q^2)$ in the left panel and for the form factor $\widetilde{F}^{(d)}_{B\to p_L}(q^2)$ in the right panel. For this, it is convenient to define the ratios

$$R^{(d)}_{B\to p_R;i} = \frac{F^{(d)}_{B\to p_R;i}}{\sum_{i\in\{3,4,5,6\}} F^{(d)}_{B\to p_R;i}}\,; \widetilde{R}^{(d)}_{B\to p_L;i} = \frac{\widetilde{F}^{(d)}_{B\to p_L;i}}{\sum_{i\in\{4,5,6\}} \widetilde{F}^{(d)}_{B\to p_L;i}}, \tag{16.7}$$

$$R^{(b)}_{B\to p_R;i} = \frac{F^{(b)}_{B\to p_R;i}}{\sum_{i\in\{3,4,5,6\}} F^{(b)}_{B\to p_R;i}}\,; \widetilde{R}^{(b)}_{B\to p_L;i} = \frac{\widetilde{F}^{(b)}_{B\to p_L;i}}{\sum_{i\in\{3,4,5,6\}} \widetilde{F}^{(b)}_{B\to p_L;i}}, \tag{16.8}$$

where $F^{(d)}_{B\to p_R;i}$ and $\widetilde{F}^{(d)}_{B\to p_L;i}$ correspond to the twist i contribution of the form

factors $F^{(d)}_{B\to p_R}$ and $\widetilde{F}^{(d)}_{B\to p_L}$, respectively. With the help of Eqs. (16.7) and (16.8), we obtain an estimate at which values of m_Ψ the OPE breaks down. The idea at this point is that once higher twist contributions become large, i.e. the ratios above become large, the twist corrections tend to dominate and the convergence is spoiled. We observe that for the form factor $F^{(d)}_{B\to p_R}(q^2)$ in the left panel of figure 16.5 the convergence breaks down for m_Ψ around 3 GeV, while the contributions to the form factor $\widetilde{F}^{(d)}_{B\to p_L}(q^2)$ are insensitive to this analysis. But for the benchmark value 2 GeV studied above, we see that the convergence of the OPE is still well established. Notice that we can not investigate values of m_Ψ larger than 6.2 GeV, since we cross the multi-hadron threshold t_+ at this point, which results into complex values of the z-parameter.
Similarly, we can perform this analysis for the (b)-operator, which we illustrate in figure 16.6.

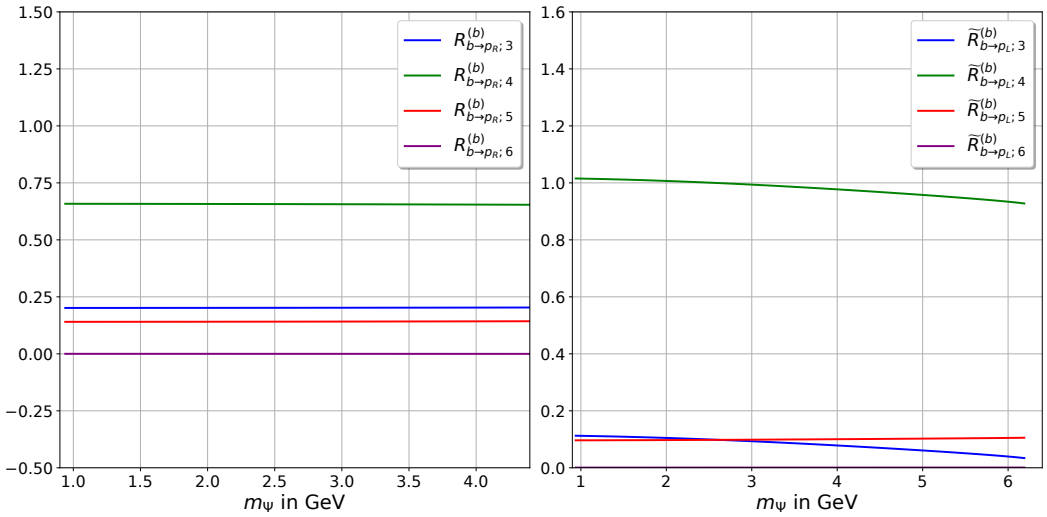

Figure 16.6: Plot for the ratios $R^{(b)}_{B\to p_R;i}$ and $\widetilde{R}^{(b)}_{B\to p_L;i}$ defined in Eqs. (16.7) and (16.8) after replacing $(d)\to(b)$ with respect to the dark fermion mass m_Ψ. The left panel contains the contributions from the form factor $F^{(b)}_{B\to p_R}$, while the right panel shows the ratios for the form factor $\widetilde{F}^{(b)}_{B\to p_L}$.

We conclude that the hierarchy in the twist expansion is well preserved for both form factors in the (b)-model, indicating that the expansion is convergent over the whole kinematically possible m_Ψ-range.

16.2 Numerical analysis: Branching fractions

In order to derive the decay width and branching fraction of the decay $B \to p\Psi$, we need to compute an expression for the matrix element $\mathcal{A}(B \to p\Psi)$ which enters both observables. This matrix element can be parameterised in terms of form factors of the transition $B \to p$ as discussed in Eq. (14.24)

$$\begin{aligned}\mathcal{A}_{(d)}(B^+ \to p\Psi) = G_{(d)} \Bigg[& F^{(d)}_{B\to p_R}(q^2)\bar{u}_{p,R}(P)u^c_\Psi(q) + F^{(d)}_{B\to p_L}(q^2)\bar{u}_{p,L}(P)u^c_\Psi(q) \\ & + \widetilde{F}^{(d)}_{B\to p_R}(q^2)\bar{u}_{p,R}(P)\frac{\not{q}}{m_p}u^c_\Psi(q) + \widetilde{F}^{(d)}_{B\to p_L}(q^2)\bar{u}_{p,L}(P)\frac{\not{q}}{m_p}u^c_\Psi(q)\Bigg] .\end{aligned} \tag{16.9}$$

With the help of the Dirac equation for a charge-conjugated field $\not{q}u^c_\Psi(q) = m_\Psi u^c_\Psi(q)$, we end up at the following expression:

$$\mathcal{A}_{(d)}(B^+ \to p\Psi) = G_{(d)}\bar{u}_p(P)\Big[A^{(d)} + B^{(d)}\gamma_5\Big]u^c_\Psi(q) , \tag{16.10}$$

where

$$A^{(d)} \equiv \frac{1}{2}\left[F^{(d)}_{B\to p_R}(q^2) + \frac{m_\Psi}{m_p}\widetilde{F}^{(d)}_{B\to p_R}(q^2)\right] + \frac{1}{2}\left[F^{(d)}_{B\to p_L}(q^2) + \frac{m_\Psi}{m_p}\widetilde{F}^{(d)}_{B\to p_L}(q^2)\right] \tag{16.11}$$

$$B^{(d)} \equiv -\frac{1}{2}\left[F^{(d)}_{B\to p_R}(q^2) + \frac{m_\Psi}{m_p}\widetilde{F}^{(d)}_{B\to p_R}(q^2)\right] + \frac{1}{2}\left[F^{(d)}_{B\to p_L}(q^2) + \frac{m_\Psi}{m_p}\widetilde{F}^{(d)}_{B\to p_L}(q^2)\right] \tag{16.12}$$

Next, Eq. (16.10) is to be inserted into the general relation for the decay width $\Gamma(B^+ \to p\Psi)$:

$$\Gamma_{(d)}(B^+ \to p\Psi) = \frac{1}{2m_B}\int \mathrm{d}\Pi\, |\mathcal{A}_{(d)}(B^+ \to p\Psi)|^2 . \tag{16.13}$$

For a two-body decay, the phase-space integration yields an analytic result in terms of the Källen function

$$\begin{aligned}\Gamma_{(d)}(B^+ \to p\Psi) &= \frac{1}{16\pi m_B^3}\lambda^{\frac{1}{2}}(m_B^2, m_p^2, m_\Psi^2)\, |\mathcal{A}_{(d)}(B^+ \to p\Psi)|^2 \\ &= |G_{(d)}|^2\, \frac{\lambda^{\frac{1}{2}}(m_B^2, m_p^2, m_\Psi^2)}{8\pi m_B^3}\left[|A^{(d)}|^2\Big(m_B^2 - (m_p - m_\Psi)^2\Big)\right. \\ &\quad \left. + |B^{(d)}|^2\Big(m_B^2 - (m_p + m_\Psi)^2\Big)\right] .\end{aligned} \tag{16.14}$$

During the derivation of Eq. (16.14), we use the on-shell conditions of the momenta, i.e. $(P+q)^2 = m_B^2$, $q^2 = m_\Psi^2$ and $P^2 = m_p^2$. Since we only encounter two of the four form factors in Eq. (14.24) in each version of the

model, it is possible to state the final expression for the decay width in terms of these form factors in the following form

$$\Gamma_{(d)}(B^+ \to p\Psi) = |G_{(d)}|^2 \Bigg\{ \left[\left(F^{(d)}_{B\to p_R}(m_\Psi^2) \right)^2 + \frac{m_\psi^2}{m_p^2} \left(\widetilde{F}^{(d)}_{B\to p_L}(m_\Psi^2) \right)^2 \right] \times \left(m_B^2 - m_p^2 - m_\Psi^2 \right) + 2m_\Psi^2 F^{(d)}_{B\to p_R}(m_\Psi^2) \widetilde{F}^{(d)}_{B\to p_L}(m_\Psi^2) \Bigg\} \frac{\lambda^{1/2}(m_B^2, m_p^2, m_\Psi^2)}{16\pi m_B^3} \,. \tag{16.15}$$

This is the final result for the desired decay width. Compared to the leading-twist three approximation in [202, 216], we additionally see that the form factor $\widetilde{F}^{(d)}_{B\to p_L}(q^2)$ contributes due to higher twist corrections. Since this form factor already appears for the (b)-model at leading-twist approximation (15.10), it is now possible to just replace $(d) \leftrightarrow (b)$ in order to obtain the relations in the second model under consideration.
The last observable of interest is the branching fraction of this decay, which can be obtained from Eq. (16.15) by inserting the form factors from Eqs. (15.14) and (F.41) to (F.43) and dividing this result by the total width of the B meson, i.e. is the inverse lifetime $\tau_{B^\pm}$, such that

$$\mathrm{Br}_{(d)}(B^+ \to p\Psi) = \Gamma_{(d)}(B^+ \to p\Psi) \cdot \tau_{B^\pm} \,. \tag{16.16}$$

Therefore, we use the $B^\pm$-lifetime $\tau_{B^\pm} = 1.638 \pm 0.004$ ps from [219].
With the expressions for the branching fractions in mind, we can next perform the numerical analysis. Since we were only able to obtain an estimate for the branching fraction to the leading-twist approximation in the original work [202], it was not immediately possible to make a statement about the convergence of the OPE in general. However, our analysis from last section, where we have included twist corrections up to twist six, allows us to study this convergence. We apply these insights in the following.
In figure 16.7, we show the branching fraction for the (d)-model including all contributions up to twist six after setting the four-fermion coupling $|G_{(d)}|^2$ to 10^{-13} GeV^{-4} and compare those to the leading twist contribution from [202, 216]. We observe good agreement between both computations in the m_Ψ-range up to 3 GeV, which is in accordance with our previous observation in figure 16.5 that around this particular value the higher twist contributions start to dominate and the convergence of the OPE is spoiled. The uncertainties on our twist six calculation are larger compared to the twist three evaluation since the error estimates on input parameters for the conformal and next-to-conformal expansion are large, especially for the parameter ξ_{10}, for which we assume a conservative error of 50% from [214]. But in general we confirm that the leading-twist result provides a good estimate for the branching fractions for the m_Ψ-range up to 3 GeV and agrees with our calculation including contributions up to twist six.

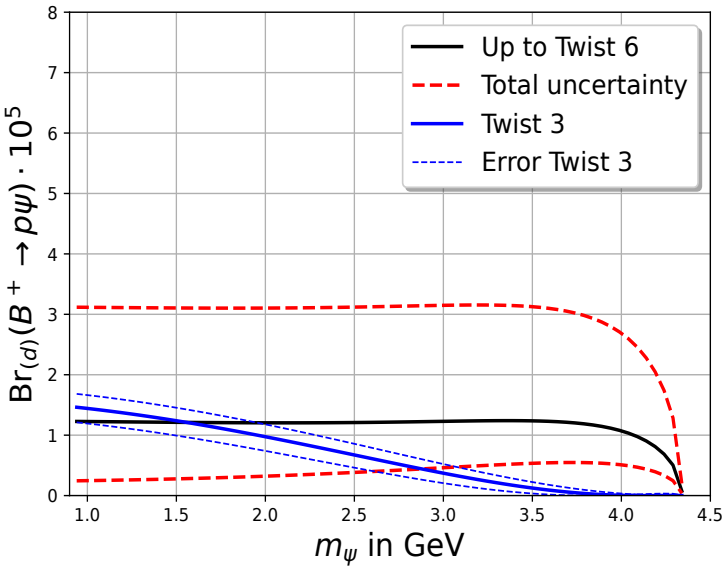

Figure 16.7: Branching fraction for the decay $B \to p\Psi$ in the (d)-model with respect to the dark matter particle mass m_Ψ. We set $|G_{(d)}|^2 = |G_{(b)}|^2 = 10^{-13}\,\mathrm{GeV}^{-4}$. The blue line with the blue dashed error band corresponds to the original twist three computation from [202], see also [216], while the black curve shows the computation including contributions up to twist six. The dashed red curves illustrate the uncertainty on this calculation, which is slightly enhanced due to the large errors on the input parameters from the conformal and next-to-conformal expansion.

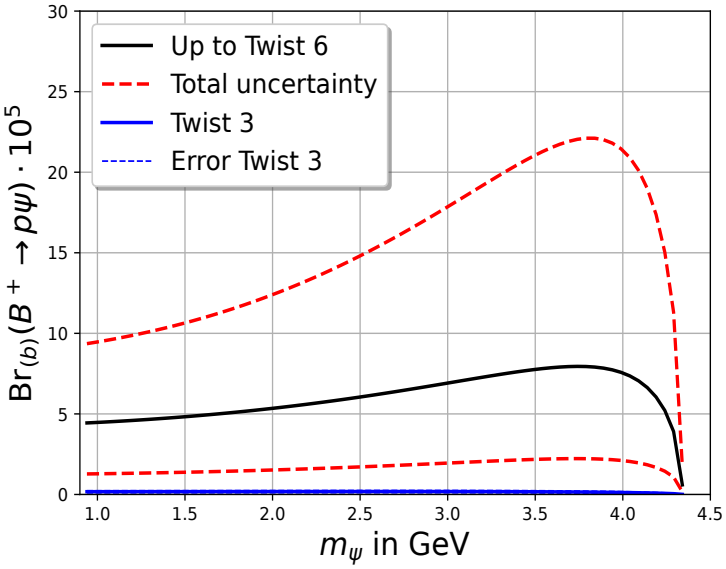

Figure 16.8: We show the same as in figure 16.7, but for the (b)-model instead. In comparison to the (d)-model, the leading-twist approximation is not sufficient here to allow for an reliable estimate of the branching fraction.

However, we observe a sizeable difference in the (b)-model between the twist-

three determination and the computation up to twist six contributions. The branching fraction gets enhanced around a factor of 20 and both calculations do not agree within the uncertainties. This difference can be traced back to the large twist four correction for both form factors in the model, see figures 16.3 and 16.4. In particular, the $\mathcal{T}_{2,4}$-contributions in the decomposition from Eq. (E.1) give a sizeable contribution and dominate this twist correction. These contributions introduce for the first time the parameter f_2^d, which is directly related to ξ_{10} via Eq. (16.5). In the (d)-model, we observe that these kind of contributions vanish during the computation. The uncertainties on the twist six computation are again large due to the same reason as for the (d)-model, in particular the upper bound uncertainty blows up for $m_\Psi > 3$ GeV. This indicates that the branching fraction becomes unreliable since $m_\Psi^2 \sim m_b^2$, which violates the key requirement for the light-cone expansion. Hence, we can conclude that the leading-twist analysis from [202] for this specific model is not sufficient and a higher twist analysis points out that the OPE does not show the typical hierarchy. But we see that the additional corrections push this particular decay into the sensitivity range of Belle-II, which lies around $3 \cdot 10^{-6}$.

Chapter 17

Conclusions

The Standard Model (SM) of particle physics has been tested to high precision in the past and provides the theoretical foundation to describe the visible sector in particle physics. Nevertheless, it is known for a long time that it does not account for the full physics of the universe. The quantisation of gravity or effects like dark matter, dark energy or neutrino masses are few examples which require different theoretical frameworks for their description. The theoretical study of dark matter is a long standing problem and led to a plethora of different approaches for its explanation, although we lack experimental confirmation for these theories so far.

In this work, we focus on the recently proposed dark matter model called B-Mesogenesis, which is of particular interest since it allows for a direct test in experiments like Belle-II. In its simplest version, a new dark matter particle Ψ, which is considered to be a fermionic antibaryon, is generated via CP-violating effects in the mixing of neutral $B^0_{d,s} - \bar{B}^0_{d,s}$-systems. With these assumptions, one observes baryon number violation in the visible SM sector, but in combination with the dark sector the baryon number is ultimately conserved.

In general, this model allows for many different decay modes. However, we have considered the decay mode $B \to p\Psi$ in more detail, where p denotes a proton. As a mediator particle between the visible sector and the dark sector, the model introduces a heavy scalar boson Y with a mass of the order of TeV, which we have integrated out to obtain an effective four-fermion interaction. In order to determine the branching fraction for this decay and test whether this decay is in the sensitivity range of Belle-II, we have investigated the $p \to B$ transition, which is related to the relevant $B \to p$ transition by a global phase. Similar to the work [213], we made use of light-cone sum rules to parameterise the long-distance effects in the operator product expansion in terms of the proton distribution amplitudes. We studied this model for two different versions (the (d)- and (b)-model), which are characterised by the operators describing the four-fermion interaction.

In the first part of this work, which led to the publication [202], we have determined the leading-twist contributions to the form factors of the $p \to B$ transition to leading order in α_s. This determination of the form factors has allowed us to calculate the corresponding branching fraction for the

$B \to p\Psi$ decay in the two realisations of this model and compare it to the sensitivity range of Belle-II. The branching fraction was in the end a function of the dark matter particle mass m_Ψ, for which we found a parameter range $0.94\,\text{GeV} \leq m_\Psi \leq 4.34\,\text{GeV}$ based on the kinematics of the two-particle decay. Moreover, we chose the effective couplings to be $|G_{(d)}|^2 = |G_{(b)}|^2 = 10^{-13}\,\text{GeV}^{-4}$. We have concluded from our analysis that the branching fraction for the (d)-model was well within the sensitivity range of Belle-II, while the branching fraction for the other model has turned out to be suppressed.

However, the leading-twist analysis in [202] did not allow to study the convergence of the OPE in general. Therefore, we have included higher twist corrections up to twist six into our analysis in a subsequent work in order to investigate the convergence of the OPE for both models and in order to see the effect of these corrections on the values of the branching fractions themselves. For the (d)-model, we were able to verify that the OPE shows good convergence in the parameter range $0.94\,\text{GeV} \leq m_\Psi \leq 3$ GeV in the sense that higher twist corrections tend to become smaller for increasing twist. For values of m_Ψ beyond 3 GeV, we have seen that the OPE expansion breaks down since higher twist contributions start to become the dominant contributions to the form factors. However, this is expected due to the light-cone condition $m_\Psi^2 \ll m_b^2$, which is not well satisfied in this parameter range. A corresponding analysis for the (b)-model has shown that the twist four contributions were dominating, but beyond twist four we confirmed the convergence of the OPE in the complete range $0.94\,\text{GeV} \leq m_\Psi \leq 4.34$ GeV.

Furthermore, we were able to make quantitative statements about the impact of higher twist corrections on our leading-twist analysis from [202]. For the (d)-model, we have observed that the branching fractions of the leading-twist analysis and the analysis including higher twist corrections were in good agreement in the convergence range. Interestingly, the (b)-model has shown a sizeable difference for the branching fractions up to a factor of 20. This pushes this particular model into the sensitivity range of Belle-II as well.

In the future, it might be interesting to include higher twist corrections for other decay channels as well. The original intention to focus on the particular decay $B \to p\Psi$ was that this analysis could be carried out in a similar way to [213] and provides a first reliable estimate for the branching fraction of these decays, since previous studies have only determined rather imprecise estimates. Furthermore, the developed techniques are easily applicable to other decay channels, which has been done in [216] to leading-twist accuracy after the publication of our results in [202]. The study of higher twist corrections in these channels is interesting as well, because they might turn out to be sizeable as in our case. Moreover, it might be interesting to analyse decays like $B \to \Delta\Psi \to p\pi\Psi$ or $B \to \Lambda\psi \to p\pi\Psi$, since the Belle-II experimental setup prefers three-particle final states over two-particle final states from a technical point of view. These decays can be computed with the methods explored in this work, albeit the distribution amplitudes for the Δ- and Λ-baryon are less known. But a leading-twist analysis might still be interesting as a rough estimate for the branching fraction. In addition to that

the ratio of the branching fraction of these decays with the branching fraction obtained here is independent of the couplings $G_{(d),(b)}$, which is another input parameter into our analysis besides the dark matter particle mass m_Ψ. In our case, we deal with this issue by normalising our branching fractions with respect to the order of magnitude of the involved couplings. However, the ratio would be directly independent of the couplings and provide a better way to study the dependence on the particle mass m_Ψ.

Appendix

Appendix A

Useful formulae and transformations

A.1 Feynman integrals and loop integrals in dimensional regularisation

In this chapter, we aim to collect the formulae which are relevant for the computation of loop integrals in project I and II. In order to combine several denominators of the propagators in the correlation functions, we make use of the Feynman parameterisation. For a general number n of denominators raised to powers k_1 to k_n, we have the relation [133]

$$\frac{1}{D_1^{k_1}...D_n^{k_n}} = \frac{\Gamma(k_1+...+k_n)}{\Gamma(k_1)...\Gamma(k_n)} \int_0^1 \mathrm{d}x_1 ... \int_0^1 \mathrm{d}x_n \frac{\delta(1-\sum_{i=1}^n x_i) x_1^{k_1-1}...x_n^{k_n-1}}{(\sum_{i=1}^n x_i D_i)^{\sum_{i=1}^n k_i}}\,, \tag{A.1}$$

where $\mathrm{Re}(k_i) > 0$ for $1 \leq i \leq n$ and we use the Γ-function above. In case we encounter a linear propagator like in applications of SCET or HQET, we make use of the slightly modified form

$$\frac{1}{D_1^{k_1} D_2^{k_2}} = \frac{\Gamma(k_1+k_2)}{\Gamma(k_1)\Gamma(k_2)} \int_0^\infty \mathrm{d}\lambda \frac{\lambda^{k_1}}{\Big[\lambda D_1 + D_2\Big]^{k_1+k_2}} \tag{A.2}$$

if D_1 corresponds to the linear propagator. In the case that we need to deal with a linear propagator and several quadratic propagators, we first combine the quadratic propagators according to Eq. (A.1) and use Eq. (A.2) subsequently.
After we combine all contributions and regularise the integrals with dimensional regularisation, we obtain phase-space integrals of the form

$$\int \frac{\mathrm{d}^d k}{(2\pi)^d} \frac{k^{2a}}{(k^2-\Delta)^b}\,, \tag{A.3}$$

which we can rewrite into the closed form expression

$$\int \frac{\mathrm{d}^d k}{(2\pi)^d} \frac{k^{2a}}{(k^2-\Delta)^b} = i(-1)^{a-b} \frac{1}{(4\pi)^{d/2}} \frac{1}{\Delta^{b-a-\frac{d}{2}}} \frac{\Gamma(a+d/2)\Gamma(b-a-d/2)}{\Gamma(b)\Gamma(d/2)} \,. \tag{A.4}$$

We employ this relation extensively in this work. Particularly interesting are tensor integrals, which can be expressed in terms of Eq. (A.4)

$$\int \frac{\mathrm{d}^d k}{(2\pi)^d} \frac{k^\mu k^\nu}{(k^2-\Delta)^b} = \frac{1}{d} g^{\mu\nu} \int \frac{\mathrm{d}^d k}{(2\pi)^d} \frac{k^2}{(k^2-\Delta)^b} \,. \tag{A.5}$$

Integrals with an odd number of tensors in the numerator like

$$\int \frac{\mathrm{d}^d k}{(2\pi)^d} \frac{k^\mu}{(k^2-\Delta)^b} \tag{A.6}$$

vanish due to the antisymmetry of the integrand. Furthermore, the special case $\Delta = 0$ is of importance since this leads to scaleless integrals in dimensional regularisation.

A.2 Anomalous dimensions

In this section, we summarise the analytic expressions for the anomalous dimensions of the observables that we encounter in this work. We start with the anomaly coefficient for the SCET-II observables transverse-momentum resummation and jet-veto resummation. For p_T-resummation, the NLO anomaly coefficient d_1 vanishes, $d_1^{q,g} = 0$. The NNLO coefficient reads [78, 79]

$$d_2^q = \left(\frac{808}{27} - 28\zeta_3\right) C_F C_A - \frac{224}{27} C_F T_F n_f \tag{A.7}$$

$$d_2^g = \left(\frac{808}{27} - 28\zeta_3\right) C_A^2 - \frac{224}{27} C_A T_F n_f \,. \tag{A.8}$$

For p_T-veto, the NLO anomaly coefficient is the same as for p_T. However the NNLO anomaly coefficients $d_2^{q,g}$ are only known semi-analytically and can be found for instance in [160] for the quark case. The gluon case is obtained via Casimir scaling.
The cusp anomalous dimensions are observable independent. They read for the quark case

$$\Gamma_0^q = 4C_F \tag{A.9}$$

$$\Gamma_1^q = \left(\frac{268}{9} - \frac{4\pi^2}{3}\right) C_F C_A - \frac{80}{9} C_F T_F n_f \tag{A.10}$$

and for the gluon case we need to replace $C_F \to C_A$.
Finally, we turn our attention to the non-cusp anomalous dimensions. At NLO, they coincide for all observables under consideration here and are $\gamma_0^q =$

$-3C_F$ and $\gamma_0^g = -\beta_0$ for the quark and gluon case at NLO, respectively. The NNLO non-cusp anomalous dimensions are the same for p_T-resummation and p_T-veto

$$\gamma_1^q = \left(-\frac{3}{2} + 2\pi^2 - 24\zeta_3 \right) C_F^2 + \left(-\frac{961}{54} - \frac{11\pi^2}{6} + 26\zeta_3 \right) C_F C_A + \left(\frac{130}{27} + \frac{2\pi^2}{3} \right) C_F T_F n_f \tag{A.11}$$

$$\gamma_1^g = \left(-\frac{692}{27} + \frac{11\pi^2}{18} + 2\zeta_3 \right) C_A^2 + \left(\frac{256}{27} - \frac{2\pi^2}{9} \right) C_A T_F n_f + 4\, C_F T_F n_f \,, \tag{A.12}$$

while these quantities become for beam thrust

$$\gamma_1^q = \left(-\frac{3}{2} + 2\pi^2 - 24\zeta_3 \right) C_F^2 + \left(-\frac{1769}{54} - \frac{11\pi^2}{9} + 40\zeta_3 \right) C_F C_A + \left(\frac{242}{27} + \frac{4\pi^2}{9} \right) C_F T_F n_f \tag{A.13}$$

$$\gamma_1^g = \left(-\frac{1096}{27} + \frac{11\pi^2}{9} + 16\zeta_3 \right) C_A^2 + \left(\frac{368}{27} - \frac{4\pi^2}{9} \right) C_A T_F n_f + 4\, C_F T_F n_f \,. \tag{A.14}$$

A.3 Splitting functions in momentum space

Here, we aim to collect the expressions for the leading order and next-to-leading order splitting functions. We expand these splitting functions similarly to Eq. (4.18) in α_s:

$$P_{i\leftarrow j}(x) = \sum_{k=0}^{\infty} \left(\frac{\alpha_s}{4\pi} \right)^{k+1} P_{i\leftarrow j}^{(k)}(x) \tag{A.15}$$

For the leading order splitting function, we observe contributions from four different channels

$$P_{q\leftarrow q}^{(0)} = 2\, C_F \cdot p_{q\leftarrow q}(x) + 3\, C_F \delta(1-x) \,, \tag{A.16}$$

$$P_{q\leftarrow g}^{(0)} = 2\, T_F \cdot p_{q\leftarrow g}(x) \,, \tag{A.17}$$

$$P_{q\leftarrow g}^{(0)} = 2\, C_F \cdot p_{g\leftarrow q}(x) \,, \tag{A.18}$$

$$P_{q\leftarrow g}^{(0)} = 2\, C_A \cdot p_{g\leftarrow g}(x) + \beta_0\, \delta(1-x) \,. \tag{A.19}$$

We have defined the splitting function kernels

$$p_{q\leftarrow q}(x) = (1+x^2) \cdot \left[\frac{1}{1-x} \right]_+ \,, \tag{A.20}$$

$$p_{q\leftarrow g}(x) = ((1-x)^2 + x^2) \,, \tag{A.21}$$

$$p_{g\leftarrow q}(x) = \frac{1}{x}(1 + (1-x)^2) \,, \tag{A.22}$$

$$p_{g\leftarrow g}(x) = 2 \cdot \left[\frac{1}{1-x} \right]_+ + \frac{2}{x} - 4 + 2x - 2x^2 \,. \tag{A.23}$$

For the NLO splitting function, we obtain for the $q \to q$ channel

$$\begin{aligned}
P^{(1)}_{q\leftarrow q}(x) =& 4\left[\frac{C_F}{2}\left(1+x^2\right)\left[\frac{1}{1-x}\right]_+\left[\left(\frac{67}{9}-\frac{\pi^2}{3}\right)C_A-\frac{20T_Fn_f}{9}\right]\right.\\
&+\delta(1-x)\left[\left(\frac{1}{8}+\frac{\pi^2}{6}\right)\beta_0C_F+C_FC_A\left(\frac{1}{4}-3\zeta(3)\right)\right.\\
&\left.+C_F^2\left(6\zeta(3)+\frac{3}{8}-\frac{\pi^2}{2}\right)\right]+C_F\left(\frac{(1+x^2)\ln(x)}{2(1-x)}-x+1\right)\beta_0\\
&+C_FC_A\left(\frac{(1+x^2)\ln(x)^2}{2(1-x)}+3(1-x)+(x+1)\ln(x)\right)\\
&+C_F^2\Bigg(-\Bigg(\frac{(1+x^2)\left(2\ln(1-x)+\frac{3}{2}\right)\ln(x)}{1-x}+5(1-x)\\
&+\frac{1}{2}(1+x)\ln(x)^2+\frac{1}{2}(7x+3)\ln(x)\Bigg)\Bigg)\\
&+C_FT_F\Bigg(-\frac{56x^2}{9}+\left(\frac{8x^2}{3}+5x+1\right)\ln(x)+6x+\frac{20}{9x}\\
&\left.-(1+x)\ln(x)^2-2\Bigg)\right]. \qquad \text{(A.24)}
\end{aligned}$$

For the $g \to q$ channel, we get

$$\begin{aligned}
P^{(1)}_{q\leftarrow g}(x) =& C_FT_F\left[8x^2(\ln(x)(\ln(x)+2)+5)-2\ln(x)^2-2\ln(x)\right.\\
&-\frac{4}{3}(2(x-1)x+1)\left(-3\ln(1-x)^2+6\ln(x)\ln(1-x)+\pi^2\right)\\
&\left.-2(x-1)(8x\ln(1-x)+2\ln(x)(\ln(x)+2)+29)-30\right]\\
&+4\,C_AT_F\Bigg[-2(2x(x+1)+1)(\mathrm{Li}_2(-x)+\ln(x)\log(x+1))\\
&+\frac{2}{9}x^2(66\ln(x)-109)-\frac{2\pi^2x}{3}+25x+\frac{20}{9x}+(-2(x-1)x-1)\\
&\times\ln(1-x)^2-3\ln(x)^2+9\ln(x)+2(x-1)(2x\ln(1-x)\\
&-(\ln(x)-4)\ln(x))-2\Bigg], \qquad \text{(A.25)}
\end{aligned}$$

where the function $H_{n_1,\ldots,n_j}(x)$ denote the harmonic polylogarithms. The splitting functions for the two gluon channels read

$$\begin{aligned}
P^{(1)}_{g\leftarrow q}(x) =& -4\,C_F^2\left[\frac{1}{2}(7x+5)+\frac{((1-x)^2+1)\ln(1-x)^2}{x}+\Big(\frac{3\left((1-x)^2+1\right)}{x}\right.\\
&\left.+2x\Big)\ln(1-x)+\frac{1}{2}(2-x)\ln(x)^2-\frac{1}{2}(7x+4)\ln(x)\right]
\end{aligned}$$

$$
\begin{aligned}
&+ 4\,C_F C_A \left[- \frac{((x+1)^2+1)\left(-2\mathrm{Li}_2(-x) - 2\ln(x)\log(x+1) - \frac{\pi^2}{6}\right)}{x} \right.\\
&+ \frac{1}{18}\left(88x^2 - x + 56\right) - \frac{1}{3}\left(8x^2 + 15x + 36\right)\ln(x) + (x+2)\ln(x)^2\\
&+ 2x\ln(1-x) + \frac{11}{3}\left(x + \frac{((1-x)^2+1)\left(\ln(1-x) + \frac{5}{3}\right)}{x}\right)\\
&\left. + \frac{((1-x)^2+1)\left(\ln(1-x)^2 - 2\ln(x)\ln(1-x) - \frac{\pi^2}{6} - \frac{101}{18}\right)}{x} \right]\\
&- \frac{16}{3}\,C_F T_F n_f \left[x + \frac{((1-x)^2+1)\left(\ln(1-x) + \frac{5}{3}\right)}{x} \right], \qquad \text{(A.26)}
\end{aligned}
$$

$$
\begin{aligned}
P^{(1)}_{g\leftarrow g}(x) = {}& C_A^2 \left[\frac{4\left(\frac{67}{9} - \frac{\pi^2}{3}\right)\left(x^2 - x + 1\right)^2}{x} \left[\frac{1}{1-x}\right]_+ + \frac{8\left(x^2 - x + 1\right)^2}{x}\left(\frac{\ln(x)}{2}\right.\right.\\
&\left. - 2\ln(1-x)\right)\ln(x)\left[\frac{1}{1-x}\right]_+ - \frac{8\left(x^2 + x + 1\right)^2}{x(x+1)}\Big(- 2\mathrm{Li}_2(-x)\\
&+ \frac{\ln(x)^2}{2} - 2\ln(x)\log(x+1) - \frac{\pi^2}{6}\Big) + \frac{44}{3}\Big(- \frac{13x^2}{6} - \frac{3(1-x)}{2}\\
&+ \frac{13}{6x} + (x+1)\ln(x)\Big) + 4\Big(\frac{277x^2}{18} - \frac{4}{3}\left(11x^2 + 9\right)\ln(x)\\
&+ 19(1-x) - \frac{277}{18x} + 4(x+1)\ln(x)^2\Big) + 4\left(3\zeta(3) + \frac{8}{3}\right)\delta(1-x)\Big]\\
&+ C_A T_F n_f \left[- \frac{80\left(x^2 - x + 1\right)^2}{9x}\left[\frac{1}{1-x}\right]_+ - \frac{16}{3}\Big(- \frac{13x^2}{6}\right.\\
&\left. - \frac{3(1-x)}{2} + \frac{13}{6x} + (x+1)\ln(x)\Big) - \frac{16}{3}\delta(1-x)\right]\\
&+ 4\,C_F T_F n_f \left[\frac{20x^2}{3} - \delta(1-x) + 8x + \frac{4}{3x} - 2(x+1)\ln(x)^2\right.\\
&\left. - 2(5x+3)\ln(x) - 16\right]. \qquad \text{(A.27)}
\end{aligned}
$$

A.4 Laplace transformation of logarithms in momentum space

In this section, we are going to collect the Laplace transformation for the logarithms in momentum space, which are relevant to compare the momentum space results for the observable beam thrust in [124, 125] to the results

in chapter 8. Starting with the highest logarithm, we observe

$$\int_0^\infty \mathrm{d}x \left[\frac{\Theta(x)\log^3(x)}{x}\right]_+ e^{x\mu^2\tau} = \frac{1}{4}\log^4(\mu^2\bar{\tau}) + \frac{\pi^2}{4}\log^2(\mu^2\bar{\tau}) + 2\zeta(3)\log\big(\mu^2\bar{\tau}\big) + \frac{3\pi^4}{80}\,, \tag{A.28}$$

where we define $x := t/\mu^2$ and $\bar{\tau} = \tau e^{\gamma_E}$. Notice that τ represents the Laplace variable in this context. Next, the squared logarithm transforms as follows:

$$\int_0^\infty \mathrm{d}x \left[\frac{\Theta(x)\log^2(x)}{x}\right]_+ e^{x\mu^2\tau} = -\frac{1}{3}\log^3(\mu^2\bar{\tau}) - \frac{\pi^2}{6}\log\big(\mu^2\bar{\tau}\big) - \frac{2}{3}\zeta(3)\,. \tag{A.29}$$

Finally, for the single logarithm and no logarithm we see

$$\int_0^\infty \mathrm{d}x \left[\frac{\Theta(x)\log(x)}{x}\right]_+ e^{x\mu^2\tau} = \frac{1}{2}\log^2(\mu^2\bar{\tau}) + \frac{\pi^2}{12}\,, \tag{A.30}$$

$$\int_0^\infty \mathrm{d}x \left[\frac{\Theta(x)}{x}\right]_+ e^{x\mu^2\tau} = -\log\big(\mu^2\bar{\tau}\big)\,. \tag{A.31}$$

In order to compare the renormalised matching kernels for beam thrust from chapter 8 to [124, 125], we need to correct the results for the constant terms which do not contain any logarithms.

A.5 Borel transformation

In this section, we introduce the Borel transformation, which is an essential tool to make the sum rules more convergent. Generally, the Borel transformation of a function $g(-q^2) \equiv g(Q^2)$ in the unphysical spacelike region $q^2 < 0$ is defined to be

$$\hat{\mathcal{B}}_{M^2} = \lim_{Q^2,n\to\infty,\, Q^2/n=M^2} \frac{(Q^2)^{n+1}}{n!}\left(-\frac{\mathrm{d}}{\mathrm{d}Q^2}\right)^n g(Q^2) \equiv g(M^2)\,. \tag{A.32}$$

The advantage of this additional transformation is to suppress the continuum and higher excited or multihadron states in the hadronic spectral density $\rho^{\text{hadr.}}$ and to remove possible substraction terms originating from the contour integral in the dispersion relation, as investigated in section 11.2. This ensures that the dependence on the quark-hadron duality gets reduced.
For special functions $g(Q^2)$, it is possible to state a closed form for the transformation in Eq. (A.32). In the case of polynomials in Q^2, we see that

$$\hat{\mathcal{B}}_{M^2}(Q^2)^k = 0, \quad k \geq 0. \tag{A.33}$$

This is for instance the reason why we rewrite the scalar product $P \cdot q$ in Eq. (15.9), since we obtain simple polynomials in $(P+q)^2$ which vanish during the Borel transformation.
The second frequently used transformation is connected to the denominators:

$$\hat{\mathcal{B}}_{M^2} \frac{1}{(s+Q^2)^k} = \frac{1}{(k-1)!} \Big(\frac{1}{M^2}\Big)^{k-1} e^{-s/M^2} \tag{A.34}$$

In our case, we deal with $k = 1, 2, 3$ and $Q^2 = -(P+q)^2$.

Appendix B

Remaining results

B.1 Jet-veto resummation in x-space

Here, we show the remaining results for the refactorised matching kernels for p_T-veto in x-space. Similarly to the plots in section 8.2, the large dots indicate numbers from our numerical approach, while the small dots, which approximately look like a solid line are semi-analytical expressions extracted from [171, 173]. The uncertainties on our computation are included, albeit not visible on the scales presented here. Notice that the results from [171, 173] do not state any uncertainties on their calculation, although some results are given in form of a grid in the variable x in the small R-expansion. We know that factorisation works in the limit $R \ll 1$, but it has been proven in many applications that results in the range $R \sim 1$ also reproduce experimental data very well [159]. Therefore, we choose the values $R = \{0.2, 0.5, 0.8\}$ in our setup.

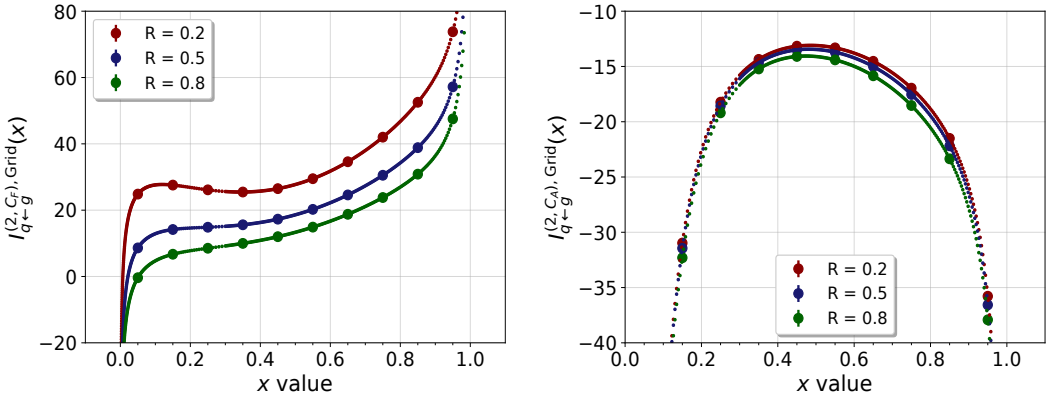

Figure B.1: Grid contribution of the refactorised matching kernel for the $g \to q$ channel for $R = \{0.2, 0.5, 0.8\}$.

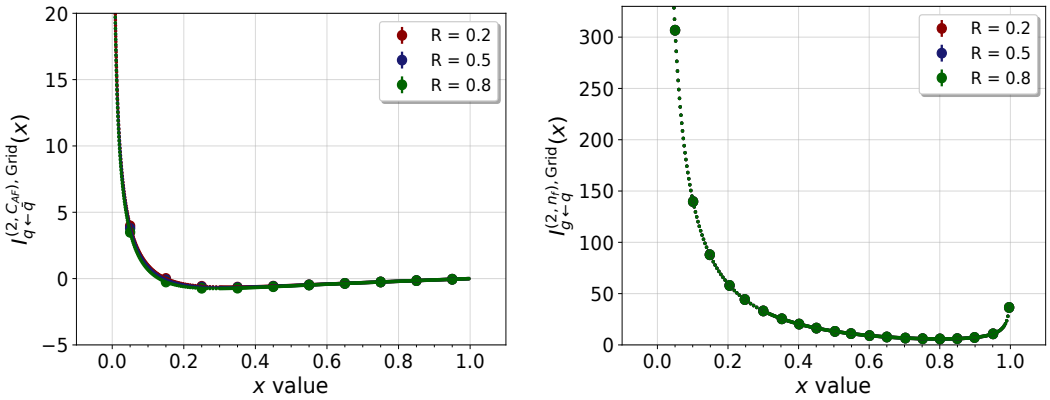

Figure B.2: Grid contribution of the refactorised matching kernel for the $\bar{q} \to q$ channel and for the $C_F T_F n_f$ colour structure of the $q \to g$ channel for $R = \{0.2, 0.5, 0.8\}$.

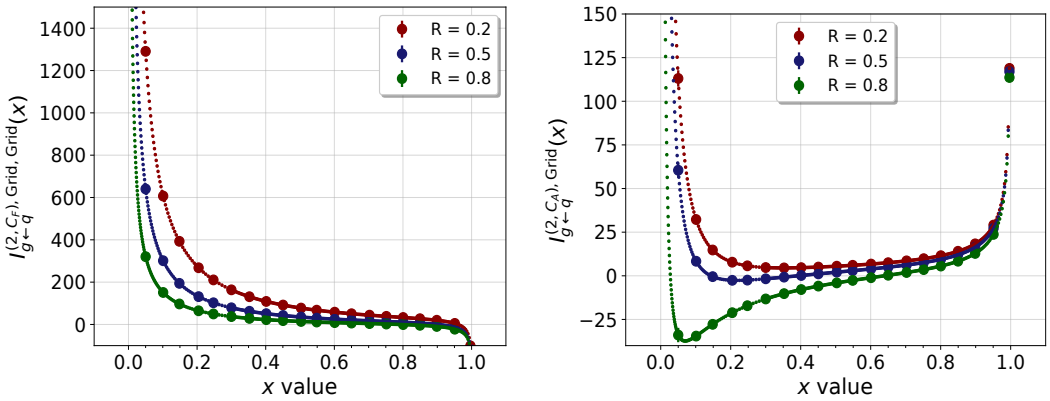

Figure B.3: Grid contribution of the refactorised matching kernel for the two remaining colour structures C_F^2 and $C_F C_A$ of the $q \to g$ channel for $R = \{0.2, 0.5, 0.8\}$.

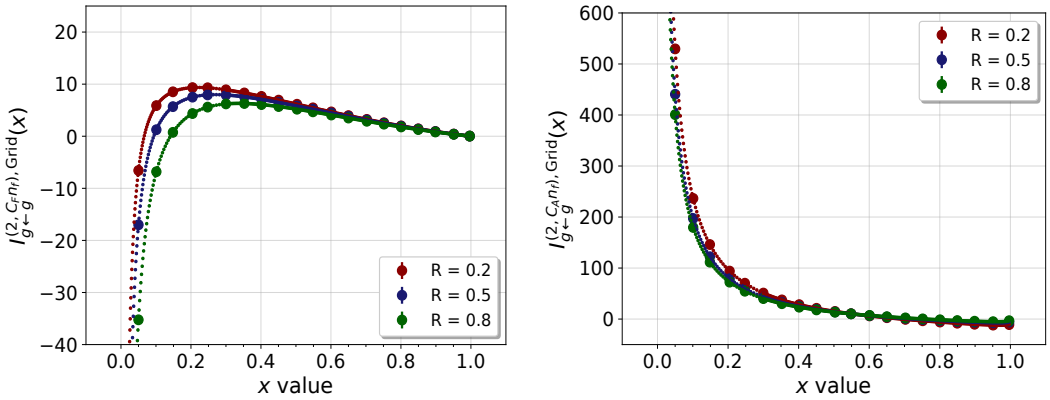

Figure B.4: Grid contribution of the refactorised matching kernel for the colour structures $C_F T_F n_f$ and $C_A T_F n_f$ of the $g \to g$ channel for $R = \{0.2, 0.5, 0.8\}$.

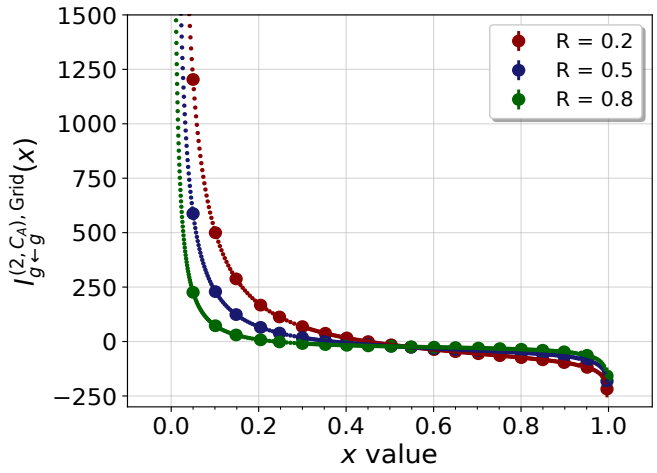

Figure B.5: Grid contribution of the refactorised matching kernel for the C_A^2 colour structure of the $g \to g$ channel for $R = \{0.2, 0.5, 0.8\}$.

It turns out that our results agree very well with the extraction from [171, 173], in particular for complicated colour structures like the C_A^2 structure in the $g \to g$ channel. Notice that also the small and large x-limit are in agreement, which are known to be difficult to resolve due to the singular behaviour in $x \to \{0, 1\}$.

B.2 Jet-veto resummation in N-space

Additionally, we collect the results for Mellin space for the off-diagonal quark channel and both gluon channels. The results for the quark channels have been published in [122] for three values of the jet radius $R = \{0.2, 0.5, 0.8\}$, which are commonly used in the literature. We extend this analysis to the gluon channels here and moreover include two additional values for R, namely $R = \{0.4, 1.0\}$.

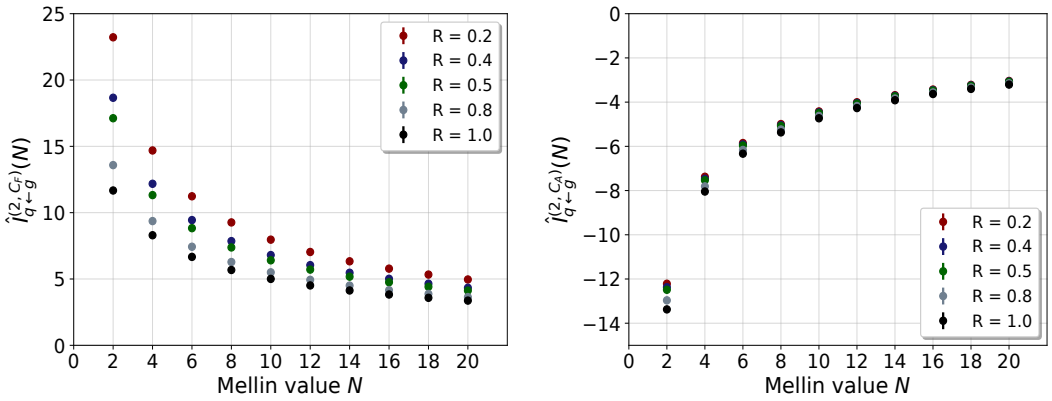

Figure B.6: Refactorised matching kernel for the $g \to q$ channel for $R = \{0.2, 0.4, 0.5, 0.8, 1.0\}$. The uncertainties are shown here on each point, but not visible.

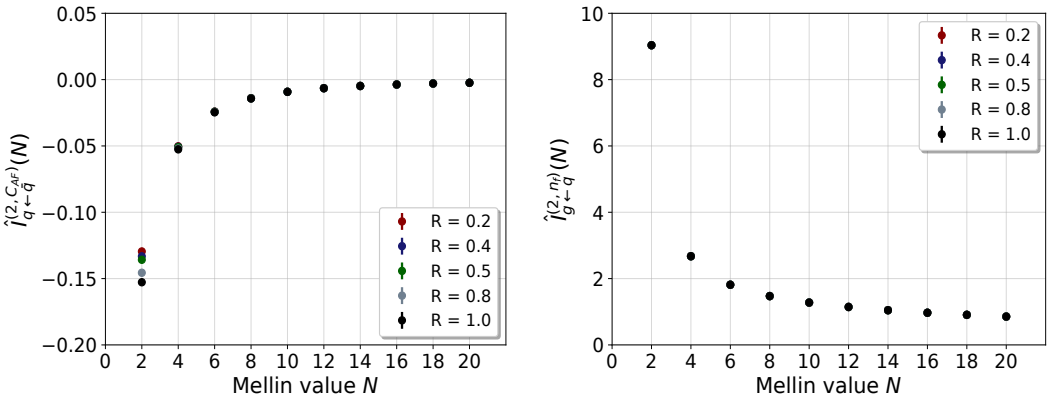

Figure B.7: Refactorised matching kernel for the $\bar{q} \to q$ channel and for the $C_F T_F n_f$ colour structure of the $q \to g$ channel for $R = \{0.2, 0.4, 0.5, 0.8, 1.0\}$ in Mellin space. The uncertainties are shown here on each point, but not visible.

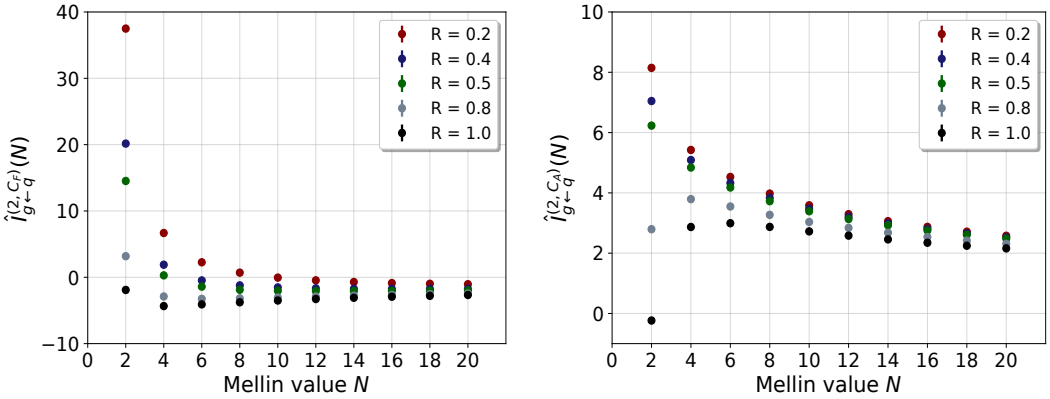

Figure B.8: Refactorised matching kernel for the two remaining colour structures C_F^2 and $C_F C_A$ of the $q \to g$ channel for $R = \{0.2, 0.4, 0.5, 0.8, 1.0\}$ in Mellin space. The uncertainties are shown here on each point, but not visible.

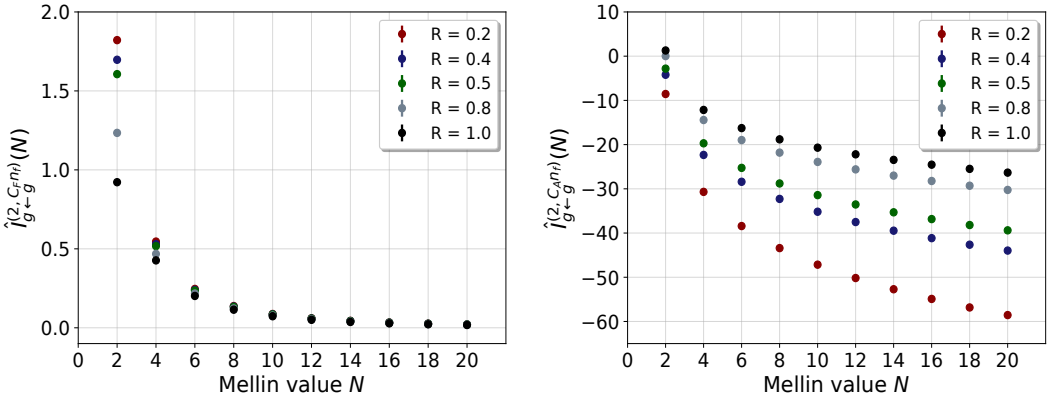

Figure B.9: Refactorised matching kernel for the colour structures $C_F T_F n_f$ and $C_A T_F n_f$ of the $g \to g$ channel for $R = \{0.2, 0.4, 0.5, 0.8, 1.0\}$ in N-space. The uncertainties are shown here on each point, but not visible.

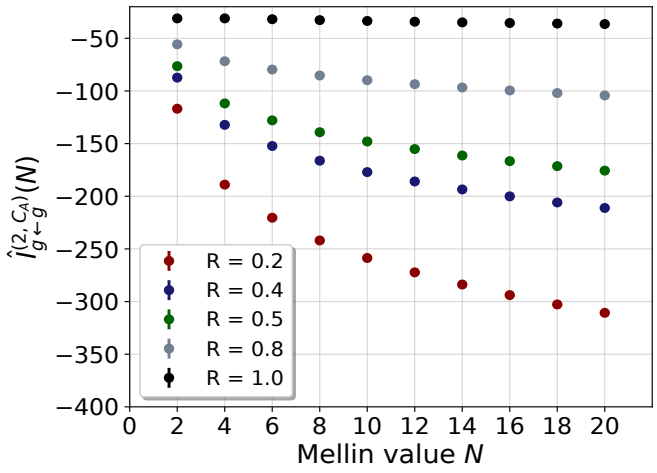

Figure B.10: Refactorised matching kernel for the C_A^2 colour structure of the $g \to g$ channel for $R = \{0.2, 0.4, 0.5, 0.8, 1.0\}$ in N-space. The uncertainties are shown here on each point, but not visible.

These results can in principle be compared to our x-space computation or to the results from [171, 173] after performing a Mellin transformation on those according to Eq. (3.9). We observe perfect agreement within the uncertainties with these results. Notice that the uncertainties on our calculation are shown in all plots, but not visible at the scales presented there. Since the factorisation for this observable is usually stated in x-space, it is necessary to perform an additional inverse Mellin transformation on these results to end up in momentum space. This procedure introduces yet another unknown systematic error on our evaluation. But since our x-space setup provides good results with reasonable uncertainties, we rather make use of this framework in order to calculate observables with factorisation theorems in x-space and employ our Mellin space framework for observables defined in N-space.

B.3 DIS-angularities in x-space

Here, we are going to state the remaining contributions for the class of observables DIS-angularities. We cover three different angularity values $A = \{-1, 0, 0.5\}$ and therefore show the applicability of our framework for all possible values of n since angularity values less or greater than 0 (n values less or greater than 1) require different treatment, as we have discussed in chapter 5 and as we will further investigate in the next chapter C. We show the x-independent coefficients for the diagonal gluon channel from Eq. (8.4) first, whereas we have listed the corresponding quark coefficients in section 8.4. Before we do that, we investigate the NNLO gluon non-cusp anomalous dimension $\gamma_1^{g,B}$ and compare it to the results from [176].

$\gamma_1^{g,B}$	$A=-1$		$A=0$		$A=0.5$	
	[176]	this work	[176]	this work	[176]	this work
$C_F T_F n_f$	4	4	4	4	4	4
$C_A T_F n_f$	7.05	7.0490(26)	9.24	9.2432(33)	12.45	12.4480(296)
C_A^2	−16.93	−16.9324(470)	−9.30	−9.2964(523)	1.94	1.9286(2918)

Table B.1: NNLO quark non-cusp anomalous dimensions for the three different angularity values $A = \{-1, 0, 0.5\}$. We compare the results obtained here to [176].

We observe very good agreement between our computation and [176] within the uncertainties. Notice that the errors on the angularity value $A = 0.5$ are worse compared to the other two angularities, as have we elaborated in section 8.4. This effect can be traced back to logarithmic and square-root divergences inside the measurement function, which require a more advanced version of the computational parameterisation than the one we have implemented so far.
Next, we state the x-independent coefficients c_{-1}^g to c_3^g, which constitute a new prediction.

c_{-1}^g	$A=-1$	$A=0$	$A=0.5$
$C_F T_F n_f$	0	0	0
$C_A T_F n_f$	6.3202(41)	−1.2379(53)	−17.4870(877)
C_A^2	−7.0118(1115)	−14.8952(922)	11.9223(7150)

Table B.2: x-independent coefficients in front of the δ-distribution for the colour structures of the diagonal gluon channel. We extract these coefficients for three different angularity values $A = \{-1, 0, 0.5\}$.

c_0^g	$A=-1$	$A=0$	$A=0.5$
$C_F T_F n_f$	0	0	0
$C_A T_F n_f$	−0.1494(34)	3.9098(33)	8.1559(197)
C_A^2	51.7720(627)	35.0279(523)	17.1790(1946)

Table B.3: We show the same as in table B.2, but for the $\left[\frac{1}{1-x}\right]_+$-distribution.

c_1^g	$A=-1$	$A=0$	$A=0.5$
$C_F T_F n_f$	0	0	0
$C_A T_F n_f$	$-11.8519(16)$	$-8.8889(12)$	$-5.9259(27)$
C_A^2	$-31.9426(348)$	$-9.7011(274)$	$9.6170(424)$

Table B.4: We show the same as in table B.2, but for the $\left[\frac{\ln(1-x)}{1-x}\right]_+$-distribution.

c_2^g	$A=-1$	$A=0$	$A=0.5$
$C_F T_F n_f$	0	0	0
$C_A T_F n_f$	4.7407(1)	2.6667(1)	1.1852(1)
C_A^2	$-13.0371(72)$	$-7.3334(48)$	$-3.2592(30)$

Table B.5: We show the same as in table B.2, but for the $\left[\frac{\ln^2(1-x)}{1-x}\right]_+$-distribution.

c_3^g	$A=-1$	$A=0$	$A=0.5$
$C_F T_F n_f$	0	0	0
$C_A T_F n_f$	0	0	0
C_A^2	14.2222(4)	8 ± 20^{-4}	3.5555(1)

Table B.6: We show the same as in table B.2, but for the $\left[\frac{\ln^3(1-x)}{1-x}\right]_+$-distribution.

We see once more that these coefficients are connected to the corresponding quark coefficients via Casimir scaling. Moreover, the value $A=0$ corresponds to beam thrust and we observe perfect agreement with the previous results within the uncertainties.

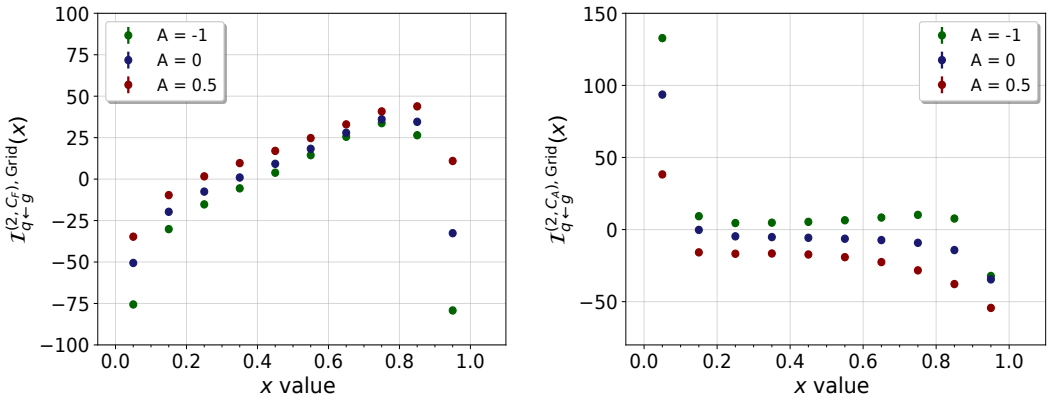

Figure B.11: Refactorised matching kernel for the off-diagonal quark channel for $A = \{-1, 0, 0.5\}$. The uncertainties are shown here on each point, but not visible.

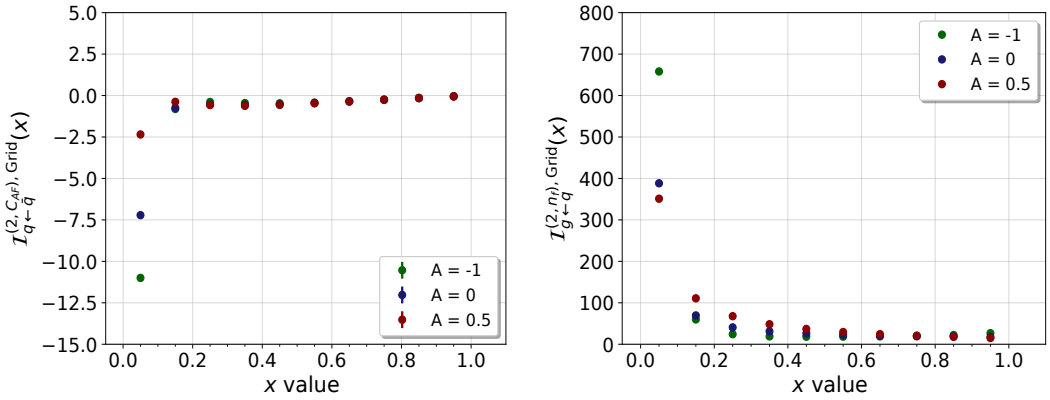

Figure B.12: Refactorised matching kernel for the $\bar{q} \to q$ channel and the $C_F T_F n_f$ colour structure of the $q \to g$ channel for $A = \{-1, 0, 0.5\}$. The uncertainties are shown here on each point, but not visible.

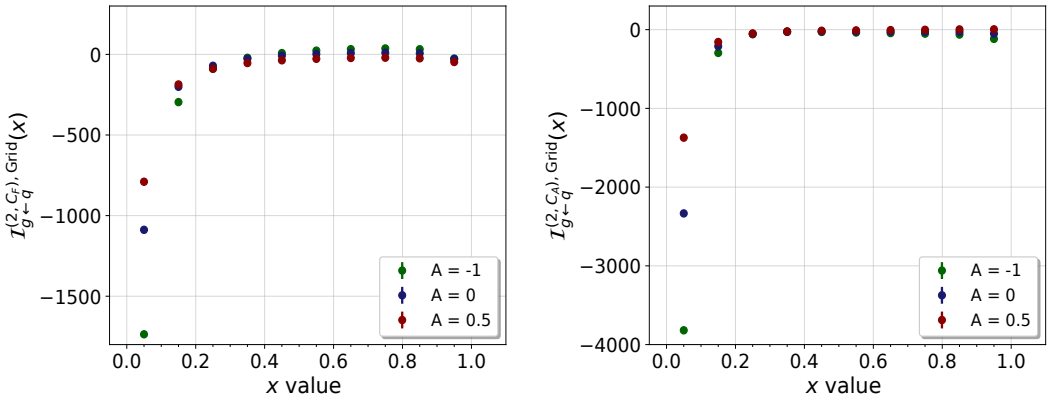

Figure B.13: Refactorised matching kernel for the remaining contributions of the off-diagonal gluon channel for $A = \{-1, 0, 0.5\}$. The uncertainties are shown here on each point, but not visible.

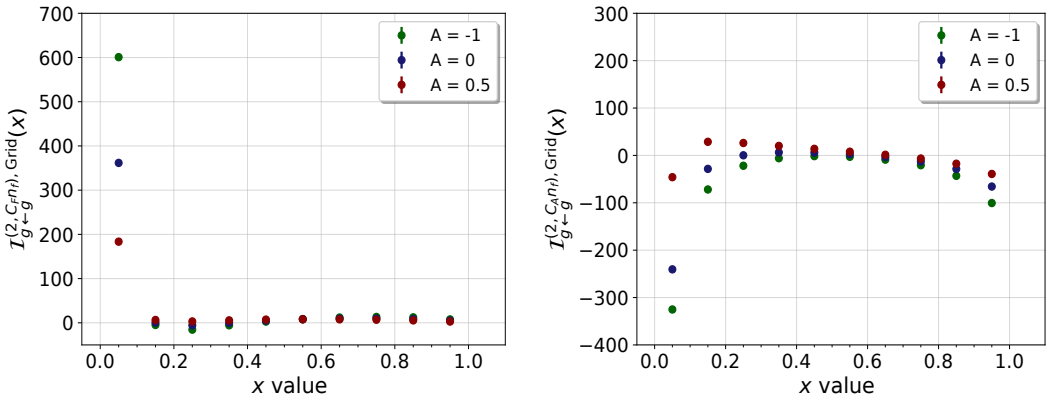

Figure B.14: Refactorised matching kernel for the colour structures $C_F T_F n_f$ and $C_A T_F n_f$ of the $g \to g$ channel for $A = \{-1, 0, 0.5\}$. The uncertainties are shown here on each point, but not visible.

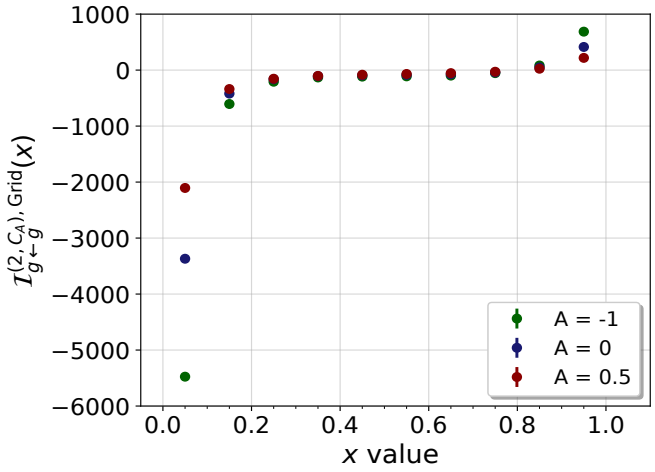

Figure B.15: Refactorised matching kernel for the colour structure C_A^2 of the $g \to g$ channel for $A = \{-1, 0, 0.5\}$. The uncertainties are shown here on each point, but not visible.

These grid contributions constitute a new prediction for the angularity values $A = \{-1, 0.5\}$ and $A = 0$ serves as a check of our approach since we can compare these numbers to our beam thrust computation. We conclude that these results are in perfect agreement within the uncertainties. These uncertainties are also shown in the plots above, albeit not visible on the scales presented above. For further discussion regarding the error estimates for this observable, we refer to section 8.4 for more details.

Appendix C

Steps to derive singularities in monomial form in all sectors

In this section, we will explicitly elaborate all steps for each matching kernel and colour structure in the RR contributions in order to derive completely factorised singularities in monomial form. We assume that we have already performed the remapping of the integrals to the unit hypercube such that the integration domain is always between 0 and 1. Moreover, we work in computational parameterisation.
In general, the decomposition is the same in our momentum-space and Mellin-space approach. We state the substitutions, which are necessary to obtain the monomial forms, the divergences in each sector and the factor ρ denoting factors which we have to remove from the measurement function in order to keep it finite and non-zero. In particular, we show the factor ρ for three different cases ($n \geq 1, 0 < n < 1, n = 0$) since they require different treatment. Generally, the allowed range for the parameter n is $n \in [0, \infty)$. The methods which are required to arrive at singularities in monomial form have been discussed in chapter 5. On the one hand, we use sector decomposition steps (SD), on the other hand we use the selector functions introduced in Eq. (5.74). In the case of the observable DIS-angularities, we preserve the n-dependence, which requires a modification of the measurement function, see chapter 5 for more details. There, we have introduced the additional substitutions in Eqs. (5.76) and (5.77)

Region	Substitution	SD	ρ
T_I	$b \to g^n;\ t \to s^{1-n}$	$s \to g \cdot \tilde{s}$	$g^{\frac{1-n^2}{2}} \cdot \tilde{s}^{\frac{(1-n)^2}{2}}$
		$g \to s \cdot \tilde{s}$	$s^{\frac{1-n^2}{2}}$
T_{II}	$t \to s^{n-1}$	$a \to g \cdot s$	$g^{(1-n)}$
		$s \to g \cdot a$	-

Table C.1: List of additional substitutions to ensure that the measurement function is still finite and non-zero in the case where we study a class of observables with unfixed parameter n.

These additional steps need to be performed if it is indicated in the following tables.
The implementation of the various contributions in this chapter is straightforward. The complete expressions for each colour structure in each channel are related to the timelike splitting functions from [135, 136, 138] via the crossing procedure described in section 5.2.4. We state each contribution separately in terms of invariant masses. For a direct implementation, the invariant masses need to be expressed in terms of the parameterisation from Eq. (5.23) and subsequently in the computational parameterisation from chapter 7. This expression is exactly the matrix element in the RR NNLO master formula in Eq. (5.49) if we remove the factors of q_T in the denominator (which we already integrated analytically to obtain the master formula). Then, we can perform the integrations indicated in the master formula.

C.1 The $\mathcal{I}^{0,(2)}_{q\leftarrow q}$ matching kernel

The first matching kernel under consideration is the diagonal $q \to q$ channel. As already discussed in much detail, we encounter four different colour structures in this case, in particular the $C_F T_F$, the $C_F T_F n_f$, C_F^2 and $C_F C_A$ structures. Contrary to the jet function case [50], there occurs an additional structure $C_F T_F$ which becomes apparent for spacelike splitting functions. For timelike splitting functions, the $C_F T_F$ and $C_F T_F n_f$ structures coincide and only yield a factor of two. We follow the same conventions as above, i.e. the different regions are defined by the substitutions:

Region	Abbreviation	Substitution
Region A	R_A	-
Region B	R_B	$a \to 1/a$
Region C	R_C	$b \to 1/b$
Region D	R_D	$a \to 1/a$ & $b \to 1/b$

Table C.2: List of the various substitutions in order to define the specific regions. We perform the remapping such that we only work on the unit hypercube if we perform numerical integrations.

$C_F T_F$ - structure

We start this discussion with the $C_F T_F$ colour structure. The complete structure is given by

$$\mathbb{P}^{C_F T_F}_{q\to\bar{q}qq^*} = \mathbb{P}^{(I_1)}_{C_F T_F} + \mathbb{P}^{(I_2)}_{C_F T_F} + \mathbb{P}^{(I_3)}_{C_F T_F}\,, \tag{C.1}$$

which we further decompose according to

$$\begin{aligned}
\mathbb{P}^{(I_1)}_{C_F T_F} &= \frac{\left((s_{13}+2s_{23})x_1 + (s_{13}-2s_{12})\right)^2}{(s^B_{123})^2 s^2_{13}(1-x_1)^2} \quad \left[-\frac{4xP_-}{2}\right], \\
\mathbb{P}^{(I_2)}_{C_F T_F} &= \frac{-4P_-}{s^B_{123}s_{13}\bar{x}_1} \quad \left[\bar{x}_2^2 + \bar{x}^2 - \epsilon\,\bar{x}_1^2\right], \\
\mathbb{P}^{(I_3)}_{C_F T_F} &= \frac{4xP_-}{(s^B_{123})^2}\left[-\frac{1-2\epsilon}{2}\right].
\end{aligned} \tag{C.2}$$

In our implementation, we combine these three pieces immediately, since the matrix element is simple enough to integrate it directly. We show them here separately to illustrate that they are related to the $C_F T_F n_f$ in Eq. (5.55) via the exchange $2 \to 3$. In table C.3, we denote how to decompose each sector in order to derive at singularities in monomial form for this particular colour structure.

Region	Substitution	Divergences	$\rho_{n\geq 1}$	$\rho_{n<1}$	$\rho_{n=0}$
R_A	-	s_5	-	-	-
R_B SD1	$a \to t \cdot b$	b, s_5	$t^{\frac{1-n}{2}}$	$t^{\frac{1-n}{2}}$	$t^{1/2}$
R_B SD2	$b \to t \cdot a$	a, s_5	-	-	-
R_C	-	s_5	-	-	-
R_D	-	s_5	-	-	-

Table C.3: All sectors for the $C_F T_F$ colour structure in the $q \to q$ channel. The factor ρ denotes the terms which needs to be removed from the measurement function. "SD" stands for sector decomposition and indicates that Region B needs an additional sector decomposition step in order to disentangle overlapping divergences in the matrix element.

$C_F T_F n_f$ - structure

Next, we discuss the $C_F T_F n_f$ colour structure. For this contribution, the matrix element and the measurement function exhibit the symmetry that the expressions in region A and D coincide, as well as in region B and C. We have already studied the complete structure and its decomposition in Eqs. (5.54) and (5.55) respectively.

Region	Substitution	Divergences	$\rho_{n\geq 1}$	$\rho_{n<1}$	$\rho_{n=0}$
R_A	$\{a,b\}\to\{u,v\}\to\{u_t,v_t\}$	x_{12},u_t,s_5	$p^{\frac{1-n}{2}}$	$p^{\frac{1-n}{2}}$	-
R_B	$\{a,b\}\to\{u,v\}\to\{u_t,v_t\}$	x_{12},u_t,s_5	$p^{\frac{1-n}{2}}$	$p^{\frac{1-n}{2}}$	-

Table C.4: All sectors for the $C_F T_F n_f$ colour structure in the $q\to q$ channel.

p corresponds to the variable a expressed in terms of $\{u_t,v_t\}$, $p=1-\left(1-(1-u_t)^2\right)\left(1-v_t^4\right)^4$. Notice that this contribution is the first colour structure which possesses a divergence in x_{12}. In our x-space framework, this divergence does not explicitly occur in our `pySecDec` code since we use Eq. (5.53) to rewrite this singularity into distributions. Contrary to that, we explicitly integrate over the x_{12}-divergence in the N-space formalism, because we perform additionally the Mellin transformation. Therefore, the singularity in x_{12} occurs explicitly.

C_F^2 - structure

In chapter 5, we have introduced the C_F^2 colour structure as the first example where sector decomposition steps are necessary. We have mentioned the complete expression as well as its decomposition in Eqs. (5.59), (5.60), (5.61) and (5.62). Therefore, we can now proceed to state all sectors individually:

Component	Region	Substitution	Divergences	$\rho_{n\geq 1}$	$\rho_{n<1}$	$\rho_{n=0}$
$\mathbb{P}^{(I_1)}_{C_F^2}$	R_A SD1	$a \to t \cdot b$	x_{12}, b, t, s_5	$t^{\frac{1-n}{2}} \cdot b^{(1-n)}$	T_I	$t^{1/2}$
	R_A SD2	$b \to t \cdot a$	x_{12}, a, t, s_5	T_{II}	-	-
	R_B SD1	$a \to t \cdot b$	x_{12}, b, t, s_5	$t^{\frac{1-n}{2}}$	$t^{\frac{1-n}{2}}$	$t^{1/2}$
	R_B SD2	$b \to t \cdot a$	x_{12}, a, t, s_5	-	-	-
$\mathbb{P}^{(I_{23})}_{C_F^2}$	R_A	-	s_5	$a^{\frac{1-n}{2}}$	$a^{\frac{1-n}{2}}$	-
	R_B SD1	$a \to t \cdot b$	b, s_5	$t^{\frac{1-n}{2}}$	$t^{\frac{1-n}{2}}$	$t^{1/2}$
	R_B SD2	$b \to t \cdot a$	a, s_5	$a^{\frac{1-n}{2}}$	$a^{\frac{1-n}{2}}$	-
$\mathbb{P}^{(I_4)}_{C_F^2}$	R_A SD1	$a \to t \cdot b$	x_{12}, b, s_5	$t^{\frac{1-n}{2}} \cdot b^{(1-n)}$	$t^{\frac{1-n}{2}}$	$t^{1/2}$
	R_A SD2	$b \to t \cdot a$	x_{12}, a, t, s_5	T_{II}	-	-
	R_B SD1	$a \to t \cdot b$	x_{12}, b, t, s_5	$t^{\frac{1-n}{2}}$	$t^{\frac{1-n}{2}}$	$t^{1/2}$
	R_B SD2	$b \to t \cdot a$	x_{12}, a, t, s_5	-	-	-
	R_C SD1	$a \to t \cdot b$	x_{12}, s_5	$t^{\frac{1-n}{2}}$	$t^{\frac{1-n}{2}}$	$t^{1/2}$
	R_C SD2	$b \to t \cdot a$	x_{12}, s_5	-	-	-
	R_D SD1	$a \to t \cdot b$	x_{12}, b, t, s_5	$t^{\frac{1-n}{2}} \cdot b^{(1-n)}$	T_I	$t^{1/2}$
	R_D SD2	$b \to t \cdot a$	x_{12}, a, s_5	$a^{(1-n)}$	-	-

Table C.5: All sectors for the C_F^2 contributions from Eq. (5.61). Sector decomposition steps (SD).

Moreover, we decompose the contributions from the identical splitting function in the following way:

Component	Region	Substitution	Divergences	$\rho_{n\geq 1}$	$\rho_{n<1}$	$\rho_{n=0}$
$\mathbb{P}^{(I_{12}),(I_3),(I_4)}_{id}$	R_A	$\{a,b\}\to\{u,v\}\to\{u_t,v_t\}$	u_t, s_5	$p^{\frac{1-n}{2}}$	$p^{\frac{1-n}{2}}$	-
	$\mathcal{S}_1\cdot R_B$	$\{a,b\}\to\{u,v\}\to\{u_t,v_t\}$	u_t, s_5	$p^{\frac{1-n}{2}}$	$p^{\frac{1-n}{2}}$	-
	$\mathcal{S}_2\cdot R_B$ SD1	$a\to t\cdot b$	b, s_5	$t^{\frac{1-n}{2}}$	$t^{\frac{1-n}{2}}$	$t^{1/2}$
	$\mathcal{S}_2\cdot R_B$ SD2	$b\to t\cdot a$	a, s_5	-	-	-
	R_C	$\{a,b\}\to\{u,v\}\to\{u_t,v_t\}$	u_t, s_5	$p^{\frac{1-n}{2}}$	$p^{\frac{1-n}{2}}$	-
	R_D	$\{a,b\}\to\{u,v\}\to\{u_t,v_t\}$	u_t, s_5	$p^{\frac{1-n}{2}}$	$p^{\frac{1-n}{2}}$	-

Table C.6: All sectors for the identical contribution of the C_F^2 colour structure. The selector functions are defined according to chapter 5

$C_F C_A$ - structure

Finally, we focus on the $C_F C_A$ colour structure. We have already discussed its general structure and the decomposition of the pure $C_F C_A$ contributions in Eqs. (5.69), (5.70) and (5.71) as the first example for the introduction of selector functions. We state all sectors in the following table.

Component	Region	Substitution	Divergences	$\rho_{n\geq 1}$	$\rho_{n<1}$	$\rho_{n=0}$
$\mathbb{P}^{(I_1)}_{C_F C_A}$	R_A, R_B	$\{a,b\} \to \{u,v\} \to \{u_t, v_t\}$	x_{12}, u_t, s_5	$p^{\frac{1-n}{2}}$	$p^{\frac{1-n}{2}}$	-
$\mathbb{P}^{(I_2)}_{C_F C_A}$	$R_A - R_D$	$\{a,b\} \to \{u,v\} \to \{u_t, v_t\}$	x_{12}, s_5	$p^{\frac{1-n}{2}}$	$p^{\frac{1-n}{2}}$	-
$\mathbb{P}^{(I_3)}_{C_F C_A}$	R_A	$\{a,b\} \to \{u,v\} \to \{u_t, v_t\}$	x_{12}, u_t, b, s_5	$p^{\frac{1-n}{2}}$	$p^{\frac{1-n}{2}}$	-
	R_B	$\{a,b\} \to \{u,v\} \to \{u_t, v_t\}$	x_{12}, u_t, b, s_5	$p^{\frac{1-n}{2}}$	$p^{\frac{1-n}{2}}$	-
	$\mathcal{S}_1 \cdot R_C$	$\{a,b\} \to \{u,v\} \to \{u_t, v_t\}$	x_{12}, u_t, b, s_5	$p^{\frac{1-n}{2}}$	$p^{\frac{1-n}{2}}$	-
	$\mathcal{S}_2 \cdot R_C$ SD1	$a \to t \cdot b$	x_{12}, b, t, s_5	$t^{\frac{1-n}{2}}$	$t^{\frac{1-n}{2}}$	$t^{1/2}$
	$\mathcal{S}_2 \cdot R_C$ SD2	$b \to t \cdot a$	x_{12}, a, t, s_5	-	-	-
	$\mathcal{S}_1 \cdot R_D$	$\{a,b\} \to \{u,v\} \to \{u_t, v_t\}$	x_{12}, u_t, b, s_5	$p^{\frac{1-n}{2}}$	$p^{\frac{1-n}{2}}$	-
	$\mathcal{S}_2 \cdot R_D$ SD1	$a \to t \cdot b$	x_{12}, b, t, s_5	$t^{\frac{1-n}{2}} \cdot b^{(1-n)}$	T_I	$t^{1/2}$
	$\mathcal{S}_2 \cdot R_D$ SD2	$b \to t \cdot a$	x_{12}, a, t, s_5	T_{II}	-	-
$\mathbb{P}^{(I_5)}_{C_F C_A}$	R_A	$\{a,b\} \to \{u,v\} \to \{u_t, v_t\}$	x_{12}, u_t, s_5	$p^{\frac{1-n}{2}}$	$p^{\frac{1-n}{2}}$	-
	R_B	$\{a,b\} \to \{u,v\} \to \{u_t, v_t\}$	x_{12}, u_t, s_5	$p^{\frac{1-n}{2}}$	$p^{\frac{1-n}{2}}$	-
	R_C	$\{a,b\} \to \{u,v\} \to \{u_t, v_t\}$	x_{12}, u_t, b, s_5	$p^{\frac{1-n}{2}}$	$p^{\frac{1-n}{2}}$	-
	R_D SD1	$a \to t \cdot b$	x_{12}, b, s_5	$t^{\frac{1-n}{2}} \cdot b^{(1-n)}$	$t^{\frac{1-n}{2}}$	$t^{1/2}$
	$\mathcal{S}_1 \cdot R_D$ SD2	$\{a,b\} \to \{u,v\} \to \{u_t, v_t\}$	x_{12}, u_t, t, s_5	$p^{(1-n)}$	-	-
	$\mathcal{S}_2 \cdot R_D$ SD2	$b \to t \cdot a$	x_{12}, a, t, s_5	-	T_I	-
$\mathbb{P}^{(I_6)}_{C_F C_A}$	R_A	$\{a,b\} \to \{u,v\} \to \{u_t, v_t\}$	x_{12}, s_5	$p^{\frac{1-n}{2}}$	$p^{\frac{1-n}{2}}$	-
	R_B SD1	$b \to t \cdot a$	x_{12}, a, s_5	-	-	-
	R_B SD2	$a \to t \cdot b$	x_{12}, b, s_5	$t^{\frac{1-n}{2}}$	$t^{\frac{1-n}{2}}$	$t^{1/2}$
	R_C	$\{a,b\} \to \{u,v\} \to \{u_t, v_t\}$	x_{12}, s_5	$p^{\frac{1-n}{2}}$	$p^{\frac{1-n}{2}}$	-
	R_D SD1	$a \to t \cdot b$	x_{12}, b, t, s_5	$t^{\frac{1-n}{2}} \cdot b^{(1-n)}$	T_I	$t^{1/2}$
	R_D SD2	$b \to t \cdot a$	x_{12}, a, s_5	$a^{(1-n)}$	-	-

Table C.7: All sectors for the $C_F C_A$ contributions from Eq. (5.71). Sector decomposition steps (SD) and selector functions are defined according to chapter 5.

C.2 The $\mathcal{I}^{0,(2)}_{q\leftarrow g}$ matching kernel

C_FT_F - structure

Similar to the C_FT_F colour structure in the $\mathcal{I}^{0,(2)}_{q\leftarrow q}$ matching kernel, the $\mathcal{I}^{0,(2)}_{q\leftarrow g}$ kernel does not exhibit any divergences in the x_{12} variable. In this structure, we observe two colour structures, namely the C_FT_F and C_AT_F colour structures. The complete C_FT_F contribution for the $g \to q$ channel is given by

$$\mathbb{P}^{C_FT_F}_{g\to gqq^*} = \frac{C_FT_F}{-\bar{\epsilon}} \left[\mathbb{P}^{(I_1)}_{C_FT_F} + \mathbb{P}^{(I_{23})}_{C_FT_F} + \mathbb{P}^{(I_4)}_{C_FT_F}\right] (1-x)\,. \tag{C.3}$$

Notice that the factor $\bar{\epsilon}$ originates from the crossing as described in section 5.2.4. Since we cross a gluon into the initial state, we need to account for its different polarisation compared to an initial-state quark.
The different components in Eq. (C.3) are given by:

$$\begin{aligned}
\mathbb{P}^{(I_1)}_{C_FT_F} &= \frac{-4x_2P_-}{s_{12}s_{23}x_1}\left[\left\{x^2+x_2^2-\epsilon(x_1^2-x_1+1)+\epsilon^2x_1\right\}\right],\\
\mathbb{P}^{(I_2)}_{C_FT_F} &= \frac{4xP_-}{(s^B_{123})^2}\left[2\epsilon(1-\epsilon)\right],\\
\mathbb{P}^{(I_3)}_{C_FT_F} &= \frac{4xP_-\left(s_{12}^2+s_{23}^2\right)}{(s^B_{123})^2s_{12}s_{23}}\left[(1-\epsilon)^2\right],\\
\mathbb{P}^{(I_{4A})}_{C_FT_F} &= \frac{4P_-}{s^B_{123}s_{12}x_1}\left[\bar{x}^3+x_2\bar{x}_2x-\epsilon(x_1^2-x_1+1)\bar{x}+\epsilon^2x_1(x-x_2)\right],\\
\mathbb{P}^{(I_{4B})}_{C_FT_F} &= \frac{4P_-}{s^B_{123}s_{23}x_1}\left[\bar{x}_2^3+x_2x\bar{x}-\epsilon(x_1^2-x_1+1)\bar{x}_2-\epsilon^2x_1(x-x_2)\right].
\end{aligned} \tag{C.4}$$

In our setup, we group these contributions again according to the power of the invariant mass s^B_{123} in the denominator. Hence, we investigate I_1 separately, while we combine $I_{23} = I_2 + I_3$ and $I_4 = I_{4A} + I_{4B}$.
The following table lists the individual sectors for each contribution in Eq. (C.3). As we have discussed in chapter 5, we need to perform a series of sector decomposition steps and implement selector functions in order to obtain completely factorised singularities in each sector.

Component	Region	Substitution	Divergences	$\rho_{n\geq 1}$	$\rho_{n<1}$	$\rho_{n=0}$
$\mathbb{P}^{(I_1)}_{C_F T_F}$	$\mathcal{S}_1 \cdot R_A$	$\{a,b\} \to \{u,v\} \to \{u_t, v_t\}$	b, u_t, s_5	$p^{\frac{1-n}{2}}$	$p^{\frac{1-n}{2}}$	-
	$\mathcal{S}_2 \cdot R_A$ SD1	$a \to t \cdot b$	b, t, s_5	$t^{\frac{1-n}{2}} \cdot b^{(1-n)}$	T_I	$t^{1/2}$
	$\mathcal{S}_2 \cdot R_A$ SD2	$b \to t \cdot a$	a, t, s_5	T_{II}	-	-
	R_B	$\{a,b\} \to \{u,v\} \to \{u_t, v_t\}$	u_t, b, s_5	$p^{\frac{1-n}{2}}$	$p^{\frac{1-n}{2}}$	-
	$\mathcal{S}_1 \cdot R_C$	$\{a,b\} \to \{u,v\} \to \{u_t, v_t\}$	u_t, s_5	$p^{\frac{1-n}{2}}$	$p^{\frac{1-n}{2}}$	-
	$\mathcal{S}_2 \cdot R_C$ SD1	$a \to t \cdot b$	t, b, s_5	$t^{\frac{1-n}{2}}$	$t^{\frac{1-n}{2}}$	$t^{1/2}$
	$\mathcal{S}_2 \cdot R_C$ SD2	$b \to t \cdot a$	a, s_5	-	-	-
	R_D	$\{a,b\} \to \{u,v\} \to \{u_t, v_t\}$	u_t, s_5	$p^{\frac{1-n}{2}}$	$p^{\frac{1-n}{2}}$	-
$\mathbb{P}^{(I_{23})}_{C_F T_F}$	R_A	$\{a,b\} \to \{u,v\} \to \{u_t, v_t\}$	u_t, s_5	$p^{\frac{1-n}{2}}$	$p^{\frac{1-n}{2}}$	-
	R_B	$\{a,b\} \to \{u,v\} \to \{u_t, v_t\}$	u_t, s_5	$p^{\frac{1-n}{2}}$	$p^{\frac{1-n}{2}}$	-
	$\mathcal{S}_1 \cdot R_C$	$\{a,b\} \to \{u,v\} \to \{u_t, v_t\}$	u_t, s_5	$p^{\frac{1-n}{2}}$	$p^{\frac{1-n}{2}}$	-
	$\mathcal{S}_2 \cdot R_C$ SD1	$a \to t \cdot b$	b, s_5	$t^{\frac{1-n}{2}}$	$t^{\frac{1-n}{2}}$	$t^{1/2}$
	$\mathcal{S}_2 \cdot R_C$ SD2	$b \to t \cdot a$	a, s_5	-	-	-
	R_D	$\{a,b\} \to \{u,v\} \to \{u_t, v_t\}$	u_t, s_5	$p^{\frac{1-n}{2}}$	$p^{\frac{1-n}{2}}$	-
$\mathbb{P}^{(I_4)}_{C_F T_F}$	$\mathcal{S}_1 \cdot R_A$	$\{a,b\} \to \{u,v\} \to \{u_t, v_t\}$	u_t, b, s_5	$p^{\frac{1-n}{2}}$	$p^{\frac{1-n}{2}}$	-
	$\mathcal{S}_2 \cdot R_A$ SD1	$a \to t \cdot b$	b, t, s_5	$t^{\frac{1-n}{2}} \cdot b^{(1-n)}$	T_I	$t^{1/2}$
	$\mathcal{S}_2 \cdot R_A$ SD2	$b \to t \cdot a$	a, t, s_5	T_{II}	-	-
	R_B	$\{a,b\} \to \{u,v\} \to \{u_t, v_t\}$	u_t, b, s_5	$p^{\frac{1-n}{2}}$	$p^{\frac{1-n}{2}}$	-
	$\mathcal{S}_1 \cdot R_C$	$\{a,b\} \to \{u,v\} \to \{u_t, v_t\}$	u_t, s_5	$p^{\frac{1-n}{2}}$	$p^{\frac{1-n}{2}}$	-
	$\mathcal{S}_2 \cdot R_C$ SD1	$a \to t \cdot b$	b, t, s_5	$t^{\frac{1-n}{2}}$	$t^{\frac{1-n}{2}}$	$t^{1/2}$
	$\mathcal{S}_2 \cdot R_C$ SD2	$b \to t \cdot a$	a, s_5	-	-	-
	R_D	$\{a,b\} \to \{u,v\} \to \{u_t, v_t\}$	u_t, s_5	$p^{\frac{1-n}{2}}$	$p^{\frac{1-n}{2}}$	-

Table C.8: All sectors for the $C_F T_F$ colour structure in the $g \to q$ channel. We introduce the selector functions $\mathcal{S}_{1,2}$, which have been defined in Eq. (5.74).

C_AT_F - structure

The C_AT_F colour structure requires a more complicated decomposition. In particular, parts of the C_FT_F structure from before and the $C_FT_Fn_f$ structure from the diagonal $q \to q$ channel enter here. Thus, the complete C_AT_F structure is given by

$$\mathbb{P}^{C_AT_F}_{g\to gqq^*} = \frac{C_AT_F}{-\bar{\epsilon}}\Bigg[\mathbb{P}^{(I_3)}_{C_AT_F} + \mathbb{P}^{(I_5)}_{C_AT_F} + \mathbb{P}^{(I_6)}_{C_AT_F} - \frac{1}{2}\left\{\mathbb{P}^{(I_1)}_{C_FT_F} + \mathbb{P}^{(I_4)}_{C_FT_F}\right\} - (1-\epsilon)\left\{\mathbb{P}^{(I_1)}_{C_AT_F} + \mathbb{P}^{(I_2)}_{C_AT_F}\right\}\Bigg](1-x)\,. \tag{C.5}$$

As we have mentioned before, the factors $\bar{\epsilon}$ are introduced during the crossing procedure. Furthermore, we state the decomposition of the pure C_AT_F contributions:

$$\begin{aligned}
\mathbb{P}^{(I_{3A})}_{C_AT_F} &= \frac{4P_-}{s_{12}s_{13}\bar{x}_1}\left[\bar{x}_1x_2x + x\bar{x} - \frac{(1-\epsilon)}{2}\Big(1+\bar{x}_1^3\Big)\right],\\
\mathbb{P}^{(I_{3B})}_{C_AT_F} &= \frac{4P_-}{s_{13}s_{23}x_1\bar{x}_1}\left[x_1\bar{x}_2x + \bar{x}_1x_2x + \frac{(1-\epsilon)}{2}\Big(x_1^3-\bar{x}_1^3\Big)\right],\\
\mathbb{P}^{(I_5)}_{C_AT_F} &= \frac{4P_-}{s_{13}s^B_{123}x_1\bar{x}_1}\Bigg[\frac{1}{2}\Big\{\bar{x}_2^4+\bar{x}^4-2x^4+x_1(x_1^2+1+12x^2)\\
&\quad - 4(x_1\bar{x}_2+\bar{x})x^2 + 2\bar{x}_1^3x - \epsilon(1+x_1)^2(x_1^2-x_1+1)\Big\}\Bigg],\\
\mathbb{P}^{(I_{6A})}_{C_AT_F} &= \frac{4P_-}{s_{12}s^B_{123}\bar{x}_1}\left[\frac{(1-\epsilon)}{2}(-\bar{x}^3+x_2^2x-x^2) + \epsilon\, x\bar{x}(1+x_2)\right.\\
&\quad \left. - \frac{\epsilon(1-\epsilon)}{2}\bar{x}_1\bar{x}_2\right],\\
\mathbb{P}^{(I_{6B})}_{C_AT_F} &= \frac{4P_-}{s_{23}s^B_{123}x_1\bar{x}_1}\left[\frac{(1-\epsilon)}{2}(\bar{x}_2^3+x_2^2x+x_1x^2) + \epsilon\,\bar{x}_2x(x_1-x_2)\right.\\
&\quad \left. - \frac{\epsilon(1-\epsilon)}{2}x_1\bar{x}_1\bar{x}\right]
\end{aligned} \tag{C.6}$$

There are two additional structures, which are connected to the $C_FT_Fn_f$ colour structure of the diagonal quark channel. However, we compute them independently according to the decomposition

$$\begin{aligned}
\mathbb{P}^{(I_1)}_{C_AT_F} &= \frac{-4xP_-}{2}\left(\frac{\big(x_1(s_{13}+2s_{23})+(s_{13}-2s_{12})\big)^2}{s_{13}^2(s^B_{123})^2(1-x_1)^2}\right),\\
\mathbb{P}^{(I_2)}_{C_AT_F} &= \frac{-4xP_-}{2}\left(\frac{1-2\epsilon}{2(s^B_{123})^2}\right).
\end{aligned} \tag{C.7}$$

In table C.9, we state the sector decomposition steps and applications of selector functions to arrive at completely factorised singularities in each sector.

Component	Region	Substitution	Divergences	$\rho_{n\geq 1}$	$\rho_{n<1}$	$\rho_{n=0}$
$\mathbb{P}^{(I_1)}_{C_A T_F}$	R_A	-	s_5	$a^{\frac{1-n}{2}}$	$a^{\frac{1-n}{2}}$	-
	R_B SD1	$a \to t \cdot b$	b, s_5	$t^{\frac{1-n}{2}}$	$t^{\frac{1-n}{2}}$	$t^{1/2}$
	R_B SD2	$b \to t \cdot a$	a, s_5	-	-	-
	R_C	-	s_5	$a^{\frac{1-n}{2}}$	$a^{\frac{1-n}{2}}$	-
	R_D	-	s_5	$a^{\frac{1-n}{2}}$	$a^{\frac{1-n}{2}}$	-
$\mathbb{P}^{(I_2)}_{C_A T_F}$	R_A, R_B	-	s_5	$a^{\frac{1-n}{2}}$	$a^{\frac{1-n}{2}}$	-
$\mathbb{P}^{(I_3)}_{C_A T_F}$	$\mathcal{S}_1 \cdot R_A$	$\{a,b\} \to \{u,v\} \to \{u_t, v_t\}$	b, u_t, s_5	$p^{\frac{1-n}{2}}$	$p^{\frac{1-n}{2}}$	-
	$\mathcal{S}_2 \cdot R_A$ SD1	$a \to t \cdot b$	b, t, s_5	$t^{\frac{1-n}{2}} \cdot b^{(1-n)}$	T_I	$t^{1/2}$
	$\mathcal{S}_2 \cdot R_A$ SD2	$b \to t \cdot a$	a, t, s_5	T_{II}	-	-
	$\mathcal{S}_1 \cdot R_B$	$\{a,b\} \to \{u,v\} \to \{u_t, v_t\}$	b, u_t, s_5	$p^{\frac{1-n}{2}}$	$p^{\frac{1-n}{2}}$	-
	$\mathcal{S}_2 \cdot R_B$ SD1	$a \to t \cdot b$	b, s_5	$t^{\frac{1-n}{2}}$	$t^{\frac{1-n}{2}}$	$t^{1/2}$
	$\mathcal{S}_2 \cdot R_B$ SD2	$b \to t \cdot a$	a, t, s_5	-	-	-
	$\mathcal{S}_1 \cdot R_C$	$\{a,b\} \to \{u,v\} \to \{u_t, v_t\}$	u_t, s_5	$p^{\frac{1-n}{2}}$	$p^{\frac{1-n}{2}}$	-
	$\mathcal{S}_2 \cdot R_C$ SD1	$a \to t \cdot b$	b, t, s_5	$t^{\frac{1-n}{2}}$	$t^{\frac{1-n}{2}}$	$t^{1/2}$
	$\mathcal{S}_2 \cdot R_C$ SD2	$b \to t \cdot a$	a, s_5	-	-	-
	R_D	$\{a,b\} \to \{u,v\} \to \{u_t, v_t\}$	u_t, s_5	$p^{\frac{1-n}{2}}$	$p^{\frac{1-n}{2}}$	-
$\mathbb{P}^{(I_5)}_{C_A T_F}$	R_A SD1	$a \to t \cdot b$	b, s_5	$t^{\frac{1-n}{2}} \cdot b^{(1-n)}$	$t^{\frac{1-n}{2}}$	$t^{1/2}$
	R_A SD2	$b \to t \cdot a$	a, t, s_5	T_{II}	-	-
	R_B SD1	$a \to t \cdot b$	b, s_5	$t^{\frac{1-n}{2}}$	$t^{\frac{1-n}{2}}$	$t^{1/2}$
	R_B SD2	$b \to t \cdot a$	a, t, s_5	-	-	-
	R_C	-	s_5	$a^{\frac{1-n}{2}}$	$a^{\frac{1-n}{2}}$	-
	R_D	-	s_5	$a^{\frac{1-n}{2}}$	$a^{\frac{1-n}{2}}$	-
$\mathbb{P}^{(I_6)}_{C_A T_F}$	$\mathcal{S}_1 \cdot R_A$	$\{a,b\} \to \{u,v\} \to \{u_t, v_t\}$	u_t, s_5	$p^{\frac{1-n}{2}}$	$p^{\frac{1-n}{2}}$	-
	$\mathcal{S}_2 \cdot R_A$ SD1	$a \to t \cdot b$	b, t, s_5	$t^{\frac{1-n}{2}} \cdot b^{(1-n)}$	T_I	$t^{2\epsilon}$
	$\mathcal{S}_2 \cdot R_A$ SD2	$b \to t \cdot a$	a, s_5	$a^{(1-n)}$	-	-
	R_B	$\{a,b\} \to \{u,v\} \to \{u_t, v_t\}$	u_t, s_5	$p^{\frac{1-n}{2}}$	$p^{\frac{1-n}{2}}$	-
	$\mathcal{S}_1 \cdot R_C$	$\{a,b\} \to \{u,v\} \to \{u_t, v_t\}$	u_t, s_5	$p^{\frac{1-n}{2}}$	$p^{\frac{1-n}{2}}$	-
	$\mathcal{S}_2 \cdot R_C$ SD1	$a \to t \cdot b$	t, b, s_5	$t^{\frac{1-n}{2}}$	$t^{\frac{1-n}{2}}$	$t^{1/2}$
	$\mathcal{S}_2 \cdot R_C$ SD2	$b \to t \cdot a$	a, s_5	-	-	-
	R_D	$\{a,b\} \to \{u,v\} \to \{u_t, v_t\}$	u_t, s_5	$p^{\frac{1-n}{2}}$	$p^{\frac{1-n}{2}}$	-

Table C.9: All sectors for the $C_A T_F$ colour structure in the $g \to q$ channel. We introduce the selector functions $\mathcal{S}_{1,2}$, which have been defined in Eq. (5.74).

C.3 The $\mathcal{I}^{0,(2)}_{g\leftarrow q}$ matching kernel

C_F^2 - structure

The real-real contributions of the off-diagonal channel for the gluon beam function consists of two colour structures, namely the C_F^2 and the $C_F C_A$ colour structure. First, the complete C_F^2 colour structure is of the form

$$\mathbb{P}^{C_F^2}_{q\to gqg^*} = C_F^2 \left[\mathbb{P}^{(I_{12})}_{C_F^2} + \mathbb{P}^{(I_3)}_{C_F^2} + \mathbb{P}^{(I_4)}_{C_F^2}\right](1-x)\,. \tag{C.8}$$

The different components are given by:

$$\begin{aligned}
\mathbb{P}^{(I_1)}_{C_F^2} &= \frac{4xP_-}{(s^B_{123})^2}\quad\left[2(1-\epsilon)\right],\\
\mathbb{P}^{(I_2)}_{C_F^2} &= 4xP_-\frac{s_{23}(s_{12}-s_{13})}{(s^B_{123})^2 s_{12}s_{13}}\quad(1-\epsilon)^2\,,\\
\mathbb{P}^{(I_3)}_{C_F^2} &= \frac{4P_-}{s_{12}s_{13}x}\quad\left[2\bar\epsilon(x_1^2+x^2)+2(x_1x+2x_2)\right],\\
\mathbb{P}^{(I_{4A})}_{C_F^2} &= \frac{4P_-}{s_{12}s^B_{123}}\quad\left[\bar\epsilon(x-2x_1)+\epsilon\bar\epsilon x+2(x_1+x_2)\right],\\
\mathbb{P}^{(I_{4B})}_{C_F^2} &= \frac{4P_-}{s_{13}s^B_{123}}\quad\left[-\bar\epsilon(x-2x_1)-\epsilon\bar\epsilon x+2(1-x_1)\right].
\end{aligned}\tag{C.9}$$

Again, we group the various contributions depending on the power of the invariant mass in the denominator. Thus, we combine $I_{12} = I_1 + I_2$ and $I_4 = I_{4A} + I_{4B}$. We state all steps to arrive at factorised singularities below.

Component	Region	Substitution	Divergences	$\rho_{n\geq 1}$	$\rho_{n<1}$	$\rho_{n=0}$
$\mathbb{P}^{(I_{12})}_{C_F^2}$	R_A	$\{a,b\} \to \{u,v\} \to \{u_t,v_t\}$	u_t, s_5	$p^{\frac{1-n}{2}}$	$p^{\frac{1-n}{2}}$	-
	$\mathcal{S}_1 \cdot R_B$	$\{a,b\} \to \{u,v\} \to \{u_t,v_t\}$	u_t, s_5	$p^{\frac{1-n}{2}}$	$p^{\frac{1-n}{2}}$	-
	$\mathcal{S}_2 \cdot R_B$ SD1	$a \to t \cdot b$	b, s_5	$t^{\frac{1-n}{2}}$	$t^{\frac{1-n}{2}}$	$t^{1/2}$
	$\mathcal{S}_2 \cdot R_B$ SD2	$b \to t \cdot a$	a, s_5	-	-	-
	R_C	$\{a,b\} \to \{u,v\} \to \{u_t,v_t\}$	u_t, s_5	$p^{\frac{1-n}{2}}$	$p^{\frac{1-n}{2}}$	-
	R_D	$\{a,b\} \to \{u,v\} \to \{u_t,v_t\}$	u_t, s_5	$p^{\frac{1-n}{2}}$	$p^{\frac{1-n}{2}}$	-
$\mathbb{P}^{(I_3)}_{C_F^2}$	R_A	$\{a,b\} \to \{u,v\} \to \{u_t,v_t\}$	b, u_t, s_5	$p^{\frac{1-n}{2}}$	$p^{\frac{1-n}{2}}$	-
	$\mathcal{S}_1 \cdot R_B$	$\{a,b\} \to \{u,v\} \to \{u_t,v_t\}$	b, u_t, s_5	$p^{\frac{1-n}{2}}$	$p^{\frac{1-n}{2}}$	-
	$\mathcal{S}_2 \cdot R_B$ SD1	$a \to t \cdot b$	b, s_5	$t^{\frac{1-n}{2}}$	$t^{\frac{1-n}{2}}$	$t^{1/2}$
	$\mathcal{S}_2 \cdot R_B$ SD2	$b \to t \cdot a$	t, a, s_5	-	-	-
	R_C	$\{a,b\} \to \{u,v\} \to \{u_t,v_t\}$	u_t, s_5	$p^{\frac{1-n}{2}}$	$p^{\frac{1-n}{2}}$	-
	R_D	$\{a,b\} \to \{u,v\} \to \{u_t,v_t\}$	u_t, s_5	$p^{\frac{1-n}{2}}$	$p^{\frac{1-n}{2}}$	-
$\mathbb{P}^{(I_4)}_{C_F^2}$	R_A	$\{a,b\} \to \{u,v\} \to \{u_t,v_t\}$	u_t, s_5	$p^{\frac{1-n}{2}}$	$p^{\frac{1-n}{2}}$	-
	$\mathcal{S}_1 \cdot R_B$	$\{a,b\} \to \{u,v\} \to \{u_t,v_t\}$	u_t, s_5	$p^{\frac{1-n}{2}}$	$p^{\frac{1-n}{2}}$	-
	$\mathcal{S}_2 \cdot R_B$ SD1	$a \to t \cdot b$	b, s_5	$t^{\frac{1-n}{2}}$	$t^{\frac{1-n}{2}}$	$t^{1/2}$
	$\mathcal{S}_2 \cdot R_B$ SD2	$b \to t \cdot a$	a, s_5	-	-	-
	R_C	$\{a,b\} \to \{u,v\} \to \{u_t,v_t\}$	u_t, s_5	$p^{\frac{1-n}{2}}$	$p^{\frac{1-n}{2}}$	-
	R_D	$\{a,b\} \to \{u,v\} \to \{u_t,v_t\}$	u_t, s_5	$p^{\frac{1-n}{2}}$	$p^{\frac{1-n}{2}}$	-

Table C.10: All sectors for the C_F^2 colour structure in the $q \to g$ channel. We introduce the selector functions $\mathcal{S}_{1,2}$, which have been defined in Eq. (5.74) and performed sector decomposition steps introduced in chapter 5.

C_FC_A - structure

For the C_FC_A colour structure, the total contribution takes the form

$$\begin{aligned}\mathbb{P}^{C_FC_A}_{q\to gqg^*} =& C_FC_A\Big[\mathbb{P}^{(I_1)}_{C_FC_A}+\mathbb{P}^{(I_{2A})}_{C_FC_A}+\mathbb{P}^{(I_{2B})}_{C_FC_A}+\mathbb{P}^{(I_{3A})}_{C_FC_A}+\mathbb{P}^{(I_{3B})}_{C_FC_A}+\mathbb{P}^{(I_4)}_{C_FC_A}\\ &+\mathbb{P}^{(I_5)}_{C_FC_A}+\mathbb{P}^{(I_6)}_{C_FC_A}\Big](1-x)\\ =& C_FC_A\Big[\mathbb{P}^{(I_1)}_{C_FC_A}+\mathbb{P}^{(I_2)}_{C_FC_A}+\mathbb{P}^{(I_3)}_{C_FC_A}+\mathbb{P}^{(I_4)}_{C_FC_A}+\mathbb{P}^{(I_5)}_{C_FC_A}+\mathbb{P}^{(I_6)}_{C_FC_A}\Big]\\ &\times(1-x)\,. \end{aligned} \tag{C.10}$$

We decompose the matrix element, which is related to the $q\to gqg^*$ splitting function as shown below

$$\begin{aligned}
\mathbb{P}^{(I_1)}_{C_FC_A} &= 4xP_-\frac{\big((s_{23}+2s_{13})x_2+(s_{23}-2s_{12})\big)^2}{(s^B_{123})^2s^2_{23}(1-x_2)^2}\quad\left[\frac{\bar\epsilon}{2}\right],\\
\mathbb{P}^{(I_{2A})}_{C_FC_A} &= \frac{4P_-}{s_{13}s_{23}x_1\bar x_2x}\quad\left[\frac{\bar\epsilon}{2}(\bar x_2^3+x_1^3)+x\bar x+2x_1x_2\right],\\
\mathbb{P}^{(I_{2B})}_{C_FC_A} &= \frac{4x_2P_-}{s_{12}s_{23}x_1\bar x_2x}\quad\left[\frac{\bar\epsilon}{2}(\bar x_2^3+x_1^3)+x_2\bar x_1x+2x_1x_2\right],\\
\mathbb{P}^{(I_{3A})}_{C_FC_A} &= \frac{-4P_-}{s_{13}s^B_{123}x_1\bar x_2}\quad\left[\frac{\bar\epsilon}{2}\bar x_1(x^2-x_1\bar x_2)+x_2\bar x_1^2\right],\\
\mathbb{P}^{(I_{3B})}_{C_FC_A} &= \frac{4P_-}{s_{12}s^B_{123}x_1\bar x_2}\quad\left[-\frac{\bar\epsilon}{2}\bar x(x^2-x_1\bar x_2)-\bar x^2\right],\\
\mathbb{P}^{(I_4)}_{C_FC_A} &= \frac{-4P_-}{s_{23}s^B_{123}x_1\bar x_2}\quad\left[\bar\epsilon(x^3-x_1^3)-x_1(1+x_2)^2+2x_2(x-x_1)\right],\\
\mathbb{P}^{(I_5)}_{C_FC_A} &= \frac{4xP_-}{(s^B_{123})^2}\quad\left[\frac{\bar\epsilon(1-2\epsilon)}{2}\right],\\
\mathbb{P}^{(I_6)}_{C_FC_A} &= \frac{-4P_-}{s_{12}s_{13}x}\quad\left[\bar\epsilon(x^2+x_1^2)+(x_1x+2x_2)\right],
\end{aligned} \tag{C.11}$$

and combine similar to the spirit above $I_2=I_{2A}+I_{2B}$ and $I_3=I_{3A}+I_{3B}$.

Component	Region	Substitution	Divergences	$\rho_{n\geq 1}$	$\rho_{n<1}$	$\rho_{n=0}$
$\mathbb{P}^{(I_1)}_{C_F C_A}$	R_A	-	s_5	$a^{\frac{1-n}{2}}$	$a^{\frac{1-n}{2}}$	-
	R_B	-	s_5	$a^{\frac{1-n}{2}}$	$a^{\frac{1-n}{2}}$	-
	R_C SD1	$a \to t \cdot b$	b, s_5	$t^{\frac{1-n}{2}}$	$t^{\frac{1-n}{2}}$	$t^{1/2}$
	R_C SD2	$b \to t \cdot a$	a, s_5	-	-	-
	R_D	-	s_5	$a^{\frac{1-n}{2}}$	$a^{\frac{1-n}{2}}$	-
$\mathbb{P}^{(I_2)}_{C_F C_A}$	$\mathcal{S}_1 \cdot R_A$	$\{a,b\} \to \{u,v\} \to \{u_t, v_t\}$	u_t, b, s_5	$p^{\frac{1-n}{2}}$	$p^{\frac{1-n}{2}}$	-
	$\mathcal{S}_2 \cdot R_A$ SD1	$a \to t \cdot b$	b, u_t, s_5	$t^{\frac{1-n}{2}} \cdot b^{(1-n)}$	T_I	$t^{1/2}$
	$\mathcal{S}_2 \cdot R_A$ SD2	$b \to t \cdot a$	a, t, s_5	T_{II}	-	-
	$\mathcal{S}_1 R_B$	$\{a,b\} \to \{u,v\} \to \{u_t, v_t\}$	u_t, b, s_5	$p^{\frac{1-n}{2}}$	$p^{\frac{1-n}{2}}$	-
	$\mathcal{S}_2 \cdot R_B$ SD1	$a \to t \cdot b$	b, s_5	$t^{\frac{1-n}{2}}$	$t^{\frac{1-n}{2}}$	$t^{1/2}$
	$\mathcal{S}_2 \cdot R_B$ SD2	$b \to t \cdot a$	a, t, s_5	-	-	-
	$\mathcal{S}_1 \cdot R_C$	$\{a,b\} \to \{u,v\} \to \{u_t, v_t\}$	u_t, b, s_5	$p^{\frac{1-n}{2}}$	$p^{\frac{1-n}{2}}$	-
	$\mathcal{S}_2 \cdot R_C$ SD1	$a \to t \cdot b$	b, t, s_5	$t^{\frac{1-n}{2}}$	$t^{\frac{1-n}{2}}$	$t^{1/2}$
	$\mathcal{S}_2 \cdot R_B$ SD2	$b \to t \cdot a$	a, s_5	-	-	-
	R_D	$\{a,b\} \to \{u,v\} \to \{u_t, v_t\}$	u_t, s_5	$p^{\frac{1-n}{2}}$	$p^{\frac{1-n}{2}}$	-
$\mathbb{P}^{(I_3)}_{C_F C_A}$	$\mathcal{S}_1 \cdot R_A$	$\{a,b\} \to \{u,v\} \to \{u_t, v_t\}$	u_t, b, s_5	$p^{\frac{1-n}{2}}$	$p^{\frac{1-n}{2}}$	-
	$\mathcal{S}_2 \cdot R_A$ SD1	$a \to t \cdot b$	b, t, s_5	$t^{\frac{1-n}{2}} \cdot b^{(1-n)}$	$t^{\frac{1-n}{2}}$	-
	$\mathcal{S}_2 \cdot R_A$ SD2	$b \to t \cdot a$	a, t, s_5	T_{II}	-	-
	$\mathcal{S}_1 \cdot R_B$	$\{a,b\} \to \{u,v\} \to \{u_t, v_t\}$	u_t, b, s_5	$p^{\frac{1-n}{2}}$	$p^{\frac{1-n}{2}}$	-
	$\mathcal{S}_2 \cdot R_B$ SD1	$a \to t \cdot b$	b, s_5	$t^{\frac{1-n}{2}}$	$t^{\frac{1-n}{2}}$	$t^{1/2}$
	$\mathcal{S}_2 \cdot R_B$ SD2	$b \to t \cdot a$	a, t, s_5	-	-	-
	R_C	$\{a,b\} \to \{u,v\} \to \{u_t, v_t\}$	u_t, s_5	$p^{\frac{1-n}{2}}$	$p^{\frac{1-n}{2}}$	-
	R_D	$\{a,b\} \to \{u,v\} \to \{u_t, v_t\}$	u_t, s_5	$p^{\frac{1-n}{2}}$	$p^{\frac{1-n}{2}}$	-
$\mathbb{P}^{(I_4)}_{C_F C_A}$	R_A SD1	$a \to t \cdot b$	b, t, s_5	$t^{\frac{1-n}{2}} \cdot b^{(1-n)}$	T_I	$t^{1/2}$
	R_A SD2	$b \to t \cdot a$	a, s_5	$a^{\frac{1-n}{2}}$	-	-
	R_B	-	s_5	$a^{\frac{1-n}{2}}$	$a^{\frac{1-n}{2}}$	-
	R_C SD1	$a \to t \cdot b$	b, t, s_5	$t^{\frac{1-n}{2}}$	$t^{\frac{1-n}{2}}$	$t^{1/2}$
	R_C SD2	$b \to t \cdot a$	a, s_5	-	-	-
	R_D	-	s_5	$a^{\frac{1-n}{2}}$	$a^{\frac{1-n}{2}}$	-
$\mathbb{P}^{(I_5)}_{C_F C_A}$	R_A, R_B	-	s_5	$a^{\frac{1-n}{2}}$	$a^{\frac{1-n}{2}}$	-
$\mathbb{P}^{(I_6)}_{C_F C_A}$	$\mathcal{S}_1 \cdot R_B$	$a \to t \cdot b$	u_t, b, s_5	$a^{\frac{1-n}{2}}$	$a^{\frac{1-n}{2}}$	-
	$\mathcal{S}_2 \cdot R_B$ SD1	$a \to t \cdot b$	b, s_5	$t^{\frac{1-n}{2}}$	$t^{\frac{1-n}{2}}$	$t^{1/2}$
	$\mathcal{S}_2 \cdot R_B$ SD2	$b \to t \cdot a$	a, t, s_5	-	-	-
	R_C	$\{a,b\} \to \{u,v\} \to \{u_t, v_t\}$	u_t, s_5	$p^{\frac{1-n}{2}}$	$p^{\frac{1-n}{2}}$	-
	R_D	$\{a,b\} \to \{u,v\} \to \{u_t, v_t\}$	u_t, s_5	$p^{\frac{1-n}{2}}$	$p^{\frac{1-n}{2}}$	-

Table C.11: All sectors for the $C_F C_A$ colour structure in the $q \to g$ channel. We introduce the selector functions $\mathcal{S}_{1,2}$, which have been defined in Eq. (5.74).

C.4 The $\mathcal{I}^{0,(2)}_{g\leftarrow g}$ matching kernel

$C_F T_F n_f$ - structure

The diagonal gluon channel contains in total three colour structures, namely the C_A^2, the $C_A T_F n_f$ and the $C_F T_F n_f$ structure. For the $C_F T_F n_f$ colour structure, we write the matrix element in terms of the splitting function decomposition

$$\begin{aligned}\mathbb{P}^{C_F T_F n_f}_{g\leftarrow \bar{q}qg^*} &= \frac{C_F T_F n_f}{\bar{\epsilon}} \left[\mathbb{P}^{(I_1)}_{C_F T_F n_f} + \mathbb{P}^{(I_2)}_{C_F T_F n_f} + \mathbb{P}^{(I_3)}_{C_F T_F n_f} + \mathbb{P}^{(I_{4A})}_{C_F T_F n_f} + \mathbb{P}^{(I_{4B})}_{C_F T_F n_f}\right] \\ &= \frac{C_F T_F n_f}{\bar{\epsilon}} \left[\mathbb{P}^{(I_{12})}_{C_F T_F n_f} + \mathbb{P}^{(I_3)}_{C_F T_F n_f} + \mathbb{P}^{(I_4)}_{C_F T_F n_f}\right] . \end{aligned} \tag{C.12}$$

We group them according to the power of the invariant mass s^B_{123} in the denominator. The various expressions in Eq. (C.12) can be stated:

$$\mathbb{P}^{(I_1)}_{C_F T_F n_f} = \frac{4xP_-}{(s^B_{123})^2} \left[-2(1-\epsilon)\right], \tag{C.13}$$

$$\mathbb{P}^{(I_2)}_{C_F T_F n_f} = 4xP_- \frac{s_{12}(s_{23}+s_{13})}{(s^B_{123})^2 s_{23}s_{13}} \left[(1-\epsilon)^2\right], \tag{C.14}$$

$$\mathbb{P}^{(I_3)}_{C_F T_F n_f} = \frac{4P_-}{s_{23}s_{13}x} \left[2\bar{\epsilon}(1+x^2) - 2(x_3+2x_1x_2)\right], \tag{C.15}$$

$$\mathbb{P}^{(I_{4A})}_{C_F T_F n_f} = \frac{4P_-}{s_{23}s_{123}} \left[\bar{\epsilon}(2+x) + \epsilon\bar{\epsilon}x - 2(1-x_2)\right], \tag{C.16}$$

$$\mathbb{P}^{(I_{4B})}_{C_F T_F n_f} = \frac{4P_-}{s_{13}s_{123}} \left[\bar{\epsilon}(2+x) + \epsilon\bar{\epsilon}x - 2(1-x_1)\right]. \tag{C.17}$$

We combine $I_1 + I_2 = I_{12}$ and $I_4 = I_{4A} + I_{4B}$.
In the following, we mention in detail all steps which are necessary in order to obtain completely factorised singularities in each sector.

Matching kernel	Region	Substitution	Divergences	$\rho_{n\geq 1}$	$\rho_{n<1}$	$\rho_{n=0}$
$\mathbb{P}^{(I_{12})}_{C_F T_F n_f}$	R_A	-	s_5	$a^{\frac{1-n}{2}}$	$a^{\frac{1-n}{2}}$	-
	R_B SD1	$a \to t \cdot b$	b, s_5	$t^{\frac{1-n}{2}}$	$t^{\frac{1-n}{2}}$	$t^{1/2}$
	R_B SD2	$b \to t \cdot a$	a, s_5	-	-	-
$\mathbb{P}^{(I_3)}_{C_F T_F n_f}$	R_A	-	s_5	$a^{\frac{1-n}{2}}$	$a^{\frac{1-n}{2}}$	-
	R_B SD1	$a \to t \cdot b$	b, s_5	$t^{\frac{1-n}{2}}$	$t^{\frac{1-n}{2}}$	$t^{1/2}$
	R_B SD2	$b \to t \cdot a$	a, s_5	-	-	-
$\mathbb{P}^{(I_4)}_{C_F T_F n_f}$	R_A	-	s_5	$a^{\frac{1-n}{2}}$	$a^{\frac{1-n}{2}}$	-
	R_B SD1	$a \to t \cdot b$	b, s_5	$t^{\frac{1-n}{2}}$	$t^{\frac{1-n}{2}}$	$t^{1/2}$
	R_B SD2	$b \to t \cdot a$	a, s_5	-	-	-

Table C.12: All sectors for the $C_F T_F n_f$ colour structure in the $g \to g$ channel. We need to perform one sector decomposition step in each region.

$C_A T_F n_f$ - structure

After investigating the $C_F T_F n_f$ structure, we focus on the more complicated $C_A T_F n_f$ colour structure. Here, we need to perform a combination of selector functions and sector decomposition. The complete colour structure is given by

$$\begin{aligned}\mathbb{P}^{C_A T_F n_f}_{g\to\bar{q}qg^*} = \frac{C_A T_F n_f}{\bar{\epsilon}}\Big[&\mathbb{P}^{(I_1)}_{C_A T_F n_f} + \mathbb{P}^{(I_2)}_{C_A T_F n_f} + \mathbb{P}^{(I_3)}_{C_A T_F n_f} + \mathbb{P}^{(I_4)}_{C_A T_F n_f} + \mathbb{P}^{(I_5)}_{C_A T_F n_f} \\ &+ \mathbb{P}^{(I_6)}_{C_A T_F n_f}\Big]\end{aligned} \tag{C.18}$$

Each contribution in Eq. (C.18) is given by

$$\begin{aligned}
\mathbb{P}^{(I_1)}_{C_A T_F n_f} &= \frac{((s_{12}-2s_{13})x_2-(s_{12}-2s_{23})x_1)^2}{(s^B_{123})^2 s^2_{12}(x_1+x_2)^2}\ \left[-\frac{4xP_-\bar{\epsilon}}{2}\right],\\
\mathbb{P}^{(I_{2A})}_{C_A T_F n_f} &= \frac{-4x_1P_-}{s_{13}s_{12}x\bar{x}}\ \left[-\frac{\bar{\epsilon}}{2}(1+\bar{x}^3)+x_1\bar{x}_2x+2x_1x_2\right],\\
\mathbb{P}^{(I_{2B})}_{C_A T_F n_f} &= \frac{-4x_2P_-}{s_{23}s_{12}x\bar{x}}\ \left[-\frac{\bar{\epsilon}}{2}(1+\bar{x}^3)+x_2\bar{x}_1x+2x_1x_2\right],\\
\mathbb{P}^{(I_{3A})}_{C_A T_F n_f} &= \frac{4P_-}{s_{13}s^B_{123}\bar{x}}\ \left[\frac{\bar{\epsilon}}{2}\bar{x}_1(x^2-\bar{x})+x_2\bar{x}_1^2\right],\\
\mathbb{P}^{(I_{3B})}_{C_A T_F n_f} &= \frac{4P_-}{s_{23}s^B_{123}\bar{x}}\ \left[\frac{\bar{\epsilon}}{2}\bar{x}_2(x^2-\bar{x})+x_1\bar{x}_2^2\right],\\
\mathbb{P}^{(I_4)}_{C_A T_F n_f} &= \frac{-4P_-}{s_{12}s^B_{123}\bar{x}}\ \left[\bar{\epsilon}(1+x^3)+(x_1-x_2)^2-2x_1x_2(1+x)\right],\\
\mathbb{P}^{(I_5)}_{C_A T_F n_f} &= \frac{4xP_-}{(s^B_{123})^2}\ \left[-\frac{\bar{\epsilon}(1-2\epsilon)}{2}\right],\\
\mathbb{P}^{(I_6)}_{C_A T_F n_f} &= \frac{4P_-}{s_{23}s_{13}x}\ \left[-\bar{\epsilon}(1+x^2)+(x+2x_1x_2)\right],
\end{aligned} \tag{C.19}$$

where we combine $I_2 = I_{2A} + I_{2B}$ and $I_3 = I_{3A} + I_{3B}$ in the end.

Matching kernel	Region	Substitution	Divergences	$\rho_{n\geq 1}$	$\rho_{n<1}$	$\rho_{n=0}$
$\mathbb{P}^{(I_1)}_{C_A T_F n_f}$	R_A, R_B	$\{a,b\} \to \{u,v\} \to \{u_t, v_t\}$	x_{12}, u_t, s_5	$p^{\frac{1-n}{2}}$	$p^{\frac{1-n}{2}}$	-
$\mathbb{P}^{(I_2)}_{C_A T_F n_f}$	R_A	$\{a,b\} \to \{u,v\} \to \{u_t, v_t\}$	u_t, s_5	$p^{\frac{1-n}{2}}$	$p^{\frac{1-n}{2}}$	-
	$\mathcal{S}_1 \cdot R_B$	$\{a,b\} \to \{u,v\} \to \{u_t, v_t\}$	u_t, s_5	$p^{\frac{1-n}{2}}$	$p^{\frac{1-n}{2}}$	-
	$\mathcal{S}_2 \cdot R_B$ SD1	$a \to t \cdot b$	b, s_5	$t^{\frac{1-n}{2}}$	$t^{\frac{1-n}{2}}$	$t^{1/2}$
	$\mathcal{S}_2 \cdot R_B$ SD2	$b \to t \cdot a$	a, s_5	-	-	-
$\mathbb{P}^{(I_3)}_{C_A T_F n_f}$	R_A	-	s_5	$a^{\frac{1-n}{2}}$	$a^{\frac{1-n}{2}}$	-
	R_B SD1	$a \to t \cdot b$	b, s_5	$t^{\frac{1-n}{2}}$	$t^{\frac{1-n}{2}}$	$t^{1/2}$
	R_B SD2	$b \to t \cdot a$	a, s_5	-	-	-
$\mathbb{P}^{(I_4)}_{C_A T_F n_f}$	R_A, R_B	$\{a,b\} \to \{u,v\} \to \{u_t, v_t\}$	x_{12}, u_t, s_5	$p^{\frac{1-n}{2}}$	$p^{\frac{1-n}{2}}$	-
$\mathbb{P}^{(I_5)}_{C_A T_F n_f}$	R_A, R_B	-	s_5	$a^{\frac{1-n}{2}}$	$a^{\frac{1-n}{2}}$	-
$\mathbb{P}^{(I_6)}_{C_A T_F n_f}$	R_A	-	s_5	$a^{\frac{1-n}{2}}$	$a^{\frac{1-n}{2}}$	-
	R_B SD1	$a \to t \cdot b$	b, s_5	$t^{\frac{1-n}{2}}$	$t^{\frac{1-n}{2}}$	$t^{1/2}$
	R_B SD2	$b \to t \cdot a$	a, s_5	-	-	-

Table C.13: All sectors for the $C_A T_F n_f$ colour structure in the $g \to g$ channel. We make use of sector decomposition to decompose all overlapping singularities.

C_A^2 - structure

Finally, we turn our attention to the most complicated colour structure in the $g \to g$ channel, namely the C_A^2 structure. The complete contributions is given by

$$\begin{aligned}\mathbb{P}^{C_A^2}_{g\to ggg^*} &= \frac{C_A^2}{2}\Big[\mathbb{P}^{(I_1)}_{C_A^2} + \mathbb{P}^{(I_2)}_{C_A^2} + \mathbb{P}^{(I_3)}_{C_A^2} + \mathbb{P}^{(I_4)}_{C_A^2} + \mathbb{P}^{(I_5)}_{C_A^2} + \mathbb{P}^{(I_6)}_{C_A^2} + \mathbb{P}^{(I_7)}_{C_A^2} + \mathbb{P}^{(I_8)}_{C_A^2} \\ &\quad + \mathbb{P}^{(I_9)}_{C_A^2} + \mathbb{P}^{(I_{10})}_{C_A^2}\Big] \\ &= \frac{C_A^2}{2}\Big[2\cdot\mathbb{P}^{(I_1)}_{C_A^2} + \mathbb{P}^{(I_3)}_{C_A^2} + \mathbb{P}^{(I_4)}_{C_A^2} + 2\cdot\mathbb{P}^{(I_5)}_{C_A^2} + \mathbb{P}^{(I_7)}_{C_A^2} + 2\cdot\mathbb{P}^{(I_8)}_{C_A^2} + \mathbb{P}^{(I_{10})}_{C_A^2}\Big]\end{aligned} \tag{C.20}$$

where we extensively exploit the $(1 \leftrightarrow 2)$-symmetry between I_1 and I_2, I_5 and I_6 as well as I_8 and I_9.

$$\begin{aligned}\mathbb{P}^{(I_1)}_{C_A^2} &= \frac{4P_-}{s_{12}s_{13}x_2\bar{x}_1 x\bar{x}}\Big[x_1\Big(x_2^2\bar{x}_1^2(x-2) + \bar{x}^2(x+2x_2)\Big) - x_2\bar{x}_1\bar{x} \\ &\quad \times (2x_1^2 - x_1 x - 4x^2) + x_2(x^4 - 2x_1x^3 + 2x_1^2x^2 + 2x_2\bar{x}_1\bar{x}) + x^2\bar{x}_1\bar{x} \\ &\quad \times (x^2 + 2x_1\bar{x}_2)\Big], \\ \mathbb{P}^{(I_2)}_{C_A^2} &= \frac{4P_-}{s_{12}s_{23}x_1\bar{x}_2 x\bar{x}}\Big[x_2\Big(x_1^2\bar{x}_2^2(x-2) + \bar{x}^2(x+2x_1)\Big) - x_1\bar{x}_2\bar{x}\end{aligned}$$

$$
\begin{aligned}
&\times (2x_2^2 - x_2 x - 4x^2) + x_1(x^4 - 2x_2x^3 + 2x_2^2x^2 + 2x_1\bar{x}_2\bar{x}) + x^2\bar{x}_2\bar{x} \\
&\times (x^2 + 2x_2\bar{x}_1)\Big]\,, \\
\mathbb{P}^{(I_3)}_{C_A^2} =& \frac{4P_-}{s_{13}s_{23}x_1\bar{x}_1x_2\bar{x}_2x}\Big[\Big(x_1^2\bar{x}_2^2(x+2x_2) + x_2^2\bar{x}_1^2(x+2x_1)\Big) + x_1\bar{x}_1x_2\bar{x}_2 \\
&\times (2 + x - 4x^2) + x_1x_2(x^4 + 2x^3 + 2x^2 + 2x_1\bar{x}_1x_2\bar{x}_2) + \bar{x}_1\bar{x}_2x^2 \\
&\times (x^2 + 2\bar{x})\Big]\,, \\
\mathbb{P}^{(I_4)}_{C_A^2} =& \frac{4P_-}{s_{12}s^B_{123}x_1\bar{x}_1x_2\bar{x}_2\bar{x}}\Big[x_1x_2\bar{x}_1\bar{x}_2\bar{x}(3x+5) - \bar{x}(x_1\bar{x}_2 + x_2\bar{x}_1)(x^2+\bar{x})^2 \\
&+ 8x_1x_2\bar{x}_1\bar{x}_2(x^2 - x_1x_2) - 2x_1x_2\bar{x}_1\bar{x}_2\bar{x}(2x^2 - x_1x_2)\Big]\,, \\
\mathbb{P}^{(I_5)}_{C_A^2} =& \frac{4P_-}{s_{13}s^B_{123}x_1\bar{x}_1x_2\bar{x}_2\bar{x}}\Big[- x_1x_2\bar{x}_1\bar{x}_2\bar{x}(3x - 5x_2) - \bar{x}_1(x_1\bar{x}_2 + \bar{x})(x^2 + x_2\bar{x}_1)^2 \\
&+ 8x_1x_2\bar{x}_2\bar{x}(x^2 + x_1) - 2x_1\bar{x}_1\bar{x}_2\bar{x}(2x^2 + x_1)\Big]\,, \\
\mathbb{P}^{(I_6)}_{C_A^2} =& \frac{4P_-}{s_{23}s^B_{123}x_1\bar{x}_1x_2\bar{x}_2\bar{x}}\Big[- x_1x_2\bar{x}_1\bar{x}_2\bar{x}(3x - 5x_1) - \bar{x}_2(x_2\bar{x}_1 + \bar{x})(x^2 + x_1\bar{x}_2)^2 \\
&+8x_1x_2\bar{x}_1\bar{x}(x^2 + x_2) - 2x_2\bar{x}_1\bar{x}_2\bar{x}(2x^2 + x_2)\Big]\,, \\
\mathbb{P}^{(I_7)}_{C_A^2} =& 4xP_- \frac{\big((s_{12} - 2s_{23})x_1 - (s_{12} - 2s_{13})x_2\big)^2}{(s^B_{123})^2 s_{12}^2 (x_1 + x_2)^2} \quad \left[\frac{\bar{\epsilon}}{2}\right]\,, \\
\mathbb{P}^{(I_8)}_{C_A^2} =& 4xP_- \frac{\big((s_{13} + 2s_{23})x_1 + (s_{13} - 2s_{12})\big)^2}{s_{123}^2 s_{13}^2 (1 - x_1)^2} \quad \left[\frac{\bar{\epsilon}}{2}\right]\,, \\
\mathbb{P}^{(I_9)}_{C_A^2} =& 4xP_- \frac{\big((s_{23} + 2s_{13})x_2 + (s_{23} - 2s_{12})\big)^2}{(s^B_{123})^2 s_{23}^2 (1 - x_2)^2} \quad \left[\frac{\bar{\epsilon}}{2}\right]\,, \\
\mathbb{P}^{(I_{10})}_{C_A^2} =& \frac{4xP_-}{(s^B_{123})^2} \quad \left[\frac{9}{2}\bar{\epsilon}\right]
\end{aligned}
\tag{C.21}
$$

For these contributions, it will be necessary to use sector decomposition and selector functions as well to obtain singularities in monomial form. We state all steps to factorise all singularities properly:

Matching kernel	Region	Substitution	Divergences	$\rho_{n\geq 1}$	$\rho_{n<1}$	$\rho_{n=0}$
$\mathbb{P}^{(I_1)}_{C^2_A}$	R_A	$\{a,b\}\to\{u,v\}\to\{u_t,v_t\}$	x_{12},u_t,b,s_5	$p^{\frac{1-n}{2}}$	$p^{\frac{1-n}{2}}$	-
	$\mathcal{S}_1\cdot R_B$	$\{a,b\}\to\{u,v\}\to\{u_t,v_t\}$	x_{12},u_t,b,s_5	$p^{\frac{1-n}{2}}$	$p^{\frac{1-n}{2}}$	-
	$\mathcal{S}_2\cdot R_B$ SD1	$a\to t\cdot b$	x_{12},b,t,s_5	$t^{\frac{1-n}{2}}$	$t^{\frac{1-n}{2}}$	$t^{1/2}$
	$\mathcal{S}_2\cdot R_B$ SD2	$b\to t\cdot a$	x_{12},a,t,s_5	-	-	-
	R_C	$\{a,b\}\to\{u,v\}\to\{u_t,v_t\}$	x_{12},u_t,b,s_5	$p^{\frac{1-n}{2}}$	$p^{\frac{1-n}{2}}$	-
	$\mathcal{S}_1\cdot R_D$	$\{a,b\}\to\{u,v\}\to\{u_t,v_t\}$	x_{12},u_t,b,s_5	$p^{\frac{1-n}{2}}$	$p^{\frac{1-n}{2}}$	-
	$\mathcal{S}_2\cdot R_D$ SD1	$a\to t\cdot b$	x_{12},b,t,s_5	$t^{\frac{1-n}{2}}\cdot b^{(1-n)}$	T_I	$t^{1/2}$
	$\mathcal{S}_2\cdot R_D$ SD2	$b\to t\cdot a$	x_{12},a,t,s_5	$a^{(1-n)}$	-	-
$\mathbb{P}^{(I_3)}_{C^2_A}$	R_A SD1	$a\to t\cdot b$	x_{12},b,t,s_5	$t^{\frac{1-n}{2}}\cdot b^{(1-n)}$	T_I	$t^{1/2}$
	R_A SD2	$b\to t\cdot a$	x_{12},a,t,s_5	T_{II}	-	-
	R_B SD1	$a\to t\cdot b$	x_{12},b,t,s_5	$t^{\frac{1-n}{2}}$	$t^{\frac{1-n}{2}}$	$t^{1/2}$
	R_B SD2	$b\to t\cdot a$	x_{12},a,t,s_5	-	-	-
$\mathbb{P}^{(I_4)}_{C^2_A}$	$\mathcal{S}_1\cdot R_A$	$\{a,b\}\to\{u,v\}\to\{u_t,v_t\}$	x_{12},u_t,b,s_5	$p^{\frac{1-n}{2}}$	$p^{\frac{1-n}{2}}$	-
	$\mathcal{S}_2\cdot R_A$ SD1	$a\to t\cdot b$	x_{12},b,t,s_5	$t^{\frac{1-n}{2}}\cdot b^{(1-n)}$	$t^{\frac{1-n}{2}}$	$t^{1/2}$
	$\mathcal{S}_2\cdot R_A$ SD2	$b\to t\cdot a$	x_{12},a,t,s_5	T_{II}	-	-
	$\mathcal{S}_1\cdot R_B$	$\{a,b\}\to\{u,v\}\to\{u_t,v_t\}$	x_{12},u_t,b,s_5	$p^{\frac{1-n}{2}}$	$p^{\frac{1-n}{2}}$	-
	$\mathcal{S}_2\cdot R_B$ SD1	$a\to t\cdot b$	x_{12},s_5	$t^{\frac{1-n}{2}}$	$t^{\frac{1-n}{2}}$	$t^{1/2}$
	$\mathcal{S}_2\cdot R_A$ SD2	$b\to t\cdot a$	x_{12},t,s_5	T_{II}	-	-
$\mathbb{P}^{(I_5)}_{C^2_A}$	R_A SD1	$a\to t\cdot b$	x_{12},b,s_5	$t^{\frac{1-n}{2}}\cdot b^{(1-n)}$	$t^{\frac{1-n}{2}}$	$t^{1/2}$
	R_A SD2	$b\to t\cdot a$	x_{12},a,s_5	T_{II}	-	-
	R_B SD1	$a\to t\cdot b$	x_{12},b,t,s_5	$t^{\frac{1-n}{2}}$	$t^{\frac{1-n}{2}}$	$t^{1/2}$
	R_B SD2	$b\to t\cdot a$	x_{12},a,t,s_5	-	-	-
	R_C SD1	$a\to t\cdot b$	x_{12},s_5	$t^{\frac{1-n}{2}}$	$t^{\frac{1-n}{2}}$	$t^{1/2}$
	R_C SD2	$b\to t\cdot a$	x_{12},s_5	-	-	-
	R_D SD1	$a\to t\cdot b$	x_{12},b,t,s_5	$t^{\frac{1-n}{2}}\cdot b^{(1-n)}$	T_I	$t^{1/2}$
	R_D SD2	$b\to t\cdot a$	x_{12},a,s_5	$a^{(1-n)}$	-	-
$\mathbb{P}^{(I_7)}_{C^2_A}$	R_A,R_B	$\{a,b\}\to\{u,v\}\to\{u_t,v_t\}$	x_{12},a,s_5	$p^{\frac{1-n}{2}}$	$p^{\frac{1-n}{2}}$	-
$\mathbb{P}^{(I_8)}_{C^2_A}$	R_A,R_C,R_D	-	s_5	$a^{\frac{1-n}{2}}$	$a^{\frac{1-n}{2}}$	-
	R_B SD1	$a\to t\cdot b$	b,s_5	$t^{\frac{1-n}{2}}$	$t^{\frac{1-n}{2}}$	$t^{1/2}$
	R_B SD2	$b\to t\cdot a$	a,s_5	-	-	-
$\mathbb{P}^{(I_{10})}_{C^2_A}$	R_A,R_B	-	s_5	$a^{\frac{1-n}{2}}$	$a^{\frac{1-n}{2}}$	-

Appendix D

Vanishing subdiagrams

In section 11.5, we mention several subdiagrams, which vanish in the evaluation of our diagrams in momentum space. Here, we explicitly prove that these subdiagrams do not contribute. In the first subdiagram, the gluon from the three-particle current in Eq. (11.4) is contracted with the heavy quark field propagator (D.3). For this, we need to define the interaction vertex of a heavy quark with an emitted gluon in HQET. The Feynman rule is given by

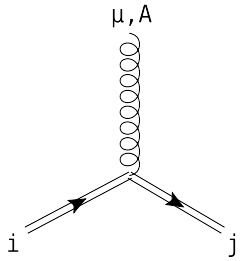

$$ig_s v^\mu t^A_{ji}$$

which we can extract for instance from [184]. With this, we are able to compute the correlation function for the subdiagram on the left in figure 11.2.

$$\begin{aligned}
\Pi_{S1} &= i\int \mathrm{d}^d x e^{-i\omega v x}\int \mathrm{d}^d y\,\langle 0|\,T\{\bar q(x)\Gamma_1 g_s G_{\mu\nu}(x) h_v\overbrace{(x)\bar h_v}(y) i g_s v^\omega \\
&\qquad\qquad \times A_\omega\overbrace{(y) h_v\overbrace{(y)\bar h_v}(0)\Gamma_2 g_s G_{\rho\sigma}}(0) q(0)\}\,|0\rangle \\
&= i g_s^3\,\langle 0|\,T\{\bar q\Gamma_1 G_{\mu\nu}(x) P_+\Gamma_2 q(0)\}\,|0\rangle\int\frac{\mathrm{d}^d l}{(2\pi)^d}\frac{1}{\omega+i0^+}\frac{1}{(l+\omega v)\cdot v+i0^+} \\
&\quad\times\frac{1}{l^2+i0^+}\Big[l_\rho g_{\sigma\omega}-l_\sigma g_{\rho\omega}\Big] \\
&= i g_s^3\,\langle 0|\,T\{\bar q\Gamma_1 G_{\mu\nu}(x) P_+ v^\omega\Gamma_2 q(0)\}\,|0\rangle\int_0^\infty \mathrm{d}x\int\frac{\mathrm{d}^d l}{(2\pi)^d}\frac{1}{(l^2-\Delta)^2} \\
&\quad\times\left[\Big(l-\frac{x}{2}v\Big)_\rho g_{\sigma\omega}-\Big(l-\frac{x}{2}v\Big)_\sigma g_{\rho\omega}\right] \\
&= -i g_s^3\,\langle 0|\,T\{\bar q\Gamma_1 G_{\mu\nu}(x) P_+\Gamma_2 q(0)\}\,|0\rangle\int_0^\infty \mathrm{d}x\,\frac{x}{2}\int\frac{\mathrm{d}^d l}{(2\pi)^d}\frac{v_\rho v_\sigma - v_\sigma v_\rho}{(l^2-\Delta)^2} \\
&= 0
\end{aligned} \tag{D.1}$$

As we have used before, the contraction between the gluon field strength tensor and a gluon field is, after performing the derivatives, a generalisation of the ordinary gluon propagator in QCD.
The second vanishing diagram states that there is no gluon condensate contribution originating from the heavy quark propagator. In order to prove this statement, it is more convenient to investigate this contribution in position space. Here, it is common to consider the gluon in background field gauge [187] and decompose it into a background and a quantum field. For the background field, we employ the fixed-point of Fock-Schwinger (FS) gauge [222, 223]

$$x_\mu A^\mu(x) = 0 \quad \text{and} \quad A_\mu(x) = \int_0^1 \mathrm{d}u\; u x^\nu G_{\nu\mu}(ux)\,, \tag{D.2}$$

which is particularly helpful due to the direct connection between the gluon field and the field strength tensor. For convenience, we set the reference point in the FS gauge to $x_0 = 0$, since the final result is expected to be independent of the explicit choice of this parameter. Generally, this gauge is a popular choice for sum rule calculations in the literature.
Furthermore, the proof requires the heavy-quark propagator in position space

$$\overbrace{h_v(0)\bar{h}_v}(x) = \Theta(-v\cdot x)\,\delta^{(d-1)}(x_\perp)\,P_+\,\mathcal{P}\exp\left(ig_s\int_{v\cdot x}^0 \mathrm{d}s\, v\cdot A(sv)\right), \tag{D.3}$$

where the gluon field A inside Eq. (D.3) corresponds to the background field. The quantity $x_\perp^\mu$ is defined in the standard definition in HQET, i.e. $x_\perp^\mu = x^\mu - (v\cdot x)v^\mu$ and $P_+ = (1+\not{v})/2$ denotes to the projection operator in HQET. $\mathcal{P}$ illustrates the path ordering operator in Eq. (D.3).
Since this contribution is a $\mathcal{O}(g_s)$ effect, it is sufficient to expand (D.3) to this order:

$$\begin{aligned}\overbrace{h_v(0)\bar{h}_v}(x) &= \Theta(-v\cdot x)\,\delta^{(d-1)}(x_\perp)\,P_+\,ig_s\int_{v\cdot x}^0 \mathrm{d}s\; v^\mu\cdot A_\mu(sv)\\ &= \Theta(-v\cdot x)\,\delta^{(d-1)}(x_\perp)\,P_+\,ig_s\int_{v\cdot x}^0 \mathrm{d}s\; v^\mu\int_0^1 \mathrm{d}u\; usv^\nu G_{\nu\mu}(usv) = 0\end{aligned} \tag{D.4}$$

In this computation, we have exploited the relation between the gluon field A_μ and the field strength tensor $G_{\mu\nu}$ in FS gauge provided in Eq. (D.2). Moreover, $v^\mu v^\nu G_{\mu\nu}(x) = 0$ due to the antisymmetry of $G_{\mu\nu}$.
The last vanishing diagram requires a one-loop calculation.

$$\begin{aligned}\Pi_{S3} = i\int \mathrm{d}^d x e^{-i\omega v\cdot x}\,\langle 0|\,T\{&\overbrace{\bar{q}(0)\Gamma_1^{\mu\nu}g_sG_{\mu\nu}(0)\int \mathrm{d}^d z\; ig_s\bar{q}(z)\gamma^\lambda A_\lambda(z)q(z)}\\ &\times \overbrace{h_v(0)\bar{h}_v}(x)\Gamma_2^{\rho\sigma}g_sG_{\rho\sigma}(x)q(x)\}\,|0\rangle\\ = i^2\int \mathrm{d}^d x\; e^{-i\omega v\cdot x}&\int \mathrm{d}^d z\; g_s^2\gamma^\lambda_{\epsilon\rho}\Gamma_{1,\alpha\beta}P_{+,\beta\gamma}\Gamma_{2,\gamma\delta}\,\langle 0|\,T\{q_\delta(0)\bar{q}_\epsilon(z)\}\,|0\rangle\end{aligned}$$

$$
\begin{aligned}
&\times \int \frac{\mathrm{d}^d k}{(2\pi)^d}\, e^{-ikx} \frac{i}{v\cdot k + i0^+} \int \frac{\mathrm{d}^d q}{(2\pi)^d}\, e^{iqz} \frac{i\not{q}}{q^2+i0^+} \int \frac{\mathrm{d}^d l}{(2\pi)^d}\, e^{-ilz} \\
&\times \left[l_\mu \frac{g_{\nu\lambda}}{l^2+i0^+} - l_\nu \frac{g_{\mu\lambda}}{l^2+i0^+} \right] \\
&= 0
\end{aligned} \tag{D.5}
$$

In the last line, we use that we are able to rewrite the d-dimensional tensor integral into a decomposition of Lorentz structures after exploiting momentum conservation given by the position space integrals in x and z

$$
\int \frac{\mathrm{d}^d l}{(2\pi)^d}\, \frac{i\not{l}}{l^2+i0^+} \Big[l_\mu \frac{g_{\nu\lambda}}{l^2+i0^+} - l_\nu \frac{g_{\mu\lambda}}{l^2+i0^+} \Big] = \int \frac{\mathrm{d}^d l}{(2\pi)^d}\, \frac{i}{d} \frac{\gamma_\mu g_{\nu\lambda} - \gamma_\nu g_{\mu\lambda}}{(l^2+i0^+)^2} = 0\,,
$$

which vanishes since we encounter a scaleless integral. Keeping these scaleless integrals in mind, we finally end up with the diagrams in section 11.5 which are left to evaluate to leading power in the OPE expansion in Eq. (11.25).

Appendix E

Nucleon distribution amplitude

Generally, the matrix element in Eq. (15.8) can be decomposed into different Lorentz structures according to symmetry considerations based on Lorentz covariance, spin and parity of the proton [116].

$$
\begin{aligned}
&4\left\langle 0\right|\epsilon^{ijk}u_{\alpha}^{i}(a_1x)u_{\beta}^{j}(a_2x)d_{\gamma}^{k}(a_3x)\left|p(P)\right\rangle \\
&\quad= \mathcal{S}_1 m_p C_{\alpha\beta}\left(\gamma_5 u_p(P)\right)_\gamma + \mathcal{S}_2 m_p^2 C_{\alpha\beta}\left(\not{x}\gamma_5 u_p(P)\right)_\gamma + \mathcal{P}_1 m_p\left(\gamma_5 C\right)_{\alpha\beta}\left(u_p(P)\right)_\gamma \\
&\quad+\mathcal{P}_2 m_p^2\left(\gamma_5 C\right)_{\alpha\beta}\left(\not{x}u_p(P)\right)_\gamma + \left(\mathcal{V}_1 + \frac{x^2 m_p^2}{4}\mathcal{V}_1^M\right)\left(\not{P}C\right)_{\alpha\beta}\left(\gamma_5 u_p(P)\right)_\gamma \\
&\quad+\mathcal{V}_2 m_p\left(\not{P}C\right)_{\alpha\beta}\left(\not{x}\gamma_5 u_p(P)\right)_\gamma + \mathcal{V}_3 m_p\left(\gamma_\mu C\right)_{\alpha\beta}\left(\gamma^\mu\gamma_5 u_p(P)\right)_\gamma \\
&\quad+\mathcal{V}_4 m_p^2\left(\not{x}C\right)_{\alpha\beta}\left(\gamma_5 u_p(P)\right)_\gamma + \mathcal{V}_5 m_p^2\left(\gamma_\mu C\right)_{\alpha\beta}\left(i\sigma^{\mu\nu}x_\nu\gamma_5 u_p(P)\right)_\gamma \\
&\quad+\mathcal{V}_6 m_p^3\left(\not{x}C\right)_{\alpha\beta}\left(\not{x}\gamma_5 u_p(P)\right)_\gamma + \left(\mathcal{A}_1 + \frac{x^2 m_p^2}{4}\mathcal{A}_1^M\right)\left(\not{P}\gamma_5 C\right)_{\alpha\beta}\left(u_p(P)\right)_\gamma \\
&\quad+\mathcal{A}_2 m_p\left(\not{P}\gamma_5 C\right)_{\alpha\beta}\left(\not{x}u_p(P)\right)_\gamma + \mathcal{A}_3 m_p\left(\gamma_\mu\gamma_5 C\right)_{\alpha\beta}\left(\gamma^\mu u_p(P)\right)_\gamma \\
&\quad+\mathcal{A}_4 m_p^2\left(\not{x}\gamma_5 C\right)_{\alpha\beta}\left(u_p(P)\right)_\gamma + \mathcal{A}_5 m_p^2\left(\gamma_\mu\gamma_5 C\right)_{\alpha\beta}\left(i\sigma^{\mu\nu}x_\nu u_p(P)\right)_\gamma \\
&\quad+\mathcal{A}_6 m_p^3\left(\not{x}\gamma_5 C\right)_{\alpha\beta}\left(\not{x}u_p(P)\right)_\gamma + \left(\mathcal{T}_1 + \frac{x^2 m_p^2}{4}\mathcal{T}_1^M\right)\left(P^\nu i\sigma_{\mu\nu}C\right)_{\alpha\beta} \\
&\quad\times\left(\gamma^\mu\gamma_5 u_p(P)\right)_\gamma + \mathcal{T}_2 m_p\left(x^\mu P^\nu i\sigma_{\mu\nu}C\right)_{\alpha\beta}\left(\gamma_5 u_p(P)\right)_\gamma + \mathcal{T}_3 m_p\left(\sigma_{\mu\nu}C\right)_{\alpha\beta} \\
&\quad\times\left(\sigma^{\mu\nu}\gamma_5 u_p(P)\right)_\gamma + \mathcal{T}_4 m_p\left(P^\nu\sigma_{\mu\nu}C\right)_{\alpha\beta}\left(\sigma^{\mu\rho}x_\rho\gamma_5 u_p(P)\right)_\gamma \\
&\quad+\mathcal{T}_5 m_p^2\left(x^\nu i\sigma_{\mu\nu}C\right)_{\alpha\beta}\left(\gamma^\mu\gamma_5 u_p(P)\right)_\gamma + \mathcal{T}_6 m_p^2\left(x^\mu P^\nu i\sigma_{\mu\nu}C\right)_{\alpha\beta}\left(\not{x}\gamma_5 u_p(P)\right)_\gamma \\
&\quad+\mathcal{T}_7 m_p^2\left(\sigma_{\mu\nu}C\right)_{\alpha\beta}\left(\sigma^{\mu\nu}\not{x}\gamma_5 u_p(P)\right)_\gamma + \mathcal{T}_8 m_p^3\left(x^\nu\sigma_{\mu\nu}C\right)_{\alpha\beta}\left(\sigma^{\mu\rho}x_\rho\gamma_5 u_p(P)\right)_\gamma
\end{aligned}
\tag{E.1}
$$

On the left side of Eq. (E.1), we consider a proton to vacuum matrix element with an on-shell proton of $P^2 = m_p^2$ in the initial state. The fields $u(x), u(0)$ and $d(0)$ display the valence quarks inside the proton, which have a spinor index attached to it denoted by Greek letters α, β, γ, as well as a colour index with Latin letters i, j, k. Notice that the valence quark structure

inside the proton requires the quarks to be totally antisymmetric in colour space. For simplicity, we suppress the gauge link factor between each valence quark which renders the expression in Eq. (E.1) gauge invariant. In addition to that we can set $a_1 = 1$ and $a_2 = a_3 = 0$ in our case. According to the previous discussion, the matrix C is the charge conjugation matrix defined as $C = \gamma_2\gamma_0$ and $u_p(P)$ is the proton spinor. The tensor $\sigma_{\mu\nu}$ is given by the standard relation $\sigma_{\mu\nu} = \frac{i}{2}[\gamma_\mu, \gamma_\nu]$.
There are in total 24 invariant functions $\mathcal{S}_i$, $\mathcal{P}_i$, $\mathcal{A}_i$, $\mathcal{V}_i$, $\mathcal{T}_i$, which do not possess a definite twist. Note that the nomenclature is chosen according to their Lorentz structure. $\mathcal{S}_i$ and $\mathcal{P}_i$ illustrate scalar and pseudoscalar contributions, which are related to distribution amplitudes only appearing at twist 4 and 5, while $\mathcal{V}_i$, $\mathcal{A}_i$ and $\mathcal{T}_i$ are connected to vector, axial-vector and tensor contributions of the DAs, respectively. In order to introduce a definite twist expansion in Eq. (E.1), we define a light-like vector of the form

$$p_\mu = P_\mu - \frac{1}{2}x_\mu \frac{m_p^2}{p\cdot x}\,, \quad p^2 = 0 \tag{E.2}$$

and therefore work in the infinite-momentum frame. Moreover, it is possible to decompose the proton spinor $u_p(P)$ into a large and a small component

$$u_p(P) = \frac{1}{2p\cdot x}(\not{p}\not{x} + \not{x}\not{p})u_p(P) = u_p^+(P) + u_p^-(P) \tag{E.3}$$

by identifying the projection operators

$$\Lambda^+ = \frac{\not{p}\not{x}}{2p\cdot x}\,, \qquad \Lambda^- = \frac{\not{x}\not{p}}{2p\cdot x}\,. \tag{E.4}$$

If we assume that the proton moves along the positive x-direction, then p^+ and x^- are the only non-vanishing contributions. The infinite-momentum frame corresponds to the limit $p^+ \sim Q \to \infty$ with fixed $P\cdot x = p\cdot x \sim 1$, where Q is the large scale of the underlying process. This power counting in Q makes it possible to perform an explicit expansion in twist. With $u_p^+(P) \sim \sqrt{p^+}$ and $u_p^-(P) \sim 1/\sqrt{p_+}$, we can replace for instance the $\mathcal{V}_\infty$ expression in terms of an expansion in twist:

$$\begin{aligned}(\not{P}C)_{\alpha\beta}(\gamma_5 u_p(P))_\gamma = {}& (\not{p}C)_{\alpha\beta}(\gamma_5 u_p^+(P))_\gamma + (\not{P}C)_{\alpha\beta}(\gamma_5 u_p^-(P))_\gamma \\ & + \frac{m_p^2}{2p\cdot x}(\not{x}C)_{\alpha\beta}(\gamma_5 u_p^+(P))_\gamma + \frac{m_p^2}{2p\cdot x}(\not{x}C)_{\alpha\beta}(\gamma_5 u_p^-(P))_\gamma\end{aligned} \tag{E.5}$$

From Eq. (E.5), we see that the first term scales as $(p_+)^{3/2}$, the second as $(p_+)^{1/2}$, the third term as $(p^+)^{-1/2}$ and the last term as $(p_+)^{-3/2}$, which can be interpreted as expansion in twist starting with the leading twist three contribution up to twist six.
The calligraphic quantities can be related to the twist amplitudes in the following way:

$$\mathcal{F}(a_1,a_2,a_3,(P\cdot x)) = \int \mathrm{d}\alpha_1\mathrm{d}\alpha_2\mathrm{d}\alpha_3\ \delta(1-\alpha_1-\alpha_2-\alpha_3)e^{-i(P\cdot x)\sum_i \alpha_i a_i}F(\alpha_i) \tag{E.6}$$

In the above expression, the variables $\alpha_{1,2,3}$ correspond to the momentum fractions of the different quarks inside the proton. Starting with twist three, we can relate the calligraphic quantities appearing in Eq. (E.1) with Eq. (E.6) to the definite twist amplitudes:

$\mathcal{F}$	integrand on r.h.s. of (E.6)
$\mathcal{V}_1$	V_1
$\mathcal{A}_1$	A_1
$\mathcal{T}_1$	T_1

The definite twist distribution amplitudes are given by

$$\begin{aligned} V_1(\alpha_i) = &\quad 120\alpha_1\alpha_2\alpha_3[\phi_3^0+\phi_3^+(1-3\alpha_3)]\,, \\ A_1(\alpha_i) = &\quad 120\alpha_1\alpha_2\alpha_3(\alpha_2-\alpha_1)\phi_3^-\,, \\ T_1(\alpha_i) = &\quad 120\alpha_1\alpha_2\alpha_3[\phi_3^0-\tfrac{1}{2}(\phi_3^+-\phi_3^-)(1-3\alpha_3)]\,. \end{aligned} \tag{E.7}$$

We are working in the conformal spin expansion, which is the physical analogue of the partial wave expansion in quantum mechanics [116]. With the help of the conformal symmetry of the QCD Lagrangian [224], we are able to disentangle the longitudinal degrees of freedom from the transverse degrees of freedom. The contributions originating from the longitudinal momentum fractions can be expressed in terms of a set of orthogonal polynomials of the collinear subgroup $SL(2,R)$ of the conformal group [116].
At the level of twist three, there are three coefficients $\phi_3^{(0,\pm)}$, which can be parameterised through the parameters f_N, the normalisation factor in leading conformal spin, and A_1^u as well as V_1^d, which belong both to the next to leading conformal spin:

$$\phi_3^0 = f_N;\quad \phi_3^+ = \frac{7}{2}f_N(1-3V_1^d);\quad \phi_3^- = \frac{21}{2}f_N A_1^u \tag{E.8}$$

In general, we can group the remaining contributions according to their twist and identify their tensor structure [116]:

	twist 3	twist 4	twist 5	twist 6
vector	V_1	V_2, V_3	V_4, V_5	V_6
pseudovector	A_1	A_2, A_3	A_4, A_5	A_6
tensor	T_1	T_2, T_3, T_7	T_4, T_5, T_8	T_6
scalar		S_1	S_2	
pseudoscalar		P_1	P_2	

With this ordering of twist for the distribution amplitudes in mind, we can group the calligraphic quantities in Eq. (E.1) into the different twist contributions. By identifying the highest twist distribution amplitude inside the calligraphic expression, we classify this expression as a contribution to this order of twist. This is equivalent to counting the powers of m_p in Eq. (E.1), since the order of the twist expansion is directly related to the power of m_p. Thus, we identify the calligraphic quantities contributing to twist 4 according to:

$\mathcal{F}$	Integrand on r.h.s. of (E.6)	Abbreviation
$\mathcal{S}_1$	S_1	
$\mathcal{P}_1$	P_1	
$2\mathcal{V}_3$	V_3	
$2\mathcal{A}_3$	A_3	
$2\mathcal{T}_3$	T_7	
$2(P\cdot x)\mathcal{V}_2$	$V_1 - V_2 - V_3$	V_{123}
$2(P\cdot x)\mathcal{A}_2$	$-A_1 + A_2 - A_3$	A_{123}
$2(P\cdot x)\mathcal{T}_2$	$T_1 + T_2$ - $2T_3$	T_{123}
$2(P\cdot x)\mathcal{T}_4$	$T_1 - T_2 - 2T_7$	T_{127}

Here, we drop the explicit renormalisation scale dependence for brevity. For consistency, the above abbreviations are chosen according to [116, 117, 213, 214]. We state the twist four DAs in the conformal expansion:

$$
\begin{aligned}
V_2(\alpha_i) &= 24\alpha_1\alpha_2[\phi_4^0 + \phi_4^+(1-5\alpha_3)]\,, \quad A_2(\alpha_i) = 24\alpha_1\alpha_2(\alpha_2-\alpha_1)\phi_4^-\,,\\
T_2(\alpha_i) &= 24\alpha_1\alpha_2[\xi_4^0 + \xi_4^+(1-5\alpha_3)]\,,\\
A_3(\alpha_i) &= 12\alpha_3(\alpha_2-\alpha_1)[(\psi_4^0+\psi_4^+) + \psi_4^-(1-2\alpha_3)]\\
V_3(\alpha_i) &= 12\alpha_3[\psi_4^0(1-\alpha_3) + \psi_4^+(1-\alpha_3-10\alpha_1\alpha_2) + \psi_4^-(\alpha_1^2+\alpha_2^2\\
&\quad - \alpha_3(1-\alpha_3))]\\
T_3(\alpha_i) &= 6\alpha_3[(\phi_4^0+\psi_4^0+\xi_4^0)(1-\alpha_3) + (\phi_4^+ + \psi_4^+ + \xi_4^+)(1-\alpha_3-10\alpha_1\alpha_2)
\end{aligned}
$$

$$
\begin{aligned}
&+(\phi_4^- - \psi_4^- + \xi_4^-)(\alpha_1^2+\alpha_2^2-\alpha_3(1-\alpha_3))]\\
T_7(\alpha_i) &= 6\alpha_3[(\phi_4^0+\psi_4^0-\xi_4^0)(1-\alpha_3)+(\phi_4^+ + \psi_4^+ - \xi_4^+)(1-\alpha_3-10\alpha_1\alpha_2)]\\
&+(\phi_4^- - \psi_4^- - \xi_4^-)(\alpha_1^2+\alpha_2^2-\alpha_3(1-\alpha_3))]\\
S_1(\alpha_i) &= 6\alpha_3(\alpha_2-\alpha_1)[(\phi_4^0+\psi_4^0+\xi_4^0+\phi_4^+ + \psi_4^+ + \xi_4^+)+(\phi_4^- - \psi_4^- + \xi_4^-)\\
&\times(1-2\alpha_3)]\\
P_1(\alpha_i) &= 6\alpha_3(\alpha_1-\alpha_2)[(\phi_4^0+\psi_4^0-\xi_4^0+\phi_4^+ + \psi_4^+ - \xi_4^+)+(\phi_4^- - \psi_4^- - \xi_4^-)\\
&\times(1-2\alpha_3)]
\end{aligned}
\tag{E.9}
$$

Here, we introduce additional parameters:

$$
\begin{aligned}
\phi_4^0 &= \frac{1}{2}(f_N+\lambda_1);\ \phi_4^+ = \frac{1}{4}(f_N(3-10V_1^d)+\lambda_1(3-10f_1^d));\\
\phi_4^- &= -\frac{5}{4}(f_N(1-2A_1^u)-\lambda_1(1-2f_1^d-4f_1^u))
\end{aligned}
\tag{E.10}
$$

$$
\begin{aligned}
\psi_4^0 &= \frac{1}{2}(f_N-\lambda_1);\ \psi_4^+ = -\frac{1}{4}(f_N(2+5A_1^u-5V_1^d)-\lambda_1(2-5f_1^d-5f_1^u));\\
\psi_4^- &= \frac{5}{4}(f_N(2-A_1^u-3V_1^d)-\lambda_1(2-7f_1^d+f_1^u))
\end{aligned}
\tag{E.11}
$$

$$
\begin{aligned}
\xi_4^0 &= \frac{1}{6}\lambda_2;\ \xi_4^+ = \frac{1}{16}\lambda_2(4-15f_2^d);\\
\xi_4^- &= \frac{5}{16}\lambda_2(4-15f_2^d)
\end{aligned}
\tag{E.12}
$$

For completeness, we state whether they belong to the leading or next-to-leading conformal spin [118]:

	Leading twist	Higher twist
Leading conformal spin	f_N	λ_1, λ_2
Next-to-leading conformal spin	A_1^u, V_1^d	f_1^u, f_1^d, f_2^d

For twist 5, we have

$$
\begin{aligned}
V_4(\alpha_i) &= 3[\psi_5^0(1-\alpha_3)+\psi_5^+(1-\alpha_3-2(\alpha_1^2+\alpha_2^2))+\psi_5^-(2\alpha_1\alpha_2\\
&-\alpha_3(1-\alpha_3))]\,,\\
A_4(\alpha_i) &= 3(\alpha_2-\alpha_1)[-\psi_5^0+\psi_5^+(1-2\alpha_3)+\psi_5^-\alpha_3]\,,\\
T_4(\alpha_i) &= \frac{3}{2}[(\phi_5^0+\psi_5^0+\xi_5^0)(1-\alpha_3)+(\phi_5^+ + \psi_5^+ + \xi_5^+)(1-\alpha_3-2(\alpha_1^2+\alpha_2^2))]\\
&+(\phi_5^- - \psi_5^- + \xi_5^-)(2\alpha_1\alpha_2-\alpha_3(1-\alpha_3))\,,\\
T_8(\alpha_i) &= \frac{3}{2}[(\phi_5^0+\psi_5^0-\xi_5^0)(1-\alpha_3)+(\phi_5^+ + \psi_5^+ - \xi_5^+)(1-\alpha_3-2(\alpha_1^2+\alpha_2^2))\\
&+(\phi_5^- - \psi_5^- + \xi_5^-)(2\alpha_1\alpha_2-\alpha_3(1-\alpha_3))]\,,
\end{aligned}
$$

$\mathcal{F}$	Integrand on r.h.s. of (E.6)	Abbreviation
$4(P\cdot x)\mathcal{V}_5$	$V_4 - V_3$	V_{43}
$4(P\cdot x)\mathcal{A}_5$	$A_3 - A_4$	A_{34}
$2(P\cdot x)\mathcal{T}_5$	$-T_1 + T_5 + 2T_8$	T_{158}
$4(P\cdot x)\mathcal{T}_7$	$T_7 - T_8$	T_{78}
$2(P\cdot x)\mathcal{S}_2$	$S_1 - S_2$	S_{12}
$2(P\cdot x)\mathcal{P}_2$	$P_2 - P_1$	P_{21}
$4(P\cdot x)\mathcal{V}_4$	$-2V_1 + V_3 + V_4 + 2V_5$	V_{1345}
$4(P\cdot x)\mathcal{A}_4$	$-2A_1 - A_3 - A_4 + 2A_5$	A_{1345}
$4(P\cdot x)^2\mathcal{T}_6$	$2T_2 - 2T_3 - 2T_4 + 2T_5 + 2T_7 + 2T_8$	T_{234578}
$\mathcal{V}_1^M$	V_1^M	
$\mathcal{A}_1^M$	A_1^M	
$\mathcal{T}_1^M$	T_1^M	

$$
\begin{aligned}
V_5(\alpha_i) &= 6\alpha_3[\phi_5^0 + \phi_5^+(1-2\alpha_3)]\,, \quad A_5(\alpha_i) = 6\alpha_3(\alpha_2-\alpha_1)\phi_5^-\,,\\
T_5(\alpha_i) &= 6\alpha_3[\xi_5^0 + \xi_5^+(1-2\alpha_3)]\,,\\
S_2(\alpha_i) &= \frac{3}{2}(\alpha_2-\alpha_1)[-(\phi_5^0+\psi_5^0+\xi_5^0) + (\phi_5^+ + \psi_5^+ + \xi_5^+)(1-2\alpha_3)\\
&\quad + (\phi_5^- - \psi_5^- + \xi_5^-)\alpha_3]\,,\\
P_2(\alpha_i) &= \frac{3}{2}(\alpha_1-\alpha_2)[-(\phi_5^0+\psi_5^0-\xi_5^0) + (\phi_5^+ + \psi_5^+ - \xi_5^+)(1-2\alpha_3)\\
&\quad + (\phi_5^- - \psi_5^- - \xi_5^-)\alpha_3]\,,
\end{aligned}
$$

The new parameters occuring in the twist 5 DAs read in the conformal expansion:

$$
\begin{aligned}
\phi_5^0 &= \frac{1}{2}(f_N + \lambda_1); \quad \phi_5^+ = -\frac{5}{6}[f_N(3+4V_1^d) - \lambda_1(1-4f_1^d)]\,,\\
\phi_5^- &= -\frac{5}{3}[f_N(1-2A_1^u) - \lambda_1(f_1^d - f_1^u)]
\end{aligned}
\tag{E.13}
$$

$$
\begin{aligned}
\psi_5^0 &= \frac{1}{2}(f_N - \lambda_1);\ \psi_5^+ = -\frac{5}{6}[f_N(5+2A_1^u-2V_1^d) - \lambda_1(1-2f_1^d-2f_1^u)]\,,\\
\psi_5^- &= \frac{5}{3}[f_N(2-A_1^u-3V_1^d) + \lambda_1(f_1^d - f_1^u)]\,,
\end{aligned}
\tag{E.14}
$$

$$
\xi_5^0 = \frac{1}{6}\lambda_2; \quad \xi_5^+ = \frac{5}{36}\lambda_2(2-9f_2^d); \quad \xi_5^- = -\frac{5}{4}\lambda_2 f_2^d\,, \tag{E.15}
$$

$\mathcal{F}$	integrand on r.h.s. of (E.6)	Abbreviations
$4(P\cdot x)^2\mathcal{V}_6$	$-V_1+V_2+V_3+V_4+V_5-V_6$	V_{123456}
$4(P\cdot x)^2\mathcal{A}_6$	$A_1-A_2+A_3+A_4-A_5+A_6$	A_{123456}
$4(P\cdot x)^2\mathcal{T}_8$	$-T_1+T_2+T_5-T_6+2T_7+2T_8$	T_{125678}

Finally, for twist 6 we get the following contributions:

$$V_6(\alpha_i) = 2[\phi_6^0 + \phi_6^+(1-3\alpha_3)]\,, \quad A_6(\alpha_i) = 2(\alpha_2-\alpha_1)\phi_6^-\,,$$
$$T_6(\alpha_i) = 2[\phi_6^0 - \frac{1}{2}(\phi_6^+ - \phi_6^-)(1-3\alpha_3)]\,. \tag{E.16}$$

The twist 6 parameters read:

$$\begin{aligned}\phi_6^+ &= \frac{1}{2}[f_N(1-4V_1^d) - \lambda_1(1-2f_1^d)]\,,\\ \phi_6^- &= \frac{1}{2}[f_N(1+4A_1^u) + \lambda_1(1-4f_1^d-2f_1^u)]\,.\end{aligned} \tag{E.17}$$

Appendix F

Expressions beyond leading twist

F.1 Higher twist corrections

Here, we collect all higher twist corrections, which contribute to the leading twist amplitudes in Eqs. (15.9) and (15.10). It turns out that the operator $\mathcal{O}_{(d)}$ receives additional contributions from the structure $\not{q} u_{p,L}$. We separate the contributions according to the different Dirac structures in Eq. (14.24). In addition to that we define $D := ((1-\alpha_1)P + q)^2 - m_b^2$.
In the expressions below, we have already performed the integrations in α_2 and α_3 from Eq. (E.6), since the exponential function does not have any dependence on these variables in our case. Thus, we introduce the notation

$$\widetilde{V}(\alpha) = \int_0^\alpha \mathrm{d}\alpha' \, V(\alpha') \tag{F.1}$$

$$\widetilde{\widetilde{V}}(\alpha) = \int_0^\alpha \mathrm{d}\alpha' \int_0^{\alpha'} \mathrm{d}\alpha'' \, V(\alpha'') \,, \tag{F.2}$$

which enters due to the partial integrations in the variable α because of the factors $1/(2P \cdot x)$. Surface terms vanish in this context.

$$\Pi^{(d)}_{\mathcal{P}_1} = \frac{m_b^2 m_p}{2} \int_0^1 \mathrm{d}\alpha \frac{P_1(\alpha)}{D} \, u_{p,R}(P) \tag{F.3}$$

$$\Pi^{(d)}_{\mathcal{V}_3} = -\frac{m_b m_p}{4} \int_0^1 \mathrm{d}\alpha_1 \frac{V_3(\alpha)}{D} \, [\not{q} u_{p,L}(P) + \, m_p(1-\alpha) u_{p,R}(P)] \tag{F.4}$$

$$\Pi^{(d)}_{\mathcal{A}_3} = \frac{m_b m_p}{4} \int_0^1 \mathrm{d}\alpha \frac{A_3(\alpha)}{D} \, [\not{q} u_{p,L}(P) + \, m_p(1-\alpha) u_{p,R}(P)] \tag{F.5}$$

$$\Pi^{(d)}_{\mathcal{S}_1} = \frac{m_b^2 m_p}{2} \int_0^1 \mathrm{d}\alpha \frac{S_1(\alpha)}{D} \, u_{p,R}(P) \tag{F.6}$$

$$\Pi^{(d)}_{\mathcal{A}_2} = -\frac{m_b m_p}{4}\int_0^1 \mathrm{d}\alpha \frac{\widetilde{A}_{123}(\alpha)}{1-\alpha}\frac{1}{D}\Bigg[\Big[1+\frac{m_b^2-q^2+m_p^2(1-\alpha)^2}{D}\Big]\not{q}u_{p,L}(P) + m_p(1-\alpha)\frac{m_b^2-q^2+m_p^2(1-\alpha)^2}{D}\,u_{p,R}(P)\Bigg] \tag{F.7}$$

$$\Pi^{(d)}_{\mathcal{V}_2} = \frac{m_b m_p}{4}\int_0^1 \mathrm{d}\alpha \frac{\widetilde{V}_{123}(\alpha)}{1-\alpha}\frac{1}{D}\Bigg[\Big[1+\frac{m_b^2-q^2+m_p^2(1-\alpha)^2}{D}\Big]\not{q}u_{p,L}(P) + m_p(1-\alpha)\frac{m_b^2-q^2+m_p^2(1-\alpha)^2}{D}\,u_{p,R}(P)\Bigg] \tag{F.8}$$

$$\Pi^{(d)}_{\mathcal{P}_2} = -\frac{m_b^2 m_p^2}{2}\int_0^1 \mathrm{d}\alpha \frac{\widetilde{P}_{21}(\alpha)}{D^2}\,[\not{q}u_{p,L}(P) + \ m_p(1-\alpha)u_{p,R}(P)] \tag{F.9}$$

$$\Pi^{(d)}_{\mathcal{S}_2} = \frac{m_b^2 m_p^2}{2}\int_0^1 \mathrm{d}\alpha \frac{\widetilde{S}_{12}(\alpha)}{D^2}\,[\not{q}u_{p,L}(P) + \ m_p(1-\alpha)u_{p,R}(P)] \tag{F.10}$$

$$\Pi^{(d)}_{\mathcal{V}_4} = \frac{m_b m_p^2}{4}\int_0^1 \mathrm{d}\alpha \frac{\widetilde{V}_{1345}(\alpha)}{D}\left[1-\frac{m_b^2}{D}\right]u_{p,R}(P) \tag{F.11}$$

$$\Pi^{(d)}_{\mathcal{A}_4} = \frac{m_b m_p^2}{4}\int_0^1 \mathrm{d}\alpha \frac{\widetilde{A}_{1345}(\alpha)}{D}\left[1-\frac{m_b^2}{D}\right]u_{p,R}(P) \tag{F.12}$$

$$\Pi^{(d)}_{\mathcal{V}_1^M} = \frac{m_b m_p^2}{4}\int_0^1 \mathrm{d}\alpha \frac{\widetilde{V}_1^M(\alpha)}{1-\alpha}\frac{1}{D}\left(1-\frac{2m_b^2}{D}\right)\left(1+\frac{m_b^2-q^2+m_p^2(1-\alpha)^2}{D}\right) \times u_{p,R}(P) \tag{F.13}$$

$$\Pi^{(d)}_{\mathcal{A}_1^M} = \frac{-m_b m_p^2}{4}\int_0^1 \mathrm{d}\alpha \frac{\widetilde{A}_1^M(\alpha)}{1-\alpha}\frac{1}{D}\left(1-\frac{2m_b^2}{D}\right)\left(1+\frac{m_b^2-q^2+m_p^2(1-\alpha)^2}{D}\right) \times u_{p,R}(P) \tag{F.14}$$

$$\Pi^{(d)}_{\mathcal{V}_6} = \frac{m_b m_p^3}{2}\int_0^1 \mathrm{d}\alpha \frac{\widetilde{\widetilde{V}}_{123456}(\alpha)}{D^2}\left[1-\frac{2m_b^2}{D}\right][\not{q}u_{p,L}(P) + \ m_p(1-\alpha)u_{p,R}(P)] \tag{F.15}$$

$$\Pi^{(d)}_{\mathcal{A}_6} = \frac{-m_b m_p^3}{2}\int_0^1 \mathrm{d}\alpha \frac{\widetilde{\widetilde{A}}_{123456}(\alpha)}{D^2}\left[1-\frac{2m_b^2}{D}\right][\not{q}u_{p,L}(P) + \ m_p(1-\alpha)u_{p,R}(P)] \tag{F.16}$$

The contributions $\Pi^{(d)}_{\mathcal{T}_2}$, $\Pi^{(d)}_{\mathcal{T}_3}$, $\Pi^{(d)}_{\mathcal{T}_4}$, $\Pi^{(d)}_{\mathcal{T}_5}$, $\Pi^{(d)}_{\mathcal{T}_6}$, $\Pi^{(d)}_{\mathcal{T}_7}$, $\Pi^{(d)}_{\mathcal{T}_8}$, $\Pi^{(d)}_{\mathcal{A}_5}$ and $\Pi^{(d)}_{\mathcal{V}_5}$ vanish due an antisymmetric contraction of Lorentz indices in the trace.
Next, we can proceed and state the results for the second operator $\mathcal{O}_{(b)}$.

$$\Pi^{(b)}_{\mathcal{P}_1} = -\frac{m_b^2 m_p}{4}\int_0^1 \mathrm{d}\alpha \frac{P_1(\alpha)}{D}\ u_{p,R}(P) \tag{F.17}$$

$$\Pi^{(b)}_{\mathcal{S}_1} = -\frac{m_b^2 m_p}{4}\int_0^1 \mathrm{d}\alpha \frac{S_1(\alpha)}{D}\ u_{p,R}(P) \tag{F.18}$$

$$\Pi^{(b)}_{\mathcal{V}_3} = \frac{m_b m_p}{2}\int_0^1 \mathrm{d}\alpha \frac{V_3(\alpha)}{D}\ [\not{q}u_{p,L}(P) + \ m_p(1-\alpha)u_{p,R}(P)] \tag{F.19}$$

$$\Pi^{(b)}_{\mathcal{A}_3} = -\frac{m_b m_p}{2}\int_0^1 \mathrm{d}\alpha \frac{A_3(\alpha)}{D}\ [\not{q}u_{p,L}(P) + \ m_p(1-\alpha)u_{p,R}(P)] \tag{F.20}$$

$$\Pi^{(b)}_{\mathcal{T}_3} = -\frac{3m_b^2 m_p}{2}\int_0^1 \mathrm{d}\alpha \frac{T_7(\alpha)}{D}\ u_{p,R}(P) \tag{F.21}$$

$$\begin{aligned}\Pi^{(b)}_{\mathcal{V}_2} = \ &-\frac{m_b m_p}{4}\int_0^1 \mathrm{d}\alpha \frac{\widetilde{V}_{123}(\alpha)}{1-\alpha}\frac{1}{D}\left[\left(1+\frac{m_b^2-q^2+m_p^2(1-\alpha)^2}{D}\right)\not{q}u_{p,L}(P)\right.\\ &\left.+ m_p(1-\alpha)\left(1-\frac{q^2-m_p^2(1-\alpha)^2}{D}\right)\ u_{p,R}(P)\right]\end{aligned} \tag{F.22}$$

$$\begin{aligned}\Pi^{(b)}_{\mathcal{A}_2} = \ &\frac{m_b m_p}{4}\int_0^1 \mathrm{d}\alpha \frac{\widetilde{A}_{123}(\alpha)}{1-\alpha}\frac{1}{D}\left[\left(1+\frac{m_b^2-q^2+m_p^2(1-\alpha)^2}{D}\right)\not{q}u_{p,L}(P)\right.\\ &\left.+ m_p(1-\alpha)\left(1-\frac{q^2-m_p^2(1-\alpha)^2}{D}\right)\ u_{p,R}(P)\right]\end{aligned} \tag{F.23}$$

$$\begin{aligned}\Pi^{(b)}_{\mathcal{T}_2} = \ &\frac{m_b^2 m_p}{8}\int_0^1 \mathrm{d}\alpha \frac{\widetilde{T}_{123}(\alpha)}{1-\alpha}\frac{1}{D}\left[\left(1+\frac{m_b^2-q^2-m_p^2(1-\alpha)^2}{D}\right)u_{p,R}(P)\right.\\ &\left.- 2m_p\frac{(1-\alpha)}{D}\not{q}u_{p,L}(P)\right]\end{aligned} \tag{F.24}$$

$$\Pi^{(b)}_{\mathcal{V}_5} = \frac{3m_b m_p^2}{8}\int_0^1 \mathrm{d}\alpha \widetilde{V}_{43}(\alpha)\frac{1}{D}\left(1-\frac{m_b^2}{D}\right)u_{p,R}(P) \tag{F.25}$$

$$\Pi^{(b)}_{\mathcal{A}_5} = \frac{3m_b m_p^2}{8}\int_0^1 \mathrm{d}\alpha \widetilde{A}_{34}(\alpha)\frac{1}{D}\left(1-\frac{m_b^2}{D}\right)u_{p,R}(P) \tag{F.26}$$

$$\Pi^{(b)}_{\mathcal{T}_5} = -\frac{3m_b^2 m_p^2}{4}\int_0^1 \mathrm{d}\alpha \widetilde{T}_{158}(\alpha)\frac{1}{D^2}\left[\not{n}u_{p,L}(P) + m_p(1-\alpha)u_{p,R}(P)\right] \tag{F.27}$$

$$\Pi^{(b)}_{\mathcal{T}_7} = -\frac{3m_b^2 m_p^2}{2}\int_0^1 \mathrm{d}\alpha \widetilde{T}_{78}(\alpha)\frac{1}{D^2}\left[\not{n}u_{p,L}(P) + m_p(1-\alpha)u_{p,R}(P)\right] \tag{F.28}$$

$$\Pi^{(b)}_{\mathcal{S}_2} = -\frac{m_b^2 m_p^2}{4}\int_0^1 \mathrm{d}\alpha_1 \widetilde{S}_{12}(\alpha)\frac{1}{D^2}\left[\not{n}u_{p,L}(P) + m_p(1-\alpha)u_{p,R}(P)\right] \tag{F.29}$$

$$\Pi^{(b)}_{\mathcal{P}_2} = \frac{m_b^2 m_p^2}{4}\int_0^1 \mathrm{d}\alpha \widetilde{P}_{21}(\alpha)\frac{1}{D^2}\left[\not{n}u_{p,L}(P) + m_p(1-\alpha)u_{p,R}(P)\right] \tag{F.30}$$

$$\Pi^{(b)}_{\mathcal{V}_4} = -\frac{m_b m_p^2}{8}\int_0^1 \mathrm{d}\alpha \widetilde{V}_{1345}(\alpha)\frac{1}{D}\left(1-\frac{m_b^2}{D}\right)u_{p,R}(P) \tag{F.31}$$

$$\Pi^{(b)}_{\mathcal{A}_4} = -\frac{m_b m_p^2}{8}\int_0^1 \mathrm{d}\alpha \widetilde{A}_{1345}(\alpha)\frac{1}{D}\left(1-\frac{m_b^2}{D}\right)u_{p,R}(P) \tag{F.32}$$

$$\Pi^{(b)}_{\mathcal{V}_1^M} = -\frac{m_b m_p^3}{4}\int_0^1 \mathrm{d}\alpha \widetilde{V}_1^M(\alpha)\frac{1}{D^2}\left(1-\frac{2m_b^2}{D}\right)\left[\not{n}u_{p,L}(P) + m_p(1-\alpha)u_{p,R}(P)\right] \tag{F.33}$$

$$\Pi^{(b)}_{\mathcal{A}_1^M} = \frac{m_b m_p^3}{4}\int_0^1 \mathrm{d}\alpha \widetilde{A}_1^M(\alpha)\frac{1}{D^2}\left(1-\frac{2m_b^2}{D}\right)\left[\not{n}u_{p,L}(P) + m_p(1-\alpha)u_{p,R}(P)\right] \tag{F.34}$$

$$\Pi^{(b)}_{\mathcal{T}_1^M} = -\frac{3m_b^4 m_p^3}{2}\int_0^1 \mathrm{d}\alpha \widetilde{T}_1^M(\alpha)\frac{1}{D^3}u_{p,R}(P) \tag{F.35}$$

$$\Pi^{(b)}_{\mathcal{V}_6} = -\frac{m_b m_p^3}{4}\int_0^1 \mathrm{d}\alpha \widetilde{\widetilde{V}}_{123456}(\alpha)\frac{1}{D^2}\left[1-\frac{2m_b^2}{D}\right]\left[\not{q}u_{p,L}(P)+m_p(1-\alpha)u_{p,R}(P)\right] \tag{F.36}$$

$$\Pi^{(b)}_{\mathcal{A}_6} = \frac{m_b m_p^3}{4}\int_0^1 \mathrm{d}\alpha \widetilde{\widetilde{A}}_{123456}(\alpha)\frac{1}{D^2}\left[1-\frac{2m_b^2}{D}\right]\left[\not{q}u_{p,L}(P)+m_p(1-\alpha)u_{p,R}(P)\right] \tag{F.37}$$

$$\Pi^{(b)}_{\mathcal{T}_8} = -\frac{3m_b^4 m_p^3}{2}\int_0^1 \mathrm{d}\alpha \widetilde{\widetilde{T}}_{125678}(\alpha)\frac{1}{D^3}u_{p,R}(P) \tag{F.38}$$

$$\begin{aligned}\Pi^{(b)}_{\mathcal{T}_6} = &-\frac{m_b^2 m_p^2}{8}\int_0^1 \mathrm{d}\alpha \frac{\widetilde{\widetilde{T}}_{234578}(\alpha)}{1-\alpha}\frac{1}{D^2}\left[2\left(1+\frac{m_p^2(1-\alpha)^2-q^2+m_b^2}{D}\right)\not{q}u_{p,L}(P)\right.\\ &\left.+m_p(1-\alpha)\left(1+2\frac{m_p^2(1-\alpha)^2-q^2-m_b^2}{D}\right)u_{p,R}(P)\right]\end{aligned} \tag{F.39}$$

$$\begin{aligned}\Pi^{(b)}_{\mathcal{T}_4} = &\frac{m_b^2 m_p}{4}\int_0^1 \mathrm{d}\alpha_1 \widetilde{T}_{127}(\alpha)\frac{1}{D}\left[\frac{-2m_p}{D}\not{q}u_{p,L}(P)\right.\\ &\left.+\left[\frac{5}{2(1-\alpha)}+\frac{5}{2(1-\alpha)}\frac{m_b^2-q^2}{D}+\frac{m_p^2(1-\alpha)}{2D}\right]u_{p,R}(P)\right]\end{aligned} \tag{F.40}$$

F.2 Form factors

In this section, we collect the remaining form factor expressions. The form factor $\widetilde{F}^{(d)}_{B\to p_L}(q^2)$ does not contribute at leading-twist three and its contributions start at twist four level. Notice that we also include the $\mathcal{O}(x^2)$-contributions to twist three, which we denote V_1^M, A_1^M and T_1^M, while the $\mathcal{O}(x^2)$-contributions to twist four are considered to be numerically negligible.

$$\begin{aligned}\widetilde{F}^{(d)}_{B\to p_L}(q^2) = &\frac{1}{m_B^2 f_B}\int_0^{\alpha_0^B}\mathrm{d}\alpha\, e^{\frac{m_B^2-s(\alpha)}{M^2}}\left\{\frac{m_b m_p}{4\bar{\alpha}}\Big(V_3(\alpha)-A_3(\alpha)\Big)+\frac{m_b^2 m_p^2}{2}\right.\\ &\times\frac{\widetilde{S}_{12}(\alpha)-\widetilde{P}_{21}(\alpha)}{\bar{\alpha}^2M^2}+\frac{m_b m_p}{4}\frac{\widetilde{A}_{123}(\alpha)-\widetilde{V}_{123}(\alpha)}{\bar{\alpha}^2}\left(1-\frac{m_p^2\bar{\alpha}^2-q^2+m_b^2}{\bar{\alpha}M^2}\right)\\ &\left.+\frac{m_b m_p^3}{2}\left(1+\frac{m_b^2}{\bar{\alpha}M^2}\right)\frac{\widetilde{\widetilde{V}}_{123456}(\alpha)-\widetilde{\widetilde{A}}_{123456}(\alpha)}{\bar{\alpha}^2M^2}\right\}\end{aligned} \tag{F.41}$$

$$
\begin{aligned}
F^{(b)}_{B\to p_R}(q^2) = \frac{1}{m_B^2 f_B}\int_0^{\alpha_0^B} \mathrm{d}\alpha\, e^{\frac{m_B^2-s(\alpha)}{M^2}} \Bigg\{ & \frac{m_b^2 m_p}{4}\left(\frac{m_p}{m_b}\Big(V_1(\alpha)+A_1(\alpha)\Big) - \frac{3}{\bar\alpha}T_1(\alpha)\right) \\
& + \frac{m_b^2 m_p}{4}\frac{P_1(\alpha)+S_1(\alpha)+6\cdot T_7(\alpha)}{\bar\alpha} + \frac{m_b m_p^2}{2}\Big(A_3(\alpha)-V_3(\alpha)\Big) \\
& + \frac{m_b m_p^2}{4}\frac{\widetilde V_{123}(\alpha)-\widetilde A_{123}(\alpha)}{\bar\alpha}\left(1+\frac{q^2-m_p^2\bar\alpha^2}{\bar\alpha M^2}\right) - \frac{m_b^2 m_p}{8}\frac{\widetilde T_{123}(\alpha)}{\bar\alpha^2} \\
& \times\left(1-\frac{m_b^2-q^2-m_p^2\bar\alpha^2}{\bar\alpha M^2}\right) - \frac{3m_b m_p^2}{8}\frac{\widetilde A_{34}(\alpha)+\widetilde V_{43}(\alpha)}{\bar\alpha}\left(1+\frac{m_b^2}{\bar\alpha M^2}\right) \\
& + \frac{m_b^2 m_p^3}{4}\frac{\widetilde P_{21}(\alpha)-\widetilde S_{12}(\alpha)}{\bar\alpha M^2} - \frac{3m_b^2 m_p^3}{4}\frac{2\cdot\widetilde T_{78}(\alpha)+\widetilde T_{158}(\alpha)}{\bar\alpha M^2} \\
& + \frac{m_b m_p^2}{8}\frac{\widetilde V_{1345}(\alpha)+\widetilde A_{1345}(\alpha)}{\bar\alpha}\left(1+\frac{m_b^2}{\bar\alpha M^2}\right) \\
& + \frac{3m_b^4 m_p^3}{4}\frac{\widetilde T_1^M}{\bar\alpha^3 M^4} - \frac{m_b^2 m_p}{4}\frac{\widetilde T_{127}(\alpha)}{\bar\alpha}\left(\frac{5}{2\bar\alpha}\left(1-\frac{m_b^2-q^2}{\bar\alpha M^2}\right)-\frac{m_p^2}{2M^2}\right) \\
& + \frac{3m_b^4 m_p^3}{4}\frac{\widetilde{\widetilde T}_{125678}(\alpha)}{\bar\alpha^3 M^4} + \frac{m_b m_p^4}{4}\frac{\widetilde{\widetilde A}_{123456}(\alpha)-\widetilde{\widetilde V}_{123456}(\alpha)}{\bar\alpha M^2}\left(1+\frac{m_b^2}{\bar\alpha M^2}\right) \\
& + \frac{m_b m_p^4}{4\bar\alpha M^2}\left(1+\frac{m_b^2}{\bar\alpha M^2}\right)\Big(\widetilde A_1^M-\widetilde V_1^M\Big)(\alpha) \\
& - \frac{m_b^2 m_p^3}{8}\frac{\widetilde{\widetilde T}_{234578}(\alpha)}{\bar\alpha^2 M^2}\left(1-\frac{m_p^2\bar\alpha^2-q^2-m_b^2}{\bar\alpha M^2}\right)\Bigg\}
\end{aligned}
\tag{F.42}
$$

$$
\begin{aligned}
\widetilde F^{(b)}_{B\to p_L}(q^2) = \frac{1}{m_B^2 f_B}\int_0^{\alpha_0^B} \mathrm{d}\alpha\, e^{\frac{m_B^2-s(\alpha)}{M^2}} \Bigg\{ & \frac{m_b m_p^2}{4\bar\alpha}(V_1(\alpha)+A_1(\alpha)) + \frac{m_b m_p}{2\bar\alpha} \\
& \times (A_3(\alpha)-V_3(\alpha)) + \frac{m_b^2 m_p^2}{4}\frac{\widetilde P_{21}(\alpha)-\widetilde S_{12}(\alpha)}{\bar\alpha^2 M^2} + \frac{m_b m_p}{4\bar\alpha^2}\Big(\widetilde V_{123}(\alpha)-\widetilde A_{123}(\alpha)\Big) \\
& \times\left(1+\frac{q^2-m_p^2\bar\alpha^2-m_b^2}{\bar\alpha M^2}\right) - \frac{3m_b^2 m_p^2}{4}\frac{2\cdot\widetilde T_{78}(\alpha)+\widetilde T_{158}(\alpha)}{\bar\alpha^2 M^2} \\
& + \frac{m_b m_p^3}{4\bar\alpha^2 M^2}\left(1+\frac{m_b^2}{\bar\alpha M^2}\right)\Big(\widetilde A_1^M(\alpha)-\widetilde V_1^M(\alpha)\Big) - \frac{m_b^2 m_p^2}{2}\frac{\widetilde T_{127}(\alpha)}{\bar\alpha^2 M^2} \\
& + \frac{m_b m_p^3}{4}\frac{\widetilde{\widetilde A}_{123456}(\alpha)-\widetilde{\widetilde V}_{123456}(\alpha)}{\bar\alpha^2 M^2}\left(1+\frac{m_b^2}{\bar\alpha M^2}\right) - \frac{m_b^2 m_p^2}{4M^2}\frac{\widetilde T_{123}(\alpha)}{\bar\alpha^2} \\
& - \frac{m_b^2 m_p^2}{4}\frac{\widetilde{\widetilde T}_{234578}(\alpha)}{\bar\alpha^3 M^2}\left(1-\frac{m_p^2\bar\alpha^2-q^2+m_b^2}{2\bar\alpha M^2}\right)\Bigg\}
\end{aligned}
\tag{F.43}
$$

Bibliography

[1] *ATLAS*. "Observation of a new particle in the search for the Standard Model Higgs boson with the ATLAS detector at the LHC". In: *Phys. Lett. B* 716 (2012), pp. 1–29. DOI: 10.1016/j.physletb.2012.08.020. arXiv: 1207.7214 [hep-ex]. №: CERN-PH-EP-2012-218.

[2] *CMS*. "Observation of a New Boson at a Mass of 125 GeV with the CMS Experiment at the LHC". In: *Phys. Lett. B* 716 (2012), pp. 30–61. DOI: 10.1016/j.physletb.2012.08.021. arXiv: 1207.7235 [hep-ex]. №: CMS-HIG-12-028 and CERN-PH-EP-2012-220.

[3] *Super-Kamiokande*. "Evidence for oscillation of atmospheric neutrinos". In: *Phys. Rev. Lett.* 81 (1998), pp. 1562–1567. DOI: 10.1103/PhysRevLett.81.1562. arXiv: hep-ex/9807003. №: BU-98-17, ICRR-REPORT-422-98-18, UCI-98-8, KEK-PREPRINT-98-95, LSU-HEPA-5-98, UMD-98-003, SBHEP-98-5, TKU-PAP-98-06, and TIT-HPE-98-09.

[4] *SNO*. "Measurement of the rate of $\nu_e + d \to p + p + e^-$ interactions produced by ^{8}B solar neutrinos at the Sudbury Neutrino Observatory". In: *Phys. Rev. Lett.* 87 (2001), p. 071301. DOI: 10.1103/PhysRevLett.87.071301. arXiv: nucl-ex/0106015. №: UPR-0240E.

[5] *SNO*. "Direct evidence for neutrino flavor transformation from neutral current interactions in the Sudbury Neutrino Observatory". In: *Phys. Rev. Lett.* 89 (2002), p. 011301. DOI: 10.1103/PhysRevLett.89.011301. arXiv: nucl-ex/0204008.

[6] S. Fartoukh et al. "LHC Configuration and Operational Scenario for Run 3" (). №: CERN-ACC-2021-0007.

[7] *Belle-II*. "The Belle II Physics Book". In: *PTEP* 2019.12 (2019). Ed. by E. Kou and P. Urquijo. [Erratum: PTEP 2020, 029201 (2020)], p. 123C01. DOI: 10.1093/ptep/ptz106. arXiv: 1808.10567 [hep-ex]. №: KEK Preprint 2018-27, BELLE2-PUB-PH-2018-001, FERMILAB-PUB-18-398-T, JLAB-THY-18-2780, INT-PUB-18-047, and UWThPh 2018-26.

[8] J. Goldstone, A. Salam, and S. Weinberg. "Broken Symmetries". In: *Phys. Rev.* 127 (1962), pp. 965–970. DOI: 10.1103/PhysRev.127.965.

[9] P. W. Higgs. "Broken symmetries, massless particles and gauge fields". In: *Phys. Lett.* 12 (1964), pp. 132–133. DOI: 10.1016/0031-9163(64)91136-9.

[10] P. W. Higgs. "Broken Symmetries and the Masses of Gauge Bosons". In: *Phys. Rev. Lett.* 13 (1964). Ed. by J. C. Taylor, pp. 508–509. DOI: 10.1103/PhysRevLett.13.508.

[11] N. Cabibbo. "Unitary Symmetry and Leptonic Decays". In: *Phys. Rev. Lett.* 10 (1963), pp. 531–533. DOI: 10.1103/PhysRevLett.10.531.

[12] M. Kobayashi and T. Maskawa. "CP Violation in the Renormalizable Theory of Weak Interaction". In: *Prog. Theor. Phys.* 49 (1973), pp. 652–657. DOI: 10.1143/PTP.49.652. №: KUNS-242.

[13] D. J. Gross and F. Wilczek. "Asymptotically Free Gauge Theories - I". In: *Phys. Rev. D* 8 (1973), pp. 3633–3652. DOI: 10.1103/PhysRevD.8.3633. №: NAL-PUB-73-49-THY and FERMILAB-PUB-73-049-T.

[14] H. D. Politzer. "Asymptotic Freedom: An Approach to Strong Interactions". In: *Phys. Rept.* 14 (1974), pp. 129–180. DOI: 10.1016/0370-1573(74)90014-3. №: PRINT-74-1223 (HARVARD).

[15] D. J. Gross and F. Wilczek. "ASYMPTOTICALLY FREE GAUGE THEORIES. 2." In: *Phys. Rev. D* 9 (1974), pp. 980–993. DOI: 10.1103/PhysRevD.9.980.

[16] C. W. Bauer, S. Fleming, D. Pirjol, and I. W. Stewart. "An Effective field theory for collinear and soft gluons: Heavy to light decays". In: *Phys. Rev. D* 63 (2001), p. 114020. DOI: 10.1103/PhysRevD.63.114020. arXiv: hep-ph/0011336. №: UCSD-PTH-00-28.

[17] C. W. Bauer, D. Pirjol, and I. W. Stewart. "Soft collinear factorization in effective field theory". In: *Phys. Rev. D* 65 (2002), p. 054022. DOI: 10.1103/PhysRevD.65.054022. arXiv: hep-ph/0109045. №: UCSD-PTH-01-15.

[18] C. W. Bauer, S. Fleming, D. Pirjol, I. Z. Rothstein, and I. W. Stewart. "Hard scattering factorization from effective field theory". In: *Phys. Rev. D* 66 (2002), p. 014017. DOI: 10.1103/PhysRevD.66.014017. arXiv: hep-ph/0202088. №: UCSD-PTH-02-03.

[19] M. Beneke, A. P. Chapovsky, M. Diehl, and T. Feldmann. "Soft collinear effective theory and heavy to light currents beyond leading power". In: *Nucl. Phys. B* 643 (2002), pp. 431–476. DOI: 10.1016/S0550-3213(02)00687-9. arXiv: hep-ph/0206152. №: PITHA-02-09.

[20] H. Georgi. "An Effective Field Theory for Heavy Quarks at Low-energies". In: *Phys. Lett. B* 240 (1990), pp. 447–450. DOI: 10.1016/0370-2693(90)91128-X. №: HUTP-90/A007.

[21] E. Eichten and B. R. Hill. "An Effective Field Theory for the Calculation of Matrix Elements Involving Heavy Quarks". In: *Phys. Lett. B* 234 (1990), pp. 511–516. DOI: 10.1016/0370-2693(90)92049-O. №: FERMILAB-PUB-89-184-T.

[22] B. Grinstein. "The Static Quark Effective Theory". In: *Nucl. Phys. B* 339 (1990), pp. 253–268. DOI: 10.1016/0550-3213(90)90349-I. №: HUTP-90/A002.

[23] T. Mannel, W. Roberts, and Z. Ryzak. "A Derivation of the heavy quark effective Lagrangian from QCD". In: *Nucl. Phys. B* 368 (1992), pp. 204–217. DOI: 10.1016/0550-3213(92)90204-O. №: HUTP-91-A017.

[24] T. Kinoshita. "Mass singularities of Feynman amplitudes". In: *J. Math. Phys.* 3 (1962), pp. 650–677. DOI: 10.1063/1.1724268.

[25] T. D. Lee and M. Nauenberg. "Degenerate Systems and Mass Singularities". In: *Phys. Rev.* 133 (1964). Ed. by G. Feinberg, B1549–B1562. DOI: 10.1103/PhysRev.133.B1549.

[26] F. Maltoni and T. Stelzer. "MadEvent: Automatic event generation with MadGraph". In: *JHEP* 02 (2003), p. 027. DOI: 10.1088/1126-6708/2003/02/027. arXiv: hep-ph/0208156.

[27] J. Alwall, M. Herquet, F. Maltoni, O. Mattelaer, and T. Stelzer. "MadGraph 5 : Going Beyond". In: *JHEP* 06 (2011), p. 128. DOI: 10.1007/JHEP06(2011)128. arXiv: 1106.0522 [hep-ph]. №: FERMILAB-PUB-11-448-T.

[28] J. Alwall et al. "The automated computation of tree-level and next-to-leading order differential cross sections, and their matching to parton shower simulations". In: *JHEP* 07 (2014), p. 079. DOI: 10.1007/JHEP07(2014)079. arXiv: 1405.0301 [hep-ph]. №: CERN-PH-TH-2014-064, CP3-14-18, LPN14-066, MCNET-14-09, and ZU-TH-14-14.

[29] G. Bevilacqua, M. Czakon, M. Kubocz, and M. Worek. "Complete Nagy-Soper subtraction for next-to-leading order calculations in QCD". In: *JHEP* 10 (2013), p. 204. DOI: 10.1007/JHEP10(2013)204. arXiv: 1308.5605 [hep-ph]. №: TTK-13-20.

[30] W. Kilian, T. Ohl, and J. Reuter. "WHIZARD: Simulating Multi-Particle Processes at LHC and ILC". In: *Eur. Phys. J. C* 71 (2011), p. 1742. DOI: 10.1140/epjc/s10052-011-1742-y. arXiv: 0708.4233 [hep-ph]. №: DESY-11-126, EDINBURGH-2010-36, FR-PHENO-2010-037, and SI-HEP-2010-18.

[31] P. Stienemeier et al. "WHIZARD 3.0: Status and News". *International Workshop on Future Linear Colliders*. Apr. 2021. arXiv: 2104.11141 [hep-ph]. №: DESY-21-050.

[32] S. Catani and M. H. Seymour. "A General algorithm for calculating jet cross-sections in NLO QCD". In: *Nucl. Phys. B* 485 (1997). [Erratum: Nucl.Phys.B 510, 503–504 (1998)], pp. 291–419. DOI: 10.1016/S0550-3213(96)00589-5. arXiv: hep-ph/9605323. №: CERN-TH-96-029 and CERN-TH-96-29.

[33] S. Catani, S. Dittmaier, M. H. Seymour, and Z. Trocsanyi. "The Dipole formalism for next-to-leading order QCD calculations with massive partons". In: *Nucl. Phys. B* 627 (2002), pp. 189–265. DOI: 10.1016/S0550-3213(02)00098-6. arXiv: hep-ph/0201036. №: CERN-TH-2001-305 and DESY-01-099.

[34] S. Frixione and B. R. Webber. "Matching NLO QCD computations and parton shower simulations". In: *JHEP* 06 (2002), p. 029. DOI: 10.1088/1126-6708/2002/06/029. arXiv: hep-ph/0204244. №: CAVENDISH-HEP-02-01, LAPTH-905-02, and GEF-TH-2-2002.

[35] Z. Nagy and D. E. Soper. "General subtraction method for numerical calculation of one loop QCD matrix elements". In: *JHEP* 09 (2003), p. 055. DOI: 10.1088/1126-6708/2003/09/055. arXiv: hep-ph/0308127.

[36] S. Frixione, P. Nason, and C. Oleari. "Matching NLO QCD computations with Parton Shower simulations: the POWHEG method". In: *JHEP* 11 (2007), p. 070. DOI: 10.1088/1126-6708/2007/11/070. arXiv: 0709.2092 [hep-ph]. №: BICOCCA-FT-07-9 and GEF-TH-21-2007.

[37] M. Czakon, H. B. Hartanto, M. Kraus, and M. Worek. "Matching the Nagy-Soper parton shower at next-to-leading order". In: *JHEP* 06 (2015), p. 033. DOI: 10.1007/JHEP06(2015)033. arXiv: 1502.00925 [hep-ph]. №: TTK-15-7.

[38] A. Gehrmann-De Ridder, T. Gehrmann, and E. W. N. Glover. "Antenna subtraction at NNLO". In: *JHEP* 09 (2005), p. 056. DOI: 10.1088/1126-6708/2005/09/056. arXiv: hep-ph/0505111. №: ZU-TH-07-05 and IPPP-05-18.

[39] S. Catani and M. Grazzini. "An NNLO subtraction formalism in hadron collisions and its application to Higgs boson production at the LHC". In: *Phys. Rev. Lett.* 98 (2007), p. 222002. DOI: 10.1103/PhysRevLett.98.222002. arXiv: hep-ph/0703012.

[40] M. Czakon. "Double-real radiation in hadronic top quark pair production as a proof of a certain concept". In: *Nucl. Phys. B* 849 (2011), pp. 250–295. DOI: 10.1016/j.nuclphysb.2011.03.020. arXiv: 1101.0642 [hep-ph]. №: TTK-10-58 and SFB-CPP-10-134.

[41] M. Czakon and D. Heymes. "Four-dimensional formulation of the sector-improved residue subtraction scheme". In: *Nucl. Phys. B* 890 (2014), pp. 152–227. DOI: 10.1016/j.nuclphysb.2014.11.006. arXiv: 1408.2500 [hep-ph]. №: TTK-14-16.

[42] R. Boughezal, K. Melnikov, and F. Petriello. "A subtraction scheme for NNLO computations". In: *Phys. Rev. D* 85 (2012), p. 034025. DOI: 10.1103/PhysRevD.85.034025. arXiv: 1111.7041 [hep-ph].

[43] F. Caola, K. Melnikov, and R. Röntsch. "Nested soft-collinear subtractions in NNLO QCD computations". In: *Eur. Phys. J. C* 77.4 (2017), p. 248. DOI: 10.1140/epjc/s10052-017-4774-0. arXiv: 1702.01352 [hep-ph]. №: CERN-TH-2017-029, IPPP-17-10, and TTP17-003.

[44] A. Banfi, G. P. Salam, and G. Zanderighi. "Principles of general final-state resummation and automated implementation". In: *JHEP* 03 (2005), p. 073. DOI: 10.1088/1126-6708/2005/03/073. arXiv: hep-ph/0407286. №: FERMILAB-PUB-04-116-T, LPTHE-04-16, and NIKHEF-2004-005.

[45] A. Banfi, H. McAslan, P. F. Monni, and G. Zanderighi. "A general method for the resummation of event-shape distributions in $e^+e^=$ annihilation". In: *JHEP* 05 (2015), p. 102. DOI: 10.1007/JHEP05(2015)102. arXiv: 1412.2126 [hep-ph]. №: OUTP-14-18P.

[46] S. Catani, L. Trentadue, G. Turnock, and B. R. Webber. "Resummation of large logarithms in e+ e- event shape distributions". In: *Nucl. Phys. B* 407 (1993), pp. 3–42. DOI: 10.1016/0550-3213(93)90271-P. №: CERN-TH-6640-92 and CAVENDISH-HEP-91-11.

[47] G. Bell, R. Rahn, and J. Talbert. "Two-loop anomalous dimensions of generic dijet soft functions". In: *Nucl. Phys. B* 936 (2018), pp. 520–541. DOI: 10.1016/j.nuclphysb.2018.09.026. arXiv: 1805.12414 [hep-ph]. №: SI-HEP-2018-16, QFET-2018-10, DESY 18-078, and DESY-18-078.

[48] G. Bell, R. Rahn, and J. Talbert. "Generic dijet soft functions at two-loop order: correlated emissions". In: *JHEP* 07 (2019), p. 101. DOI: 10.1007/JHEP07(2019)101. arXiv: 1812.08690 [hep-ph]. №: DESY-18-209.

[49] G. Bell, R. Rahn, and J. Talbert. "Generic dijet soft functions at two-loop order: uncorrelated emissions". In: *JHEP* 09 (2020), p. 015. DOI: 10.1007/JHEP09(2020)015. arXiv: 2004.08396 [hep-ph]. №: SI-HEP-2020-11, QFET-2020-01, NIKHEF 2020-007, and DESY-19-157.

[50] K. M. Brune. "Automation of jet function calculations in Soft-Collinear Effective theory". PhD thesis. Siegen U., 2022. DOI: 10.25819/ubsi/10228.

[51] M. A. Shifman, A. I. Vainshtein, and V. I. Zakharov. "QCD and Resonance Physics. Theoretical Foundations". In: *Nucl. Phys. B* 147 (1979), pp. 385–447. DOI: 10.1016/0550-3213(79)90022-1. №: ITEP-73-1978 and ITEP-80-1978.

[52] M. A. Shifman, A. I. Vainshtein, and V. I. Zakharov. "QCD and Resonance Physics: Applications". In: *Nucl. Phys. B* 147 (1979), pp. 448–518. DOI: 10.1016/0550-3213(79)90023-3. №: ITEP-94-1978 and ITEP-81-1978.

[53] V. A. Novikov, M. A. Shifman, A. I. Vainshtein, and V. I. Zakharov. "Calculations in External Fields in Quantum Chromodynamics. Technical Review". In: *Fortsch. Phys.* 32 (1984), p. 585. №: ITEP-140-1983.

[54] I. I. Balitsky. "STRING OPERATOR EXPANSION OF THE T PRODUCT OF TWO CURRENTS NEAR THE LIGHT CONE". In: *Phys. Lett. B* 124 (1983), pp. 230–236. DOI: 10.1016/0370-2693(83)91442-9.

[55] I. I. Balitsky and V. M. Braun. "Evolution Equations for QCD String Operators". In: *Nucl. Phys. B* 311 (1989), pp. 541–584. DOI: 10.1016/0550-3213(89)90168-5. №: LENINGRAD-87-1351.

[56] M. Beneke and V. A. Smirnov. "Asymptotic expansion of Feynman integrals near threshold". In: *Nucl. Phys. B* 522 (1998), pp. 321–344. DOI: 10.1016/S0550-3213(98)00138-2. arXiv: hep-ph/9711391. №: CERN-TH-97-315.

[57] B. Jantzen. "Foundation and generalization of the expansion by regions". In: *JHEP* 12 (2011), p. 076. DOI: 10.1007/JHEP12(2011)076. arXiv: 1111.2589 [hep-ph]. №: TTK-11-53 and SFB-CPP-11-61.

[58] T. Becher, A. Broggio, and A. Ferroglia. *Introduction to Soft-Collinear Effective Theory*. Vol. 896. Springer, 2015. DOI: 10.1007/978-3-319-14848-9. arXiv: 1410.1892 [hep-ph]. №: PSI-PR-14-12.

[59] I. Moult, I. W. Stewart, G. Vita, and H. X. Zhu. "First Subleading Power Resummation for Event Shapes". In: *JHEP* 08 (2018), p. 013. DOI: 10.1007/JHEP08(2018)013. arXiv: 1804.04665 [hep-ph]. №: MIT-CTP 4978 and MIT-CTP-4978.

[60] Z. L. Liu and M. Neubert. "Factorization at subleading power and endpoint-divergent convolutions in $h \to \gamma\gamma$ decay". In: *JHEP* 04 (2020), p. 033. DOI: 10.1007/JHEP04(2020)033. arXiv: 1912.08818 [hep-ph]. №: MITP/19-078.

[61] Z. L. Liu, B. Mecaj, M. Neubert, and X. Wang. "Factorization at subleading power and endpoint divergences in $h \to \gamma\gamma$ decay. Part II. Renormalization and scale evolution". In: *JHEP* 01 (2021), p. 077. DOI: 10.1007/JHEP01(2021)077. arXiv: 2009.06779 [hep-ph]. №: MITP/20-047.

[62] M. Beneke, M. Garny, S. Jaskiewicz, J. Strohm, R. Szafron, L. Vernazza, and J. Wang. "Next-to-leading power endpoint factorization and resummation for off-diagonal "gluon" thrust". In: *JHEP* 07 (2022), p. 144. DOI: 10.1007/JHEP07(2022)144. arXiv: 2205.04479 [hep-ph]. №: IPPP/22/25 and TUM-HEP-1398/22.

[63] G. Bell, P. Böer, and T. Feldmann. "Muon-electron backward scattering: a prime example for endpoint singularities in SCET". In: *JHEP* 09 (2022), p. 183. DOI: 10.1007/JHEP09(2022)183. arXiv: 2205.06021 [hep-ph]. №: MITP-22-034, SI-HEP-2022-10, and P3H-22-049.

[64] T. Feldmann, N. Gubernari, T. Huber, and N. Seitz. "Contribution of the electromagnetic dipole operator O7 to the $B^- s \to \mu^+ \mu^-$ decay amplitude". In: *Phys. Rev. D* 107.1 (2023), p. 013007. DOI: 10.1103/PhysRevD.107.013007. arXiv: 2211.04209 [hep-ph]. №: SI-HEP-2022-33 and P3H-22-110.

[65] Z. L. Liu, M. Neubert, M. Schnubel, and X. Wang. "Factorization at next-to-leading power and endpoint divergences in gg → h production". In: *JHEP* 06 (2023), p. 183. DOI: 10.1007/JHEP06(2023)183. arXiv: 2212.10447 [hep-ph]. №: CERN-TH-22-211, MITP/22-109, and TUM-HEP-1441/22.

[66] T. Hurth and R. Szafron. "Refactorisation in subleading $B^- \to X_s\gamma$". In: *Nucl. Phys. B* 991 (2023), p. 116200. DOI: 10.1016/j.nuclphysb.2023.116200. arXiv: 2301.01739 [hep-ph].

[67] J. C. Collins, D. E. Soper, and G. F. Sterman. "Does the Drell-Yan Cross-section Factorize?" In: *Phys. Lett. B* 109 (1982), pp. 388–392. DOI: 10.1016/0370-2693(82)91097-8. №: ITP-SB-81-59.

[68] J. C. Collins, D. E. Soper, and G. F. Sterman. "Factorization for Short Distance Hadron - Hadron Scattering". In: *Nucl. Phys. B* 261 (1985), pp. 104–142. DOI: 10.1016/0550-3213(85)90565-6. №: OITS-287.

[69] G. T. Bodwin. "Factorization of the Drell-Yan Cross-Section in Perturbation Theory". In: *Phys. Rev. D* 31 (1985). [Erratum: Phys.Rev.D 34, 3932 (1986)], p. 2616. DOI: 10.1103/PhysRevD.34.3932. №: ANL-HEP-PR-84-64-REV and ANL-HEP-PR-84-64.

[70] C. W. Bauer, B. O. Lange, and G. Ovanesyan. "On Glauber modes in Soft-Collinear Effective Theory". In: *JHEP* 07 (2011), p. 077. DOI: 10.1007/JHEP07(2011)077. arXiv: 1010.1027 [hep-ph]. №: SI-HEP-2010-14.

[71] J. F. Donoghue, B. K. El-Menoufi, and G. Ovanesyan. "Regge behavior in effective field theory". In: *Phys. Rev. D* 90.9 (2014), p. 096009. DOI: 10.1103/PhysRevD.90.096009. arXiv: 1405.1731 [hep-ph]. №: ACFI-T14-09.

[72] J. R. Gaunt. "Glauber Gluons and Multiple Parton Interactions". In: *JHEP* 07 (2014), p. 110. DOI: 10.1007/JHEP07(2014)110. arXiv: 1405.2080 [hep-ph]. №: DESY-14-067.

[73] T. Becher and G. Bell. "Analytic Regularization in Soft-Collinear Effective Theory". In: *Phys. Lett. B* 713 (2012), pp. 41–46. DOI: 10.1016/j.physletb.2012.05.016. arXiv: 1112.3907 [hep-ph].

[74] Y. Li, D. Neill, and H. X. Zhu. "An exponential regulator for rapidity divergences". In: *Nucl. Phys. B* 960 (2020), p. 115193. DOI: 10.1016/j.nuclphysb.2020.115193. arXiv: 1604.00392 [hep-ph]. №: FERMILAB-PUB-16-090-PPD-T and MIT-CTP-4795.

[75] T. Becher and M. Neubert. "Drell-Yan Production at Small q_T, Transverse Parton Distributions and the Collinear Anomaly". In: *Eur. Phys. J. C* 71 (2011), p. 1665. DOI: 10.1140/epjc/s10052-011-1665-7. arXiv: 1007.4005 [hep-ph]. №: HD-THEP-10-13 and MZ-TH-10-26.

[76] J.-y. Chiu, A. Jain, D. Neill, and I. Z. Rothstein. "The Rapidity Renormalization Group". In: *Phys. Rev. Lett.* 108 (2012), p. 151601. DOI: 10.1103/PhysRevLett.108.151601. arXiv: 1104.0881 [hep-ph].

[77] J.-Y. Chiu, A. Jain, D. Neill, and I. Z. Rothstein. "A Formalism for the Systematic Treatment of Rapidity Logarithms in Quantum Field Theory". In: *JHEP* 05 (2012), p. 084. DOI: 10.1007/JHEP05(2012)084. arXiv: 1202.0814 [hep-ph]. №: INT-PUB-11-057 and CALT-68-2864.

[78] T. Lübbert. "Transverse parton distribution functions at next-to-next-to-leading order". PhD thesis. Zurich U., 2014. DOI: 10.5167/uzh-164334.

[79] T. Lübbert, J. Oredsson, and M. Stahlhofen. "Rapidity renormalized TMD soft and beam functions at two loops". In: *JHEP* 03 (2016), p. 168. DOI: 10.1007/JHEP03(2016)168. arXiv: 1602.01829 [hep-ph]. №: DESY-16-024 and MITP-16-017.

[80] M.-x. Luo, T.-Z. Yang, H. X. Zhu, and Y. J. Zhu. "Unpolarized quark and gluon TMD PDFs and FFs at N^{3}LO". In: *JHEP* 06 (2021), p. 115. DOI: 10.1007/JHEP06(2021)115. arXiv: 2012.03256 [hep-ph].

[81] M. A. Ebert, B. Mistlberger, and G. Vita. "TMD fragmentation functions at N^{3}LO". In: *JHEP* 07 (2021), p. 121. DOI: 10.1007/JHEP07(2021)121. arXiv: 2012.07853 [hep-ph]. №: MIT-CTP 5261, SLAC-PUB-17577, and MPP-2020-220.

[82] J. F. Nieves and P. B. Pal. "Generalized Fierz identities". In: *Am. J. Phys.* 72 (2004), pp. 1100–1108. DOI: 10.1119/1.1757445. arXiv: hep-ph/0306087. №: SINP-TNP-03-16.

[83] M. Neubert. "Heavy quark effective theory". In: *Subnucl. Ser.* 34 (1997). Ed. by A. Zichichi, pp. 98–165. arXiv: hep-ph/9610266. №: CERN-TH-96-281.

[84] A. G. Grozin and M. Neubert. "Asymptotics of heavy meson form-factors". In: *Phys. Rev. D* 55 (1997), pp. 272–290. DOI: 10.1103/PhysRevD.55.272. arXiv: hep-ph/9607366. №: BUDKER-INP-1996-45, BINP-96-45, and CERN-TH-96-144.

[85] T. Nishikawa and K. Tanaka. "QCD Sum Rules for Quark-Gluon Three-Body Components in the B Meson". In: *Nucl. Phys. B* 879 (2014), pp. 110–142. DOI: 10.1016/j.nuclphysb.2013.12.007. arXiv: 1109.6786 [hep-ph]. №: J-PARC-TH-0032.

[86] M. Beneke, G. Buchalla, M. Neubert, and C. T. Sachrajda. "QCD factorization for B —> pi pi decays: Strong phases and CP violation in the heavy quark limit". In: *Phys. Rev. Lett.* 83 (1999), pp. 1914–1917. DOI: 10.1103/PhysRevLett.83.1914. arXiv: hep-ph/9905312. №: SLAC-PUB-8146, CERN-TH-99-126, and SHEP-99-04.

[87] M. Beneke, G. Buchalla, M. Neubert, and C. T. Sachrajda. "QCD factorization for exclusive, nonleptonic B meson decays: General arguments and the case of heavy light final states". In: *Nucl. Phys. B* 591 (2000), pp. 313–418. DOI: 10.1016/S0550-3213(00)00559-9. arXiv: hep-ph/0006124. №: CERN-TH-2000-159, CLNS-00-1675, PITHA-00-06, and SHEP-00-06.

[88] M. Beneke, G. Buchalla, M. Neubert, and C. T. Sachrajda. "QCD factorization in B —> pi K, pi pi decays and extraction of Wolfenstein parameters". In: *Nucl. Phys. B* 606 (2001), pp. 245–321. DOI: 10.1016/S0550-3213(01)00251-6. arXiv: hep-ph/0104110. №: CERN-TH-2001-107, CLNS-01-1728, PITHA-01-01, and SHEP-01-11.

[89] M. Beneke and S. Jager. "Spectator scattering at NLO in non-leptonic b decays: Tree amplitudes". In: *Nucl. Phys. B* 751 (2006), pp. 160–185. DOI: 10.1016/j.nuclphysb.2006.06.010. arXiv: hep-ph/0512351. №: PITHA-05-21.

[90] M. Beneke and S. Jager. "Spectator scattering at NLO in non-leptonic B decays: Leading penguin amplitudes". In: *Nucl. Phys. B* 768 (2007), pp. 51–84. DOI: 10.1016/j.nuclphysb.2007.01.016. arXiv: hep-ph/0610322. №: PITHA-06-09.

[91] G. Bell. "NNLO vertex corrections in charmless hadronic B decays: Imaginary part". In: *Nucl. Phys. B* 795 (2008), pp. 1–26. DOI: 10.1016/j.nuclphysb.2007.09.006. arXiv: 0705.3127 [hep-ph]. №: LMU-ASC-32-07, TTP07-08, and SFB-CPP-07-20.

[92] G. Bell. "NNLO vertex corrections in charmless hadronic B decays: Real part". In: *Nucl. Phys. B* 822 (2009), pp. 172–200. DOI: 10.1016/j.nuclphysb.2009.07.012. arXiv: 0902.1915 [hep-ph]. №: TTP09-02 and SFB-CPP-09-14.

[93] M. Beneke, T. Huber, and X.-Q. Li. "NNLO vertex corrections to non-leptonic B decays: Tree amplitudes". In: *Nucl. Phys. B* 832 (2010), pp. 109–151. DOI: 10.1016/j.nuclphysb.2010.02.002. arXiv: 0911.3655 [hep-ph]. №: PITHA-09-28, SFB-CPP-09-106, and SI-HEP-2009-17.

[94] G. Bell, M. Beneke, T. Huber, and X.-Q. Li. "Two-loop current–current operator contribution to the non-leptonic QCD penguin amplitude". In: *Phys. Lett. B* 750 (2015), pp. 348–355. DOI: 10.1016/j.physletb.2015.09.037. arXiv: 1507.03700 [hep-ph]. №: OUTP-15-15P, TUM-HEP-1005-15, SI-HEP-2015-17, and QFET-2015-23.

[95] G. Bell, M. Beneke, T. Huber, and X.-Q. Li. "Two-loop non-leptonic penguin amplitude in QCD factorization". In: *JHEP* 04 (2020), p. 055. DOI: 10.1007/JHEP04(2020)055. arXiv: 2002.03262 [hep-ph]. №: TUM-HEP-1250/20, SI-HEP-2019-17, and QFET-2019-12.

[96] V. M. Braun, D. Y. Ivanov, and G. P. Korchemsky. "The B meson distribution amplitude in QCD". In: *Phys. Rev. D* 69 (2004), p. 034014. DOI: 10.1103/PhysRevD.69.034014. arXiv: hep-ph/0309330. №: LPT-ORSAY-03-63.

[97] M. Beneke and J. Rohrwild. "B meson distribution amplitude from B –> \gamma l \nu". In: *Eur. Phys. J. C* 71 (2011), p. 1818. DOI: 10.1140/epjc/s10052-011-1818-8. arXiv: 1110.3228 [hep-ph]. №: TTK-11-51 and SFB-CPP-11-56.

[98] V. M. Braun and A. Khodjamirian. "Soft contribution to $B \to \gamma\ell\nu_\ell$ and the B-meson distribution amplitude". In: *Phys. Lett. B* 718 (2013), pp. 1014–1019. DOI: 10.1016/j.physletb.2012.11.047. arXiv: 1210.4453 [hep-ph]. №: SI-HEP-2012-19.

[99] Y.-M. Wang. "Factorization and dispersion relations for radiative leptonic B decay". In: *JHEP* 09 (2016), p. 159. DOI: 10.1007/JHEP09(2016)159. arXiv: 1606.03080 [hep-ph]. №: UWTHPH-2016-10.

[100] Y.-M. Wang and Y.-L. Shen. "Subleading-power corrections to the radiative leptonic $B \to \gamma\ell\nu$ decay in QCD". In: *JHEP* 05 (2018), p. 184. DOI: 10.1007/JHEP05(2018)184. arXiv: 1803.06667 [hep-ph].

[101] M. Beneke, V. M. Braun, Y. Ji, and Y.-B. Wei. "Radiative leptonic decay $B \to \gamma\ell\nu_\ell$ with subleading power corrections". In: *JHEP* 07 (2018), p. 154. DOI: 10.1007/JHEP07(2018)154. arXiv: 1804.04962 [hep-ph]. №: TUM-HEP-1135-18.

[102] Y.-L. Shen, Z.-T. Zou, and Y.-B. Wei. "Subleading power corrections to $B \to \gamma l\nu$ decay in PQCD approach". In: *Phys. Rev. D* 99.1 (2019), p. 016004. DOI: 10.1103/PhysRevD.99.016004. arXiv: 1811.08250 [hep-ph].

[103] A. Khodjamirian, R. Mandal, and T. Mannel. "Inverse moment of the B_s-meson distribution amplitude from QCD sum rule". In: *JHEP* 10 (2020), p. 043. DOI: 10.1007/JHEP10(2020)043. arXiv: 2008.03935 [hep-ph]. №: SI-HEP-2020-20 and P3H-20-039.

[104] M. Beneke and T. Feldmann. "Factorization of heavy to light form-factors in soft collinear effective theory". In: *Nucl. Phys. B* 685 (2004), pp. 249–296. DOI: 10.1016/j.nuclphysb.2004.02.033. arXiv: hep-ph/0311335. №: PITHA-03-11 and CERN-TH-2003-286.

[105] T. Feldmann, B. O. Lange, and Y.-M. Wang. "B -meson light-cone distribution amplitude: Perturbative constraints and asymptotic behavior in dual space". In: *Phys. Rev. D* 89.11 (2014), p. 114001. DOI: 10.1103/PhysRevD.89.114001. arXiv: 1404.1343 [hep-ph]. №: SI-HEP-2013-18, QFET-2013-14, TTK-14-05, SFB-CPP-14-07, and TUM-HEP-928-14.

[106] A. M. Galda, M. Neubert, and X. Wang. "Factorization and Sudakov resummation in leptonic radiative B decay — a reappraisal". In: *JHEP* 07 (2022), p. 148. DOI: 10.1007/JHEP07(2022)148. arXiv: 2203.08202 [hep-ph]. №: MITP/22-024.

[107] T. Feldmann, P. Lüghausen, and D. van Dyk. "Systematic parametrization of the leading B-meson light-cone distribution amplitude". In: *JHEP* 10 (2022), p. 162. DOI: 10.1007/JHEP10(2022)162. arXiv: 2203.15679 [hep-ph]. №: SI-HEP-2022-05, P3H-22-029, and TUM-HEP-1388/22.

[108] B. O. Lange and M. Neubert. "Renormalization group evolution of the B meson light cone distribution amplitude". In: *Phys. Rev. Lett.* 91 (2003), p. 102001. DOI: 10.1103/PhysRevLett.91.102001. arXiv: hep-ph/0303082. №: CLNS-03-1822.

[109] G. Bell, T. Feldmann, Y.-M. Wang, and M. W. Y. Yip. "Light-Cone Distribution Amplitudes for Heavy-Quark Hadrons". In: *JHEP* 11 (2013), p. 191. DOI: 10.1007/JHEP11(2013)191. arXiv: 1308.6114 [hep-ph]. №: OUTP-13-15P, SI-HEP-2013-05, QFET-2013-05, TTK-13-19, SFB-CPP-13-60, IPPP-13-55, DCPT-13-110, and TUM-HEP-899-13.

[110] V. M. Braun, Y. Ji, and A. N. Manashov. "Higher-twist B-meson Distribution Amplitudes in HQET". In: *JHEP* 05 (2017), p. 022. DOI: 10.1007/JHEP05(2017)022. arXiv: 1703.02446 [hep-ph]. №: DESY-17-037.

[111] V. M. Braun, Y. Ji, and A. N. Manashov. "Scale-dependence of the B-meson LCDA beyond leading order from conformal symmetry". *14th International Symposium on Radiative Corrections: Application of Quantum Field Theory to Phenomenology*. Dec. 2019. DOI: 10.22323/1.375.0037. arXiv: 1912.03210 [hep-ph].

[112] V. M. Braun, Y. Ji, and A. N. Manashov. "Two-loop evolution equation for the B-meson distribution amplitude". In: *Phys. Rev. D* 100.1 (2019), p. 014023. DOI: 10.3204/PUBDB-2019-02451. arXiv: 1905.04498 [hep-ph]. №: DESY-19-080.

[113] A. M. Galda and M. Neubert. "Evolution of the B-Meson Light-Cone Distribution Amplitude in Laplace Space". In: *Phys. Rev. D* 102 (2020), p. 071501. DOI: 10.1103/PhysRevD.102.071501. arXiv: 2006.05428 [hep-ph]. №: MITP/20-031.

[114] P. Ball, V. M. Braun, Y. Koike, and K. Tanaka. "Higher twist distribution amplitudes of vector mesons in QCD: Formalism and twist - three distributions". In: *Nucl. Phys. B* 529 (1998), pp. 323–382. DOI: 10.1016/S0550-3213(98)00356-3. arXiv: hep-ph/9802299. №: FERMILAB-PUB-98-028-T, NORDITA-98-6-P, and JUPD-9811.

[115] H. Kawamura, J. Kodaira, C.-F. Qiao, and K. Tanaka. "B-meson light cone distribution amplitudes in the heavy quark limit". In: *Phys. Lett. B* 523 (2001). [Erratum: Phys.Lett.B 536, 344–344 (2002)], p. 111. DOI: 10.1016/S0370-2693(01)01299-0. arXiv: hep-ph/0109181. №: DESY-01-135, HUPD-0108, and JUPD-0191.

[116] V. Braun, R. J. Fries, N. Mahnke, and E. Stein. "Higher twist distribution amplitudes of the nucleon in QCD". In: *Nucl. Phys. B* 589 (2000). [Erratum: Nucl.Phys.B 607, 433–433 (2001)], pp. 381–409. DOI: 10.1016/S0550-3213(00)00516-2. arXiv: hep-ph/0007279. №: TPR-00-10.

[117] V. M. Braun, A. Lenz, N. Mahnke, and E. Stein. "Light cone sum rules for the nucleon form-factors". In: *Phys. Rev. D* 65 (2002), p. 074011. DOI: 10.1103/PhysRevD.65.074011. arXiv: hep-ph/0112085.

[118] A. Lenz, M. Gockeler, T. Kaltenbrunner, and N. Warkentin. "The Nucleon Distribution Amplitudes and their application to nucleon form factors and the $N \to \Delta$ transition at intermediate values of Q^2". In: *Phys. Rev. D* 79 (2009), p. 093007. DOI: 10.1103/PhysRevD.79.093007. arXiv: 0903.1723 [hep-ph].

[119] *RQCD*. "Light-cone distribution amplitudes of octet baryons from lattice QCD". In: *Eur. Phys. J. A* 55.7 (2019), p. 116. DOI: 10.1140/epja/i2019-12803-6. arXiv: 1903.12590 [hep-lat].

[120] G. Bell, K. Brune, G. Das, and M. Wald. "Automation of Beam and Jet functions at NNLO". In: *SciPost Phys. Proc.* 7 (2022), p. 021. DOI: 10.21468/SciPostPhysProc.7.021. arXiv: 2110.04804 [hep-ph]. №: SI-HEP-2021-25 and P3H-21-069.

[121] G. Bell, K. Brune, G. Das, and M. Wald. "Automated Calculation of Beam Functions at NNLO". In: *PoS LL* 2022 (2022), p. 026. DOI: 10.22323/1.416.0026. arXiv: 2208.04847 [hep-ph]. №: SI-HEP-2022-18 and P3H-22-085.

[122] G. Bell, K. Brune, G. Das, and M. Wald. "The NNLO quark beam function for jet-veto resummation". In: *JHEP* 01 (2023), p. 083. DOI: 10.1007/JHEP01(2023)083. arXiv: 2207.05578 [hep-ph]. №: SI-HEP-2022-13 and P3H-22-064.

[123] T. Becher and X. Garcia i Tormo. "Factorization and resummation for transverse thrust". In: *JHEP* 06 (2015), p. 071. DOI: 10.1007/JHEP06(2015)071. arXiv: 1502.04136 [hep-ph].

[124] J. R. Gaunt, M. Stahlhofen, and F. J. Tackmann. "The Quark Beam Function at Two Loops". In: *JHEP* 04 (2014), p. 113. DOI: 10.1007/JHEP04(2014)113. arXiv: 1401.5478 [hep-ph]. №: DESY-14-001.

[125] J. Gaunt, M. Stahlhofen, and F. J. Tackmann. "The Gluon Beam Function at Two Loops". In: *JHEP* 08 (2014), p. 020. DOI: 10.1007/JHEP08(2014)020. arXiv: 1405.1044 [hep-ph]. №: DESY-14-004.

[126] R. H. Boels, T. Huber, and G. Yang. "Four-Loop Nonplanar Cusp Anomalous Dimension in N=4 Supersymmetric Yang-Mills Theory". In: *Phys. Rev. Lett.* 119.20 (2017), p. 201601. DOI: 10.1103/PhysRevLett.119.201601. arXiv: 1705.03444 [hep-th]. №: SI-HEP-2017-10.

[127] J. M. Henn, T. Peraro, M. Stahlhofen, and P. Wasser. "Matter dependence of the four-loop cusp anomalous dimension". In: *Phys. Rev. Lett.* 122.20 (2019), p. 201602. DOI: 10.1103/PhysRevLett.122.201602. arXiv: 1901.03693 [hep-ph]. №: MPP-2019-3, MITP/19-001, and ZU-TH 01/19.

[128] J. M. Henn, G. P. Korchemsky, and B. Mistlberger. "The full four-loop cusp anomalous dimension in $\mathcal{N} = 4$ super Yang-Mills and QCD". In: *JHEP* 04 (2020), p. 018. DOI: 10.1007/JHEP04(2020)018. arXiv: 1911.10174 [hep-th]. №: IPhT-T19/155, MIT-CTP/5160, and MPP-2019-233.

[129] F. Herzog, B. Ruijl, T. Ueda, J. A. M. Vermaseren, and A. Vogt. "The five-loop beta function of Yang-Mills theory with fermions". In: *JHEP* 02 (2017), p. 090. DOI: 10.1007/JHEP02(2017)090. arXiv: 1701.01404 [hep-ph]. №: NIKHEF-2017-001 and LTH-1117.

[130] T. Luthe, A. Maier, P. Marquard, and Y. Schroder. "The five-loop Beta function for a general gauge group and anomalous dimensions beyond Feynman gauge". In: *JHEP* 10 (2017), p. 166. DOI: 10.1007/JHEP10(2017)166. arXiv: 1709.07718 [hep-ph]. №: BI-TP-2017-13, DESY-17-142, and IPPP-17-68.

[131] R. N. Lee, A. von Manteuffel, R. M. Schabinger, A. V. Smirnov, V. A. Smirnov, and M. Steinhauser. "Quark and Gluon Form Factors in Four-Loop QCD". In: *Phys. Rev. Lett.* 128.21 (2022), p. 212002. DOI: 10.1103/PhysRevLett.128.212002. arXiv: 2202.04660 [hep-ph]. №: MSUHEP-22-003, P3H-22-014, and TTP22-008.

[132] A. Chakraborty et al. "Hbb vertex at four loops and hard matching coefficients in SCET for various currents". In: *Phys. Rev. D* 106.7 (2022), p. 074009. DOI: 10.1103/PhysRevD.106.074009. arXiv: 2204.02422 [hep-ph]. №: MSUHEP-22-014, P3H-22-034, TTP22-020, and SI-HEP-2022-06.

[133] M. E. Peskin and D. V. Schroeder. *An Introduction to quantum field theory*. Reading, USA: Addison-Wesley, 1995. ISBN: 978-0-201-50397-5.

[134] R. J. Eden, P. V. Landshoff, D. I. Olive, and J. C. Polkinghorne. *The analytic S-matrix*. Cambridge: Cambridge Univ. Press, 1966. ISBN: 978-0-521-04869-9.

[135] M. Ritzmann and W. J. Waalewijn. "Fragmentation in Jets at NNLO". In: *Phys. Rev. D* 90.5 (2014), p. 054029. DOI: 10.1103/PhysRevD.90.054029. arXiv: 1407.3272 [hep-ph]. №: NIKHEF-2014-015.

[136] S. Catani and M. Grazzini. "Collinear factorization and splitting functions for next-to-next-to-leading order QCD calculations". In: *Phys. Lett. B* 446 (1999), pp. 143–152. DOI: 10.1016/S0370-2693(98)01513-5. arXiv: hep-ph/9810389. №: CERN-TH-98-325 and ETH-TH-98-27.

[137] G. F. R. Sborlini, D. de Florian, and G. Rodrigo. "Double collinear splitting amplitudes at next-to-leading order". In: *JHEP* 01 (2014), p. 018. DOI: 10.1007/JHEP01(2014)018. arXiv: 1310.6841 [hep-ph]. №: LPN-13-069 and IFIC-13-73.

[138] J. M. Campbell and E. W. N. Glover. "Double unresolved approximations to multiparton scattering amplitudes". In: *Nucl. Phys. B* 527 (1998), pp. 264–288. DOI: 10.1016/S0550-3213(98)00295-8. arXiv: hep-ph/9710255. №: DTP-97-82.

[139] T. Binoth and G. Heinrich. "An automatized algorithm to compute infrared divergent multiloop integrals". In: *Nucl. Phys. B* 585 (2000), pp. 741–759. DOI: 10.1016/S0550-3213(00)00429-6. arXiv: hep-ph/0004013. №: LAPTH-789-00 and LPT-ORSAY-00-37.

[140] G. Heinrich. "Sector Decomposition". In: *Int. J. Mod. Phys. A* 23 (2008), pp. 1457–1486. DOI: 10.1142/S0217751X08040263. arXiv: 0803.4177 [hep-ph]. №: IPPP-08-16 and DCPT-08-32.

[141] S. Borowka, G. Heinrich, S. P. Jones, M. Kerner, J. Schlenk, and T. Zirke. "SecDec-3.0: numerical evaluation of multi-scale integrals beyond one loop". In: *Comput. Phys. Commun.* 196 (2015), pp. 470–491. DOI: 10.1016/j.cpc.2015.05.022. arXiv: 1502.06595 [hep-ph]. №: FR-PHENO-2015-001, MPP-2015-27, and ZU-TH-1-15.

[142] M. Czakon. "A novel subtraction scheme for double-real radiation at NNLO". In: *Phys. Lett. B* 693 (2010), pp. 259–268. DOI: 10.1016/j.physletb.2010.08.036. arXiv: 1005.0274 [hep-ph].

[143] T. Becher, G. Bell, and M. Neubert. "Factorization and Resummation for Jet Broadening". In: *Phys. Lett. B* 704 (2011), pp. 276–283. DOI: 10.1016/j.physletb.2011.09.005. arXiv: 1104.4108 [hep-ph]. №: MZ-TH-11-08.

[144] T. Hahn. "CUBA: A Library for multidimensional numerical integration". In: *Comput. Phys. Commun.* 168 (2005), pp. 78–95. DOI: 10.1016/j.cpc.2005.01.010. arXiv: hep-ph/0404043. №: MPP-2004-40.

[145] T. Hahn. "The CUBA library". In: *Nucl. Instrum. Meth. A* 559 (2006). Ed. by J. Blumlein, W. Friebel, T. Naumann, T. Riemann, P. Wegner, and D. Perret-Gallix, pp. 273–277. DOI: 10.1016/j.nima.2005.11.150. arXiv: hep-ph/0509016. №: MPP-2005-89.

[146] T. Hahn. "Concurrent Cuba". In: *Comput. Phys. Commun.* 207 (2016), pp. 341–349. DOI: 10.1016/j.cpc.2016.05.012.

[147] S. Borowka, G. Heinrich, S. Jahn, S. P. Jones, M. Kerner, J. Schlenk, and T. Zirke. "pySecDec: a toolbox for the numerical evaluation of multi-scale integrals". In: *Comput. Phys. Commun.* 222 (2018), pp. 313–326. DOI: 10.1016/j.cpc.2017.09.015. arXiv: 1703.09692 [hep-ph]. №: MPP-2017-42, CERN-TH-2017-063, and IPPP-17-24.

[148] S. Borowka, G. Heinrich, S. Jahn, S. P. Jones, M. Kerner, and J. Schlenk. "A GPU compatible quasi-Monte Carlo integrator interfaced to pySecDec". In: *Comput. Phys. Commun.* 240 (2019), pp. 120–137. DOI: 10.1016/j.cpc.2019.02.015. arXiv: 1811.11720 [physics.comp-ph]. №: CERN-TH-2018-246, MPP-2018-279, ZU-TH 43/18, and IPPP/18/100.

[149] G. Heinrich et al. "Expansion by regions with pySecDec". In: *Comput. Phys. Commun.* 273 (2022), p. 108267. DOI: 10.1016/j.cpc.2021.108267. arXiv: 2108.10807 [hep-ph]. №: KA-TP-19-2021, P3H-21-055, MPP-2021-131, IPPP/21/20, ZU-TH 35/21, and PSI-PR-21-17.

[150] J. Carter and G. Heinrich. "SecDec: A general program for sector decomposition". In: *Comput. Phys. Commun.* 182 (2011), pp. 1566–1581. DOI: 10.1016/j.cpc.2011.03.026. arXiv: 1011.5493 [hep-ph]. №: IPPP-10-94 and DCPT-10-188.

[151] S. Borowka, J. Carter, and G. Heinrich. "Numerical Evaluation of Multi-Loop Integrals for Arbitrary Kinematics with SecDec 2.0". In: *Comput. Phys. Commun.* 184 (2013), pp. 396–408. DOI: 10.1016/j.cpc.2012.09.020. arXiv: 1204.4152 [hep-ph]. №: IPPP-12-22, DCPT-12-44, and MPP-2012-75.

[152] J. A. M. Vermaseren. "New features of FORM" (Oct. 2000). arXiv: math-ph/0010025.

[153] J. Kuipers, T. Ueda, and J. A. M. Vermaseren. "Code Optimization in FORM". In: *Comput. Phys. Commun.* 189 (2015), pp. 1–19. DOI: 10.1016/j.cpc.2014.08.008. arXiv: 1310.7007 [cs.SC]. №: NIKHEF-2013-036, TTP13-031, and SFB-CPP-13-80.

[154] B. Ruijl, T. Ueda, and J. Vermaseren. "FORM version 4.2" (July 2017). arXiv: 1707.06453 [hep-ph].

[155] G. P. Lepage. "VEGAS: AN ADAPTIVE MULTIDIMENSIONAL INTEGRATION PROGRAM" (Mar. 1980). №: CLNS-80/447.

[156] A. Banfi, G. P. Salam, and G. Zanderighi. "NLL+NNLO predictions for jet-veto efficiencies in Higgs-boson and Drell-Yan production". In: *JHEP* 06 (2012), p. 159. DOI: 10.1007/JHEP06(2012)159. arXiv: 1203.5773 [hep-ph]. №: CERN-PH-TH-2012-065, OUTP-12-04P, and LPN12-043.

[157] T. Becher and M. Neubert. "Factorization and NNLL Resummation for Higgs Production with a Jet Veto". In: *JHEP* 07 (2012), p. 108. DOI: 10.1007/JHEP07(2012)108. arXiv: 1205.3806 [hep-ph]. №: MZ-TH-12-18.

[158] F. J. Tackmann, J. R. Walsh, and S. Zuberi. "Resummation Properties of Jet Vetoes at the LHC". In: *Phys. Rev. D* 86 (2012), p. 053011. DOI: 10.1103/PhysRevD.86.053011. arXiv: 1206.4312 [hep-ph]. №: DESY-12-104.

[159] A. Banfi, P. F. Monni, G. P. Salam, and G. Zanderighi. "Higgs and Z-boson production with a jet veto". In: *Phys. Rev. Lett.* 109 (2012), p. 202001. DOI: 10.1103/PhysRevLett.109.202001. arXiv: 1206.4998 [hep-ph]. №: CERN-PH-TH-2012-173, LPN12-061, OUTP-12-14P, and ZU-ZH-10-12.

[160] T. Becher, M. Neubert, and L. Rothen. "Factorization and N^3LL_p+NNLO predictions for the Higgs cross section with a jet veto". In: *JHEP* 10 (2013), p. 125. DOI: 10.1007/JHEP10(2013)125. arXiv: 1307.0025 [hep-ph]. №: MITP-13-37 and PHY11-25915.

[161] I. W. Stewart, F. J. Tackmann, J. R. Walsh, and S. Zuberi. "Jet p_T resummation in Higgs production at $NNLL' + NNLO$". In: *Phys. Rev. D* 89.5 (2014), p. 054001. DOI: 10.1103/PhysRevD.89.054001. arXiv: 1307.1808 [hep-ph]. №: DESY-13-122 and MIT-CTP-4479.

[162] D. Y. Shao, C. S. Li, and H. T. Li. "Resummation Prediction on Higgs and Vector Boson Associated Production with a Jet Veto at the LHC". In: *JHEP* 02 (2014), p. 117. DOI: 10.1007/JHEP02(2014)117. arXiv: 1309.5015 [hep-ph].

[163] Y. Li and X. Liu. "High precision predictions for exclusive VH production at the LHC". In: *JHEP* 06 (2014), p. 028. DOI: 10.1007/JHEP06(2014)028. arXiv: 1401.2149 [hep-ph].

[164] P. Jaiswal and T. Okui. "Explanation of the WW excess at the LHC by jet-veto resummation". In: *Phys. Rev. D* 90.7 (2014), p. 073009. DOI: 10.1103/PhysRevD.90.073009. arXiv: 1407.4537 [hep-ph].

[165] Y. Wang, C. S. Li, and Z. L. Liu. "Resummation prediction on gauge boson pair production with a jet veto". In: *Phys. Rev. D* 93.9 (2016), p. 094020. DOI: 10.1103/PhysRevD.93.094020. arXiv: 1504.00509 [hep-ph].

[166] S. Dawson, P. Jaiswal, Y. Li, H. Ramani, and M. Zeng. "Resummation of jet veto logarithms at $\mathrm{N^3LL}_a$ + NNLO for W^+W^- production at the LHC". In: *Phys. Rev. D* 94.11 (2016), p. 114014. DOI: 10.1103/PhysRevD.94.114014. arXiv: 1606.01034 [hep-ph]. №: YITP-SB-16-24 and FERMILAB-PUB-16-210-PPD-T.

[167] F. J. Tackmann, W. J. Waalewijn, and L. Zeune. "Impact of Jet Veto Resummation on Slepton Searches". In: *JHEP* 07 (2016), p. 119. DOI: 10.1007/JHEP07(2016)119. arXiv: 1603.03052 [hep-ph]. №: NIKHEF-2016-010 and DESY-16-044.

[168] M. A. Ebert, S. Liebler, I. Moult, I. W. Stewart, F. J. Tackmann, K. Tackmann, and L. Zeune. "Exploiting jet binning to identify the initial state of high-mass resonances". In: *Phys. Rev. D* 94.5 (2016), p. 051901. DOI: 10.1103/PhysRevD.94.051901. arXiv: 1605.06114 [hep-ph]. №: DESY-16-086, MIT-CTP-4804, and NIKHEF-2016-019.

[169] B. Fuks and R. Ruiz. "A comprehensive framework for studying W' and Z' bosons at hadron colliders with automated jet veto resummation". In: *JHEP* 05 (2017), p. 032. DOI: 10.1007/JHEP05(2017)032. arXiv: 1701.05263 [hep-ph]. №: IPPP-17-1.

[170] L. Arpino, A. Banfi, S. Jäger, and N. Kauer. "BSM WW production with a jet veto". In: *JHEP* 08 (2019), p. 076. DOI: 10.1007/JHEP08(2019)076. arXiv: 1905.06646 [hep-ph].

[171] S. Abreu, J. R. Gaunt, P. F. Monni, L. Rottoli, and R. Szafron. "Quark and gluon two-loop beam functions for leading-jet p_T and slicing at NNLO". In: *JHEP* 04 (2023), p. 127. DOI: 10.1007/JHEP04(2023)127. arXiv: 2207.07037 [hep-ph]. №: CERN-TH-2022-118 and ZU-TH 30/22.

[172] A. Banfi, F. Caola, F. A. Dreyer, P. F. Monni, G. P. Salam, G. Zanderighi, and F. Dulat. "Jet-vetoed Higgs cross section in gluon fusion at N^3LO+NNLL with small-R resummation". In: *JHEP* 04 (2016), p. 049. DOI: 10.1007/JHEP04(2016)049. arXiv: 1511.02886 [hep-ph]. №: CERN-PH-TH-2015-261 and OUTP-15-29P.

[173] S. Abreu, J. R. Gaunt, P. F. Monni, and R. Szafron. "The analytic two-loop soft function for leading-jet p_T". In: *JHEP* 08 (2022), p. 268. DOI: 10.1007/JHEP08(2022)268. arXiv: 2204.02987 [hep-ph]. №: CERN-TH-2022-059.

[174] I. W. Stewart, F. J. Tackmann, and W. J. Waalewijn. "The Quark Beam Function at NNLL". In: *JHEP* 09 (2010), p. 005. DOI: 10.1007/JHEP09(2010)005. arXiv: 1002.2213 [hep-ph]. №: MIT-CTP-4097.

[175] J. Zhu, D. Kang, and T. Maji. "Angularity in DIS at next-to-next-to-leading log accuracy". In: *JHEP* 11 (2021), p. 026. DOI: 10.1007/JHEP11(2021)026. arXiv: 2106.14429 [hep-ph].

[176] G. Bell, A. Hornig, C. Lee, and J. Talbert. "e^+e^- angularity distributions at NNLL′ accuracy". In: *JHEP* 01 (2019), p. 147. DOI: 10.1007/JHEP01(2019)147. arXiv: 1808.07867 [hep-ph]. №: SI-HEP-2018-19, LA-UR-18-24071, DESY-18-083, and DESY 18-083.

[177] M. Rahimi and M. Wald. "QCD sum rules for parameters of the B-meson distribution amplitudes". In: *Phys. Rev. D* 104.1 (2021), p. 016027. DOI: 10.1103/PhysRevD.104.016027. arXiv: 2012.12165 [hep-ph]. №: P3H-20-082 and SI-HEP-2020-35.

[178] K. G. Wilson. "Nonlagrangian models of current algebra". In: *Phys. Rev.* 179 (1969), pp. 1499–1512. DOI: 10.1103/PhysRev.179.1499.

[179] D. J. Broadhurst and A. G. Grozin. "Operator product expansion in static quark effective field theory: Large perturbative correction". In: *Phys. Lett. B* 274 (1992), pp. 421–427. DOI: 10.1016/0370-2693(92)92009-6. arXiv: hep-ph/9908363. №: OUT-4102-31.

[180] A. A. Penin and M. Steinhauser. "Heavy light meson decay constant from QCD sum rules in three loop approximation". In: *Phys. Rev. D* 65 (2002), p. 054006. DOI: 10.1103/PhysRevD.65.054006. arXiv: hep-ph/0108110. №: DESY-01-112.

[181] H. Cartan. *Elementary Theory of Analytic Functions of One Or Several Complex Variables*. Adiwes international series in mathematics. Éditions scientifiques Hermann., 1963. URL: books.google.de/books?id=DXguAAAAIAAJ.

[182] E. C. Poggio, H. R. Quinn, and S. Weinberg. "Smearing the Quark Model". In: *Phys. Rev. D* 13 (1976), p. 1958. DOI: 10.1103/PhysRevD.13.1958. №: PRINT-75-1056 (HARVARD).

[183] R. Hofmann. "Operator product expansion and local quark hadron duality: Facts and riddles". In: *Prog. Part. Nucl. Phys.* 52 (2004), pp. 299–376. DOI: 10.1016/j.ppnp.2004.02.003. arXiv: hep-ph/0312130.

[184] M. Neubert. "Heavy meson form-factors from QCD sum rules". In: *Phys. Rev. D* 45 (1992), pp. 2451–2466. DOI: 10.1103/PhysRevD.45.2451. №: SLAC-PUB-5712.

[185] P. Colangelo and A. Khodjamirian. "QCD sum rules, a modern perspective" (Oct. 2000). Ed. by M. Shifman and B. Ioffe, pp. 1495–1576. DOI: 10.1142/9789812810458_0033. arXiv: hep-ph/0010175. №: CERN-TH-2000-296 and BARI-TH-2000-394.

[186] P. Pascual and R. Tarrach. *QCD: RENORMALIZATION FOR THE PRACTITIONER*. Vol. 194. 1984.

[187] S. N. Nikolaev and A. V. Radyushkin. "Vacuum Corrections to QCD Charmonium Sum Rules: Basic Formalism and O (G^3) Results". In: *Nucl. Phys. B* 213 (1983), pp. 285–304. DOI: 10.1016/0550-3213(83)90513-8. №: JINR-E2-82-521.

[188] R. Thomas, T. Hilger, and B. Kampfer. "Four-quark condensates in nucleon QCD sum rules". In: *Nucl. Phys. A* 795 (2007), pp. 19–46. DOI: 10.1016/j.nuclphysa.2007.08.012. arXiv: 0704.3004 [hep-ph].

[189] R. N. Lee. "LiteRed 1.4: a powerful tool for reduction of multiloop integrals". In: *J. Phys. Conf. Ser.* 523 (2014). Ed. by J. Wang, p. 012059. DOI: 10.1088/1742-6596/523/1/012059. arXiv: 1310.1145 [hep-ph].

[190] F. V. Tkachov. "A Theorem on Analytical Calculability of Four Loop Renormalization Group Functions". In: *Phys. Lett. B* 100 (1981), pp. 65–68. DOI: 10.1016/0370-2693(81)90288-4.

[191] G. 't Hooft. "Dimensional regularization and the renormalization group". In: *Nucl. Phys. B* 61 (1973), pp. 455–468. DOI: 10.1016/0550-3213(73)90376-3.

[192] V. Shtabovenko, R. Mertig, and F. Orellana. "FeynCalc 9.3: New features and improvements". In: *Comput. Phys. Commun.* 256 (2020), p. 107478. DOI: 10.1016/j.cpc.2020.107478. arXiv: 2001.04407 [hep-ph]. №: P3H-20-002, TTP19-020, and TUM-EFT 130/19.

[193] A. Grozin, J. M. Henn, G. P. Korchemsky, and P. Marquard. "The three-loop cusp anomalous dimension in QCD and its supersymmetric extensions". In: *JHEP* 01 (2016), p. 140. DOI: 10.1007/JHEP01(2016)140. arXiv: 1510.07803 [hep-ph]. №: DESY-15-186, IPHT-T15-174, and MITP-15-088.

[194] F. Herren and M. Steinhauser. "Version 3 of RunDec and CRunDec". In: *Comput. Phys. Commun.* 224 (2018), pp. 333–345. DOI: 10.1016/j.cpc.2017.11.014. arXiv: 1703.03751 [hep-ph]. №: TTP17-011.

[195] *Particle Data Group.* "Review of Particle Physics". In: *PTEP* 2022 (2022), p. 083C01. DOI: 10.1093/ptep/ptac097.

[196] M. Jamin. "Flavor symmetry breaking of the quark condensate and chiral corrections to the Gell-Mann-Oakes-Renner relation". In: *Phys. Lett. B* 538 (2002), pp. 71–76. DOI: 10.1016/S0370-2693(02)01951-2. arXiv: hep-ph/0201174. №: HD-THEP-0201.

[197] P. Gubler and D. Satow. "Recent Progress in QCD Condensate Evaluations and Sum Rules". In: *Prog. Part. Nucl. Phys.* 106 (2019), pp. 1–67. DOI: 10.1016/j.ppnp.2019.02.005. arXiv: 1812.00385 [hep-ph].

[198] V. M. Belyaev and B. L. Ioffe. "Determination of Baryon and Baryonic Resonance Masses from QCD Sum Rules. 1. Nonstrange Baryons". In: *Sov. Phys. JETP* 56 (1982), pp. 493–501. №: ITEP-59-1982.

[199] P. Gambino, A. Melis, and S. Simula. "Extraction of heavy-quark-expansion parameters from unquenched lattice data on pseudoscalar and vector heavy-light meson masses". In: *Phys. Rev. D* 96.1 (2017), p. 014511. DOI: 10.1103/PhysRevD.96.014511. arXiv: 1704.06105 [hep-lat]. №: PREPRINT-RM3-TH-17-3.

[200] *Flavour Lattice Averaging Group (FLAG).* "FLAG Review 2021". In: *Eur. Phys. J. C* 82.10 (2022), p. 869. DOI: 10.1140/epjc/s10052-022-10536-1. arXiv: 2111.09849 [hep-lat]. №: CERN-TH-2021-191, JLAB-THY-21-3528, and FERMILAB-PUB-21-620-SCD-T.

[201] A. Khodjamirian. "Upper bounds on f(D) and f(D(s)) from two-point correlation function in QCD". In: *Phys. Rev. D* 79 (2009), p. 031503. DOI: 10.1103/PhysRevD.79.031503. arXiv: 0812.3747 [hep-ph]. №: SI-HEP-2008-19.

[202] A. Khodjamirian and M. Wald. "B-meson decay into a proton and dark antibaryon from QCD light-cone sum rules". In: *Phys. Lett. B* 834 (2022), p. 137434. DOI: 10.1016/j.physletb.2022.137434. arXiv: 2206.11601 [hep-ph]. №: SI-HEP-2022-08 and P3H-22-060.

[203] A. Boushmelev and M. Wald. "Higher twist corrections to B-meson decays into a proton and dark antibaryon from QCD light-cone sum rules" (Nov. 2023). arXiv: 2311.13482 [hep-ph]. №: SI-HEP-2023-29 and P3H-23-093.

[204] A. Khodjamirian. *Hadron Form Factors: From Basic Phenomenology to QCD Sum Rules.* Boca Raton, FL, USA: CRC Press, Taylor & Francis Group, 2020. ISBN: 978-1-138-30675-2, 978-1-315-14200-5.

[205] G. Elor, M. Escudero, and A. Nelson. "Baryogenesis and Dark Matter from B Mesons". In: *Phys. Rev. D* 99.3 (2019), p. 035031. DOI: 10.1103/PhysRevD.99.035031. arXiv: 1810.00880 [hep-ph]. №: KCL-18-53 and IFIC-18-35.

[206] G. Alonso-Álvarez, G. Elor, and M. Escudero. "Collider signals of baryogenesis and dark matter from B mesons: A roadmap to discovery". In: *Phys. Rev. D* 104.3 (2021), p. 035028. DOI: 10.1103/PhysRevD.104.035028. arXiv: 2101.02706 [hep-ph]. №: TUM-HEP 1299/20.

[207] G. Alonso-Álvarez, G. Elor, M. Escudero, B. Fornal, B. Grinstein, and J. Martin Camalich. "Strange physics of dark baryons". In: *Phys. Rev. D* 105.11 (2022), p. 115005. DOI: 10.1103/PhysRevD.105.115005. arXiv: 2111.12712 [hep-ph]. №: TUM-HEP-1373/21 and MITP-21-060.

[208] *Planck*. "Planck 2015 results. XIII. Cosmological parameters". In: *Astron. Astrophys.* 594 (2016), A13. DOI: 10.1051/0004-6361/201525830. arXiv: 1502.01589 [astro-ph.CO].

[209] *Planck*. "Planck 2018 results. VI. Cosmological parameters". In: *Astron. Astrophys.* 641 (2020). [Erratum: Astron.Astrophys. 652, C4 (2021)], A6. DOI: 10.1051/0004-6361/201833910. arXiv: 1807.06209 [astro-ph.CO].

[210] R. H. Cyburt, B. D. Fields, K. A. Olive, and T.-H. Yeh. "Big Bang Nucleosynthesis: 2015". In: *Rev. Mod. Phys.* 88 (2016), p. 015004. DOI: 10.1103/RevModPhys.88.015004. arXiv: 1505.01076 [astro-ph.CO]. №: UMN-TH-3432-15 and FTPI-MINN-15-19.

[211] *Particle Data Group*. "Review of Particle Physics". In: *Phys. Rev. D* 98.3 (2018), p. 030001. DOI: 10.1103/PhysRevD.98.030001.

[212] A. D. Sakharov. "Violation of CP Invariance, C asymmetry, and baryon asymmetry of the universe". In: *Pisma Zh. Eksp. Teor. Fiz.* 5 (1967), pp. 32–35. DOI: 10.1070/PU1991v034n05ABEH002497.

[213] A. Khodjamirian, C. Klein, T. Mannel, and Y. .-. Wang. "Form Factors and Strong Couplings of Heavy Baryons from QCD Light-Cone Sum Rules". In: *JHEP* 09 (2011), p. 106. DOI: 10.1007/JHEP09(2011)106. arXiv: 1108.2971 [hep-ph]. №: SI-HEP-2011-05.

[214] V. M. Braun, A. Lenz, and M. Wittmann. "Nucleon Form Factors in QCD". In: *Phys. Rev. D* 73 (2006), p. 094019. DOI: 10.1103/PhysRevD.73.094019. arXiv: hep-ph/0604050.

[215] I. V. Anikin, V. M. Braun, and N. Offen. "Nucleon Form Factors and Distribution Amplitudes in QCD". In: *Phys. Rev. D* 88 (2013), p. 114021. DOI: 10.1103/PhysRevD.88.114021. arXiv: 1310.1375 [hep-ph].

[216] G. Elor and A. W. M. Guerrera. "Branching fractions of B meson decays in Mesogenesis". In: *JHEP* 02 (2023), p. 100. DOI: 10.1007/JHEP02(2023)100. arXiv: 2211.10553 [hep-ph].

[217] C. Bourrely, I. Caprini, and L. Lellouch. "Model-independent description of B —> pi l nu decays and a determination of |V(ub)|". In: *Phys. Rev. D* 79 (2009). [Erratum: Phys.Rev.D 82, 099902 (2010)], p. 013008. DOI: 10.1103/PhysRevD.82.099902. arXiv: 0807.2722 [hep-ph]. №: CPT-P36-2007.

[218] C. G. Boyd, B. Grinstein, and R. F. Lebed. "Model independent extraction of |V(cb)| using dispersion relations". In: *Phys. Lett. B* 353 (1995), pp. 306–312. DOI: 10.1016/0370-2693(95)00480-9. arXiv: hep-ph/9504235. №: UCSD-PTH-95-03.

[219] *Particle Data Group*. "Review of Particle Physics". In: *PTEP* 2020.8 (2020), p. 083C01. DOI: 10.1093/ptep/ptaa104.

[220] A. Khodjamirian and A. V. Rusov. "$B_s \to K\ell\nu_\ell$ and $B_{(s)} \to \pi(K)\ell^+\ell^-$ decays at large recoil and CKM matrix elements". In: *JHEP* 08 (2017), p. 112. DOI: 10.1007/JHEP08(2017)112. arXiv: 1703.04765 [hep-ph]. №: SI-HEP-2017-03 and QFET-2017-03.

[221] A. Khodjamirian, B. Melić, Y.-M. Wang, and Y.-B. Wei. "The $D^*D\pi$ and $B^*B\pi$ couplings from light-cone sum rules". In: *JHEP* 03 (2021), p. 016. DOI: 10.1007/JHEP03(2021)016. arXiv: 2011.11275 [hep-ph]. №: SI-HEP-2020-29, P3H-20-071, RBI-ThPhys-2020-13, and TUM-HEP-1297/20.

[222] V. Fock. "Proper time in classical and quantum mechanics". In: *Phys. Z. Sowjetunion* 12 (1937), pp. 404–425.

[223] J. S. Schwinger. "On gauge invariance and vacuum polarization". In: *Phys. Rev.* 82 (1951). Ed. by K. A. Milton, pp. 664–679. DOI: 10.1103/PhysRev.82.664.

[224] G. Mack and A. Salam. "Finite component field representations of the conformal group". In: *Annals Phys.* 53 (1969), pp. 174–202. DOI: 10.1016/0003-4916(69)90278-4. №: IC-68-68.

Acknowledgements

First of all, I would like to thank Prof. Dr. Guido Bell for accepting me as a PhD student and for allowing me to work under his supervision. I am grateful for the countless discussions, support and feedback during the past years and in particular during the final stages of this work. Additionally, I would like to thank Dr. Kevin Brune and Dr. Goutam Das for discussions, support, proof reading of this work and bug fixing, especially in the final stages of this thesis.
Moreover, I thank Prof. Dr. Alexander Khodjamirian for his encouragement, support, feedback and time during our collaboration. I am particularly thankful for his help in my first project, which he proposed, but did not participate as a collaborator. Nevertheless, he was always available for discussions, feedback and pointed out several subtleties during the analysis which turned out to be of major importance in the end. In this context I would also like to thank Prof. Dr. Thomas Mannel and Prof. Dr. A. Pivovarov for their support.
Special thanks goes to Dr. Muslem Rahimi and Anastasia Boushmelev, which I enjoyed collaborating with and which I also enjoyed spending time apart from work. The many hours of interesting and fruitful discussions were fun, helped me to improve myself as well as my abilities and turned gray and monotonous office days into an adventure.
I also thank the whole TP1 theory department for a nice work atmosphere and lunch times. In this context I would like to stress that the freedom in research and the variety of different research fields in this institute are certainly unique and should be definitely more appreciated. Especially younger students should use this opportunity to improve their skills and master the field of particle physics.
Finally and most importantly, I thank my family for their constant support and help during my studies and during my PhD time. Without your understanding, willingness to help and love I would not have made it this far.